# Synthesis, Structure-Property Relationship, and Orbital Engineering of Transition Metal-Substituted Sandwich Polyoxometalates

A Thesis Submitted in the fulfillment for the degree of Doctor of Philosophy

Ganga Singh 2018CYZ0015



Department of Chemistry
Indian Institute of Technology Ropar
India

August 2024

© Indian Institute of Technology Ropar - 2024 All rights reserved

## Declaration

I hereby declare that this thesis entitled "Synthesis, Structure-Property Relationship, and Orbital Engineering of Transition Metal-Substituted Sandwich Polyoxometalates" is the outcome of original research work performed by me under the able guidance of Dr. Debaprasad Mandal, Associate Professor at the Department of Chemistry, Indian Institute of Technology Ropar. I solemnly declare that the contents of this thesis both in part or complete has not been submitted elsewhere for the award of any degree or diploma.

Ganga Singh
(2018CYZ0015)

Department of Chemistry
Indian Institute of Technology Ropar

# Certificate

This is to certify that the thesis entitled "Synthesis, Structure-Property Relationship, and Orbital Engineering of Transition Metal-Substituted Sandwich Polyoxometalates" submitted by Mr. Ganga Singh for the award of the degree of "Doctor of Philosophy" in Chemistry is based on the results of studies carried out by him under my guidance and supervision.

The thesis or any part thereof has not been previously submitted for the award of any other degree or diploma.

धियो यो नः प्रचोदयात्

Dr. Debaprasad Mandal

Associate Professor
Department of Chemistry
Indian Institute of Technology Ropar
Rupnagar 140001
Punjab, INDIA

# Coursework Certificate

This is to certify that **Mr. Ganga Singh** have undertaken the following coursework for the fulfillment of the degree of Doctor of Philosophy;

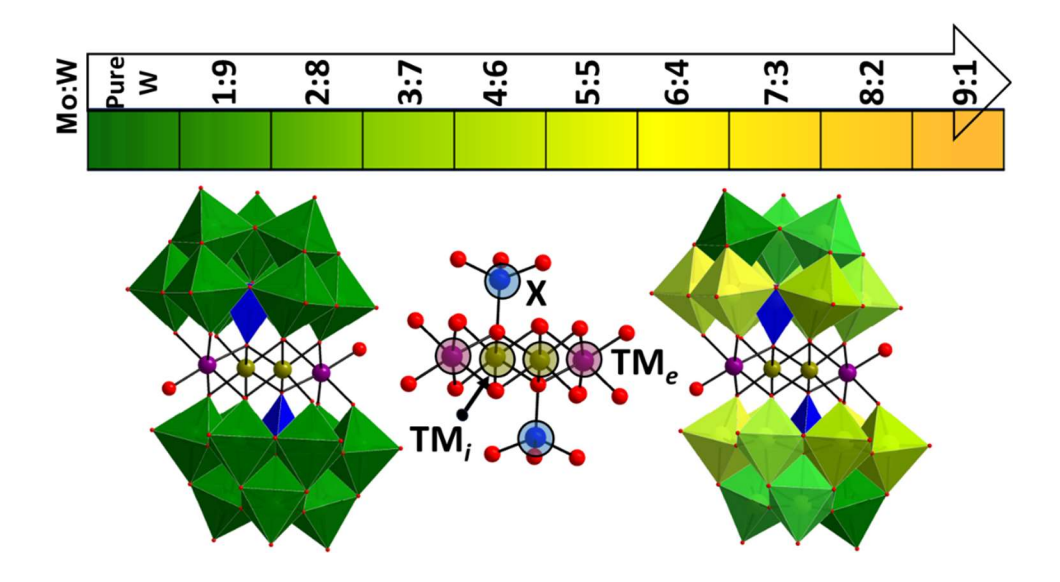
अधिकी ः

CYL701	Molecular Spectroscopy
CYL511	Instrumentation analysis
CYL622	Applied Electrochemistry
CYL613	The Chemistry of Metal-Carbon bond
CYL423	Solid-state chemistry
	SAE OF LECHMO.
	धियो यो नः प्रचोदयात्

Dr. Debaprasad Mandal

Associate Professor
Department of Chemistry
Indian Institute of Technology Ropar
Rupnagar 140001
Punjab, INDIA

# **TOC** of the thesis



## Dedicated

to

My Parents, Family and Almighty God

## **Acknowledgements**

I would like to express my sincere gratitude to all who have helped me to bring this study into reality. I am very delighted to express my gratitude to all of them. At the very beginning, I would like to express my sincere gratitude to the almighty for inducing adequate abilities along with patience and courage to pursue this program.

I am very thankful to my thesis supervisor, Dr. Debaprasad Mandal for his continuous support and help throughout my PhD career. I am proud that I have worked under his guidance. I am thankful to him for giving me the opportunity to work with him and to create my interest in crystallography. His constant inspiration, encouragement and patience helped me a lot throughout this endeavour. He has helped me cultivate scientific thoughts and supported me to improve my thesis with many good ideas and suggestions. His influence has been profound, pushing me to exceed my limits and achieve more than I thought possible. One thing about him is that whenever I needed him, he was always available for scientific discussion, especially after my 2<sup>nd</sup> year. I can never forget our long discussions (sometimes more than 1 hour) about research projects and ideas. Apart from scientific discussions, his humanity bound me to respect him. Outside the institute, he was more like a friend than a mentor with whom I could discuss so many things apart from lab work. Finally, "Thank you sir for all the constructive discussions and support throughout my PhD journey, bearing me whenever I was unruly for some time and my everlasting gratitude goes to you."

I would like to express my sincere gratitude to my doctoral committee members Dr. Avijit Goswami, Dr. Indranil Chatterjee, Dr. Anshu Dhar Jayal, Dr. Dheeraj K. Mahajan, and Dr. T. J. Dhilip for their evaluation, suggestions, and help. I would like to express my sincere gratitude to Dr. Tharamani C.N. for continuously motivating me and for suggestions throughout my PhD journey. I would also thank my M.Sc. thesis supervisor Prof. Pradeep C. Parmeswaran for creating my interest in inorganic chemistry, especially in the beauty of polyoxometalate chemistry.

I would like to express my sincere thanks to all the faculty members of Chemistry department, Indian Institute of Technology Ropar for their help and suggestions. I am thankful

to Indian Institute of Technology Ropar for the impeccable research environment and Council of Scientific and Industrial Research for financial support. I wish to thank all the supporting staff of the Chemistry department, IIT Ropar, especially Mr. Nagender Singh, Mrs. Poonam Kataria, Mr. Sushil Kumar, Mrs. Samita Saini, Mr. Manish, Mr. Kamlesh, Mr. Amit Kumar, who has helped me throughout this journey.

I would like to thank my all lab-mates for their help and support. Especially, I would like to thank my senior Dr. Subhasis Das Adhikary for giving me essential and valuable training of laboratory techniques and lab culture regarding polyoxometalates synthesis and characterizations. I am thankful to him for his help inside or outside the laboratory whenever it was needed. Special thanks to my seniors Dr. Sinchen, Dr. Anil, Dr. Gaje Singh, Diksha for their support in my research work. I am thankful to them for various technical supports and also for the cheerful moments we spent together. Special thanks to Dr. Gaje Singh and Diksha, who were always there to help with my projects. Their gossips in my tea and lunch breaks always give me time to laugh and relax. Diksha has supported me a lot throughout this journey, and we have exchanged many innovative ideas, especially regarding polymer design in one of our collaborative projects. I must thank my present lab mates Tino Thomas, Aayushi Sinha, Rahul Maurya, Rajpal Singh, Ruchika, Kirti and Dr. Amandeep for their cooperation and maintaining a pleasant atmosphere in the laboratory. Special thanks to Ruchika and Amit Thapliyal without whom it was difficult for me to finish this much thesis work. I express my thanks to all the lab-members of Dr. Tharamani C.N. research group for their help and support in my research work and for the cheerful moments we spent together. I wish to thank M.Sc. students Swarnima, Jiyad KM, Naseeb Araham, and intern Shambhavi Sah for their help in my research work.

Outside lab, I am especially thankful to Dr. Pankaj Kumar, Dr. Debarshi Saha, Dr. Navpreet Kaur, Dr. Majid, Dr. Mukesh Kumar, Dr. Neha Thakur, Dr. Alankar, Dr. Divyani Gupta, Dr. Parsoon Raj Singh, Dr. Manisha Lamba, Dr. Daisy Mehta, Dr. Chandresh Kumari, Dr. Moumita Halder, Dr. Anoop, Dr. Manish Kumar, Dr. Rakesh and Shain Kadir, Vishal, Gulshan, Himanshu, Brij Gopal, Ketan, Ganesh, Amit, Dinesh, Sourav, Man Singh for their support throughout this journey and for the joyful moments shared with me. Special thanks to Dr. Manish Kumar, who always supported me outside my lab. He's the person I reach out to

whenever I feel low in the lab. His simple sentence, "Come out of the lab and let's go for dinner," always manages to lift my spirits and help me forget my worries, even if just for a while.

Finally, I wish to express my sincere gratitude to my family members, my doctoral study could not have been completed without their enormous support, blessing and always trusting me. I would like to express my deepest gratitude to my parents, grandma and dedicating my thesis to them. I also wish to express my sincere gratitude to brother (Parmveer Singh), sister-in-law (Jyoti) and Sisters (Sarita, Sukarma), brother-in-law (Sumit, Ankur) for their blessings, love and care throughout the journey. I am also thankful to my beloved ones (Chanchal, Divyansh, Jayash, Lavik, Prisha, and Dev) for their love and affection for me. A special thanks to Chanchal for pushing me to finish my doctoral work and praying on my behalf. Apart from them, I am also thankful to my friends from school and college days (M Ashraf, Dr. Deepak Kumar, Dr. Parveen, Dr. Tushar, Vicky, Shubham, Dr. Reetu, Sanjhal, Navneet, Anu, Ankita, Sakshi, Shilpa, Vikul, Sanjeev, Rohit, Anjit, Sanjay, Deepak, Manoj) who always supported me during this journey. In every footstep of my life and career, they are the main motivators.

Ganga Singh

### **Preface**

In today's world, the scientific community is facing two major challenges namely energy crisis and global warming. Our energy sources are currently dependent on non-renewable energy mainly fossil fuels which are predicted to be depleted within the century and will significantly limit our quality of life. Additionally, these non-renewable energy resources emit greenhouse gases which result in major global climate problems. In this scenario, the utilization of renewable and sustainable energy sources are the best alternative for the economic, environmental and increased energy demand of industries and common households. In this scenario, many catalytic reactions such as water splitting, CO<sub>2</sub> and N<sub>2</sub> reduction becomes very important. For example, water splitting has long been perceived as Holy Grail in this regard because of the production of hydrogen (a clean, renewable fuel) and oxygen without any unwanted by-products. Similarly, CO<sub>2</sub> reduction not only minimise the greenhouse effect but also can be efficient as fuel in the form of methanol. CO<sub>2</sub>/N<sub>2</sub> reduction requires coupling of multiple electron and proton for its reduction through proton-coupled electron transfer (PCET). Water is the best proton source for CO<sub>2</sub>/N<sub>2</sub> reduction, however, water splitting suffers from its high oxidation potential and sluggish kinetics. Therefore, in last few decades, much more attention has been paid to develop the highly efficient water oxidation catalysts (WOCs). For this purpose, the tetra-metal substituted sandwich polyoxometalates are of particular interest because of their robust nature, multi-electron redox property, easily accessible active sites and scope of various transition metal incorporation. The tetra-metal core, heteroatom and addenda atoms are highly tuneable for the construction of distinct sandwich polyoxometalate clusters and subsequently, the physical and electrochemical properties can be tuned. Even after three decades of research on sandwich POMs, with more than 50 sandwich POMs reported so far, there is still a lack of structureproperties relations of these POMs which can be used for designing the best catalyst.

Also, for efficient PCET, orbital engineering becomes very important in terms of controlling electron transfer kinetics. To bridge this research gap, a comprehensive study is necessary

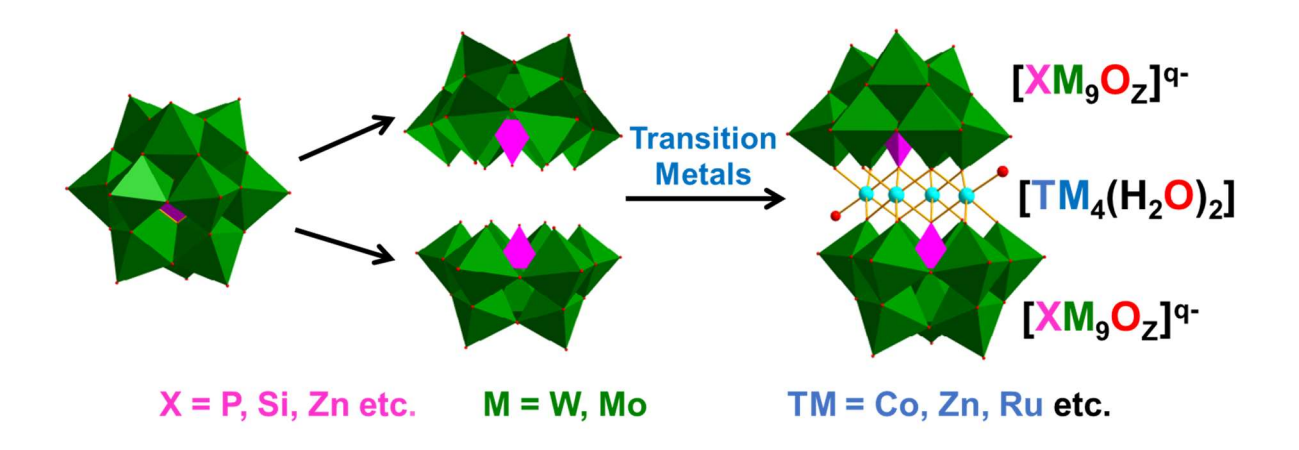
including the effect of different transition metals at the sandwich position and the role of mixed addenda framework in orbital engineering and hence activities of these POMs.

Here, we propose mixed metals at sandwich position along with mixed addenda in the framework of polyoxometalates to modulate the frontier molecular orbitals (FMO) in these POMs. This thesis presents a systematic cooperative mix-metal approach, demonstrating the successful synthesis of mixed metal-mixed addenda POMs. We meticulously characterized all the POMs by Single crystal-XRD, ESI-MS and XPS analysis and validated the orbital modulation by various spectroscopy and DFT studies.

Our cooperative mix-metal approach proves to be a versatile synthetic strategy for mixed metal-mixed addenda POMs and also served as an effective tool for orbital engineering. It influences the overall band gap, charge transfer (especially metal to POM charge transfer - MPCT), modulation of electron density, and SOMO and HOMO-LUMO orbitals, which was further complemented by the DFT calculations. We have also extended this approach for the synthesis of POM-based 1D-frameworks (POM-based coordination polymers), which recently gained attention, and for the synthesis of mixed addenda Banana-type POMs, a previously unexplored POM. Also, using cooperative mixed metal strategy along with organic ligands, we could be able to synthesize pure Mo-based sandwich POMs. We believe that our cooperative mix metal approach presents a robust synthetic analogy, suitable for designing new POMs and hybrid POM complexes with tuneable orbital for designing more active catalysts.

#### Description of the research work

The tetra-metal sandwich polyoxometalates can be synthesized in two ways. Firstly, the synthesis and isolation of tri-vacant or di-vacant polyoxometalate fragments followed by the sandwich polyoxometalate synthesis in the second step. Secondly, sandwich polyoxometalates can be synthesized in 'one-pot' without isolating the lacunary or fragment POMs. The oxygen atoms of lacunary sites of tri-vacant Keggin fragments (or tri-vacant lacunary polyoxometalates) are sufficiently active to accommodate the transition metal atoms to form the sandwich polyoxometalates as shown in Scheme X.



**Scheme X**. Schematic presentation of the synthesis of tetra-metal sandwich POMs.

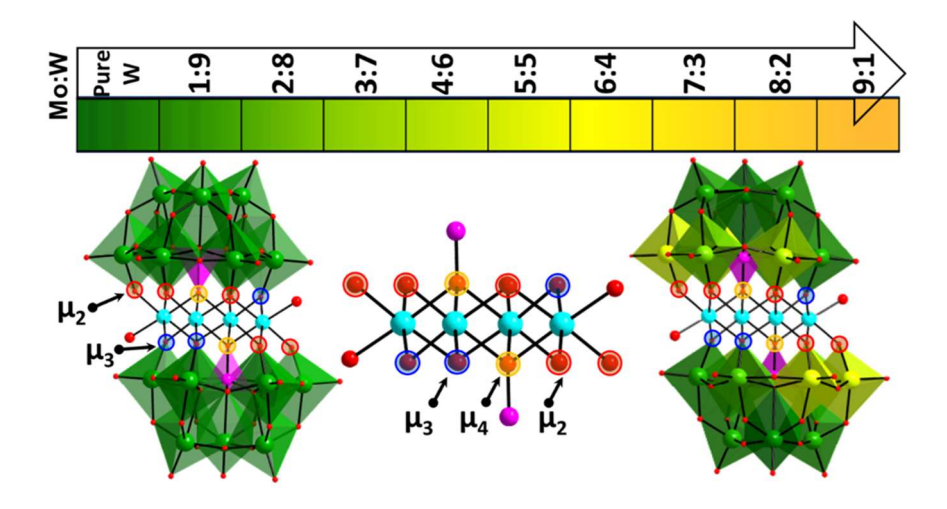
#### **Chapter 1: Introduction to Polyoxometalates**

This chapter represents an overview of polyoxometalate chemistry, especially the structure, and properties with further emphasis on the band gap modulation in Sandwich POMs. Sandwich polyoxometalates are transition metal substituted polyoxometalate where transition metals are sandwiched between the lacunary polyoxometalate fragments. Because of their remarkable structural similarity to naturally occurring enzymes and cofactors, and potential uses in a variety of catalysis, medical, and electrochemistry-related fields, sandwich-type compounds are among the most important transition metal-substituted polyoxometalates (TMSPs) which have been discussed in the introduction.

# Chapter 2: Modulation of Band Gap and Redox Properties in Mixed-Addenda Sandwich Polyoxometalates

In this chapter, we have targeted transition metal-based Sandwich POMs with phosphorus as heteroatom with the formula  $[(TM)_4(H_2O)_2(PMo_xW_{9-x}O_{34})_2]^{10-}$  **P-(TM)\_4Mo\_xW\_{18-x}** where TM=Mn/Co/Ni/Zn. Due to the wide range of applications of band-gap engineering in optoelectronics and photocatalysis, the rational design of polyoxometalate (POM) frameworks is highly desired. Here, we have successfully synthesized a series of mixed addenda (Mo and W) sandwich POMs by systematically varying pH, concentrations of salts, and counterions in Weakley-type sandwich POMs by incorporating Mo into the framework of tetrasubstituted sandwich POMs. Crystallographic analysis reveals the centrosymmetric structure; with variation in Mo to W ratio, Mo preferentially binds to  $\mu_2$  oxygen connected to

transition metals in the sandwich position. UV-visible spectroscopy, electrochemical, and theoretical modelling rationalize the band-gap modulations. Theoretical studies and cyclic voltammograms indicate that during the reduction, the incoming electrons preferentially go to substituted transition metals followed by Mo. Flat band potential calculated from the Mott-Schottky enables tuning of the electronic properties of composites based on these sandwich POMs. Moreover, the dioxygen binding and activation studies of these polyoxometalates have been highlighted. Further, orbital engineering using mixed metals at sandwich position have been performed.



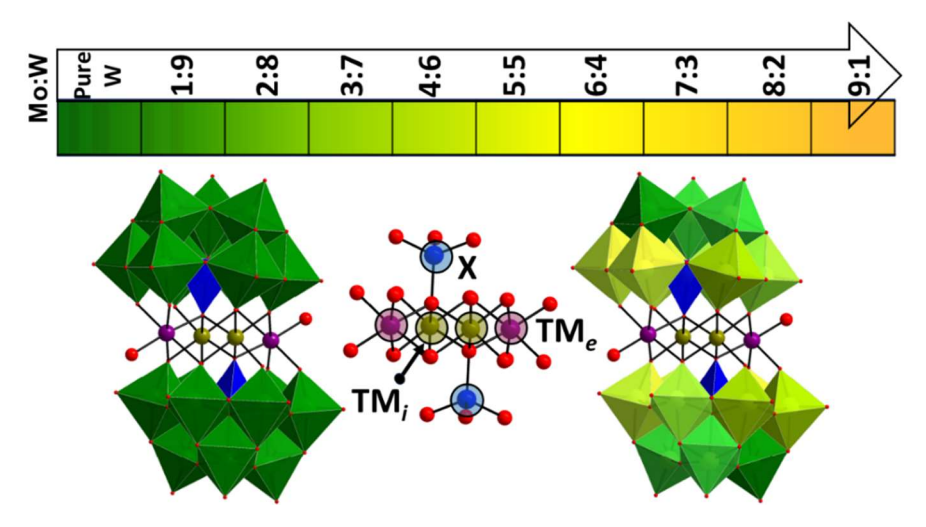
Chapter 3: Construction of Mixed Addenda Polyoxometalates by Cooperative Self-assembly and tuning of their Optoelectronic Properties

This chapter deals with the incorporation of high oxidation state transition metals at an internal sandwich position to modulate optoelectronic properties as well as incorporating mixed addenda in sandwich POMs. Using low oxidation state precursor metals introduces the formation of frameworks in sandwich POMs. This chapter is further divided into two sections (3A and 3B).

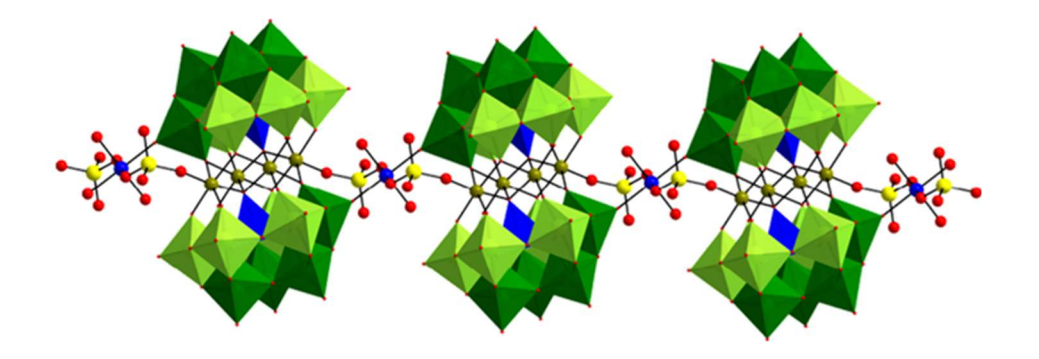
#### Section 3A: Interplay of Transition Metals at an internal Sandwich Position Towards Modulation of the Optoelectronic Properties

The orbital engineering by the cooperative effect of different transition metals (TM) proves to be a highly impactful and versatile approach for regulating the chemistry of polyoxometalates (POMs) either by introducing novel POMs or through POM-hybrids for

designing more effective catalysts. Here we present a cooperative mix-metal strategy for the synthesis of mixed addenda (Mo/W) sandwich POMs, denoted as  $[(TM_i)_2(TM_e)_2(H_2O)_2(XMo_xW_{9-x}O_{34})_2]^{n-}$  ( $TM_i(III)=Mn/Fe$  and  $TM_e(II)=X=Zn/Co/Fe$ ). Structural analysis of these POMs show that the incorporation of Mo addenda in (Mo/W) POM framework is highly influenced by the variation of transition metals at sandwich core and their oxidation states and pH of the media. ESI-MS analysis provides detailed POM compositions, while UV-vis spectra, and complementary density functional theory (DFT) analysis reveal orbital engineering through distinctive charge transfer processes.



Section 3B: Role of Charge Density towards the formation of Framework Structures in Sandwich Polyoxometalates



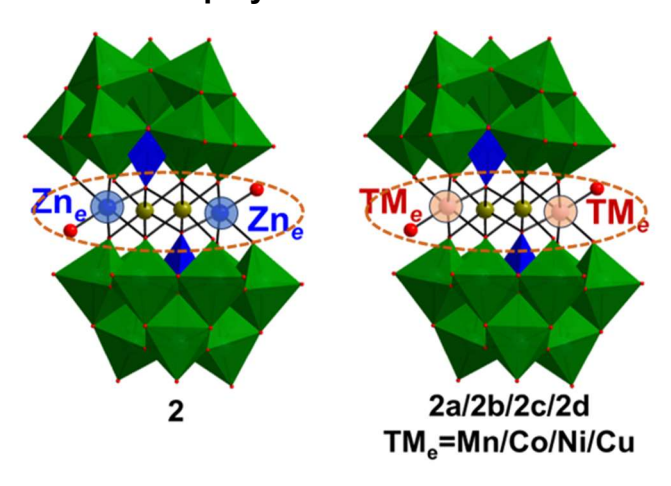
This section deals with the role of charge density or oxidation state of precursor metals towards the formation of framework compounds in sandwich POMs. The formation of frameworks has been further understood through the DFT study. Further, the role of framework towards Mo incorporation has been highlighted. This cooperative mixed metal-

mix addenda strategy has been extended to the formation of 1-D polyoxometalate cluster frameworks (POMCFs), where oxidation state of precursor metals plays a vital role impacting the overall structural attributes.

# Chapter 4: Construction Of Trimetallic Sandwich Polyoxometalates towards Optoelectronic Properties Modulation

This chapter deals with the introduction of high oxidation state transition metals at the internal sandwich position thus facilitating the substitution of transition metals at the external sandwich position while changing heteroatoms results in structural modifications in these TMSPs thus impacting their physiochemical as well as optoelectronic properties. This chapter has been divided in two sections (4A and 4B)

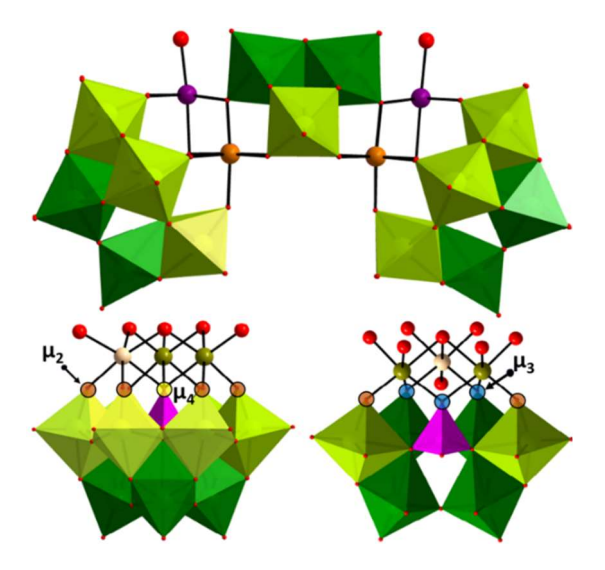
Section 4A: Modulation of Optoelectronic Properties in Trimetallic Sandwich Polyoxometalates via the interplay of External Sandwich Position



The physico- and electrochemical behavior of a series of [Zn<sub>2</sub>Fe<sub>2</sub>(H<sub>2</sub>O)<sub>2</sub>(ZnW<sub>9</sub>O<sub>34</sub>)<sub>2</sub>]<sup>14-</sup> **Zn-Zn<sub>2</sub>Fe<sub>2</sub>**, [Co<sub>2</sub>Fe<sub>2</sub>(H<sub>2</sub>O)<sub>2</sub>(CoW<sub>9</sub>O<sub>34</sub>)<sub>2</sub>]<sup>14-</sup> **Co-Co<sub>2</sub>Fe<sub>2</sub>**, and its first-row transition metal) substituted analogues [(TM)<sub>2</sub>Fe<sub>2</sub>(ZnW<sub>9</sub>O<sub>34</sub>)<sub>2</sub>]<sup>q-</sup> **Zn-Zn<sub>2</sub>(TM)<sub>2</sub>** (where, TM= Mn/Ni/Fe/Cu) are reported. Various spectroscopic studies FT-IR, UV-visible, ESI-mass and Raman etc., show similar spectral patterns in all sandwich POMs because of their isostructural geometry and constancy of overall negative charge (-14). However, the electronic properties highly depend on the transition metals at the 'sandwich core' and correlate well with DFT study. Further, depending on the substituted TM-atoms, there is decrease in HOMO-LUMO bandgap

energy in these TMSP complexes w.r.t **Zn-Zn<sub>2</sub>Fe<sub>2</sub>** as confirmed by diffuse reflectance spectroscopy and DFT study.

Section 4B: Framework Switch in Trimetallic Sandwich Polyoxometalates Control by Heteroatom and Oxidation State



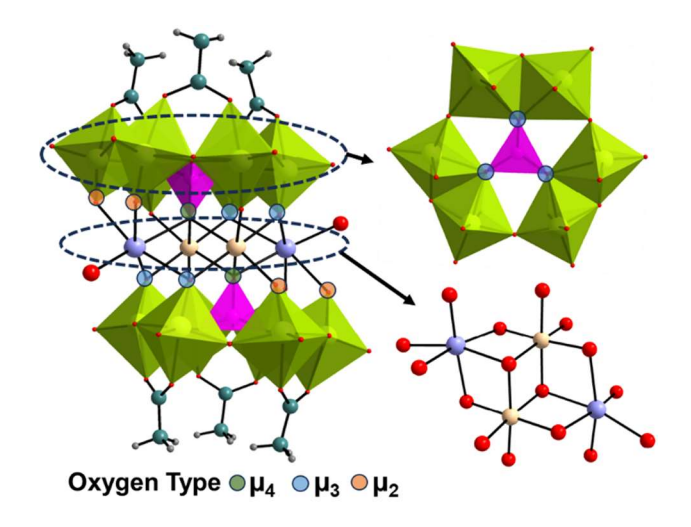
This chapter deals with the role of transition metals at the hetero-position towards structural transformation thus facilitating the functionalization of transition metals at the external sandwich position using organic ligands thus impacting their physiochemical as well as optoelectronic properties.

# Chapter 5: Design of Polyoxometalates-based Inorganic-Organic Hybrids for Task-Specific Application

Apart from structural parameters, these TMSPs can be used to form POM-organic hybrids either by covalent functionalization (class-A hybrids) or by electrostatic interaction by exchanging countercations (class-B hybrids). The countercations and organic anchoring groups largely impact the electronic, crystallographic, and solubility properties of the polyoxometalates. In this regard, class-A hybrids have been synthesized (Chapter 5A) while Class-B hybrids have been used for adhesive application in seawater and anticorrosive coatings (Chapter 5B).

# Section 5A: Microwave-assisted Synthesis of Transition Metals Substituted Sandwich Phosphomolybdates

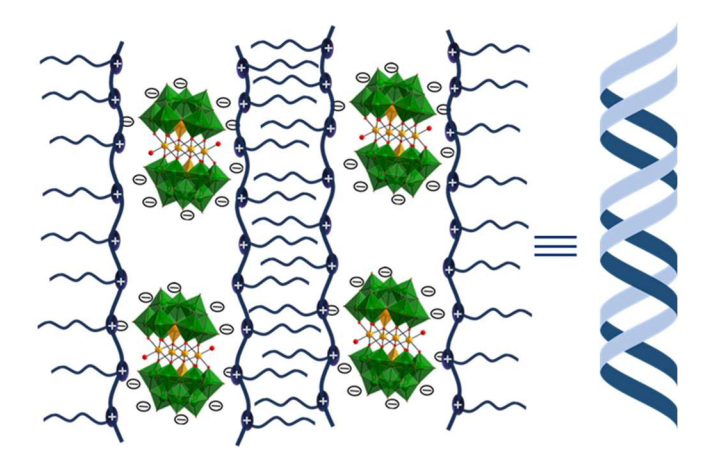
Here, we have targeted the synthesis of molybdenum-based sandwich POMs synthesis using cooperative effect of transition metals at sandwich position and organic ligands using covalent bonds. Using this cooperative effect, sandwich POMs with the formula [Na<sub>2</sub>(TM)<sub>2</sub>(H<sub>2</sub>O)<sub>2</sub>(PMo<sub>6</sub>O<sub>22</sub>)<sub>2</sub>(R)<sub>6</sub>]<sup>n-</sup> where TM=Mn/Co/Ni/Zn, and R= OAc, Ogly, OOCCH<sub>3</sub> have been isolated and characterised.



Section 5B: Self-assembled Polyoxometalate-based Nanohybrids for Corrosion-Resistant Underwater Adhesive

Designing underwater adhesives with fast and strong adhesion is in high demand in many applications, including underwater repair, soft robotics, medical devices, and water-based energy devices. However, shortening the bonding period usually leads to premature bonding and thus weak adhesion. Such trade-off becomes more pronounced in the presence of interfacial water especially saltwater which disrupts adhesive-adherend interactions. Here we report a facile synthesis for hydrophobic polyoxometalates-polymer adhesive which shows outstanding underwater adhesion strength of up to 3.5 MPa with remarkable reversibility, and a substantially faster bonding time of 1 minute.

These adhesives are versatile and can stick to a wide range of surfaces, including glass, metals, and polymers with high strength. Interestingly, they exhibit excellent stability at very low temperatures as well as under submerged seawater conditions and ambient air at room temperature with a remarkable corrosive inhibition efficiency of 85% at stainless steel substrate in seawater.



**Chapter 6: Conclusion and Future Aspects** 

In this chapter, the summary of the whole work has been narrated.

## **Contents**

Chapter 1	. Introduction to Polyoxometalates	3-32
1.1 Intro	duction	05
1.2 Cons	struction of Polyoxometalates by self-assembly	06
1.3 Strue	ctural diversity of polyoxometalates	07
1.4 Gen	eral characterization methods of polyoxometalates	10
1.5 Synt	hetic strategy for sandwich polyoxometalates and its requirement	12
1.6 Stru	cture-property relationship	14
1.7 Redo	ox properties of POMs	15
1.8 Elec	tronic properties of POMs	16
1.9 Mo	ecular orbital engineering	18
1.10 Stru	ctural description in sandwich POMs	20
1.11 Org	anic-inorganic hybrid polyoxometalates	21
1.12 Ain	of Thesis	22
1 12 Dof	erences	29
1.13 Kel	Dictions	2)
	2. Modulation of Band Gap and Redox Properties in	
Chapter		
Chapter	2. Modulation of Band Gap and Redox Properties in la Sandwich Polyoxometalates	Mixed
Chapter Addender 2.1 Intro	2. Modulation of Band Gap and Redox Properties in la Sandwich Polyoxometalates	Mixed- 33-98
Chapter Addender 2.1 Intro	2. Modulation of Band Gap and Redox Properties in la Sandwich Polyoxometalates  duction	<b>Mixed</b> -33-98
Chapter Addender 2.1 Intro 2.2 Resu	2. Modulation of Band Gap and Redox Properties in la Sandwich Polyoxometalates duction lts & Discussion	<b>Mixed- 33-98</b> 35 37
Chapter Addender 2.1 Intro 2.2 Resu 2.2.1	2. Modulation of Band Gap and Redox Properties in la Sandwich Polyoxometalates duction llts & Discussion Reaction chemistry of mixed addenda sandwich polyoxometalates	<b>Mixed</b> - <b>33-98</b> 35 37 37
Chapter Addende 2.1 Intro 2.2 Resu 2.2.1 2.2.2	2. Modulation of Band Gap and Redox Properties in la Sandwich Polyoxometalates duction lits & Discussion Reaction chemistry of mixed addenda sandwich polyoxometalates Characterization of mixed addenda sandwich polyoxometalates	<b>Mixed- 33-98</b> 35 37 37 39
2.1 Intro 2.2 Resu 2.2.1 2.2.2 2.2.3	2. Modulation of Band Gap and Redox Properties in la Sandwich Polyoxometalates  duction  lits & Discussion  Reaction chemistry of mixed addenda sandwich polyoxometalates  Characterization of mixed addenda sandwich polyoxometalates  Properties of mixed addenda sandwich polyoxometalates	<b>Mixed</b> 33-98  35  37  37  39  49
Chapter Addender 2.1 Intro 2.2 Resu 2.2.1 2.2.2 2.2.3 2.2.4	2. Modulation of Band Gap and Redox Properties in la Sandwich Polyoxometalates duction dits & Discussion Reaction chemistry of mixed addenda sandwich polyoxometalates Characterization of mixed addenda sandwich polyoxometalates Properties of mixed addenda sandwich polyoxometalates Density Functional Theory (DFT) study Molecular oxygen binding/activation	<b>Mixed</b> 33-98  35  37  37  39  49  55
Chapter Addender 2.1 Intro 2.2 Resu 2.2.1 2.2.2 2.2.3 2.2.4 2.2.5 2.3 Cond	2. Modulation of Band Gap and Redox Properties in la Sandwich Polyoxometalates duction dits & Discussion Reaction chemistry of mixed addenda sandwich polyoxometalates Characterization of mixed addenda sandwich polyoxometalates Properties of mixed addenda sandwich polyoxometalates Density Functional Theory (DFT) study Molecular oxygen binding/activation	<b>Mixed</b> 33-98  35  37  37  39  49  55  62
Chapter Addender 2.1 Intro 2.2 Resu 2.2.1 2.2.2 2.2.3 2.2.4 2.2.5 2.3 Cond	2. Modulation of Band Gap and Redox Properties in la Sandwich Polyoxometalates duction lts & Discussion Reaction chemistry of mixed addenda sandwich polyoxometalates Characterization of mixed addenda sandwich polyoxometalates Properties of mixed addenda sandwich polyoxometalates Density Functional Theory (DFT) study Molecular oxygen binding/activation elusion erimental Section	<b>Mixed</b> 33-98  35  37  37  39  49  55  62  63

Chapter 3. C	Cooperative Self-Assembly Assisted Construction o	f Sandwich
Polyoxom	etalates and its Mixed Addenda Analogue	99-102
3.1 Introduc	etion	101
3.2 Referen	ces	102
Chapter 3: S	Section A: Construction of Mixed Addenda Polyox	ometalates
by Coop	erative Self-Assembly and Tuning their Opt	oelectronic
Properties		103-152
3A.1 Introdu	action	105
3A.2 Results	s and Discussion	107
3A.2.1 Syr	athetic Chemistry	107
3A.2.2 Str	actural Description	115
3A.2.2a	Structural Description and Characterizations of 1 and 1-M	115
3A.2.2b	Structural Description and Characterizations of 2 and 2-M	118
3A.2.2c	Structural Description and Characterizations of 3 and 3-M	123
3A.2.2d	Structural Description and Characterizations of 4 and 4-M	127
3A.2.2e	Structural Description and Characterizations of 5 and 5-M	131
3A.3 Conclu	asion	134
3A.4 Experi	mental Section	134
3A.5 Refere	nces	138
Annexure-II		141
Chapter 3: S	Section B: Role of charge density towards formatio	n of
framewor	k structures in sandwich Polyoxometalates	153-170
3B.1 Introdu	action	155
3B.2 Results	s and Discussion	155
3B.2.1 Syr	thetic Chemistry	155
3B.2.2 Str	actural Description	158
3B.2.2a St	ructural Description and Characterizations of 6 and 6-M	158
3B.2.2b St	ructural Description and Characterizations of 7 and 8	160
3B.3 Conclu	sion	163
3B.4 Experi	mental Section	163

3B.5 References	165
Annexure-III	167
Chapter 4. Modulation of Optoelectronic Properties and Framev	vork in
Trimetallic Sandwich Polyoxometalates	171-174
4.1 Introduction	173
4.2 References	174
Chapter 4. Section A: Modulation of Optoelectronic Properties in	n
Trimetallic Sandwich Polyoxometalates via the Interplay of Ex	
Sandwich Position	175-212
4A.1 Introduction	177
4A.2 Results and Discussion	179
4A.2.1 Reaction Chemistry	179
4A.2.2 When W(VI) is present at internal sandwich position	180
4A.2.3 When Fe(III) is present at internal sandwich position	183
$4A.2.3a$ With Zn as heteroatom and $TM_e=Mn/Co/Ni/Cu/Zn$	183
$4A.2.3b$ With Co as heteroatom and $TM_e=Mn/Co/Ni/Cu/Zn$	188
4A.2.4 When Mn(III) is present at the internal sandwich position	193
4A.2.4a With Zn as heteroatom and TM <sub>e</sub> =Fe	193
4A.3 Conclusion	197
4A.4 Experimental Section	197
4A.5 References	200
Annexure-IV	203
Chapter 4. Section B: Framework Switch in Trimetallic Sandwic	eh
Polyoxometalates Control by Heteroatom and oxidation state	213-242
4B.1 Introduction	215
4B.2 Results and Discussion	215
4B.2.1 Cooperative Effects of Mixed Metals with Phosphorous as the hetero	oatom 215
$4B.2.1a\ Characterization\ analysis\ of\ P-Mn_2Co_2Mo_xW_{18-x}\ and\ P-Ni_2Zn_2Mo_xW_{18-x}$	$W_{18-x}$ 217
4B.2.1b Effect of the oxidation state of precursor transition metals: Sys	nthesis and
Characterization of mixed addenda Banana Polyoxometalates	220

4B.2.2 Cooperative Effects of Mixed Metals with Bismuth as the heteroatom				
4B.2.2a Synthesis and characterization of Krebs Polyoxometalates using c	ooperative			
mixed metals strategy	225			
4B.3 Conclusion	228			
4B.4 Experimental Section	228			
4B.5 References	231			
Annexure-V	233			
Chapter 5. Design of Polyoxometalates-based inorganic-organic h	ybrids			
for task-specific application	243-246			
5.1 Introduction	245			
5.2 References	245			
Chapter 5. Section A: Microwave-assisted synthesis of transition substituted sandwich Phosphomolybdates	metals 247-274			
5A.1 Introduction	248			
5A.2 Results and Discussion	250			
5A.2.1 Synthesis of Inorganic-organic Hybrids	251			
5A.3 Conclusion	258			
5A.4 Experimental Section	258			
5A.5 References	261			
Annexure-VI	263			
Chapter 5. Section B: Self-assembled Polyoxometalate-based				
Nanohybrids for Corrosion-Resistant Underwater Adhesive	275-292			
5B.1 Introduction	277			
5B.2 Results and Discussion	278			
5B.2.1 Synthesis of [C <sub>25</sub> H <sub>54</sub> N][Co-WCo <sub>3</sub> ] hybrids for Underwater adhesion	278			
5B.2.2 Synthesis [q-PEI-hexyl][Co-WCo <sub>3</sub> ] hybrids for Underwater adhesion	281			
5B.3 Conclusion	286			
5B.4 Experimental Section	287			
5B.5 References	289			
Annexure-VII	291			

Chapter 6. Conclusion and Future perspective	293-298	
6.1 Summary	295	
6.2 Future Perspective	297	
6.3 References	298	

#### **Abstract**

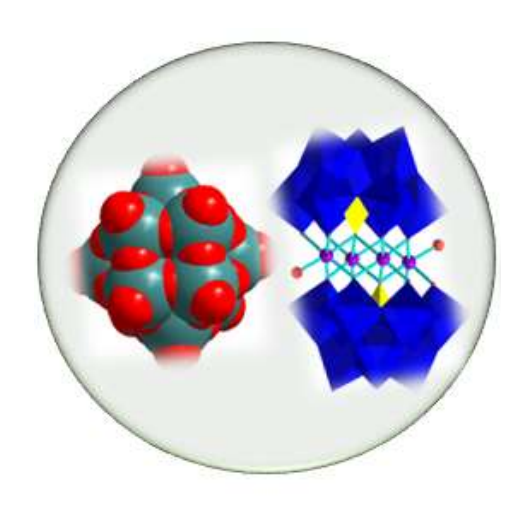
A class of anionic polynuclear metal—oxo clusters with distinct, chemically modifiable structures are known as polyoxometalates (POMs), constructed mainly by early transition metals (V, Mo, W, Nb) in their highest oxidation states. POMs can act as electron reservoirs due to their tunable reactivity, reversible multi-electron transfer, and UV-visible light absorption capabilities. Sandwich polyoxometalates are transition metal substituted polyoxometalate where transition metals are sandwiched between the lacunary polyoxometalate fragments. Because of their remarkable structural similarity to naturally occurring enzymes and cofactors, and potential uses in a variety of catalysis, medical, and electrochemistry-related fields, sandwich-type compounds are among the most important transition metal-substituted polyoxometalates (TMSPs) which have been discussed in the introduction.

Sandwich POM has a robust structure and their catalytic activity highly depends on the transition metal core [TM<sub>4</sub> consists of internal (TM<sub>i</sub>) and external transition metals (TM<sub>e</sub>)], heteroatom, and the addenda framework. Despite three decades of research into these tetrasubstituted TMSPs with over 50 structures reported to date, however, it is still unknown how altercating TM at a particular position (internal or external sandwich position/heteroposition/framework position) entirely changes the catalytic activity of these POMs. Here, in this thesis, we have explored the chemistry of sandwich POMs that can be useful for designing these POMs for task-specific applications. We focussed on the orbital engineering of sandwich POMs using mixed addenda (Mo/W) to modulate optoelectronic and electrochemical properties in sandwich POMs. Apart from structural parameters, these TMSPs can be used to form POM-organic hybrids either by covalent functionalization (class-A hybrids) or by electrostatic interaction by exchanging countercations (class-B hybrids). In this regard, class-A hybrids have been synthesized and explored for modulating solid-state luminescence properties while Class-B hybrids have been used for adhesive application in seawater and anticorrosive coatings.

Overall, this thesis focuses on all the possible ways of orbital engineering in sandwich POMs based on 3d transition metals using experimental as well as theoretical study. It gives a trend of band gap engineering that can be useful for designing POMs-based materials in photo and electrocatalysis, photovoltaics, and enhanced optoelectronics in material science. Moreover, the interplay of intrinsically anionic POMs with organic anchoring groups is crucial in controlling the self-assembly, stabilization, solubility, and functions of POMs.

### **Chapter 1**

### **Introduction to Polyoxometalates**



#### 1.1 Introduction

Polyoxometalates<sup>1</sup> (POMs) represent a class of anionic polynuclear metal—oxo clusters, predominantly constructed from early transition metals (V, Mo, W, Nb, Ta) in their highest oxidation states.<sup>2-4</sup> POMs consist of a large, closed three-dimensional structure made up of shared oxygen atoms connecting addenda metal centres that vary in size, shape, and nuclearity.<sup>2, 5</sup> POMs have garnered renewed attention due to their unique properties, which include solubility in a wide range of media, potential applications in catalysis, magnetism, and therapeutics as well as their wide structural diversity, acidity, and redox activity controlled by the exchange of counter cations.<sup>6-8</sup>

POMs have been an evolving field in inorganic chemistry for the past two centuries.<sup>9</sup> In 1826, Berzelius reported the first example of a POM compound, phosphomolybdate, ([PMo<sub>12</sub>O<sub>40</sub>]<sup>3-</sup>). A significant milestone occurred in 1933 when Keggin interpreted the crystal structure of phosphotungstic acid (H<sub>3</sub>PW<sub>12</sub>O<sub>40</sub>.xH<sub>2</sub>O) for the first time from the X-ray diffraction data, and these structures were named after Keggin.<sup>10</sup> This finding marked the first major milestone in POM chemistry. Subsequently, several important POM motifs were identified, such as the Lindqvist, Preyssler, Waugh, Wells-Dawson, and Anderson POMs (Figure 1.1).

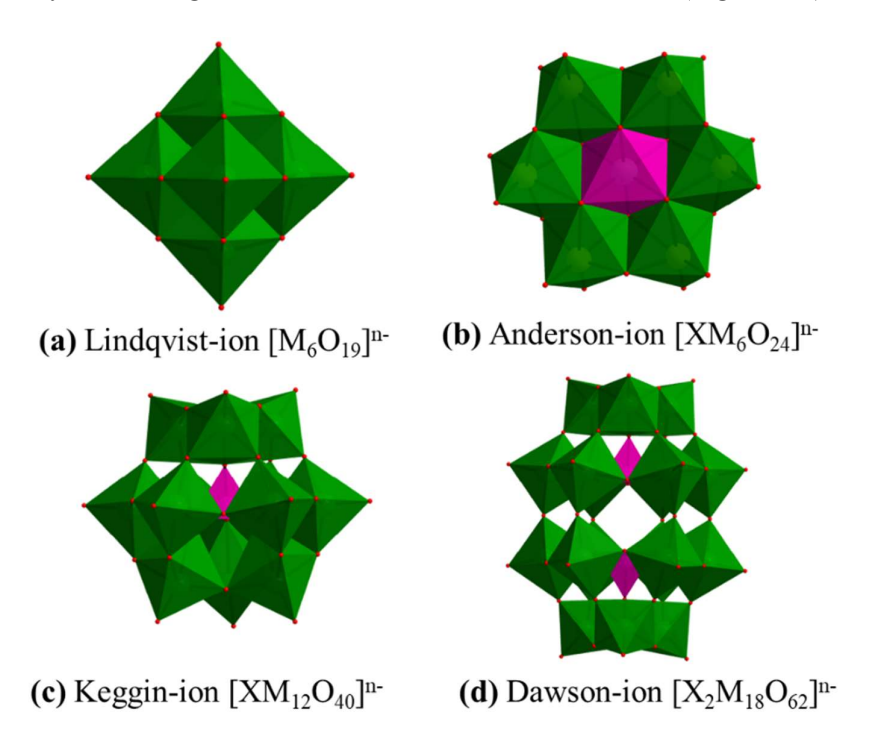
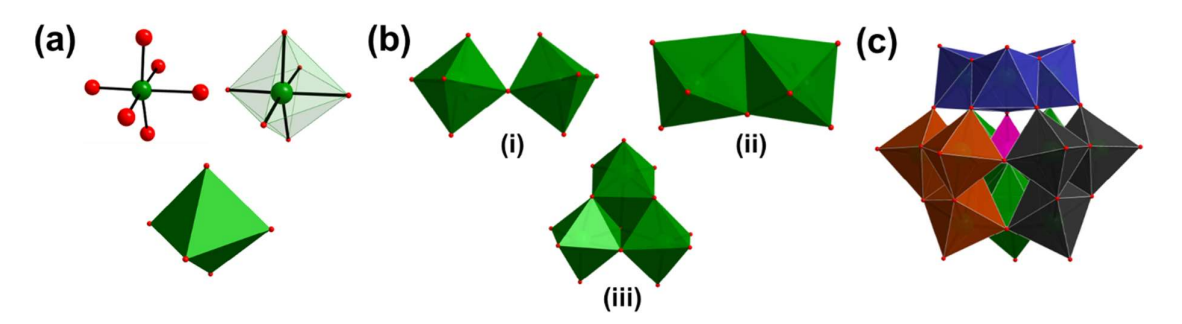


Figure 1.1 Classification of POMs based on the number of addenda atoms.

#### 1.2 Construction of Polyoxometalates by self-assembly

Polyoxometalates are typically formed by oligo-condensation of oxometallate precursors, with corner as well as edge shared and highly tunable cluster architecture.<sup>11</sup>



**Figure 1.2** (a) MO<sub>6</sub> octahedra (Addenda); (b) Condensation of addenda atoms (i) corner shared (ii) edge shared (iii) triads formations; (c) Keggin POMs with different triads (highlighted in a different colour) with a pink coloured templating agent.

Low-nuclearity monomeric metal oxoanions such as  $MoO_4^{2-}$ ,  $WO_4^{2-}$  or  $VO_4^{3-}$  ions are used to synthesize POMs. The acidification of these monomeric oxoanions initiates protonation-condensation processes which are necessary for the synthesis to occur in aqueous media.<sup>3</sup> The fundamental structural motif of POMs centers around the monomeric  $MO_x$  units, where M=Mo/W/V and x typically varies from 4 to 7. These units often assemble into  $MO_6$  octahedra, known as addenda (Figure 1.2a).

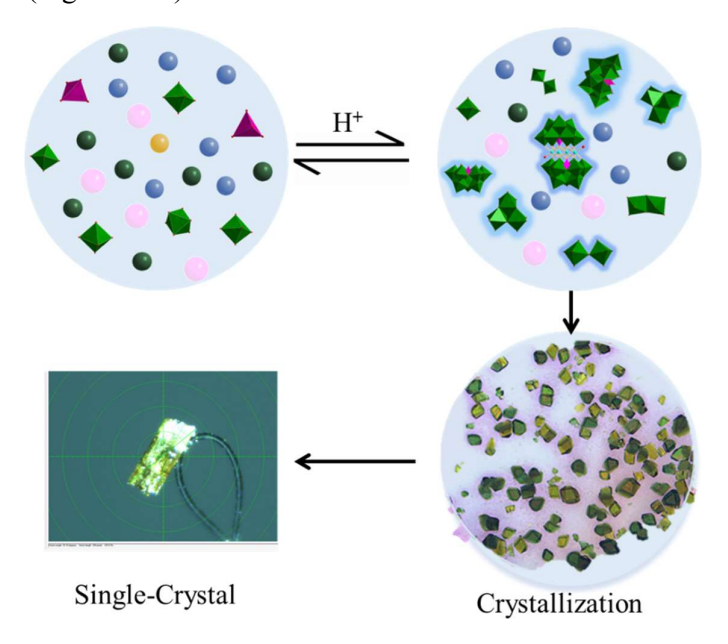


Figure 1.3 Self-assembly assisted crystallization of POMs via controlling pH, concentration and countercations.

The addenda  $MO_6$  is coordinated to six oxygen atoms which forms the bridging M-O-M bonds through coordinative bonding and terminal M=O bonds through strong  $p\pi$ -d $\pi$  interactions. Three main types of condensation are possible for the octahedral metal centres in POMs: face-sharing (involving three oxygen atoms), edge-sharing (involving two oxygen atoms), and corner-sharing (involving one oxygen). Among these, corner-sharing and edge-sharing are most prevalent in POM structures (Figure 1.2b (i, ii)). The process of assembling these small  $MO_x$  monomeric units into complex polymeric structures is commonly referred to as "self-assembly", a complex phenomenon in chemistry. This "self-assembly" process, results in  $[W_3O_{10}(OH)]^{3-}$ , the basic building block known as triads (Figure 1.2b(iii)), which aggregate in the presence of templating agents (usually P/Si or 3d transition metals) to higher nuclearities such as Keggin, Dawson etc. (Figure 1.2c). However, the tunability or the synthesis of polyoxometalate clusters depends on synthetic variables, like (a) concentration/type of metal-oxide anion, (b) concentration/type of heteroatom, (c) pH, (d) ionic strength, (e) additional ligand/reducing agent, (f) counter ions, (g) temperature and reaction processing (e.g., microwave, hydrothermal and reflux) (Figure 1.3).  $^{13}$ 

#### 1.3 Structural diversity of polyoxometalates

Polyoxometalates are broadly classified into three subcategories based on their composition and structure (i) Isopolyoxometalates or Isopolyanions, ii) Heteropolyoxometalates or Heteropolyanions and (iii) High nuclearity POMs (Mo-blue and Mo-brown clusters)<sup>1</sup>

#### (i) Isopolyoxometalates or isopolyanions

Polyoxometalates with a general formula of  $[M_mO_y]^{p-}$  [where M is termed as 'addenda atom' (M = W, Mo, V, Nb, etc.) are known as Isopolyoxometalates or Isopolyanions. Due to less robust structural motifs, this subset of polyoxometalates is much smaller without any heteroatom present e.g. Lindqvist POMs.

#### (ii) Heteropolyoxometalates or heteropolyanions

POMs framework with general formula  $[X_xM_mO_y]^{q-}$  [where M is W/Mo/V and X is 'heteroatom' like P, Si, Ge, Al, etc. or transition metals like Co, Zn, Cu,] are known as heteropolyoxometalates or heteropolyoxometalates are the most explored subset of polyoxometalate families because of their diverse structural variation, inherent

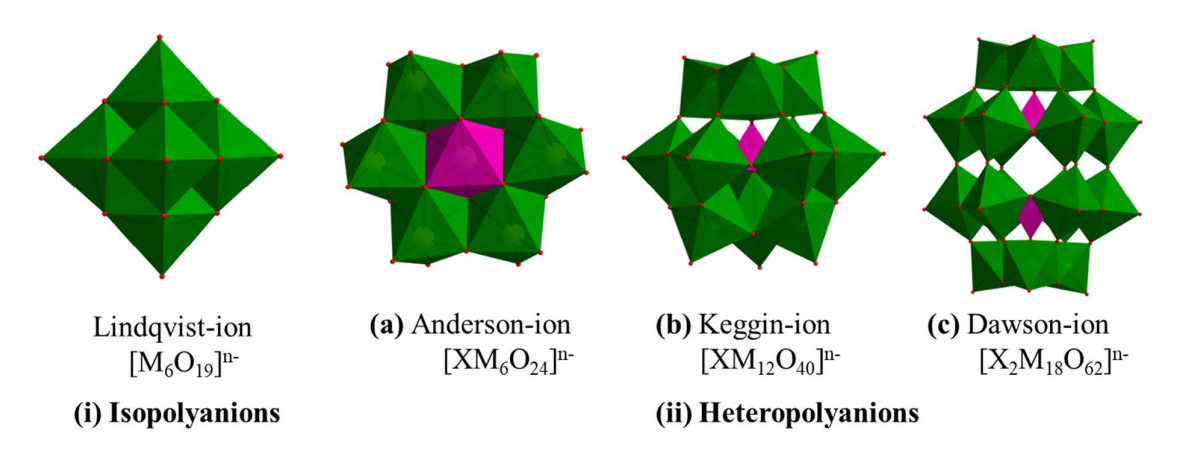


Figure 1.4 Classification of Polyoxometalates based on composition.

stability, and adjustable redox/ electronic properties e.g. Keggin, Anderson, Dawson POMs etc. (Figure 1.4)

#### (iii) Mo-blue/brown as reduced polyoxometalate clusters

Mo-blue and Mo-brown polyoxometalates are predominantly composed of molybdenum-based reduced polyoxometalate clusters. However, Muller et al. extensively worked on the exceptional size and structural complexity of such POMs and reported Mo<sub>154</sub> with high nuclearities and ring topology. All these subcategories of POMs are well documented; however, this thesis is mainly based on the heteropolyanions i.e. heteroatom containing POMs. These heteropolyanions can be further modified to lacunary and sandwich POMs as follows.

#### 1.3.1 Lacunary Polyoxometalate and transition metal substitution

Lacunary polyoxometalate clusters can be derived from Keggin/Dawson POMs by the removal of one or more addenda atoms. <sup>14</sup> These Lacunary POMs are then further used for the synthesis of transition metal-substituted polyoxometalates. <sup>15</sup> Depending on the number of removed addenda atoms, lacunary POMs are classified as mono-, di-, or tri-lacunary polyoxometalates. Figure 1.5 illustrates the polyhedral representation of mono-vacant and tri-vacant polyoxometalates. Removal of the entire M<sub>3</sub>O<sub>13</sub> triad group from the Keggin unit generates 'tri-vacant' or 'tri-lacunary' Keggin fragments, which serve as building blocks for multi-transition metal-substituted polyoxometalates such as sandwich or banana POMs. This thesis primarily focuses on tri-vacant lacunary Keggin POMs with various heteroatoms substitution of different 3d transition metals to form various sandwich and banana-type POMs. <sup>16</sup>

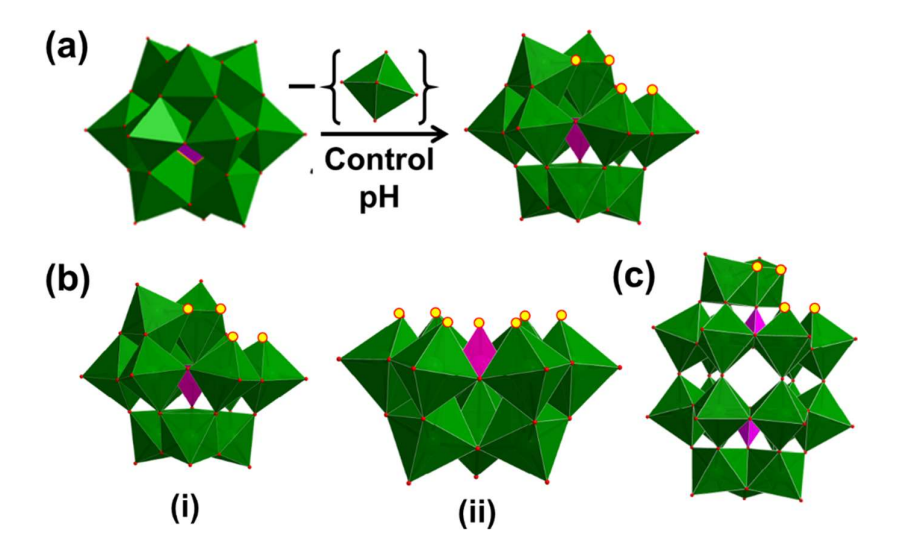
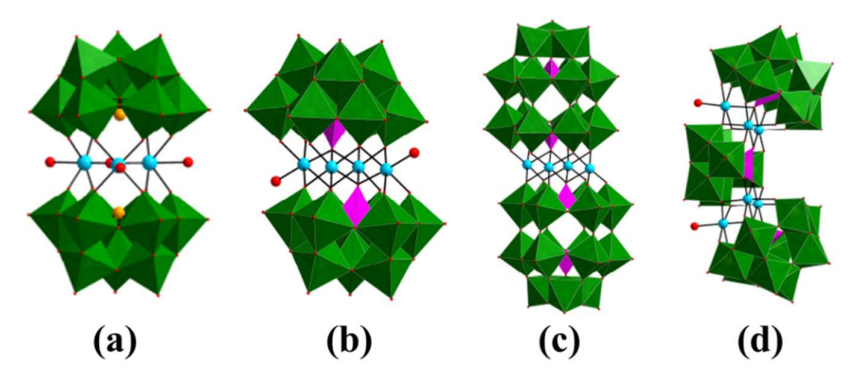


Figure 1.5 (a) Mono-vacant or mono-lacunary and (b) (i) mono and (ii) tri-vacant lacunary Keggin fragments; (c) mono-vacant Dawson POMs.

#### 1.3.2 Sandwich Polyoxometalates

Transition-metal substituted sandwich POMs (TMSPs) are potentially produced from trivacant lacunary POMs by the incorporation of lanthanide or transition metals in their vacant sites. <sup>17</sup> The Keggin and Wells Dawson POMs are more prone to produce these sandwich-like forms. Trivacant Keggin species, self-assemble in the presence of transition metals to form the sandwich structure, sometimes called the Weakley or Tourne structures. <sup>16</sup> This specific structure involves two tri-lacunary Keggin moieties {PW<sub>9</sub>O<sub>34</sub>}



**Figure 1.6** Transition metals substituted sandwich POMs based on tri-lacunary Keggin and Dawson POMs.

linked together by four cobalt centres, resulting in a sandwich-type polyanion denoted as  $[\text{Co}_4(\text{H}_2\text{O})_2(\text{PW}_9\text{O}_{34})_2]^{10}$ .

Because of their remarkable structural similarity to naturally occurring enzymes and cofactors, sandwich-type compounds are among the most important transition metal-substituted polyoxometalates. Because of their highly tunable structure and potential uses in a variety of catalysis, medical, and electrochemistry-related fields, tetrasubstituted sandwich-type transition-metal substituted polyoxometalates (TMSPs) based on Keggin POMs are the largest subclass thus gaining attention among TMSPs (Figure 1.6b). 18, 19

These tetrasubstituted sandwich-type TMSPs obtained from trivacant Keggin fragments  $[XW_9O_{33}]^{n-}$  or  $[XW_9O_{34}]^{n-}$  can be further divided into two subgroups : 1. Polyanions with central heteroatom X having no lone pair of electrons.

 $[M_4(H_2O)_2(XW_9O_{34})_2]^{n-}$  where X=P(V), Si(IV), Zn(II), Co(II), As(V). They are also known as Weakley POMs.<sup>20, 21</sup>

2. Polyanions with central heteroatom X having lone pair of electrons.

 $[(M_xM'_{6-x})(XW_9O_{33})_2]^{n-}$  where X=Bi(III), As(III), Sb(III), Te(IV) And  $[(M_2M'_2)(XW_9O_{34})_2]^{n-}$  where X=Bi(III), Sb(III) known as Krebs POMs.<sup>22</sup>

#### 1.4 General characterization methods of polyoxometalates

For the characterization of polyoxometalate clusters, several techniques like vibrational spectroscopy (Infrared, Raman), electrospray ionization mass (ESI-MS) spectrometry, single-crystal X-ray diffraction (SC-XRD) analysis, UV-visible spectroscopy, diffuse reflectance spectroscopy (DRS), nuclear magnetic resonance (NMR) spectroscopy, and electrochemical techniques are commonly used. Each of these methods contributed to the final molecular structure or the characteristics of electronic properties of polyoxometalates.

**Infrared (IR) and Raman spectroscopy** are the preliminary techniques for the characterization of polyoxometalates. FT-IR/Raman spectra of polyoxometalates show intense peaks in the range of 600-1100 cm<sup>-1</sup> for M=O<sub>t</sub>, X-O, and M-O<sub>c/e</sub>-M (M = W, Mo, V, etc., addenda atoms; and X = P, Si, etc., heteroatom, O<sub>t</sub> is terminal oxygen and O<sub>c/e</sub> is corner or edge sharing oxygen) bond vibrations which predominate over the TM-O (TM = transition metal) bond vibrations in transition metal substituted polyoxometalates.<sup>23</sup> However, without a reference spectrum of the pure chemical, it is challenging to distinguish between a mixture of identical polyoxometalate structures.

**Nuclear magnetic resonance (NMR) spectroscopy** is a useful spectroscopic technique for identifying the NMR active nucleus (<sup>31</sup>P, <sup>51</sup>V, <sup>29</sup>Si, <sup>183</sup>W, etc.) in the solution to characterize and determine the purity of POMs. <sup>16</sup> For example, <sup>31</sup>P/<sup>51</sup>V NMR is crucial for study of

decomposition of POMs in solution. Recently, solid state <sup>183</sup>W NMR have drawn attention due to their uniqueness in identifying isomeric structures as well as presence of different type of POMs at a time.

**Electrospray ionization mass spectrometry (ESI-MS)** is also used to investigate the stability of polyoxometalate anions in the solution state. Generally, ESI-MS spectra show the single or multiple envelopes of peaks with their associated charges of polyoxometalate anions present in the solution. ESI-MS detection is little cumbersome, however, give very accurate information of the polyanion species along with total charge at POM cluster.<sup>24</sup>

**Single Crystal X-ray diffraction (SC-XRD) analysis** is the most promising tool for studying polyoxometalates in solid-state. Since the most polyoxometalates are crystalline solids, SC-XRD analysis is the most convenient and traditional method for the structural investigation of polyoxometalates.

**Powder X-ray diffraction (PXRD) analysis.** PXRD analysis is mostly used to characterize polyoxometalate-based composite materials. It demonstrates the existence of parent polyoxometalate in the final composite as well as potential interactions between them. Another important information from PXRD can be obtained is comparison between the simulated XRD pattern of SC-XRD and bulk of the crystals.<sup>25</sup>

**Thermogravimetric analysis (TGA):** The number of hydrated water molecules in a polyoxometalate molecule and the thermal stability of polyoxometalates are calculated using TGA. The weight percentage of polyoxometalates in the composite may also be determined from the comparative TGA traces of the parent polyoxometalate and polyoxometalate-based composite materials.<sup>26</sup>

**UV-visible spectroscopy** is used to understand the electronic properties as well as the stability of polyoxometalates in solution. POMs usually show a strong absorption band due to ligand-to-metal charge transfer (LMCT) spectra (O  $\rightarrow$  transition metal) along with the d-d transition of the transition metal (TM) present in TMSP complexes. Sometimes, they show a feeble peak of metal-to-polyoxometalate charge transfer (MPCT) in the visible region in the range of 400-600 nm.  $^{27-29}$ 

**Diffuse Reflectance spectroscopy (DRS)** is used to calculate optical band gap of POMs using Kubelka-Munk equation and plotting the graph between the energy axis and Kubelka-Munk function.<sup>30</sup> The optical band gap in POMs is generally defined as the difference between the

oxo band (highest occupied molecular orbital, HOMO) and the empty metal band (lowest unoccupied molecular orbital, LUMO).

#### **Computational studies of POMs**

Several research groups have carried out theoretical investigations on the electronic and redox properties of POMs in the past decades, the primary goal being to characterise the properties of their most important molecular orbitals. Using the model potential Xα technique, N. Yamazoe and colleagues pioneered POM computational analysis in 1986. M. Bénard, M. M. Rohmer, and associates used the more accurate Hartree-Fock Self-Consistent Field (HF-SCF) approach in their studies in the early 1990s. To evaluate the relative basicity of the exterior oxygen sites of the [V<sub>10</sub>O<sub>28</sub>]<sup>6</sup> anion, they performed ab initio calculations. However, for transition metals, the HF-SCF approach usually produces significant inaccuracies, which led to a move towards Density Functional Theory (DFT) techniques, which are carried out with the use of programmes such as the Gaussian package.<sup>31</sup> DFT methods can process simulations with hundreds of atoms, although they need a substantial amount of computing time. However, they provide reliable information on the electronic characteristics and geometrical arrangements of various atomic species, including big molecules and metals. Modern DFT computations now incorporate a linear combination of Gaussian-type functions (GTOs) as atomic orbitals, along with the incorporation of additional physical effects such as hybrid functionals, large atomic basis sets, solvation effects, and relativistic effects, which were previously overlooked.<sup>32, 33</sup> Incorporation of the solvent effects as an approximation by continuum models such as COSMO and PCM revealed fundamentals for the accurate modelling of various POMs properties, such as reactivity and electrochemistry. 32, 34

A basis set is a mathematical set of orbitals employed in theoretical calculations to approximate the electronic structure of a system. In molecules, each atom is assigned a group of basis functions to describe its orbitals. For atoms like transition metals Mo and W in POMs, a common choice is the standard 2-double-zeta LANL2DZ basis set. Oxygen atoms are typically described using the 6-31G (d, p) basis set.<sup>35</sup> One significant advantage of using Gaussian computational software is its efficient implementation of hybrid functionals. These functionals combine aspects of both Hartree-Fock theory and density functional theory, allowing for accurate and computationally feasible calculations of electronic properties in complex molecules like POMs.

#### 1.5 Synthetic strategy for sandwich polyoxometalates and its requirement

Polyoxometalates (POMs), particularly sandwich-type POMs, have emerged as promising candidates for water oxidation, facilitating the development of robust and efficient catalysts under neutral conditions. Although numerous POMs-based water oxidation catalysts have been documented in the past two decades, however, breakthrough research is non-noble metal-based tetra-cobalt sandwich polyoxometalate [Co<sub>4</sub>(H<sub>2</sub>O)<sub>2</sub>(PW<sub>9</sub>O<sub>34</sub>)<sub>2</sub>]<sup>10</sup> for its higher activity for oxygen evolution reaction in 2010. After that, congeners structure such as  $[Co_4(H_2O)_2(VW_9O_{34})_2]^{10-} \; ; \; [Co_4(H_2O)_2(PMo_xW_{9-x}O_{34})_2]^{10-} \; and \; [Co_2Ni_2(H_2O)_2(PW_9O_{34})_2]^{10-}$ have shown promising water oxidation activity at neutral pH conditions.<sup>36, 37</sup> Due to the extensive range of possible structural designs, ongoing research aims to identify and optimize efficient water oxidation catalysts based on polyoxometalates, especially tetrasubstituted sandwich POMs. Tetrasubstituted sandwich POMs can be synthesized via two different methods. The first method involves the synthesis and isolation of tri-vacant polyoxometalate fragments, followed by the addition of transition metals in a separate step and subsequent synthesis of sandwich polyoxometalates. Alternatively, sandwich polyoxometalates can be synthesized directly in a single "one-pot" reaction without isolating the lacunary or fragment polyoxometalates. In both approaches, the oxygen atoms located at the lacunary sites of trivacant Keggin fragments (or tri-vacant lacunary polyoxometalates) exhibit sufficient reactivity to accommodate transition metal atoms, facilitating the formation of sandwich polyoxometalates. Typically, tetra-metal sandwich polyoxometalates are constructed from Keggin and Wells-Dawson-based lacunary fragments. However, this thesis focuses only on tetra-metal or tetrasubstituted sandwich POMs based on lacunary fragments obtained from Keggin POMs.<sup>38</sup>

As POMs are widely used in photocatalysis, electrocatalysis, and photochromism because of their reversible redox characteristics and well-defined structures.<sup>39, 40</sup> Without compromising their structural integrity, these can reversibly accept multiple electrons. Because of this nature, POMs have the potential to operate as "electron switches," improving the efficiency and selectivity of electrocatalytic processes. POMs help to improve reaction activity and selectivity in electrochemical processes by facilitating the control of electron transfer routes with in catalytically active species. For example, uncontrolled multiple electron/protons coupling activities in the carbon dioxide reduction reaction (CO<sub>2</sub>RR) provide multiple reaction pathways that result in a range of products. Low selectivity and low faradaic efficiency are the results of this complexity. The CO<sub>2</sub>RR process is further complicated by the extra competitive response brought about by this closeness in potentials.<sup>41</sup>

These days, it is acknowledged that controlling proton transfer mechanisms in electrocatalytic reactions is essential for streamlining reaction pathways and enhancing product selectivity and faradaic efficiency. Similar to this, the process of electron transfer has a major influence on the kinetics, thermodynamics, and different paths of electrocatalytic processes. For instance, the quantity of electrons transported can have a significant impact on the reaction's results. For instance, methane requires eight electrons to be created, but carbon monoxide just needs two. These reaction pathways can be controlled using POMs, however, it is equally important to choose a particular POM to control the selectivity of the product. For that, we need to study the structure-property relationships in POMs, which can be helpful for target reactions based on their structural properties.

#### 1.6 Structure-property relationship

Polyoxometalates exhibit versatile behaviour as both Lewis acids and bases due to their composition featuring oxygen atoms and transition metals in high oxidation states. The metal ions within their structure can act as Lewis acids by accepting electrons, while the surface oxygen atoms of POMs can donate electrons, functioning as soft Lewis bases. For example, Keggin POMs, such as  $H_n[XM_{12}O_{40}]$  (where X = P, Si; M = W or Mo; and n = 3, 4), possess significantly higher Bronsted acidity compared to conventional mineral acids. However, a variety of factors, including solvent, POM and cation interactions, and covalently linked organic groups can influence the redox properties of POMs.<sup>40</sup>

POMs are highly valued for their exceptional ability to participate in multi-electron redox reactions and their considerable electrons donating and accepting capacity, making them effective electron reservoirs in diverse chemical reactions. The basicity of POMs can be influenced and stabilized by protic solvents, while electron transfer between POMs and covalently bonded organic group can modulate their electron up take and donation capabilities. Additionally, the electrical, structural, and solubility properties of polyoxometalates are significantly impacted by the nature of their counter cations. <sup>43</sup> To maintain charge balance in POMs, a large varieties of counterions can be utilized by Ion exchange processes to facilitate the substitution of different cations. Inorganic cations (e.g., H<sup>+</sup>, Na<sup>+</sup>, K<sup>+</sup>, Cs<sup>+</sup>, NH<sub>4</sub><sup>+</sup>) are commonly used in various applications. While, organic cations offer additional benefits due to their ability for required modification with diverse functional groups and metals, offering tailored properties suitable to meet specific application requirements. The unique solubility characteristics of POMs in a wide range of solvents, including aqueous, non-aqueous, and fluorous (particularly perfluorinated) solvents, distinguish them as "molecular" metal oxides

with highly specialized capabilities. Adjusting the counter cations, POMs can be dissolved across a broad range of solvents, encompassing organic, aqueous, and highly nonpolar fluorous solvents (Figure 1.7b). This capability contrasts sharply with traditional metal oxides like zeolites, which typically exhibit limited solubility in such a diverse solvent environment. <sup>44</sup> In aqueous media, POMs readily dissolve when paired with smaller counter cations such as H<sup>+</sup>, Li<sup>+</sup>, Na<sup>+</sup>, K<sup>+</sup> etc. This adaptability highlights the distinct solvation behaviour of POMs, enabling their application in various solvent-dependent processes and technologies. <sup>45</sup>

POMs exhibit versatility in their solubility across organic and fluorous solvents, supporting applications in both homogeneous and heterogeneous catalysis. This solubility is achieved by substituting their counter cations with organic or fluorous cations that feature suitable alkyl and perfluoroalkyl chains. Conversely, employing counter cations like Cs<sup>+</sup>, NH<sub>4</sub><sup>+</sup>, or cationic polymers can render POMs insoluble. <sup>43</sup> Beyond their role in catalysis, this adjustable solubility distinguishes POMs by enabling the creation of multifunctional composite materials. <sup>46-48</sup> These

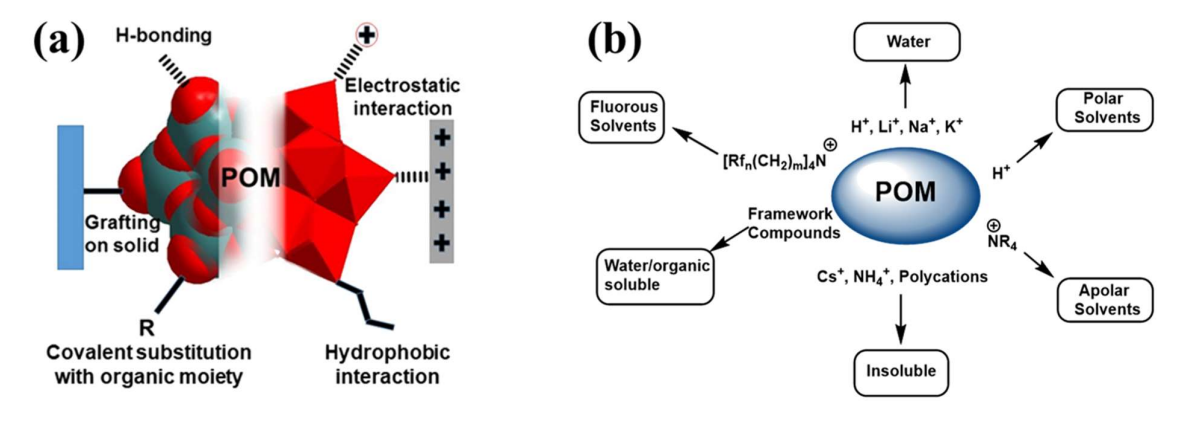


**Figure 1.7** (a) Different types of interactions in POM-based materials; (b) Counter ion-dependent diversified tunable solubility of POMs.

materials leverage the unique properties of polyoxometalates for diverse real-world applications, highlighting their potential in fields requiring tailored solvation properties.

#### 1.7 Redox properties of POMs

The formal redox potential is strongly influenced by several variables, including the type and nature of addenda and heteroatom. <sup>49</sup> For example, the redox potential of the incorporated metal increases proportionally with the formal charge on the heteropolyanion. As size and electronegativity of X decrease, the redox potential increases for a given oxidation state. Specifically, Mn(III/II) redox potential increases with X, where X follows the order  $B < Zn < Si\backslash Ge \backslash P$ . <sup>50, 51</sup>

Pope classified POMs into three categories based on the coordination environments of their addenda atoms<sup>52</sup>. In type-I polyanions, each addendum is coordinated to one terminal oxo ligand. Type-II polyanions feature two terminal oxo ligands per addendum atom, while type-III polyanions exhibit characteristics of both type-I and type-II. According to molecular orbital theory, octahedral metals in type-I polyanions, with one unshared oxo ligand possess an unoccupied non-bonding  $t_{2g}$  orbital that can be filled during reduction processes. It has been hypothesized and experimentally observed that only type-I and type-III polyanions possess reversible reduction capabilities. In type-II polyanions, the  $t_{2g}$  orbitals are usually involved in  $\pi$ -bonding interactions, thus making  $t_{2g}$  orbitals unavailable for non-bonding. For example, no reduction has been reported up to now for the octamolybdates ([Mo<sub>8</sub>O<sub>26</sub>]<sup>4-</sup>) or Anderson-type anions ([XMo<sub>6</sub>O<sub>24</sub>]<sup>n-</sup>, where X is a heteroatom and M is Mo/W).

Compared to isostructural polyoxotungstates; POM(W), which are the heavier Group VI complexes, polyoxomolybdates; POM(Mo) shows lower reduction potentials. As a result, reduction preferentially occurs at Mo sites in mixed-addenda (Mo/W) POMs. POM(Mo) usually show redox potentials around 400 mV more positive than those of corresponding POM(W)<sup>53</sup>. For example, in acetone, the redox couple for Mo is observed at -468 mV, while for W, it is observed at -895 mV for the  $[PM_{12}O_{40}]^{3-/4-}$  system. Also, in Keggin structure,  $[XM_{12}O_{40}]^{n-}$  (X = heteroatom; M = Mo/W), Mo derivative can accommodate up to 12 electrons, while the corresponding W derivative can only accept up to 6 electrons. By tuning the oxidation potential of addenda atoms in type I POMs in the order V(+5) > Mo(+6) > W(+6), it is possible to improve the electrochemical activity of these compounds and ensure consistent redox characteristics. For example, using mixed-addenda polyoxometalate, redox potential can be tuned as electron localization preferentially happens at the more reducible atom at room temperature. Set

#### 1.8 Electronic properties of POMs

J. M. Poblet and co-workers have been pioneers in the theoretical study of polyoxometalates (POMs) using Density Functional Theory  $(DFT)^{31,\,55}$ . They have extensively investigated the electronic and magnetic properties of the Keggin anion  $[XM_{12}O_{40}]^{n-}$ , where M = W/Mo, and X represents Si/P/Fe/Co, as well as  $[SiM_{11}VO_{40}]^{n-}$  POMs, where  $M = Mo/W^{31,\,56}$ . Their research has greatly contributed to the understanding of the structural, electronic, and magnetic properties of POMs, which are crucial for their potential applications in various fields of chemistry and materials science<sup>57</sup>. The Keggin POMs  $[XM_{12}O_{40}]^{n-}$ , the most prevalent type, features a straightforward electronic structure with doubly occupied orbitals predominantly

centered on the oxo ligands, distinctly separated from the unoccupied orbitals centered mainly on the metal atoms. The high oxidation states of the metal d-orbitals interact with the adjacent oxygen p-orbitals, leading to distortions in the  $MO_6$  octahedra from ideal  $O_h$  symmetry in fully oxidized Keggin POMs.<sup>58</sup>

Current understanding highlights the increased significance of orbital overlap between the metal's d<sub>xz</sub> and d<sub>yz</sub> orbitals and the terminal oxygen atom (O<sub>t</sub>) due to the shortened M-O<sub>t</sub> bond length and favourable orientations. As a result, the lowest unoccupied molecular orbital (LUMO) of POMs is characterized by symmetry-adapted combinations of dxy-like orbitals, with very low energy levels, making fully oxidized POMs readily reducible in solution<sup>59</sup>. In Keggin POMs, the energy gap between the occupied and unoccupied bands remains constant regardless of the heteroatom. Maestre et al. reported a steady HOMO-LUMO energy gap of approximately 2.8 eV for tungstates with various heteroatoms, while this value decreases to 2 eV for molybdates. The lower energy of the metal d-orbitals in molybdates makes them more easily reducible compared to tungstates. For instance, SiMo<sub>12</sub> and GeMo<sub>12</sub> exhibit stronger oxidizing capabilities, with an estimated 0.5 V advantage over their tungstate counterparts. Mixed-addenda POMs, where one or more M<sup>n+</sup>O<sub>6</sub> octahedra in [XM<sub>12</sub>O<sub>40</sub>]<sup>n-</sup> are replaced by units containing metals such as V<sup>5+</sup>, Nb<sup>5+</sup>, Mo<sup>6+</sup>, etc., significantly alter the electronic structure of the symmetric Keggin POMs. 60 Each substitution influences the energy and composition of the LUMO orbitals, thereby modifying the redox properties of the POM. The electron affinity of the M<sup>n+</sup> ion dictates the extent of these LUMO energy changes. The substitution of early transition metals such as V<sup>V</sup>, Nb<sup>V</sup> by W<sup>VI</sup> or Mo<sup>VI</sup> ions, has a profound impact on the redox characteristics of mixed addenda POMs, as observed theoretically and experimentally.

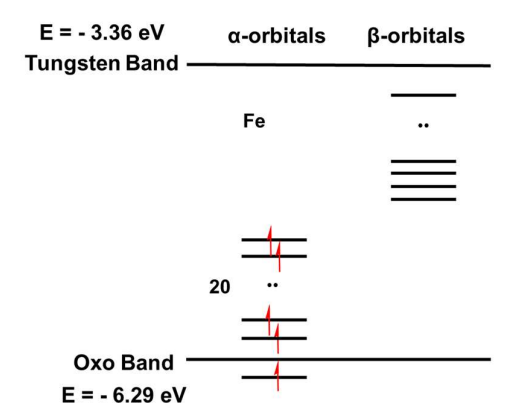


Figure 1.8 Representation of the electronic arrangements in [Fe<sub>4</sub>(H<sub>2</sub>O)<sub>2</sub>(PW<sub>9</sub>O<sub>34</sub>)<sub>2</sub>]<sup>6</sup>-.

The inclusion of transition metals in lower oxidation states (Co<sup>II</sup>, Ni<sup>II</sup>, Fe<sup>III</sup>, etc.) introduces additional complexity. This complexity is particularly notable in sandwich polyoxometalates, which have applications in catalysis and other fields; and are based on structures like Keggin and Wells-Dawson frameworks. In sandwich polyoxotungstates, a series of orbitals centred on the transition metals of the sandwich POMs are located between the "oxo band," consisting of the HOMO centred on oxygen atoms, and the "tungsten band," encompassing the LUMOs primarily associated with tungsten atoms. For instance, in the sandwich POM [Fe<sub>4</sub>(H<sub>2</sub>O)<sub>2</sub>(PW<sub>9</sub>O<sub>34</sub>)<sub>2</sub>]<sup>6-</sup>, the LUMO and HOMO (doubly occupied orbital) are found at -3.35 and -6.29 eV, respectively<sup>61, 62</sup>. Between these bands, 20 α spin orbitals (singly occupied molecular orbitals; SOMOs) centred on the Fe atoms are observed (Figure 1.8). Interestingly, the energy gap between these two bands remains consistent across different complexes, although it may vary depending on the functional parameters such as heteroatom or addenda atoms. The oxidizing capability of POMs arises from multiple metal centres in high oxidation states represents a crucial attribute as previously noted. M. T. Pope first described the influence of anionic charge by studying the electrochemical behaviour of different isostructural [XM<sub>12</sub>O<sub>40</sub>]<sup>n-</sup> Keggin POMs with varying heteroatoms. His research revealed that the reduction potential decreases by approximately -0.18 V per additional negative charge. 63

By systematically considering the total negative charge (q) and the number of metal atoms (m) within a POM framework, J. M. Poblet group demonstrated the broad applicability of the anion charge effect across POMs of various sizes and charges. They also established a mathematical correlation between a POM's oxidizing potential and the q/m ratio, which serves as a metric of molecular charge density. This ratio was initially introduced by the same group to highlight the importance of solvent effects in POM modelling. Notably, POMs with high q/m values, example of species like the Nb<sub>6</sub>O<sub>19</sub><sup>8</sup>- anion, require modelling description within an external field or solvent to avoid inaccuracies in molecular orbital energies and interatomic distances. Conversely, Keggin and Wells-Dawson POMs, with low-to-intermediate q/m ratios, maintain well-defined structures and are generally unaffected by solvation effects.<sup>64</sup> However, accounting for solvation effects consistently improves the accuracy of geometric parameters in these systems.

#### 1.9 Molecular orbital engineering

As molecular catalysts, the atomically precise structures of POMs make them ideal models to investigate the structure-property relationships. More importantly, their electronic structures can be easily tuned by choosing appropriate constituent elements (e.g., addenda atoms), metal

substitution, and functionalization with organic groups, leading to varied energy levels of highest occupied molecular orbital (HOMO) and lowest unoccupied molecular orbital (LUMO). 57, 65 The adjustment of electronic structures through molecular orbital engineering strategy can undoubtedly affect the catalytic efficiency such as, photocatalytic hydrogen evolution activity.<sup>66</sup> Recent studies have demonstrated the engineering of POMs HOMO/LUMO levels by the incorporation of organic ligands into lacunary POMs or by changing the composition of addenda atoms, leading to different electronic structures, light absorption profiles, and photocatalytic activities<sup>36</sup>. For example, a giant Mo/Ta/W ternary mixed-addenda POM was reported to show good catalytic activity in the oxidative coupling of primary amines to imines, which was attributed to its enhanced visible-light-responsive charge transfer ability by lowering the LUMO position through the introduction of Mo atom<sup>67</sup>. In photocatalytic hydrogen-evolving systems, the energy-level difference between the LUMO positions of the POM catalyst and the photosensitizer determines the electron transfer kinetics, thereby influencing the photocatalytic performance. 47, 68-70 In this context, we believe that the modulation of the LUMO energy level of POM catalysts via molecular orbital engineering strategy is an promising approach for optimizing the catalytic activity of POMs. 71 A simple strategy to tune the LUMO position would be introducing constitutional mix-addenda atoms.<sup>72</sup> Additionally, the incorporation of transition metals into these POMs raises the energy of HOMO energy, further tuning the band gap. Overall, incorporation of transition metals along with mixed addenda in the framework of sandwich POMs reduces the band gap from both directions (raising HOMO energy and lowering LUMO energy) thus making these POMs wellsuited for visible light absorption (Figure 1.9). 73 A considerable progress has been made in orbital engineering within Keggin and Dawson POMs, like a mixed-addenda approach by the inclusion of few Mo/V/Nb into W-based Keggin and Dawson POMs is reported for modulating the HOMO-LUMO levels. 74, 75 However, only a little known for sandwich and banana POMs. Tetrasubstituted Sandwich POMs [(TM)<sub>4</sub>(H<sub>2</sub>O)<sub>2</sub>(XW<sub>9</sub>O<sub>34</sub>)<sub>2</sub>]<sup>n-</sup> [TM=transition metal, X= hetero atoms, example P, Si, Zn, Co) have gained a lot of interest as efficient catalysts for various catalytic activities like energy conversion and storage devices, sensing, organic transformation, etc. The robust nature of sandwich POM and their catalytic activity is highly dependent on the transition metal core (TM<sub>4</sub>) and the addenda framework. <sup>76, 77</sup> Orbital engineering strategies in these POMs can offer versatile tool for fast electron transfer and large electron storage capacity, making them very impactful in catalytic applications. E.g., Cronin et. al. reported mixed addenda POM [Co<sub>4</sub>(H<sub>2</sub>O)<sub>2</sub>(PMo<sub>x</sub>W<sub>9-x</sub>O<sub>34</sub>)<sub>2</sub>]<sup>n-</sup>, which can overcome the sluggish kinetics in oxygen evolution reaction.<sup>36</sup>

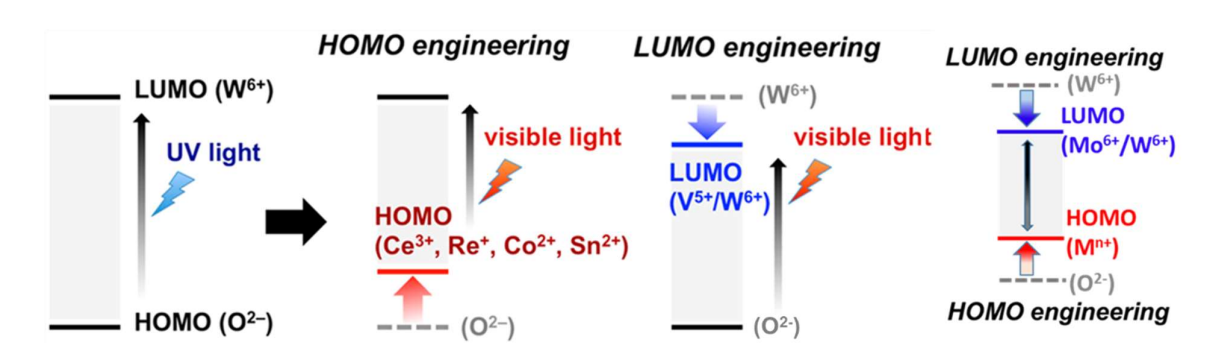
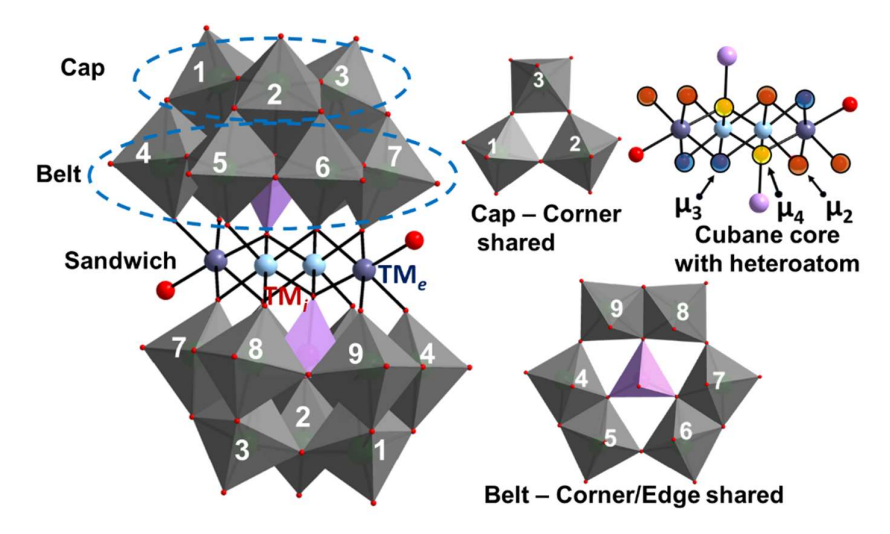


Figure 1.9 Different ways of band gap engineering in POMs.

#### 1.10 Structural description in sandwich POMs

Combined polyhedral/ball and stick representation of tetrasubstituted sandwich POMs<sup>16</sup> shows the position and type of oxygen present (corner/belt shared) as well as internal ( $TM_i$ ) and external ( $TM_e$ ) transition metals in sandwich position.  $\mu_2$ ,  $\mu_3$ , and  $\mu_4$  indicate the denticity of the different kinds of oxygen atoms connected to the transition metals. The 3D structure of these sandwich polyoxometalates can be broken into two parts: (I) tetranuclear cubane framework consisting of 3d transition metals at the sandwich position and (II) the trivacant Keggin framework. The trilacunary Keggin moiety contains a tetrahedrally bound transition metal or P-atom at the center as a templating agent to form triads of addenda W/Mo atoms. Four transition metals in the tetrasubstituted sandwich core are termed internal { $TM_i$ } and external atoms { $TM_e$ } (Figure 1.10).



**Figure 1.10** Different positions of substituted transition metals in sandwich POMs and their coordination mode with the POM framework.

Two internal transition metal atoms are connected with the Keggin framework octahedrally via oxygen atoms, while the external transition metal atoms  $\{TM_e\}$  are pentacoordinated with the trivacant framework through oxygen, while the sixth coordination is occupied by one water molecule making it pseudo-octahedral. There are a total of 34 oxygen atoms in the asymmetric unit of these sandwich POMs, of which 6 oxygen are corner shared  $(O_e)$ , 12 are edge shared  $(O_e)$ , 9 are terminal oxygen  $(O_t)$  atoms, and 7 oxygen atoms are bridging transition metals at the sandwich position with the trivacant framework; heteroatoms are tetrahedrally bound through  $\mu_4$ -oxygen. Both the internal transition metal atoms  $\{TM_i\}$  are bound to both side heteroatom through  $\mu_4$  oxygen and the framework through  $\mu_2$  and  $\mu_3$  oxygen, each type of oxygen lying on both sides of the transition metal. However, each external transition metal atom  $\{TM_e\}$  is bound to only one side heteroatom through  $\mu_4$  oxygen, while it is bound to the framework metals through two  $\mu_2$  oxygen on one side and two  $\mu_3$  oxygen on the opposite side with a water molecule as the sixth coordination site (Figure 1.10).

#### 1.11 Organic-inorganic hybrid polyoxometalates

Polyoxometalates can form an enormous number of functional organic-inorganic hybrids either by tuning the organic countercation or by tuning the polyoxometalate cluster anion. The organic-inorganic hybrids can be classified into two categories depending on the nature of the interaction (non-covalent or covalent) between the inorganic part of the polyoxometalate cluster and organic moiety.<sup>78</sup> In one category, organic-inorganic hybrids are formed either through electrostatic force of interactions or hydrogen bonding and/or van der Waals interactions. In another category, organic moieties are covalently linked to the inorganic polyoxometalate clusters to form the hybrid material (Figure 1.11). The modification of inorganic polyoxometalate clusters by organic moieties by either of these two categories leads to the formation of novel polyoxometalate-based hybrids.<sup>79</sup>

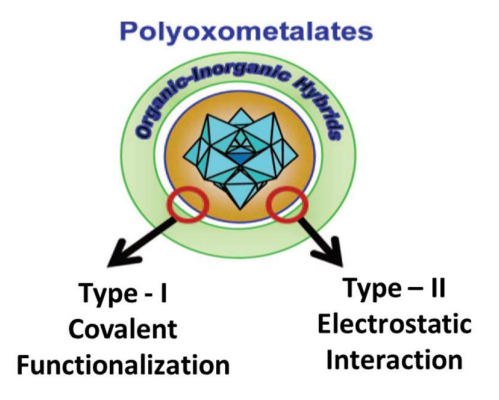


Figure 1.11 Classification of POMs-based inorganic-organic hybrids based on different interactions.

Polyoxometalates show various mode of interactions because of their negative charge and surface oxygen atoms. Since polyoxometalates are anionic, they can interact electrostatically with the cationic species or positively charged solid surface of material, and they can also interact with proton donors by hydrogen bonding. Additionally, the covalently attached organic moieties of polyoxometalates can interact with other molecules, complexes, and polymers via non-covalent interactions. The organic moieties can be covalently attached to the polyoxometalate cluster via addenda organometallic compounds.

#### 1.12 Aim of thesis

The tetra-metal substituted sandwich polyoxometalates are of particular interest because of their robust nature, multi-electron redox property, easily accessible active sites and scope of various transition metal incorporation. 80,81 The tetra-metal core, heteroatom and addenda atoms are highly tuneable for the construction of distinct sandwich polyoxometalate clusters and subsequently, the physical and electrochemical properties can be tuned.<sup>7, 70, 82, 83</sup> The sandwiched transition metal atoms can be replaced by other transition metal atoms to construct mixed metal sandwich polyoxometalates. For example, by substituting the external Zn-atoms of tetra-metal sandwich polyoxometalate  $[Zn_2Fe_2(H_2O)_2(ZnW_9O_{34})_2]^{14}$  **Zn-Zn<sub>2</sub>Fe<sub>2</sub>**, various transition metal substituted polyoxometalates [(TM)<sub>2</sub>Fe<sub>2</sub>(ZnW<sub>9</sub>O<sub>34</sub>)<sub>2</sub>]<sup>q-</sup> **Zn-Zn<sub>2</sub>(TM)<sub>2</sub>** (where, TM= Mn, Ni, Fe, Cu) are prepared. We also propose a mixed addenda with mixed metal (TM<sub>4</sub> core) strategy to modulate the frontier molecular orbitals (FMO) in these POMs. But neither such mixed addenda with mixed metal sandwich POMs are known nor any synthetic strategy. This thesis presents a systematic cooperative mix-metal approach, demonstrating the successful synthesis of mixed metal-mixed addenda POMs. We meticulously characterized all the POMs by Single crystal-XRD, ESI-MS and XPS analysis and validated the orbital modulation by various spectroscopy and DFT studies.

This thesis addresses the following key aims in polyoxometalate science -

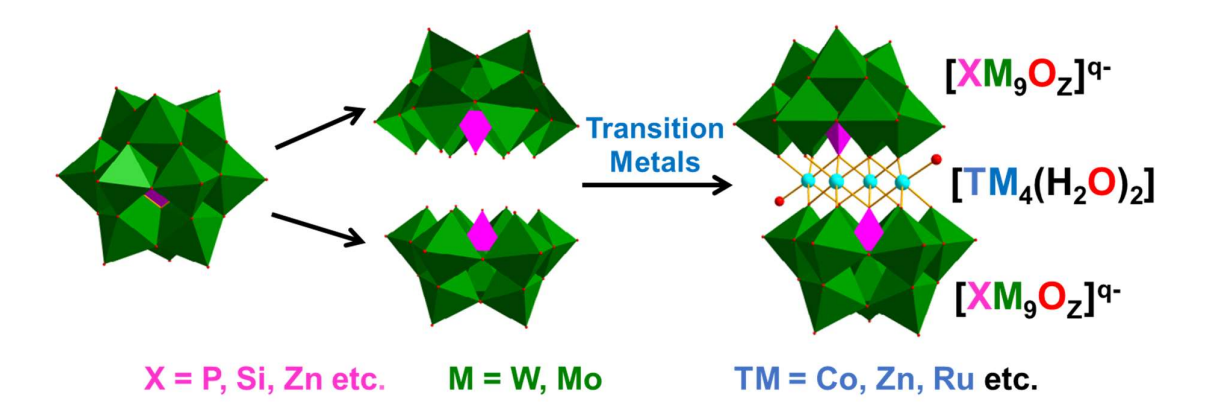
- (i) Mixed addenda in Sandwich and Banana POMs Mixed addenda in sandwich POMs can be an effective tool for orbital engineering. So far, transition metal incorporation raises HOMO levels but using mixed addenda in these POMs can be used for LUMO engineering. This approach can be further explored for the synthesis of mixed addenda Banana-type POMs, a previously unexplored POM.
- (ii) Cooperative mixed metal approach In sandwich POMs, typically a single type of transition metals at sandwich position (M<sub>4</sub>) is known, however, it possesses synthetic challenges for various transition metal, as only a few transition metals have been

reported. Here, we propose mixed metals (M<sub>2</sub>M'<sub>2</sub>) at the sandwich position in the same or different oxidation states to understand their cooperative effect. The cooperative mixmetal approach would be a versatile synthetic strategy for mixed metal-mixed addenda POMs synthesis and also as an effective tool for orbital engineering, which can influence the overall band gap, charge transfer (especially metal to POM charge transfer - MPCT), modulation of electron density, and SOMO; HOMO-LUMO orbitals.

(iii) Cooperative effect inorganic-organic hybrids - A cooperative mixed metal strategy with organic ligands approach is proposed for the design and synthesis of new inorganic-organic hybrids with tuneable orbital for designing more active catalysts. This approach can help in substantial progress in the development of novel heterogeneous materials based on POMs and opens the access to a broader range of structural modifications with diverse functionalities.

#### Description of the research work

The tetra-metal sandwich polyoxometalates can be synthesized in two ways. Firstly, the synthesis and isolation of tri-vacant or di-vacant polyoxometalate fragments followed by the sandwich polyoxometalate synthesis in the second step. Secondly, sandwich polyoxometalates can be synthesized in 'one-pot' without isolating the lacunary or fragment POMs.



**Scheme 1.1** Schematic presentation of the synthesis of tetra-metal sandwich POMs.

The oxygen atoms of lacunary sites of tri-vacant Keggin fragments (or tri-vacant lacunary polyoxometalates) are sufficiently active to accommodate the transition metal atoms to form the sandwich polyoxometalates as shown in Scheme 1.1

#### **Chapter 1: Introduction to Polyoxometalates**

This chapter represents an overview of polyoxometalate chemistry, especially the structure, and properties with further emphasis on the band gap modulation in Sandwich POMs. Sandwich polyoxometalates are transition metal substituted polyoxometalate where transition metals are sandwiched between the lacunary polyoxometalate fragments. Because of their remarkable structural similarity to naturally occurring enzymes and cofactors, and potential uses in a variety of catalysis, medical, and electrochemistry-related fields, sandwich-type compounds are among the most important transition metal-substituted polyoxometalates (TMSPs) which have been discussed in the introduction.

## Chapter 2: Modulation of Band Gap and Redox Properties in Mixed-Addenda Sandwich Polyoxometalates

In this chapter, we have targeted transition metal-based Sandwich POMs with phosphorus as heteroatom with the formula  $[(TM)_4(H_2O)_2(PMo_xW_{9-x}O_{34})_2]^{10}$  **P-(TM)**<sub>4</sub>**Mo**<sub>x</sub>**W**<sub>18-x</sub> where TM=Mn/Co/Ni/Zn. Due to the wide range of applications of band-gap engineering in optoelectronics and photocatalysis, the rational design of polyoxometalate (POM) frameworks is highly desired. Here, we have successfully synthesized a series of mixed addenda (Mo and W) sandwich POMs by systematically varying pH, concentrations of salts, and counterions in Weakley-type sandwich POMs by incorporating Mo into the framework of tetrasubstituted sandwich POMs. Crystallographic analysis reveals the centrosymmetric structure; with variation in Mo to W ratio, Mo preferentially binds to  $\mu_2$  oxygen connected to transition metals in the sandwich position. UV-visible spectroscopy, electrochemical, and theoretical modelling rationalize the band-gap modulations. Theoretical studies and cyclic voltammograms indicate that during the reduction, the incoming electrons preferentially go to substituted transition metals followed by Mo. Flat band potential calculated from the Mott-Schottky enables tuning of the electronic properties of composites based on these sandwich POMs. Moreover, the binding and activation studies of these polyoxometalates have been highlighted. Further, orbital engineering using mixed metals at sandwich position have been performed.

# Chapter 3: Construction of mixed addenda polyoxometalates by cooperative self-assembly and tuning of optoelectronic properties

This chapter deals with the incorporation of high oxidation state transition metals at an internal sandwich position to modulate optoelectronic properties as well as incorporating mixed addenda in sandwich POMs. Using low oxidation state precursor metals introduces the formation of frameworks in sandwich POMs. This chapter is further divided into two sections (3A and 3B).

## Section 3A: Interplay of transition metals at an internal sandwich position towards modulation of the optoelectronic properties

The orbital engineering by the cooperative effect of different transition metals (TM) proves to be a highly impactful and versatile approach for regulating the chemistry of polyoxometalates (POMs) either by introducing novel POMs or through POM-hybrids for designing more effective catalysts. Here we present a cooperative mix-metal strategy for the synthesis of mixed addenda (Mo/W) sandwich POMs, denoted as [(TM<sub>i</sub>)<sub>2</sub>(TM<sub>e</sub>)<sub>2</sub>(H<sub>2</sub>O)<sub>2</sub>(XMo<sub>x</sub>W<sub>9-x</sub>O<sub>34</sub>)<sub>2</sub>]<sup>n</sup>-(TM<sub>i</sub>(III)=Mn/Fe and TM<sub>e</sub>(II)=X=Zn/Co/Fe). Structural analysis of these POMs show that the incorporation of Mo addenda in (Mo/W) POM framework is highly influenced by the variation of transition metals at sandwich core and their oxidation states and pH of the media. ESI-MS analysis provides detailed POM compositions, while UV-vis spectra, and complementary density functional theory (DFT) analysis reveal orbital engineering through distinctive charge transfer processes.

### Section 3B: Role of charge density towards framework structures in sandwich Polyoxometalates

This section deals with the role of charge density or oxidation state of precursor metals towards the formation of framework compounds in sandwich POMs. The formation of frameworks has been further understood through the DFT study. Further, the role of framework towards Mo incorporation has been highlighted. This cooperative mixed metal-mix addenda strategy has been extended to the formation of 1-D polyoxometalate cluster frameworks (POMCFs), where oxidation state of precursor metals plays a vital role impacting the overall structural attributes.

### Chapter 4: Construction of trimetallic sandwich polyoxometalates towards optoelectronic properties modulation

This chapter deals with the introduction of high oxidation state transition metals at the internal sandwich position thus facilitating the substitution of transition metals at the external sandwich position while changing heteroatoms results in structural modifications in these TMSPs thus impacting their physiochemical as well as optoelectronic properties. This chapter has been divided in two sections (4A and 4B)

### Section 4A: Modulation of optoelectronic properties in trimetallic sandwich polyoxometalates via the interplay of external sandwich position

The physico- and electrochemical behavior of a series of  $[Zn_2Fe_2(H_2O)_2(ZnW_9O_{34})_2]^{14}$  **Zn-Zn<sub>2</sub>Fe<sub>2</sub>**,  $[Co_2Fe_2(H_2O)_2(CoW_9O_{34})_2]^{14}$  **Co-Co<sub>2</sub>Fe<sub>2</sub>**, and its first-row transition metal)

substituted analogues [(TM)<sub>2</sub>Fe<sub>2</sub>(ZnW<sub>9</sub>O<sub>34</sub>)<sub>2</sub>]<sup>q-</sup> **Zn-Zn<sub>2</sub>(TM)<sub>2</sub>** (where, TM= Mn/Ni/Fe/Cu) are reported. Various spectroscopic studies FT-IR, UV-visible, ESI-mass and Raman etc., show similar spectral patterns in all sandwich POMs because of their isostructural geometry and constancy of overall negative charge (-14). However, the electronic properties highly depend on the transition metals at the 'sandwich core' and correlate well with DFT study. Further, depending on the substituted TM-atoms, there is decrease in HOMO-LUMO bandgap energy in these TMSP complexes w.r.t **Zn-Zn<sub>2</sub>Fe<sub>2</sub>** as confirmed by diffuse reflectance spectroscopy and DFT study.

### Section 4B: Framework Switch in Trimetallic Sandwich Polyoxometalates Control by Heteroatom and Oxidation State

This chapter deals with the role of transition metals at the hetero-position towards structural transformation thus facilitating the functionalization of transition metals at the external sandwich position using organic ligands thus impacting their physiochemical as well as optoelectronic properties.

### Chapter 5: Design of Polyoxometalates-based inorganic-organic hybrids for task-specific application

Apart from structural parameters, these TMSPs can be used to form POM-organic hybrids either by covalent functionalization (class-A hybrids)<sup>84</sup> or by electrostatic interaction by exchanging countercations (class-B hybrids).<sup>43</sup> The countercations and organic anchoring groups largely impact the electronic, crystallographic, and solubility properties of the polyoxometalates. In this regard, class-A hybrids have been synthesized and explored for modulating solid-state luminescence properties (**Chapter 5A**) while Class-B hybrids have been used for adhesive application in seawater and anticorrosive coatings (**Chapter 5B**).

# Section 5A: Microwave-assisted synthesis of transition metals substituted sandwich Phosphomolybdates

Here, we have targeted the synthesis of molybdenum-based sandwich POMs synthesis using cooperative effect of transition metals at sandwich position and organic ligands using covalent bonds. Using this cooperative effect, sandwich POMs with the formula  $[Na_2(TM)_2(H_2O)_2(PMo_6O_{22})_2(R)_6]^{n-}$  where TM=Mn/Co/Ni/Zn, and R= OAc, Ogly, OOCCH<sub>3</sub> and these have been further investigated towards solid state luminescence.

#### Section 5B: Self-assembled Polyoxometalate-based Nanohybrids for Corrosion-Resistant Underwater Adhesive

The development of underwater adhesives with rapid and strong adhesion is crucial for various applications, including underwater repairs, soft robotics, medical devices, and water-based energy systems. However, shortening the time for bonding process often leads to premature bonding and weakend adhesion. Such trade-off becomes more pronounced in the presence of interfacial water especially saltwater, which disrupts the adhesive-adherend interactions. Here we present a simple synthesis for hydrophobic polyoxometalates-polymer adhesives that exhibit outstanding underwater adhesion strength of up to 3.5 MPa with remarkable reversibility and a significantly faster bonding time of 1 minute. These adhesives are versatile and capable of bonding a wide range of surfaces, including glass, metals, and polymers with high strength. Interestingly, they demonstrate excellent stability at very low temperatures. Additionally, they maintain performance under submerged seawater conditions with a remarkable corrosive inhibition efficiency of 85% at stainless steel substrate in seawater.

#### **Chapter 6. Conclusions and future aspects:**

This doctoral thesis explores various possibilities of orbital engineering in sandwich POMs based on 3d transition metals through experimental as well as theoretical studies (Figure 1.12).

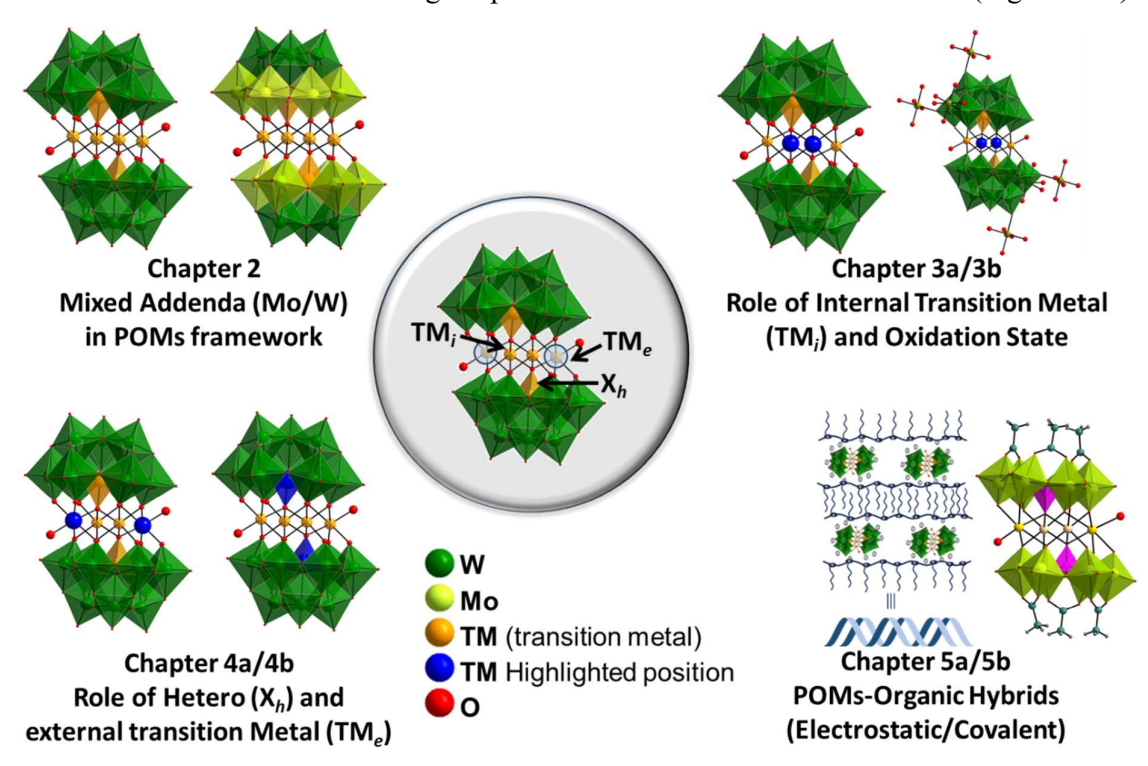


**Figure 1.12** Orbital engineering highlighting the role of various positions towards structure-property relationship in sandwich POMs.

It presents a comprehensive analysis of band gap engineering trends in sandwich POMs, offering insights that could guide the design of POMs-based materials for applications in photocatalysis, electrocatalysis, photovoltaics, and advancement in optoelectronics. Additionally, the interplay between inherently anionic POMs and organic anchoring groups plays a crucial role in influencing the self-assembly, stabilization, solubility, and functions of POMs. So, chapter 5 delves into how these POMs can be customized for specific applications by adjusting the covalent or electrostatic attachment of organic anchoring groups.

#### 1.13 References

- 1. Pope, M. T.; Jeannin, Y.; Fournier, M., Heteropoly and isopoly oxometalates. Springer: 1983; Vol. 8.
- 2. Miras, H. N.; Yan, J.; Long, D.-L.; Cronin, L., Engineering polyoxometalates with emergent properties. *Chem. Soc. Rev.* **2012**, *41* (22), 7403-7430.
- Miras, H.; Long, D.-L.; Cronin, L., Exploring self-assembly and the self-organization of nanoscale inorganic polyoxometalate clusters. In *Advances in Inorganic Chemistry*, Elsevier: 2017; Vol. 69, pp 1-28.
- 4. Jeannin, Y. P., The nomenclature of polyoxometalates: how to connect a name and a structure. *Chem. Rev.* **1998**, *98* (1), 51-76.
- 5. Ma, P.; Hu, F.; Wang, J.; Niu, J., Carboxylate covalently modified polyoxometalates: From synthesis, structural diversity to applications. *Coord Chem Rev* **2019**, *378*, 281-309.
- 6. Katsoulis, D. E., A survey of applications of polyoxometalates. Chem. Rev. 1998, 98 (1), 359-388.
- 7. Suzuki, K.; Mizuno, N.; Yamaguchi, K., Polyoxometalate photocatalysis for liquid-phase selective organic functional group transformations. *ACS Catal.* **2018**, *8* (11), 10809-10825.
- 8. Yamase, T., Photo-and electrochromism of polyoxometalates and related materials. *Chem. Rev.* **1998**, 98 (1), 307-326.
- 9. Baker, L.; Glick, D. C., Present General Status of Understanding of Heteropoly Electrolytes and a Tracing of Some Major Highlights in the History of Their Elucidation. *Chem. Rev.* **1998**, *98* (1), 3-50.
- 10. Keggin, J., Structure of the crystals of 12-phosphotungstic acid. *Nature* **1933**, *132* (3331), 351-351.
- 11. Long, D.-L.; Burkholder, E.; Cronin, L., Polyoxometalate clusters, nanostructures and materials: From self assembly to designer materials and devices. *Chem. Soc. Rev.* **2007**, *36* (1), 105-121.
- 12. Vilà-Nadal, L.; Cronin, L., Design and synthesis of polyoxometalate-framework materials from cluster precursors. *Nat. Rev. Mater.* **2017**, *2* (10), 1-15.
- 13. Gumerova, N. I.; Rompel, A., Polyoxometalates in solution: speciation under spotlight. *Chem. Soc. Rev.* **2020**, *49* (21), 7568-7601.
- 14. Liu, L.-L.; Wang, L.; Xiao, X.-Y.; Yang, P.; Zhao, J.; Kortz, U., Structural overview and evolution paths of lacunary polyoxometalates. *Coord. Chem. Rev.* **2024**, *506*, 215687.
- 15. Zhao, J.-W.; Zhang, J.; Zheng, S.-T.; Yang, G.-Y., Combination of Lacunary Polyoxometalates and High-Nuclear Transition-Metal Clusters under Hydrothermal Conditions. 5. A Novel Tetrameric Cluster of [{FeIIFeIII12 (μ3-OH) 12 (μ4-PO4) 4}(B-α-PW9O34) 4] 22. *Inorg. Chem.* **2007**, *46* (26), 10944-10946.
- Finke, R. G.; Droege, M. W.; Domaille, P. J., Trivacant heteropolytungstate derivatives. 3. Rational syntheses, characterization, two-dimensional tungsten-183 NMR, and properties of tungstometallophosphates P2W18M4 (H2O) 2O6810-and P4W30M4 (H2O) 2O11216-(M= cobalt, copper, zinc). *Inorg. Chem.* 1987, 26 (23), 3886-3896.
- 17. Nyman, M.; Burns, P. C., A comprehensive comparison of transition-metal and actinyl polyoxometalates. *Chem. Soc. Rev.* **2012**, *41* (22), 7354-7367.
- 18. Tourné, C. M.; Tourné, G. F.; Zonnevijlle, F., Chiral polytungstometalates [WM 3 (H 2 O) 2 (XW 9 O 34) 2] 12–(X= M= Zn or Co II) and their M-substituted derivatives. Syntheses, chemical, structural and spectroscopic study of some D, L sodium and potassium salts. *J. Chem. Soc., Dalton trans.* 1991, (1), 143-155.
- 19. Dhifallah, F.; Belkhiria, M. S.; Parent, L.; Leclerc, N.; Cadot, E., A series of octahedral first-row transition-metal ion complexes templated by wells—dawson polyoxometalates: synthesis, crystal structure, spectroscopic, and thermal characterizations, and electrochemical properties. *Inorg. Chem.* **2018**, *57* (19), 11909-11919.
- Gomez-Garcia, C. J.; Coronado, E.; Gómez-Romero, P.; Casan-Pastor, N., A tetranuclear rhomblike cluster of manganese (II). Crystal structure and magnetic properties of the heteropoly complex K10 [Mn4 (H2O) 2 (PW9O34) 2]. cntdot. 20H2O. *Inorg. Chem.* 1993, 32 (15), 3378-3381.
- 21. Fang, X.; Anderson, T. M.; Neiwert, W. A.; Hill, C. L., Yttrium polyoxometalates. Synthesis and characterization of a carbonate-encapsulated sandwich-type complex. *Inorg. Chem.* **2003**, *42* (26), 8600-8602.
- 22. von Allmen, K. D.; Grundmann, H.; Linden, A.; Patzke, G. R., Synthesis and characterization of 0D–3D copper-containing tungstobismuthates obtained from the lacunary precursor Na9 [B-α-BiW9O33]. *Inorg. Chem.* **2017**, *56* (1), 327-335.

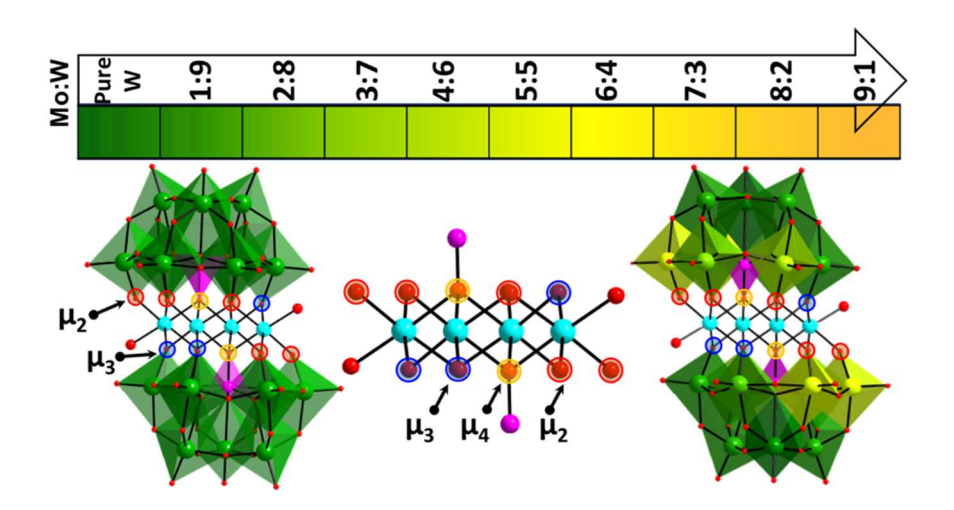
- 23. Thouvenot, R.; Fournier, M.; Franck, R.; Rocchiccioli-Deltcheff, C., Vibrational investigations of polyoxometalates. 3. Isomerism in molybdenum (VI) and tungsten (VI) compounds related to the Keggin structure. *Inorg. Chem.* 1984, 23 (5), 598-605.
- Wilson, E. F.; Miras, H. N.; Rosnes, M. H.; Cronin, L., Real-Time Observation of the Self-Assembly of Hybrid Polyoxometalates Using Mass Spectrometry. *Angew. Chem. Int. Ed.* 2011, 50 (16), 3720-3724.
- 25. Dias, J. A.; Dias, S. C. L.; Caliman, E.; Bartis, J.; Francesconi, L., Keggin structure polyoxometalates. *Inorganic Syntheses: Volume 36* **2014**, 210-217.
- Adhikary, S. D.; Tiwari, A.; Nagaiah, T. C.; Mandal, D., Stabilization of cobalt-polyoxometalate over poly (ionic liquid) composites for efficient electrocatalytic water oxidation. ACS Appl. Mater. Interfaces 2018, 10 (45), 38872-38879.
- 27. Dey, S.; Ricciardo, R. A.; Cuthbert, H. L.; Woodward, P. M., Metal-to-metal charge transfer in AWO4 (A= Mg, Mn, Co, Ni, Cu, or Zn) compounds with the wolframite structure. *Inorg. Chem.* **2014**, *53* (9), 4394-4399.
- 28. Glass, E. N.; Fielden, J.; Huang, Z.; Xiang, X.; Musaev, D. G.; Lian, T.; Hill, C. L., Transition metal substitution effects on metal-to-polyoxometalate charge transfer. *Inorg. Chem.* **2016**, *55* (9), 4308-4319
- 29. Glass, E. N.; Fielden, J.; Kaledin, A. L.; Musaev, D. G.; Lian, T.; Hill, C. L., Extending Metal-to-Polyoxometalate Charge Transfer Lifetimes: The Effect of Heterometal Location. *Chem. Eur. J* **2014**, 20 (15), 4297-4307.
- 30. Ross-Medgaarden, E. I.; Wachs, I. E., Structural determination of bulk and surface tungsten oxides with UV- vis diffuse reflectance spectroscopy and Raman spectroscopy. *J. Phys. Chem. C* **2007**, *111* (41), 15089-15099.
- 31. López, X.; Bo, C.; Poblet, J. M., Electronic properties of polyoxometalates: Electron and proton affinity of mixed-addenda Keggin and Wells—Dawson anions. *J. Am. Chem. Soc.* **2002**, *124* (42), 12574-12582.
- 32. López, X.; Miró, P.; Carbó, J. J.; Rodríguez-Fortea, A.; Bo, C.; Poblet, J. M., Current trends in the computational modelling of polyoxometalates. *Theor. Chem. Acc.* **2011**, *128*, 393-404.
- 33. Gil, A.; Carbó, J. J., Computational modelling of the interactions between polyoxometalates and biological systems. *Theor. Chem. Acc.* **2022**, *10*, 876630.
- 34. Bridgeman, A. J., Computational study of solvent effects and the vibrational spectra of Anderson Polyoxometalates. *Chem. Eur. J* **2006**, *12* (7), 2094-2102.
- 35. Duclusaud, H.; Borshch, S. A., Electron delocalization and magnetic state of doubly-reduced polyoxometalates. *J. Am. Chem. Soc.* **2001**, *123* (12), 2825-2829.
- 36. Martin-Sabi, M.; Soriano-López, J.; Winter, R. S.; Chen, J.-J.; Vilà-Nadal, L.; Long, D.-L.; Galán-Mascarós, J. R.; Cronin, L., Redox tuning the Weakley-type polyoxometalate archetype for the oxygen evolution reaction. *Nat. Catal.* **2018**, *1* (3), 208-213.
- 37. Yin, Q.; Tan, J. M.; Besson, C.; Geletii, Y. V.; Musaev, D. G.; Kuznetsov, A. E.; Luo, Z.; Hardcastle, K. I.; Hill, C. L., A fast soluble carbon-free molecular water oxidation catalyst based on abundant metals. *Science* **2010**, *328* (5976), 342-345.
- 38. Oms, O.; Dolbecq, A.; Mialane, P., Diversity in structures and properties of 3d-incorporating polyoxotung states. *Chem. Soc. Rev.* **2012**, *41* (22), 7497-7536.
- 39. Wang, S.-S.; Yang, G.-Y., Recent advances in polyoxometalate-catalyzed reactions. *Chem. Rev.* **2015**, *115* (11), 4893-4962.
- 40. Weinstock, I. A.; Schreiber, R. E.; Neumann, R., Dioxygen in polyoxometalate mediated reactions. *Chem. Rev.* **2017**, *118* (5), 2680-2717.
- 41. Du, J.; Ma, Y.-Y.; Tan, H.; Kang, Z.-H.; Li, Y., Progress of electrochemical CO2 reduction reactions over polyoxometalate-based materials. *Chin J Catal.* **2021**, *42* (6), 920-937.
- 42. Du, J.; Lang, Z.-L.; Ma, Y.-Y.; Tan, H.-Q.; Liu, B.-L.; Wang, Y.-H.; Kang, Z.-H.; Li, Y.-G., Polyoxometalate-based electron transfer modulation for efficient electrocatalytic carbon dioxide reduction. *Chem. Sci.* **2020**, *11* (11), 3007-3015.
- 43. Misra, A.; Kozma, K.; Streb, C.; Nyman, M., Beyond charge balance: counter-cations in polyoxometalate chemistry. *Angew. Chem. Int. Ed.* **2020**, *59* (2), 596-612.
- 44. Chen, L.; Turo, M. J.; Gembicky, M.; Reinicke, R. A.; Schimpf, A. M., Cation-Controlled Assembly of Polyoxotungstate-Based Coordination Networks. *Angew. Chem. Int. Ed.* **2020**, *59* (38), 16609-16615.

- 45. Feng, L.; Li, Z.; Liu, Y.; Hua, L.; Wei, Z.; Cheng, Y.; Zhang, Z.; Xu, B., Counterion Engineering toward High-Performance and pH-Neutral Polyoxometalates-Based Hole-Transporting Materials for Efficient Organic Optoelectronic Devices. *ACS nano* **2024**, *18* (4), 3276-3285.
- 46. Li, Y.-W.; Guo, L.-Y.; Su, H.-F.; Jagodic, M.; Luo, M.; Zhou, X.-Q.; Zeng, S.-Y.; Tung, C.-H.; Sun, D.; Zheng, L.-S., Two unprecedented POM-based inorganic-organic hybrids with concomitant heteropolytungstate and molybdate. *Inorg. Chem.* **2017**, *56* (5), 2481-2489.
- 47. Nagaiah, T. C.; Gupta, D.; Adhikary, S. D.; Kafle, A.; Mandal, D., Tuning polyoxometalate composites with carbonaceous materials towards oxygen bifunctional activity. *J. Mater. Chem. A* **2021**, 9 (14), 9228-9237.
- 48. Sap, A.; Van Tichelen, L.; Mortier, A.; Proost, P.; Parac-Vogt, T. N., Tuning the selectivity and reactivity of metal-substituted polyoxometalates as artificial proteases by varying the nature of the embedded Lewis acid metal ion. *Eur. J. Inorg. Chem* **2016**, 2016 (32), 5098-5105.
- 49. Sadakane, M.; Steckhan, E., Electrochemical properties of polyoxometalates as electrocatalysts. *Chem. Rev.* **1998**, *98* (1), 219-238.
- 50. López, X.; Fernández, J. A.; Poblet, J. M., Redox properties of polyoxometalates: new insights on the anion charge effect. *Dalton Trans.* **2006**, (9), 1162-1167.
- 51. Ueda, T., Electrochemistry of polyoxometalates: from fundamental aspects to applications. *ChemElectroChem* **2018**, *5* (6), 823-838.
- 52. Gumerova, N. I.; Rompel, A., Synthesis, structures and applications of electron-rich polyoxometalates. *Nat. Rev. Chem* **2018**, *2* (2), 0112.
- Cadot, E.; Fournier, M.; Tézé, A.; Hervé, G., Electrochemical Properties and ESR Characterization of Mixed Valence α-[XMo3-x V x W9O40] n-Heteropolyanions with X= PV and SiIV, x= 1, 2, or 3. *Inorg. Chem.* 1996, 35 (2), 282-288.
- 54. Amin, S. S.; Cameron, J. M.; Winslow, M.; Davies, E. S.; Argent, S. P.; Robinson, D.; Newton, G. N., A Mixed-Addenda Mo/W Organofunctionalised Hybrid Polyoxometalate. *Eur. J. Inorg. Chem* **2022**, *2022* (10), e202200019.
- 55. López, X.; Carbó, J. J.; Bo, C.; Poblet, J. M., Structure, properties and reactivity of polyoxometalates: a theoretical perspective. *Chem. Soc. Rev* **2012**, *41* (22), 7537-7571.
- 56. Maestre, J. M.; Lopez, X.; Bo, C.; Poblet, J.-M.; Casan-Pastor, N., Electronic and magnetic properties of α-keggin anions: A DFT Study of [XM12O40] n-,(M= W, Mo; X= AlIII, SiIV, PV, FeIII, CoII, CoIII) and [SiM11VO40] m-(M= Mo and W). *J. Am. Chem. Soc.* **2001**, *123* (16), 3749-3758.
- 57. Poblet, J. M.; López, X.; Bo, C., Ab initio and DFT modelling of complex materials: towards the understanding of electronic and magnetic properties of polyoxometalates. *Chem. Soc. Rev.* **2003**, *32* (5), 297-308.
- 58. Mbomekallé, I.-M.; López, X.; Poblet, J. M.; Sécheresse, F.; Keita, B.; Nadjo, L., Influence of the heteroatom size on the redox potentials of selected polyoxoanions. *Inorg. Chem.* **2010**, *49* (15), 7001-7006.
- 59. Falaise, C.; Mpacko Priso, G.; Leclerc, N.; Haouas, M.; Cadot, E., Making Heterometallic Metal—Metal Bonds in Keggin-Type Polyoxometalates by a Six-Electron Reduction Process. *Inorg. Chem.* **2023**, *62* (6), 2494-2502.
- 60. Guan, W.; Yan, L. K.; Su, Z. M.; Wang, E. B.; Wang, X. H., Density functional study of protonation sites of α-Keggin isopolyanions. *Int. J. Quantum Chem.* **2006**, *106* (8), 1860-1864.
- 61. Romo, S.; Fernandez, J. A.; Maestre, J. M.; Keita, B.; Nadjo, L.; de Graaf, C.; Poblet, J. M., Density functional theory and ab initio study of electronic and electrochemistry properties of the tetranuclear sandwich complex [FeIII4 (H2O) 2 (PW9O34) 2] 6. *Inorg. Chem.* **2007**, *46* (10), 4022-4027.
- 62. López, X.; Weinstock, I. A.; Bo, C.; Sarasa, J. P.; Poblet, J. M., Structural evolution in polyoxometalates: a DFT study of dimerization processes in Lindqvist and Keggin cluster anions. *Inorg. Chem.* **2006**, *45* (16), 6467-6473.
- 63. López, X.; Fernández, J. A.; Romo, S.; Paul, J. F.; Kazansky, L.; Poblet, J. M., Are the solvent effects critical in the modeling of polyoxoanions? *J Comput. Chem.* **2004**, *25* (12), 1542-1549.
- 64. Nyman, M., Polyoxoniobate chemistry in the 21st century. Dalton Trans. 2011, 40 (32), 8049-8058.
- 65. Chi, M.; Zeng, Y.; Lang, Z.-L.; Li, H.; Xin, X.; Dong, Y.; Fu, F.; Yang, G.-Y.; Lv, H., Molecular Orbital Engineering of Mixed-Addenda Polyoxometalates Boosts Light-Driven Hydrogen Evolution Activity. *ACS Catal* **2024**, *14*, 5006-5015.
- 66. Chi, M.; Zeng, Y.; Lang, Z.-L.; Li, H.; Xin, X.; Dong, Y.; Fu, F.; Yang, G.-Y.; Lv, H., Molecular Orbital Engineering of Mixed-Addenda Polyoxometalates Boosts Light-Driven Hydrogen Evolution Activity. *ACS Catal.* **2024**, *14* (7), 5006-5015.

- 67. Li, S.; Li, G.; Ji, P.; Zhang, J.; Liu, S.; Zhang, J.; Chen, X., A giant Mo/Ta/W ternary mixed-addenda polyoxometalate with efficient photocatalytic activity for primary amine coupling. *ACS Appl. Mater. Interfaces* **2019**, *11* (46), 43287-43293.
- 68. Kibler, A. J.; Tsang, N.; Winslow, M.; Argent, S. P.; Lam, H. W.; Robinson, D.; Newton, G. N., Electronic structure and photoactivity of organoarsenic hybrid polyoxometalates. *Inorg. Chem.* **2023**, 62 (8), 3585-3591.
- 69. Moors, M.; Warneke, J.; Lopez, X.; de Graaf, C.; Abel, B.; Monakhov, K. Y., Insights from adsorption and electron modification studies of polyoxometalates on surfaces for molecular memory applications. *Acc. Chem. Res* **2021**, *54* (17), 3377-3389.
- 70. Tucher, J.; Schlicht, S.; Kollhoff, F.; Streb, C., Photocatalytic reactivity tuning by heterometal and addenda metal variation in Lindqvist polyoxometalates. *Dalton Trans.* **2014**, *43* (45), 17029-17033.
- 71. Li, C.; Suzuki, K.; Mizuno, N.; Yamaguchi, K., Polyoxometalate LUMO engineering: a strategy for visible-light-responsive aerobic oxygenation photocatalysts. *Chem. Commun.* **2018**, *54* (52), 7127-7130.
- 72. Laurans, M.; Mattera, M.; Salles, R.; K'bidi, L.; Gouzerh, P.; Renaudineau, S.; Volatron, F.; Guillemot, G.; Blanchard, S.; Izzet, G., When identification of the reduction sites in mixed molybdenum/tungsten Keggin-type polyoxometalate hybrids turns out tricky. *Inorg. Chem.* **2022**, *61* (20), 7700-7709.
- 73. Suzuki, K.; Mizuno, N.; Yamaguchi, K., Polyoxometalate photocatalysis for liquid-phase selective organic functional group transformations. *ACS Catal* **2018**, *8* (11), 10809-10825.
- 74. Aparicio, P. A.; Poblet, J. M.; López, X., Tungsten Redox Waves in [XMW11O40] n–(X= P, Si, Al and M= W, Mo, V, Nb, Ti) Keggin Compounds–Effect of Localised/Delocalised Charges. *Eur. J. Inorg. Chem* 2013, 2013 (10-11), 1910-1916.
- 75. Cameron, J. M.; Fujimoto, S.; Kastner, K.; Wei, R. J.; Robinson, D.; Sans, V.; Newton, G. N.; Oshio, H. H., Orbital engineering: Photoactivation of an organofunctionalized polyoxotungstate. *Chem. Eur. J* **2017**, *23* (1), 47-50.
- 76. Sarma, B. B.; Efremenko, I.; Neumann, R., Oxygenation of methylarenes to benzaldehyde derivatives by a polyoxometalate mediated electron transfer—oxygen transfer reaction in aqueous sulfuric acid. *J. Am. Chem. Soc.* **2015**, *137* (18), 5916-5922.
- 77. von Allmen, K.; Moré, R.; Müller, R.; Soriano-López, J.; Linden, A.; Patzke, G. R., Nickel-Containing Keggin-Type Polyoxometalates as Hydrogen Evolution Catalysts: Photochemical Structure–Activity Relationships. *ChemPlusChem* **2015**, *80* (9), 1389-1398.
- 78. Dolbecq, A.; Dumas, E.; Mayer, C. R.; Mialane, P., Hybrid organic– inorganic polyoxometalate compounds: from structural diversity to applications. *Chem. Rev.* **2010**, *110* (10), 6009-6048.
- 79. Song, Y. F.; Long, D. L.; Ritchie, C.; Cronin, L., Nanoscale polyoxometalate-based inorganic/organic hybrids. *Chem Rec* **2011**, *11* (3), 158-171.
- 80. Neumann, R.; Gara, M., Highly active manganese-containing polyoxometalate as catalyst for epoxidation of alkenes with hydrogen peroxide. *J. Am. Chem. Soc.* **1994**, *116* (12), 5509-5510.
- 81. Neumann, R.; Gara, M., The manganese-containing polyoxometalate, [WZnMnII2 (ZnW9O34) 2] 12-, as a remarkably effective catalyst for hydrogen peroxide mediated oxidations. *J. Am. Chem. Soc.* **1995**, *117* (18), 5066-5074.
- 82. Singh, V.; Adhikary, S. D.; Tiwari, A.; Mandal, D.; Nagaiah, T. C., Sustainable non-noble metal bifunctional catalyst for oxygen-depolarized cathode and Cl2 evolution in HCl electrolysis. *Chem. Mater* **2017**, *29* (10), 4253-4264.
- 83. Singh, V.; Padhan, A. K.; Adhikary, S. D.; Tiwari, A.; Mandal, D.; Nagaiah, T. C., Poly (ionic liquid)—zinc polyoxometalate composite as a binder-free cathode for high-performance lithium—sulfur batteries. *J. Mater. Chem. A* **2019**, *7* (7), 3018-3023.
- 84. Anyushin, A. V.; Kondinski, A.; Parac-Vogt, T. N., Hybrid polyoxometalates as post-functionalization platforms: from fundamentals to emerging applications. *Chem. Soc. Rev* **2020**, *49* (2), 382-432.

### **Chapter 2**

# Modulation of Band Gap and Redox Properties in Mixed-Addenda Sandwich Polyoxometalates



#### 2.1 Introduction

Polyoxometalates (POMs)<sup>1</sup>, as molecular metal oxides, exhibit astonishing redox characteristics that are easily customizable in accordance with their molecular structure, the nature of the counter cations, heteroatoms, and the metal addenda atoms. Their wide range of structural diversity, ease of synthesis, and tuneable solubility influence their physical and chemical properties at the molecular level, such as self-assembly, acidity/basicity, redox behaviour, electronic/optical properties.<sup>2-5</sup> Polyoxometalates have continued to fascinate in developing novel structures, in pursuit of their unexplored applications and properties. polyoxometalates, with Weakley-type sandwich especially the formula [M<sub>4</sub>(H<sub>2</sub>O)<sub>2</sub>(PW<sub>9</sub>O<sub>34</sub>)<sub>2</sub>]<sup>n</sup>- have found applications in a wide range of areas such as catalysis, <sup>6</sup> magnetism,<sup>7</sup> energy storage,<sup>8</sup> and electrochemical applications.<sup>9</sup> These sandwich motifs have two trivacant Keggin subunits (PW<sub>9</sub>O<sub>34</sub>) joining tetrasubstituted transition metal core at the center. These trivacant subunits are usually made of tungstates but rarely from molybdates due to the higher kinetic lability of molybdates in aqueous solution compared to tungstates. Recently, one molybdates-based tetrasubstituted sandwich POMs have been isolated in acetonitrile using protecting group strategy. <sup>10</sup>

Mo incorporation into W-based Keggin and Dawson POMs is known to decrease the lowest unoccupied molecular orbitals (LUMO) energy level and reduce the HOMO-LUMO gap. 11 Mixed addenda POMs combining W and Mo are proposed to take the advantage of kinetic stability of W and electronic properties of Mo. Cronin et al. effectively applied this strategy in tetrasubstituted sandwich polyoxometalates to reduce over potential in water oxidation. 12 Various studies on mixed addenda Lindqvist, 13 Lacunary, 14 Keggin, 15 and Wells-Dawson POMs<sup>16</sup> with combinations like (W/V, W/Mo, Mo/V, Nb/W) have shown improved activity in applications like photocatalysis, energy storage, and conversions. For example, lacunary POMs were engineered for visible light-driven photocatalytic aerobic oxidation of sulfides to sulfoxides.<sup>17</sup> HOMO (highest occupied molecular orbitals) and LUMO of Dawson-based mixed addenda POMs were engineered by incorporating Moaddenda for optoelectronic device applications. 18 Mixed addenda Keggin POM [PV<sub>2</sub>Mo<sub>10</sub>O<sub>40</sub>]<sup>5-</sup> was demonstrated as an excellent robust catalyst in many organic group transformations. 19 Also, ternary mixed addenda polyoxometalates were employed in visible light-driven amine coupling reactions.<sup>20</sup> These examples signify the effectiveness of mixed addenda strategy in tuning the electronic properties as well as kinetic stability of the POMs,

potentially leading to enhanced photocatalytic and electrocatalytic activity by orbital engineering to give a low-lying LUMO along with a lower HOMO-LUMO gap and push the LMCT into the visible region.<sup>21</sup>

### (a) Trivacant Keggin subunits with transition metals in an aqueous solution aqueous solution $[PW_9O_{34}]^{9-}$ $[PW_{11}MO_{40}]^{x-}$ $[M_4(H_2O)_2(PW_9O_{34})_2]^{y-1}$ aqueous solution [PMo<sub>9</sub>O<sub>34</sub>]9- $[PMo_{12}O_{40}]^{3-}$ $[PMo_{11}MO_{40}]^{x-}$ (b) This work $[M_4(H_2O)_2(PMo_xW_{9-x}O_{34})_2]^{y-}$ $[M_4(H_2O)_2(PW_9O_{34})_2]^{\gamma-}$ **Metal Precursors**

**Scheme 2.1** (a) Behaviour of trivacant Keggin subunits of pure tungstates and molybdates in presence of transition metals (b) Synthesis of transition metals substituted tetrasubstituted sandwich POMs from precursors.

Additionally, substituting some of the W atoms with Mo strengthens the Lewis basicity of bridging oxygen (W-O-W) in the framework.<sup>22</sup> So, theoretically it is highly predictable that more number of Mo incorporation in the framework would potentially increase its basicity.

Also, Mo-based POMs have the advantage of higher electron storage capacity compared to isostructural W-based POMs due to their higher tendency to form metal-metal bonds within the POM framework.<sup>23</sup> The mixed addenda strategy proves particularly useful in stabilizing Mo-based tetrasubstituted sandwich POMs in an aqueous solution, enabling band gap tuning to such an extent that these POMs exhibit shifting the absorption band towards visible light and improved electrocatalytic properties. Thus, the design and synthesis of novel mixed-addenda POMs will have significant and promising pursuits, offering unprecedented performance potential.

In this study, we introduced a series of mixed addenda sandwich POMs, with the formula,  $[(TM)_4(H_2O)_2(PMo_xW_{9-x}O_{34})_2]^{10-}$ , where TM= Mn, Co, Ni, and Zn. We proposed two different synthesis methods (1) synthesis of transition metal substituted sandwiched tungstate POMs followed by Mo-addenda incorporation in solution, and (2) introducing Mo, W addenda, and transition metals simultaneously in aqueous solutions while maintaining the appropriate pH as outlined in Scheme 1. Band gap tuning has been explored experimentally and theoretically. DFT study reveals the preferred positions of Mo incorporation in the framework and matches well with crystal structure of the reported mixed addenda sandwich POMs.

#### 2.2 Results and Discussion

#### 2.2.1 Reaction chemistry of mixed addenda sandwich polyoxometalates

All the compounds with the formula Na<sub>10</sub>[(TM)<sub>4</sub>(H<sub>2</sub>O)<sub>2</sub>(PMo<sub>x</sub>W<sub>9-x</sub>O<sub>34</sub>)<sub>2</sub>].nH<sub>2</sub>O {**P**-(TM)<sub>4</sub>Mo<sub>x</sub>W<sub>18-x</sub>} were synthesized under microwave heating using a mixture of Na<sub>2</sub>MoO<sub>4</sub>.2H<sub>2</sub>O, Na<sub>2</sub>WO<sub>4</sub>.2H<sub>2</sub>O and Na<sub>2</sub>HPO<sub>4</sub>.2H<sub>2</sub>O at 85 °C after adjusting appropriate pH followed by the addition of transition metal salts. All the syntheses were optimized by varying pH, temperature, time duration and with different ratios of molybdenum to tungsten as shown in table 2.S2. We have also studied the effect of pH on the ratio of molybdenum to tungsten incorporation as well as the impact on the formation of sandwich structure over Keggin framework. It was also found that the heteroatom as well as the transition metals play important role in directing the formation of the sandwich structure. For example, Mn and Co effectively direct the sandwich structure at pH ranges from 5.0 to 6.5, while Ni and Zn direct the sandwich structure at a specific pH. However, best yields in terms of Mo/W

ratio for Mn (13/5) & Co (5/4) was obtained at final pH 6.5, while for Ni & Zn, it is pH 6.9. Crystals obtained from each reaction by varying the Mo amount from 30 to 70%, shows that the maximum amount of Mo incorporation was obtained with 60% Mo content, as confirmed from ESI-MS. However, the sandwich structure could not be obtained for Cu & Fe applying the same experimental approach. Instead, a mono substituted Keggin structure was obtained having P as heteroatom and Cu/Fe as substituting atom at one of the addenda positions (Scheme 2.1, ESI-MS characterization details later, Figure 2.S9-2.S10). Thus, transition metal also plays an important role in controlling the formation of Keggin

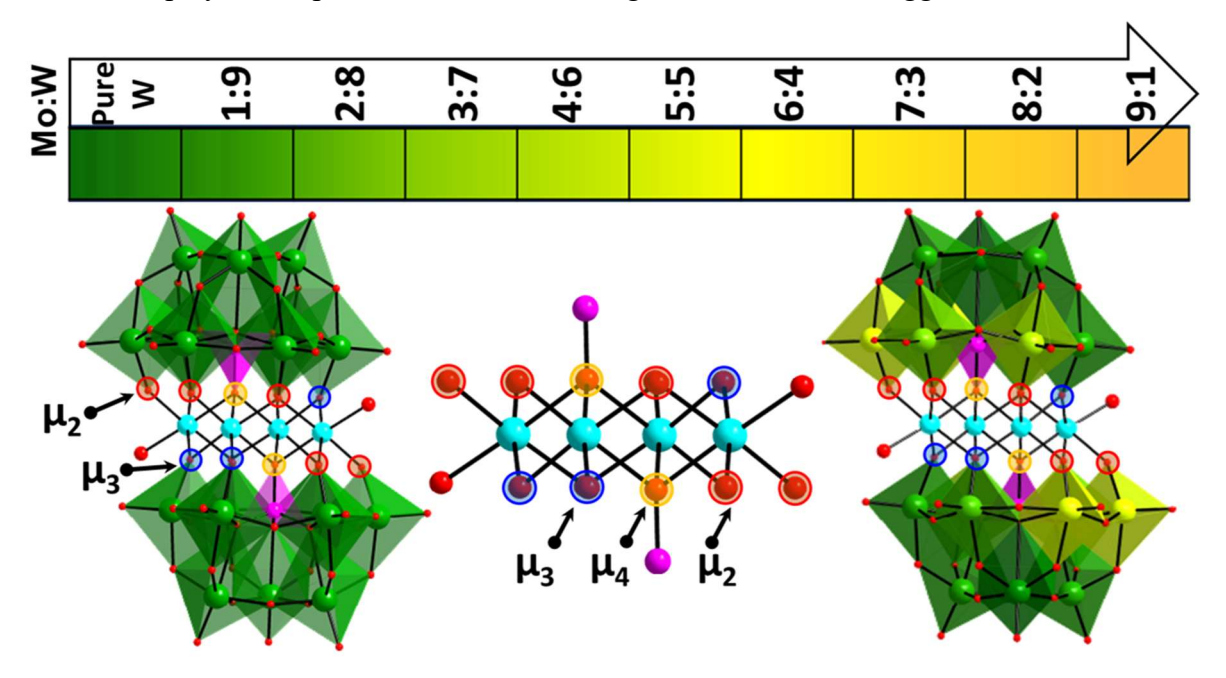


**Figure 2.1** RGB representation of Mo to W ratios in the framework of tetrasubstituted sandwich POMs. (colour bar code: Pure W-Green, Pure Mo - Yellow, Ni - cyan, O - red, P-Pink,  $\mu_2$ ,  $\mu_3$ ,  $\mu_4$  indicating the denticity of the different kinds of oxygen atoms)

versus sandwich structure. The effect of counter-cation and different acids towards the formation of these sandwich POMs have been studied e.g., K<sup>+</sup> is better for the formation of these sandwich structures with acetic acid and Na<sup>+</sup> is better with nitric acid. Among various synthetic methods, microwave method was found to be best in terms of yield, reaction time as well as higher Mo/W ratio. The crystals so obtained for all the mixed addenda sandwich POMs have been characterized using different spectroscopic techniques such as FTIR, ESI-MS, and SC-XRD and their electrochemical stability were studied at different pH.

# 2.2.2 Characterisation of mixed addenda sandwich polyoxometalates

diffraction analysis. The Single crystal X-ray molecular structures of  $[(TM)_4(H_2O)_2(PMo_xW_{9-x}O_{34})_2]^{10-}$  [P-(TM)<sub>4</sub>Mo<sub>x</sub>W<sub>18-x</sub>] where M= transition metals; have been determined by single-crystal X-ray diffraction analysis. All the crystal data, data collection and refinement parameters are summarized in Table 2.1 and 2.S1, Supporting Information. All the mixed addenda [P-(TM)4MoxW18-x] POMs structures so obtained are isostructural to their tungstate-analogues [(TM)<sub>4</sub>(H<sub>2</sub>O)<sub>2</sub>(PW<sub>9</sub>O<sub>34</sub>)<sub>2</sub>]<sup>10-</sup> [P-(TM)<sub>4</sub>W<sub>18</sub>] POMs with the same anionic charge (Z=-10) (Figure 2.3). All the compounds [P-(TM)<sub>4</sub>Mo<sub>x</sub>W<sub>18</sub>x crystallize in a triclinic centrosymmetric system with P-1 space group except P-Zn<sub>4</sub>Mo<sub>x</sub>W<sub>18-x</sub>. The 3D structure of these sandwich polyoxometalates can be broken into two parts (I) tetranuclear cubane framework consisting of 3d transition metals at the sandwich position and (II) tri-vacant Keggin framework. The tri-lacunary Keggin moiety contains a tetrahedral phosphate anion in the center as a templating agent to triads of addenda W/Mo atoms. Four transition metals in the tetrasubstituted sandwich core are referred to as internal {T and external atoms {TMe} (Figure 2.2). Two internal transition metal atoms are connected with the Keggin framework octahedrally via oxygen atoms while the external transition metal atoms {TM<sub>e</sub>} are penta-coordinated with the trivacant framework through oxygens, while the sixth coordination is occupied by one water molecule making it pseudooctahedral.

There are total of 34 oxygen atoms in the asymmetric unit of these sandwich POMs; of which 6 oxygens are corner shared (Oc), 12 are edge shared (Oe), 9 are terminal oxygens (Ot) and 7 oxygen atoms are bridging transition metals at the sandwich position with trivacant framework (Figure 2.2). Tetrahedral phosphate anion is binding through  $\mu_4$ -oxygens with an average P-O bond length of ca. 1.55 Å in both [P-(TM)<sub>4</sub>Mo<sub>x</sub>W<sub>18-x</sub>] and [P-(TM)<sub>4</sub>W<sub>18</sub>]. Both the internal transition metal atoms {TM<sub>i</sub>} are bound to both sides to tetrahedral phosphate anion through  $\mu_4$  oxygens and framework through  $\mu_2$  and  $\mu_3$  oxygens, each type of oxygen lying on both sides of transition metal. However, each external transition metal atoms {TM<sub>e</sub>} are bound to only one side to phosphate anion through  $\mu_4$  oxygen, while it is bound to the framework metals through two  $\mu_2$  oxygens on one side and two  $\mu_3$  oxygens on the opposite side with water molecule as the sixth coordination side (Figure 2.2).

Analysing the crystal structures of all the mixed addenda sandwich POMs, it was found that the positional occupancy of Mo atoms also depends on the nature of transition metals at the sandwiched position. Moreover, Mo prefers to bind  $\mu_2$  oxygens which are connected to transition metals at the sandwich positions. Comparing tungstate-based sandwich POMs and mixed addenda sandwich POMs, slight variations in bond lengths and bond angles (Table 2.S3, 2.S4) have been observed which have been detailed in the structural description. Bond valence sum (BVS) calculations show that all transition metals at sandwich position are in +2-oxidation state while P is in +5, W/Mo is in a +6 oxidation state in all the reported POMs (Table 2.S5).

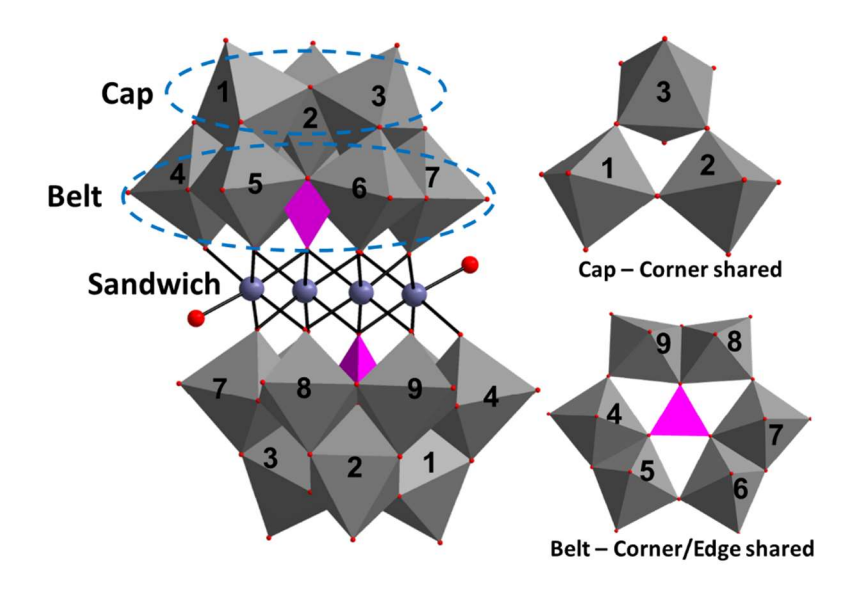


**Figure 2.2** Representative polyhedral view of tetrasubstituted sandwich POMs showing the position and type of oxygen present (corner/belt shared)

Structure description of  $P\text{-}Mn_4Mo_xW_{18\text{-}x}$ . From the crystal structure of  $Na_{10}[Mn_4(H_2O)_2(PMo_xW_{9\text{-}x}O_{34})_2]$  (Figure 2.3a), the distance between manganese atoms in the internal and external position is 3.32 Å while it is 3.45 Å between two internal manganese atoms (Figure 2.5a). Comparing  $P\text{-}Mn_4Mo_xW_{18\text{-}x}$  with  $P\text{-}Mn_4W_{18}$  as shown in (Figure 2.S2a), the bond lengths are almost equal, with slight variations (Table 2.S3). The average  $M\text{-}O_t$  bond length in  $P\text{-}Mn_4Mo_xW_{18\text{-}x}$  is 1.73 Å while the average bond length in  $P\text{-}Mn_4W_{18}$  is 1.72 Å. The average  $M\text{-}O_{c/e}\text{-}M$  ( $O_{c/e}$  – corner/edge-shared oxygen, M=W or M0) bond length of  $P\text{-}Mn_4Mo_xW_{18\text{-}x}$  is slightly smaller than  $P\text{-}Mn_4W_{18}$  due to molybdenum

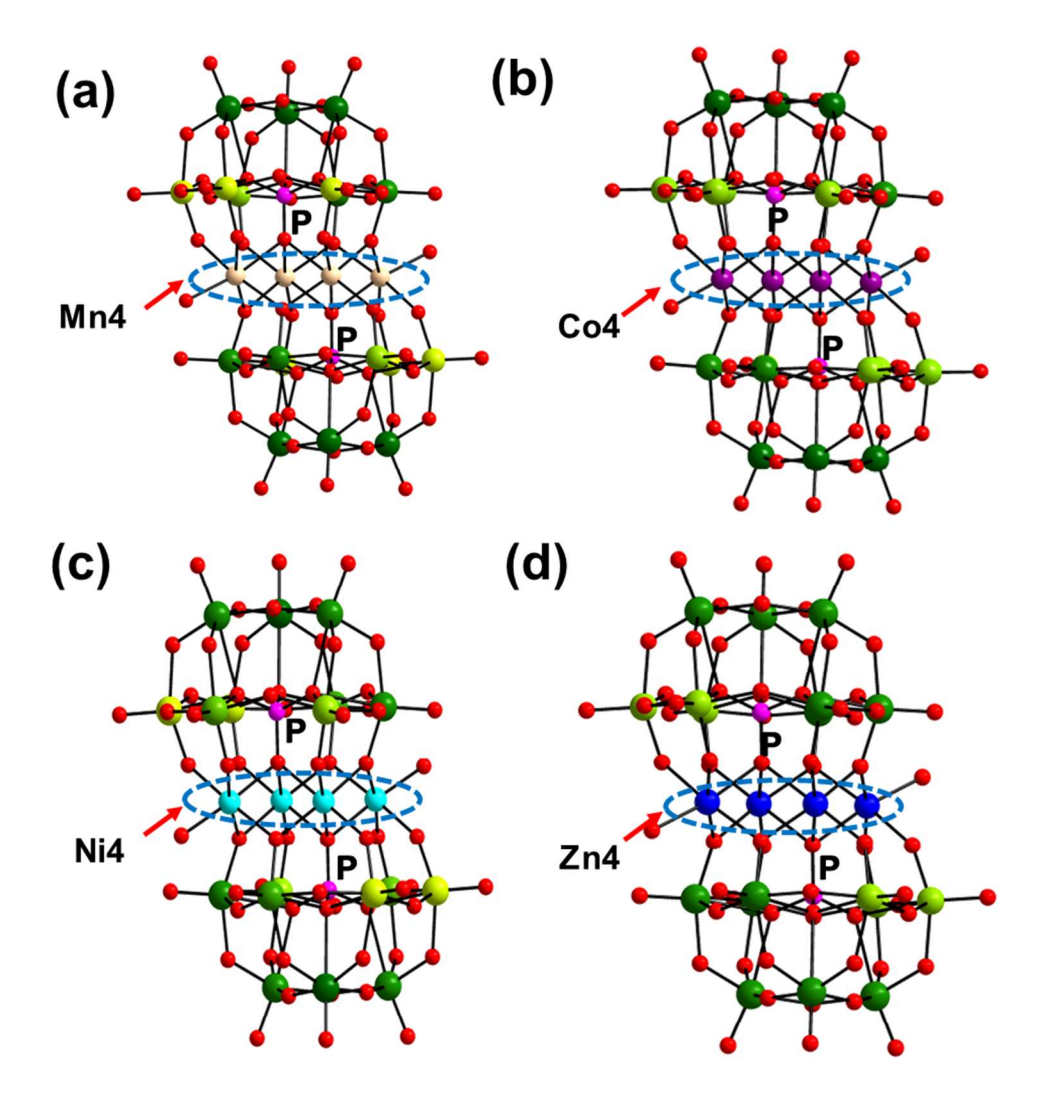


**Figure 2.3** Single-crystal X-ray structure (ball-stick model) of (a)  $[Mn_4(H_2O)_2(PMo_xW_{9-x}O_{34})_2]^{10-}$  (P-Mn<sub>4</sub>Mo<sub>x</sub>W<sub>18-x</sub>), (b) Co<sub>4</sub>(H<sub>2</sub>O)<sub>2</sub>(PMo<sub>x</sub>W<sub>9-x</sub>O<sub>34</sub>)<sub>2</sub>]<sup>10-</sup> (P-Co<sub>4</sub>Mo<sub>x</sub>W<sub>18-x</sub>) (c) Ni<sub>4</sub>(H<sub>2</sub>O)<sub>2</sub>(PMo<sub>x</sub>W<sub>9-x</sub>O<sub>34</sub>)<sub>2</sub>]<sup>10-</sup> (P-Ni<sub>4</sub>Mo<sub>x</sub>W<sub>18-x</sub>); counter ions and hydrogen atoms are omitted for clarity (colour bar code: Pure W-Green, Pure Mo-Yellow, Mn-Tan, Co-Purple, Ni-cyan, Zn-blue, O-red, P-Pink).

incorporation in mixed addenda POMs (Table 2.S3). Further, it was found that average bond angles M-O<sub>c</sub>-M (cap) and M-O<sub>e</sub>-M (belt) in P-Mn<sub>4</sub>Mo<sub>x</sub>W<sub>18-x</sub> found to be slightly higher (0.28) compared to P-Mn<sub>4</sub>W<sub>18</sub> while the reverse was observed for M-O<sub>c</sub>-M (belt) (M=Mo/W, table 2.S3). From the comparison of P-Mn<sub>4</sub>Mo<sub>x</sub>W<sub>18-x</sub> with the figure 2.2 structure, it is clear that Mo incorporation is favourable at 4/5 positions of the belt followed by positions 6 and 9 (Figure 2.4a), which are connected to transition metals in the sandwich position through

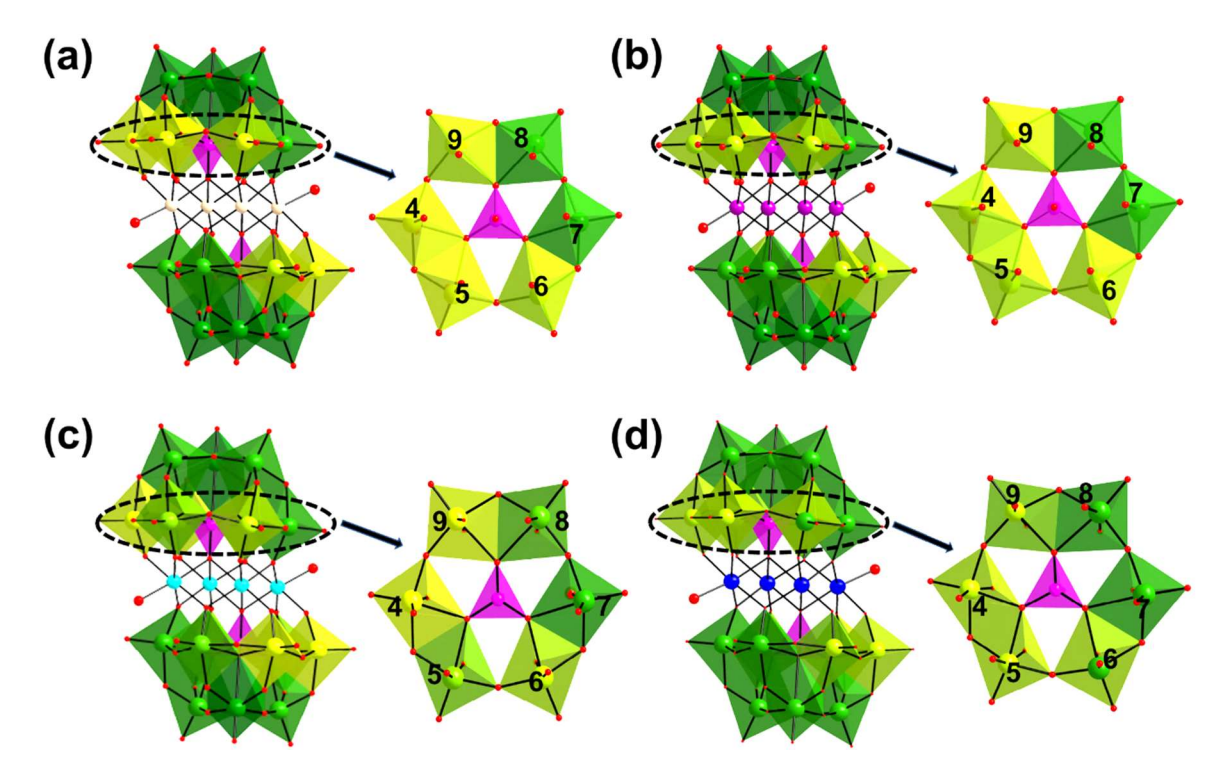
 $\mu_2$  oxygens as shown in Figure 2.1. The other positions in the belt as well as in the cap are comparatively less favourable for Mo incorporation.

Table 2.1 Crystal data, data collection, and refinement parameters for $P\text{-}M_4\text{Mo}_x\text{W}_{18\text{-}x}$						
	P-Mn <sub>4</sub> Mo <sub>x</sub> W <sub>18-x</sub>	P-Co <sub>4</sub> Mo <sub>x</sub> W <sub>18-x</sub>	P-Ni <sub>4</sub> Mo <sub>x</sub> W <sub>18-x</sub>	P-Zn <sub>4</sub> Mo <sub>x</sub> W <sub>18-x</sub>		
CCDC number	2290789	2290788	2290785	2290784		
empirical formula	$\begin{array}{c} H_{33.4}Mn_4Mo_{3.9}Na_{11}O_{10} \\ {}_2P_2W_{14.1} \end{array}$	$Co_4H_{28}Mo_{3.6}Na_{13}O_{100} \\ P_2W_{14.4}$	$\begin{array}{c} H_{24.4}Mo_{6.1}Na_{20}Ni_4O_1 \\ _{05}P_2W_{11.9} \end{array}$	$\begin{array}{c} H_{28}K_4Mo_{2.1}Na_8O_{100}P_2 \\ W_{15.9}Zn_4 \end{array}$		
formula weight	5166.71	5217.58	5234.22	5416.65		
temp (K)	293(2)	298(2)	293(2)	293(2)		
crystal system	Triclinic	Triclinic	Triclinic	Monoclinic		
space group	P <del>1</del>	P <del>1</del>	P1	P2 <sub>1</sub> /n		
unit cell dimension						
a (Å)	11.610(6)	11.5500(6)	11.5080(15)	12.8956(7)		
<i>b</i> (Å)	12.924(7)	12.8878(7)	13.2450(17)	16.5732(12)		
c (Å)	17.397(8)	17.2384(9)	18.128(2)	21.5702(13)		
α (deg)	97.510(1)	97.447(2)	70.576(2)	90		
$\beta$ (deg)	106.844(1)	107.016(2)	74.004(4)	103.953(2)		
γ (deg)	111.488(1)	111.167(2)	73.618(5)	90		
$V(Å^3)$	2240.9(2)	2207.0(2)	2449.1(5)	4474.0(5)		
Z	1	1	1	2		
ρ (calculated) (g/cm³)	3.829	3.926	3.549	4.021		
F (000)	2308	2326	2363	4814.0		
crystal size (mm³)	0.28 x 0.24 x 0.13	0.31 x 0.20 x 0.18	0.38 x 0.27 x 0.22	0.34 x 0.17 x 0.15		
index ranges	-14\left\left\left\left\left\left\left\left	-15 <h<15, -16<k<17,<br="">-22&lt;1&lt;23</h<15,>	-14 <h<14, -<br="">16<k<16, -23<1<23<="" td=""><td>-12 &lt; h &lt; 16, -20 &lt; k &lt; 20, -26 &lt; 1 &lt; 26</td></k<16,></h<14,>	-12 < h < 16, -20 < k < 20, -26 < 1 < 26		
no. of reflection collected /unique	59333/9253	47990/10927	40065/10773	41488/9164		
GOF on $F^2$	1.064	1.089	1.048	1.154		
final $R$ indices $(I > 2\sigma(I))$	R1=0.025, wR2=0.070	Rl=0.031, wR2=0.081	R1=0.030, wR2=0.071	R1= 0.035, wR2 = 0.092		
R indices (all data)	R1=0.026, wR2=0.071	R1=0.034, wR2=0.083	R1=0.039, wR2=0.075	R1 = 0.036, wR2 = 0.093		
data/restraints/par am	9253/0/647	10927/0/631	10773/0/706	9164/1/623		

Structure description of P-Co<sub>4</sub>Mo<sub>x</sub>W<sub>18-x</sub>. The crystal structural description of [Co<sub>4</sub>(H<sub>2</sub>O)<sub>2</sub>(PMo<sub>x</sub>W<sub>9-x</sub>O<sub>34</sub>)<sub>2</sub>]<sup>10-</sup> (Figure 2.3b) is similar to [Mn<sub>4</sub>(H<sub>2</sub>O)<sub>2</sub>(PMo<sub>x</sub>W<sub>9-x</sub>O<sub>34</sub>)<sub>2</sub>]<sup>10-</sup> except Mn<sub>4</sub> cubane replaced by Co<sub>4</sub> cubane along with the slight variation in the Mo to W ratio in the crystal structure (Figure 2.3b). In P-Co<sub>4</sub>Mo<sub>x</sub>W<sub>18-x</sub>, the distance between cobalt atoms in the internal and external position is 3.19 Å while it is 3.28 Å between two internal cobalt atoms which is slightly smaller when compared to P-Mn<sub>4</sub>Mo<sub>x</sub>W<sub>18-x</sub>. Also, comparing P-Co<sub>4</sub>Mo<sub>x</sub>W<sub>18-x</sub> and P-Co<sub>4</sub>W<sub>18</sub> (Table 2.S3), the bond length of mixed addenda POMs is almost equal to tungstate-based POMs, with slight variations. The average M-O<sub>t</sub> bond length in P-Co<sub>4</sub>Mo<sub>x</sub>W<sub>18-x</sub> is 1.71 Å while the average bond length in P-Co<sub>4</sub>W<sub>18</sub> is 1.73 Å. Further, it was found that average bond angles M-O<sub>c</sub>-M (belt/cap) in P-Co<sub>4</sub>Mo<sub>x</sub>W<sub>18-x</sub> found to be slightly higher when compared to P-Mn<sub>4</sub>W<sub>18</sub> while the reverse was observed for M-O<sub>c</sub>-M (belt) (M=Mo/W, table 2.S4). From the comparison of P-Co<sub>4</sub>Mo<sub>x</sub>W<sub>18-x</sub> with a sandwich structure (Figure 2.2), belt positions 4, 5, 6 and 9 are found to be favourable for Mo incorporation (Figure 2.4b) similar to P-Mn<sub>4</sub>Mo<sub>x</sub>W<sub>18-x</sub> which are connected to transition metals at sandwich position through μ<sub>2</sub> oxygens (Figure 2.1).

Structure description of P-Ni<sub>4</sub>Mo<sub>x</sub>W<sub>18-x</sub>. In [Ni<sub>4</sub>(H<sub>2</sub>O)<sub>2</sub>(PMo<sub>x</sub>W<sub>9-x</sub>O<sub>34</sub>)<sub>2</sub>]<sup>10-</sup> (P-Ni<sub>4</sub>Mo<sub>x</sub>W<sub>18-x</sub>, Figure 2.3c), the distance between nickel atoms in the internal to external position and between two internal nickel atoms is the same i.e., 3.13 Å unlike in P-Mn<sub>4</sub>Mo<sub>x</sub>W<sub>18-x</sub> and P-Co<sub>4</sub>Mo<sub>x</sub>W<sub>18-x</sub> (Figure 2.S5). Also, comparing P-Ni<sub>4</sub>Mo<sub>x</sub>W<sub>18-x</sub> with P-Ni<sub>4</sub>W<sub>18</sub> (table 2.S3), it was found that the bond length of mixed addenda POMs is equal to bond lengths in tungstate-based POMs, with slight variations. The average M-O<sub>t</sub> bond length in P-Ni<sub>4</sub>Mo<sub>x</sub>W<sub>18-x</sub> is 1.707 Å while the average bond length in P-Ni<sub>4</sub>W<sub>18</sub> is 1.731 Å. Further, it was found that average bond angles M-O<sub>c</sub>-M (cap) and M-O<sub>e</sub>-M (belt) in P-Ni<sub>4</sub>Mo<sub>x</sub>W<sub>18-x</sub> found to be slightly higher when compared to P-Ni<sub>4</sub>W<sub>18</sub> while the reverse was observed for M-O<sub>c</sub>-M (belt) (M=Mo/W, Table 2.S4). From the comparison of P-Ni<sub>4</sub>Mo<sub>x</sub>W<sub>18-x</sub> with a sandwich structure (Figure 2.2), belt positions 4, and 9 are most favourable for Mo incorporation followed by 6 and 5 (Figure 2.4c) which are connected to transition metals in the sandwich position through μ<sub>2</sub> oxygens as shown in Figure 2.1.

**Structure description of P-Zn<sub>4</sub>Mo<sub>x</sub>W<sub>18-x</sub>**. In [Zn<sub>4</sub>(H<sub>2</sub>O)<sub>2</sub>(PMo<sub>x</sub>W<sub>9-x</sub>O<sub>34</sub>)<sub>2</sub>]<sup>10-</sup> (P-Zn<sub>4</sub>Mo<sub>x</sub>W<sub>18-x</sub>, Figure 2.3d) the distance between zinc atoms in the internal and external positions is 3.21



**Figure 2.4** Polyhedral representation of mixed addenda sandwich POMs depicting different ratio of molybdenum to tungsten in tetrasubstituted sandwich POMs; (a) [Mn<sub>4</sub>(H<sub>2</sub>O)<sub>2</sub>(PMo<sub>x</sub>W<sub>9-x</sub>O<sub>34</sub>)<sub>2</sub>]<sup>10-</sup> (P-Mn<sub>4</sub>Mo<sub>x</sub>W<sub>18-x</sub>), (b) Co<sub>4</sub>(H<sub>2</sub>O)<sub>2</sub>(PMo<sub>x</sub>W<sub>9-x</sub>O<sub>34</sub>)<sub>2</sub>]<sup>10-</sup> (P-Co<sub>4</sub>Mo<sub>x</sub>W<sub>18-x</sub>) (c) Ni<sub>4</sub>(H<sub>2</sub>O)<sub>2</sub>(PMo<sub>x</sub>W<sub>9-x</sub>O<sub>34</sub>)<sub>2</sub>]<sup>10-</sup> (P-Ni<sub>4</sub>Mo<sub>x</sub>W<sub>18-x</sub>); counter ions and hydrogen atoms are omitted for clarity (colour bar code: Pure W-Green, Pure Mo-Yellow, Mn-Tan, Co-Purple, Ni - cyan, Zn-blue, O - red, P-Pink).

and 3.23 Å while it is 3.38 Å between two internal zinc atoms (Figure 2.5d). Also, comparing P-Zn<sub>4</sub>Mo<sub>x</sub>W<sub>18-x</sub> with P-Zn<sub>4</sub>W<sub>18</sub> (Table 2.S3), it was found that the bond length of mixed addenda POMs is equal to bond lengths in tungstate-based POMs, with slight variations. The average M-O<sub>t</sub> bond length in P-Zn<sub>4</sub>Mo<sub>x</sub>W<sub>18-x</sub> is 1.726 Å while the average bond length in P-Zn<sub>4</sub>W<sub>18</sub> is 1.723 Å. Further, it was found that average bond angles in P-Zn<sub>4</sub>Mo<sub>x</sub>W<sub>18-x</sub> almost equal when compared to P-Zn<sub>4</sub>W<sub>18</sub> except for M-O<sub>c</sub>-M (cap) found to be higher in case of P-Zn<sub>4</sub>W<sub>18</sub>. From the comparison of P-Zn<sub>4</sub>Mo<sub>x</sub>W<sub>18-x</sub> with a sandwich structure (Figure 2.2), belt positions 4, 5, 6, and 9 are most favorable for Mo incorporation which are connected to transition metals in the sandwich position through μ<sub>2</sub> oxygens as shown in figure 2.1. However, Mo/W ratio is very low in P-Zn<sub>4</sub>Mo<sub>x</sub>W<sub>18-x</sub> compared to other mixed addenda sandwich POMs as confirmed from other characterisation techniques.

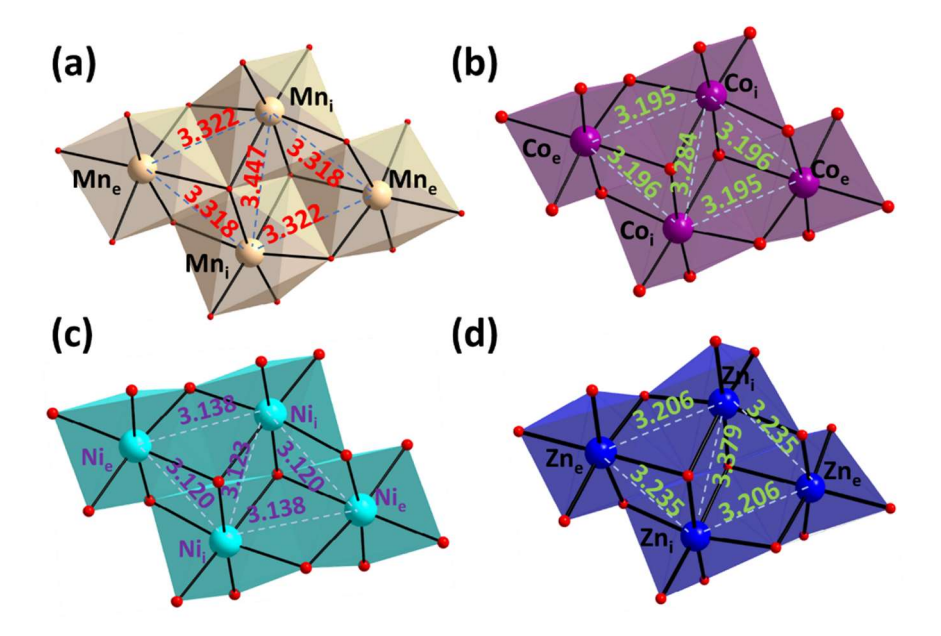


**Figure 2.5** Cubane core of mixed addenda sandwich POMs (ball-stick model) showing the interatomic distance between transition metals in (a)  $[Mn_4(H_2O)_2(PMo_xW_{9-x}O_{34})_2]^{10-}$  (P-Mn<sub>4</sub>Mo<sub>x</sub>W<sub>18-x</sub>), (b)  $Co_4(H_2O)_2(PMo_xW_{9-x}O_{34})_2]^{10-}$  (P-Co<sub>4</sub>Mo<sub>x</sub>W<sub>18-x</sub>) (c)  $Ni_4(H_2O)_2(PMo_xW_{9-x}O_{34})_2]^{10-}$  (P-Ni<sub>4</sub>Mo<sub>x</sub>W<sub>18-x</sub>) (d)  $Zn_4(H_2O)_2(PMo_xW_{9-x}O_{34})_2]^{10-}$  (P-Zn<sub>4</sub>Mo<sub>x</sub>W<sub>18-x</sub>);  $TM_i$  and  $TM_e$  are transition metals at internal and external sandwich positions in mixed addenda POMs.

# Electrospray ionization and Inductively coupled plasma mass spectrometry (ESI-MS and ICP-MS)

ESI-MS (negative mode) demonstrates molecular mass (along with charge state) present in an aqueous solution and their transient stability. ESI-MS show excellent bulk purity of all the reported sandwich POMs. The ESI-mass spectra of the tungstate-based POMs show only a single envelop of peaks of the cluster having charge -3, in the range of m/z 1555-1575 (Figure 2.S11-2.S14, Table 2.S14-2.S17) while mixed addenda sandwich POMs show the isotopic multiple envelopes of peaks attributed to varying ratios of molybdenum to tungsten (Figure 2.6). The mixed addenda POMs show envelope of peaks (Figure 2.S3-2.S8) in the range of m/z 1300-1480 for [{M<sub>4</sub>(H<sub>2</sub>O)<sub>2</sub>(PMo<sub>x</sub>W<sub>9-x</sub>)<sub>2</sub>}<sup>3-</sup>], m/z 900-1150 for [{M<sub>4</sub>(H<sub>2</sub>O)<sub>2</sub>(PMo<sub>x</sub>W<sub>9-x</sub>)<sub>2</sub>}<sup>2-</sup>] and m/z 2000-2300 for [{M<sub>4</sub>(H<sub>2</sub>O)<sub>2</sub>(PMo<sub>x</sub>W<sub>9-x</sub>)<sub>2</sub>}<sup>2-</sup>] where M= Mn, Co and Ni as shown in Table 2.S6-2.S9. However, in case of Zn-based mixed addenda sandwich POMs, the envelope shifts to m/z 1500-1580 for [{Zn<sub>4</sub>(H<sub>2</sub>O)<sub>2</sub>(PMo<sub>x</sub>W<sub>9-x</sub>)<sub>2</sub>}<sup>3-</sup>] suggesting Mo incorporation is minimum among all reported here.

The maximum number of isotopic structures and the highest Mo:W ratio were obtained in P-Mn<sub>4</sub>Mo<sub>x</sub>W<sub>18-x</sub> (Figure 2.S3). The most abundant anion in P-Mn<sub>4</sub>Mo<sub>x</sub>W<sub>18-x</sub> has a composition of Mo:W (5:4) with the formula  $\lceil \{Mn_4(H_2O)_2(PMo_5W_4O_{34})_2\}^{10} \rceil$ , while Mo:W ratio varies from 13:5 to 7:11 maintaining a constant cluster charge of -10 (Table 2.S6). Among all these POMs containing different transition metals, the most abundant peak in P-Mn<sub>4</sub>Mo<sub>x</sub>W<sub>18-x</sub> exhibits the highest Mo:W ratio. The most abundant anion in Co as TM has the Mo:W ratio 7:11 (Figure 2.S4), which varies from 5:4 to 5:13 with the same charge (Table 2.S7). Lowering the pH results in the incorporation of higher Mo:W ratio (Figure 2.S7), however, it results in the formation of Keggin framework along with the sandwich framework (Table 2.S10). The most abundant anion peak of P-Ni<sub>4</sub>Mo<sub>x</sub>W<sub>18-x</sub>, gives the composition of Mo:W (7:11) with the formula  $[\{Ni_4(H_2O)_2(PMo_{3.5}W_{5.5}O_{34})_2\}^{10}]$ , while Mo to W ratio varies from 5:4 to 5:13 with a constant -10 charge of the cluster (Figure 2.S5). Unlike Co<sub>4</sub>Mo<sub>x</sub>W<sub>18-x</sub>, lowering the pH does not improve the Mo:W ratio, instead, it promotes the formation of Keggin framework along with the sandwich framework (Figure 2.S8 and Table 2.S11), and further lowering pH leads to the formation of complete Keggin structure. For P-Zn<sub>4</sub>Mo<sub>x</sub>W<sub>18-x</sub>, the shift in the isotopic envelope towards higher m/z ratio indicates lower Mo incorporation compared to other metals (Table 2.S9). The most abundant anion has a Mo:W composition of 1:5, formulated as  $[{Zn_4(H_2O)_2(PMo_{1.5}W_{7.5}O_{34})_2}^{10}]$ . Up to 5 Mo atoms can be incorporated into the P-Zn<sub>4</sub>Mo<sub>x</sub>W<sub>18-x</sub> framework at the reported pH, while lowering the pH results in the formation of Keggin framework.

The ESI-mass of Cu-substituted mixed addenda POMs exhibit isotopic envelope of peaks in the m/z range of 1200-1400 with a -2 charge and m/z 850-950 with a -3 charge, suggesting formation of Keggin POMs rather than sandwich frameworks (Fig. 2.S9, Table 2.S12). Up to 3 Mo atoms can be incorporated into the Cu-substituted Keggin framework. Similarly, Fe-substituted mixed addenda Keggin POM show isotopic envelopes of peaks in the range of m/z 1130-1310 with a -2 charge and m/z 750-880 with a -3 charge having the maximum Mo:W ratio of 6:5 (Figure 2.S10, Table 2.S13). Further, pH plays crucial role in tuning the extent of Mo addenda incorporation in these mixed addenda POMs.

To better understand the factors controlling of Mo/W ratio in the sandwich framework of Mn and Co, a systematic synthetic study was performed with varying pH. The detailed study is given in supporting information (Figure 2.S15-2.S16). ESI-MS analysis

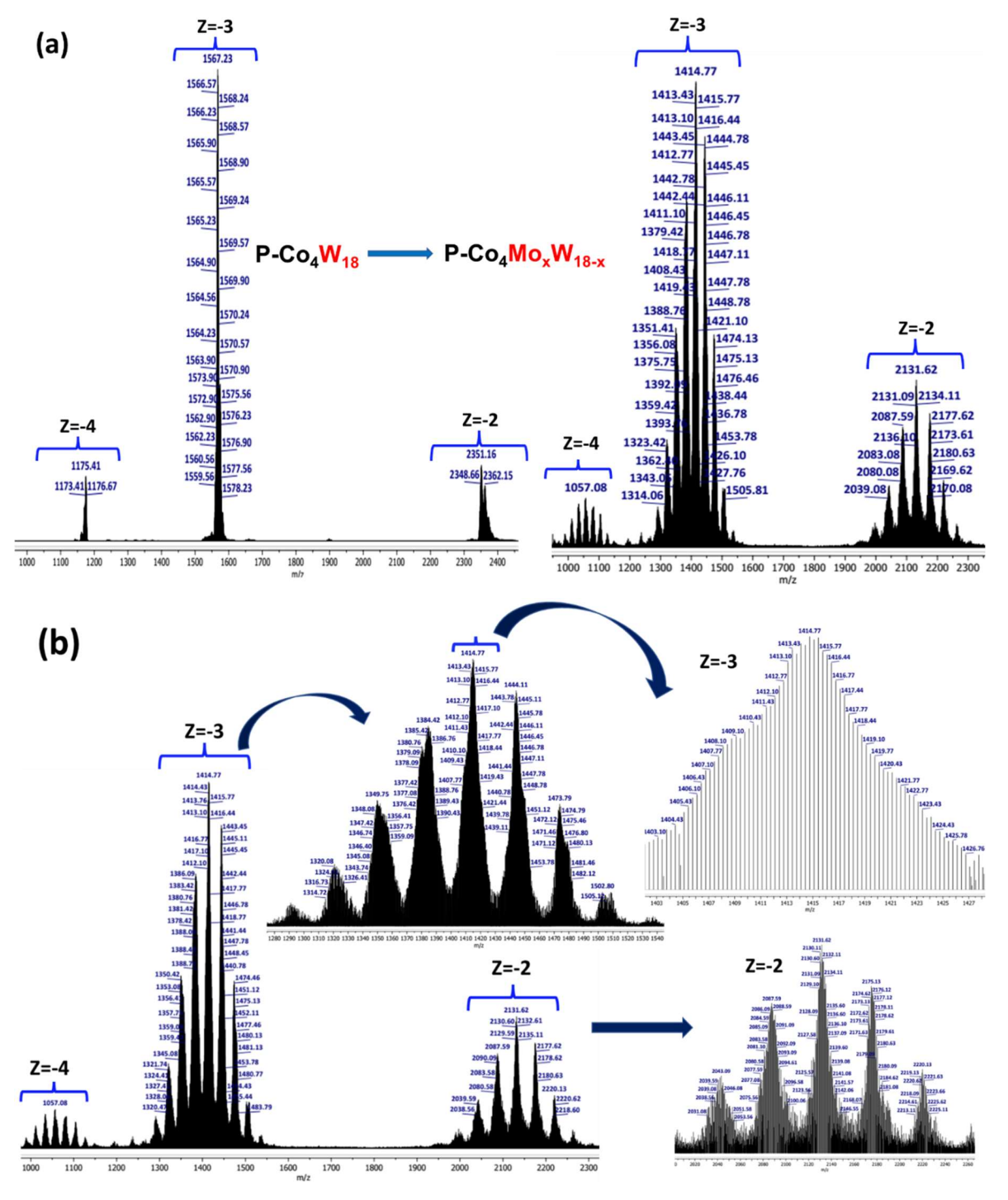


Figure 2.6 ESI-MS showing (a) single peaks in P-Co<sub>4</sub>W<sub>18</sub> and envelope of peaks for P-Co<sub>4</sub>Mo<sub>x</sub>W<sub>18-x</sub> (b) constancy of charges in envelope of peaks for P-Co<sub>4</sub>Mo<sub>x</sub>W<sub>18-x</sub>.

revealed that the Mo/W ratio of the most abundant peak increases on decreasing the pH from 7.5 to 6.5, but further decrease in pH leads to the formation of mixture of Keggin framework along with sandwich.

Further, inductively coupled plasma mass spectrometry (ICP-MS) analysis helped to assess the definitive Mo content, complementary to the ESI-mass spectrometry data (Table 2.S18). All the compounds show good thermal stability, with very little weight loss in between 30-800 °C (Figure 2.S17). The two steps weight loss from 30-200 °C suggests two types of water molecules, lattice and hydrated. The energy-dispersive X-ray analysis (EDX) analysis confirmed the bulk purity of all compounds (Figure 2.S18). The atomic percentage indicates that all elements are uniformly distributed as per the atomic composition ratio of all mixed addenda POMs.

# Vibrational spectroscopy (FTIR and Raman spectroscopy)

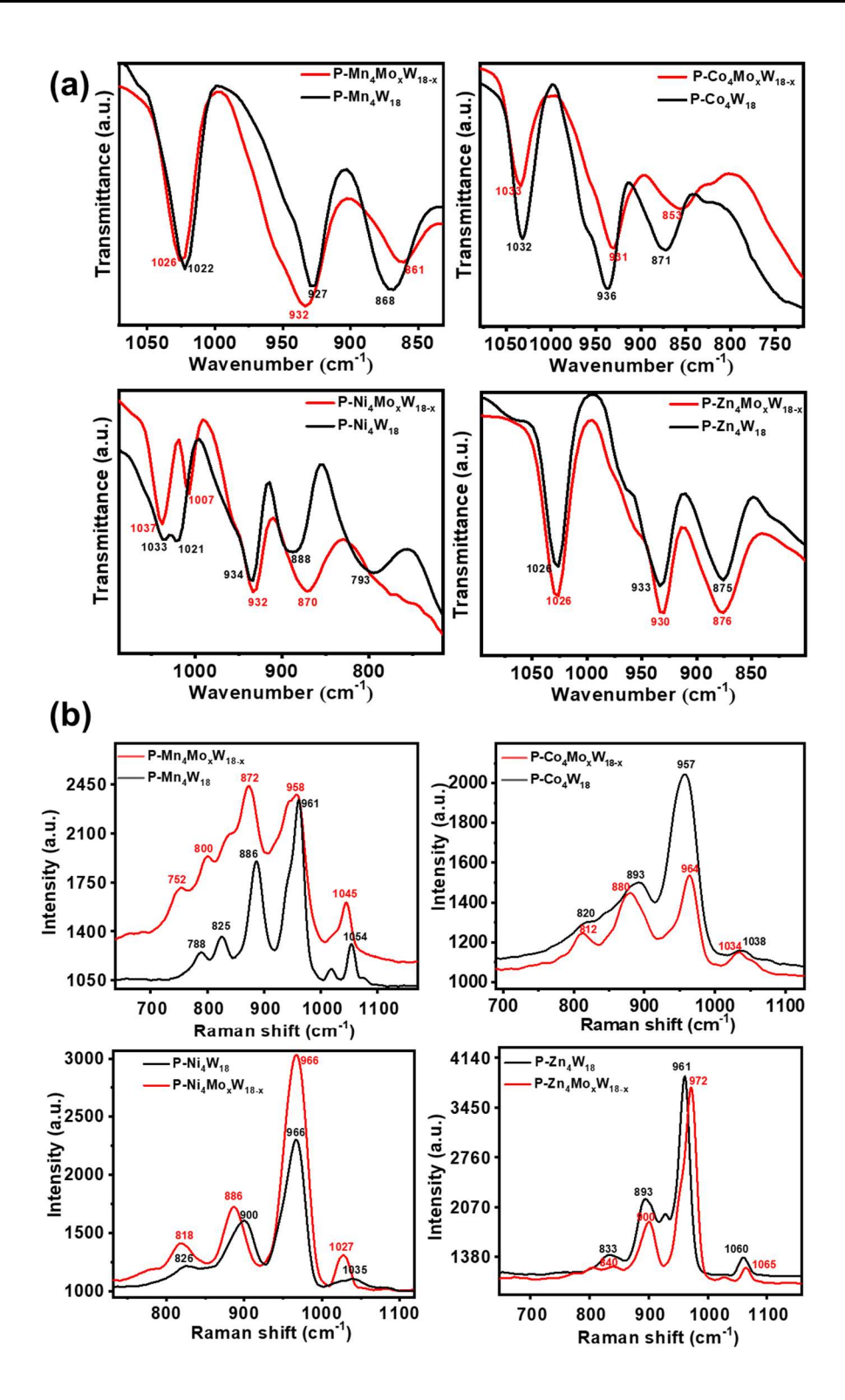
Vibrational spectra of POMs show their typical characteristics stretching vibrations of P-O, M=Ot, M-Oc-M, and M-Oc-M. Table 2.2 shows that these mixed addenda POMs have similar FT-IR as well as Raman patterns to their tungstate-based sandwich POM analogues due to their structural similarity and constancy of overall negative charge. The FT-IR spectra exhibit characteristic vibration bands of Keggin subunits (Figure 2.S19), while Raman spectra show characteristic bands of transition metal-oxygen bonds along with the Keggin subunits (Figure 2.S20). The notable difference in characteristics FT-IR and Raman peaks in these different transition metals-based mixed addenda sandwich POMs is due to different Mo:W ratios. Also, comparing the stretching frequencies of tetrasubstituted mixed addenda sandwich POMs with corresponding tungstate-only sandwich POMs, there is a subtle variation in the characteristic peaks (Figure 2.7) depending upon the number of Mo atoms incorporated in the framework structure. The P-O bond peak shifts to slightly higher values in mixed addenda while other characteristic peaks of M=Ot shift to lower values in FT-IR while this trend is reversed in Raman spectra with few exceptions (Table 2.2).

While going from tungstate-only to mixed addenda POMs, both FT-IR and Raman follow the same trend for M-O-M bonds. The maximum shift of M-O-M bond was found in Co & Ni, correlating a higher number of Mo incorporation in the framework structure, while in Zn-based sandwich POMs, there is negligible shift indicating significantly less Mo atom in the framework, which correlates well with SC-XRD as well as ESI-MS. The Raman spectroscopy (solid state) of mixed addenda sandwich POMs exhibits strong bands in the

range of 950-975 cm<sup>-1</sup> and 875-900 cm<sup>-1</sup> due to W=O<sub>t</sub> symmetric and asymmetric stretching, respectively. M-O-M M=W or Mo) stretching and bending modes of Keggin units ([PM<sub>9</sub>O<sub>34</sub>]<sup>10-</sup>) appears at 500-820 and 200-250 cm<sup>-1</sup>, respectively (Figure 2.7, Table 2.2). All tetrasubstituted sandwich POMs, the peaks in the range of 320-430 cm<sup>-1</sup> appear due to presence of transition metal-oxygen bonds in the sandwich position.

# 2.2.3 Properties of mixed addenda sandwich polyoxometalates

UV-vis spectroscopy (solid state) and bandgap measurements All the sandwich POM exhibit broad absorption band in UV-visible region due to ligand to metal charge transfer (LMCT)  $(O_{2p} \rightarrow W_{5d})$  as well as d-d transitions. The d-d transition along with LMCT is observed for Mn, Co and Ni-based sandwich POMs, while only LMCT is observed in Zn- based sandwich POMs, which is also reflected from their colour difference (Figure 2.8, inset photo). Moreover, a significant contribution of Mo is evident in mixed addenda sandwich POMs through a red shift in the UV-visible spectra compared to W-based sandwich POMs (Figure 2.8). This red shift can be explained from the changes in band gap of these POMs, which were investigated using diffuse reflectance spectroscopy (DRS). The optical band gap of these crystalline samples was calculated form DRS using Kubelka-Munk equation and plotting the graph between the energy axis and Kubelka-Munk function (Figure 2.8b). The optical band gap in POMs is generally defined as the difference between the oxo band (highest occupied molecular orbital, HOMO) and the empty metal band (lowest unoccupied molecular orbital, LUMO). The incorporation of Mo into the framework significantly impacts the optical band gap of these sandwich POMs, and the HOMO-LUMO gap decreases as the number of Mo atoms increases in the framework. The reduction in band gap is particularly prominent in P-Co<sub>4</sub>Mo<sub>x</sub>W<sub>18-x</sub> and P-Ni<sub>4</sub>Mo<sub>x</sub>W<sub>18-x</sub> compared to P-Mn<sub>4</sub>Mo<sub>x</sub>W<sub>18-x</sub> and P-Zn<sub>4</sub>Mo<sub>x</sub>W<sub>18-x</sub>, which is attributed to the combining factors of higher number of Mo atoms in the framework as well as nature of transition metal in the sandwich position. Furthermore, it is observed that the increase in the band gap follows a regular trend in both mixed addenda and W-based POMs moving from left to right in the periodic table. Also, in P-Co<sub>4</sub>Mo<sub>x</sub>W<sub>18-x</sub> and P-Ni<sub>4</sub>Mo<sub>x</sub>W<sub>18-x</sub>, a small peak was observed towards the lower band gap region due to d-d transitions, which is absent in P-Mn<sub>4</sub>Mo<sub>x</sub>W<sub>18-x</sub> and P-Zn<sub>4</sub>Mo<sub>x</sub>W<sub>18-x</sub>.



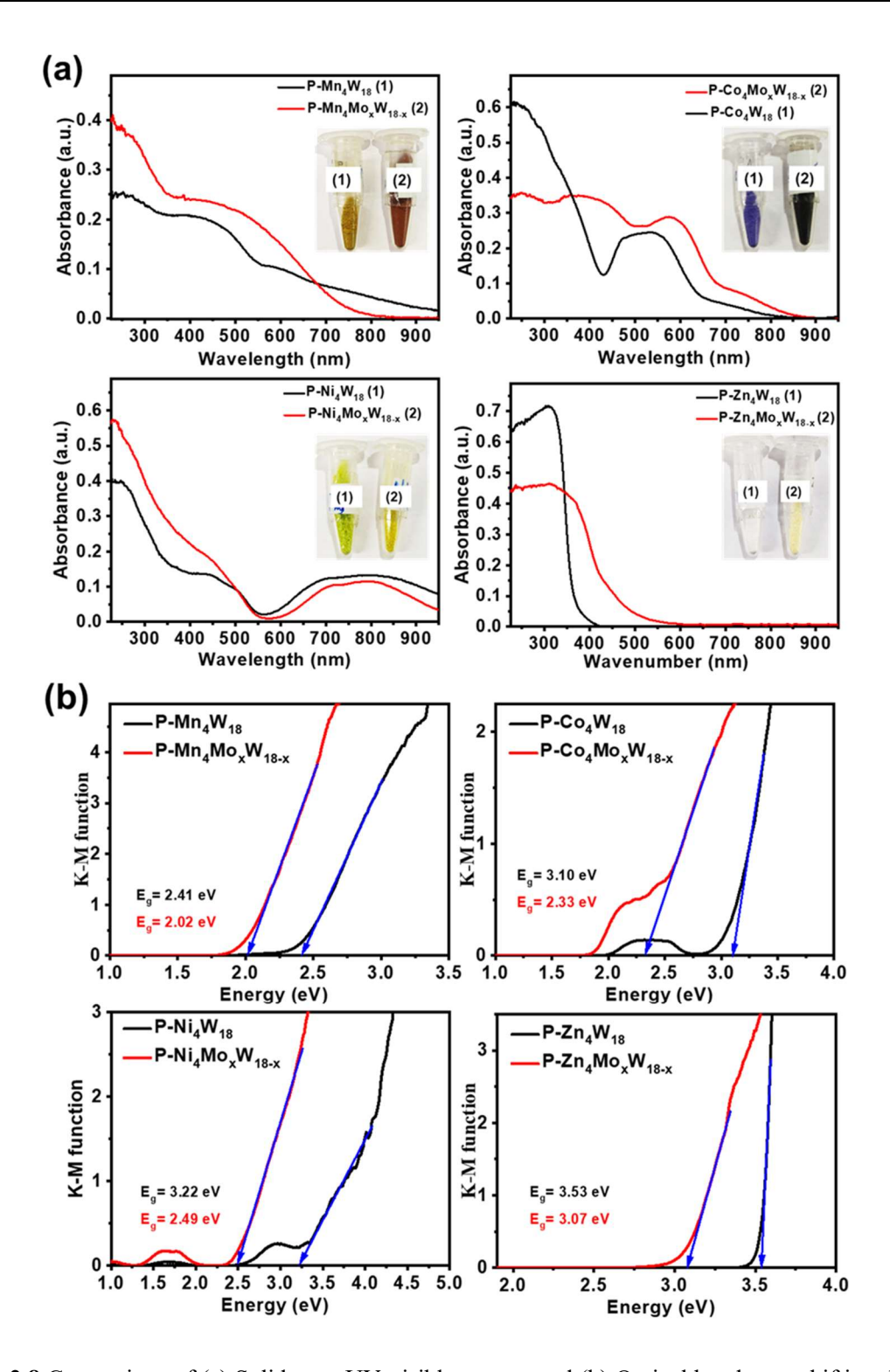
**Figure 2.7** Effect of molybdenum incorporation in the framework of tetrasubstituted sandwich POMs in terms of shifting of characteristics peaks in (a) FTIR and (b) Raman for P-(TM)<sub>4</sub>M<sub>18</sub> where TM=Mn/Co/Ni/Zn and M= Mo/W.

Table 2.2. FT-IR and Raman spectra peaks

Sandwich POMs	Raman (c		cm <sup>-1</sup> ) FT-IR (cm <sup>-1</sup>		n <sup>-1</sup> )	
	ν <sub>s</sub> (P-O)	$\nu_s(M\text{-}O_t)$	$v_s(M-O_c-M)$ ,	ν(Ρ-Ο)	$\nu_s(M\text{-}O_t)$	$\nu_s(M\text{-}O_c\text{-}M),$
			$\nu_{as}(M\text{-}O_c\text{-}M)$			$\nu_{as}(M\text{-}\mathrm{O}_c\text{-}M)$
P-Mn <sub>4</sub> W <sub>18</sub>	1054	961	886, 825	1022	927	868
P-Mn <sub>4</sub> Mo <sub>x</sub> W <sub>18-x</sub>	1045	958	872, 800	1026	932	861
P-Co <sub>4</sub> W <sub>18</sub>	1038	957	893, 820	1032	936	871
P-Co <sub>4</sub> Mo <sub>x</sub> W <sub>18-x</sub>	1034	964	880, 812	1033	931	853
P-Ni <sub>4</sub> W <sub>18</sub>	1033	966	900, 826	1035	934	888, 793
$P\text{-}Ni_{4}Mo_{x}W_{18\text{-}x}$	1037	966	886, 818	1027	932	870, 793
P-Zn <sub>4</sub> W <sub>18</sub>	1060	961	893, 833	1026	933	875
P-Zn <sub>4</sub> Mo <sub>x</sub> W <sub>18-x</sub>	1065	972	900, 840	1026	930	876

Cyclic Voltammetry In order to investigate the effect of the structural modulation on the electrochemical properties of mixed addenda sandwich POMs, cyclic voltammetry (CV) was performed in an aqueous solution with different scan rates at different pH. These sandwich POMs do not show redox peaks at pH >7.0, and only a few feeble peaks were observed at pH 5.0. At lower pH (typically pH<1.5), the tungstate/molybdate-based POMs generally demonstrate proton-coupled electron transfer, leading to hydrogen evolution.<sup>24</sup> Hence, all the electrochemical studies were performed at pH 3.5, where all the reported POMs show mostly quasi-reversible redox characteristics (Figure 2.9). The CV of tungstate-based sandwich POMs shows three quasi-reversible redox peaks of W on the negative side (ca.  $E_{1/2} < -200$  mV), while the TMs at sandwich position show quasi-reversible peaks toward the positive side (>200 mV) versus Ag/AgCl/3M KCl. 25 In mixed addenda analogues, along with these peaks for W and TM, Mo shows quasi-reversible redox peaks in the potential range of +0.65 V to -0.25 V with successive reduction of different Mo and W centers (Table 2.3). These peaks are assigned based on decreasing oxidizing power, TM > Mo > W. There are few redox peaks between -0.15 V to -0.50 V common for Mo and W. These POMs exhibit quasi-reversible redox couples in CV, characterized by their half-wave potentials

 $(E_{1/2})$  and peak separations ( $\Delta E_p = |E_{pc} - E_{pa}|$ ), as shown in Figure 2.9 (Table 2.3). CV of P- $Mn_4Mo_xW_{18-x}$  exhibits quasi-reversible redox couples with  $E_{1/2}$  0.30 V ( $\Delta E_p = 122$  mV) for Mn(II/III), 0.62 V ( $\Delta E_p = 77 \text{ mV}$ ), -0.10 V ( $\Delta E_p = 152 \text{ mV}$ ) attributed to successive redox Mo(V/VI) couple of two Mo centres. The redox couples at -0.61 V ( $\Delta E_p = 224$  mV), -0.98V ( $\Delta E_p = 112 \text{ mV}$ ) are assigned to W(V/VI) center (Figure 2.9a). Similarly, P-Co<sub>4</sub>Mo<sub>x</sub>W<sub>18</sub>-<sub>x</sub> shows quasi-reversible redox couples at  $E_{1/2}$  0.23 V ( $\Delta E_p = 139$  mV) corresponding to Co(II/III),  $E_{1/2}$  0.65 V ( $\Delta E_p = 66$  mV), -0.01 V ( $\Delta E_p = 198$  mV) and -0.13 V (133 mV) corresponding to Mo(V/VI) and  $E_{1/2}$  –0.39 V ( $\Delta E_p = 82$  mV), –0.63 V ( $\Delta E_p = 198$  mV), – 0.91 ( $\Delta E_p = 228 \text{ mV}$ ) corresponding to W(V/VI) center (Figure 2.9b). P-Ni<sub>4</sub>Mo<sub>x</sub>W<sub>18-x</sub> POM shows quasi-reversible redox couples at 0.32 V ( $\Delta E_p = 157$  mV) for Ni(II/III), -0.05 V ( $\Delta E_p$ = 184 mV) corresponding to Mo(V/VI) and two irreversible reductive response at -0.61 V, -0.88 V corresponding to W(V/VI) at 100 mV scan rate (Figure 2.9c). In the case of P-Zn<sub>4</sub>Mo<sub>x</sub>W<sub>18-x</sub>, quasi-reversible redox peaks at 0.64 V ( $\Delta E_p = 108 \text{ mV}$ ), +0.35 V ( $\Delta E_p = 128 \text{ mV}$ ) mV), -0.11 V ( $\Delta E_p = 137 \text{ mV}$ ) corresponding to Mo(V/VI) and -0.61 V ( $\Delta E_p = 228 \text{ mV}$ ), -1.01 V ( $\Delta E_p = 182$  mV), corresponding to W(V/VI) center were observed. It also exhibits two irreversible reductive responses at -0.94 V and -1.27 V, corresponding to W(V/VI) (Figure 2.9d). Also, the peak current varies with different scan rates while the peak potential remains almost constant thus showing the quasi-reversible nature of redox peaks (Figure 2.S21-2.S22). In tungstate-only POMs, tungsten accepts electrons in preference to transition metal during reduction while in mixed addenda (Table 2.3, Figure 2.9e/2.9f), Mo controls the directionality of electron transfer due to its higher affinity for accepting electrons than W and transition metals during the redox activity. Notably, comparing mixed addenda sandwich POMs with W-only, it was found that the redox peaks of W shift significantly towards higher reduction potentials, possibly due to a shift in the electron density towards more electronegative Mo within the framework. The first reduction for Co and Ni mixed addenda takes place at lower potential (-0.01 to -0.05 V) compared to Mn and Zn (-0.10 V) and this can be correlated with the low-lying LUMO of these mixed addenda POMs in DFT. Hence, these findings highlight the influence of mixed addenda on the electron density distribution during redox processes and the reversible nature of the redox processes based on the constant peak potential. The observed electrochemical behaviour provides insights into the electron transfer rates, directionality, and redox activities of these polyoxometalates.



**Figure 2.8** Comparison of (a) Solid state UV-visible spectra and (b) Optical band gaps shifting derived from Kubelka-Munk equation in P-(TM)<sub>4</sub>M<sub>18</sub> where TM=Mn/Co/Ni/Zn and M= Mo/W.

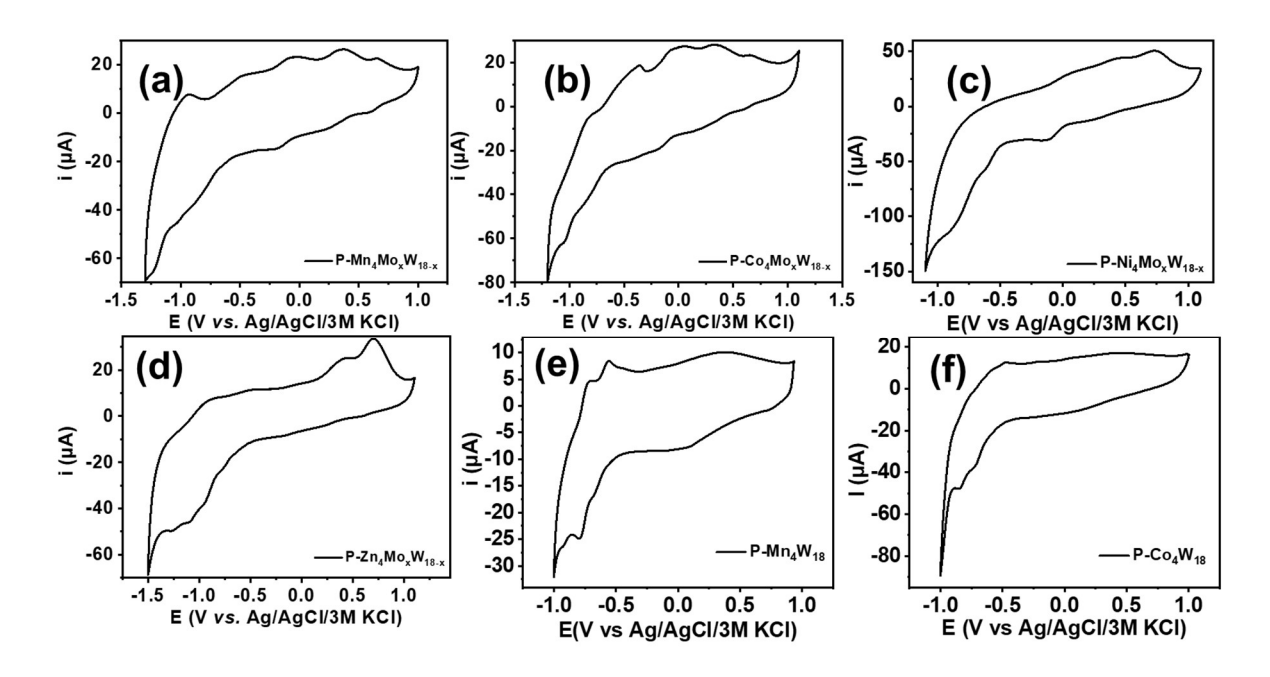


**Figure 2.9** Cyclic voltammograms of 0.2 mM concentration of (a) P-Mn<sub>4</sub>Mo<sub>x</sub>W<sub>18-x</sub>, (b) P-Co<sub>4</sub>Mo<sub>x</sub>W<sub>18-x</sub> (c) P-Ni<sub>4</sub>Mo<sub>x</sub>W<sub>18-x</sub>, and (d) P-Zn<sub>4</sub>Mo<sub>x</sub>W<sub>18-x</sub> and CV study of W-based sandwich POMs; (e) P-Mn<sub>4</sub>W<sub>18</sub>, (f) P-Co<sub>4</sub>W<sub>18</sub> in 0.5 M Na<sub>2</sub>SO<sub>4</sub> solution at pH 3.5 (pH of the solution adjusted by 2M H<sub>2</sub>SO<sub>4</sub>); Glassy carbon (WE): Pt wire, (CE): Ag/AgCl/3 M KCl (RE).

<b>Table 2.3</b> Cyclic voltammetry data of P-TM <sub>4</sub> Mo <sub>x</sub> W <sub>18-x</sub> and P-TM <sub>4</sub> W <sub>18</sub> , where TM=Mn, Co, Ni, and Zn (pH 3.5).							
		Mixed addenda	u /	W-only POMs			
Sandwich POMs	3d TMs $E_{1/2} (\Delta E_{\rm p})$ [V] [mV]	<b>W/Mo peaks</b> $E_{1/2}(\Delta E_p)$ [V] [mV]		3d TMs $E_{1/2} (\Delta E_{\rm p})$ [V] [mV]	W peaks $E_{1/2} (\Delta E_{\rm p})$ [V] [mV]		
	[ • ] [111 • ]	Mo	W	[ • ] [111 • ]	[v][mv]		
P-Mn <sub>4</sub> Mo <sub>x</sub> W <sub>18-x</sub>	0.30 (122)	0.62 (77), -0.10 (152),	-0.61 (224), -0.98 (112)	0.24 (240)	-0.55 (232), -0.68 (236), -0.81 (220),		
P-Co <sub>4</sub> Mo <sub>x</sub> W <sub>18-x</sub>	0.23 (139)	0.65 (66), -0.01 (198), -0.13 (133)	-0.39 (82), -0.63 (198), -0.91 (228)	0.31 (180)	-0.38 (198) -0.63 (136), -0.78 (85)		
P-Ni <sub>4</sub> Mo <sub>x</sub> W <sub>18-x</sub>	0.32 (157)	0.74 <sup>[a]</sup> , -0.05 (184)	-0.61 <sup>[b]</sup> , -0.88 <sup>[b]</sup>				
P-Zn <sub>4</sub> Mo <sub>x</sub> W <sub>18-x</sub>	-	0.64 (108), 0.35 (128), -0.11 (137)	-0.61 (228), -0.94 <sup>[b]</sup> , -1.01 (182), -1.27 <sup>[b]</sup>				

<sup>&</sup>lt;sup>[a]</sup>values refer to  $E_{\rm pa}$ , <sup>[b]</sup>values refer to  $E_{\rm pc}$ 

These phenomena can be understood better using the Mott Schottky plot.

Mott-Schottky plot and flat band potential Mott-Schottky measurements were conducted using a Biologic VSP-300 electrochemical workstation to investigate these mixed addenda sandwich POMs influence the energy band positions and charge transfer transitions. Mott-Schottky curves were recorded using a three-electrode system consisting of platinum as working, Ag/AgCl/3M KCl as reference, and graphite electrodes as the counter electrodes in a 0.5 mmol sandwich POMs dissolved in a 0.1 M Na<sub>2</sub>SO<sub>4</sub> solution electrolyte by varying the potential from -1.5 V to 1.0 V at frequencies of 631 Hz and 794 Hz. The obtained curves exhibited positive slopes, indicating the n-type semiconducting properties of all the reported POMs (Figure 2.10). The Fermi level, referenced to the normal hydrogen electrode (NHE) and considered to be approximately 0.2 eV more positive than the band positions obtained through the Mott-Schottky plot (Figure 2.11). The flat band potential for the valence band was determined using the equation  $E_g = VB-CB$ , where  $E_g$  represents the optical band gap calculated from the Kubelka-Munk function in DRS, VB represents the valence band, and CB represents the flat band potential of the conduction band. The flat band potential for the tungstate-only sandwich POMs were observed to be -1.22 V, -0.81 V, -0.92 V, and -1.29, which change to -1.09 V, -0.69 V, -0.70 V, and -1.19 V for the mixed addenda POMs for P-Mn4, P-Co4, P-Ni4, and P-Zn4, respectively. It is also observed that reduction in LUMO position is maximum in case of Co and Ni based sandwich POMs which can be correlated with the higher number of Mo incorporation as well as higher electronegativity of transition metal thus taken. This observation suggests that incorporation of Mo into the framework structure changes the flat band potential of these tetrasubstituted sandwich POMs due to the change in HOMO and LUMO positions.

# 2.2.4 Density Functional Theory (DFT) study

To understand the impact of mixed addenda on the electrical and redox characteristics of these sandwich POMs, systematic Density-functional theory (DFT) simulations were carried out using B3LYP functional with water as the solvent, implicitly using CPCM model. DFT studies were carried out using different spin states with unrestricted configuration considered with/without coupling. All the optimized molecular structures were found to be in good agreement with the corresponding SC-XRD structures in terms of bond parameters (Table 2.S19-2.S20). The energy and composition of LUMO define how the mixed addenda would affect the redox properties of these Weakley-type sandwich POMs (Figure 2.12a). The

detailed DFT studies aim to analyze the impact of non-equivalent Mo addenda atoms at different positions in the framework on the acidity/basicity, the band gap and redox behaviour of a series of W, Mo, and mixed addenda (Mo/W) sandwich POMs. From the spin coupling effects, the free energy increases from high spin to low spin state, (Table 2.4) suggesting that the ground state of all these POMs is high spin state thus suggesting the substituted transition metals are high spin (Table 2.4). Under the same computational parameter, the stability order of these POMs was found to be W-only > mixed addenda > Mo-only based on free energy (Table 2.S21).

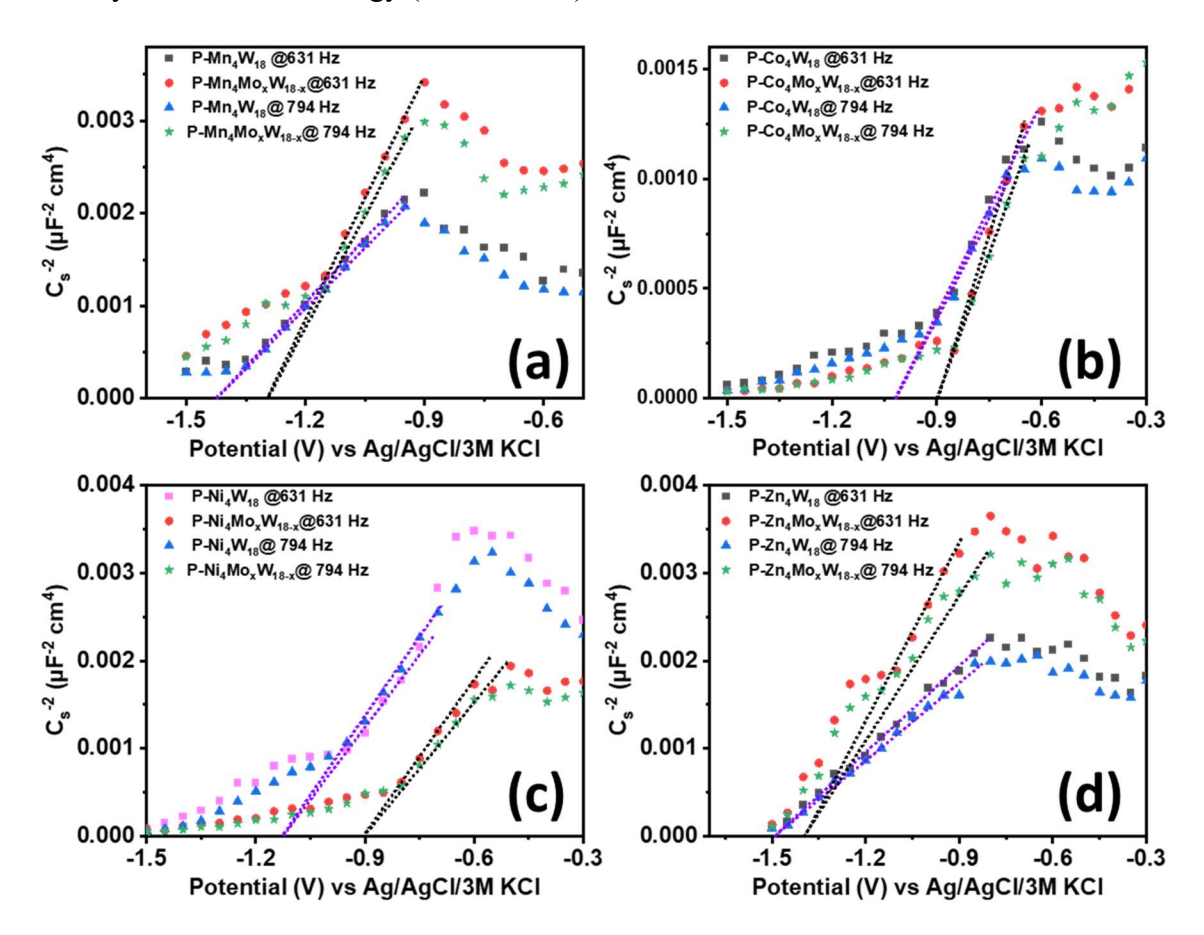


**Figure 2.10** Mott-Schottky Plot of (a) P-Mn<sub>4</sub>M<sub>18</sub>, (b) P-Co<sub>4</sub>M<sub>18</sub>, (c) P-Ni<sub>4</sub>M<sub>18</sub>, and (d) P-Zn<sub>4</sub>M<sub>18</sub> where M=W and Mo/W.

In order to identify the most suitable position for Mo substitution, one Mo-substituted at each addenda position in the mixed addenda sandwich POM were investigated (Table 2.6).

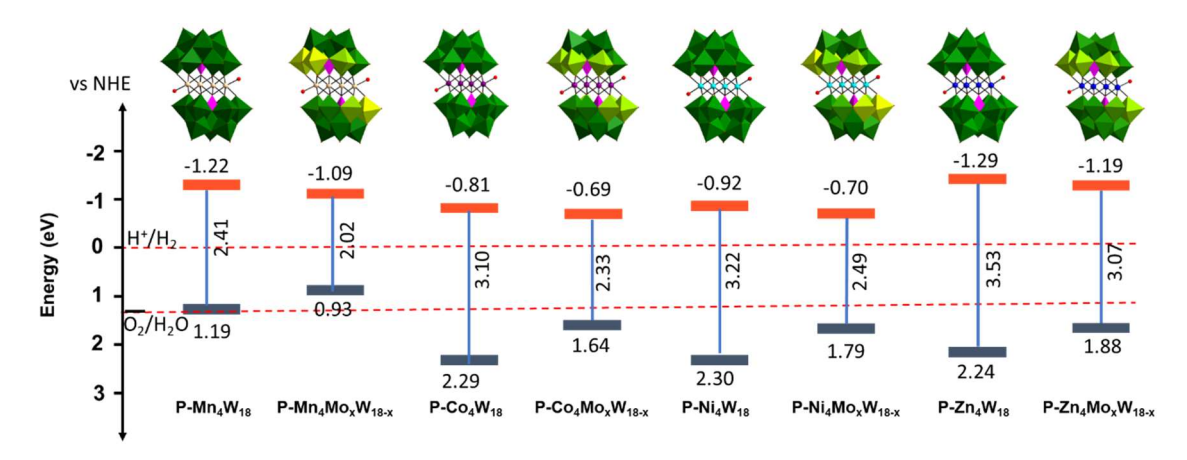
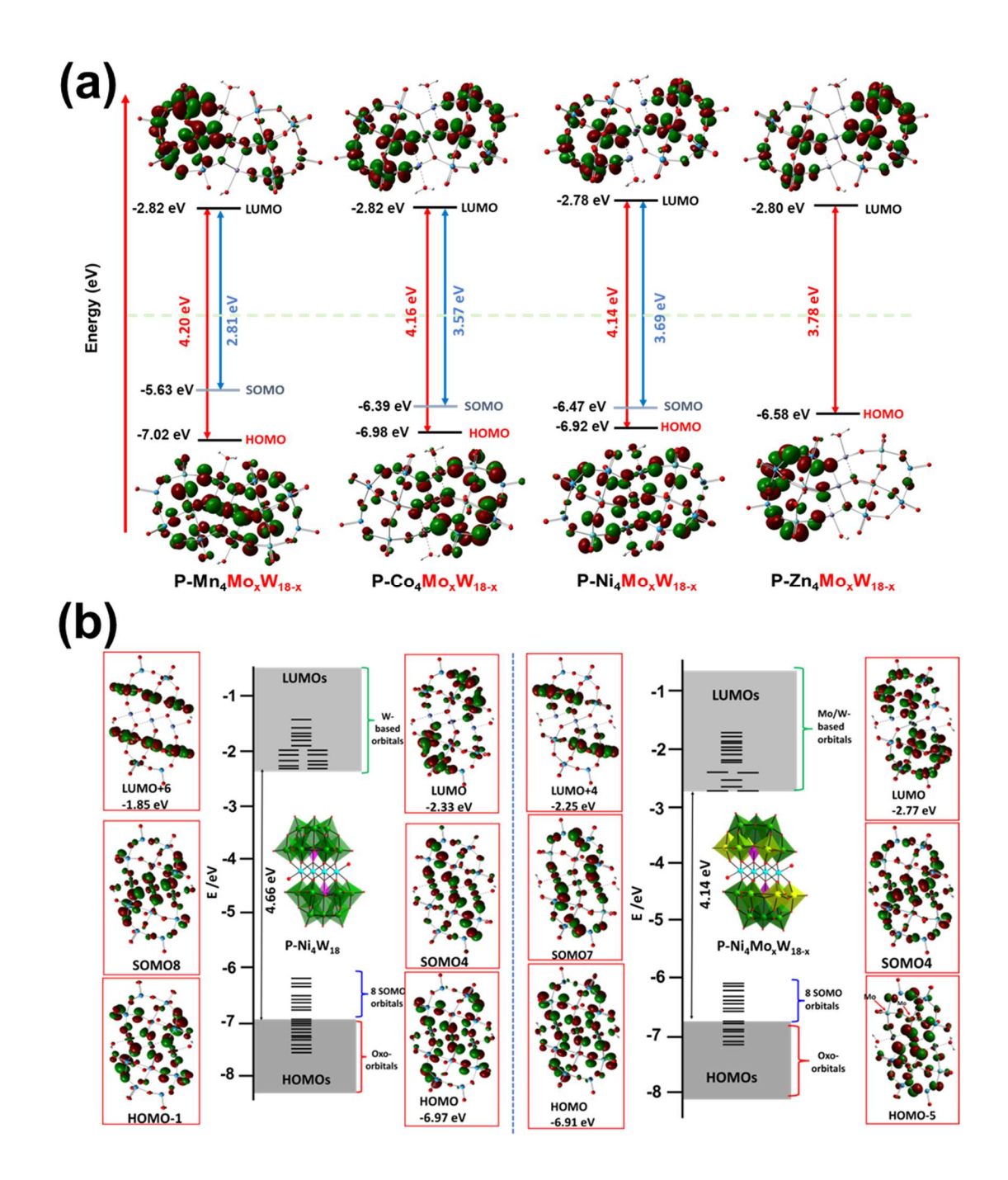


Figure 2.11 Diagram showing the frontier orbitals of tetrasubstituted sandwich POMs.

<b>Table 2.4</b> Energy Difference ( $\Delta E$ , in kcal mol <sup>-1</sup> ) between the Low-lying Spin States (High									
Spin, without spin coupling) and higher-energy Spin States (after spin coupling)									
POMsStates $\Delta E$ POMsStates $\Delta E$									
	(2S+1)	(kcal mol <sup>-1</sup> )		(2S+1)	(kcal mol <sup>-1</sup> )				
Mn <sub>4</sub> Mo <sub>x</sub> W <sub>18-x</sub>	21	0.0	Co <sub>4</sub> Mo <sub>x</sub> W <sub>18-x</sub>	13	0.0				
	1 (singlet)	262.67		1 (singlet)	223.70				
Ni <sub>4</sub> Mo <sub>x</sub> W <sub>18-x</sub>	9 (Nonet)	0.0	$Zn_4Mo_xW_{18-x}$	1 (Singlet)	0.0				
	7 (Septet) 17.29								
	1 (Singlet)	208.02							

Comparing the relative energies of P-Zn<sub>4</sub>W<sub>18</sub> with that of P-Zn<sub>4</sub>Mo<sub>18</sub>, each Mo dissipates 35.33 kcal/mol per Mo atom i.e. a minimum of 70.66 kcal/mol per position. From Table 2.6, position 6 dissipates 70.87 kcal/mol of energy and is highly vulnerable to the incoming molybdenum. Additionally, positions 4, 5, 6, and 9 (connected to  $\mu_2$  oxygen in the belt position) also exhibit high susceptibility to Mo-atom. In contrast positions 7 and 8 (connected to  $\mu_3$  oxygen in belt position), as well as cap positions 1, 2, and 3, are least susceptible, it seems the bridging oxygen plays an important role in dictating the positioning of Mo in these sandwich POMs. Moreover, due to the lower charge density of  $\mu_2$  oxygen compared to  $\mu_3$  oxygen,  $\mu_2$  oxygen preferentially binds with softer Mo atom. Further, the influence of transition metal at the sandwich position on the Mo:W (4:5) ratio in these sandwich POMs was studied (Table 2.S21). The highest Mo:W ratio follows the order of Mn>Ni>Co>Zn, which is consistent with the observed highest intensity peaks in ESI-MS analysis.



**Figure 2.12** (a) Frontier molecular orbitals showing band gaps of tetrasubstituted mixed addenda sandwich POMs. (b) Molecular orbitals showing HOMOs, LUMOs and SOMOs of P-Ni4W18 (left) and P-Ni4MoxW18-x POMs (right).

Typically, the bridged oxygens (M-O-M) of a POM exhibits higher basicity than terminals (M=O<sub>term</sub>) (M-O-M > M=O<sub>term</sub>, M=Mo/W). While the basicity order for bridged oxygen in mixed addenda Keggin POMs, was found to be Mo-O-Mo > Mo-O-W > W-O-W. In

sandwich POMs, the basicity of bridged oxygen in M-O-M was also found to be higher than M=O<sub>term</sub>, but the order changes for both bridged and terminal oxygen i.e., W-O-W > Mo-O-W > Mo-O-W > Mo-O-Mo and W=O<sub>term</sub> > Mo=O<sub>term</sub> (belt region) due to the presence of transition metals at the sandwich position (Table 2.S22) In the optimized structures of all the reported POMs, the highest occupied molecular orbitals (HOMO) lie on the corner and edge shared oxygens while the lowest occupied molecular orbitals (LUMO) majorly contribution from the addenda atoms (i.e., W/Mo) (Figure 2.S23-2.S26). In the TM substituted sandwich POMs, in between the oxo and LUMO band, a series of singly occupied molecular orbitals (SOMO) is contributed from the TM present, where the number of unpaired electrons depends on the nature of TM.

<b>Table 2.5</b> Effect of protonation on the different sites in Ni-based sandwich POMs							
$H_2[P\text{-}Ni_4Mo_8W_{10}]$							
Protonation site (oxygen)	Charge	2S+1	Reduction energy ΔE (eV)				
W-Ot (cap)	-10	7	-27.22				
W-O <sub>t</sub> (belt)	-10	7	-28.18				
Mo-Ot (belt)	-10	7	-28.25				
Mo-O-Mo (belt)	-10	7	-29.19				
Mo-O-W (belt)	-10	7	-29.11				
Nie-O-Wbelt	-10	7	-27.22				
Nie-O-Mobelt	-10	7	-33.51				
Nii-O-Mobelt	-10	7	-30.92				
	P-Ni <sub>4</sub>	$W_{18}$	1				
-	-10	9	-				
Nie-O-W <sub>belt</sub>	-10	7	-32.00				
P-Ni <sub>4</sub> Mo <sub>18</sub>							
-	-10	9	-				
-	-8	7	11.42				
Nie-O-Mobelt	-10	7	-33.48				

A representation of the HOMO-LUMO gap and their associated energy is shown in Figure 2.12. The HOMO-LUMO gap of 4.66 eV in case of W-only (P-Ni4) POM is reduced to 4.14 eV in mixed addenda analogue (Figure 2.12b). Consequently, HOMO-LUMO band gap in

mixed addenda sandwich POM falls between that of W-only and Mo-only sandwich POMs (Figure 2.13). This suggests that mixed addenda POMs are easy to reduce and powerful oxidizing agents compared to W-only POMs.

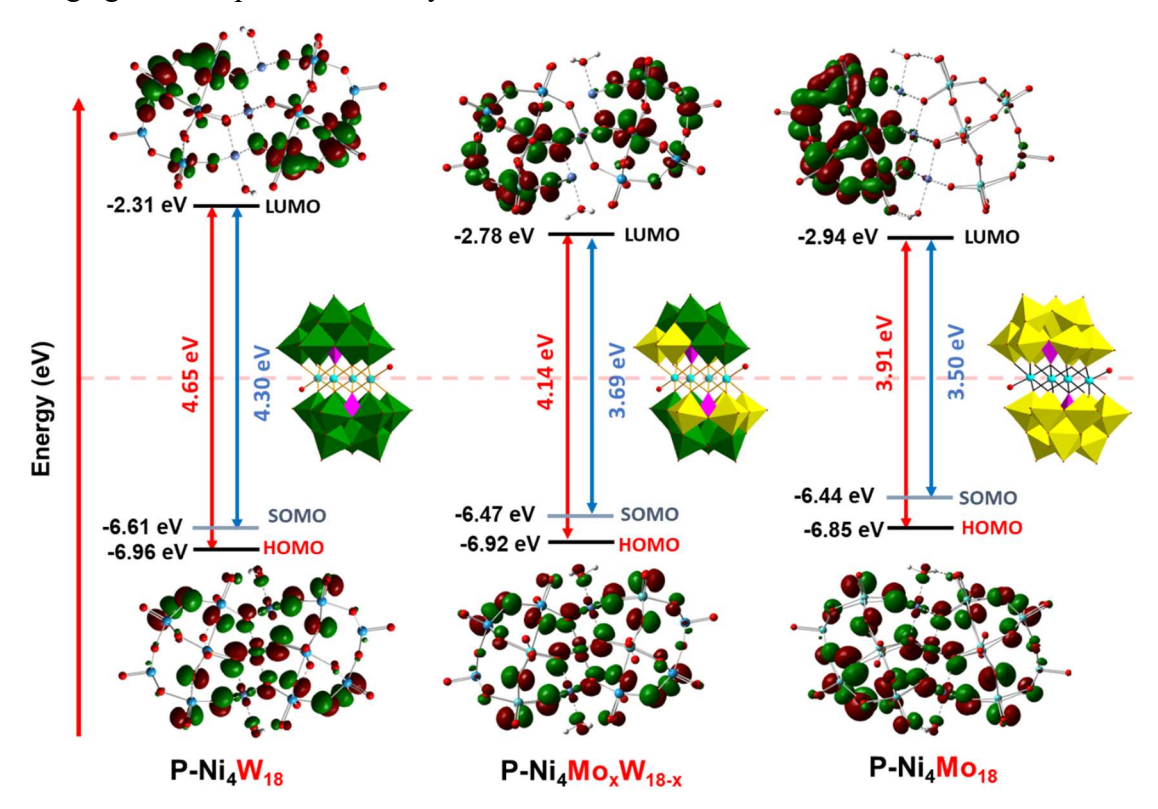


**Figure 2.13** Frontier molecular orbitals of tetrasubstituted sandwich POMs showing the effect of Modoping on band gaps as well as shifting of electron density on addenda atoms.

The LUMO energy as well as the band gap energy (HOMO-LUMO) drops as going from W-only to mixed addenda or even Mo-only POMs (Figure 2.13), which also correlates well in UV-visible spectroscopy. A similar trend was also reported in Keggin POMs. <sup>11</sup> The band positions and overall charge on the POM play a crucial role in defining their redox characteristics. While the overall charge being constant in all these sandwich POMs, the relatively lower LUMO energy in mixed addenda POMs correlates well with the higher electron affinity compared to their corresponding W-analogues. For analysis of the reduction properties, Ni4-substituted sandwich POMs (W-only vs mixed addenda), were taken as representative for DFT studies. From DFT optimization, it was found that 2e reduction

Table 2.6 Energy differen	nce for Mo ir		on at different sites in					
Zii-t	P-Zn <sub>4</sub> Mo <sub>2</sub> W <sub>16</sub>							
Molybdenum site (x)	Charge	2S+1	ΔE (kcal/mol)					
P-Zn <sub>4</sub> Mo <sub>2</sub> W <sub>16</sub> (1)	-10	0	73.2901					
P-Zn <sub>4</sub> Mo <sub>2</sub> W <sub>16</sub> (2)	-10	0	73.7147					
P-Zn <sub>4</sub> Mo <sub>2</sub> W <sub>16</sub> (3)	-10	0	73.4009					
P-Zn <sub>4</sub> Mo <sub>2</sub> W <sub>16</sub> (4)	-10	0	70.9975					
P-Zn <sub>4</sub> Mo <sub>2</sub> W <sub>16</sub> (5)	-10	0	71.2235					
P-Zn <sub>4</sub> Mo <sub>2</sub> W <sub>16</sub> (6)	-10	0	70.8721					
P-Zn <sub>4</sub> Mo <sub>2</sub> W <sub>16</sub> (7)	-10	0	74.7689					
P-Zn <sub>4</sub> Mo <sub>2</sub> W <sub>16</sub> (8)	-10	0	74.1038					
P-Zn <sub>4</sub> Mo <sub>2</sub> W <sub>16</sub> (9)	-10	0	71.0289					
P-Zn <sub>4</sub> W <sub>18</sub>	-10	0						
	P-Zn <sub>4</sub> Mo <sub>x</sub> V	W <sub>18-x</sub>						
P-Zn <sub>4</sub> Mo <sub>4</sub> W <sub>14</sub> (7, 8)	-10	0	146.5795					
P-Zn <sub>4</sub> Mo <sub>6</sub> W <sub>12</sub> (4, 5, 6)	-10	0	208.2047					
P-Zn <sub>4</sub> Mo <sub>8</sub> W <sub>10</sub> (6, 7, 8, 9)	-10	0	284.1723					
P-Zn <sub>4</sub> Mo <sub>8</sub> W <sub>10</sub> (4, 5, 6, 9)	-10	0	277.0875					
$\begin{array}{c} P\text{-}Zn_4Mo_{10}W_8 \\ (1,2,3,7,8) \end{array}$	-10	0	359.4872					

was unattainable without coupling simultaneous proton transfer, which was also evident from pH dependent redox behaviour in electrochemical reduction. So, the DFT optimization was done considering the  $2e^{-}/2H^{+}$  reduction. This phenomenon was better understood from the computed energy for protonation of different oxygen atoms within the framework considering the  $2e^{-}/2H^{+}$  reduction process (Table 2.5). Interestingly, the corner shared  $\mu_{2}$  oxygen atom situated between external Ni<sub>e</sub> and Mo atom exhibited a preference for accepting the protons over other oxygen sites. This preference was further corroborated by the NBO charge distribution analysis (detailed in Table 2.S22). The charge distribution table unequivocally confirmed that the oxygen bonded to external TM<sub>e</sub> and Mo from the belt has the highest charge density.

Unlike Keggin POMs, the addenda within sandwich POMs are not equivalent, leading to the different contributions from various position of addenda atoms while adding the electrons during 2e reduction. This is very clear during the 2e/2H+ reduction of mixed addenda POMs, where, the Mo atoms are reduced first before W, and the corner shared  $\mu_2$  oxygen atom between external TM and connecting Mo addenda atoms directs the proton and the electron localized on Mo (Figure 2.S26). Furthermore, the mixed addenda strategy introduces a significant shift in LUMO. For example, the LUMO of Ni4 sandwich POMs in W-only (Figure 2.13) mainly located on the W-atoms at the cap as well as the W-atom of belt region connected to  $\mu_3$  oxygen. While in case of Mo-only (P-Ni4Mo9), the LUMO is the contribution from all Mo-atoms of the framework (cap and belt region). However, the LUMO in mixed addenda is constituted mainly from two Mo-atoms at the belt region connected to the  $\mu_2$  oxygen, which was also contributing for the incoming electron during 2H+/2e reduction. Thus, the mixed addenda strategy controls the direction of incoming electrons during 2H+/2e reduction.

# 2.2.5 Molecular oxygen binding/activation

The activation of molecular oxygen (O<sub>2</sub>) by sandwich POMs have been found very effective in many organic transformation reactions. As sandwich POMs have specific binding sites for binding of molecular oxygen, it imparts selectivity in the product. Recently, our group of Zn-based have shown dioxygen activation sandwich **POMs** [{ZnWM<sub>2</sub>(H<sub>2</sub>O)<sub>2</sub>(ZnW<sub>9</sub>O<sub>34</sub>)<sub>2</sub>}<sup>n-</sup>] where M=Mn, Co, Fe, Ni and Cu have been found to be active for catalytic imine synthesis.<sup>27</sup> Here, binding ability of O<sub>2</sub> have been investigated using mixed addenda sandwich POMs towards the formation of POM-O2 adduct. Following the reported procedure, O<sub>2</sub> binding ability of [P-(TM)<sub>4</sub>Mo<sub>x</sub>W<sub>18-x</sub>] (M=Mn, Co, Ni and Zn) was checked in toluene as heterogenous system, and heated at 110 °C after purging with O<sub>2</sub> for 5 h. From FT-IR study of O<sub>2</sub> activated [P-(TM)<sub>4</sub>Mo<sub>x</sub>W<sub>18-x</sub>], two peaks in the range of 1150-1160 cm<sup>-1</sup> and 1200-1210 cm<sup>-1</sup> have been observed in all these POMs indicating the formation of O<sub>2</sub> binding POM (Figure 2.14). Along with these two peaks, P-Mn<sub>4</sub>Mo<sub>x</sub>W<sub>18-x</sub> and P-Co<sub>4</sub>Mo<sub>x</sub>W<sub>18-x</sub> exhibit one more peak in the region 530-650 cm<sup>-1</sup>, possibly due to formation of peroxo complex. Also, when comparing the O<sub>2</sub> binding ability of P-Co<sub>4</sub>W<sub>18</sub> with P-Co<sub>4</sub>Mo<sub>x</sub>W<sub>18-x</sub>, it was found that mixed addenda show better activity for O<sub>2</sub> activation (Figure 2.S27).

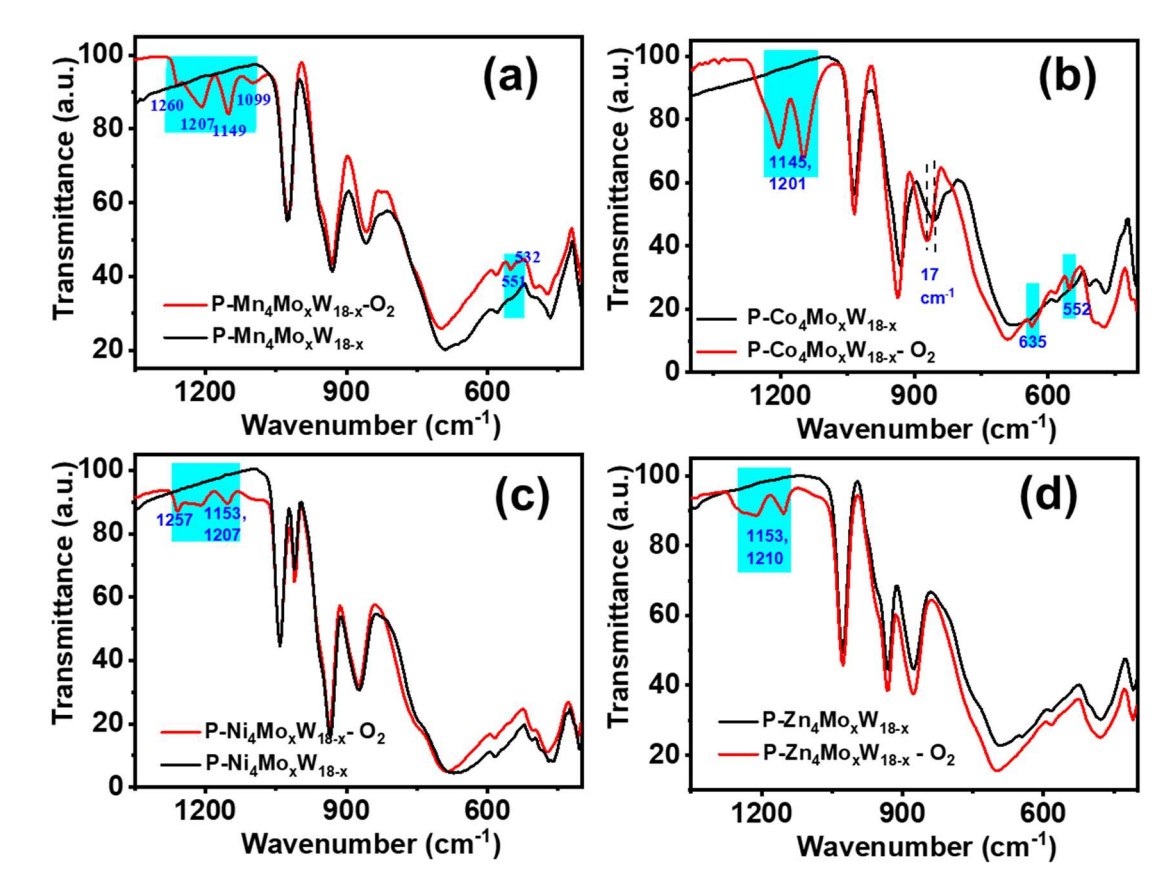


**Figure 2.14** Comparative FT-IR spectroscopy of mixed addenda sandwich POMs before and after  $O_2$  treatment in toluene for (a)  $[Mn_4(H_2O)_2(PMo_xW_{9-x}O_{34})_2]^{10-}$  (P-Mn<sub>4</sub>Mo<sub>x</sub>W<sub>18-x</sub>), (b)  $Co_4(H_2O)_2(PMo_xW_{9-x}O_{34})_2]^{10-}$  (P-Co<sub>4</sub>Mo<sub>x</sub>W<sub>18-x</sub>) (c)  $Ni_4(H_2O)_2(PMo_xW_{9-x}O_{34})_2]^{10-}$  (P-Ni<sub>4</sub>Mo<sub>x</sub>W<sub>18-x</sub>) and (d)  $Zn_4(H_2O)_2(PMo_xW_{9-x}O_{34})_2]^{10-}$  (P-Zn<sub>4</sub>Mo<sub>x</sub>W<sub>18-x</sub>).

## 2.3 Conclusion

In this study, we have successfully synthesized mixed addenda sandwich POMs and extensively characterized them in the both solid as well as in solution states. Through a combination of experimental and theoretical methods, we have identified and validated the relative stabilities of their structural isomers with different Mo distributions. ESI-MS analysis confirmed different ratios of Mo to W in the mixture of tetrasubstituted sandwich POMs, where Mn, Co and Ni has most abundance Mo/W ratio of 9/9, 7/11, 7/11, respectively. The introduction of mixed addenda into these POMs has proven to be a powerful strategy for lowering the overall band gap, thereby enabling precise engineering of HOMO and LUMO gaps. This lowering of the LUMO energy significantly impacts

molecular properties, such as reduction of onset potential, and absorption maxima at higher wavelengths, which was also correlated with the DFT calculations.

We propose that this orbital engineering strategy have significant implications for the designing of POM-based photo and electrocatalysts. Given the enormous potential for further fine-tuning through counter ion exchange and composite design through host-guest interaction with various dimensional materials; we believe this approach leads to significant advances in the generation of POMs-based novel heterogeneous materials. Using our mixed addenda design strategy, further variation in substituted transition metals as well as heteroatom we anticipate a broader spectrum of structural tuning in a variety of mixed-addenda sandwich POMs.

# 2.4 Experimental Section

#### 2.4.1 General Information and Instrumentation

#### 2.4.1a Materials and Methods

Deionized water used in the experiments was from Millipore system (>18 M $\Omega$  cm<sup>-1</sup>). The transition metal salts used in synthesis were obtained from Alfa Aesar (purity > 99.9%) and used without further purification. [(TM)<sub>4</sub>(H<sub>2</sub>O)<sub>2</sub>(PW<sub>9</sub>O<sub>34</sub>)<sub>2</sub>].nH<sub>2</sub>O where M=Mn, Co, Ni and Zn were synthesized according to the reported procedure.<sup>7, 28, 29</sup> All polyoxometalates were recrystallized from an aqueous solution before characterization and electrochemical analysis.

#### 2.4.1b Instrumentation

**Bond Valence Sum (BVS) Calculations**: BVS values of selected atoms were calculated using the expression

$$V_i = \sum_j \exp\left(\frac{R_o - R_{ij}}{B}\right)$$

Where  $V_i$  is bond valence parameter of atom i, B is a constant equal to 0.37 Å.  $R_{ij}$  is variation in bond length between two atoms i and j,  $R_o$  is the bond valence parameter of given pair of atoms. BVS was calculated from the obtained crystal structure of all the synthesized POMs

to calculate oxidation state of transition metals and further correlated with oxidation states calculated from the XPS analysis.

Ultraviolet-Visible spectroscopy (UV-Vis). UV-visible spectra were recorded in Shimadzu (UV-2600) spectrophotometer. Diffuse reflectance spectra were recorded in Shimadzu UV-2600 using integrating sphere units (ISR-2600). The optical band gap of these crystalline samples was calculated from diffuse reflectance spectroscopy (DRS) using the Kubelka-Munk equation. A graph was plotted between the energy axis and the Kubelka-Munk function as the intersection point between the energy axis and line obtained by extrapolating the linear portion of the absorption edge in the plot of the Kubelka-Munk function versus energy. The Kubelka-Munk function, (1-R)<sup>2</sup>/2R, was calculated from the recorded reflectance data, where R is the reflectance of the layer of TMSP. Absorbance was also calculated from the reflectance spectra using K-M function.

**Fourier Transform Infrared spectroscopy (FT-IR).** FT-IR spectra were recorded in the range of 400–4000 cm<sup>-1</sup> using Shimadzu spectrometer with a spectral resolution of 4 cm<sup>-1</sup> and 100 scan.

**Raman spectra** were recorded on a LabRAM HR Evolution Raman spectrometer (Horiba Scientific) in the range of 200-4000 cm-1 by using a 532 nm laser as the excitation source.

**Thermal gravimetric analysis (TGA).** Measurements were performed using a Mettler Toledo TGA/DSC 3, STARe System apparatus under nitrogen flow at a heating rate of 10 °C min<sup>-1</sup> up to 600 °C. The water of crystallization was determined from the weight loss based on the first derivative plot below 220 °C.

## **Optical Images (Camera)**

The optical images of the crystalline compounds were taken in OLYMPUS equipment (V-TV0.5XC-3, T7).

**Electrospray ionization mass spectrometry (ESI-MS)** The ESI-MS spectra of all the polyoxometalates were recorded on Waters XEVO G2-XS QTOF mass spectrometer. Sample was prepared by adding 2.5 mL of milli-Q water to the sample vial (5-10 mg), sonicated for 10 minutes to obtain a clear solution, and filtered using a syringe filter (organic solvents like acetonitrile should be avoided, which may precipitate POM). The sample was

run in the HRMS using negative ionization mode in the range of m/z 100-3000 with different z values (single peak/envelope of peaks).

**Powder X-ray diffraction (PXRD)** studies were performed to affirm the phase purity of the compounds over PANalytical's X'Pert Pro MPD with Cu K $\alpha$  radiation.

**X-ray photoelectron spectra (XPS)** were recorded using a Thermo Scientific NEXSA surface analysis system with a microfocused (400  $\mu$ m, 72 W, 12000 V) monochromatic Al K $\alpha$  (1486.6 eV) hemispherical analyzer and 128 channel plate detectors under a ultrahigh vacuum (UHV 8-10 mbar).

Energy dispersive X-ray analysis (EDX) were performed for the elemental analysis using EDX; Oxford, INCAx-act, 51-ADD0013 instruments.

Single crystal X-ray diffraction analysis. The molecular structures of all the sandwich POMs were revealed from single crystal X-ray diffraction (SC-XRD) analysis. Diffraction quality crystals were coated by Paratone-N oil, mounted on a cryoloop and subjected to collect single crystal X-ray data using graphite monochromated Mo  $K\alpha$  radiation ( $\lambda$  = 0.71073 Å) on a Bruker D8 SMART APEX2 CMOS diffractometer at 300 K. Data integration was performed using scalable automated integrations of reflections (SAINT). Routine Lorentz and polarization corrections were applied to all structures, and empirical absorption corrections were performed using SADABS. Olex2 were used to solve all the structures, and refinement was performed using SHELXL2013. In Olex 2 software, an electron density contour map along with refinements (variation in R1/wR2 values) was used to assign crystallographic mixed addenda (Mo/W) position in the framework. Crystal data, data collection parameters, refinement statistics and the Cambridge Crystallographic Data Centre; CCDC number (1511657, 2290783, 2290784, 2290785, 2290786, 2290787, 2290788, 2290789) for studied crystals are summarized in Table 2.1 and 2.S1.

# 2.4.1c Density Functional Theory (DFT) Calculation

DFT calculations were performed with the Gaussian 09 programs using Becke's three-parameter hybrid exchange functional and the Lee-Yang-Parr correlation functional (B3LYP). The double- $\zeta$  basis set of Hay and Wadt (LanL2DZ) with an effective core potential (ECP) was used for W, Mo, Zn, Ni, Co, Mn to represent the innermost electrons of these atoms and the O-atom was described using the 6-31G+(d,p) basis sets. The calculations

were performed considering the solvation effects of water in conductor-like screening model (CPCM) model. The closed-shell geometry optimization calculations in P-M<sub>4</sub>W<sub>18</sub>, P-M<sub>4</sub>Mo<sub>x</sub>W<sub>18-x</sub>, and P-M<sub>4</sub>Mo<sub>18</sub> complexes (where M=Mn, Co, Ni, and Zn) were performed using the atomic coordinates provided by the X-ray structures of the respective anions.

#### 2.4.1d Electrochemical studies

Cyclic voltammograms were recorded on a Metrohm Autolab 204 using a standard three-electrode set-up equipped with a 3 mm diameter glassy carbon working electrode (WE), Pt wire counter electrode (CE) and Ag/AgCl/3 M KCl as reference electrode (RE) using 0.2 mM POM @10 mV/s scan rate. Mott-Schottky measurements were conducted on a Biologic (VSP 300) potentiostat.

# 2.4.2 Synthesis

Synthesis of Na<sub>10</sub>[Mn<sub>4</sub>(H<sub>2</sub>O)<sub>2</sub>(PMo<sub>x</sub>W<sub>9-x</sub>O<sub>34</sub>)<sub>2</sub>].18H<sub>2</sub>O (P-Mn<sub>4</sub>Mo<sub>x</sub>W<sub>18-x</sub>). A mixture of Na<sub>2</sub>WO<sub>4</sub>.2H<sub>2</sub>O (4.12 g, 12.50 mmol), Na<sub>2</sub>MoO<sub>4</sub>.2H<sub>2</sub>O (3.02 g, 12.50 mmol), Na<sub>2</sub>HPO<sub>4</sub>.2H<sub>2</sub>O (0.38 g, 2.76 mmol) was dissolved in 25 mL DI H<sub>2</sub>O. After fixing pH 6.5 using nitric acid, the clear solution was heated for 30 min at 85 °C. A solution of MnCl<sub>2</sub>.4H<sub>2</sub>O (1.08 g, 5.49 mmol) dissolved in 10 mL DI water was then added to the above solution with stirring and transferred to a Teflon microwave vial. The mixture was microwave irradiated by controlled pressure programming with a power ramp for 5 min. and holding for 45 min. at 85 °C, under 300 W maximum power. The resultant solution was hot filtered and potassium nitrate was added to the reaction mixture resulting in a small amount of precipitate which was filtered again. The dark red-colored solution thus obtained was left for crystallization at room temperature. After 3 days, dark red colored cylindrical shaped crystals appeared (Figure 2.S1), which filtered and clear filtrate gave few more crystal on keeping for further 3-4 days. These crystals were collected and recrystallized from water, and dried at ~60 °C under vacuum to get the P-Mn<sub>4</sub>Mo<sub>x</sub>W<sub>18-x</sub> sandwich POMs. Yield: 2.02 g (36.6%). FT-IR (cm<sup>-1</sup>): 1026, 932, 861. Raman (solid, cm<sup>-1</sup>): 1045, 958, 872, 800.

Synthesis of Na<sub>10</sub>[Co<sub>4</sub>(H<sub>2</sub>O)<sub>2</sub>(PMo<sub>x</sub>W<sub>9-x</sub>O<sub>34</sub>)<sub>2</sub>].16H<sub>2</sub>O (P-Co<sub>4</sub>Mo<sub>x</sub>W<sub>18-x</sub>). The synthetic procedure of P-Mn<sub>4</sub>Mo<sub>x</sub>W<sub>18-x</sub> was repeated using Co(NO<sub>3</sub>)<sub>2</sub>.6H<sub>2</sub>O (1.60 g, 5.49 mmol) in place of MnCl<sub>2</sub>. After microwave irradiation, brown colored solution thus obtained was left for crystallization. After 2 hours, dark brown colored cylindrical-shaped (Figure 2.S1)

crystals appeared. These crystals were recrystallized with 1M aqueous potassium nitrate solution. The crystals thus obtained were collected by filtration, and dried at  $\sim$ 60 °C under vacuum to get the P-Co<sub>4</sub>Mo<sub>x</sub>W<sub>18-x</sub>. Yield: 2.40 g (43.4%). FT-IR (cm<sup>-1</sup>): 1033, 931, 853. Raman (solid, cm<sup>-1</sup>): 1034, 964, 880, 812.

Synthesis of Na<sub>10</sub>[Ni<sub>4</sub>(H<sub>2</sub>O)<sub>2</sub>(PMo<sub>x</sub>W<sub>9-x</sub>O<sub>34</sub>)<sub>2</sub>].14H<sub>2</sub>O (P-Ni<sub>4</sub>Mo<sub>x</sub>W<sub>18-x</sub> POM). In a typical procedure, a mixture of Na<sub>2</sub>WO<sub>4</sub>.2H<sub>2</sub>O (3.29 g, 10.00 mmol), Na<sub>2</sub>MoO<sub>4</sub>.2H<sub>2</sub>O (3.63 g, 15.00 mmol), Na<sub>2</sub>HPO<sub>4</sub>.2H<sub>2</sub>O (0.38 g, 2.76 mmol) was dissolved in 25 mL DI H<sub>2</sub>O. After fixing pH 7.15 using glacial acetic acid, the clear solution was heated for 30 minutes at 85 °C (solution A). A solution of Ni(OAc)<sub>2</sub>.4H<sub>2</sub>O (1.36 g, 5.49 mmol) dissolved in 10 mL DI water was then added to the above solution with stirring and transferred to a Teflon microwave vial. The sample mixture was microwave irradiated by controlled pressure programming with a power ramp for 5 min. and holding for 45 min. at 85 °C, under 300 W maximum power. The resultant solution was hot-filtered resulting in the formation of greenish crystalline powder in the solution after 20 minutes. The crystalline powder was dissolved in the solution again and final pH of the solution thus obtained was fixed at 6.8 using dilute KOH. The resulting solution was further heated at 85 °C for 1 h resulting in the formation of light yellow-colored clear solution which was left for crystallization. After 2 days, yellow colored cylindrical shaped crystal (Figure 2.S1) appears which were collected by filtration, recrystallized from water, and dried at ~60 °C under vacuum to get the Ni4-based mixed addenda sandwich Polyoxometalates. Yield: 1.65 g (29.9%) FT-IR (cm<sup>-1</sup>):1027, 932, 870, 793. Raman (solid, cm<sup>-1</sup>):1037, 966, 886, 818.

# Synthesis of Na<sub>10</sub>[Zn<sub>4</sub>(H<sub>2</sub>O)<sub>2</sub>(PMo<sub>x</sub>W<sub>9-x</sub>O<sub>34</sub>)<sub>2</sub>]•10H<sub>2</sub>O (P-Zn<sub>4</sub>Mo<sub>x</sub>W<sub>18-x</sub>)

The synthetic procedure of P-Zn<sub>4</sub>Mo<sub>x</sub>W<sub>18-x</sub> POM is likewise P-Ni<sub>4</sub>Mo<sub>x</sub>W<sub>18-x</sub> with slight modification. A solution of Zn(OAc)<sub>2</sub>.4H<sub>2</sub>O (1.41 g, 5.49 mmol) in 10 mL DI H<sub>2</sub>O was used in place of Ni(OAc)<sub>2</sub>.4H<sub>2</sub>O was transferred to solution A with stirring. The sample mixture was microwave irradiated by controlled pressure programming with a power ramp for 5 min. and holding for 45 min. at 85 °C, under 300 W maximum power. The resultant solution was hot-filtered resulting in yellowish clear solution and the pH of the solution thus obtained was fixed at 6.8 using dilute NaOH. To this solution, 0.20 g potassium acetate was added and stirred for 30 min. and filtered the resulting clear solution. After 2 days, colourless block shaped crystals appear (Figure 2.S1), which were collected by filtration. Recrystallized the

crystals from water and dried under vacuum to get the desired P- $Zn_4Mo_xW_{18-x}$  POMs. Yield: 1.26 g (21.7%). FT-IR (cm<sup>-1</sup>): 1026, 930, 876. Raman (solid, cm<sup>-1</sup>): 1065, 972, 900, 840.

# 2.4.3 Molecular oxygen binding of $Na_{10}[M_4(H_2O)_2(PMo_xW_{9-x}O_{34})_2].nH_2O$ (P-M<sub>4</sub>Mo<sub>x</sub>W<sub>18-x</sub>) where M=Mn, Co, Ni and Zn

A Schlenk tube was charged with 10  $\mu$ mol P-M<sub>4</sub>Mo<sub>x</sub>W<sub>18-x</sub> and 1 mL toluene (non-coordinating solvent) and heated at 110 °C for 24 h under 1 atm. O<sub>2</sub> pressure. After cooling to room temperature, the mixture was filtered and dried at 80 °C under a vacuum to obtain dioxygen-activated P-M<sub>4</sub>Mo<sub>x</sub>W<sub>18-x</sub>.

## 2.5 References

- 1. Pope, M. T.; Jeannin, Y.; Fournier, M., *Heteropoly and isopoly oxometalates*. Springer: 1983; Vol. 8.
- 2. Song, Y.-F.; Tsunashima, R., Recent advances on polyoxometalate-based molecular and composite materials. *Chem. Soc. Rev* **2012**, *41* (22), 7384-7402.
- 3. Wang, L.-S.; Wang, Y.; Lv, C.-L.; Guo, C.; Xing, F.-Y.; Dong, Y.-J.; Xie, Z.; Zhou, S.-Y.; Wei, Y.-G., Polyoxometalates with tunable third-order nonlinear optical and super broad band optical limiting properties. *Inorg. Chem. Front.* **2022**, *9* (17), 4413-4424.
- 4. Song, B.-J.; Ma, Z.; Li, B.; Wu, X.-T.; Lin, H.; Zhu, Q.-L., Structural Modulation from Cu<sub>3</sub>PS<sub>4</sub> to Cu<sub>5</sub>Zn<sub>0.5</sub>P<sub>2</sub>S<sub>8</sub>: Single-Site Aliovalent-Substitution-Driven Second-Harmonic-Generation Enhancement. *Inorg. Chem.* **2021**, *60* (7), 4357-4361.
- 5. Chen, H.; Wei, W.-B.; Lin, H.; Wu, X.-T., Transition-metal-based chalcogenides: A rich source of infrared nonlinear optical materials. *Coord. Chem. Rev* **2021**, *448*, 214154.
- 6. Yin, Q.; Tan, J. M.; Besson, C.; Geletii, Y. V.; Musaev, D. G.; Kuznetsov, A. E.; Luo, Z.; Hardcastle, K. I.; Hill, C. L., A fast soluble carbon-free molecular water oxidation catalyst based on abundant metals. *Science* **2010**, *328* (5976), 342-345.
- 7. Gomez-Garcia, C. J.; Coronado, E.; Gómez-Romero, P.; Casan-Pastor, N., A tetranuclear rhomblike cluster of manganese (II). Crystal structure and magnetic properties of the heteropoly complex K10 [Mn<sub>4</sub>(H<sub>2</sub>O)<sub>2</sub>(PW<sub>9</sub>O<sub>34</sub>)<sub>2</sub>].20H<sub>2</sub>O. *Inorg. Chem.* **1993**, *32*, 3378-3381.
- 8. Nagaiah, T. C.; Gupta, D.; Adhikary, S. D.; Kafle, A.; Mandal, D., Tuning polyoxometalate composites with carbonaceous materials towards oxygen bifunctional activity. *J. Mater. Chem. A* **2021**, *9* (14), 9228-9237.
- 9. Adhikary, S. D.; Tiwari, A.; Nagaiah, T. C.; Mandal, D.; interfaces, Stabilization of cobalt-polyoxometalate over poly (ionic liquid) composites for efficient electrocatalytic water oxidation. *ACS Appl. Mater. Interfaces* **2018**, *10* (45), 38872-38879.
- 10. Li, C.; Jimbo, A.; Yamaguchi, K.; Suzuki, K., A protecting group strategy to access stable lacunary polyoxomolybdates for introducing multinuclear metal clusters. *Chem. Sci.* **2021**, *12* (4), 1240-1244.
- 11. Lopez, X.; Maestre, J. M.; Bo, C.; Poblet, J.-M., Electronic properties of polyoxometalates: A DFT study of α/β-[XM<sub>12</sub>O<sub>40</sub>] n-relative stability (M= W, Mo and X a main group element). *J. Am. Chem. Soc.* **2001**, *123* (39), 9571-9576.
- 12. Martin-Sabi, M.; Soriano-López, J.; Winter, R. S.; Chen, J.-J.; Vilà-Nadal, L.; Long, D.-L.; Galán-Mascarós, J. R.; Cronin, L., Redox tuning the Weakley-type polyoxometalate archetype for the oxygen evolution reaction. *Nat. Catal* **2018**, *I* (3), 208-213.

- 13. Spillane, S.; Sharma, R.; Zavras, A.; Mulder, R.; Ohlin, C. A.; Goerigk, L.; O'Hair, R. A.; Ritchie, C., Non-Aqueous Microwave-Assisted Syntheses of Deca-and Hexa-Molybdovanadates. *Angew. Chem. Int. Ed.* **2017**, *56* (29), 8568-8572.
- Laurans, M.; Mattera, M.; Salles, R.; K'bidi, L.; Gouzerh, P.; Renaudineau, S.; Volatron, F.; Guillemot, G.; Blanchard, S.; Izzet, G., When Identification of the Reduction Sites in Mixed Molybdenum/Tungsten Keggin-Type Polyoxometalate Hybrids Turns Out Tricky. *Inorg. Chem.* 2022, 61 (20), 7700-7709.
- 15. Falaise, C.; Mpacko Priso, G.; Leclerc, N.; Haouas, M.; Cadot, E., Making Heterometallic Metal–Metal Bonds in Keggin-Type Polyoxometalates by a Six-Electron Reduction Process. *Inorg. chem.* **2023**, *62* (6), 2494-2502.
- 16. Fang, Y.; Zhang, Q.; Li, F.; Xu, L., Exploring Inorganic Hole Collection Materials from Mixed-Metal Dawson-Type Polyoxometalates for Efficient Organic Photovoltaic Devices. *Sol. RRL* **2022**, *6* (2), 2100827.
- 17. Li, C.; Suzuki, K.; Mizuno, N.; Yamaguchi, K., Polyoxometalate LUMO engineering: a strategy for visible-light-responsive aerobic oxygenation photocatalysts. *Chem. Commun.* **2018**, *54* (52), 7127-7130.
- 18. Yang, Y.; Xu, B.; Hou, J., Mixed-Addenda Dawson-Type Polyoxometalates as High-Performance Anode Interlayer Materials for Efficient Organic Optoelectronic Devices. *Adv. Energy Mater* **2023**, *13* (14), 2204228.
- 19. Tiwari, C. K.; Baranov, M.; Neyman, A.; Neumann, R.; Weinstock, I. A., Selective oxidation by H5[PV2Mo10O40] in a highly acidic medium. *Inorg. Chem.* **2020**, *59* (17), 11945-11952.
- 20. Li, S.; Li, G.; Ji, P.; Zhang, J.; Liu, S.; Zhang, J.; Chen, X., A giant Mo/Ta/W ternary mixed-addenda polyoxometalate with efficient photocatalytic activity for primary amine coupling. *ACS Appl. Mater. Interfaces* **2019**, *11* (46), 43287-43293.
- 21. Suzuki, K.; Mizuno, N.; Yamaguchi, K., Polyoxometalate photocatalysis for liquid-phase selective organic functional group transformations. *ACS Catal.* **2018**, *8* (11), 10809-10825.
- 22. López, X.; Bo, C.; Poblet, J. M., Electronic properties of polyoxometalates: Electron and proton affinity of mixed-addenda Keggin and Wells–Dawson anions. *J. Am. Chem. Soc.* **2002**, *124* (42), 12574-12582.
- 23. Gumerova, N. I.; Rompel, A., Synthesis, structures and applications of electron-rich polyoxometalates. *Nat. Rev. Chem* **2018**, *2* (2), 0112.
- 24. Chen, J.-J.; Symes, M. D.; Cronin, L., Highly reduced and protonated aqueous solutions of [P2W18O62]6– for on-demand hydrogen generation and energy storage. *Nat. Chem* **2018**, *10* (10), 1042-1047.
- 25. Balula, M. S.; Gamelas, J. A.; Carapuça, H. M.; Cavaleiro, A. M.; Schlindwein, W., Electrochemical behaviour of first row transition metal substituted polyoxotungstates: A comparative study in acetonitrile. *Eur. J. Inorg. Chem.* **2004**, *2004* (3), 619-628.
- 26. López, X.; Carbó, J. J.; Bo, C.; Poblet, J. M., Structure, properties and reactivity of polyoxometalates: a theoretical perspective. *Chem. Soc. Rev* **2012**, *41* (22), 7537-7571.
- 27. Singh, G.; Das Adhikary, S.; Mandal, D., Physico-and Electrochemical Properties of First-Row Transition-Metal-Substituted Sandwich Polyoxometalates. *Inorg. chem.* **2023**, *62* (22), 8551–8564.
- 28. Finke, R. G.; Droege, M. W.; Domaille, P. J., Trivacant heteropolytungstate derivatives. 3. Rational syntheses, characterization, two-dimensional tungsten-183 NMR, and properties of tungstometallophosphates P<sub>2</sub>W<sub>18</sub>M<sub>4</sub>(H<sub>2</sub>O)<sub>2</sub>O<sub>68</sub><sup>10-</sup> and P<sub>4</sub>W<sub>30</sub>M<sub>4</sub>(H<sub>2</sub>O)<sub>2</sub>O<sub>112</sub><sup>16-</sup>(M= cobalt, copper, zinc). *Inorganic Chemistry* **1987**, *26* (23), 3886-3896.

# **Annexure-I**

	D 3.4 337	D.C. W	D 31, 111	D 7 111
GGD G 1	P-Mn <sub>4</sub> W <sub>18</sub>	P-Co <sub>4</sub> W <sub>18</sub>	P-Ni <sub>4</sub> W <sub>18</sub>	P-Zn <sub>4</sub> W <sub>18</sub>
CCDC number	2290783	1511657	2290786	2290787
empirical formula	$\begin{array}{c} H_{17.6}Mn_4Na_{13}O_{98}P \\ {}_2W_{18} \end{array}$	$Co_{4}H_{18}K_{6}Na_{6}O_{92}  P_{2}W_{18}$	$H_{12}K_6Na_6Ni_4O_9$ ${}_1P_2W_{18}$	$\begin{array}{c} H_{12}K_{10}Na_4O_{86}P_2 \\ W_{18}Zn_4 \end{array}$
formula weight	5475.61	5469.64	5446.71	5503.78
temp (K)	273.15	293 (2)	293 (15)	273.15
crystal system	Triclinic	Monoclinic	Monoclinic	Monoclinic
space group	$P\overline{1}$	$P2_1/n$	$P2_1/n$	$P2_1/n$
unit cell dimension				
a (Å)	11.618(9)	11.871(9)	11.8463(5)	12.318(6)
b (Å)	12.924(11)	16.676(14)	16.5493(6)	21.362(11)
c (Å)	17.465(15)	21.219(18)	21.1131(9)	15.822(7)
α (deg)	97.832(3)	90	90	90
$\beta$ (deg)	106.602(2)	100.389(3)	100.320(2)	92.088(1)
γ (deg)	111.474(2)	90	90	90
$V(Å^3)$	2251.9(3)	4132.0(6)	4072.2(3)	4161.1(3)
Z	1	2	2	2
ρ (calculated) (g/cm³)	4.038	4.396	4.442	4.393
F (000)	2407.0	4808	4788	4832
crystal size (mm <sup>3</sup> )	$0.26 \times 0.16 \times 0.12$	0.24 x 0.22 x 0.16	0.21 x 0.18 x 0.14	0.31 x 0.24 x 0.21
index ranges	-14 <h<14, -16≤k≤<br="">16, -18&lt;1&lt;21</h<14,>	$ \begin{array}{l} -15 \le h \le 15, -22 \\ \le k \le 22, -28 \le 1 \\ \le 28 \end{array} $	-15≤h<15, - 22 <k≤22, -<br="">28&lt;1&lt;28</k≤22,>	-15≤h<15, - 26 <k<26, -19<br="">&lt;1&lt;19</k<26,>
no. of reflection collected /unique	9197/27608	112516 / 10329	89007/10107	83569/8547
GOF on $F^2$	1.081	1.037	1.065	1.122
final $R$ indices $(I > 2\sigma(I))$	R1 =0.043, wR2 = 0.080	R1 = 0.038, wR2 = 0.093	R1=0.033, wR2 = 0.084	R1 = 0.018, wR2 = 0.046

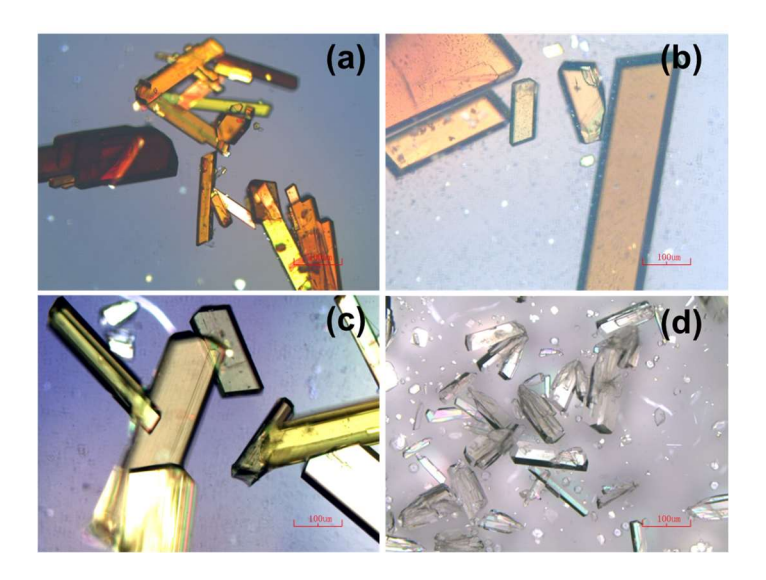
R indices (all data)	R1 = 0.058, wR2	R1 = 0.044, wR2	R1=0.038,	R1 =0.019, wR2
	= 0.086	= 0.097	wR2 = 0.087	= 0.047
data/restraints/para	9197/0/638	10329/0/589	10107/0/589	8547/2/570

**Table 2.S2** Reaction parameters showing the effect of pH, mmol on total yield and type of POM framework obtained. (M= transition metal in the sandwich position in  $[M_4(P_2Mo_xW_{18-x}O_{68})]^{10-}$  and in the framework of Keggin  $[M(PMo_xW_{18-x}O_{68})]^{15-}$ )

the framework of Keggin   N	$M(PMo_xW_{11-x}O_{39}) ^{5-})$
-----------------------------	---------------------------------

	ik of Keggili [wi(r				T :
Transition metal (3d)	Na <sub>2</sub> WO <sub>4</sub> .2H <sub>2</sub> O g (mmol)	Na <sub>2</sub> MoO <sub>4</sub> .2H <sub>2</sub> O g (mmol)	pH (Sol A)	Yield (%) (P-based)	POM Framework Type [M <sub>4</sub> (P <sub>2</sub> Mo <sub>x</sub> W <sub>18-x</sub> O <sub>68</sub> )] <sup>10-</sup> ( <b>A</b> ) or [M(PMo <sub>x</sub> W <sub>11-x</sub> O <sub>39</sub> )] <sup>5-</sup> ( <b>B</b> )
M=Mn	3.29 (10.00)	3.63 (15.00)	6.5	26.20	A
M=Mn	4.12 (12.50)	3.02 (12.50)	6.5	36.60	A
M=Mn	4.94 (15.00)	2.42 (10.00)	6.5	28.30	A
M=Mn	4.12 (12.50)	3.02 (12.50)	8.0		
M=Mn	4.12 (12.50)	3.02 (12.50)	7.0	13.30	A
M=Mn	4.12 (12.50)	3.02 (12.50)	6.0	22.30	A
M=Mn	4.12 (12.50)	3.02 (12.50)	5.0	4.80	A
M=Mn	4.12 (12.50)	3.02 (12.50)	4.0		
M=Co	2.47 (7.50)	4.23 (17.50)	6.5	32.40	A
M=Co	3.29 (10.00)	3.63 (15.00)	6.5	43.40	A
M=Co	4.12 (12.50)	3.02 (12.50)	6.5	34.40	A
M=Co	3.29 (10.00)	3.63 (15.00)	8.0		
M=Co	3.29 (10.00)	3.63 (15.00)	7.0	18.60	A
M=Co	3.29 (10.00)	3.63 (15.00)	6.0	26.60	A
M=Co	3.29 (10.00)	3.63 (15.00)	5.0	15.80	A
M=Co	3.29 (10.00)	3.63 (15.00)	4.0		A + B
M=Ni	2.47 (7.50)	4.23 (17.50)	7.15	22.70	A
M=Ni	3.29 (10.00)	3.63 (15.00)	7.15	29.90	A
M=Ni	4.12 (12.50)	3.02 (12.50)	7.15	24.40	A
M=Ni	3.29 (10.00)	3.63 (15.00)	6.5		A + B
M=Ni	3.29 (10.00)	3.63 (15.00)	6.5		A + B
M=Ni	3.29 (10.00)	3.63 (15.00)	8.0		
	1	l	1	l	

M=Ni	3.29 (10.00)	3.63 (15.00)	6.0		A + B
M=Ni	3.29 (10.00)	3.63 (15.00)	5.0	9.40	В
M=Ni	3.29 (10.00)	3.63 (15.00)	4.0		
M=Zn	2.47 (7.50)	4.23 (17.50)	7.15	16.60	A
M=Zn	3.29 (10.00)	3.63 (15.00)	7.15	21.70	A
M=Zn	4.12 (12.50)	3.02 (12.50)	7.15	18.90	A
M=Zn	4.12 (12.50)	3.02 (12.50)	8.0		
M=Zn	4.12 (12.50)	3.02 (12.50)	6.5		A + B
M=Zn	4.12 (12.50)	3.02 (12.50)	6.0		A + B
M=Zn	4.12 (12.50)	3.02 (12.50)	5.0		
M=Cu	3.29 (10.00)	3.63 (15.00)	7.2		
M=Cu	3.29 (10.00)	3.63 (15.00)	6.5	14.40	В
M=Cu	3.29 (10.00)	3.63 (15.00)	6.0	10.30	В
M=Fe	3.29 (10.00)	3.63 (15.00)	7.2		<del></del>
M=Fe	3.29 (10.00)	3.63 (15.00)	6.5	7.80	В
M=Fe	3.29 (10.00)	3.63 (15.00)	6.0	4.20	В



 $\label{eq:Figure 2.S1} \textbf{Figure 2.S1} \ \ \textbf{Optical images of mixed addenda sandwich POMs; (a)} \ \ P-Mn_4Mo_xW_{18-x}, \ \ (b) \ \ P-Co_4Mo_xW_{18-x} \ \ \ (c) \ P-Ni_4Mo_xW_{18-x} \ \ and \ \ (d) \ P-Zn_4Mo_xW_{18-x}$ 

**Table 2.S3** Comparison of bond lengths between SC-XRD structure of mixed addenda (Mo/W) and W-only tetrasubstituted sandwich POMs. ( $TM_i = transition metal at internal sandwich position, <math>TM_e = transition metal at external sandwich position; M(1)-M(9) are different addenda atom positions$ 

according to the structure in Figure 2.2 (main text).

M (Ma/W)	P-M		_ `	Co4	P-1	P-Ni4		P-Zn4	
M (Mo/W)	Mo/W	W	Mo/W	W	Mo/W	W	Mo/W	W	
	1.708	1.713	1.710	1.710	1.705	1.714	1.723	1.706	
	1.945	1.937	1.955	1.925	1.956	1.915	1.952	1.932	
M(1)	1.954	1.944	1.926	1.908	1.924	1.909	1.926	1.935	
	2.553	2.579	2.528	2.483	2.518	2.487	2.496	2.549	
	1.887	1.872	1.867	1.884	1.877	1.888	1.863	1.860	
	1.844	1.855	1.856	1.876	1.858	1.802	1.867	1.867	
	1.724	1.723	1.709	1.719	1.711	1.711	1.711	1.712	
	1.873	1.865	1.927	1.921	1.950	1.918	1.898	1.904	
M(2)	1.902	1.884	1.862	1.874	1.857	1.896	1.919	1.916	
. ,	2.543	2.578	2.528	2.532	2.516	2.523	2.488	2.548	
	1.903	1.898	1.899	1.880	1.883	1.896	1.903	1.904	
	1.927	1.913	1.901	1.914	1.900	1.935	1.877	1.879	
	1.723	1.723	1.720	1.705	1.709	1.716	1.702	1.713	
M(3)	1.866	1.862	1.893	1.898	1.893	1.880	1.875	1.891	
141(3)	1.883	1.910	1.861	1.884	1.877	1.871	1.889	1.872	
	2.557	2.552	2.520	2.510	2.505	2.533	2.492	2.532	
	1.900	1.916	1.917	1.927	1.921	1.920	1.918	1.932	
	1.920	1.933	1.902	1.923	1.881	1.941	1.875	1.900	
	1.713	1.725	1.712	1.724	1.697	1.721	2.036	2.026	
	2.067	2.021	1.933	1.927	1.932	1.933	2.452	2.396	
M(4)	1.922	1.935	1.918	1.928	1.943	1.928	1.942	1.919	
	2.432	2.428	2.432	2.423	2.431	2.455	1.758	1.776	
	1.765	1.773	2.043	2.022	2.044	2.015	1.718	1.726	
	1.943	1.937	1.764	1.777	1.758	1.781	1.947	1.929	
	1.719	1.714	1.715	1.713	1.697	1.727	2.024	2.028	
	2.011	2.046	2.021	2.025	2.028	2.010	2.424	2.436	
M(5)	1.933	1.919	1.936	1.929	1.926	1.934	1.917	1.926	
	2.429	2.438	2.430	2.453	2.423	2.434	1.766	1.779	
	1.764	1.776	1.768	1.772	1.773	1.774	1.715	1.719	
	1.950	1.919	1.933	1.939	1.957	1.933	1.937	1.935	
	1.716	1.718	1.707	1.711	1.703	1.730	2.015	2.002	
	1.984	1.903	2.028	2.015	2.032	1.999	1.986	1.974	
M(6)	2.025	1.979	1.991	1.969	1.989	1.945	1.723	1.713	
	2.476	2.463	2.453	2.425	2.421	2.402	1.762	1.793	
	1.903	1.777	1.766	1.771	1.756	1.828	1.898	1.900	

	1.766	1.718	2.028	1.898	1.900	1.886	2.426	2.445
	1.723	1.716	1.715	1.710	1.710	1.722	1.998	2.001
	1.953	1.946	1.830	1.811	1.998	1.993	1.725	1.716
M(7)	1.909	1.904	1.891	1.903	1.885	1.890	1.829	1.830
	2.418	2.424	2.405	2.446	2.427	2.433	1.892	1.893
	1.823	1.820	1.928	1.928	1.827	1.782	2.427	2.413
	1.989	2.004	1.999	1.993	1.935	1.985	1.936	1.925
	1.718	1.719	1.706	1.721	1.701	1.717	1.831	1.830
	1.822	1.820	1.825	1.826	1.824	1.839	1.905	1.920
M(8)	1.897	1.912	1.900	1.901	1.905	1.898	2.409	2.412
	2.432	2.417	2.434	2.422	2.456	2.403	1.706	1.711
	2.001	1.996	2.000	1.999	2.005	2.007	1.996	1.993
	1.918	1.926	1.930	1.917	1.917	1.927	1.908	1.921
	1.716	1.713	1.708	1.718	1.711	1.724	1.770	1.777
	1.787	1.768	1.773	1.778	1.763	1.777	1.893	1.903
M(9)	1.903	1.903	1.898	1.896	1.906	1.897	1.714	1.718
	2.434	2.455	2.435	2.443	2.399	2.420	2.441	2.435
	2.030	2.032	2.019	2.008	2.022	2.042	2.014	2.004
	1.976	1.984	1.973	1.976	1.978	1.965	1.981	1.963
	2.074	2.067	2.003	2.003	1.986	1.983	2.203	2.272
$TM_i$	2.293	2.301	2.208	2.217	2.145	2.163	2.135	2.083
1 1411	2.145	2.151	2.072	2.073	2.045	2.038	2.050	2.080
	2.353	2.362	2.257	2.217	2.157	2.177	2.000	2.005
	2.081	2.094	2.031	2.010	1.999	1.996	2.310	2.286
	2.140	2.161	2.065	2.068	2.042	2.043	2.027	2.013
	2.117	2.108	2.040	2.030	2.018	2.006	2.050	2.055
•	2.142	2.145	2.041	2.042	2.025	2.008	2.084	2.093
TMe	2.318	2.331	2.205	2.210	2.159	2.151	2.213	2.198
	2.156	2.155	2.088	2.042	2.047	2.039	2.065	2.059
	2.162	2.162	2.098	2.114	2.053	2.055	2.106	2.122
	2.143	2.175	2.093	2.099	2.064	2.057	2.083	2.070
	1.538	1.524	1.536	1.538	1.536	1.537	1.532	1.534
P	1.542	1.541	1.538	1.539	1.537	1.538	1.538	1.541
1	1.543	1.547	1.538	1.544	1.540	1.541	1.546	1.542
	1.557	1.550	1.538	1.548	1.551	1.558	1.551	1.543

**Table 2.S4** Comparison of few bond angles (average) of W-only vs. mixed addenda; (M= Mo/W,  $TM_i$  = internal transition metal and  $TM_e$  = external transition metal at sandwich position,  $O_c$  = Corner shared oxygen,  $O_e$  = edge shared oxygen

Bond angles	P-Mn4	P-Co4	P-Ni4	P-Zn4

	Mo/W	W	Mo/W	W	Mo/W	W	Mo/W	W
M-O <sub>c</sub> -M(cap)	152.48	152.20	152.12	151.97	152.52	151.66	151.98	152.11
M-O <sub>c</sub> -M(belt)	147.86	148.72	147.68	147.55	146.24	147.01	148.60	148.58
M-O <sub>e</sub> -M(belt)	124.66	124.58	123.71	124.01	123.19	122.75	123.70	123.69
M-Oµ2-TMi	136.66	136.20	137.13	137.36	137.40	137.08	137.68	137.36
M-Oµ3-TMi	125.33	125.92	125.20	125.87	124.75	125.29	124.82	125.68
M-Oμ <sub>2</sub> -TM <sub>e</sub>	136.65	136.09	137.88	136.95	139.27	139.50	137.66	137.21
M-Oμ <sub>3</sub> -TM <sub>e</sub>	132.15	131.74	132.71	132.26	133.58	132.74	132.00	132.68

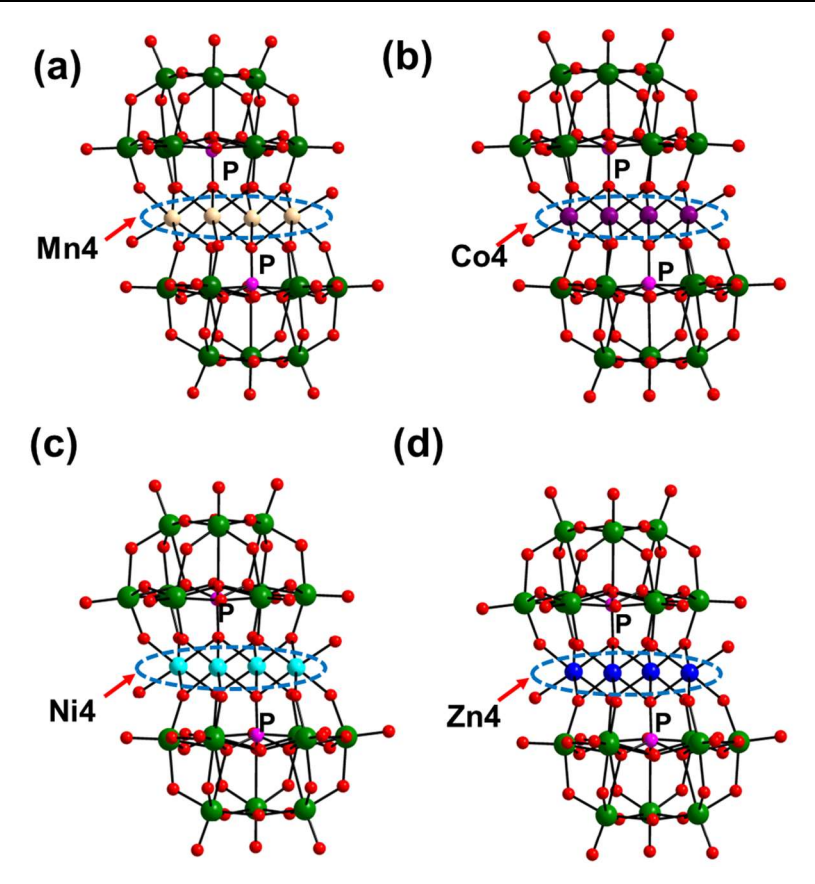


Table 2.S5 Bond valence parameter of selected atoms calculated from the SC-XRD structure of mixed addenda sandwich POMs						
POMs	Transition metal	Bond valence sum value	Oxidation state			
P-Mn <sub>4</sub> Mo <sub>x</sub> W <sub>18-x</sub>	P Mn Mo/W	5.144 2.162 6.081	5 2 6			

P-Co <sub>4</sub> Mo <sub>x</sub> W <sub>18-x</sub>	P	5.049	5
	Co	2.016	2
	Mo/W	6.056	6
P-Ni <sub>4</sub> Mo <sub>x</sub> W <sub>18-x</sub>	P	5.094	5
	Ni	2.140	2
	Mo/W	6.014	6
P-Zn <sub>4</sub> Mo <sub>x</sub> W <sub>18-x</sub>	P	5.104	5
	Zn	2.076	2
	Mo/W	6.070	6

## **ESI-Mass spectrometry**

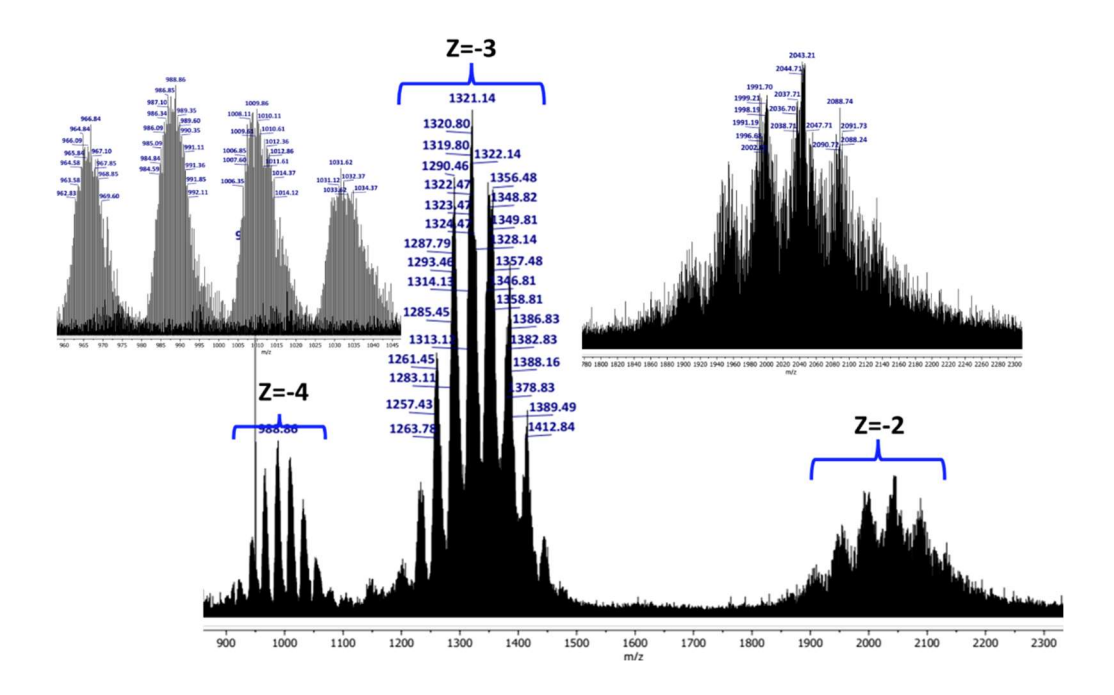


Figure 2.S3 ESI-MS spectra of P-Mn<sub>4</sub>Mo<sub>x</sub>W<sub>18-x</sub> in the range of m/z 870-2330 for different z values.

Charge	m/z (obs.)	m/z (calc.)	Mol. Wt.	Assigned probable fragment
-4	1031.62	1032.49	4129.96	Na <sub>5</sub> K[Mn <sub>4</sub> (P <sub>2</sub> Mo <sub>8</sub> W <sub>10</sub> O <sub>68</sub> )]
-4	1009.62	1010.48	4041.92	Na <sub>5</sub> K[Mn <sub>4</sub> (P <sub>2</sub> Mo <sub>9</sub> W <sub>9</sub> O <sub>68</sub> )]
-4	988.86	988.47	3953.88	Na <sub>5</sub> K[Mn <sub>4</sub> (P <sub>2</sub> Mo <sub>10</sub> W <sub>8</sub> O <sub>68</sub> )]
-4	966.84	966.46	3865.84	Na <sub>5</sub> K[Mn <sub>4</sub> (P <sub>2</sub> Mo <sub>11</sub> W <sub>7</sub> O <sub>68</sub> )]
-3	1415.52	1413.67	4241.01	Na <sub>6</sub> K[Mn <sub>4</sub> (P <sub>2</sub> Mo <sub>7</sub> W <sub>11</sub> O <sub>68</sub> )]
-3	1385.50	1384.32	4152.96	Na <sub>6</sub> K[Mn <sub>4</sub> (P <sub>2</sub> Mo <sub>8</sub> W <sub>10</sub> O <sub>68</sub> )]

-3	1351.15	1349.65	4048.95	Na <sub>7</sub> [Mn <sub>4</sub> (P <sub>2</sub> Mo <sub>9</sub> W <sub>9</sub> O <sub>68</sub> )]
-3	1321.14	1320.30	3960.90	Na <sub>7</sub> [Mn <sub>4</sub> (P <sub>2</sub> Mo <sub>10</sub> W <sub>8</sub> O <sub>68</sub> )]
-3	1290.46	1290.96	3872.88	Na <sub>7</sub> [Mn <sub>4</sub> (P <sub>2</sub> Mo <sub>11</sub> W <sub>7</sub> O <sub>68</sub> )]
-3	1261.78	1261.61	3784.83	Na <sub>7</sub> [Mn <sub>4</sub> (P <sub>2</sub> Mo <sub>12</sub> W <sub>6</sub> O <sub>68</sub> )]
-3	1233.10	1232.26	3699.30	$Na_{7}[Mn_{4}(P_{2}Mo_{13}W_{5}O_{68})]$
-2	2088.74	2087.98	4175.96	Na <sub>7</sub> K[Mn <sub>4</sub> (P <sub>2</sub> Mo <sub>10</sub> W <sub>8</sub> O <sub>68</sub> )]
-2	2043.21	2043.96	4087.92	Na <sub>7</sub> K[Mn <sub>4</sub> (P <sub>2</sub> Mo <sub>9</sub> W <sub>9</sub> O <sub>68</sub> )]
-2	1991.70	1991.95	3983.90	$Na_{8}[Mn_{4}(P_{2}Mo_{10}W_{8}O_{68})]$

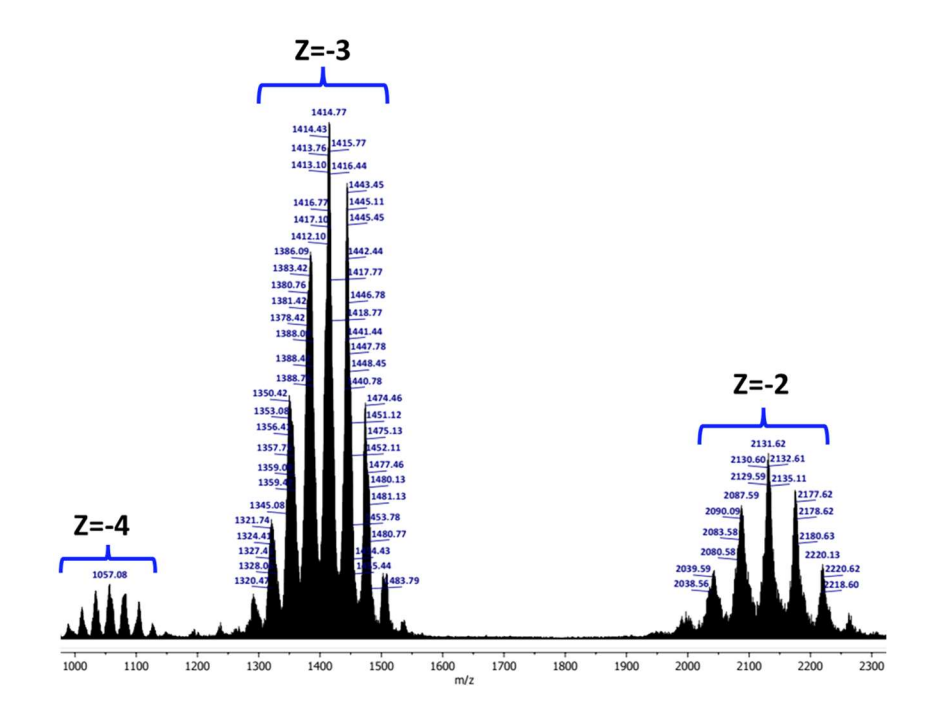
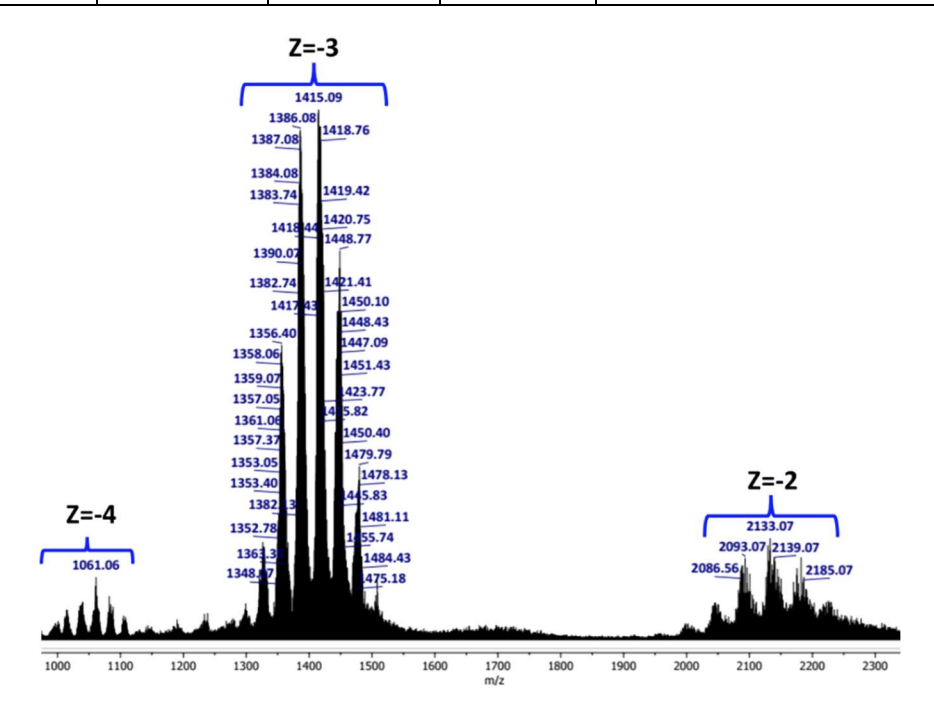


Figure 2.S4 ESI-MS spectra of P-Co<sub>4</sub>Mo<sub>x</sub>W<sub>18-x</sub> in the range of m/z 980-2320 for different z.

	Table 2.S7 Assignment of ESI-mass peaks of P-Co <sub>4</sub> Mo <sub>x</sub> W <sub>18-x</sub>						
Charge	m/z (obs.)	m/z (calc.)	Mol. Wt.	Assigned probable fragment			
-4	1011.57	1010.48	4041.92	Na <sub>6</sub> [Co <sub>4</sub> (P <sub>2</sub> Mo <sub>9</sub> W <sub>9</sub> O <sub>68</sub> )]			
-4	1033.57	1032.49	4129.96	Na <sub>6</sub> [Co <sub>4</sub> (P <sub>2</sub> Mo <sub>8</sub> W <sub>10</sub> O <sub>68</sub> )]			
-4	1057.08	1058.50	4234.00	Na <sub>5</sub> K[Co <sub>4</sub> (P <sub>2</sub> Mo <sub>7</sub> W <sub>11</sub> O <sub>68</sub> )]			
-4	1083.34	1084.25	4337.00	Na <sub>4</sub> K <sub>2</sub> [Co <sub>4</sub> (P <sub>2</sub> Mo <sub>6</sub> W <sub>12</sub> O <sub>68</sub> )]			
-4	1104.09	1102.27	4409.08	Na <sub>5</sub> K[Co <sub>4</sub> (P <sub>2</sub> Mo <sub>5</sub> W <sub>13</sub> O <sub>68</sub> )]			

-3	1350.42	1350.97	4052.92	$K_2Na_3H_2[Co_4(P_2Mo_9W_9O_{68})]$
-3	1386.09	1384.32	4152.96	Na <sub>7</sub> [Co <sub>4</sub> (P <sub>2</sub> Mo <sub>8</sub> W <sub>10</sub> O <sub>68</sub> )]
-3	1414.77	1413.34	4240.02	Na <sub>7</sub> [Co <sub>4</sub> (P <sub>2</sub> Mo <sub>7</sub> W <sub>11</sub> O <sub>68</sub> )]
-3	1443.45	1442.68	4328.04	Na <sub>7</sub> [Co <sub>4</sub> (P <sub>2</sub> Mo <sub>6</sub> W <sub>12</sub> O <sub>68</sub> )]
-3	1473.46	1472.03	4416.09	Na <sub>7</sub> [Co <sub>4</sub> (P <sub>2</sub> Mo <sub>5</sub> W <sub>13</sub> O <sub>68</sub> )]
-3	1502.80	1501.38	4504.14	Na <sub>7</sub> [Co <sub>4</sub> (P <sub>2</sub> Mo <sub>4</sub> W <sub>14</sub> O <sub>68</sub> )]
-2	2087.59	2087.98	4175.96	Na <sub>8</sub> [Co <sub>4</sub> (P <sub>2</sub> Mo <sub>8</sub> W <sub>10</sub> O <sub>68</sub> )]
-2	2131.62	2131.50	4263.00	Na <sub>8</sub> [Co <sub>4</sub> (P <sub>2</sub> Mo <sub>7</sub> W <sub>11</sub> O <sub>68</sub> )]
-2	2175.13	2175.52	4351.04	Na <sub>8</sub> [Co <sub>4</sub> (P <sub>2</sub> Mo <sub>6</sub> W <sub>12</sub> O <sub>68</sub> )]
-2	2220.62	2219.54	4439.08	$Na_{8}[Co_{4}(P_{2}Mo_{5}W_{13}O_{68})]$



**Figure 2.S5** ESI-MS spectra of P-Ni<sub>4</sub>Mo<sub>x</sub>W<sub>18-x</sub> in the range of m/z 980-2350 for different values of z.

Charge	m/z (obs.)	m/z (calc.)	Mol. Wt.	Assigned probable fragment
-4	1061.06	1059.75	4239.00	Na <sub>7</sub> [Ni <sub>4</sub> (P <sub>2</sub> Mo <sub>7</sub> W <sub>11</sub> O <sub>68</sub> )]
-3	1355.06	1354.65	4063.95	Na <sub>7</sub> [Ni <sub>4</sub> (P <sub>2</sub> Mo <sub>9</sub> W <sub>9</sub> O <sub>68</sub> )]
-3	1386.08	1389.32	4167.96	Na <sub>6</sub> K[Ni <sub>4</sub> (P <sub>2</sub> Mo <sub>8</sub> W <sub>10</sub> O <sub>68</sub> )]

-3	1415.09	1413.01	4239.03	Na <sub>7</sub> [Ni <sub>4</sub> (P <sub>2</sub> Mo <sub>7</sub> W <sub>11</sub> O <sub>68</sub> )]
-3	1448.77	1448.36	4345.08	Na <sub>7</sub> [Ni <sub>4</sub> (H <sub>2</sub> O)(P <sub>2</sub> Mo <sub>6</sub> W <sub>12</sub> O <sub>68</sub> )]
-3	1480.11	1477.70	4433.10	Na <sub>7</sub> [Ni <sub>4</sub> (H <sub>2</sub> O)(P <sub>2</sub> Mo <sub>5</sub> W <sub>13</sub> O <sub>68</sub> )]
-2	2086.56	2086.99	4173.98	Na <sub>8</sub> [Ni <sub>4</sub> (H <sub>2</sub> O)(P <sub>2</sub> Mo <sub>8</sub> W <sub>10</sub> O <sub>68</sub> )]
-2	2133.07	2131.51	4263.02	$Na_{8}[Ni_{4}(P_{2}Mo_{7}W_{11}O_{68})]$

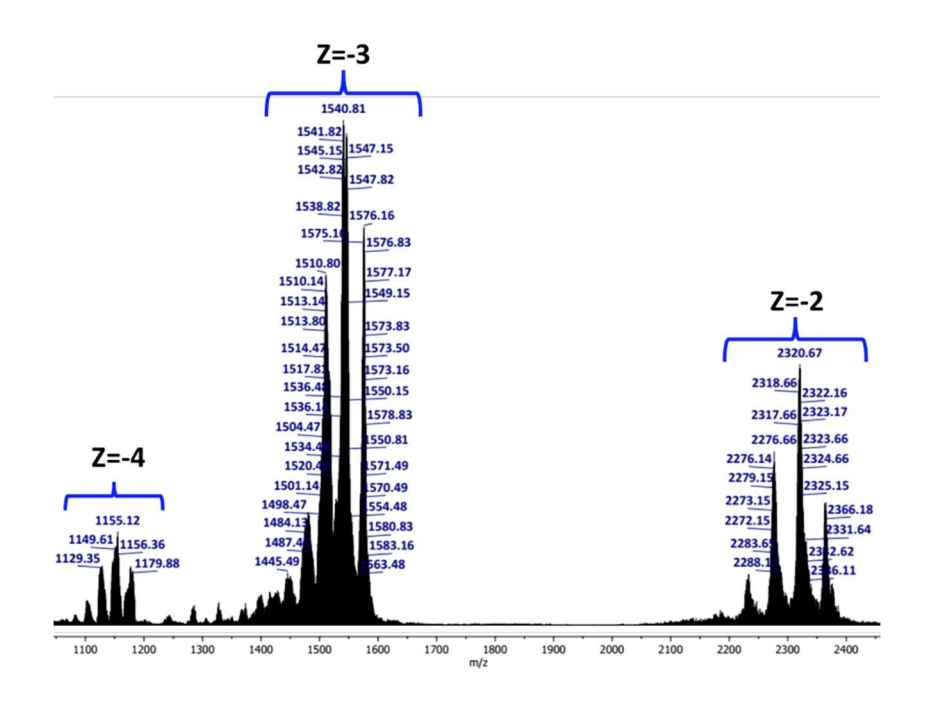


Figure 2.S6 ESI-MS spectra of P-Zn<sub>4</sub>Mo<sub>x</sub>W<sub>18-x</sub> in the range of m/z 1050-2460

Table 2.S9	Table 2.S9 Assignment of ESI-mass peaks of P-Zn <sub>4</sub> Mo <sub>x</sub> W <sub>18-x</sub>						
Charge	m/z (obs.)	m/z (calc.)	Mol. Wt.	Assigned probable fragment			
-4	1129.35	1130.77	4523.11	Na <sub>5</sub> K[Zn <sub>4</sub> (P <sub>2</sub> Mo <sub>4</sub> W <sub>14</sub> O <sub>68</sub> )]			
-4	1155.12	1157.54	4630.16	$Na_{6}[Zn_{4}(H_{2}O)_{2}(P_{2}Mo_{3}W_{15}O_{68})]$			
-4	1179.88	1179.55	4718.20	$Na_{6}[Zn_{4}(H_{2}O)_{2}(P_{2}Mo_{2}W_{16}O_{68})]$			
-3	1480.80	1480.69	4442.07	Na <sub>7</sub> [Zn <sub>4</sub> (P <sub>2</sub> Mo <sub>5</sub> W <sub>13</sub> O <sub>68</sub> )]			
-3	1510.80	1510.04	4530.12	$Na_{7}[Zn_{4}(P_{2}Mo_{4}W_{14}O_{68})]$			
-3	1540.80	1539.05	4617.15	$Na_{7}[Zn_{4}(P_{2}Mo_{3}W_{15}O_{68})]$			
-3	1576.16	1574.40	4723.20	Na <sub>7</sub> [Zn <sub>4</sub> (H <sub>2</sub> O)(P <sub>2</sub> Mo <sub>2</sub> W <sub>16</sub> O <sub>68</sub> )]			

-2	2232.65	2232.53	4465.06	$Na_{8}[Zn_{4}(P_{2}Mo_{5}W_{13}O_{68})]$
-2	2276.66	2276.55	4553.10	$Na_{8}[Zn_{4}(P_{2}Mo_{4}W_{14}O_{68})]$
-2	2320.67	2320.07	4640.14	$Na_{8}[Zn_{4}(P_{2}Mo_{3}W_{15}O_{68})]$
-2	2364.67	2364.09	4728.18	$Na_{8}[Zn_{4}(P_{2}Mo_{2}W_{16}O_{68})]$

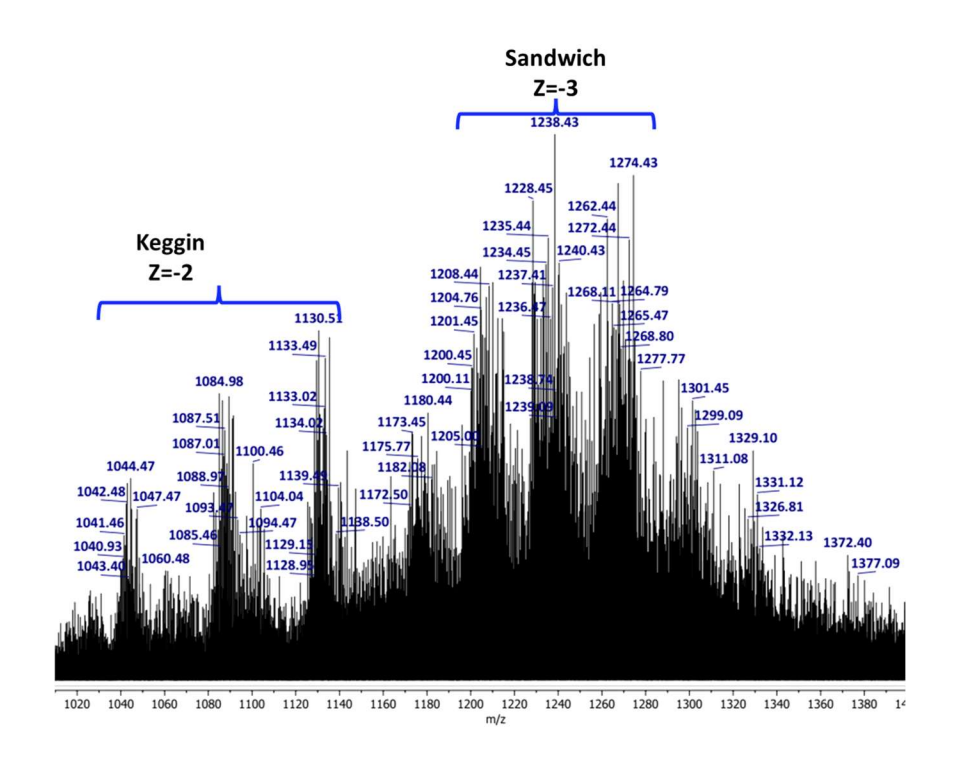


Figure 2.S7 ESI-MS spectra showing Co-substituted Keggin and sandwich POMs.

<b>Table 2.S10</b> Assignment of ESI-mass peaks of Co-substituted mix-addenda Keggin and sandwich POMs							
Charge	m/z (obs.)	m/z (calc.)	Mol. Wt.	Assigned probable fragment			
-3	1238.43	1237.59	3712.78	Na <sub>7</sub> [Co <sub>4</sub> (P <sub>2</sub> Mo <sub>13</sub> W <sub>5</sub> O <sub>68</sub> )]			
-3	1208.44	1208.24	3624.74	Na <sub>7</sub> [Co <sub>4</sub> (P <sub>2</sub> Mo <sub>14</sub> W <sub>4</sub> O <sub>68</sub> )]			
-2	1130.50	1127.93	2255.87	$Na_2H[Co(PW_5Mo_6O_{39})]$			
-2	1084.98	1083.91	2167.83	Na <sub>2</sub> H[Co(PW <sub>4</sub> Mo <sub>7</sub> O <sub>39</sub> )]			

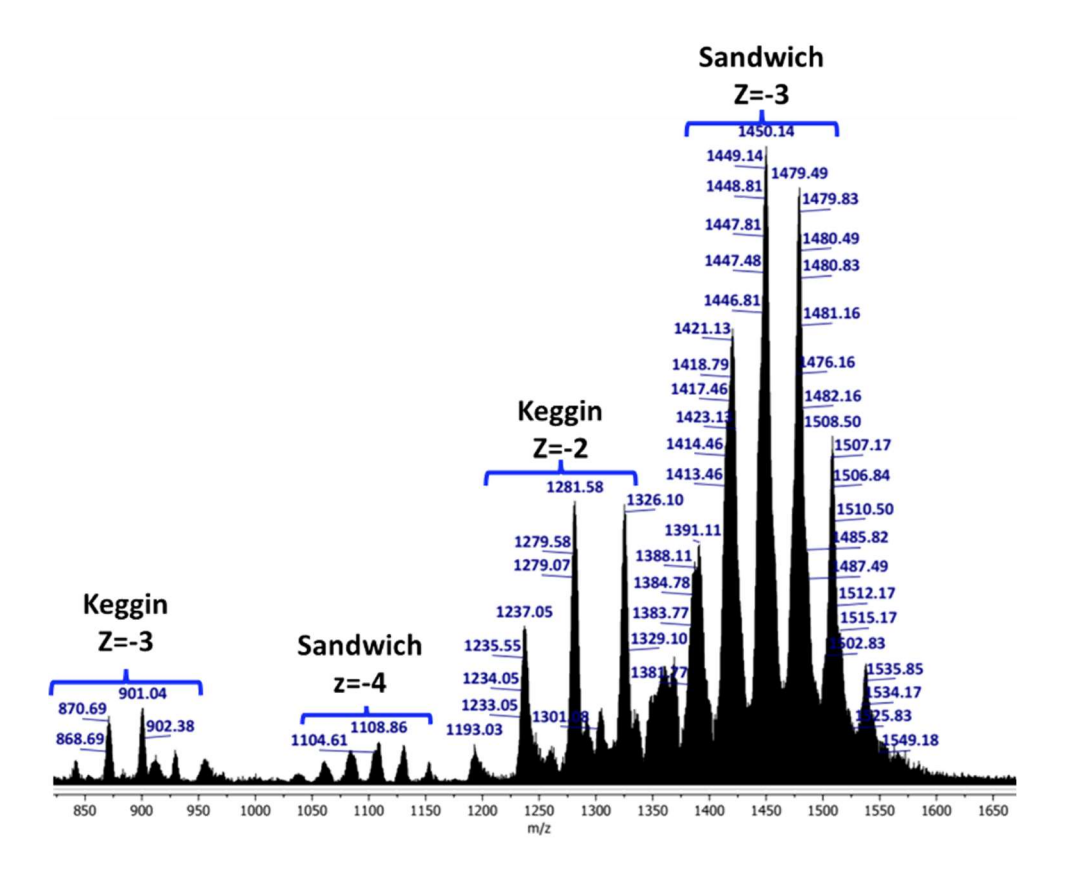


Figure 2.S8 ESI-MS spectra showing Ni-substituted mix-addenda Keggin and sandwich POMs

POMs	Assignment of	ESI-mass peaks	of N1-substitu	ted mix-addenda Keggin and sandwic
Charge	m/z (obs.)	m/z (calc.)	Mol. Wt.	Assigned probable fragment
-3	1479.79	1477.70	4191.98	Na <sub>7</sub> [Ni <sub>4</sub> (H <sub>2</sub> O)(P <sub>2</sub> Mo <sub>5</sub> W <sub>13</sub> O <sub>68</sub> )]
-3	1450.14	1448.36	4345.08	Na <sub>7</sub> [Ni <sub>4</sub> (H <sub>2</sub> O)(P <sub>2</sub> Mo <sub>6</sub> W <sub>12</sub> O <sub>68</sub> )]
-3	1421.13	1419.01	4257.04	Na <sub>7</sub> [Ni <sub>4</sub> (H <sub>2</sub> O)(P <sub>2</sub> Mo <sub>7</sub> W <sub>11</sub> O <sub>68</sub> )]
-2	1326.10	1325.55	2651.10	H <sub>3</sub> [Ni(PW <sub>10</sub> MoO <sub>39</sub> )]
-2	1281.58	1281.53	2563.06	H <sub>3</sub> [Ni(PW <sub>9</sub> Mo <sub>2</sub> O <sub>39</sub> )]
-2	1237.05	1237.51	2475.02	H <sub>3</sub> [Ni(PW <sub>8</sub> Mo <sub>3</sub> O <sub>39</sub> )]
-4	1108.86	1109.07	4436.31	$H_7[Ni_4(P_2Mo_3W_{15}O_{68})]$
-3	901.04	898.02	2694.06	Na <sub>2</sub> [Ni(PW <sub>10</sub> MoO <sub>39</sub> )]
-3	870.69	868.67	2606.02	Na <sub>2</sub> [Ni(PW <sub>9</sub> Mo <sub>2</sub> O <sub>39</sub> )]

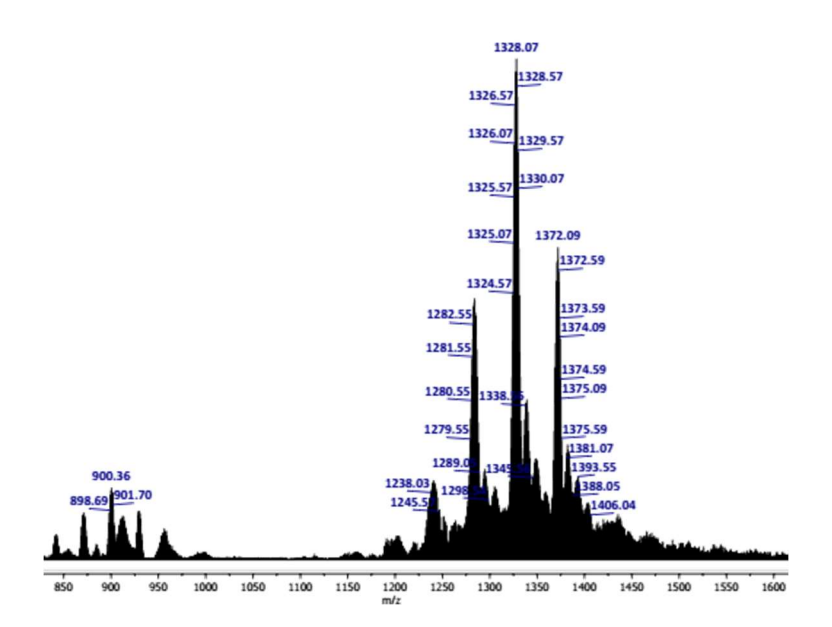


Figure 2.S9 ESI-MS spectra of P-CuMo $_{x}W_{11-x}$  in the range of m/z 830-1650.

Table 2.S12 Assignment of ESI-mass peaks of P-CuPMo <sub>x</sub> W <sub>11-x</sub>								
Charge	m/z (obs.)	m/z (calc.)	Mol. Wt.	Assigned probable fragment				
-2	1284.07	1284.03	2568.06	$H_3[Cu(PW_9Mo_2O_{39})]$				
-2	1328.09	1328.05	2656.10	$H_3[Cu(PW_{10}MoO_{39})]$				
-2	1372.09	1372.07	2744.14	$H_3[Cu(PW_{11}O_{39})]$				
-3	-3 870.35 870		2611.02	$Na_3[Cu(PW_9Mo_2O_{39})]$				
-3	900.36	899.68	2699.04	$Na_3[Cu(PW_{10}MoO_{39})]$				

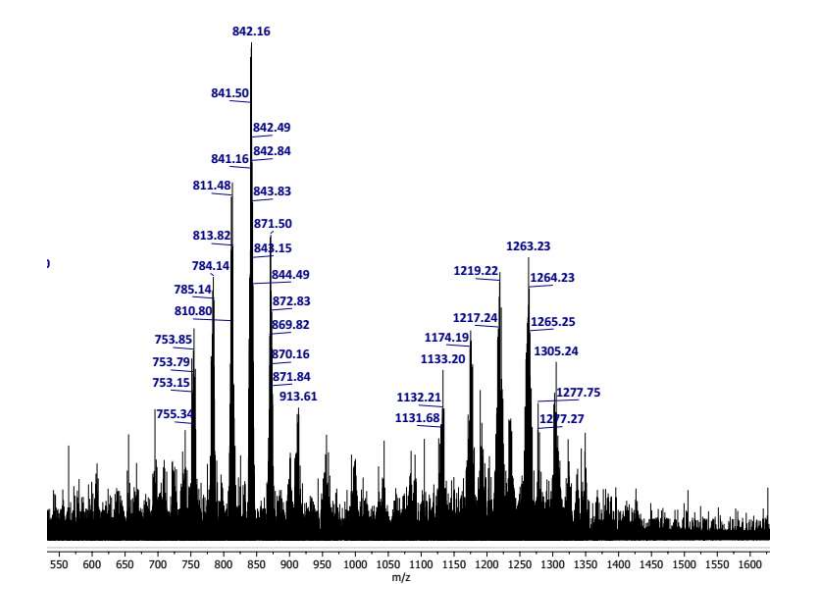


Figure 2.S10 ESI-MS spectra of P-FeMo<sub>x</sub>W<sub>11-x</sub> in the range of m/z 1050-1400

Table 2.S13 Assignment of ESI-mass peaks of P-FeMo <sub>x</sub> W <sub>11-x</sub> POM							
Charge	m/z (obs.)	m/z (obs.) m/z (calc.)		Assigned probable fragment			
-2	1219.22	1219.97	2439.94	K[Fe(H2O)(PW7Mo4O39)]			
-2	1263.23	1263.49	2526.98	K[Fe(H2O)(PW8Mo3O39)]			
-2	1305.24	1307.51	2615.02	K[Fe(H2O)(PW9Mo2O39)]			
-3	753.85	754.28	2262.84	K[Fe(H2O)(PW5Mo6O39)]			
-3	784.14	783.63	2350.89	K[Fe(H2O)(PW6Mo5O39)]			
-3	811.48	812.98	2438.94	K[Fe(H2O)(PW7Mo4O39)]			

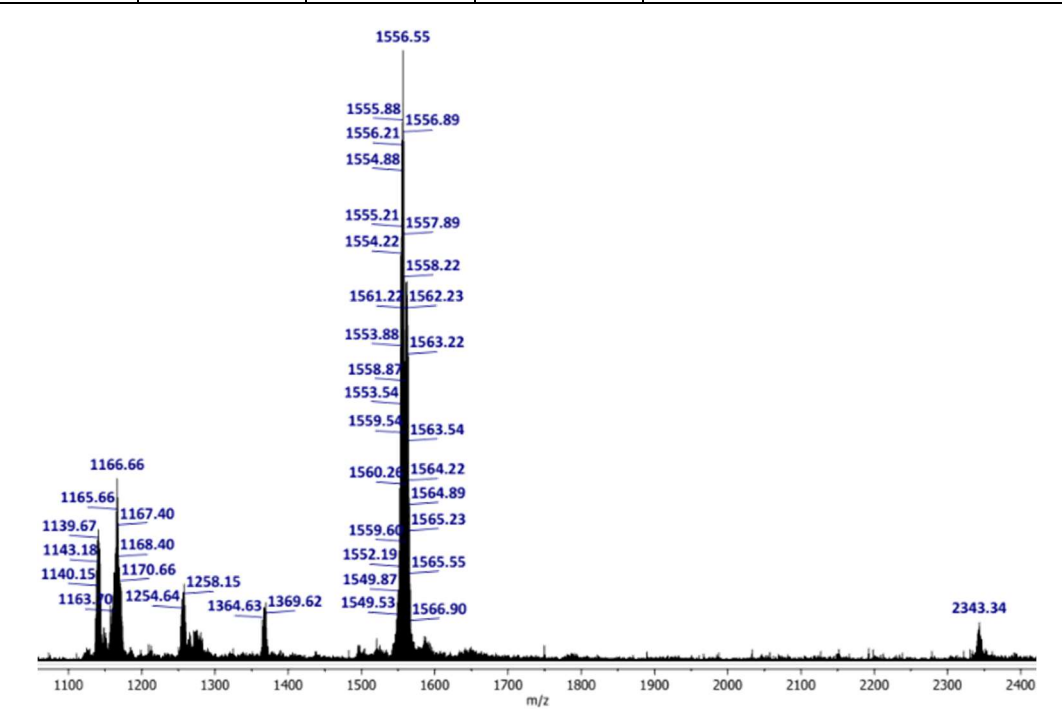
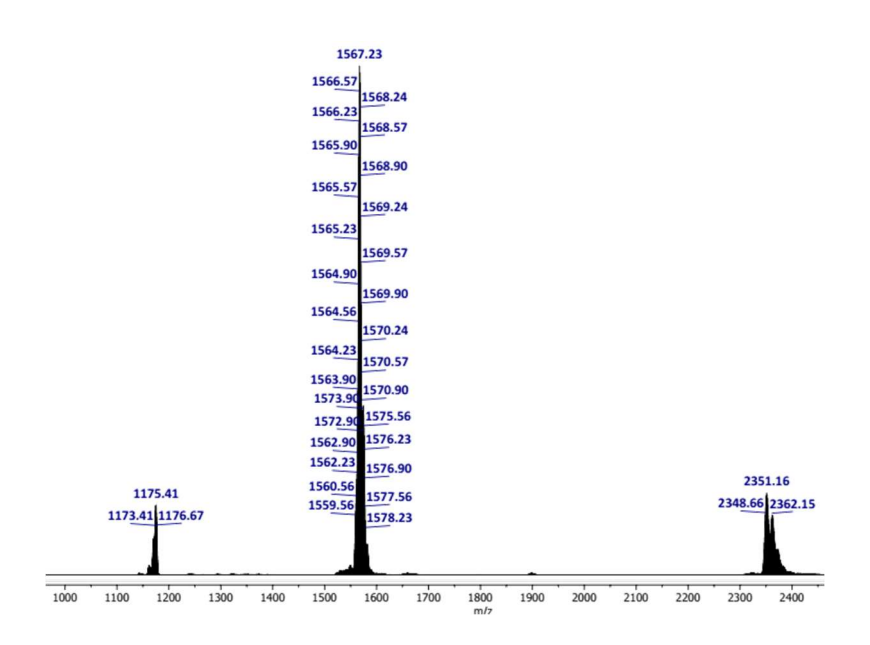


Figure 2.S11 ESI-MS spectra of P-Mn<sub>4</sub>W<sub>18</sub> in the range of m/z 1070-2420.

	Table 2.S14 Assignment of ESI-mass peaks of P-Mn <sub>4</sub> W <sub>18</sub>								
Charge	m/z (obs.)	m/z (calc.)	Mol. Wt.	Assigned probable fragment					
-4	1166.66	1166.60	4666.43	H <sub>4</sub> [Mn <sub>4</sub> (PW <sub>9</sub> O <sub>33</sub> ) <sub>2</sub> O]					
-3	1562.22	1561.48	4685.44	H <sub>7</sub> [Mn <sub>4</sub> (PW <sub>9</sub> O <sub>34</sub> ) <sub>2</sub> ]					
-2	2343.34	2343.22	4686.45	H <sub>8</sub> [Mn <sub>4</sub> (PW <sub>9</sub> O <sub>34</sub> ) <sub>2</sub> ]					



**Figure 2.S12** ESI-MS spectra of P-Co<sub>4</sub>W<sub>18</sub> in the range of m/z 980-2450.

Charge	m/z (obs.)	m/z (calc.)	Mol. Wt.	Assigned probable fragment	
-4	1175.16	1175.10	4700.42	H <sub>6</sub> [Co <sub>4</sub> (PW <sub>9</sub> O <sub>34</sub> ) <sub>2</sub> ]	
-3	1567.17	1567.14	4701.42	H <sub>7</sub> [Co <sub>4</sub> (PW <sub>9</sub> O <sub>34</sub> ) <sub>2</sub> ]	
-2	2351.16	2351.21	4702.43	H <sub>8</sub> [Co <sub>4</sub> (PW <sub>9</sub> O <sub>34</sub> ) <sub>2</sub> ]	

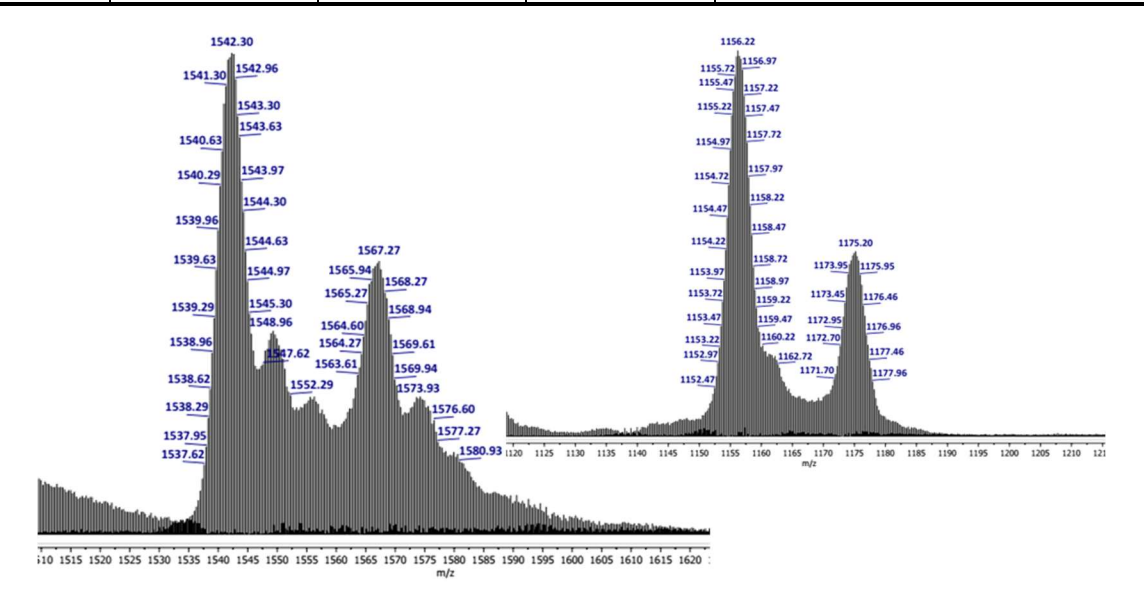


Figure 2.S13 ESI-MS spectra of  $P-Ni_4W_{18}$  in the range of m/z 1120-1630 (z=-3)

Г <b>able 2.</b> S16 <i>A</i>	Assignment of ESI-n	nass peaks of P-Ni4	$\mathbf{W}_{18}$	
Charge	m/z (obs.)	m/z (calc.)	Mol. Wt.	Assigned probable fragment
-4	1175.20	1175.10	4700.43	$H_6[Ni_4(PW_9O_{34})_2]$
-3	1567.37	1566.81	4700.43	H <sub>7</sub> [Ni <sub>4</sub> (PW <sub>9</sub> O <sub>34</sub> ) <sub>2</sub> ]

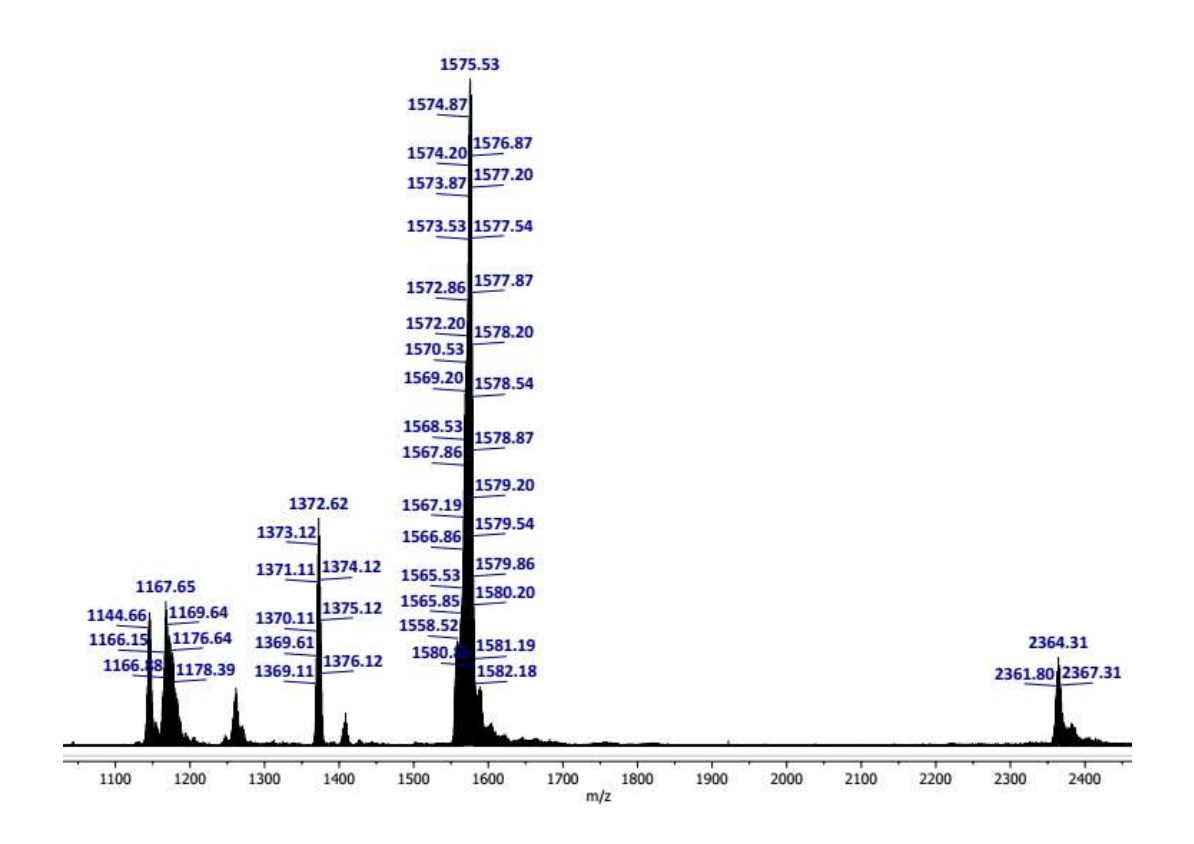


Figure 2.S14 ESI-MS spectra of P-Zn<sub>4</sub>W<sub>18</sub> in the range of m/z 1050-2450.

Table 2.S17 Assignment of ESI-mass peaks of P-Zn <sub>4</sub> W <sub>18</sub>								
Charge	m/z (obs.)	m/z (calc.)	Mol. Wt.	Assigned probable fragment				
-3	1575.54	1575.80	4727.41	$H_7[Zn_4(PW_9O_{34})_2]$				
-2	2364.31	2364.21	4728.42	$H_8[Zn_4(PW_9O_{34})_2]$				

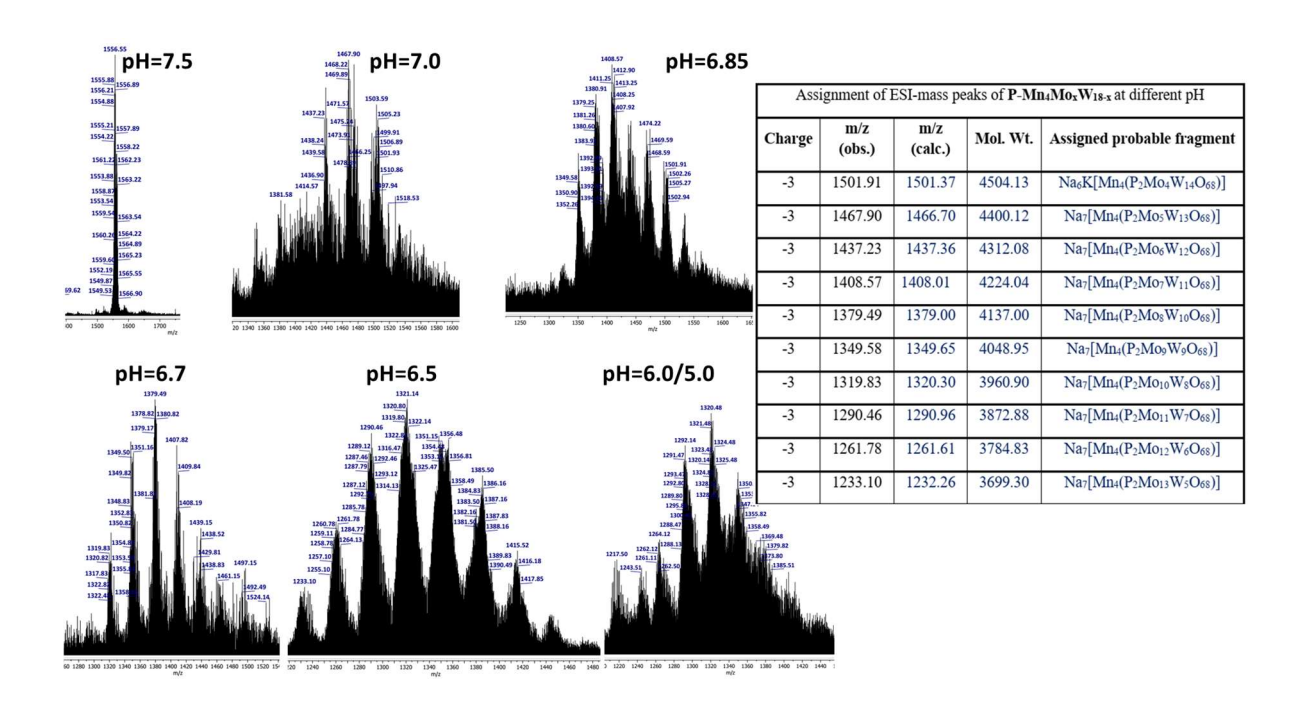


Figure 2.S15 pH dependent ESI-MS spectra of P-Mn<sub>4</sub>Mo<sub>x</sub>W<sub>18-x</sub> with charge (z)= -3

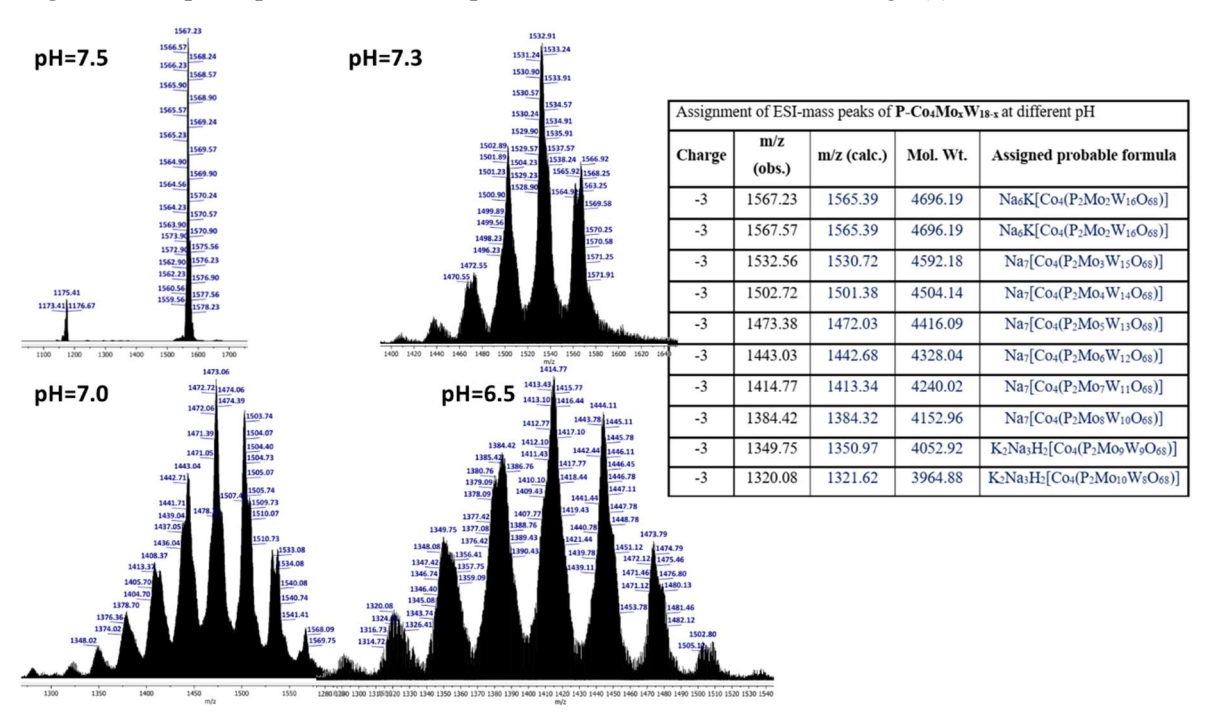


Figure 2.S16 pH-dependent ESI-MS spectra of P-Co<sub>4</sub>Mo<sub>x</sub>W<sub>18-x</sub> with charge (z)= -3

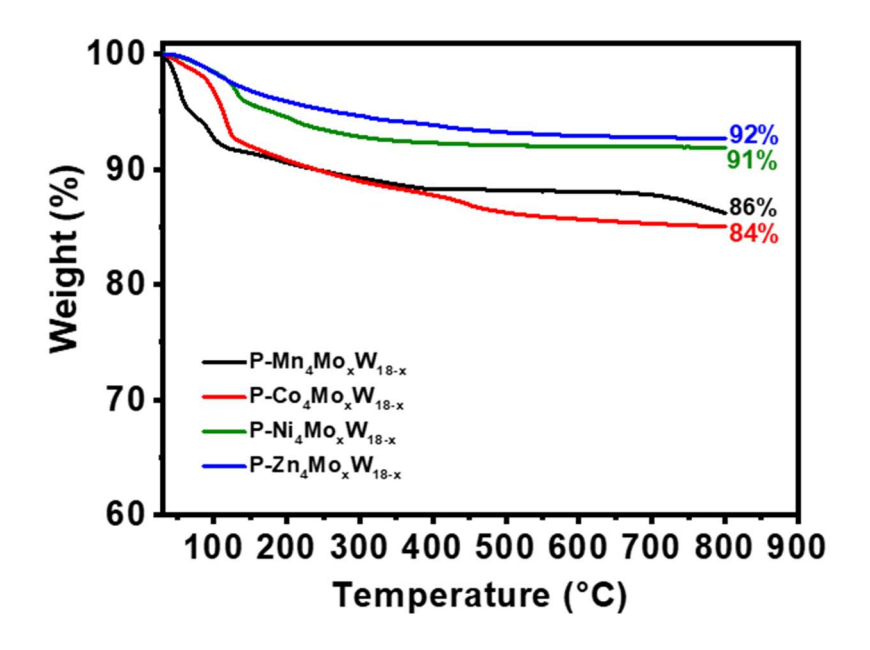
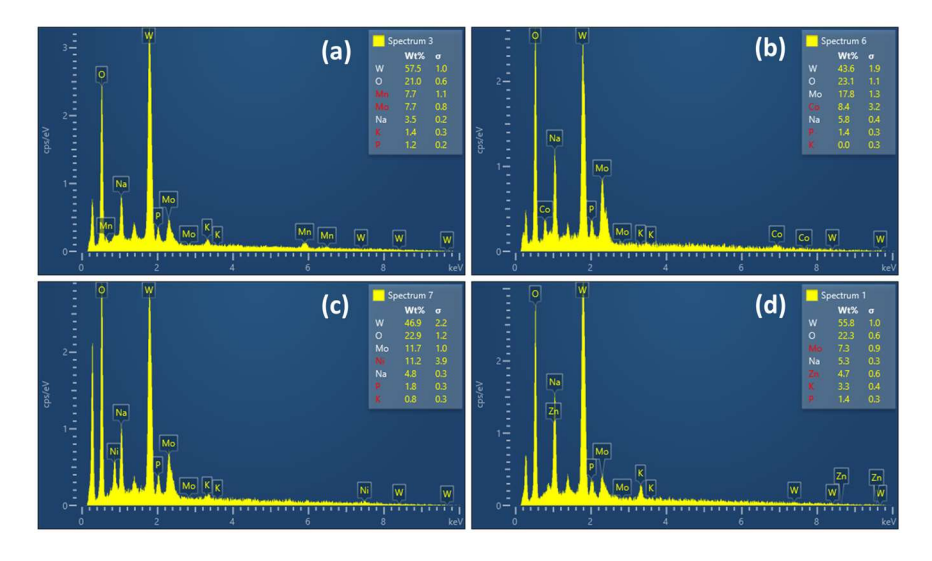


Figure 2.S17 TGA curves of mixed addenda sandwich POMs.



**Figure 2.S18** EDX mapping for mixed addenda sandwich POMs (a) P-Mn<sub>4</sub>Mo<sub>x</sub>W<sub>18-x</sub>, (b) P-Co<sub>4</sub>Mo<sub>x</sub>W<sub>18-x</sub> (c) P-Ni<sub>4</sub>Mo<sub>x</sub>W<sub>18-x</sub> and (d) P-Zn<sub>4</sub>Mo<sub>x</sub>W<sub>18-x</sub>

Atomic percentage for

- (a) **P-Mn<sub>4</sub>Mo<sub>x</sub>W<sub>18-x</sub>**; W= 15.08, Mo=3.87, P=1.86, Mn=6.76, O=63.34, Na=7.34, K=1.72 and bulk composition  $K_{1.72}Mn_{6.76}Mo_{3.87}Na_{7.34}O_{63.34}P_{1.86}W_{15.08}$
- (b) **P-Co<sub>4</sub>Mo<sub>x</sub>W<sub>18-x</sub>**; W=10.28, Mo=8.03, P=1.95, Co=6.17, O=62.61, Na=10.93 and bulk composition  $Co_{6.17}Mo_{8.03}Na_{10.93}O_{62.61}P_{1.95}W_{10.28}$
- (c) (c)  $P-Ni_4Mo_xW_{18-x}$ ; W=11.15, Mo=5.33, P=2.54, Ni=8.34, O=62.61, Na=9.12, K=0.89 and bulk composition  $K_{0.89}Ni_{8.34}Mo_{5.33}Na_{9.12}O_{62.61}P_{2.54}W_{11.15}$

(d) (d) **P-Zn<sub>4</sub>Mo<sub>x</sub>W<sub>18-x</sub>**; W= 13.75, Mo=3.45, P=2.05, Zn=3.26, O=63.20, Na=10.45, K=3.82 and bulk composition  $K_{3.82}Zn_{13.75}Mo_{3.45}Na_{10.45}O_{63.20}P_{2.05}W_{13.7}$ 

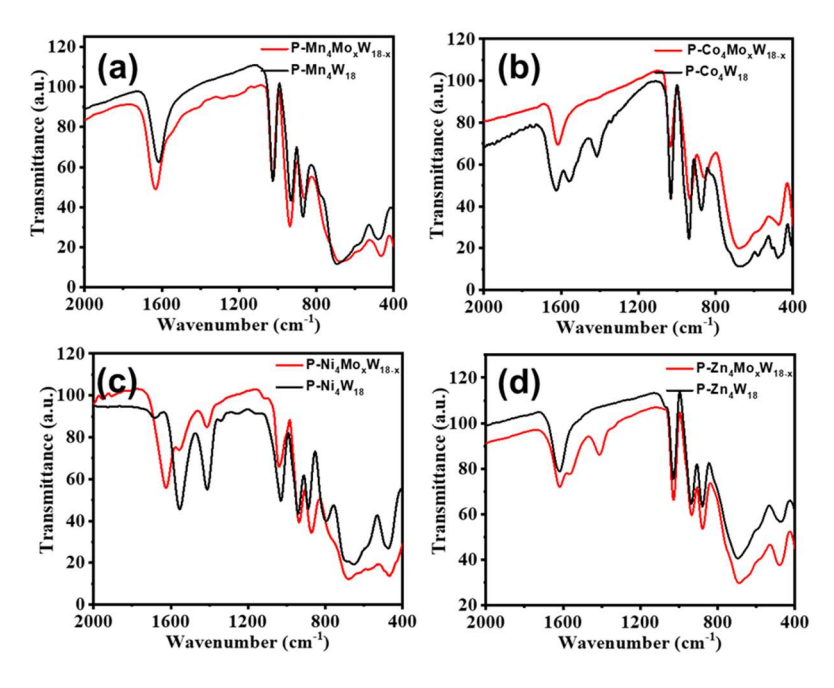


**Figure 2.S19** Comparison of FT-IR spectra of W-only with mixed addenda sandwich POMs (a) P-Mn<sub>4</sub>M<sub>18</sub>, (b) P-Co<sub>4</sub>M<sub>18</sub>, (c) P-Ni<sub>4</sub>M<sub>18</sub>, and (d) P-Zn<sub>4</sub>M<sub>18</sub>, (M=W or Mo/W).

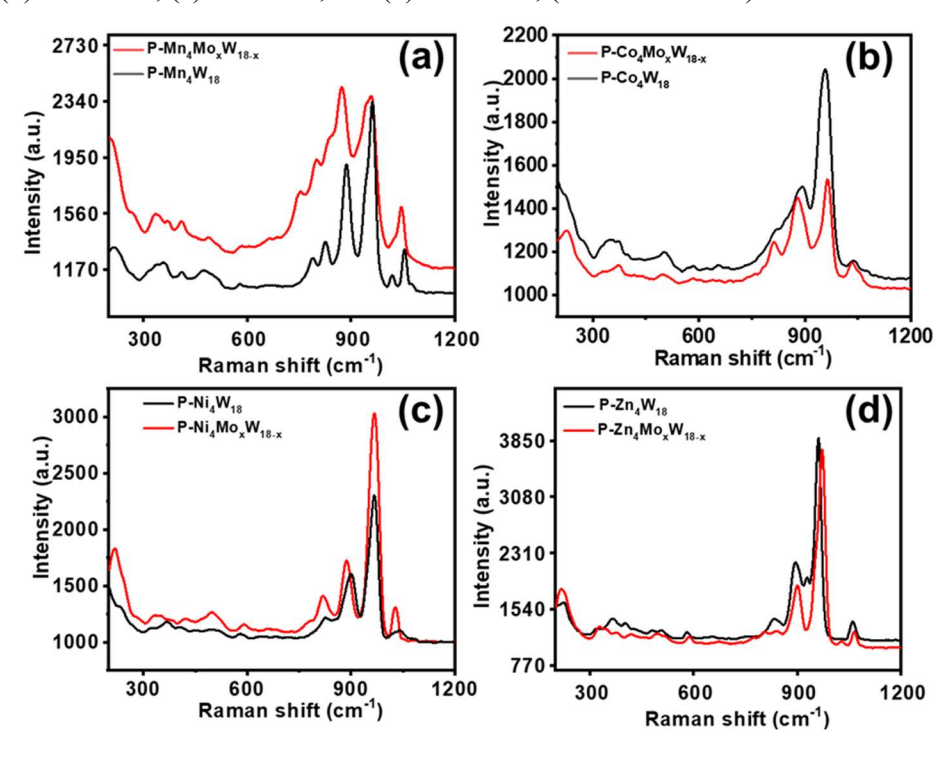


**Figure 2.S20** Comparison of Raman spectra of W-only with the mixed addenda sandwich POMs; (a) P-Mn<sub>4</sub>M<sub>18</sub>, (b) P-Co<sub>4</sub>M<sub>18</sub>, (c) P-Ni<sub>4</sub>M<sub>18</sub>, and (d) P-Zn<sub>4</sub>M<sub>18</sub>, (M=W or Mo/W).

Table 2.S18 Inductively coupled plasma mass spectrometry (ICP-MS) data for mixed addenda sandwich POMs								
POM	TM %	Mo %	W %	Na %	К%			
P-Mn4MoxW18-x	4.52	10.22	43.03	1.01	7.55			
P- Co <sub>4</sub> Mo <sub>x</sub> W <sub>18-x</sub>	5.58	22.36	37.26	3.55	5.43			
P- Ni <sub>4</sub> Mo <sub>x</sub> W <sub>18-x</sub>	3.64	26.98	29.88	1.01	7.7			
P- Zn <sub>4</sub> Mo <sub>x</sub> W <sub>18-x</sub>	3.17	7.67	32.51		9.86			

 $\textbf{P-Mn4Mo}_{x}W_{18-x} \text{ with bulk composition } [NaK_{9}\{Mn_{4}(H_{2}O)_{2}(P_{2}Mo_{5.5}W_{12.5}O_{68})\}.35H_{2}O]$ 

 $P-Co_4Mo_xW_{18-x}$  with bulk composition [Na<sub>2</sub>K<sub>8</sub>{Co<sub>4</sub>(H<sub>2</sub>O)<sub>2</sub>(P<sub>2</sub>Mo<sub>9.5</sub>W<sub>8.5</sub>O<sub>68</sub>)}]

**P-Ni**<sub>4</sub>**Mo**<sub>x</sub>**W**<sub>18-x</sub> with bulk composition  $[Na_2K_8Ni_4(H_2O)_2(P_2Mo_{11.5}W_{6.5}O_{68})]$ .8H<sub>2</sub>O]

**P-Zn<sub>4</sub>Mo<sub>x</sub>W<sub>18-x</sub>** with bulk composition [ $Na_2K_8\{Zn_4(H_2O)_2(P_2Mo_{5.5}W_{12.5}O_{68})\}.118H_2O$ ]

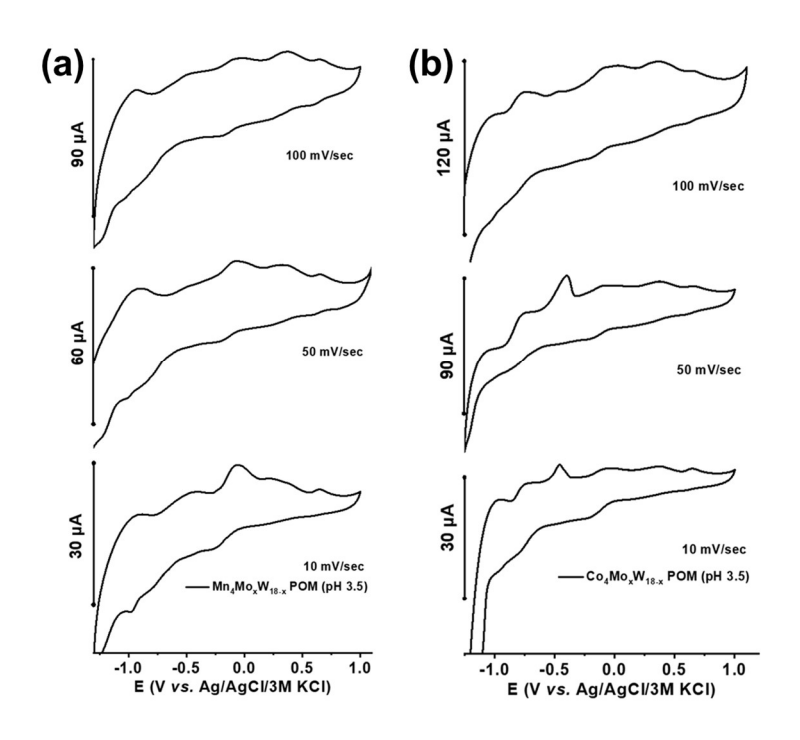


**Figure 2.S21** CV showing the effect of scan rate in mixed addenda sandwich POMs; (a) P-Mn<sub>4</sub>Mo<sub>x</sub>W<sub>18-x</sub>, (b) P-Co<sub>4</sub>Mo<sub>x</sub>W<sub>18-x</sub> at pH=3.5; Glassy carbon (WE): Pt wire, (CE): Ag/AgCl/3 M KCl (RE).

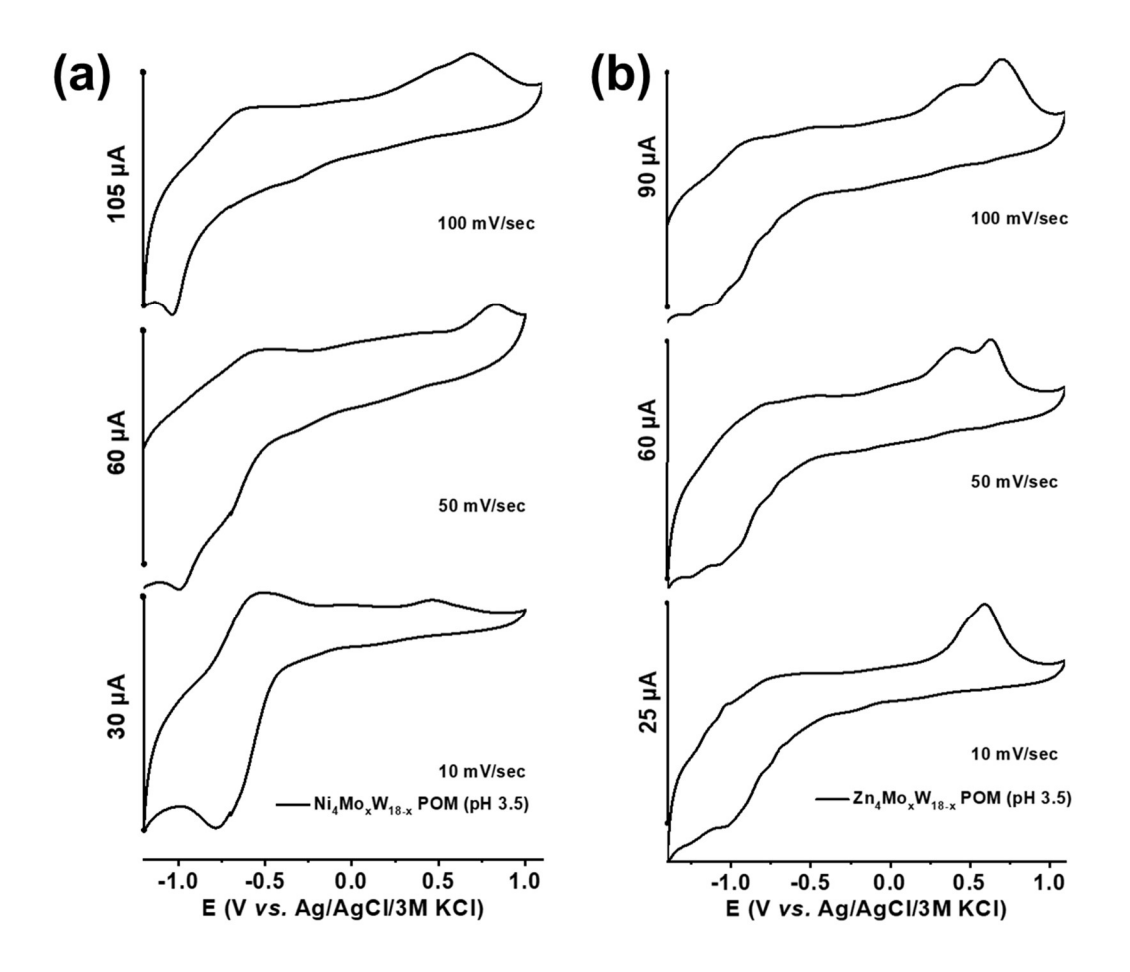


**Figure 2.S22** CV showing the effect of scan rate in mixed addenda sandwich POMs; (a) P-Ni<sub>4</sub>Mo<sub>x</sub>W<sub>18-x</sub>, and (b) P-Zn<sub>4</sub>Mo<sub>x</sub>W<sub>18-x</sub> at pH=3.5; Glassy carbon (WE): Pt wire, (CE): Ag/AgCl/3 M KCl (RE).

### DFT study.

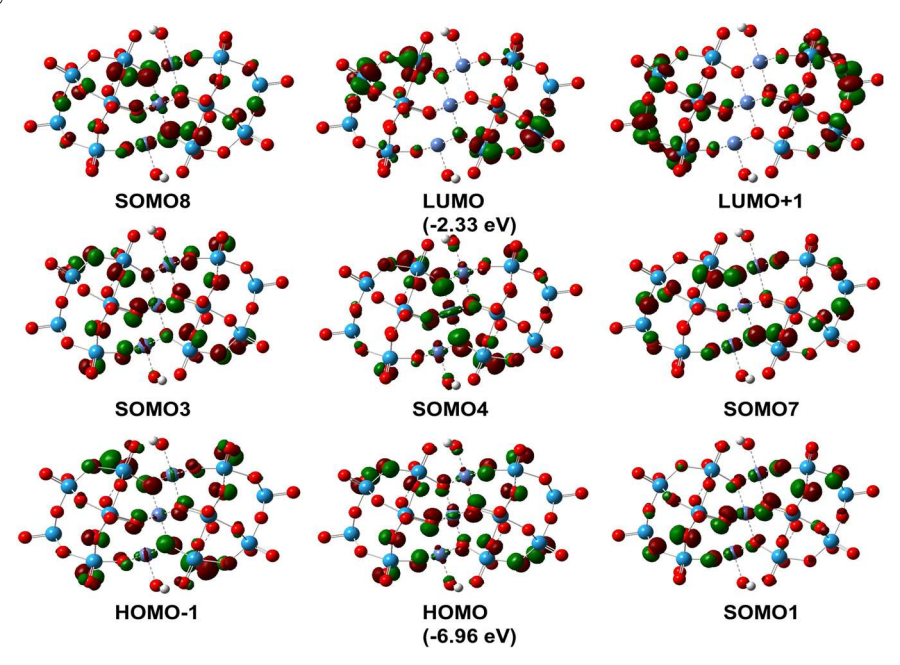


Figure 2.S23 HOMO, LUMO, and SOMO of P-Ni<sub>4</sub>W<sub>18</sub>.

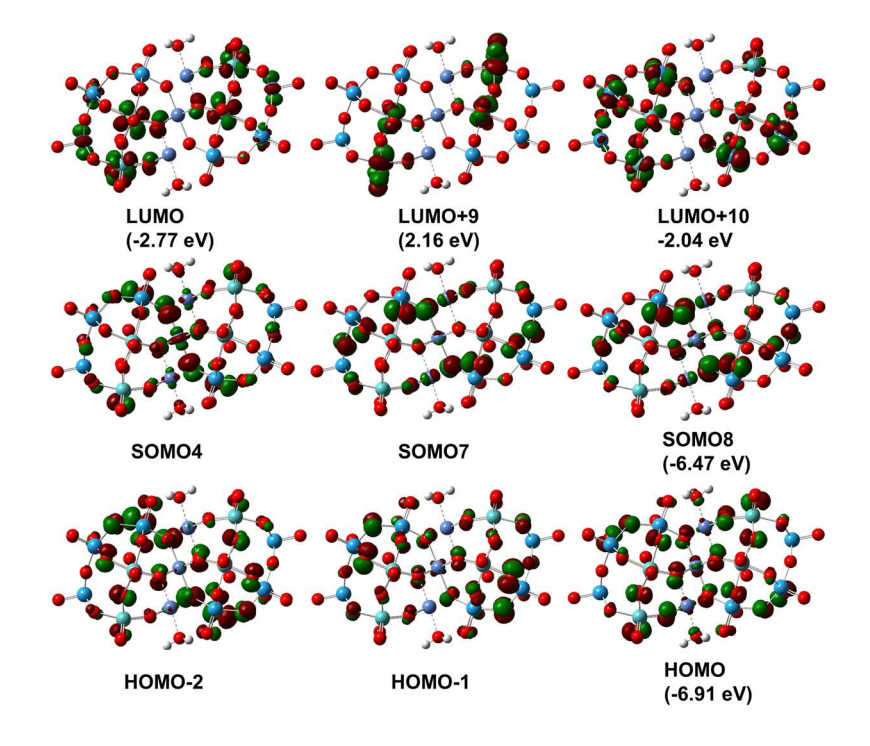


Figure 2.S24 HOMO, LUMO, and SOMO of P-Ni<sub>4</sub>Mo<sub>x</sub>W<sub>18-x</sub>.

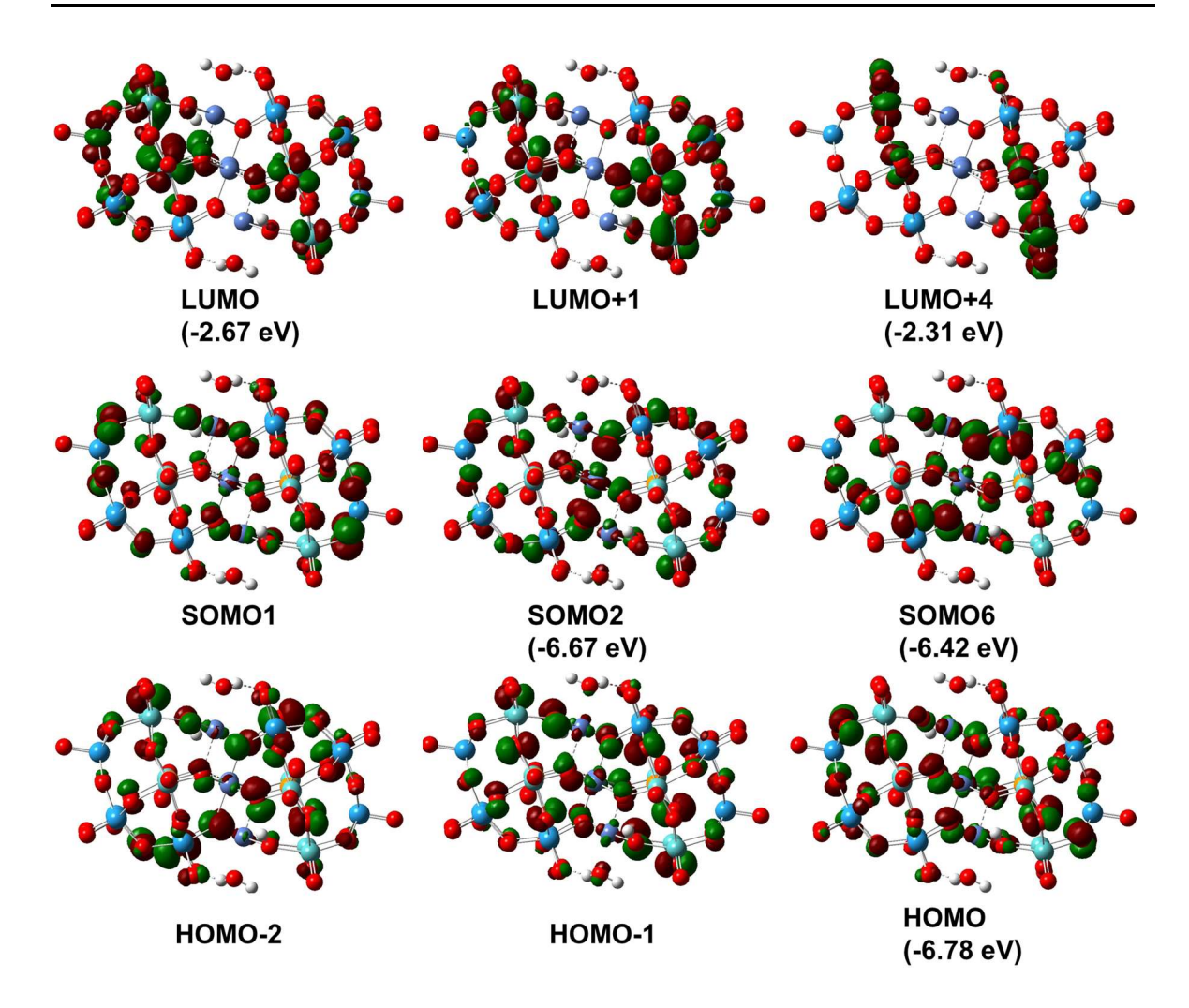
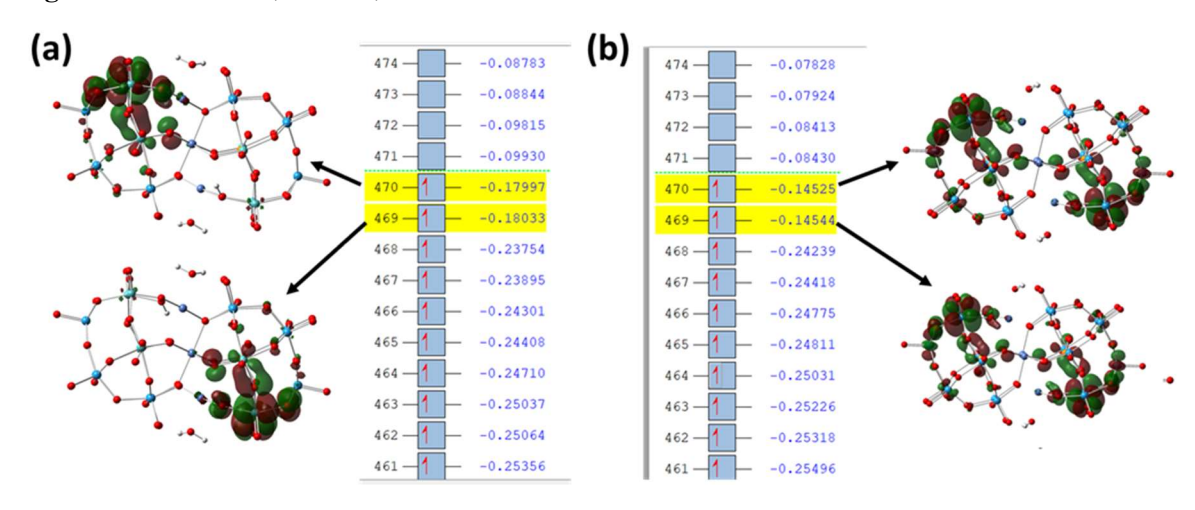


Figure 2.S25 HOMO, LUMO, and SOMO of 2e/2H<sup>+</sup> reduced P-Ni<sub>4</sub>Mo<sub>x</sub>W<sub>18-x</sub>.



**Figure 2.S26** HOMOs for 2e/2H+ reduced (a) P-Ni<sub>4</sub>Mo<sub>x</sub>W<sub>18-x</sub> and (b) P-Ni<sub>4</sub>W<sub>18</sub> without spin coupling.

POMs	P-Mn <sub>4</sub> Mo <sub>2</sub>	$W_{18-x}$	P-Co <sub>4</sub> Mo <sub>2</sub>	$W_{18-x}$	P-Ni <sub>4</sub> Mo <sub>x</sub> W <sub>18-x</sub>		P-Zn <sub>4</sub> Mo <sub>x</sub> W <sub>18-x</sub>	
(positions)	SC-XRD	DFT	SC-XRD	DFT	SC-XRD	DFT	SC-XRD	DFT
	1.708	1.755	1.710	1.754	1.705	1.754	1.723	1.761
	1.945	1.945	1.955	1.949	1.956	1.948	1.952	1.942
M(1)	1.954	1.943	1.926	1.941	1.924	1.941	1.926	1.953
	2.553	2.487	2.528	2.471	2.518	2.472	2.496	2.483
	1.887	1.887	1.867	1.891	1.877	1.893	1.863	1.897
	1.844	1.893	1.856	1.892	1.858	1.893	1.867	1.896
	1.724	1.754	1.709	1.754	1.711	1.754	1.711	1.750
-	1.873	1.905	1.927	1.902	1.950	1.900	1.898	1.900
M(2)	1.902	1.901	1.862	1.934	1.857	1.937	1.919	1.948
111(2)	2.543	2.531	2.528	2.491	2.516	2.491	2.488	2.509
	1.903	1.921	1.899	1.926	1.883	1.928	1.903	1.92
	1.927	1.929	1.901	1.902	1.900	1.901	1.877	1.89
	1.723	1.754	1.720	1.753	1.709	1.753	1.702	1.75
1.6(2)	1.866	1.895	1.893	1.916	1.893	1.915	1.875	1.90
M(3)	1.883	1.904	1.861	1.897	1.877	1.899	1.889	1.90
-	2.557	2.531	2.520	2.498	2.505	2.496	2.492	2.50
	1.900	1.923	1.917	1.934	1.921	1.921	1.918	1.94
-	1.920	1.936	1.902	1.920	1.881	1.932	1.875	1.92
	1.713	1.748	1.712	1.748	1.697	1.749	2.036	2.03
-	2.067	2.032	1.933	2.030	1.932	1.968	2.452	2.41
M(4)	1.922	1.947	1.918	1.968	1.943	1.964	1.942	1.969
111(1)	2.432	2.465	2.432	2.464	2.431	2.465	1.758	1.80
	1.765	1.808	2.043	2.033	2.044	2.033	1.718	1.74
	1.943	1.992	1.764	1.806	1.758	1.803	1.947	1.97
	1.719	1.749	1.715	1.748	1.697	1.749	2.024	2.03
	2.011	2.010	2.021	2.033	2.028	2.031	2.424	2.46
M(5)	1.933	1.930	1.936	1.968	1.926	1.979	1.917	1.92
	2.429	2.473	2.430	2.469	2.423	2.464	1.766	1.80
	1.764	1.800	1.768	1.806	1.773	1.802	1.715	1.75
	1.950	2.037	1.933	1.964	1.957	1.954	1.937	1.76
	1.716	1.749	1.707	1.749	1.703	1.749	2.015	2.01
<u> </u>	1.984	2.074	2.028	2.041	2.032	2.045	1.986	2.05
M(6)	2.025	2.026	1.991	1.949	1.989	2.024	1.723	1.75
	2.476	2.471	2.453	2.465	2.421	2.460	1.762	1.884
	1.903	1.891	1.766	1.803	1.756	1.800	1.898	1.91
	1.766	1.805	2.028	2.028	1.900	1.919	2.426	2.473

	1.723	1.772	1.715	1.749	1.710	1.775	1.998	1.999
	1.953	1.950	1.830	1.803	1.998	1.990	1.725	1.763
M(7)	1.909	1.885	1.891	2.041	1.885	1.868	1.829	1.862
`	2.418	2.377	2.405	2.465	2.427	2.371	1.892	1.945
	1.823	1.864	1.928	1.909	1.827	1.895	2.427	2.406
	1.989	2.002	1.999	2.028	1.935	1.936	1.936	2.016
	1.718	1.771	1.706	1.748	1.701	1.756	1.831	1.864
	1.822	1.862	1.825	1.806	1.824	1.869	1.905	1.902
M(8)	1.897	1.917	1.900	1.959	1.905	1.904	2.409	2.407
`	2.432	2.377	2.434	2.469	2.456	2.397	1.706	1.774
	2.001	2.001	2.000	2.034	2.005	2.008	1.996	1.992
	1.918	1.921	1.930	1.971	1.917	1.940	1.908	1.935
	1.716	1.747	1.708	1.749	1.711	1.749	1.770	1.802
	1.787	1.804	1.773	1.802	1.763	1.800	1.893	1.926
M(9)	1.903	1.943	1.898	1.917	1.906	1.923	1.714	1.757
	2.434	2.474	2.435	2.465	2.399	2.454	2.441	2.473
	2.030	2.021	2.019	2.024	2.022	2.023	2.014	2.025
	1.976	2.004	1.973	2.035	1.978	2.027	1.981	2.042
	2.074	2.106	2.003	2.047	1.986	2.035	2.203	2.261
	2.293	2.304	2.208	2.220	2.145	2.160	2.135	2.115
$TM_i$	2.145	2.154	2.072	2.101	2.045	2.079	2.050	2.071
	2.353	2.316	2.257	2.233	2.157	2.169	2.000	2.082
	2.081	2.101	2.031	2.052	1.999	2.035	2.310	2.259
	2.140	2.157	2.065	2.085	2.042	2.079	2.027	2.105
	2.117	2.128	2.040	2.050	2.018	2.044	2.050	2.108
	2.142	2.169	2.041	2.120	2.025	2.073	2.084	2.112
$TM_e$	2.318	2.244	2.205	2.156	2.159	2.120	2.213	2.201
	2.156	2.186	2.088	2.116	2.047	2.068	2.065	2.141
	2.162	2.184	2.098	2.124	2.053	2.098	2.106	2.143
	2.143	2.224	2.093	2.157	2.064	2.114	2.083	2.170
	1.538	1.657	1.536	1.651	1.536	1.648	1.532	1.659
P	1.542	1.657	1.538	1.654	1.537	1.651	1.538	1.654
	1.543	1.656	1.538	1.659	1.540	1.667	1.546	1.657
	1.557	1.649	1.538	1.647	1.551	1.644	1.551	1.652

<b>Table 2.S20</b> Comparison table of few important bond angles of mixed addenda POMs: SC-XRD versus optimized structure (DFT) (M= Mo/W, $TM_i$ = internal transition metal, $TM_e$ = external transition metal at								
_	sandwich position)							
Bond angles	P-Mn4(W/Mo)		P-Co4(W/Mo)		P-Ni4(W/Mo)		P-Zn4(W/Mo)	
Bona ungres	SC-XRD DFT		SC-XRD	DFT	SC-XRD	DFT	SC-XRD	DFT
M-O <sub>c</sub> -M(cap)	152.48	153.41	152.12	153.30	152.52	153.38	151.98	153.32

-10

-10

-10

-10

-10

-10

M-O <sub>c</sub> -M(belt)	147.86	153.13	147.68	152.14	146.24	151.84	148.60	152.42
M-O <sub>e</sub> -M(belt)	124.66	124.59	123.71	124.49	123.19	124.27	123.70	124.91
M-Oμ <sub>2</sub> -TM <sub>i</sub>	136.66	141.89	137.13	142.03	137.40	141.58	137.68	141.18
M-Oµ <sub>3</sub> -TM <sub>i</sub>	125.33	125.75	125.20	125.75	124.75	125.53	124.82	125.24
M-Oμ <sub>2</sub> -TM <sub>e</sub>	136.65	140.77	137.88	142.18	139.27	141.21	137.66	140.89
M-Oμ <sub>3</sub> -TM <sub>e</sub>	132.15	133.32	132.71	134.64	133.58	134.99	132.00	132.22

POMs	Charge	2S+1	Energy (Hartree)	ΔE (kcal/mol)
P-Mn <sub>4</sub> Mo <sub>18</sub>	-10	21	-7585.99365	
P-Mn <sub>4</sub> W <sub>18</sub>	-10	21	-7592.50966	
P-Mn <sub>4</sub> Mo <sub>8</sub> W <sub>10</sub>	-10	21	-7589.62104	276.4945
P-Co <sub>4</sub> W <sub>18</sub>	-10	13	-7756.95029	
P-Co <sub>4</sub> Mo <sub>8</sub> W <sub>10</sub>	-10	13	-7754.06093	276.9564

-7847.31597

-7853.83094

-7850.94173

-7432.50494

-7439.02651

-7436.13699

276.8704

277.0562

9

9

9

1

1

1

**Table 2.S21** Stabilization of **P-(TM)<sub>4</sub>Mo<sub>8</sub>W<sub>10</sub>** ( $\Delta E$ , in kcal mol<sup>-1</sup>) with respect to

Table 2.S22	Table 2.S22 Average charge distribution on oxygen atoms at different positions in P-(TM) <sub>4</sub> W <sub>18</sub> and								
	P-(TM) <sub>4</sub> Mo <sub>8</sub> W <sub>10</sub> tetrasubstituted POMs (TM=Mn, Co, Ni, Zn; M=Mo/W)								
Atom/Group	P-Mn <sub>4</sub> W <sub>18</sub>	P-Mn <sub>4</sub>	P-C04W18	P-Co <sub>4</sub>	P-	P-Ni <sub>4</sub>	P-Zn <sub>4</sub> W <sub>18</sub>	P-Zn <sub>4</sub>	
		$Mo_8W_{10}$		$Mo_8W_{10} \\$	Ni <sub>4</sub> W <sub>18</sub>	$Mo_8W_{10}$		$Mo_8W_{10}$	
P	2.48	2.47	2.49	2.48	2.50	2.49	2.49	2.48	
O <sub>µ4</sub> (belt)	-0.95	-0.95	-0.95	-0.95	-0.95	-0.95	-0.95	-0.95	
<b>P-O</b> <sub>μ4</sub> -TM	-1.07	-1.07	-1.05	-1.05	-1.04	-1.03	-1.15	-1.15	
M <sub>belt</sub> -O <sub>μ2-</sub> TM <sup>e</sup>	-0.73	-0.61	-0.71	-0.59	-0.69	-0.58	-0.76	-0.63	
M <sub>belt</sub> -O <sub>μ3</sub> -	-0.82	-0.84	-0.81	-0.82	-0.79	-0.80	-0.88	-0.91	
TM <sup>e</sup>									
M <sub>belt</sub> -O- M <sub>cap</sub>	-0.72	-0.69	-0.72	-0.69	-0.72	-0.69	-0.72	-0.69	
<b>O</b> (H <sub>2</sub> O)	-0.99	-0.98	-0.97	-0.97	-0.96	-0.95	-1.02	-1.01	
$M_{belt} = O_t$	-0.61	-0.54	-0.61	-0.54	-0.62	-0.54	-0.62	-0.54	
$W_{cap} = O_t$	-0.59	-0.60	-0.59	-0.60	-0.59	-0.59	-0.59	-0.60	
W-O-W (cap)	-0.72	-0.72	-0.72	-0.72	-0.72	-0.72	-0.72	-0.72	
W-O-W	-0.72	-0.72	-0.72	-0.72	-0.72	-0.72	-0.72	-0.72	
(belt)									

P-Ni<sub>4</sub>Mo<sub>18</sub>

P-Ni<sub>4</sub>W<sub>18</sub>

P-Ni<sub>4</sub>Mo<sub>8</sub>W<sub>10</sub>

P-Zn<sub>4</sub>Mo<sub>8</sub>W<sub>10</sub>

P-Zn<sub>4</sub>Mo<sub>18</sub>

P-Zn<sub>4</sub>W<sub>18</sub>

Mo- <b>O</b> -W (belt)	-	-0.68	-	-0.68	-	-0.68	-	-0.68
Mo- <b>O</b> -Mo (belt)	-	-0.62	-	-0.62	-	-0.62	-	-0.62
TM (ext.)	1.24	1.22	1.13	1.12	1.07	1.06	1.39	1.38
TM (int.)	1.21	1.20	1.14	1.13	1.01	1.07	1.37	1.36

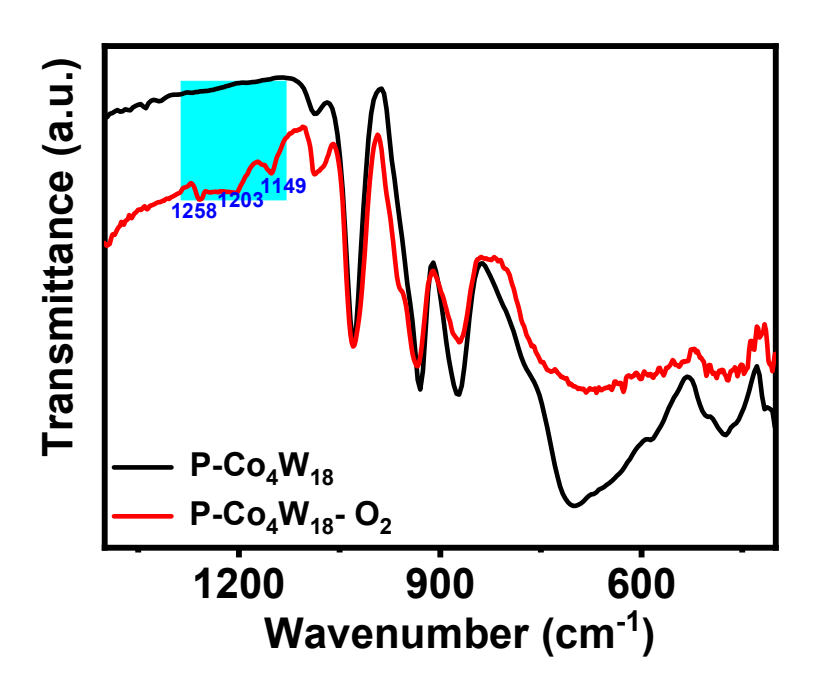


Figure 2.S27 Comparative FT-IR spectroscopy of P-Co $_4$ W $_{18}$  sandwich POMs before and after O $_2$  treatment.

# **Chapter 3**

Cooperative Self-Assembly Assisted Construction of Sandwich Polyoxometalates and its Mixed Addenda Analogue

#### 3.1 Introduction

Polyoxometalates (POMs) have garnered significant attention due to their tunable reactivity, reversible electron transfer, and UV-visible light absorption capabilities.<sup>1</sup> This has led to significant advancements in POM-based photo and electrocatalysis in material science.<sup>2</sup>

A considerable progress has been made in orbital engineering within Keggin and Dawson POMs, like a mixed addenda approach by the inclusion of few Mo/V/Nb into W-based Keggin and Dawson POMs is reported for modulating the HOMO-LUMO levels.<sup>3,4</sup> However, there is very little known about sandwich POMs and frameworks based on these POMs. Tetrasubstituted Sandwich POM [(TM)<sub>4</sub>(H<sub>2</sub>O)<sub>2</sub>(XW<sub>9</sub>O<sub>34</sub>)<sub>2</sub>]<sup>n-</sup> (TM=transition metal, X= hetero atoms, example P, Si, Zn, Co) has gained a lot of interest as efficient catalyst for various catalytic activities like energy conversion and storage devices, sensing, organic transformation, etc. Sandwich POM has robust structure and their catalytic activity highly depend on the transition metal core (TM<sub>4</sub>) and the addenda framework. Orbital engineering strategies in these POMs can be seen as versatile tools for fast electron transfer and large electron storage capacity and become very impactful.<sup>5</sup> In Chapter 2, we understood the orbital engineering in P as heteroatom based sandwich POMs. Here, we propose a mixed addenda with mixed metal (TM<sub>4</sub> cubane core) strategy to modulate the frontier molecular orbitals (FMO) in sandwich POMs with transition metals (Fe/Co/Zn) as heteroatoms.

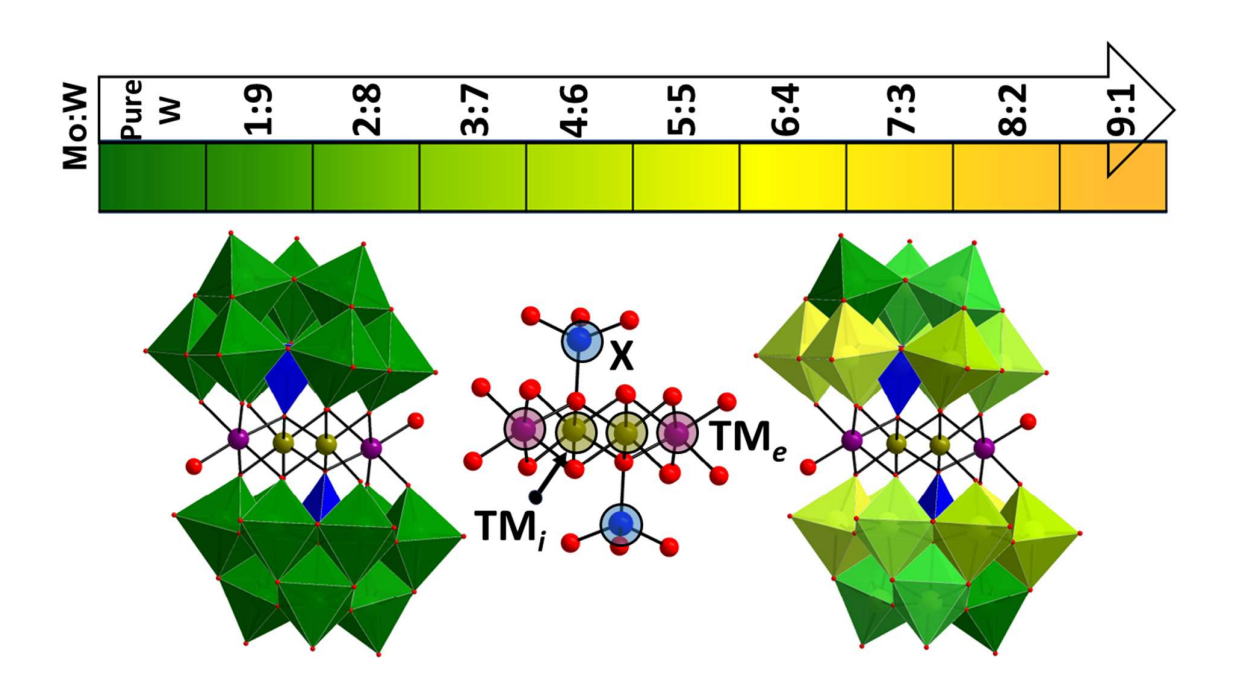
In section A of chapter 3, we explored a cooperative mix-metal approach for the synthesis of mixed metal-mixed addenda polyoxometalates (POMs) in sandwich-type architectures with transition metals (Fe/Co/Zn) as heteroatoms. Recently, POM based coordination frameworks have gained attention due to their properties like enhanced conductivities and catalytic activities. Fo, in section B of chapter 3, we have extended this cooperative mixed metal approach for the synthesis of POMs 1D-coordination frameworks (POMCFs), with its complimentary DFT study to explain how charge density of these POMs plays a crucial role in the formation of these POMCFs. This chapter presents a systematic cooperative mix-metal approach, demonstrating the successful synthesis of mixed metal-mixed addenda POMs. Using this cooperative mix-metal approach we have synthesized 6 new mixed metal-mixed addenda sandwich POMs, five W-based new POMs, four POM 1D-coordination frameworks (POMCFs). We meticulously characterized all the POMs by Single crystal-XRD, ESI-MS and XPS analysis and validated the orbital modulation by various spectroscopy and DFT studies.

#### 3.2 References

- 1. Cameron, J. M.; Fujimoto, S.; Kastner, K.; Wei, R. J.; Robinson, D.; Sans, V.; Newton, G. N.; Oshio, H. H., Orbital engineering: Photoactivation of an organofunctionalized polyoxotungstate. *Chem. Eur. J* **2017**, *23* (1), 47-50.
- 2. Katsoulis, D. E., A survey of applications of polyoxometalates. *Chem. Rev.* **1998**, *98* (1), 359-388.
- 3. López, X.; Bo, C.; Poblet, J. M., Electronic properties of polyoxometalates: Electron and proton affinity of mixed-addenda Keggin and Wells-Dawson anions. *J. Am. Chem. Soc.* **2002**, *124* (42), 12574-12582.
- 4. Lopez, X.; Maestre, J. M.; Bo, C.; Poblet, J.-M., Electronic properties of polyoxometalates: A DFT study of α/β-[XM12O40] n-relative stability (M= W, Mo and X a main group element). *J. Am. Chem. Soc.* **2001**, *123* (39), 9571-9576.
- 5. Amin, S. S.; Cameron, J. M.; Winslow, M.; Davies, E. S.; Argent, S. P.; Robinson, D.; Newton, G. N., A Mixed-Addenda Mo/W Organofunctionalised Hybrid Polyoxometalate. *Eur. J. Inorg. Chem* **2022**, *2022* (10), e202200019.
- 6. Guo, K.-K.; Yang, Y.-L.; Dong, S.-M.; Li, F.-Y.; Jiang, X.-Y.; Xu, L., Decomposition—Reassembly Synthesis of a Silverton-Type Polyoxometalate 3D Framework: Semiconducting Properties and Photocatalytic Applications. *Inrog. Chem.* **2022**, *61* (17), 6411-6420.
- 7. Zhao, M.; Zhang, X.-W.; Wu, C.-D. J. A. C., Structural transformation of porous polyoxometalate frameworks and highly efficient biomimetic aerobic oxidation of aliphatic alcohols. *ACS Catal.* **2017**, *7* (10), 6573-6580.

# Chapter 3 Section A

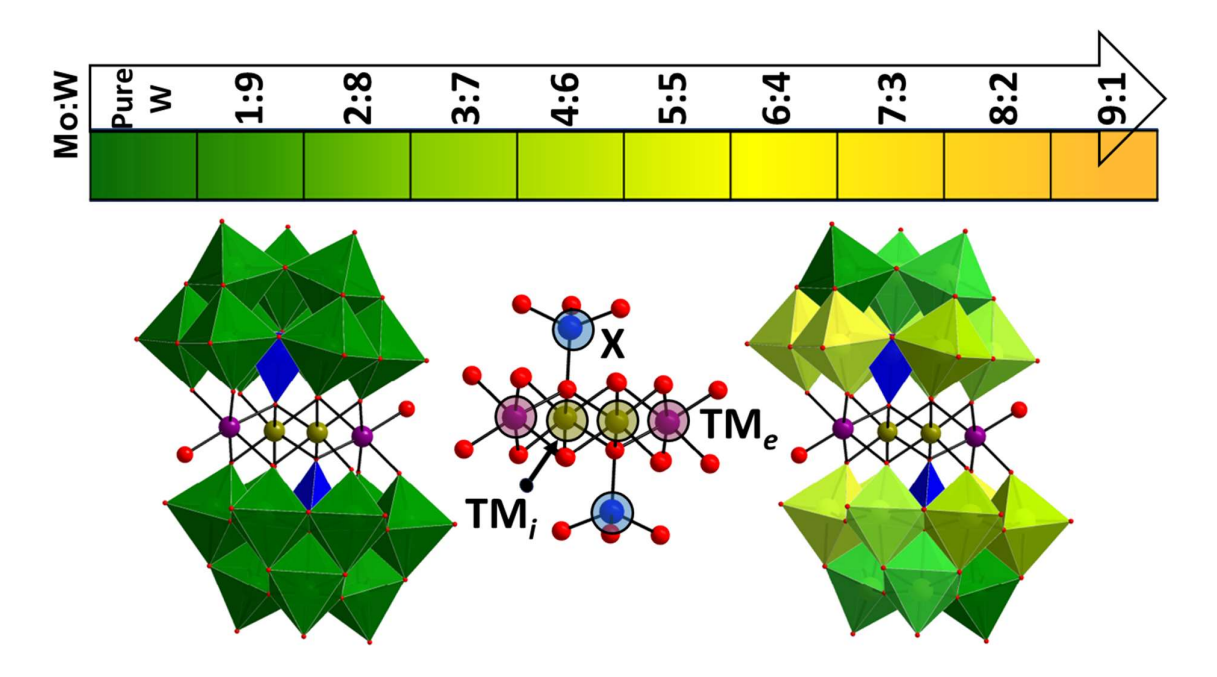
Construction of Mixed Addenda Polyoxometalates
by Cooperative Self-Assembly and Tuning
their Optoelectronic Properties



#### **3A.1 Introduction**

Polyoxometalates<sup>1</sup> (POMs), with their diverse structural architectures and properties, applied across diverse fields such as catalysis, nanotechnology, magnetism, material science, and medicine.<sup>2,3</sup> Our particular focus delves into exploring the binding affinity of various transition metals to lacunary POMs<sup>4-8</sup> to form transition metals substituted sandwich POMs (TMSPs); specifically, tetrasubstituted TMSPs with the formula [(TM)<sub>4</sub>(H<sub>2</sub>O)<sub>2</sub>(XW<sub>9</sub>O<sub>34</sub>)<sub>2</sub>]<sup>n</sup> (where TM = transition metals, X = P/Zn/Co, etc.). By selecting appropriate addenda atoms and substituting transition metals, the electronic structures of these TMSPs can be tuned, resulting in distinct positions for the highest occupied molecular orbital (HOMO) and lowest unoccupied molecular orbital (LUMO). These TMSPs having transition metals at the core and W as addenda atoms, exhibit robust structural diversity.9, 10 Incorporation of other addenda atoms (Mo and V) in TMSPs remains challenging, possibly due to higher kinetic lability. Recently, using a protecting group strategy, a Mo-based tetrasubstituted TMSP was isolated in acetonitrile. <sup>5</sup> Conversely, a mixed addenda approach by the inclusion of few Mo/V/Nb into Wbased Keggin and Dawson POMs is reported for modulating the HOMO-LUMO levels, which significantly impacting molecular properties, such as improving absorption towards the visible region. 11, 12 Cronin group has reported mixed addenda (Mo, W) TMSP, [Co<sub>4</sub>(H<sub>2</sub>O)<sub>2</sub>(PMo<sub>x</sub>W<sub>9</sub>- $_{\rm x}O_{34})_2$ ]<sup>n-</sup>, thus overcoming the sluggish kinetics in oxygen evolution reaction (OER).<sup>13</sup>

In Chapter 2, we have demonstrated fine-tuning of the optical and redox properties in mixed addenda sandwich POMs, [(TM)<sub>4</sub>(H<sub>2</sub>O)<sub>2</sub>(PMo<sub>x</sub>W<sub>9-x</sub>O<sub>34</sub>)<sub>2</sub>]<sup>n-</sup>, which opens up opportunities of a wide range of possibilities for the synthesis of these TMSPs with desired properties.<sup>14</sup> Conversely, another set of TMSPs with d-block elements as heteroatoms  $[(TM)_4(H_2O)_2(XW_9O_{34})_2]^{n-}$  (where TM = X = Mn/Fe/Ni/Cu) and  $[W(TM)_3(H_2O)_2(XW_9O_{34})_2]^{n-}$ (where TM = X = Co/Zn), with W addenda atoms have been reported. 15-18 Despite these advantages, the mixed addenda POM with the incorporation of Mo, V, or Nb alongside W in these tetrasubstituted TMSPs remains unexplored, which holds potential for fine-tuning the optical and redox properties. Alternatively, a mixed transition metal approach is widely used for the synthesis of W-only Keggin and Dawson-based tetrasubstituted sandwich, Banana, Cap, **TMSPs** towards improved catalytic activity. Tetramer  $[Ni_2Co_2(H_2O)_2(PW_9O_{34})_2]^{10-}$  and  $[Fe_2Co_2(H_2O)_2(CoW_9O_{34})_2]^{14-}$  reported as highly active OER catalyst. 19-23



**Scheme 3A.1**. Transition metals substituted tetrasubstituted sandwich POMs (W only and Mo/W based) indicating the role of transition metals at internal sandwich  $(TM_i)$ , external sandwich  $(TM_e)$ , and heteroatom position (X).

However, a systematic study of transition metal variations at different positions, such as heteroatom-position, sandwich (internal and external) positions, and mixed metals toward Mo addenda incorporation in the framework, and its impact on their band gap modulation, is still lacking. Also, the effect of charge densities of lacunary POMs (overall charge divided by number of atoms, Table 3A.1) on binding with transition metals remains unexplored in these TMSPs, as observed in Nb-based POMs.<sup>24, 25</sup>

Table 3A.1 Charge densities of lacunary POMs with different heteroatoms (bold)							
Formula	Charge (-ve)	(non-H) atoms	Charge density (Charge/atoms)				
ZnW <sub>9</sub> O <sub>34</sub> or ZnMo <sub>x</sub> W <sub>9-x</sub> O <sub>34</sub>	12	44	0.27				
CoW <sub>9</sub> O <sub>34</sub> or CoMo <sub>x</sub> W <sub>9-x</sub> O <sub>34</sub>	12	44	0.27				
FeW <sub>9</sub> O <sub>34</sub> or FeMo <sub>x</sub> W <sub>9-x</sub> O <sub>34</sub>	11	44	0.25				
PW <sub>9</sub> O <sub>34</sub> or PMo <sub>x</sub> W <sub>9-x</sub> O <sub>34</sub>	9	44	0.20				
$ZnW_{12}O_{40}$	6	53	0.11				
PW <sub>12</sub> O <sub>40</sub>	3	53	0.05				

Thus, we propose TMSPs with mixed addenda to leverage the combined advantages of W and Mo along with various transition metals at the sandwich core and heteroatom position (Scheme 3A.1). In this Chapter, our efforts focus on the systematic approach for the synthesis of mixed metal-mixed addenda TMSPs featuring mixed late 3d transition metals with the general formula  $[(TM_e)_2(TM_i)_2(H_2O)_2(XMo_xW_{9-x}O_{34})_2]^{14-}$   $(TM_e = X = Zn/Co/Fe, TM_i = Mn/Fe)$ .

All these POMs are characterized using SC-XRD, ESI-MS, FT-IR, Raman, XPS, TGA, and their role in dioxygen activation<sup>26-30</sup> has been emphasized. Further, electronic, and optical properties are elucidated through UV-vis spectra and DFT studies.<sup>31-34</sup>

#### 3A.2 Results and Discussion

#### 3A.2.1 Synthetic Chemistry

**TMSPs with TM as heteroatom:** TMSPs with the same transition metals in the sandwich as well as heteroatom position;  $[(TM)_4(H_2O)_2(XW_9O_{34})_2]^{n-}$  are well known<sup>9</sup> when TM = X =Mn/Fe/Ni/Cu, however, analogues mixed addenda of these structures are still unknown. In this context, first we synthesized mixed addenda Na<sub>14</sub>[Fe<sub>4</sub>(H<sub>2</sub>O)<sub>2</sub>(FeMo<sub>x</sub>W<sub>9-x</sub>O<sub>34</sub>)<sub>2</sub>].20H<sub>2</sub>O (1-M, TM = X = Fe) analogous to  $Na_{14}[Fe_4(H_2O)_2(FeW_9O_{34})_2].22H_2O$  (1) obtained from FeCl<sub>2</sub>. 1-M has been synthesized via microwave heating at 85 °C at pH 6.6; increasing the pH results in the formation of 1, while lowering the pH does not give the desired product. ESI-MS of 1 (aq. solution) shows the isotopic single envelope of peaks at m/z 1580 (z=-3), which shifts to isotopic multiple envelopes of peaks in the range of m/z 1400-1550 (z=-3) for 1-M with different compositions of Mo/W ratio (Fig. 3A.4), thus indicating the incorporation of Mo addenda in the POM framework. The most abundant anion of 1-M has the composition of Mo:W (3:15) with the formula  $[Fe_4(H_2O)_2(FeMo_3W_{15}O_{34})_2]^{7-}$  while Mo:W ratio varies from 1:17 to 6:12 in the cluster. Due to the Mo addenda incorporation FT- IR (W=O<sub>term</sub> at 931 cm<sup>-1</sup> in 1, W/Mo=O<sub>term</sub> 911 cm<sup>-1</sup> in 1-M) peaks shifts to lower values (Fig. 3A.5a). SC-XRD study confirms the light yellow colored block shape crystals of 1-M with  $P\overline{1}$  space group and the molecular formula of [Fe<sub>4</sub>(H<sub>2</sub>O)<sub>2</sub>(FeMo<sub>1.1</sub>W<sub>7.9</sub>O<sub>34</sub>)<sub>2</sub>]<sup>10</sup>, while 1 crystallizes with P2<sub>1</sub>/n space group with formula [Fe<sub>4</sub>(H<sub>2</sub>O)<sub>2</sub>(FeW<sub>9</sub>O<sub>34</sub>)<sub>2</sub>]<sup>12</sup>. Bond valence sum (BVS) calculation<sup>35</sup> indicates all Fe in +3 oxidation state in 1-M, which was confirmed from XPS analysis (Fig. 3A.S2).

While Fe is in +2 oxidation state at external sandwich positions (TM<sub>e</sub>) and +3 at heteroatom and internal sandwich position (TM<sub>i</sub>) in **1**. The characteristics Fe-O bond lengths are between 1.8-2.1 Å with X-O $\mu_4$ -TM<sub>i</sub> (X = TM<sub>i</sub> = Fe) distances was found to be 3.87 Å. FeCl<sub>2</sub> imparts a crucial role towards incorporating mixed addenda in these POMs as FeCl<sub>3</sub> as a precursor favors

precipitation after some time, which couldn't be analyzed further. FeCl<sub>2</sub> over FeCl<sub>3</sub> not only facilitates crystallization but also maintains the required solution pH. FeCl<sub>3</sub> drastically decreases the pH to <4 from 6.6, whereas the pH decreases to 5.0 in FeCl<sub>2</sub>. The crystallization of **1-M** is slow and took approximately 15 days. Use of Fe<sup>3+</sup> instead of Fe<sup>2+</sup> results in fast precipitation rather than gradual crystallization.

Effect of TM at Internal Sandwich Position Interestingly, in [(TM)<sub>4</sub>(H<sub>2</sub>O)<sub>2</sub>(XW<sub>9</sub>O<sub>34</sub>)<sub>2</sub>]<sup>n-</sup>, TM = X = Mn/Fe/Ni/Cu are well known, but  $(TM = X = Co \text{ or } Zn) \text{ e.g.}, [Zn_4(H_2O)_2(ZnW_9O_{34})_2]^{n-1}$ and [Co<sub>4</sub>(H<sub>2</sub>O)<sub>2</sub>(CoW<sub>9</sub>O<sub>34</sub>)<sub>2</sub>]<sup>n</sup> are unknown. Instead of (TM)<sub>4</sub> core in Zn/Co, one W(+6) atom incorporation at the sandwich position [W(TM)<sub>3</sub>(H<sub>2</sub>O)<sub>2</sub>(XW<sub>9</sub>O<sub>34</sub>)<sub>2</sub>]<sup>n</sup> was always observed, which must be the cooperative effect/interplay between the transition metals at sandwich core and heteroatom.<sup>36-38</sup> From several sandwich POMs having 3d transition metals as the heteroatom, we observed that the X-Oµ4-TMi bond distances connected through Oµ4 are generally in between 3.87 and 4.0 Å, and the structures with X-O $\mu_4$ -TM<sub>i</sub> bond length >4.0 Å found to be distorted as observed in reported structures of Bi-POMs (Table 3A.S5). 39, 40 Further, DFT optimization of the auxiliary structure of [Zn<sub>4</sub>(H<sub>2</sub>O)<sub>2</sub>(ZnW<sub>9</sub>O<sub>34</sub>)<sub>2</sub>]<sup>16</sup> suggests that the X-Ou<sub>4</sub>-TM<sub>i</sub> distance of 4.03 Å with one of the Zn-O bond length (3.01 Å) elongation results in the distortion of the structure (Fig. 3A.S4). Moreover, it was observed that the introduction of W(VI) in the sandwich position of these POMs not only enhances the structural stability but also facilitates the substitution of TMs at the external sandwich position within these sandwich POMs. <sup>36, 41, 42</sup> Similarly, other higher oxidation state transition metals at the internal sandwich position also enhance the structural stability in these mixed metal TMSP. For example, Fe<sup>3+</sup>,  $Ru^{4+}$  substituted TMSP,  $[Co_2Fe_2(H_2O)_2(CoW_9O_{34})_2]^{14-}$  and  $[Zn_2Ru_2(H_2O)_2(ZnW_9O_{34})_2]^{12-}$ reported as highly stable under the strong oxidizing condition of OER.<sup>21, 43</sup> Given the good structural stability and TM substitution possibilities at the external sandwich position in Zn and Co-based TMSPs motivated us to exploit the potential impact of mixed TMs, particularly with those high oxidation state TM at the sandwich position. In this context, different transition metals such as V(IV), Cr(III), Mn(III), Fe(III), Y(III), Zr(IV) were tried for sandwich POMs with Zn/Co as heteroatom; out of which Mn(III) and Fe(III) show excellent stability when taken as mix metals precursors along with Zn/Co salts. Other TM either give insoluble precipitate or forms [Zn<sub>3</sub>W(H<sub>2</sub>O)<sub>2</sub>(ZnW<sub>9</sub>O<sub>34</sub>)<sub>2</sub>]<sup>12</sup>- in our condition (pH range 6-8). Four compounds with the general formula  $[(TM_e)_2(TM_i)_2(H_2O)_2(XW_9O_{34})_2]^{14}$  (where  $TM_i =$ Fe(III)/Mn(III),  $X = TM_e = Zn/Co$  were obtained in situ from the mixture of Zn/Co, Fe/Mn and W salts solution after microwave heating at 80 °C for 45 min at pH 7.8, which crystallized out

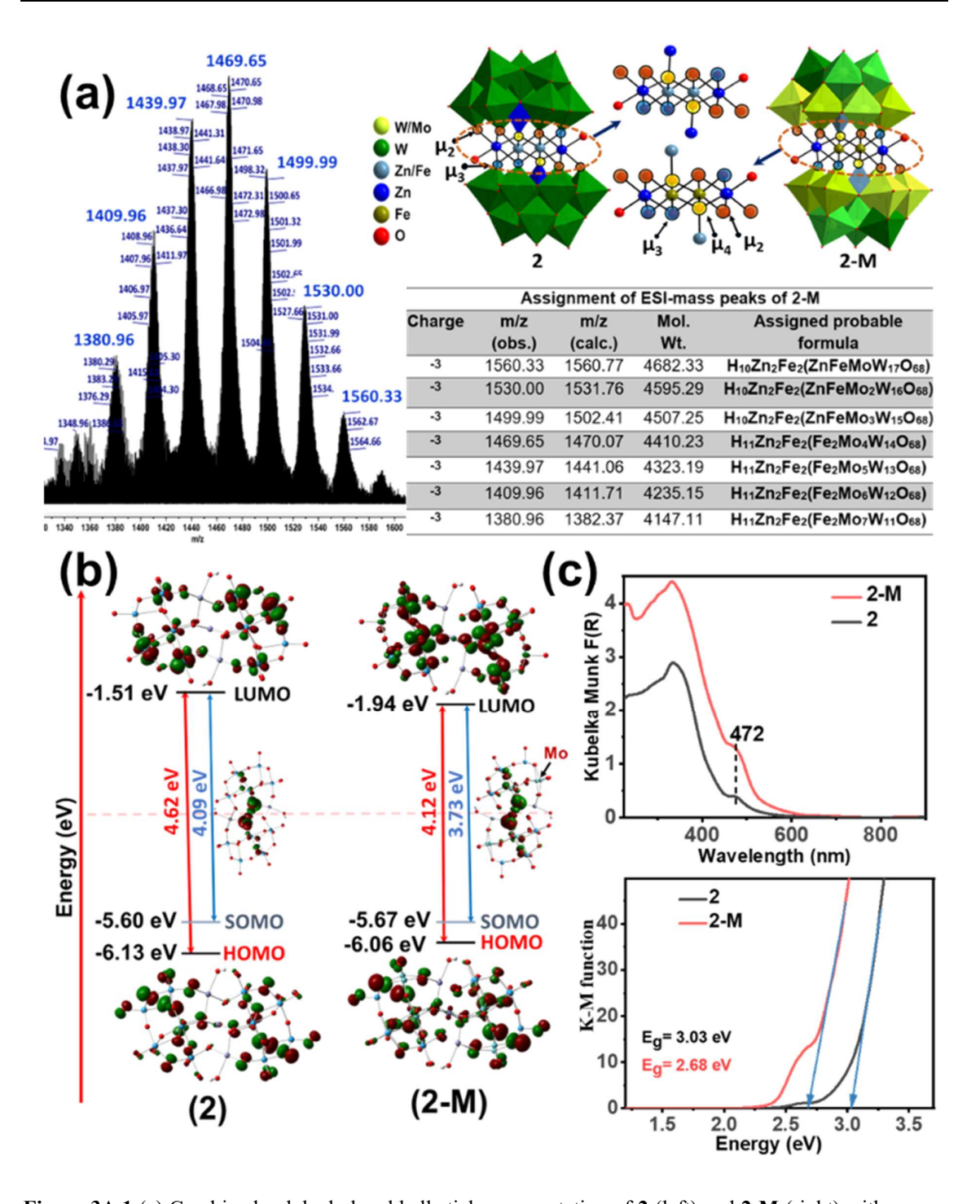


Figure 3A.1 (a) Combined polyhedral and ball-stick representation of 2 (left) and 2-M (right) with  $\mu_2$ ,  $\mu_3$ ,  $\mu_4$  oxygen atoms (counter cations and hydrogen atoms are omitted for clarity); ESI-MS envelope of peaks with assigned formula table for 2-M (Full spectra Fig. 3A.7, Table 3A.S7). (b) Frontier molecular orbitals from DFT optimized structure with theoretically calculated band gap and (c) solid-state UV-vis spectra and corresponding optical band-gap derived from the Kubelka-Munk (K-M) equation in 2 and 2-M.

in 2 h as monoclinic ( $P2_1/n$ ) lattice (Table 3A.S1, 3A.S2). Except  $\mathbf{3}^{21}$ , all these POMs are new and the obtained SC-XRD structures are:

```
Na_{14}[Fe_4(H_2O)_2(FeW_9O_{34})_2].22H_2O~(\textbf{1});\\ Na_{14}[(Zn_e)_2(Fe_i)_2(H_2O)_2(ZnW_9O_{34})_2].23H_2O~(\textbf{2});\\ Na_{14}[(Co_e)_2(Fe_i)_2(H_2O)_2(CoW_9O_{34})_2].15H_2O~(\textbf{3});\\ Na_{14}[(Zn_e)_2(Mn_i)_2(H_2O)_2(ZnW_9O_{34})_2].24H_2O~(\textbf{4});\\ Na_{14}[(Co_e)_2(Mn_i)_2(H_2O)_2(CoW_9O_{34})_2].22H_2O~(\textbf{5})\\ And their mixed addenda POMs are\\ Na_{14}[Fe_4(H_2O)_2(FeMo_xW_{9-x}O_{34})_2].20H_2O~(\textbf{1-M});\\ Na_{14}[Zn_2Fe_2(H_2O)_2(ZnMo_xW_{9-x}O_{34})_2].23H_2O~(\textbf{2-M});\\ Na_{14}[Co_2Fe_2(H_2O)_2(CoMo_xW_{9-x}O_{34})_2].19H_2O~(\textbf{3-M});\\ Na_{14}[(Zn_e)_2(Mn_i)_2(H_2O)_2(ZnMo_xW_{9-x}O_{34})_2].22H_2O~(\textbf{4-M});\\ Na_{14}[(Co_e)_2(Mn_i)_2(H_2O)_2(CoMo_xW_{9-x}O_{34})_2].19H_2O~(\textbf{5-M}),\\ Na_{14}[(Co_e)_2(Mn_i)_2(H_2O)_2(CoMo_xW_{9-x}O_{34})_2].20H_2O~(\textbf{5-M}),\\ Na_{14}[(Co_e)_2(Mn_i)_2(H_2O)_2(CoMo_xW_{9-x}O_{34})_2].
```

BVS calculation indicates all TM<sub>i</sub> in +3 and TM<sub>e</sub>/X is in +2 oxidation state with characteristics TM<sub>i</sub>-O bond lengths average found to be 2.04 Å. In case of 4/5, two TM<sub>i</sub>-O bond lengths found to be longer (2.30 Å) than average of other four TM<sub>i</sub>-O bond length (1.94 Å) due to z-out Jahn Teller distortions in 3d<sup>4</sup> {Mn(III)} configurations. The X-(O $\mu$ 4)-TM<sub>i</sub> bond distance was found to be 3.86-3.93 Å. These POMs were then characterized using FT-IR (W=O<sub>t</sub> at 900-930 cm<sup>-1</sup>, W-O<sub>c</sub>-W at 835-840 cm<sup>-1</sup>) and the ESI-MS confirms the fragments of H<sub>11</sub>[2] at m/z 1594 (z= -3), H<sub>11</sub>[3] at 1585 (z= -3), H<sub>11</sub>[4] at 1593 (z= -3), and H<sub>11</sub>[5] at 1584 (z= -3). From the SC-XRD of 2, it was observed that Fe also competes with Zn for the internal sandwich position (Zn:Fe = 1:1) but ESI-MS revealed that the dominant structure is with Fe at the internal sandwich position, where it gives only a single peak at m/z 1594. The FT-IR study of O<sub>2</sub>-activated 2/3, two peaks at 1149, 1203/1205 cm<sup>-1</sup> indicates dioxygen activation, which was further confirmed in Raman spectra (peaks at 722,1063 cm<sup>-1</sup>) (Figure 3A.8a, 3A.13b).

This cooperative mix-metal approach seems useful for the synthesis of mixed-metal sandwiched POMs, and we have extended it for the synthesis of mixed addenda with Zn/Co heteroatom. Using Fe<sup>3+</sup> along with Zn<sup>2+</sup>/Co<sup>2+</sup> as mixed transition metals resulting in the formation of mixed metal- mixed addenda sandwich POMs with the formula Na<sub>14</sub>[Zn<sub>2</sub>Fe<sub>2</sub>(H<sub>2</sub>O)<sub>2</sub>(ZnMo<sub>x</sub>W<sub>9-x</sub>O<sub>34</sub>)<sub>2</sub>].23H<sub>2</sub>O (2-M) and Na<sub>14</sub>[Co<sub>2</sub>Fe<sub>2</sub>(H<sub>2</sub>O)<sub>2</sub>(CoMo<sub>x</sub>W<sub>9-x</sub>O<sub>34</sub>)<sub>2</sub>].19H<sub>2</sub>O (3-M). The SC-XRD of 2-M (light yellow-colored) and 3-M (purple-colored) confirm the structures with space group  $P2_1/n$  (Fig. 3A.2). Distribution of the Mo addenda show preferential binding with  $\mu_2$  oxygen connected to substituted transition metals. The higher binding affinity of Mo to  $\mu_2$  oxygens with lower charge density compared to other oxygens ( $\mu_3$ 

and  $\mu_4$ ) can be attributed to its lower effective nuclear charge and higher  $\pi$ -acceptor ability compared to W. Shifts in characteristics FT-IR peaks indicate Mo incorporation in the POM framework (Fig. 3A.1, 3A.S13c).

Similar to 2, Fe competes with Zn at heteroatom position in 2-M. BVS indicates Fe<sub>i</sub> in +3, Zn<sub>e</sub> in +2, and Zn at heteroatom in +2 with a 0.5 discrepancies indicating the presence of Fe(+3) along with Zn in 2-M, which was further confirmed by ESI-MS (Table 3A.S7) and  $^{57}$ Fe

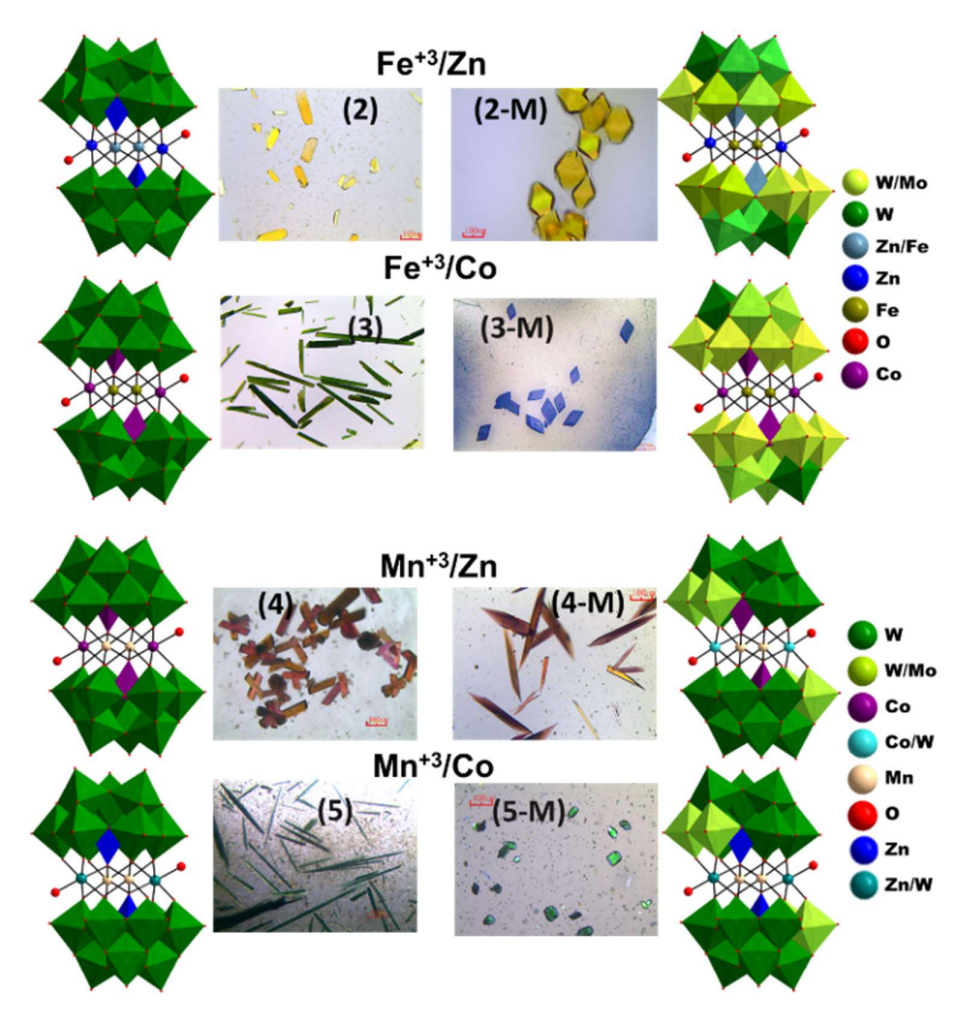


**Figure 3A.2** Combined polyhedral and ball-stick representation of SC-XRD structures and corresponding optical images of **2**, **2-M**, **3**, **3-M**, **4**, **4-M**, **5**, and **5-M**. (green-Pure W, yellowish green - varrying Mo/W ratios, counter cations and hydrogen atoms are omitted for clarity.

Mössbauer spectroscopy showing the presence of two types of Fe in the structure (two singlets) (Fig 3A.8d). In ESI-MS, the isotopic single envelope of peaks at m/z 1594 (z=-3) for 2 shifts to isotopic multiple envelopes of peaks ranging from m/z 1340-1565 (z=-3) for 2-M due to incorporation of Mo addenda atoms. Similarly, the isotopic single envelope of peaks at m/z 1585 (z=-3) for 3 shifts to isotopic multiple envelopes of peaks ranging from m/z 1320-1550

(z=-3) in **3-M**. The most abundant anion in **2-M** gave the composition of Mo:W(2:7) with the formula  $[Zn_2Fe_2(H_2O)_2(ZnFeMo_4W_{14}O_{34})]^{10}$ , while Mo:W ratio varies from 1:17 to 8:10 with constant -14 charge on the cluster. In 3-M, the most abundant anion has a Mo:W ratio of 5:13 with the formula  $[Co_2Fe_2(H_2O)_2(CoFeMo_5W_{13}O_{34})]^{10}$ , while the Mo:W ratio varies from 3:15 to 7:11 with -14 charge of the cluster (Fig. 3A.12).

We have also done the pH-dependent studies, which indicates that the Mo/W ratio increases for the most abundant peak by decreasing in the pH from 7.5 to 6.0 for **2-M** and **3-M**. However, a further decrease in pH results in the formation of the Keggin framework, indicating the crucial role of pH in obtaining maximum Mo incorporation in the framework (details, Fig. 3A.S5, 3A.S7). BVS indicates Fe<sub>i</sub> in +3, Co<sub>e</sub> in +2, and Co at the heteroatom in +2 with 0.5 discrepancies, supporting the presence of Fe(+3) along with Co<sup>2+</sup> in **3-M**, which was confirmed by XPS analysis, otherwise difficult to predict from SC-XRD and ESI-MS. The UV-visible spectra show the LMCT, d-d transition as well as a small intensity oxygen to Fe<sup>3+</sup> charge transfer peaks (at 473/480 nm) in **2/3** and **2-M/3-M**. The band gap calculated from the Kubelka Munk plot was found to be less in case of **2-M/3-M** when compared to **2/3** (e.g., 3.03 eV in **2** to 2.68 eV in **2-M**, Fig. 3A.1c). The DFT optimizations of mixed addenda TMSPs show that LUMO lies at Mo atoms rather than W (Fig. 3A.10, 3A.14), resulting in the reduction of the band gap, which is also observed from UV-vis spectra.

Using a similar approach, mix addenda were introduced in  $Mn^{3+}$  based sandwich POMs. SCXRD and ESI-MS confirms the molecular formula of  $Na_{14}[(Zn_e)_2(Mn_i)_2(H_2O)_2(ZnMo_xW_9_xO_{34})_2].22H_2O$  (4-M) and  $Na_{14}[(Co_e)_2(Mn_i)_2(H_2O)_2(CoMo_xW_{9-x}O_{34})_2].19H_2O$  (5-M), with only a little Mo addenda incorporation (highest Mo:W ratio obtained 2:16). SC-XRD reveals Mo at only two addenda positions connected with the transition metal at external sandwich position through  $\mu_2$  oxygen, (Fig. 3A.15c). Thus, when we go from 2 to 4 (3 to 5, Table 3A.2, 3A-3), optical band gap decreases, which was also observed from DFT study; indicating the significant effect of change in transition metal at the internal sandwich position. Also, going from 2-M to 4-M, it was observed that TM at the internal sandwich position impacts the Mo incorporation in the framework.

From the synthesis of these mixed-metal based W-only/mixed-addenda TMSPs, it was observed that two factors play a crucial role in the self-assembly (a) the charge density of trivacant lacunary part due to the heteroatom, (b) cooperative effects of transition metals (TMs) at the sandwich position. This cooperative effect is especially prominent in the TMSPs with higher charge density lacunary POMs with transition metal at heteroatom, which also allows

Mo addenda incorporation into these TMSPs. In terms of Mo incorporation in these TMSPs, the cooperative effect of mixed metals like Zn/Fe<sup>3+</sup> or Co/Fe<sup>3+</sup> were found to be superior.

The following few essential points are discussed as the synthetic strategy for these TMSPs: (1) TMs as heteroatom (Zn, Co) form high charge density trivacant lacunary POMs (e.g. ZnW<sub>9</sub>O<sub>34</sub>), while P-heteroatom forms relatively low charge density trivacant lacunary POMs (e.g. PW<sub>9</sub>O<sub>34</sub>) (Table 3A.1). (2) TMs as heteroatom in high charge density lacunary POMs preferentially bind with TMs of high oxidation state (e.g., W<sup>6+</sup>, Ru<sup>4+</sup>, Fe<sup>3+</sup>) at internal sandwich positions to form TMSPs. E.g. Zn as heteroatom (i.e. ZnW<sub>9</sub>O<sub>34</sub>) forms TMSPs with Fe<sup>3+</sup> in 3,

**Table 3A.2** Effect of Mo incorporation, charge density of lacunary POMs, position and oxidation states of TMs towards optical band gap, Mo/W Ratio. Optical Band gap from DRS (eV) Mo:W ratio **POMs** (Reference Code) Abundant Maximum Mo:W Mo:W A. Effect of changing transition metal at internal sandwich positions 2 vs 4 3.03 vs 2.31 3 vs 5 1.98 vs 1.37 2-M vs 4-M 2.68 vs 1.65 4:14 **→** 1:17 7:11 **→** 2:16 3-M vs 5-M 1.73 vs 1.29 5:13 → 1:17 7:11 **→** 2:16 B. Effect of changing heteroatom along with external sandwich positions (using same metal) 3.03 vs 1.98 2 vs 3 2.31 vs 1.37 4 vs 5 2.68 vs 1.73 **2-M** vs **3-M** 4:14 **→** 5:13 7:11 **→** 7:11 4-M vs 5-M 1.65 vs 1.29 1:17 → 1:17 2:16 **→** 2:16 C. Effect of Mo incorporation in framework 1 vs 1-M 2.24 vs 1.82 3:15 (1-M) 6:12 (**1-M**) 2 vs 2-M 3.03 vs 2.68 4:14 (2-M) 7:11 **(2-M)** 1.98 vs 1.73 3 vs 3-M 5:13 (**3-M**) 7:11 **(3-M)** 4 vs 4-M 1.84 vs 1.65 1:17 (**4-M**) 2:16 (**4-M**) 1.37 vs 1.29 5 vs 5-M 1:17 (**5-M**) 2:16 (**5-M**)

(3) In TM-heteroatom based TMSPs, TM at internal sandwich positions has a pronounced impact on Mo incorporation in the mixed addenda as compared to external sandwich position and heteroatom position. E.g. Fe<sup>3+</sup> favors more Mo incorporation in 2 than Mn<sup>3+</sup> in 4 at internal sandwich position. Following the synthesis of various mixed-metal, mixed-addenda TMSPs and theoretical analysis of these POMs using DFT, it is evident that orbital engineering and electronic bandgap align with the optical bandgap, as summarized in Table 3A.2. The data in Table 3A.2 indicate that modifying a transition metal at internal sandwich positions within these TMSPs or incorporating Mo addenda significantly impacts bandgap modulation, a trend also supported by theoretical calculations (Table 3A.3).

Table 3A.3	Table 3A.3 Effect of Mo incorporation, charge density of lacunary					
POMs, posit	POMs, positions and oxidation states of TMs towards electronic band					
gap, position	n of highest SOMC	and LUMC	(from DI	FT)		
POMs	Band gap (eV) Atom/group of LUMO position LMCT (O → atoms at which (eV)					
	W/Mo) / <b>MPCT</b> (SOMO → W/Mo)	Highest SOMO	LUMO			
A. Effect of o	changing transition	metal at into	ernal sand	wich position		
2 vs 4	4.62/4.09 vs 4.01/3.78	Fe <sup>3+</sup> vs O <sub>c</sub> ; Mn <sup>3+</sup>	$\begin{array}{ c c c }\hline W & vs \\ Mn^{3+} \end{array}$	-1.51 vs -2.09		
B. Effect of c	hange in heteroato sition	m along with	transition	metal at external		
2 vs 3	4.62/4.09 vs 4.70/3.64	Fe <sup>3+</sup> for both	W for both	-1.51 vs -1.58		
2-M vs 3-M	4.12/3.73 vs 4.32/3.29	Fe <sup>3+</sup> for both	Mo for both	-1.94 vs -1.95		
C. Effect of I	Mo incorporation:	W-only vs W	//Mo TMS	Ps		
2 vs 2-M	4.62/4.09 vs 4.12/3.73	Fe <sup>3+</sup> for both	W vs Mo	-1.51 vs -1.94		
3 vs 3-M	4.70/3.64 vs 4.32/3.29	Fe <sup>3+</sup> for both	W vs Mo	-1.58 vs -1.95		
4 vs 4-M	4.01/3.78 vs 3.97/3.36	$O_c+Mn^{3+};$ $O_c+Mn^{3+}$	W vs Mn	-2.09 vs -2.07		

Furthermore, a significant decrease in the bandgap was observed due to the combined effects of the heteroatom and the external sandwich position while moving from TMSP 2 to 3. Notably,

incorporation of Mo in mixed addenda POMs not only decreases the bandgap but also changes the LUMO position, e.g. the LUMO, which is located at W in TMSP 2, shifts entirely to Mo in 2-M. While both factors reduce the bandgap, the internal sandwich position (Fe to Mn) has a more pronounced impact on lowering the bandgap and providing a lower-lying LUMO compared to Mo incorporation, as supported by theoretical calculations (Table 3A.3). The heteroatom effect is most pronounced with Co as the heteroatom, while the other position has comparatively less impact on the bandgap.

Following the trends of decrease in band gap, TMSPs with Co as heteroatom, Mn at the internal sandwich position along with mixed addenda reveal the lowest band gap, which was indeed experimentally observed in **5-M** (1.29 eV) among all the reported TMSPs here due to the combined effect of with Co, Mn<sup>3+</sup>, and W/Mo.

Similarly, **3-M** shows a lower bandgap with Co as heteroatom but higher than **5-M** due to Fe instead of Mn at the sandwich position. Although the optical band gap is slightly lowered (by 0.2 eV) in **4-M** compared to **4**, the DFT shows that the LUMO of **4-M** remains entirely on Mn for both **4** and **4-M**, thereby minimising the effect of Mo incorporation (bandgap of -2.09 vs - 2.07 eV from DFT).

## 3A.2.2 Structural Description

## 3A.2.2a Structural Description and Characterizations of 1 and 1-M.

Compounds 1 and 1-M were characterized using SC-XRD, FT-IR, ESI-MS, and UV-vis spectroscopy (Figure 3A.3-3A.5). The structure was confirmed by SC-XRD (CCDC 2330248, 2330238). The light yellow colored crystals (Figure 3A.3a) of 1 crystallize in monoclinic with  $P2_1/n$  space group, while 1-M crystallize in triclinic with space group  $P\overline{1}$  (Table 3A.S1). BVS calculation indicates that all addenda atoms are in their +6 oxidation state and Fe in +3 oxidation states in 1-M while BVS in the case of 1 indicates that Fe in +2 oxidation state at external sandwich position while Fe at internal sandwich position and heteroatom position in +3 oxidation states (Table 3A.S4) which was further confirmed from XPS analysis. The XP spectra of 1 revealed the presence of W, Fe, and oxygen (Figures 3A.S1), while 1-M revealed the presence of W, Fe, Mo and oxygen (Figure 3A.S2). Two peaks at 710.3 and 724.3 eV in 1-M can be attributed to the presence of Fe in a +3 oxidation state, while 1 give one additional peak at lower side apart from these two peaks, indicating the presence of Fe in +2 oxidation state. The W 4f doublet appears between 33-37 eV, corresponding to W  $4f_{7/2}$  and  $4f_{5/2}$  in both 1/1-M. The shift to higher values in 1-M compared to 1 can be attributed to strong anion-anion interaction in 1-M due to the less overall negative charge and also due to the presence of Mo

in the framework. From the comparison of [ $\{Fe_4(H_2O)_2(FeMo_xW_{9-x})_2\}^{3-}$ ], with the reference structure (Figure 3A.3c), it is clear that Mo incorporation is favorable at 4/5/9 positions of the belt, which are connected to transition metals in the sandwich position through  $\mu_2$  oxygens followed by positions 6 and 8. The other positions in the belt as

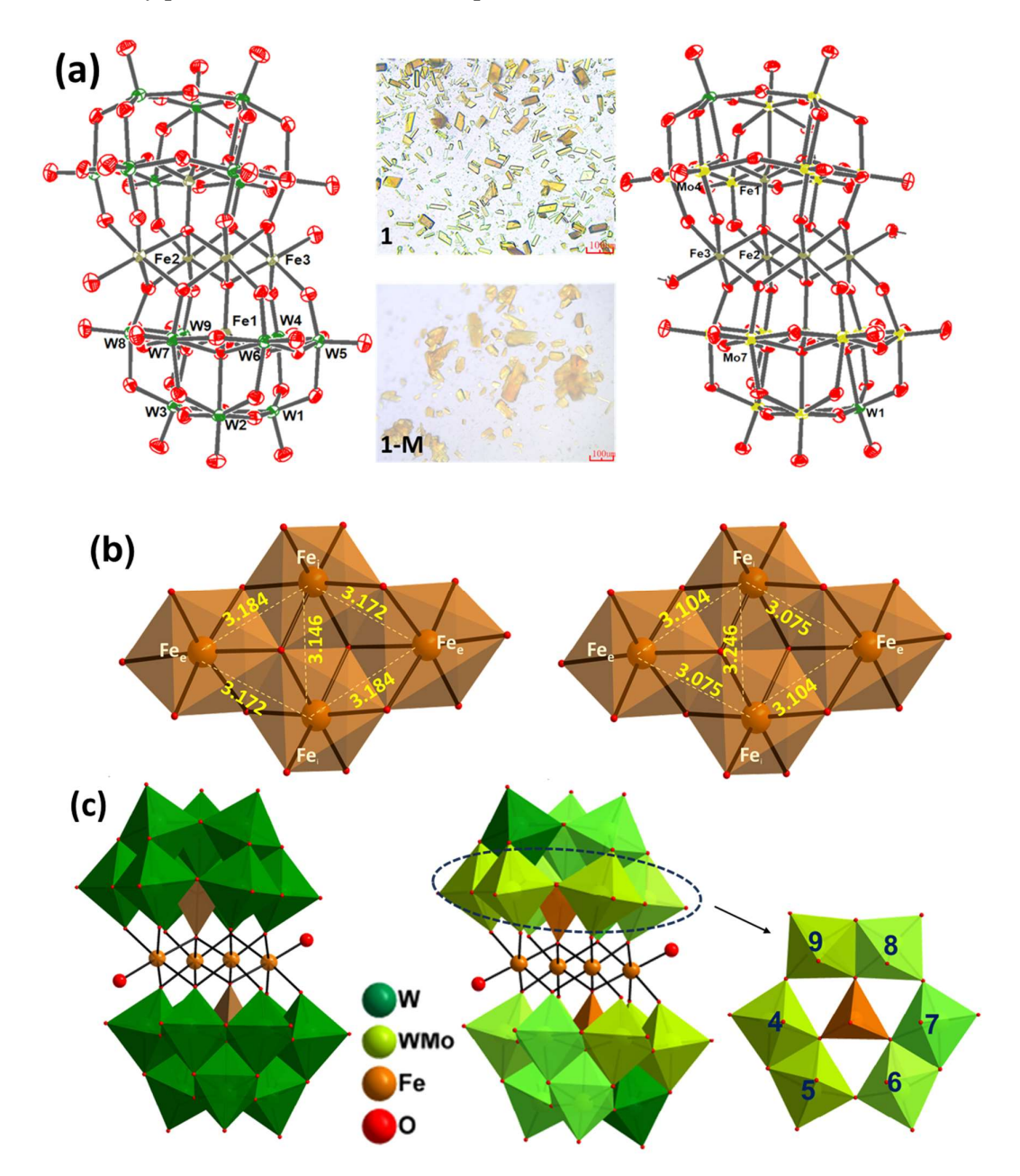


**Figure 3A.3** (a) ORTEP drawing (with 60% ellipsoid probability) and Optical images of sandwich POMs; **1** (left) and **1-M** (right); (b) Cubane core showing the interatomic distances between TMs in **1** (left) and **1-M** (right); (c) combined polyhedral/ball and stick representation **1** (left) and **1-M** (right), belt 2 depicting different Mo to W ratios in **1-M**; (Countercations and hydrogen atoms are omitted for clarity).

well as in the cap are comparatively less favorable for Mo incorporation. The distance between Fe atoms in the internal and external positions is 3.18 Å, while it is 3.14 Å between two internal Fe atoms in 1, however, in 1-M the distance between Fe atoms in the internal and external positions is 3.10 Å, while it is 3.24 Å between two internal Fe atoms.

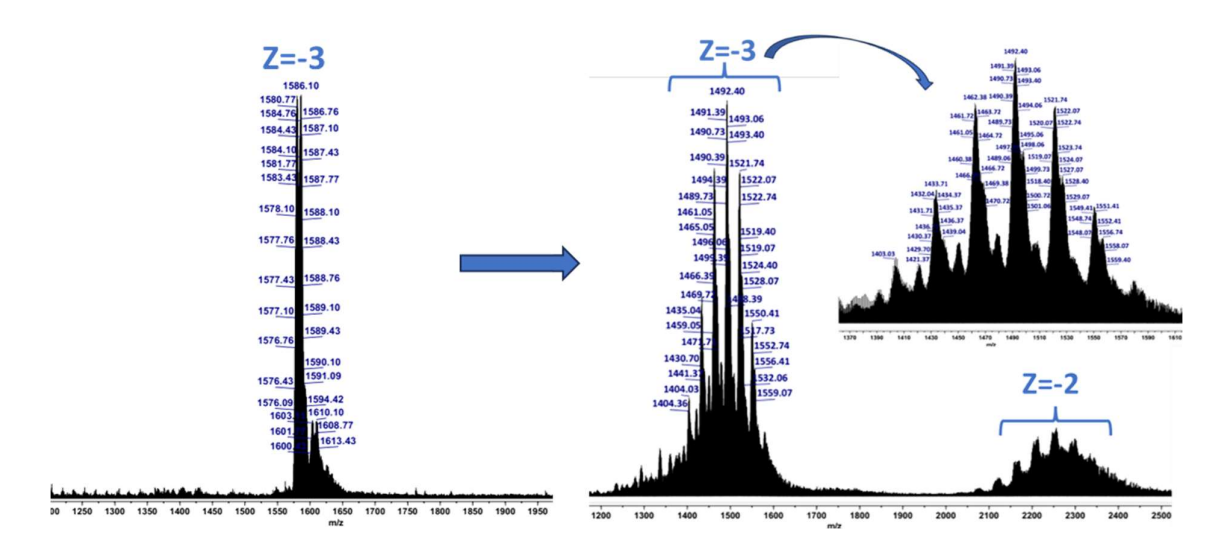


Figure 3A.4 ESI-MS spectra of 1/1-M in the range of m/z 1200-2500 for different z values.

ESI-mass spectrum of **1** (Figure 3A.4, Table 3A.S3) shows the envelope of peaks at m/z 1580.33 (z=-3), while the analog mixed addenda POM shows the isotopic multiple envelopes of peaks attributed to varying ratios of Mo to W. The mixed addenda sandwich POM **1-M** show the envelopes of peaks in the range of m/z 1390-1550 for [{Fe<sub>4</sub>(H<sub>2</sub>O)<sub>2</sub>(FeMo<sub>x</sub>W<sub>9-x</sub>)<sub>2</sub>}<sup>3-</sup>], and m/z 2100-2400 for [{Fe<sub>4</sub>(H<sub>2</sub>O)<sub>2</sub>(FeMo<sub>x</sub>W<sub>9-x</sub>)<sub>2</sub>}<sup>2-</sup>]. The most abundant anion in **1-M** has the composition of Mo/W (3:15) with the formula [{Fe<sub>4</sub>(H<sub>2</sub>O)<sub>2</sub>(FeMo<sub>1.5</sub>W<sub>7.5</sub>O<sub>34</sub>)<sub>2</sub>}<sup>10-</sup>], while the Mo/W ratio varies from 1:17 to 5:13 with a constant charge of the cluster, i.e., -10. Comparing the stretching frequencies of tetrasubstituted mixed addenda sandwich POMs with corresponding W-only sandwich POMs, there is a subtle variation in the characteristic peaks (Figure 3A.5a) depending upon the number of Mo atoms incorporated in the framework structure. The FT-IR spectra of **1** show the peaks in the region 650-950 cm<sup>-1</sup> with characteristics peaks at 931 cm<sup>-1</sup> (W=O<sub>term</sub>), 839, 661 cm<sup>-1</sup> (W-O-W) cm<sup>-1</sup>. The FT-IR spectra of **1-M** show characteristic peaks similar to **1** in the region 650-950 cm<sup>-1</sup> with slight shifting due to Mo incorporation in the framework. The M=O<sub>term</sub> characteristics peaks shift to 911 cm<sup>-1</sup> while the M-O-M (M=Mo/W) peak shifts to 832 and 678 cm<sup>-1</sup>, respectively.

Both 1 and 1-M exhibit broad absorption bands in the UV region due to ligand to metal charge transfer (LMCT) (O2p  $\rightarrow$  W5d) while in visible region due to d-d transitions. Moreover,

a significant contribution of Mo is evident in 1-M through a red shift in the UV-vis spectra compared to that of 1 (Figure 3A.5c). This red shift can be explained by the changes in the band gap of these POMs, which were investigated using DRS. It was observed that the band

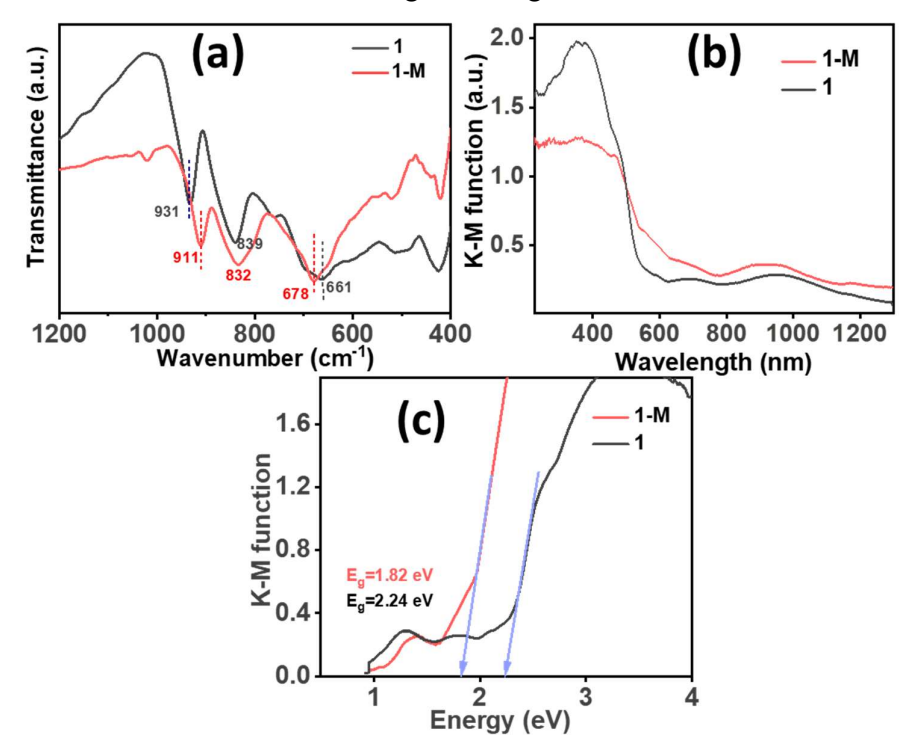


Figure 3A.5 (a) FT-IR, and (b) solid-state UV-vis. spectra and (c) optical band-gap shifting derived from the Kubelka-Munk equation in 1 and 1-M.

gap reduced to 1.82 eV (1-M) from 2.24 eV (1). These results were further supported by the DFT study, where the electron density in LUMO shifts to Mo in 1-M (representative 1-M formula is taken as Fe<sub>4</sub>(H<sub>2</sub>O)<sub>2</sub>(FeMo<sub>4</sub>W<sub>5</sub>)<sub>2</sub>}<sup>10-</sup>) while in case of 1 (Figure 3A.S3) the electron density lies at W. It was observed that optimization was not feasible with an overall charge of -14/-16 in 1-M which also supports our experimental findings where it was found that all Fe is in a +3 oxidation state leading to an overall charge of -10. Further, charge -16 in 1 leads to elongation of Fe-O(H<sub>2</sub>O) (discussed later). Thus overall charge as well as the nature of addenda/substituted TM at the sandwich position play crucial roles in defining the redox characteristics of these POMs.

#### 3A.2.2b Structural Description and Characterizations of 2 and 2-M.

Compounds 2 and 2-M were characterized using SC-XRD, FT-IR, ESI-MS, and UV-visible spectroscopy (Figure 3A.6-3A.10). The framework structure was confirmed by SC-XRD (CCDC 2330240 and 2330247). The light yellow colored crystals of 2 and 2-M crystallize in monoclinic with P2<sub>1</sub>/n space group (Table 3A.S1). BVS calculation indicates that all addenda

atoms are in their highest oxidation state (+6) and Zn, Fe in +2 and +3 oxidation states respectively (Table 3A.S6). The 3D SC-XRD structure of **2** and **2-M** shows that the tri-lacunary Keggin moiety contains a tetrahedrally bound zinc atom in the center as a templating agent to triads of addenda W/Mo atoms. The tetrasubstituted sandwich core consists of Fe at the internal  $\{TM_i\}$  position and Zn as external atoms  $\{TM_e\}$  (Fig. 3A.6b).

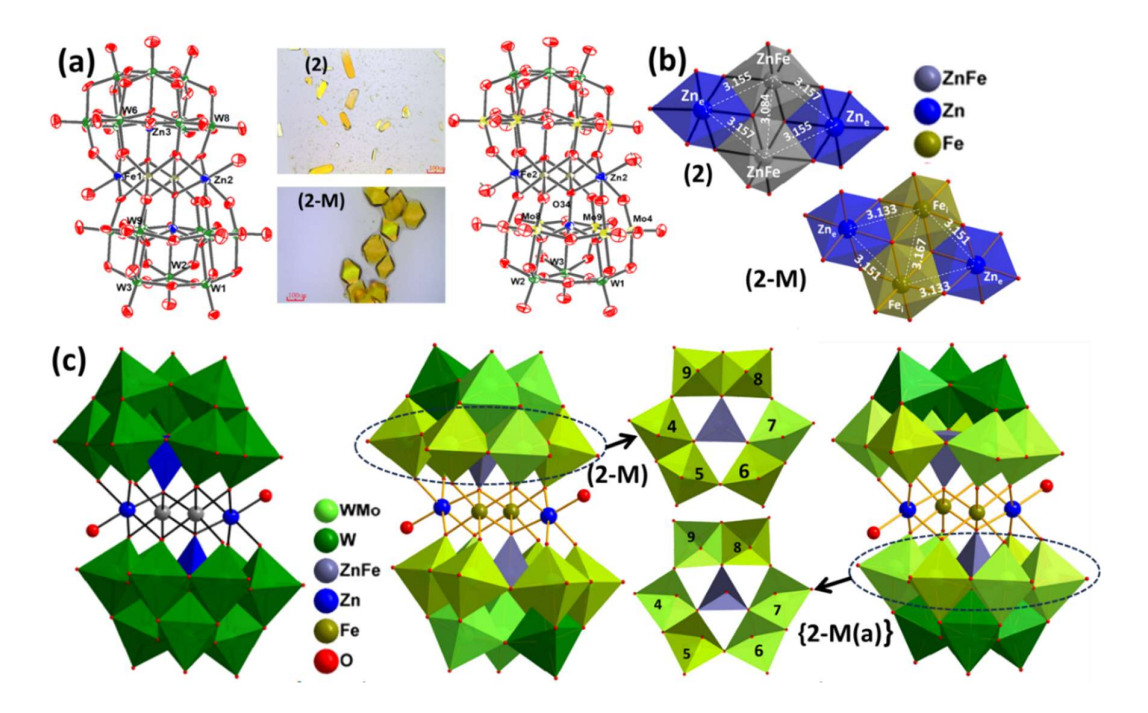


Figure 3A.6 (a) ORTEP drawing (with 60% ellipsoid probability) and Optical images of sandwich POMs; 2 (left) and 2-M (right); (b) Cubane core showing the interatomic distance between transition metals in 2 (left) and 2-M (right); (c) combined polyhedral/ball and stick representation of the single-crystal X-ray structure of polyoxometalate 2(left) and 2-M/2-M(a) (right), belt 2 depicting different ratios of molybdenum to tungsten in 2-M/2-M(a); Countercations and hydrogen atoms are omitted for clarity.

From the comparison of  $[{Zn_2Fe_2(H_2O)_2(ZnFeMo_xW_{9-x})_2}^{14-}]$ , with the reference structure (Figure 1.10), it is clear that Mo incorporation is favorable at the entire belt position, most favorable at 4/5 which are connected to transition metals in the sandwich position through  $\mu_2$  oxygens (Figure 3A.6c). The other positions in the cap are comparatively less favorable for Mo incorporation. The distance between Zn atoms at the external and Zn/Fe at the internal positions is 3.15 Å in 2/2-M, however, the distance between Zn/Fe atoms in the internal positions is 3.08 Å in 2 and 3.16 Å in 2-M. It was observed that at a particular pH, analyzing different crystals from the same mother liquor indicates the different ratio of Mo to W (Figure 3A.6c) as observed in 2-M(a) (CCDC 2330252) which was further confirmed from ESI-MS. The ESI-mass spectrum of 2 in (Figure 3A.7, Table 3A.S7) shows the envelope of peaks at m/z 1593 (z=-3)

while the analog mixed addenda POMs (2-M) structure shows the isotopic multiple envelopes of peaks attributed to varying ratios of Mo to W.

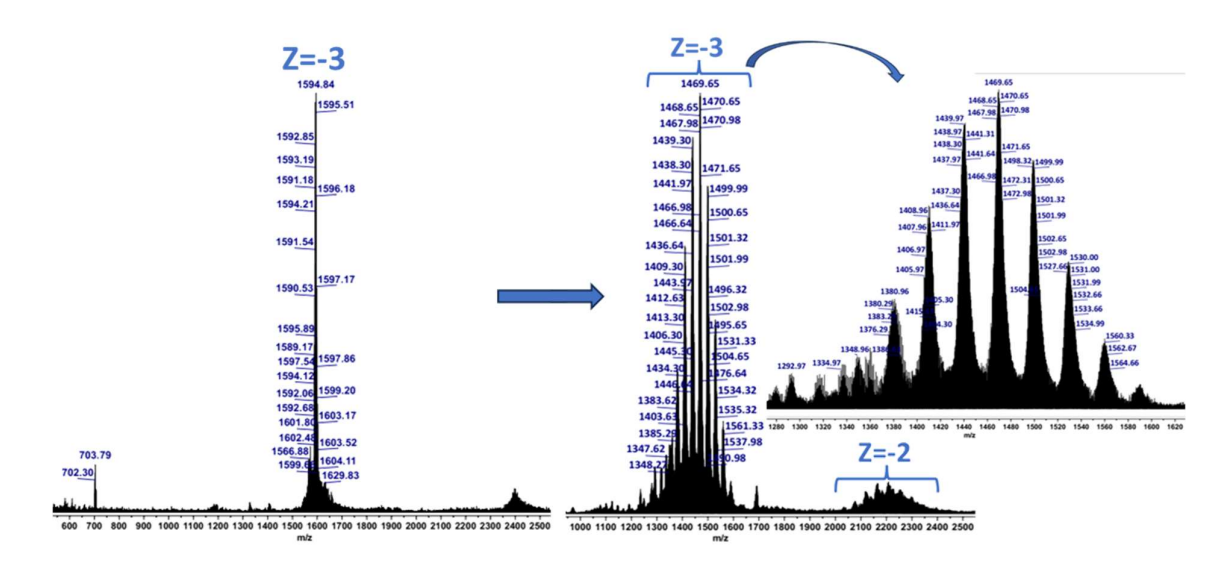
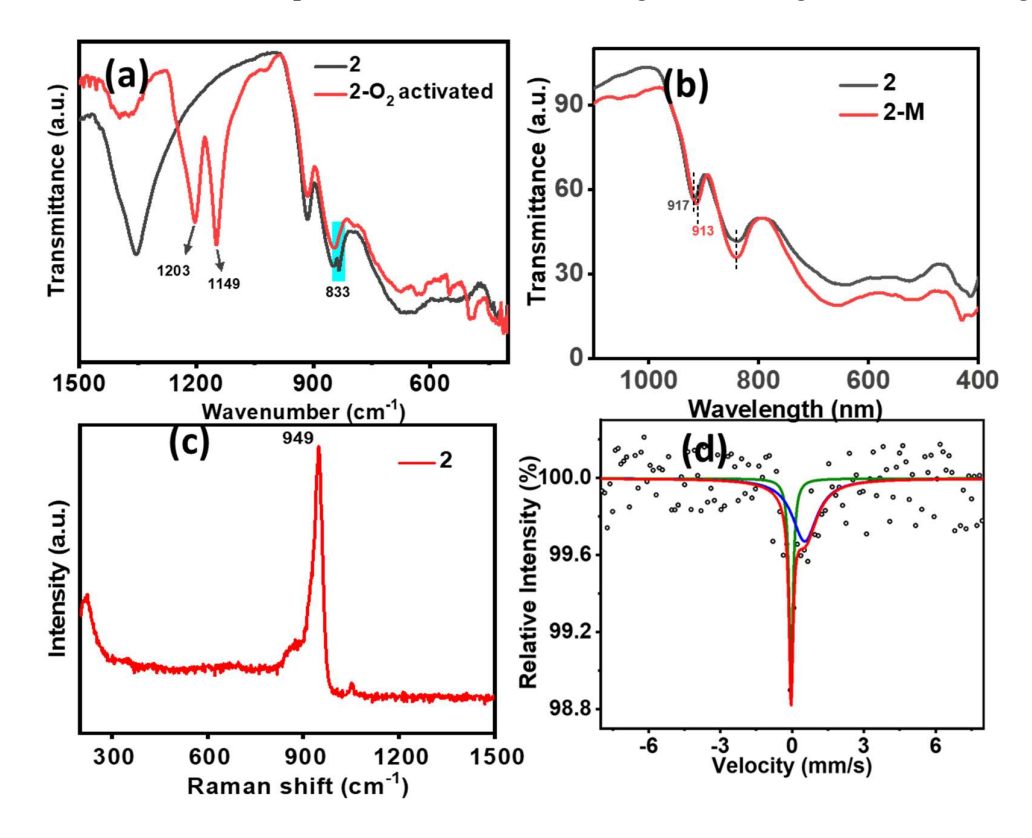


Figure 3A.7 ESI-MS spectra of 2 (left)/2-M (right) in the range of m/z 1000-2500 for different z values.

**2-M** show the envelopes of peaks (Figure 3A.7, Table 3A.S7) in the range of *m/z* 1380-1560 for [H{Zn<sub>2</sub>Fe<sub>2</sub>(H<sub>2</sub>O)<sub>2</sub>(ZnFeMo<sub>x</sub>W<sub>9-x</sub>)<sub>2</sub>}<sup>3-</sup>], and *m/z* 2100-2400 for [{Zn<sub>2</sub>Fe<sub>2</sub>(H<sub>2</sub>O)<sub>2</sub>(ZnFeMo<sub>x</sub>W<sub>9-x</sub>)<sub>2</sub>}<sup>2-</sup>]. The most abundant anion in **2-M** has the composition of Mo/W (2:7) with the formula [{Zn<sub>2</sub>Fe<sub>2</sub>(H<sub>2</sub>O)<sub>2</sub>(FeMo<sub>2</sub>W<sub>7</sub>O<sub>34</sub>)<sub>2</sub>}<sup>14-</sup>], while the Mo/W ratio varies from 1:17 to 7:11 with a constant charge of the cluster, i.e., -14. Further, in tuning the amount of Mo addenda incorporation, pH plays a crucial role. Hence, to understand the controlling of the Mo/W ratio in the sandwich framework of **2-M**, an ESI-MS-based systematic study was performed by varying pH. From ESI-MS, it was found that for the most abundant peak, the Mo/W ratio increases by decreasing the pH from 7.5 to 6.0; however, a further decrease in the pH results in the formation of the Keggin framework (Figure 3A.S5, Table 3A.S8).

Comparing the stretching frequencies of tetrasubstituted mixed addenda sandwich POMs with corresponding tungstate-only sandwich POMs, there is a subtle variation in the characteristic peaks. The FT-IR/Raman spectra of **2** show the characteristics peaks in the region 650-920 cm<sup>-1</sup> with characteristics peaks at 917 cm<sup>-1</sup> (W=O<sub>term</sub>), 835, 657 cm<sup>-1</sup> (W-O-W) cm<sup>-1</sup> (Figure 3A.1c). The FT-IR spectra of **2-M** show characteristics peaks similar to **2** in the region 650-920 cm<sup>-1</sup> with slight shifting due to Mo incorporation in the framework. The M=O<sub>term</sub> charcateristics peaks shifts to 913 cm<sup>-1</sup> while M-O-M (M=Mo/W) peak shifts is negligible. From the FT-IR study of O<sub>2</sub>-activated **2**, two peaks at 1149, 1203 cm<sup>-1</sup> along with 833 cm<sup>-1</sup>

have been observed, indicating dioxygen activation using these POMs (Figure 3A.8a). Both 2 and 2-M exhibit broad absorption bands in the UV-vis region due to ligand to metal charge



**Figure 3A.8** (a) FT-IR spectra of **2** before and after O<sub>2</sub> treatment in toluene; (b) FT-IR of **2** and **2-M**; (c) Raman spectra of **2**; (d) <sup>57</sup>Fe Mössbauer spectrum of **2-M**.

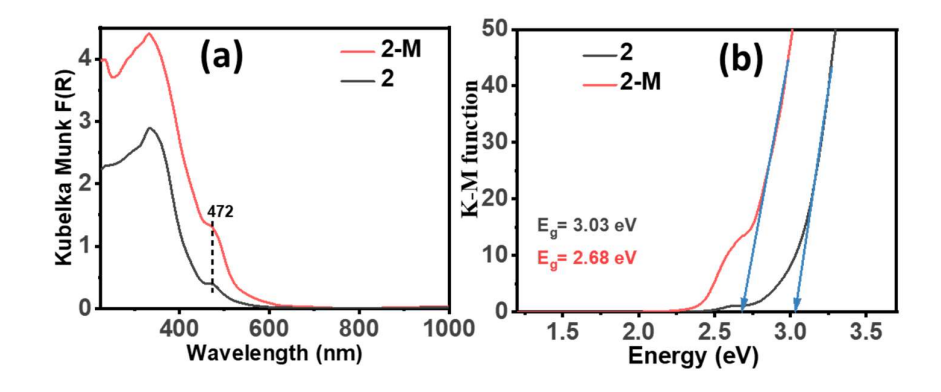


**Figure 3A.9** (a) solid-state UV-vis spectra and (b) optical band-gap shifting derived from the Kubelka-Munk equation in **2** and **2-M**.

transfer (LMCT) ( $O_{2p} \rightarrow W_{5d}$ ) and a feeble peak is observed for transition metal to POM charge transfer at 472 nm (TM  $\rightarrow$  W<sub>5d</sub>) indicating Metal to metal charge transfer (MMCT). Moreover, a significant contribution of Mo is evident in mixed addenda sandwich POMs through a red

shift in the UV-vis spectra compared to that of W-based sandwich POMs (Figure 3A.8b). This red shift can be explained by the changes in the band gap of these POMs, which were investigated using DRS.

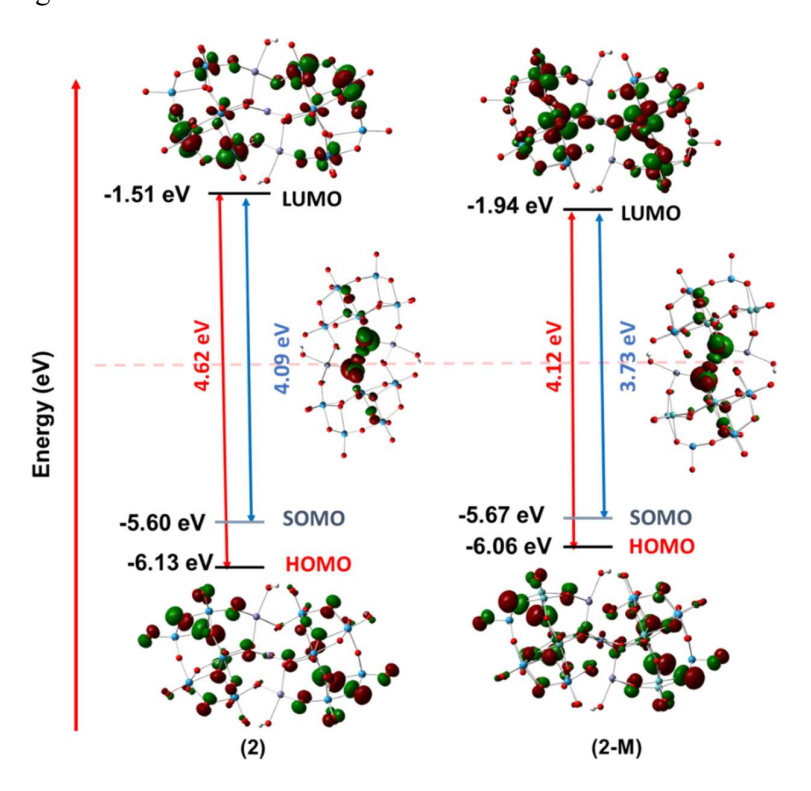


**Figure 3A.10** Frontier molecular orbitals of tetrasubstituted sandwich POMs showing the effect of Mo doping on band gaps as well as shifting of electron density on addenda atoms in 2 and 2-M.

These results were further supported with DFT study, where the HOMO-LUMO band gap in 2-M (representative structure of 2-M is taken with the formula [Zn<sub>2</sub>Fe<sub>2</sub>(H<sub>2</sub>O)<sub>2</sub>(ZnMo<sub>4</sub>W<sub>5</sub>)<sub>2</sub>]<sup>14-</sup> falls lower than that of 2 (Figure 3A.10). The LUMO energy as well as the band gap energy (HOMO-LUMO) drop as going from 2 to 2-M, which also correlates well with UV-visible spectroscopy. The band positions and overall charge on the POM play crucial roles in defining their redox characteristics e.g. 2-M is easy to reduce and a powerful oxidizing agent compared to 2. While the overall charge is constant in all of these sandwich POMs, the relatively lower LUMO energy in mixed addenda POMs correlates well with the higher electron affinity compared to their corresponding W-analogues. To identify the most suitable position for Mo substitution, one Mo-substituted at each addenda position in the mixed addenda sandwich POM was investigated using DFT study in our previous report<sup>14</sup> where it was observed that it is the μ<sub>2</sub> oxygen which dissipates lowest energy in Mo incorporation in the framework of these POMs.

#### 3A.2.2c Structural Description and Characterizations of 3 and 3-M.

Compounds **3** and **3-M** were characterized using SC-XRD, FT-IR, ESI-MS, XPS, and UV-visible spectroscopy (Figure 3A.11-3A.14). The framework structure was confirmed by SC-XRD (CCDC 2330239, 2330253) (Table 3A.S1). The needle-shaped green-colored crystals (Figure 3A.11a) of **3** and dark purple-colored crystals of **3-M** crystallize in monoclinic with P2<sub>1</sub>/n space group.

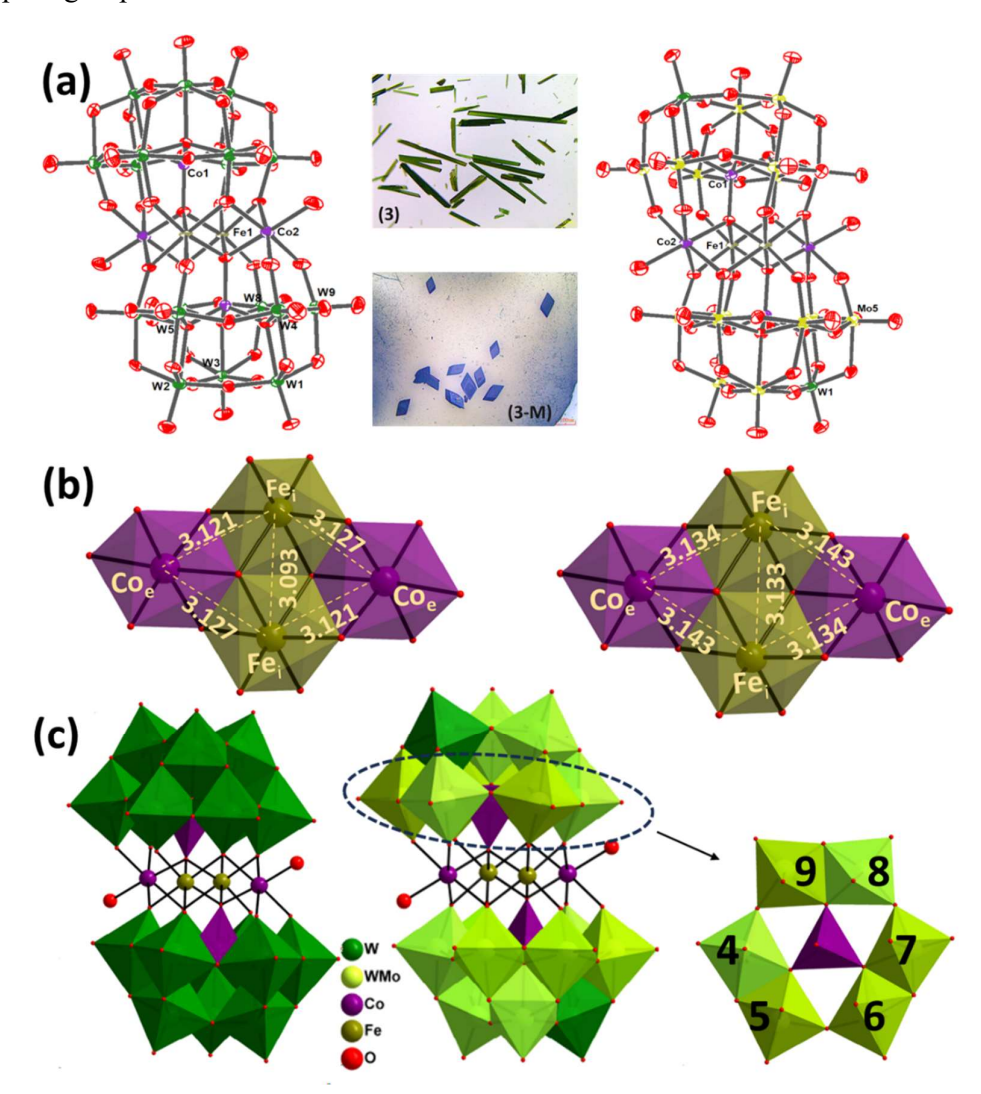
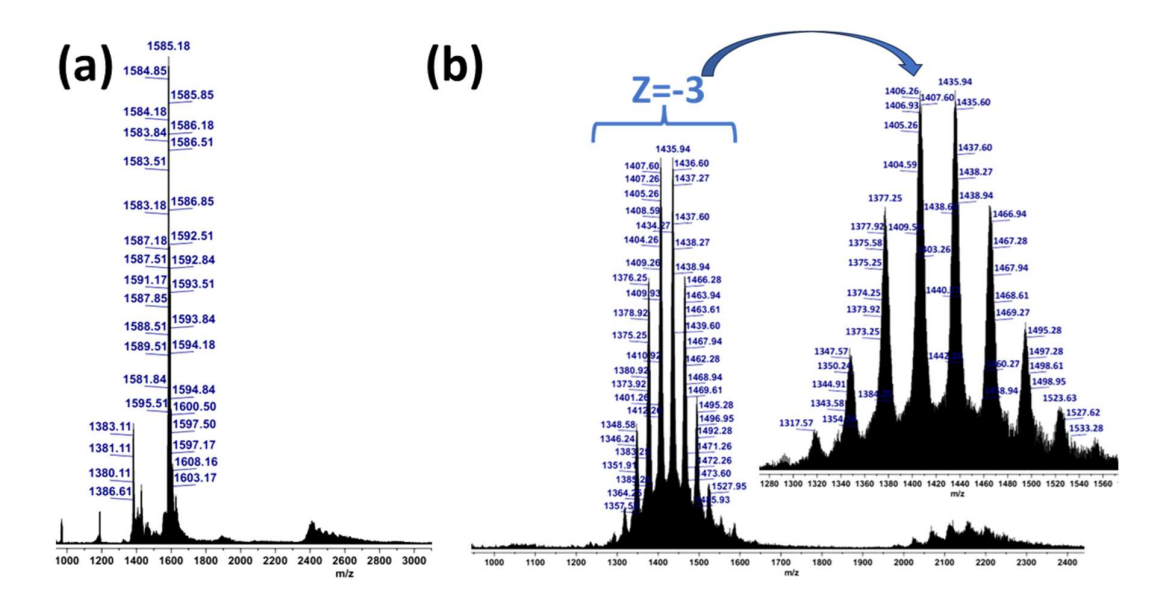


Figure 3A.11 (a) ORTEP drawing (with 60% ellipsoid probability) and Optical images of sandwich POMs 3 (left) and 3-M (right); (b) Cubane core showing the interatomic distance between TMs in 3 (left) and 3-M (right); (c) combined polyhedral/ball and stick representation of 3 (left) and 3-M (right), belt 2 depicting different ratios of molybdenum to tungsten in 3-M; (Countercations and hydrogen atoms are omitted for clarity).

The 3D SC-XRD structure of 3 and 3-M shows that the trilacunary Keggin moiety contains a tetrahedrally bound cobalt/iron atom in the center as a templating agent to triads of addenda W/Mo atoms (Figure 3A.11c). The tetrasubstituted sandwich core consists of Fe at the internal  $\{TM_i\}$  position and Co as external atoms  $\{TM_e\}$ . From the comparison of **3-M** with the reference structure (Figure 3A.11c), it is clear that Mo incorporation is favorable at all the belt positions. Except for position 1, other positions in the cap are comparatively more favorable for Mo incorporation than 1-M and 2-M. The distance between Co atoms at the external and Fe at the internal positions is 3.12-3.15 Å in 3/3-M, however, the distance between Zn/Fe atoms in the internal positions is 3.09 Å in 3 and 3.13 Å in 3-M (Figure 3A.11b). BVS calculation indicates that all addenda atoms are in their highest oxidation state (+6) and Co, Fe in +2 and +3 oxidation states respectively (Table 3A.S9). Apart from the BVS, the oxidation states of all of the atoms in 3 were determined from XPS analysis. The XP spectra of 3 revealed the presence of tungsten (W), iron (Fe), cobalt (Co), and oxygen. The two peaks at 713.2 and 723.5 eV in 3 can be attributed to the presence of Fe in a +3 oxidation state. The W 4f doublet appears between 36.2 and 38.4 eV, corresponding to W  $4f_{7/2}$  and  $4f_{5/2}$  in 3-M respectively (Figure 3A.S6).



**Figure 3A.12** ESI-MS spectra of (a) **3** (left) and (b) **3-M** (right) in the range of m/z 1000-2500 for different z values.

ESI-mass spectrum of **3** in (Figure 3A.12a, Table 3A.S10) shows the envelope of peaks at m/z 1585 (z=-3) while the analog mixed addenda POMs structure shows the isotopic multiple envelopes of peaks attributed to varying ratios of Mo to W. The mixed addenda sandwich

POMs 3-M show the envelopes of peaks (Figure 3A.12b, Table 3A.S10) in the range of m/z $[\{Co_2Fe_2(H_2O)_2(CoMo_xW_{9-x})_2\}^{3-}],$ 1300-1530 for and m/z2050-2300 for  $[\{Co_2Fe_2(H_2O)_2(CoMo_xW_{9\text{-}x})_2\}^{2\text{-}}].$  The most abundant anion in 3-M has the composition of Mo/W (5:13) with the formula  $[{Co_2Fe_2(H_2O)_2(CoMo_{2.5}W_{6.5}O_{34})_2}^{14-}]$ , while the Mo/W ratio varies from 1:5 to 7:11 with a constant charge of the cluster, i.e., -14. Further, in tuning the amount of Mo addenda incorporation, pH plays a crucial role. Hence, to understand the controlling of the Mo/W ratio in the sandwich framework of 3-M, an ESI-MS-based systematic study was performed by varying pH (Figure 3A.S7, Table 3A.S11). From ESI-MS, it was found that for the most abundant peak, the Mo/W ratio increases by decreasing the pH from 7.5 to 6.5; however, a further decrease in the pH results in the formation of the Keggin framework along with the sandwich POM.

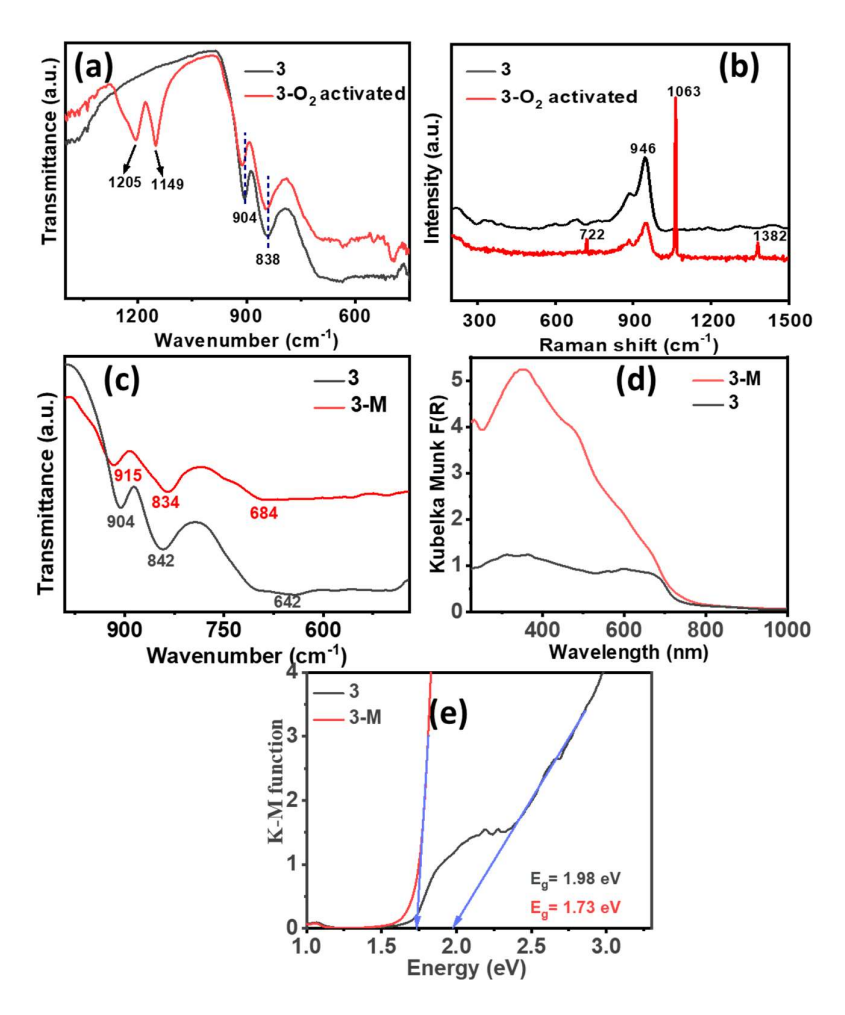


**Figure 3A.13** (a) FT-IR and (b) Raman spectra of **3** before and after O<sub>2</sub> treatment; (c) FT-IR and (d) solid-state UV-vis spectra of **3** and **3-M** (e) corresponding optical band-gap derived from the Kubelka-Munk equation in **3** and **3-M**.

From the FT-IR study of O<sub>2</sub>-activated **3**, two peaks at 1149, 1205 cm<sup>-1</sup> have been observed, indicating the formation of O<sub>2</sub> activation using these POMs (Figure 3A.13a). This was further supported in Raman spectra where peaks at 722, 1063 cm<sup>-1</sup> have been observed in the O<sub>2</sub> activated **3** (Figure 3A.13b). Comparing the stretching frequencies of **3-M** with **3**, there is a subtle variation in the characteristic peaks. The FT-IR spectra of **3** show the characteristics peaks in the region 650-920 cm<sup>-1</sup> with characteristics peaks at 904 cm<sup>-1</sup> (W=O<sub>term</sub>), 842, 642 cm<sup>-1</sup> (W-O-W) cm<sup>-1</sup> (Figure 3A.13c). The FT-IR spectra of **3-M** show characteristic peaks similar to **3** in the region 650-920 cm<sup>-1</sup> with slight shifting due to Mo incorporation in the framework. The M=O<sub>term</sub> characteristics peaks shift to 915 cm<sup>-1</sup> while M-O-M (M=Mo/W) peak shifts to 834, 684 in **3-M** (Figure 3A.13c) after Mo incorporation in the framework structure.

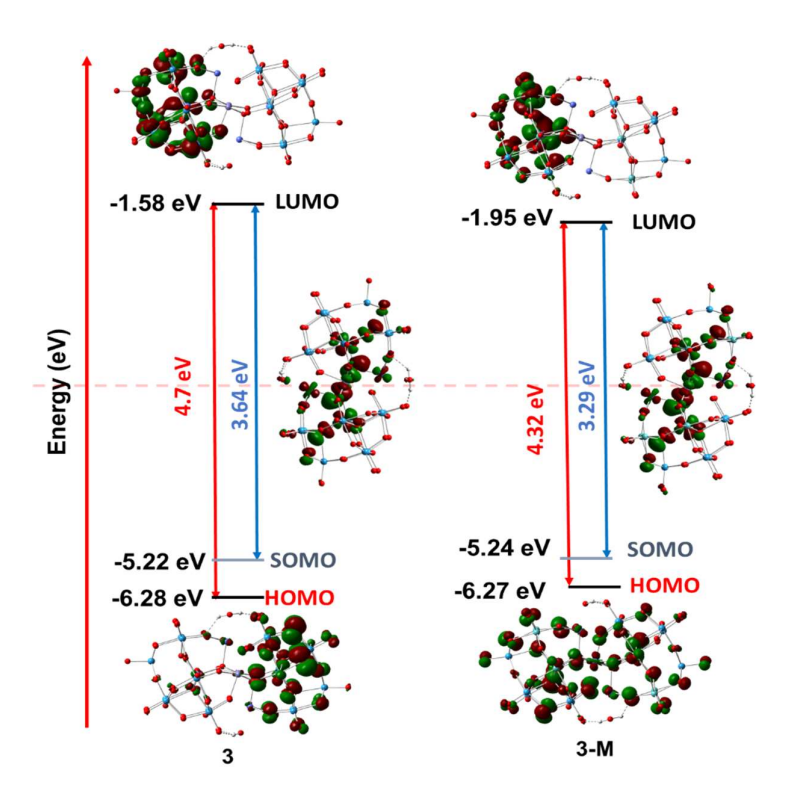


**Figure 3A.14** Frontier molecular orbitals of tetrasubstituted sandwich POMs showing the effect of Mo doping on band gaps as well as shifting of electron density on addenda atoms in 3 and 3-M.

Both 3 and 3-M exhibit broad absorption bands in the UV-vis region due to ligand-to-metal charge transfer (LMCT) ( $O_{2p} \rightarrow W_{5d}$ ), as well as d-d transitions, and the feeble peak is observed for transition metal to POM charge transfer (MMCT) at 478 nm (TM  $\rightarrow$  W<sub>5d</sub>). Moreover, a significant contribution of Mo is evident in mixed addenda sandwich POMs through a red shift in the UV-vis spectra compared to that of W-based sandwich POMs (Figure 3A.13d). This red

shift can be explained by the changes in the band gap of these POMs, which were investigated using DRS. These results were further supported with DFT study, where the HOMO-LUMO band gap in **3-M** (representative structure of **3-M** is taken with formula  $\{Co_2Fe_2(H_2O)_2(CoMo_4W_5)_2\}^{10-}$ ) falls lower than that of **3** (Figure 3A.14). The LUMO energy as well as the band gap energy (HOMO-LUMO) drop as going from **3** to **3-M** (Figure 3A.13e), which also correlates well with UV-visible spectroscopy. The band positions and overall charge on the POM play crucial roles in defining their redox characteristics. While the overall charge is constant in all of these sandwich POMs, the relatively lower LUMO energy in mixed addenda POMs correlates well with the higher electron affinity compared to their corresponding W-analogues.

#### 3A.2.2d Structural Description and Characterizations of 4 and 4-M.

Compounds **4** and **4-M** were characterized using SC-XRD, FT-IR, ESI-MS, XPS, and UV-visible spectroscopy (Figure 3A.15-3A.18). The framework structure was confirmed by SC-XRD (CCDC **2330242**, **2330243**). The dark pink colored crystals of **4** and **4-M** crystallize in monoclinic with P2<sub>1</sub>/n space group (Table 3A.S2).

The 3D SC-XRD structure of 4 and 4-M shows that the trilacunary Keggin moiety contains a tetrahedrally bound zinc atom in the center as a templating agent to triads of addenda W/Mo atoms (Figure 3A.15). The tetrasubstituted sandwich core consists of Mn at the internal  $\{TM_i\}$ position and Zn/W (80:20) as external atoms  $\{TM_e\}$ . From the comparison of 4-M with the reference structure (Figure 1.10), it is clear that Mo incorporation is favorable at only 4/5 positions of the belt, which are connected to transition metals in the sandwich position through  $\mu_2$  oxygens. (Figure 3A.15c). The other positions in the belt as well as the cap are not favorable for Mo incorporation. The distance between Zn atoms at the external and Mn at the internal positions is 3.19-3.21 Å in 4/4-M, however, the distance between Zn/Fe atoms in the internal positions is 2.95 Å in 4/4-M (Figure 3A.15b). BVS calculation indicates that all addenda atoms are in their highest oxidation state (+6) and Zn, and Mn in +2 and +3 oxidation states respectively (Table 3A.S12). Apart from the BVS, the oxidation states of all of the atoms in 4 and 4-M were determined from XPS analysis. The XP spectra of 4-M revealed the presence of W, Mo, Mn, and oxygen. The two peaks at 641.5 and 653.2 eV in 4-M can be attributed to the presence of Mn in a +3 oxidation state. The W 4f doublet appears at 34.5 and 36.7 eV, corresponding to W 4f<sub>7/2</sub> and 4f<sub>5/2</sub> and Mo 3d doublet appears at 231.8 and 234.9 eV, corresponding to Mo 3d<sub>5/2</sub> and 3d<sub>3/2</sub> respectively in 4-M.

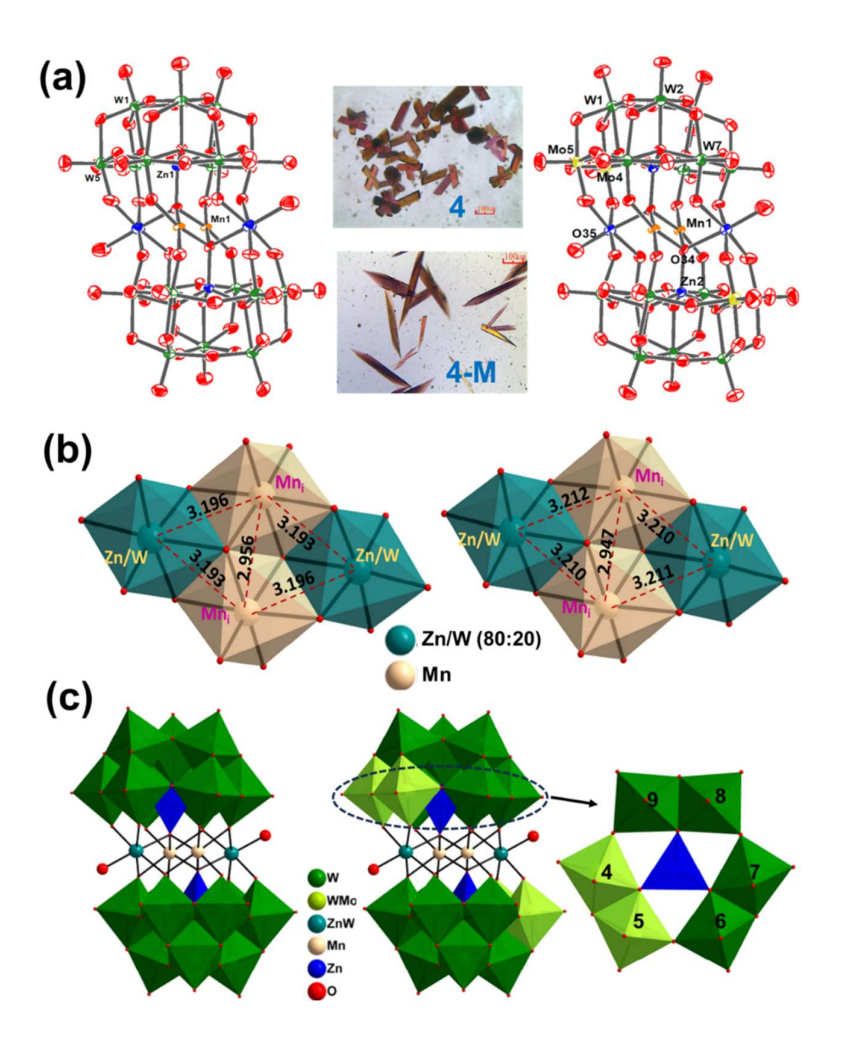


**Figure 3A.15** (a) ORTEP drawing (with 60% ellipsoid probability) and Optical images of sandwich POMs; **4** (left) and **4-M** (right); (b) Cubane core showing the interatomic distance between transition metals in **4** (left) and **4-M** (right); (c) combined polyhedral/ball and stick representation of the single-crystal X-ray structure of polyoxometalate **4** (left) and **4-M** (right), belt 2 depicting different ratios of molybdenum to tungsten in **4-M**;. Countercations and hydrogen atoms are omitted for clarity.

The ESI-mass spectrum of **4** in (Figure 3A.16, Table 3A.S13) shows the envelope of peaks at m/z 1592.75 (z=-3) due to the presence of fragment  $\{Zn_2Mn_2(H_2O)_2(ZnW_9O_{34})_2\}^{3-}$  while a relatively small peak at 1607.07 (z=-3) indicates the presence of analog structure with W-substituted at the external position. These results have been supported by complementary results in SC-XRD. The analog mixed addenda POMs structure **4-M** shows the isotopic multiple envelopes of peaks attributed to varying ratios of Mo to W. The mixed addenda sandwich POMs **4-M** show the envelopes of peaks (Figure 3A.16b, Table 3A.S13) at m/z1576.71 for  $[\{Zn_2Mn_2(H_2O)_2(Zn_2MoW_{17})\}^{3-}]$ , and m/z 1607.73 for  $[\{WMn_3(H_2O)_2(Zn_2MoW_{17}O_{68})\}^{3-}]$ .

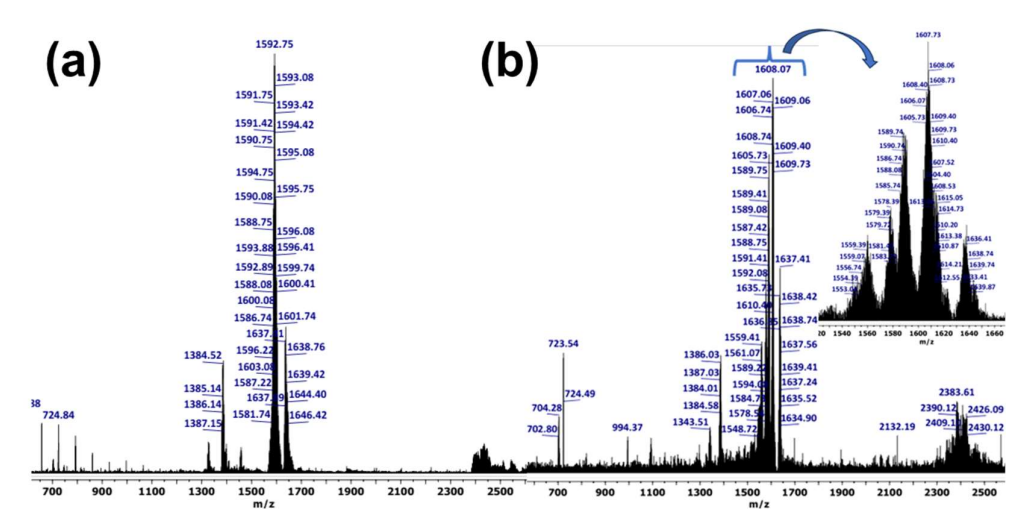


**Figure 3A.16** ESI-MS spectra of (a) **4** (left) and (b) **4-M** (right) in the range of m/z 1000-2500 for different z values.

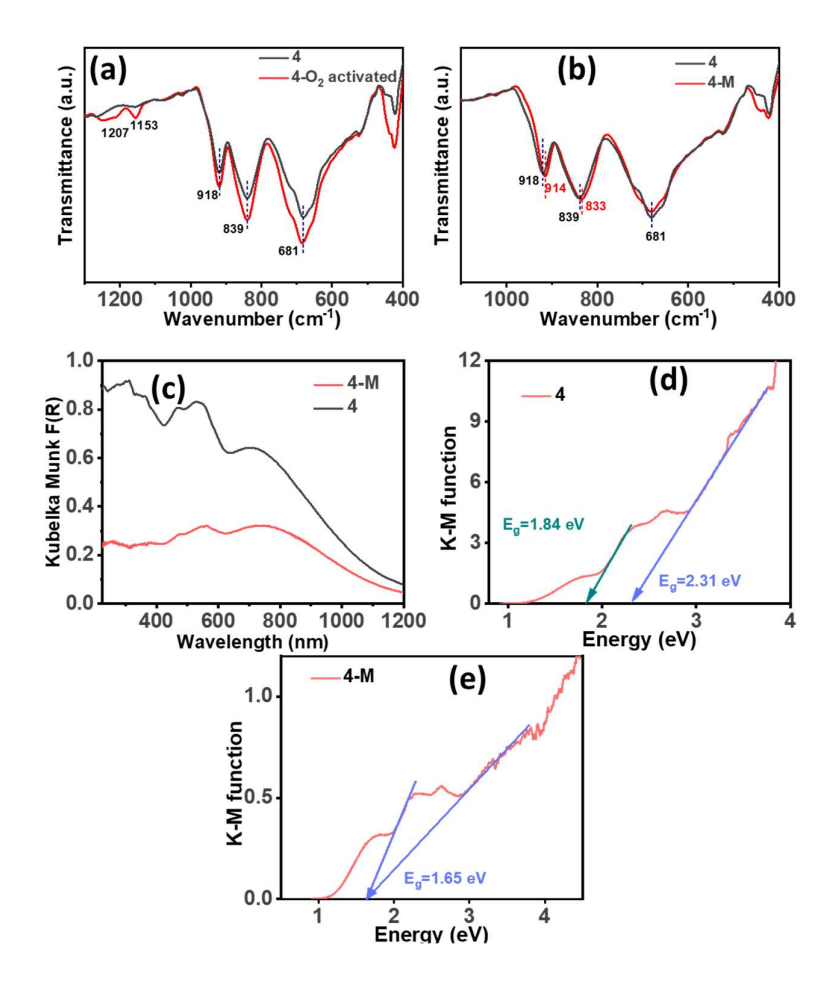


**Figure 3A.17** (a) FT-IR spectra of **4** before and after O<sub>2</sub> treatment; (b) FT-IR and (c) solid-state UV-vis spectra of **4** and **4-M** and corresponding optical band-gap derived from the Kubelka-Munk equation in (d) **4** and (e) **4-M**.

From the FT-IR study of O<sub>2</sub>-activated **4**, two feeble peaks in the range at 1153, 1207 cm<sup>-1</sup> have been observed, indicating the formation of O<sub>2</sub> activation using these POMs (Figure 3A.17a). Comparing the stretching frequencies of **4-M** with **4**, there is a subtle variation in the characteristic's peaks at 918 cm<sup>-1</sup> (**4**, W=O<sub>term</sub>) to 914 (**4-M**, M=O<sub>term</sub>, M=Mo/W), 839 cm<sup>-1</sup> (**4**, W-O-W) to 833 cm<sup>-1</sup> (**4-M**, M-O-M, M=Mo/W) (Figure 3A.17b). Both **4** and **4-M** exhibit broad absorption bands in the UV-vis region due to LMCT ( $O_{2p} \rightarrow W_{5d}$ ), as well as d-d transitions and sharp peak, is observed for transition MPCT at 470 nm and 527/563 nm (TM  $\rightarrow$  LUMO ( $W_{5d}/Mn_{3d}$ ) (Figure 3A.17c). Also, broad peak at 700/733 can be assigned to d-d transition in **4/4-M** respectively. Moreover, the contribution of Mo is evident in mixed addenda sandwich POMs can be explained by the changes in the band gap (2.31 eV in **4** decreases to 1.65 eV in **4-M**) of these POMs, which were investigated using DRS (Figure 3A.17d/e).

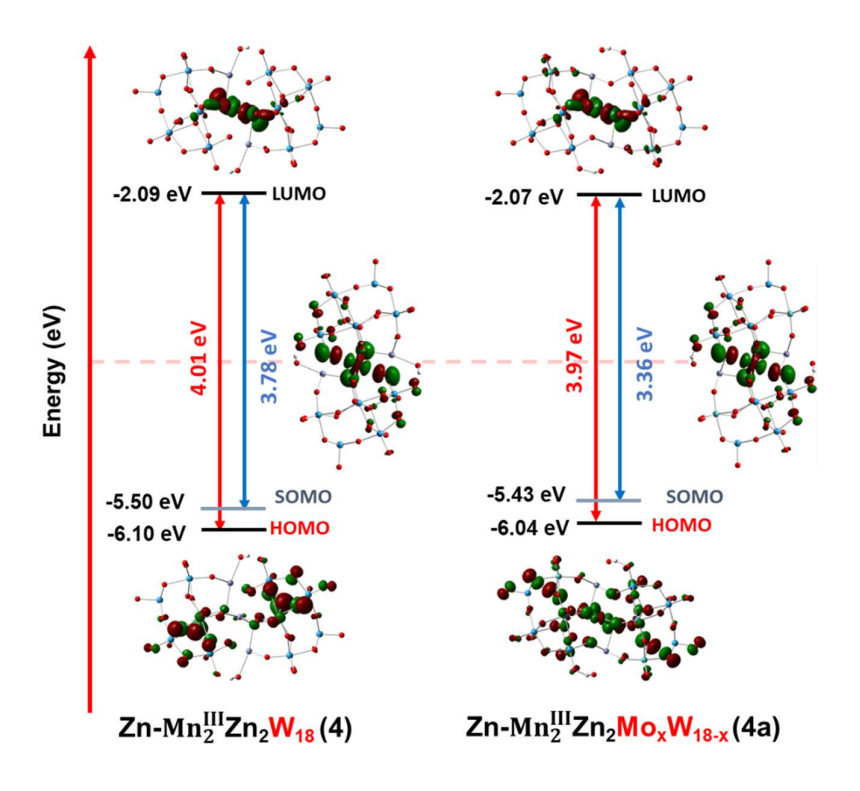


**Figure 3A.18** Frontier molecular orbitals of tetrasubstituted sandwich POMs showing the effect of Mo doping on band gaps as well as shifting of electron density on addenda atoms in **4** and **4-M**.

These results were further supported with DFT study, where the HOMO-LUMO band gap in **4-M** (representative structure of **4-M** is taken with formula  $\{Zn_2Mn_2(H_2O)_2(ZnMo_2W_7O_{34})_2\}^{14-}$  falls lower than that of **4** (Figure 3A.18). Interestingly, LUMO/LUMO+1 of **4** lies at Mn(III) while LUMO+2 lies at W(VI) centre which also supports UV-visible spectroscopy e.g. MPCT at 470 nm can be assigned to TM  $\rightarrow$  W and peak at 527

nm stand for oxygen  $\rightarrow$  Mn<sup>3+</sup> in 4 (Figure 3A.17c). In 4-M, LUMO lies at Mn while LUMO+1 lies at Mo(VI) (Figure 3A.S10). Thus, in 4-M; MPCT at 470 nm can be assigned to TM  $\rightarrow$  Mo and peak at 527 nm stand for TM  $\rightarrow$  Mn<sup>3+</sup> in 4-M. Thus incorporation of Mn at internal sandwich position responsible for the MPCT in these POMs while mixed addenda changes the electron density in LUMO lie at Mo rather than W thus decreasing the overall band gap.

#### 3A.2.2e Structural Description and Characterizations of 5 and 5-M.

Compounds 5 and 5-M were characterized using SC-XRD, FT-IR, ESI-MS, and UV-visible spectroscopy (Figure 3A.19-3A.21). The framework structure was confirmed by SC-XRD (CCDC 2330255, 2330245). The dark green colored crystals of 5 (needle-shaped) and 5-M (cubic) crystallize in monoclinic with P2<sub>1</sub>/n space group (Table 3A.S2).

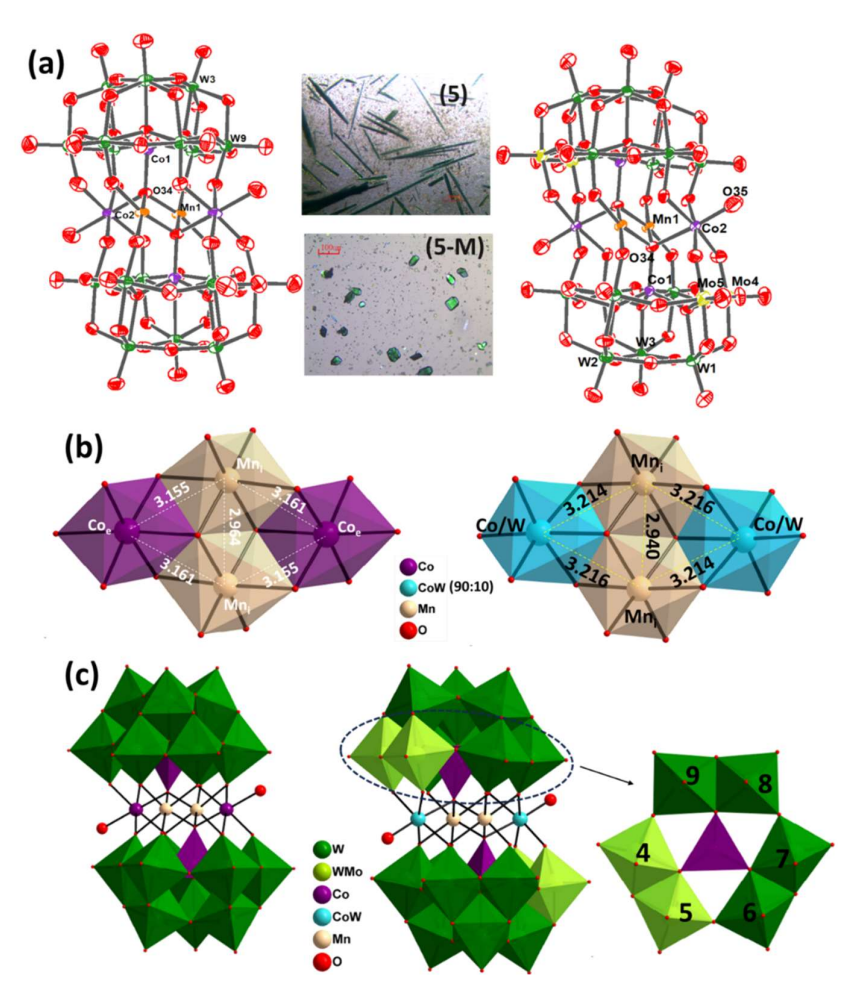


**Figure 3A.19** (a) ORTEP drawing (with 60% ellipsoid probability) and Optical images of sandwich POMs; **5** (left) and **5-M** (right); (b) Cubane core showing the interatomic distance between transition metals in **5** (left) and **5-M** (right); (c) combined polyhedral/ball and stick representation of the single-crystal X-ray structure of polyoxometalate **5** (left) and **5-M** (right), belt 2 depicting different ratios of molybdenum to tungsten in **5-M**;. Countercations and hydrogen atoms are omitted for clarity.

The 3D SC-XRD structure of **5** and **5-M** shows that the trilacunary Keggin moiety contains a tetrahedrally bound cobalt atom in the center as a templating agent to triads of addenda W/Mo atoms. The tetrasubstituted sandwich core consists of Mn at the internal  $\{TM_i\}$  position and Co/W (90:10) as external atoms  $\{TM_e\}$  (Figure 3A.19). From the comparison of **5-M** with the reference structure (Figure 1.10), it is clear that Mo incorporation is favorable at only 4/5 positions of the belt similar to **4-M**, which are connected to transition metals in the sandwich position through  $\mu_2$  oxygens (Figure 3A.19c). The other positions in the cap and belt are not favorable for Mo incorporation. The distance between Co atoms at the external and Mn at the internal positions is 3.15 Å in **5** while 3.21 Å in **5-M**, however, the distance between Mn atoms in the internal positions is 2.9 Å in **5/5-M** (Figure 3A.19b). BVS calculation indicates that all addenda atoms are in their highest oxidation state +6 and Co, and Mn in +2, +3 oxidation state respectively (Table 3A.S14).

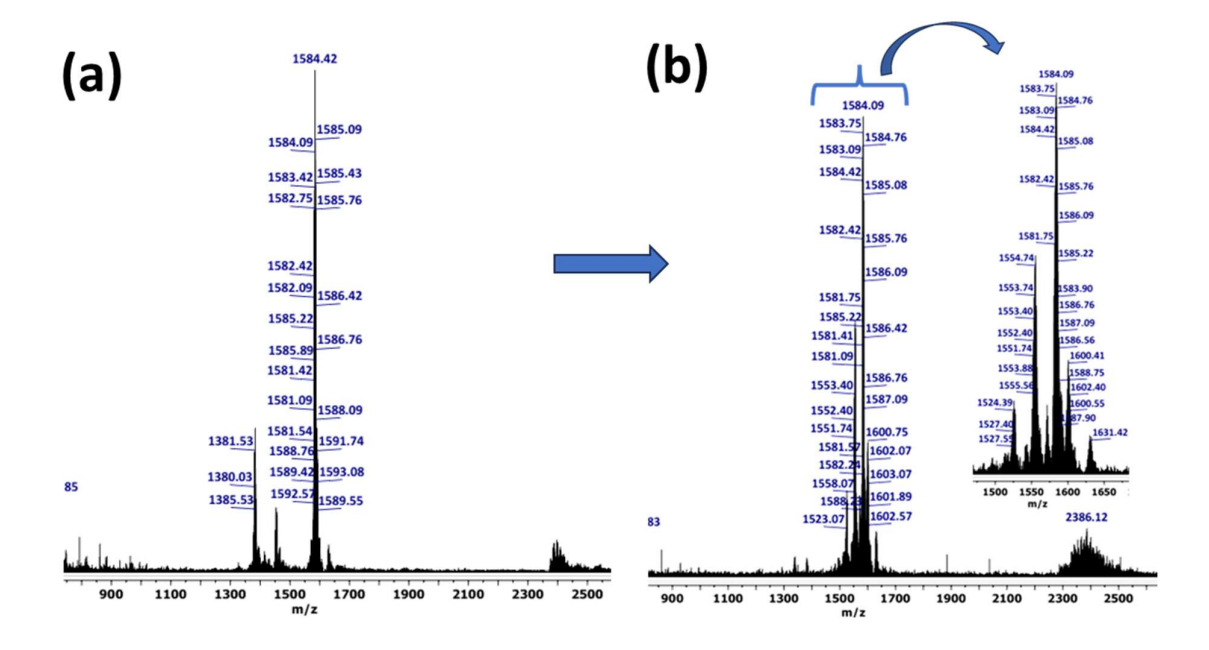


**Figure 3A.20** ESI-MS spectra of (a) **5** (left) and (b) **5-M** (right) in the range of m/z 1000-2500 for different z values.

ESI-mass spectrum of **5** in (Figure 3A.20) shows the envelope of peaks at m/z 1584 (z=-3) for the fragment  $[{Co_2Mn_2(H_2O)_2(CoW_9O_{34})_2}]^{3-}]$ , while the analog mixed addenda **5-M** structure shows the isotopic multiple envelopes of peaks attributed to varying ratios of Mo to W with maximum 2 Mo incorporated in the framework. **5-M** show the envelopes of peaks (Figure 3A.20, Table 3A.S15) at m/z 1554 for  $[H_{11}{Co_2Mn_2(CoMoW_{17}O_{68})}]^{3-}$ , and m/z 1524 for  $[H_{11}{Co_2Mn_2(CoMo_2W_{16}O_{68})}]^{3-}$  while the incorporation of W at external sandwich position

is indicated by the small peaks at 1631 due to fragments  $[H_6Na\{CoWMn_2(Co_2W_{18}O_{68})\}]^{3-}$  with corresponding mixed addenda peaks at 1600 due to probable fragment  $[H_7Na\{WMn_3(Co_2MoW_{17}O_{68})\}]^{3-}$ . Comparing the stretching frequencies of **4-M** with **4**, there is a subtle variation in the characteristic's peaks at 930 cm<sup>-1</sup> (**5**, W=O<sub>term</sub>) to 914 (**5-M**, M=O<sub>term</sub>, M=Mo/W), 836 cm<sup>-1</sup> (**5**, W-O-W) to 834 cm<sup>-1</sup> (**5-M**, M-O-M, M=Mo/W) (Figure 3A.21a).

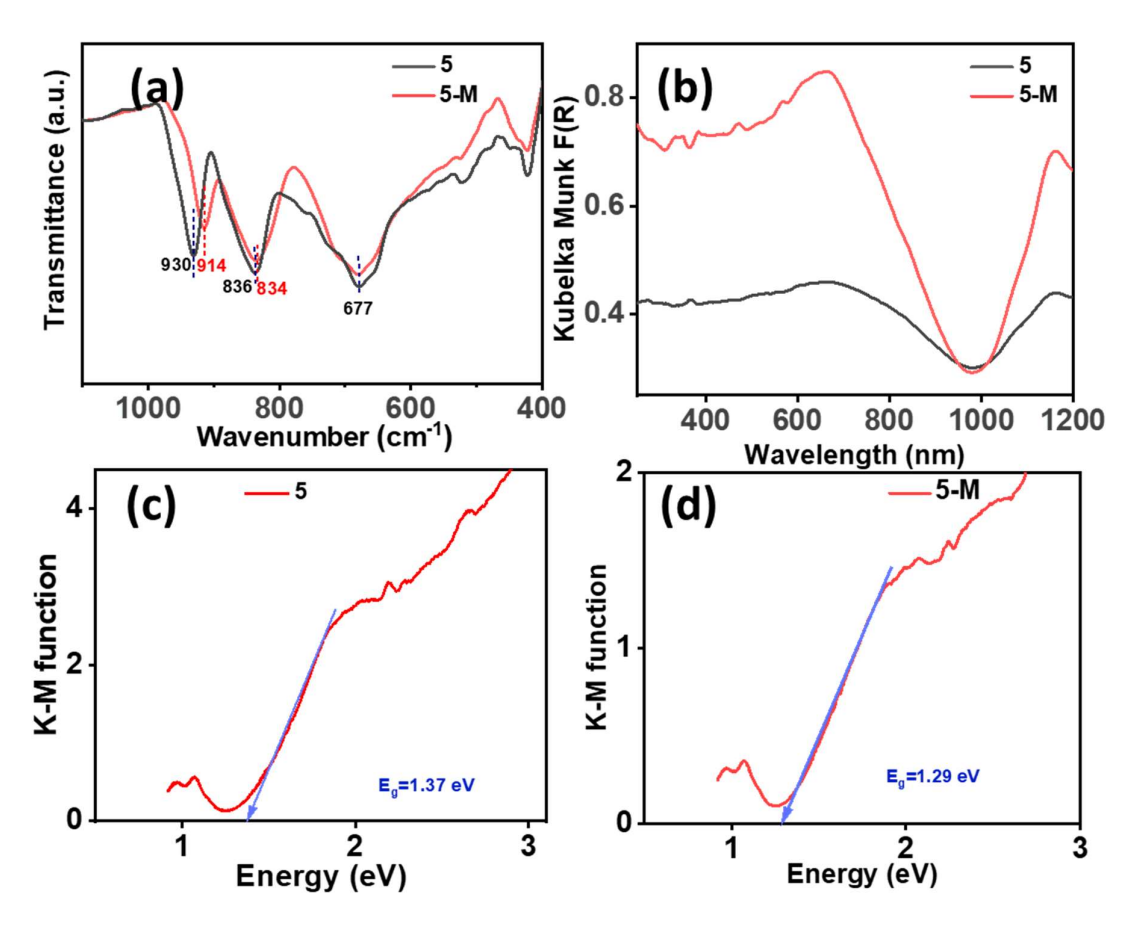


**Figure 3A.21** (a) FT-IR and (b) solid-state UV-vis spectra of **5** and **5-M** and corresponding optical bandgap derived from the Kubelka-Munk equation in (c) **5** and (d) **5-M**.

Both 5 and 5-M exhibit broad absorption bands in the UV-vis region due to (LMCT) (O2p → W5d), d-d transitions as well absorption in Near IR region (Figure 3A.21b). The peak at 660/666 nm can be assigned to d-d transition in 5/5-M respectively while peaks at 1160 nm can be assigned to NIR absorption. Interestingly Mo incorporation has very little effect on its absorption properties which can be further confirmed from band gap calculated from DRS (slight change in band gap; 1.37 eV in 5 to 1.29 eV in 5-M).

#### 3A.3 Conclusion

In conclusion, our study highlights the strategic role of different transition metals in the rational design of one-pot self-assembly, contributing to the formation of mixed metal-mixed addenda structures in sandwich POMs. This cooperative mixed metal-mixed addenda approach expands the applicability of mixed addenda POMs and demonstrates the versatility of the approach across diverse POM frameworks, including mixed addenda sandwich POMs and coordination frameworks. Introducing mixed addenda using mixed transition metals into these POMs proves to be an effective orbital engineering strategy, influencing the overall band gap, molecular properties, and absorption characteristics, which was also supported by the DFT calculations. This study not only showcases the versatility of mixed addenda TMSPs in sandwich POMs but also extends their relevance to other frameworks such as coordination frameworks.

#### 3A.4 Experimental section

## 3A.4.1 General Information and Instrumentation

**3A.4.1a** Materials and Methods. Deionized water used in the experiments was from the Millipore system (>18 M $\Omega$  cm-1). The transition metal salts used in synthesis were obtained from Alfa Aesar (purity > 99.9 %) and used without further purification. All polyoxometalates were recrystallized from an aqueous solution before characterization. All the synthetic procedures were optimized in terms of pH and the different ratios of Mo to W salt as mentioned in our previously reported article. <sup>14</sup> The optimization in the case of mixed addenda POMs was done regarding the maximum Mo: W ratio in the final compound using pH dependent study.

#### 3A.4.1b Instrumentation

Already mentioned in section 2.4.1b (chapter 2)

Crystal data, data collection parameters, refinement statistics, and the Cambridge Crystallographic Data Centre; CCDC number (2330238, 2330239, 2330240, 2330241, 2330242, 2330243, 2330244, 2330245, 2330246, 2330247, 2330248, 2330249, 2330250, 2330251, 2330252, 2330253, 2330254, 2330255, 2330256, 2330257, 2330258, 2330259, 2330260, 2330261).

#### 3A.4.1c Density Functional Theory (DFT) Calculation.

Already mentioned in section 2.4.1c (chapter 2)

#### 3A.4.2 Synthesis

#### Na<sub>14</sub>[Fe<sub>4</sub>(H<sub>2</sub>O)<sub>2</sub>(FeW<sub>9</sub>O<sub>34</sub>)<sub>2</sub>].22H<sub>2</sub>O (1)

Na<sub>2</sub>WO<sub>4</sub>.2H<sub>2</sub>O (4.00 g, 12.12 mmol) was dissolved in 15 mL DI water completely. Using 6M HCl, the pH of the solution was fixed at 7.26 (precipitate formed during HCl addition were

dissolved with vigorous stirring), the resultant solution was put in Teflon microwave vials of 100 mL volume and microwave irradiated under controlled pressure with a power ramp for 15 min and power hold for 45 min at 85 °C under 400 W maximum power. To this solution, FeCl<sub>2</sub>.4H<sub>2</sub>O (0.80 g, 4.04 mmol) was added and irradiated again in the microwave for 1 h at 85 °C following the previous parameter. The orange solution thus obtained was filtered hot and filtrate was kept for crystallization. After one day, block-shaped orange-colored crystals appeared, which were collected by filtration and dried at 60 °C under vacuum. Yield: 0.84 g (22.8%). FT-IR (cm<sup>-1</sup>): 931 (W=O<sub>t</sub>), 839 (W-O<sub>c</sub>-W), 661 (W-O<sub>e</sub>-W).

## Na<sub>14</sub>[Fe<sub>4</sub>(H<sub>2</sub>O)<sub>2</sub>(FeMo<sub>x</sub>W<sub>9-x</sub>O<sub>34</sub>)<sub>2</sub>].20H<sub>2</sub>O (1-M)

A mixture of Na<sub>2</sub>WO<sub>4</sub>.2H<sub>2</sub>O (2.67 g, 8.08 mmol) and Na<sub>2</sub>MoO<sub>4</sub>.2H<sub>2</sub>O (0.98 g, 4.04 mmol) was dissolved in 15 mL DI water completely. Using 6M HCl, the pH of the solution was fixed at 6.6, the resultant solution was put in Teflon microwave vials of 100 mL volume and microwave irradiated under controlled pressure with a power ramp for 15 min and power hold for 45 min at 85 °C under 400 W maximum power. To this solution, FeCl<sub>2</sub>.4H<sub>2</sub>O (0.80 g, 4.04 mmol) was added and irradiated again in the microwave for 1 h at 85 °C following the previous parameter. The orange solution thus obtained was filtered hot and 0.3 g of KCl was added to the filtrate with vigorous stirring. A small amount of precipitate thus formed, which was filtered and the final pH of the filtrate was found to be 5.6. After 15 days, block-shaped orange-colored crystals appeared which were collected by filtration and dried at 60 °C under vacuum. Yield: 0.45 g (13.1%). FT-IR (cm<sup>-1</sup>): 911 (M=O<sub>t</sub>), 832 (M-O<sub>c</sub>-M), 678 (M-O<sub>c</sub>-M) (M=Mo/W).

# $Na_{14}[Zn_{2}Fe_{2}^{III}(H_{2}O)_{2}(ZnW_{9}O_{34})_{2}].23H_{2}O$ (2)

Na<sub>2</sub>WO<sub>4</sub>.2H<sub>2</sub>O (4.00 g, 12.12 mmol) was dissolved in 15 mL DI water completely to which 0.5 mL nitric acid was added dropwise (precipitates formed during HNO<sub>3</sub> addition were dissolved with vigorous stirring), the resultant solution was put in Teflon microwave vials and microwave irradiated under controlled pressure with a power ramp for 15 min and hold for 45 min at 85 °C under 400 W maximum power. Zn(NO<sub>3</sub>)<sub>2</sub>.6H<sub>2</sub>O (0.80 g, 2.68 mmol) followed by Fe(NO<sub>3</sub>)<sub>3</sub>.9H<sub>2</sub>O (0.54 g, 1.34 mmol) was added to the above solution with vigorous stirring and irradiated again in the microwave for 1 h at 85 °C maintaining the previous parameter. The light orange solution thus obtained was filtered hot and filtrate was kept for crystallization. The pH of the final solution was found to be 7.7. After 2 h, block-shaped yellow-colored crystals appeared, which were collected by filtration and dried at 60 °C under vacuum. Yield: 0.73 g (19.6%). FT-IR (cm<sup>-1</sup>): 917 (W=O<sub>1</sub>), 839 (W-O<sub>c</sub>-W), 635 (W-O<sub>e</sub>-W).

# $Na_{14}[Zn_{2}Fe_{2}^{III}(H_{2}O)_{2}(ZnMo_{x}W_{9-x}O_{34})_{2}].23H_{2}O$ (2-M)

A mixture of Na<sub>2</sub>WO<sub>4</sub>.2H<sub>2</sub>O (2.00 g, 6.06 mmol) and Na<sub>2</sub>MoO<sub>4</sub>.2H<sub>2</sub>O (1.47 g, 6.06 mmol) in 15 mL DI water was dissolved completely. Using nitric acid, the pH of the solution was fixed at 6.5, the resultant solution was put in Teflon microwave vials and microwave irradiated under controlled pressure with a power ramp for 15 min and power hold for 45 min at 85 °C under 400 W maximum power. Zn(NO<sub>3</sub>)<sub>2</sub>.6H<sub>2</sub>O (0.80 g, 2.68 mmol) followed by Fe(NO<sub>3</sub>)<sub>3</sub>.9H<sub>2</sub>O (0.54 g, 1.34 mmol) was added to the above solution with vigorous stirring and irradiated again in the microwave for 30 min at 85 °C maintaining the previous parameter. The dark orange solution thus obtained was filtered hot and filtrate was kept for crystallization. The pH of the final solution was found to be 6.25 from which block-shaped orange-colored crystals appeared after 2 days. These crystals were collected by filtration and dried at 60 °C under vacuum. Yield: 0.67 g (19.3%). FT-IR (cm<sup>-1</sup>): 913 (M=O<sub>t</sub>), 840 (M-O<sub>c</sub>-M), 656 (M-O<sub>c</sub>-M) (M=Mo/W).

## $Na_{14}[Co_2Fe_2^{III}(H_2O)_2(CoW_9O_{34})_2].15H_2O$ (3)

The synthetic procedure of compound (2) was followed with slight modification. In place of Zn(NO<sub>3</sub>)<sub>2</sub>.6H<sub>2</sub>O, Co(NO<sub>3</sub>)<sub>2</sub>.6H<sub>2</sub>O (0.78 g, 2.68 mmol) was used. The dark green solution thus obtained was filtered hot and filtrate was kept for crystallization. After 2 h, dark green long needle-shaped crystals appeared which were collected by filtration and dried at 60 °C under vacuum. Yield: 0.89 g (24.7%). FT-IR (cm<sup>-1</sup>): 904 (W=O<sub>t</sub>), 838 (W-O<sub>c</sub>-W), 699 (W-O<sub>c</sub>-W).

## $Na_{14}[C_{02}Fe_{2}^{III}(H_{2}O)_{2}(C_{0}M_{0x}W_{9-x}O_{34})_{2}].19H_{2}O$ (3-M)

The synthetic procedure of compound (2-M) was followed with slight modification.  $Co(NO_3)_2.6H_2O$  (0.78 g, 2.68 mmol) was used instead of  $Zn(NO_3)_2.6H_2O$ . The pH of the final solution was found to be 6.3, from which dark colored crystals appeared after 5 days. The crystals were collected by filtration and dried at 60 °C under vacuum. Yield: 0.58 g (17.0%). FT-IR (cm<sup>-1</sup>): 911 (M=O<sub>t</sub>), 832 (M-O<sub>c</sub>-M), 678 (M-O<sub>e</sub>-M) (M=Mo/W). FT-IR (cm<sup>-1</sup>): 915 (M=O<sub>t</sub>), 834 (M-O<sub>c</sub>-M), 634 (M-O<sub>e</sub>-M) (M=Mo/W).

# $Na_{14}[Zn_2Mn_2^{III}(H_2O)_2(ZnW_9O_{34})_2].24H_2O$ (4)

A solution of Na<sub>2</sub>WO<sub>4</sub>.2H<sub>2</sub>O (4.00 g, 12.12 mmol) in 15 mL DI water was dissolved completely. Using glacial acetic acid, the pH of the solution was fixed at 7.2, the resultant solution was put in Teflon microwave vials and microwave irradiated under controlled pressure with a power ramp for 15 min and held for 45 min at 85 °C under 400 W maximum power. Zn(OAc)<sub>2</sub>.2H<sub>2</sub>O (0.58 g, 2.68 mmol) followed by Mn(OAc)<sub>3</sub>.2H<sub>2</sub>O (0.36 g, 1.34 mmol) was added to the above solution with vigorous stirring and irradiated again in the microwave for 30 min at 85 °C following previous parameter. The purple solution thus obtained was filtered hot and filtrate was kept for crystallization. After 2 h, block-shaped purple-colored crystals

appeared which were collected by filtration and dried at 60 °C under vacuum. Yield: 1.13 g (30.3%). FT-IR (cm<sup>-1</sup>): 918 (W=O<sub>t</sub>), 839 (W-O<sub>c</sub>-W), 681 (W-O<sub>e</sub>-W).

# $Na_{14}[Zn_{2}Mn_{2}^{III}(H_{2}O)_{2}(ZnMo_{x}W_{9-x}O_{34})_{2}],22H_{2}O\ (4-M)$

A mixture of Na<sub>2</sub>WO<sub>4</sub>.2H<sub>2</sub>O (2.67 g, 8.08 mmol) and Na<sub>2</sub>MoO<sub>4</sub>.2H<sub>2</sub>O (0.98 g, 4.04 mmol) was dissolved in 15 mL DI water completely. The pH of the solution was fixed at 6.5 using glacial acetic acid. The resultant solution was put in Teflon microwave vials and microwave irradiated under controlled pressure with a power ramp for 15 min and power hold for 45 min at 85 °C under 400 W maximum power. Zn(OAc)<sub>2</sub>.2H<sub>2</sub>O (0.58 g, 2.68 mmol) followed by Mn(OAc)<sub>3</sub>.2H<sub>2</sub>O (0.36 g, 1.34 mmol) was added to the above solution with vigorous stirring and irradiated again in the microwave for 30 min at 85 °C maintaining the previous parameter. The resultant solution was filtered hot and the pH of the final solution was found to be 5.8 which was further fixed to 4.5 using glacial acetic acid, then heated at 85 °C with stirring for 30 min. The dark-colored solution gives pink needle shaped crystals after 1 day. These crystals were collected and dried at 60 °C under vacuum. Yield: 0.82 g (22.9%). FT-IR (cm<sup>-1</sup>): 914 (M=O<sub>1</sub>), 833 (M-O<sub>c</sub>-M), 681 (M-O<sub>c</sub>-M) (M=Mo/W).

## $Na_{14}[Co_2Mn_2^{III}(H_2O)_2(CoW_9O_{34})_2].22H_2O$ (5)

The synthetic procedure of compound **(4)** was followed with slight modification. In place of Zn(OAc)<sub>2</sub>.2H<sub>2</sub>O, Co(OAc)<sub>2</sub>.2H<sub>2</sub>O (0.66 g, 2.68 mmol) was used. The pH of the final solution was found to be 6.3, from which dark colored crystals appeared after 5 days. The crystals were collected by filtration and dried at 60 °C under vacuum. Yield: 0.94 g (25.5%). FT-IR (cm<sup>-1</sup>): 930 (W=O<sub>t</sub>), 836 (W-O<sub>c</sub>-W), 677 (W-O<sub>e</sub>-W).

## $Na_{14}[Co_2Mn_2^{III}(H_2O)_2(CoMo_xW_{9-x}O_{34})_2].19H_2O$ (5-M)

The synthetic procedure of compound (4-M) was followed with slight modification. In place of Zn(OAc)<sub>2</sub>.2H<sub>2</sub>O, Co(OAc)<sub>2</sub>.2H<sub>2</sub>O (0.66 g, 2.68 mmol) was used. The dark green solution thus obtained was filtered hot and filtrate was kept for crystallization after fixing the pH of the final solution 4.5 which gave dark green block-shaped crystals. These crystals were collected by filtration and dried at 60 °C under vacuum. Yield: 0.62 g (17.6%). FT-IR (cm<sup>-1</sup>): 914 (M=O<sub>t</sub>), 834 (M-O<sub>c</sub>-M), 677 (M-O<sub>e</sub>-M) (M=Mo/W).

## 3A.4.3 Molecular oxygen binding experiment

A Schlenk tube was charged with 10 μmol of POM and 1 mL toluene and heated at 110 °C for 12 h under 1 atm. O<sub>2</sub> pressure. After cooling to room temperature, the mixture was filtered and

dried at 80 °C under a vacuum to obtain dioxygen-activated POM characterized via FT-IR and Raman.

#### 3A-5. References

- 1. Pope, M. T.; Jeannin, Y.; Fournier, M., *Heteropoly and isopoly oxometalates*. Springer: 1983; Vol. 8.
- 2. Li, N.; Liu, J.; Dong, B. X.; Lan, Y. Q., Polyoxometalate-based compounds for photo-and electrocatalytic applications. *Angew. Chem. Int. Ed* **2020**, *59* (47), 20779-20793.
- 3. Katsoulis, D. E., A survey of applications of polyoxometalates. *Chem. Rev* **1998**, *98* (1), 359-388.
- 4. Liu, L.-L.; Wang, L.; Xiao, X.-Y.; Yang, P.; Zhao, J.; Kortz, U., Structural overview and evolution paths of lacunary polyoxometalates. *Coord Chem Rev* **2024**, *506*, 215687.
- 5. Li, C.; Jimbo, A.; Yamaguchi, K.; Suzuki, K., A protecting group strategy to access stable lacunary polyoxomolybdates for introducing multinuclear metal clusters. *Chem. Sci.* **2021**, *12* (4), 1240-1244.
- 6. Azmani, K.; Besora, M.; Soriano-Lopez, J.; Landolsi, M.; Teillout, A.-L.; de Oliveira, P.; Mbomekallé, I.-M.; Poblet, J. M.; Galán-Mascarós, J.-R., Understanding polyoxometalates as water oxidation catalysts through iron vs. cobalt reactivity. *Chem. Sci* **2021**, *12* (25), 8755-8766.
- 7. Gumerova, N. I.; Rompel, A., Polyoxometalates in solution: speciation under spotlight. *Chem. Soc. Rev* **2020**, *49* (21), 7568-7601.
- 8. Mulkapuri, S.; Ravi, A.; Nasani, R.; Kurapati, S. K.; Das, S. K., Barrel-shaped-polyoxometalates exhibiting electrocatalytic water reduction at neutral pH: A synergy effect. *Inorg. Chem.* **2022**, *61* (35), 13868-13882.
- 9. Zheng, S.-T.; Yang, G.-Y., Recent advances in paramagnetic-TM-substituted polyoxometalates (TM= Mn, Fe, Co, Ni, Cu). *Chem. Soc. Rev* **2012**, *41* (22), 7623-7646.
- 10. Miras, H. N.; Yan, J.; Long, D.-L.; Cronin, L., Engineering polyoxometalates with emergent properties. *Chem. Soc. Rev* **2012**, *41* (22), 7403-7430.
- 11. Suzuki, K.; Mizuno, N.; Yamaguchi, K., Polyoxometalate photocatalysis for liquid-phase selective organic functional group transformations. *ACS Catal* **2018**, *8* (11), 10809-10825.
- 12. Chi, M.; Zeng, Y.; Lang, Z.-L.; Li, H.; Xin, X.; Dong, Y.; Fu, F.; Yang, G.-Y.; Lv, H., Molecular Orbital Engineering of Mixed-Addenda Polyoxometalates Boosts Light-Driven Hydrogen Evolution Activity. *ACS Catal* **2024**, *14*, 5006-5015.
- 13. Martin-Sabi, M.; Soriano-López, J.; Winter, R. S.; Chen, J.-J.; Vilà-Nadal, L.; Long, D.-L.; Galán-Mascarós, J. R.; Cronin, L., Redox tuning the Weakley-type polyoxometalate archetype for the oxygen evolution reaction. *Nat. Catal* **2018**, *1* (3), 208-213.
- 14. Singh, G.; Mandal, D., Modulation of the Band Gap and Redox Properties by Mixed Addenda in Sandwich Polyoxometalates. *Inorg. Chem* **2023**, *62* (48), 19648-19663.
- 15. Compain, J. D.; Mialane, P.; Dolbecq, A.; Mbomekallé, I. M.; Marrot, J.; Sécheresse, F.; Rivière, E.; Rogez, G.; Wernsdorfer, W., Iron Polyoxometalate Single-Molecule Magnets. *Angew. Chem. Int. Ed* **2009**, *48* (17), 3077-3081.
- 16. Limanski, E.; Piepenbrink, M.; Droste, E.; Burgemeister, K.; Krebs, B., Syntheses and X-ray Characterization of Novel [M<sub>4</sub>(H<sub>2</sub>O)<sub>2</sub>(XW<sub>9</sub>O<sub>34</sub>)<sub>2</sub>]<sup>n-</sup>(M= Cu II, X= Cu II; and M= Fe III, X= Fe III) Polyoxotungstates. *J. Clust. Sci* **2002**, *13*, 369-379.
- 17. Tourné, C. M.; Tourné, G. F.; Zonnevijlle, F., Chiral polytungstometalates [WM<sub>3</sub>(H<sub>2</sub>O) <sub>2</sub>(XW<sub>9</sub>O<sub>34</sub>)<sub>2</sub>]<sup>12-</sup> (X= M= Zn or Co II) and their M-substituted derivatives. Syntheses, chemical, structural and spectroscopic study of some D, L sodium and potassium salts. *J. Chem. Soc., Dalton trans.* **1991**, (1), 143-155.
- 18. Wang, J.; Ma, P.; Shen, Y.; Niu, J., A novel polyoxotungstate [Ni4(H2O)2(α-NiW9O34) 2] 16-based on an old structure with a new component. *Cryst. Growth Des* **2007**, *7* (4), 603-605.
- 19. Wang, Z.; Xin, X.; Zhang, M.; Li, Z.; Lv, H.; Yang, G.-Y., Recent advances of mixed-transition-metal-substituted polyoxometalates. *Sci China Chem* **2022**, *65* (8), 1515-1525.
- 20. Tao, M.; Yin, Q.; Kaledin, A. L.; Uhlikova, N.; Lu, X.; Cheng, T.; Chen, Y.-S.; Lian, T.; Geletii, Y. V.; Musaev, D. G., Structurally Precise Two-Transition-Metal Water Oxidation Catalysts: Quantifying Adjacent 3d Metals by Synchrotron X-Radiation Anomalous Dispersion Scattering. *Inorg. Chem* **2022**, *61* (16), 6252-6262.

- Soriano-López, J.; Steuber, F. W.; Mulahmetović, M.; Besora, M.; Clemente-Juan, J. M.; O'Doherty, M.; Zhu, N.-Y.; Hill, C. L.; Coronado, E.; Poblet, J. M., Accelerating water oxidation—a mixed Co/Fe polyoxometalate with improved turnover characteristics. *Chem. Sci.* 2023, 14 (47), 13722-13733.
- 22. Ibrahim, M.; Lan, Y.; Bassil, B. S.; Xiang, Y.; Suchopar, A.; Powell, A. K.; Kortz, U., Hexadecacobalt (II)-containing polyoxometalate-based single-molecule magnet. *Angew. Chem. Int. Ed* **2011**, *50* (20), 4708-4711.
- 23. Jia, J.; Niu, Y.; Zhang, P.; Zhang, D.; Ma, P.; Zhang, C.; Niu, J.; Wang, J., A Monomeric Tricobalt (II)-Substituted Dawson-Type Polyoxometalate Decorated by a Metal Carbonyl Group: [P2W15O56Co3(H2O)3(OH)3Mn(CO)3]8–. *Inorg. Chem* **2017**, *56* (17), 10131-10134.
- 24. Nyman, M., Polyoxoniobate chemistry in the 21st century. *Dalton Trans* **2011**, *40* (32), 8049-8058.
- 25. Nyman, M.; Burns, P. C., A comprehensive comparison of transition-metal and actinyl polyoxometalates. *Chem. Soc. Rev* **2012**, *41* (22), 7354-7367.
- 26. Neumann, R.; Dahan, M., A ruthenium-substituted polyoxometalate as an inorganic dioxygenase for activation of molecular oxygen. *Nature* **1997**, *388* (6640), 353-355.
- 27. Neumann, R.; Dahan, M., Molecular oxygen activation by a ruthenium-substituted "sandwich" type polyoxometalate. *J. Am. Chem. Soc.* **1998**, *120* (46), 11969-11976.
- 28. Weinstock, I. A.; Schreiber, R. E.; Neumann, R., Dioxygen in polyoxometalate mediated reactions. *Chem. Rev* **2017**, *118* (5), 2680-2717.
- 29. Barats, D.; Leitus, G.; Popovitz-Biro, R.; Shimon, L. J.; Neumann, R., A Stable "End-On" Iron (III)—Hydroperoxo Complex in Water Derived from a Multi-Iron (II)-Substituted Polyoxometalate and Molecular Oxygen. *Angew. Chem. Int. Ed* **2008**, *47* (51), 9908-9912.
- 30. Neumann, R., Activation of molecular oxygen, polyoxometalates, and liquid-phase catalytic oxidation. *Inorg. Chem.* **2010**, *49* (8), 3594-3601.
- 31. López, X.; Bo, C.; Poblet, J. M., Electronic properties of polyoxometalates: Electron and proton affinity of mixed-addenda Keggin and Wells—Dawson anions. *J. Am. Chem. Soc* **2002**, *124* (42), 12574-12582.
- 32. Glass, E. N.; Fielden, J.; Huang, Z.; Xiang, X.; Musaev, D. G.; Lian, T.; Hill, C. L., Transition metal substitution effects on metal-to-polyoxometalate charge transfer. *Inorg. Chem.* **2016**, *55* (9), 4308-4319.
- 33. Glass, E. N.; Fielden, J.; Kaledin, A. L.; Musaev, D. G.; Lian, T.; Hill, C. L., Extending Metal-to-Polyoxometalate Charge Transfer Lifetimes: The Effect of Heterometal Location. *Chem. Eur. J* **2014**, *20* (15), 4297-4307.
- 34. López, X.; Carbó, J. J.; Bo, C.; Poblet, J. M., Structure, properties and reactivity of polyoxometalates: a theoretical perspective. *Chem. Soc. Rev.* **2012**, *41* (22), 7537-7571.
- 35. Brown, I. D.; Altermatt, D., Bond-valence parameters obtained from a systematic analysis of the inorganic crystal structure database. *Acta. Crystallogr. B. Struct. Sci. Cryst. Eng* **1985**, *41* (4), 244-247.
- 36. Singh, G.; Das Adhikary, S.; Mandal, D., Physico-and Electrochemical Properties of First-Row Transition-Metal-Substituted Sandwich Polyoxometalates. *Inorg. Chem* **2023**, *62* (48), 8551–8564.
- 37. Singh, G.; Adhikary, S. D.; Mandal, D., Stabilization and activation of polyoxometalate over poly (vinyl butylimidazolium) cations towards electrocatalytic water oxidation in alkaline media. *Chem. Commun.* **2023**, *59* (32), 4774-4777.
- 38. Neumann, R.; Gara, M., The manganese-containing polyoxometalate, [WZnMnII2(ZnW9O34) 2] 12-, as a remarkably effective catalyst for hydrogen peroxide mediated oxidations. *J. Am. Chem. Soc* **1995**, *117* (18), 5066-5074.
- 39. Evangelisti, F.; Car, P.-E.; Blacque, O.; Patzke, G. R., Photocatalytic water oxidation with cobalt-containing tungstobismutates: tuning the metal core. *Catal. Sci. Technol* **2013**, *3* (12), 3117-3129.
- Rafieeshad, M.; Gumerova, N. I.; Tanuhadi, E.; Giester, G.; Čipčić-Paljetak, H.; Verbanac, D.; Rompel, A., Synthesis, Characterization, and Antibacterial Activity of Ni-Substituted Krebs-type Sandwich-Tungstobismuthates Functionalized with Amino Acids. *Inorg. Chem.* 2023, 62 (24), 9484-9490.
- 41. Morris, A. M.; Anderson, O. P.; Finke, R. G., Reinvestigation of a Ru2-Incorporated Polyoxometalate Dioxygenase Precatalyst, "[WZnRu2<sup>III</sup>(H2O)(OH)(ZnW9O34)2]11-": Evidence

- For Marginal,  $\leq$  0.2 Equivalents of Ru Incorporation Plus Faster Catalysis by Physical Mixtures of [RuII(DMSO)4Cl2] and the Parent Polyoxometalate [WZn3(H2O)2(ZnW9O34)2]12–. *Inorg. Chem.* **2009**, 48 (10), 4411-4420.
- 42. Neumann, R.; Khenkin, A. M., Noble Metal (RuIII, PdII, PtII) Substituted" Sandwich" Type Polyoxometalates: Preparation, Characterization, and Catalytic Activity in Oxidations of Alkanes and Alkenes by Peroxides. *Inorg. Chem* **1995**, *34* (23), 5753-5760.
- 43. Howells, A. R.; Sankarraj, A.; Shannon, C., A diruthenium-substituted polyoxometalate as an electrocatalyst for oxygen generation. *J. Am. Chem. Soc* **2004**, *126* (39), 12258-12259.

# Annexure - II

3A.S1 Crystal o	lata, data coll	ection, and refi	nement param	eters for 1, 2, 3 and	d 1-M, 2-M, 3-N	М
	1	1-M	2	2-M	3	3-M
CCDC number	2330248	2330238	2330240	2330247	2330239	2330253
empirical	$Fe_6H_{22}Na_{13}$	Fe <sub>6</sub> H <sub>20</sub> Mo <sub>2.24</sub> N	H <sub>12</sub> FeNa <sub>16</sub> O <sub>10</sub>	Fe <sub>6</sub> H <sub>64</sub> K <sub>4</sub> Mo <sub>5.4</sub> Na	Co <sub>4</sub> Fe <sub>2</sub> H <sub>12</sub> Na <sub>1</sub>	Co <sub>4</sub> Fe <sub>2</sub> H <sub>24.6</sub> Mo <sub>2.84</sub>
formula	$O_{108}W_{18}$	$a_{11}O_{102}W_{15.8}$	$_{9}W_{18}Zn_{5}$	$_{24}O_{192}W_{30.6}Zn_{6}$	$_{6}\mathrm{O}_{106}\mathrm{W}_{18}$	$Na_{12}O_{108.02}W_{15.16}$
formula weight	5693.44	5352.53	5815.94	10715.87	5732.66	5436.05
Temperature/K	273.15	273.15	273.15	273.15	273.15	273.15
crystal system	Monoclinic	Triclinic	monoclinic	monoclinic	monoclinic	Monoclinic
space group	P2 <sub>1</sub> /n	P1	P2 <sub>1</sub> /n	P2 <sub>1</sub> /n	P2 <sub>1</sub> /n	P2 <sub>1</sub> /n
unit cell dimension						
a (Å)	13.0961(2)	12.920(3)	13.091(5)	12.8933(5)	13.064(3)	13.0895(6)
b (Å)	17.8110(4)	13.135(3)	17.747(6)	16.4920(6)	17.740(4)	17.7586(8)
c (Å)	21.1982(5)	15.044(4)	21.132(7)	21.6243(7)	21.015(6)	21.1435(11)
a (deg)	90	101.492(8)	90	90	90	90
β (deg)	93.5170(10)	96.826(8)	93.655(12)	104.6600(4)	93.599(9)	93.488(2)
γ (deg)	90	114.429(7)	90	90	90	90
$V(\mathring{A}^3)$	4935.27(18)	2219.3(10)	4899(3)	4448.4(3)	4861(2)	4905.7(4)
Z	2	1	2	1	2	2
ρ (calculated)	3.818	4.005	3.942	4.000	3.917	3.680
(g/cm <sup>3</sup> )						
$\mu/mm^{-1}$	21.910	21.764	22.575	21.597	22.348	19.163
F (000)	5034.0	2373.0	5136	4767.0	5056.0	4844.0
crystal size	0.31 x 0.24 x	0.25 x 0.22 x	0.34 x 0.32 x	0.35 x 0.27 x 0.17	0.41 × 0.41 ×	$0.32\times0.32\times0.32$
(mm <sup>3</sup> )	0.14	0.12	0.24		0.22	
2Θ range for	3.85 to	4.016 to	4.414 to	4.094 to 52.854	4.248 to 53.12	4.408 to 52.842
data	52.81	52.744	50.054			
collection/°						
index ranges	$-16 \le h \le 16$ ,	$-16 \le h \le 16, -16$	$-15 \le h \le 15, -$	$-16 \le h \le 16, -20$	$-16 \le h \le 15, -$	$-15 \le h \le 16, -22$
	$-22 \le k \le 22,$	$15 \le k \le 16$ , -	$20 \le k \le 20$ , -	$\leq k \leq 20, -26 \leq l \leq$	$19 \le k \le 21$ , -	$\leq k \leq 22, -23 \leq l \leq$
	<b>-</b> 26 ≤ 1 ≤ 26	$18 \le l \le 18$	$25 \le l \le 25$	26	$26 \le l \le 18$	26
no. of reflection collected /unique	64932/10134	23031/9026	30093/8365	47592/9082	24711/9975	41028/10022
GOF on F <sup>2</sup>	1.044	1.040	1.039	1.104	1.029	1.086
final $R$ indices $(I > 2\sigma(I))$	R1=0.025, wR2=0.05	R1=0.050, wR2=0.136	R1=0.048, wR2=0.120	Rl=0.029, wR2=0.074	$R_1 = 0.039,$ $wR_2 = 0.094$	$R_1 = 0.028, wR_2 = 0.070$

R indices (all	R1=0.031,	R1=0.055,wR	R1=0.067,	R1=0.032,	$R_1 = 0.050,$	$R_1 = 0.030, wR_2 =$
data)	wR2=0.063	2=0.142	wR2=0.136	wR2=0.075	$wR_2 = 0.100$	0.071
data/restraints	10134/1/680	9026/0/628	8365/0/685	9082/0/626	9975/0/671	10022/0/675
/param						
Largest diff.	1.44/-1.23	3.00/-3.50	2.17/-3.97	2.49/-1.27	3.01/-1.46	2.39/-1.36
peak/hole/e Å-3						

	4	4-M	5	5-M
CCDC number	2330243	2330242	2330255	2330245
empirical formula	$\begin{array}{c} H_{48}Mn_4Na_{24}O_{216} \\ W_{36.6}Zn_{7.4} \end{array}$	$\begin{array}{c} H_{16}Mn_2Mo_{0.24}Na_{14} \\ O_{106}W_{18.16}Zn_{3.6} \end{array}$	Co <sub>8</sub> H <sub>38</sub> Mn <sub>4</sub> Na <sub>24</sub> O <sub>216</sub> W <sub>36</sub>	$\begin{array}{c} Co_{3.8}H_{16}Mn_2Mo_{0.4}Na_{12}O_{108}W_{17.8} \end{array}$
formula weight	11488.55	5740.94	11355.86	5664.73
temp (K)	273.15	273.15	273.15	273.15
crystal system	monoclinic	Monoclinic	monoclinic	monoclinic
space group	P2 <sub>1</sub> /n	P2 <sub>1</sub> /n	P2 <sub>1</sub> /n	P2 <sub>1</sub> /n
unit cell dimension				
a (Å)	13.094(5)	13.152(2)	13.090(4)	13.1630(17)
b (Å)	17.717(7)	17.774(3)	17.795(6)	17.768(3)
c (Å)	21.014(8)	21.019(3)	21.125(8)	21.106(3)
α (deg)	90	90	90	90
β (deg)	93.582(12)	93.447(6)	93.497(11)	93.538(5)
γ (deg)	90	90	90	90
$V(\mathring{\mathbf{A}}^3)$	4865(3)	4904.4(14)	4912(3)	4926.7(12)
Z	1	2	1	2
ρ (calculated) (g/cm³)	3.921	3.888	3.839	3.819
μ/mm <sup>-1</sup>	22.857	22.523	22.061	21.778
F (000)	5070.0	5060.0	5010.0	4997.0
crystal size (mm³)	0.34 × 0.27 × 0.22	$0.32 \times 0.31 \times 0.25$	$0.27 \times 0.22 \times 0.21$	$0.23 \times 0.21 \times 0.14$
2Θ range for data collection/°	3.872 to 53.02	4.234 to 52.904	3.864 to 54.984	3.866 to 55.066
index ranges	$-16 \le h \le 14, -22$	$-16 \le h \le 16, -22 \le k$	$-16 \le h \le 14, -23 \le k$	$-16 \le h \le 17, -23 \le k$
	$\leq$ k $\leq$ 22, -26 $\leq$ 1	$\leq 22, -26 \leq 1 \leq 26$	$\leq 22, -27 \leq 1 \leq 27$	$\leq 23, -27 \leq 1 \leq 27$
	≤ 26			
no. of reflection collected /unique	39686/ 10042	34878/ 10078	44089/11193	50057/11315

GOF on F <sup>2</sup>	1.036	1.063	1.050	1.050
final R indices	$R_1 = 0.0367,$	$R_1 = 0.0333, wR_2 =$	$R_1 = 0.0339, wR_2 =$	$R_1 = 0.0387, WR_2 =$
$(I > 2\sigma(I))$	$wR_2 = 0.0794$	0.0836	0.0872	0.0902
R indices (all data)	$R_1 = 0.052,$	$R_1 = 0.039, WR_2 =$	$R_1 = 0.041, wR_2 =$	$R_1 = 0.054, wR_2 =$
	$wR_2 = 0.087$	0.086	0.092	0.099
data/restraints/par	10042/0/666	10078/0/665	11193/0/663	11315/0/663
am				
Largest diff.	2.38/-1.87	2.17/-1.55	2.56/-1.58	2.34/-1.95
peak/hole / e Å-3				

Table 3A.S3 Assignment of ESI-mass peaks of 1/1-M						
Charge	m/z (obs.)	m/z (calc.)	Mol. Wt.	Assigned probable formula		
-3	1580.77	1580.46	4741.40	H <sub>9</sub> Fe <sub>4</sub> (Fe <sub>2</sub> W <sub>18</sub> O <sub>68</sub> )		
-3	1586.10	1587.12	4761.36	$NaH_6Fe_4(Fe_2W_{18}O_{68})$		
-3	1551.41	1550.44	4651.34	$H_7Fe_4(Fe_2MoW_{17}O_{68})$		
-3	1521.74	1521.10	4563.30	$H_7Fe_4(Fe_2Mo_2W_{16}O_{68})$		
-3	1492.40	1491.75	4475.26	$H_7Fe_4(Fe_2Mo_3W_{15}O_{68})$		
-3	1462.38	1462.40	4387.22	$H_7Fe_4(Fe_2Mo_4W_{14}O_{68})$		
-3	1433.71	1433.06	4299.18	$H_7Fe_4(Fe_2Mo_5W_{13}O_{68})$		

Table 3A.S4 Bond valence parameter (BVS) of selected atoms calculated							
from the SC-XRD structure 1 and 1-M							
POMs	Transition metal	Oxidation state					
		value					
	W	6.061	+6				
1	Fe1	3.121	+3				
	Fe2	3.029	+3				
	Fe3	2.006	+2				
	Mo	6.147	+6				
	W	6.053	+6				
1-M	Fe1	3.167	+3				
	Fe2	3.044	+3				
	Fe3	3.012	+3				

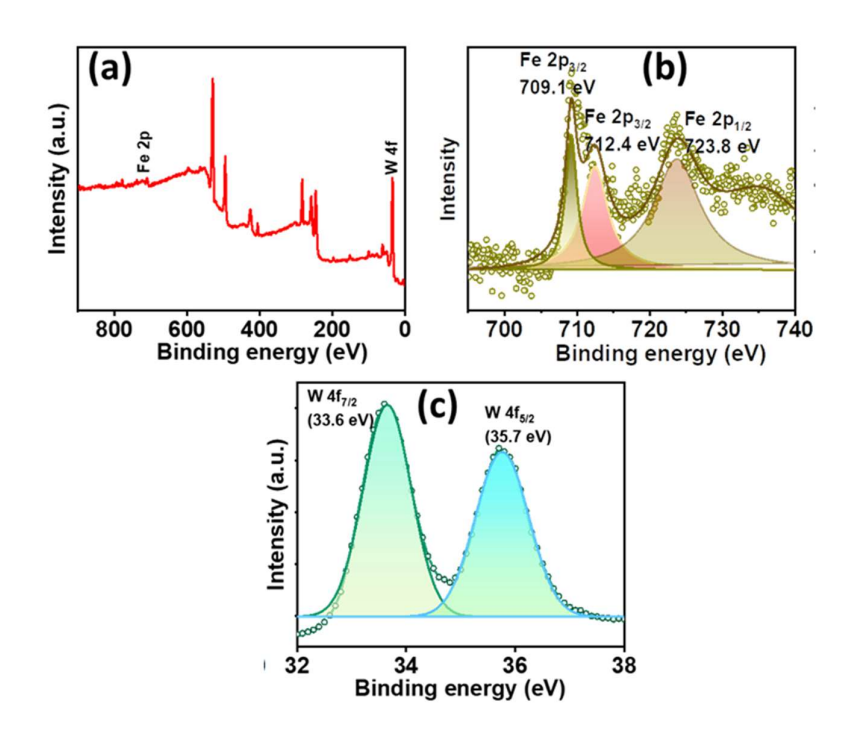


Figure 3A.S1 XP spectra of 1 showing (a) Survey spectra of 1, (b) Fe 2p, and (c) W 4f<sub>7/2</sub> and 4f<sub>5/2</sub>.

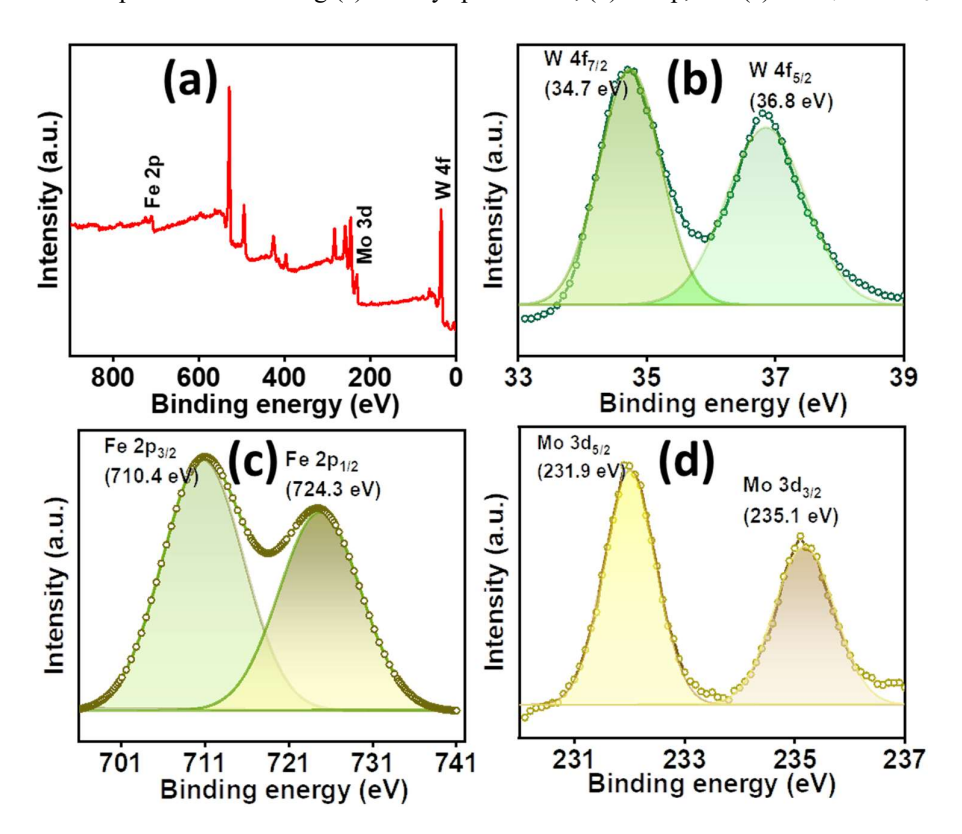
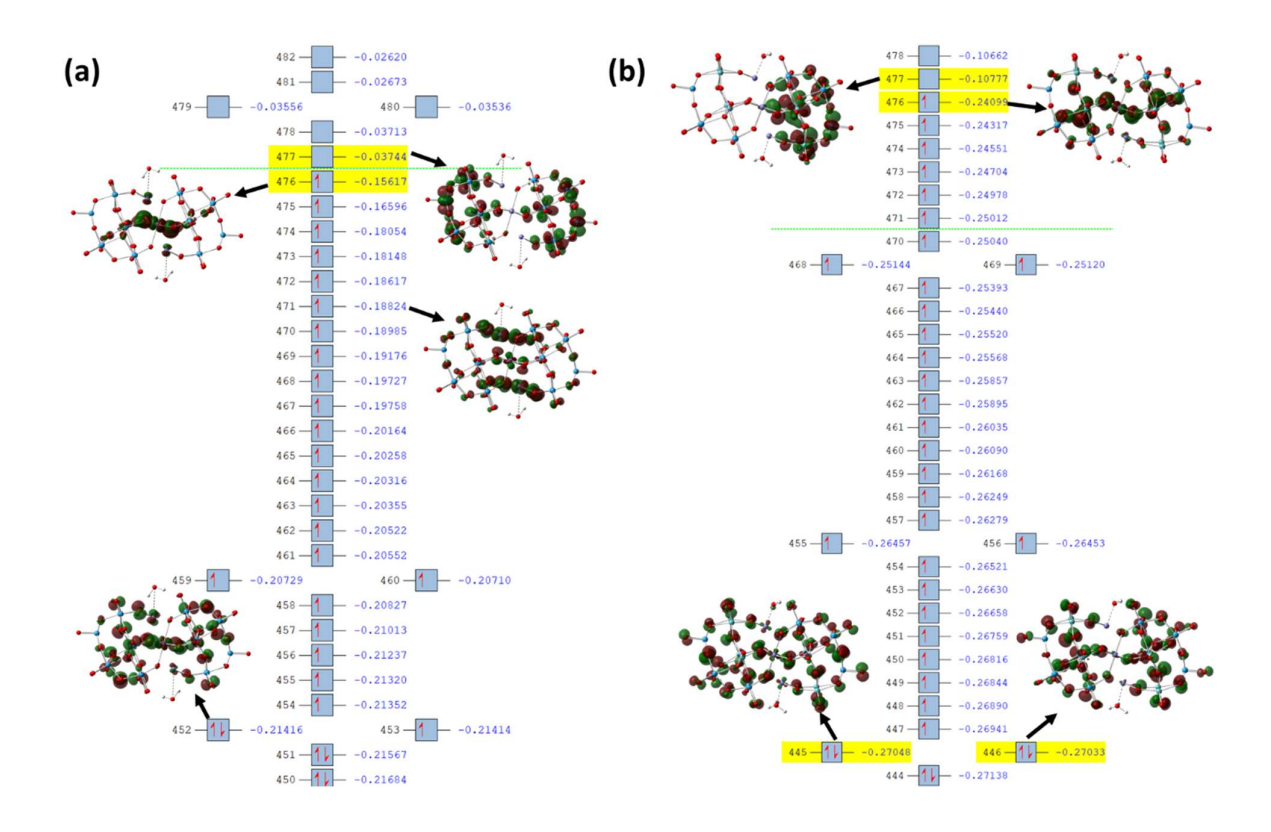


Figure 3A.S2 XP spectra of 1-M (a) Survey spectra, (b) W  $4f_{7/2}$  and  $4f_{5/2}$  (c) Fe 2p, and (d) Mo 3d.



**Figure 3A.S3** Frontier Molecular orbitals (FMOs) showing HOMOs, LUMOs, and some of the SOMOs of representative structures of (a) 1 and (b) 1-M.

Sandwich POMs	TMx-O <sub>h</sub>	Ομ4-	Oμ4-TMe	TM <sub>e</sub> -O <sub>c</sub> (μ <sub>2</sub>	Oc-W/Mo	Sum of bond
TM <sub>x</sub> -(TM) <sub>4</sub> W <sub>18</sub>		TMi		oxygen)		lengths $X-O_h$ and $O\mu_4-TM_i$
Fe-Fe <sub>2</sub> Co <sub>2</sub> W <sub>18</sub>	1.880	2.024	2.015	2.095	1.774	3.904
Co-Co <sub>2</sub> Bi <sub>2</sub> W <sub>18</sub>	1.955	2.112	2.016	2.153	1.856	4.067 (distorted)
Cu-Cu <sub>4</sub> W <sub>18</sub>	1.866	2.016	2.022	2.090	1.774	3.872
Fe-Fe <sub>2</sub> Dy <sub>2</sub> W <sub>18</sub>	1.849	2.049	2.514	2.246	1.772	3.898
Fe-Fe <sub>4</sub> W <sub>18</sub>	1.852	2.048	2.047	1.990	1.803	3.900
Fe-Fe <sub>2</sub> Mn <sub>2</sub> W <sub>18</sub>	1.848	2.041	2.076	2.033	1.807	3.889
Fe-Fe <sub>2</sub> Ni <sub>2</sub> W <sub>18</sub>	1.832	2.039	2.034	1.997	1.824	3.871
Ni-Ni <sub>4</sub> W <sub>18</sub>	1.849	2.063	1.992	2.074	1.814	3.912
Zn-Zn <sub>2</sub> Bi <sub>2</sub> W <sub>18</sub>	1.944	2.164	2.076	2.178	2.326	4.108 (distorted)
Zn-Ru <sub>2</sub> Zn <sub>2</sub> W <sub>18</sub>	1.932	2.033	2.060	2.072	1.769	3.965
Zn-WZn <sub>3</sub> W <sub>18</sub>	1.930	2.039	2.043	2.070	1.768	3.969
Zn-WZnMn <sub>2</sub> W <sub>18</sub>	1.936	2.025	2.142	2.114	1.780	3.961

Co-WCo <sub>3</sub> W <sub>18</sub>	1.938	2.030	2.049	2.074	1.771	3.968
Zn-WZnCo <sub>2</sub> W <sub>18</sub>	1.927	2.048	2.051	2.062	1.782	3.975
Zn-WZnNi <sub>2</sub> W <sub>18</sub>	1.923	2.019	2.022	2.043	1.771	3.942
Zn-WZnCu <sub>2</sub> W <sub>18</sub>	1.936	2.063	2.069	2.079	1.757	3.999

 $TM_X$ = transition metal/P at heteroposition,  $TM_i$  = transition metal at internal sandwich position,  $O\mu_4$  = tetradentate oxygen ligand between heteroatom and transition metal,  $TM_e$  = transition metal at external position,  $O_c$  = corner shared oxygen

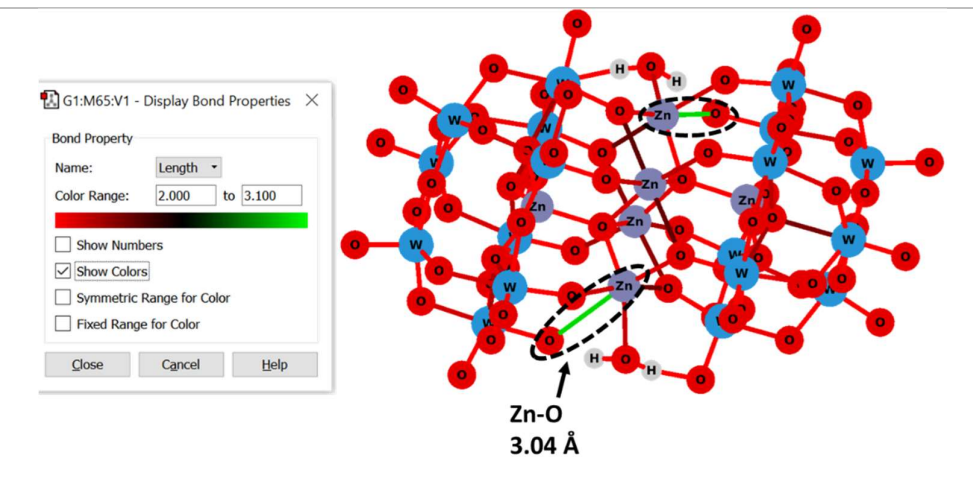


**Figure 3A.S4** DFT optimized auxiliary structure of Zn-based POM [ $\{Zn_4(H_2O)_2(ZnW_9O_{34})_2\}^{16-}$ ] (elongated bond length shown in green).

<b>Table 3A.S6</b> BVS of selected atoms calculated from the SC-XRD structure of <b>2</b> and <b>2-M.</b>						
POMs	Transition metal	Bond valence sum value	Oxidation state			
	W	6.123	+6			
	Fe1	3.145	+3			
2	Zn1	2.461	+2			
	Zn2	2.100	+2			
	Zn3	2.267	+2			
	Mo	6.154	+6			
	W	6.044	+6			
2-M	Zn1	2.501	+2			
2-IVI	Zn2	2.345	+2			
	Fe1	3.098	+3			
	Fe2	3.027	+3			

Charge Mol. Wt. m/z  $\mathbf{m}/\mathbf{z}$ Assigned probable formula (obs.) (calc.) -3 1594.84 1593.79 4762.39  $H_{11}Zn_{2}Fe_{2}(Zn_{2}W_{18}O_{68}) \\$ -2 2412.64 2413.17 4826.34  $H_{10}Na_{2}Zn_{2}Fe_{2}(Zn_{2}W_{18}O_{68}) \\$ -3 1560.33 1560.77 4682.33  $H_{10}Zn_2Fe_2(ZnFeMoW_{17}O_{68})$ 

4595.29

 $H_{10}Zn_2Fe_2(ZnFeMo_2W_{16}O_{68})$ 

Table 3A.S7 Assignment of ESI-mass peaks of 2/2-M

1531.76

146

-3

1530.00

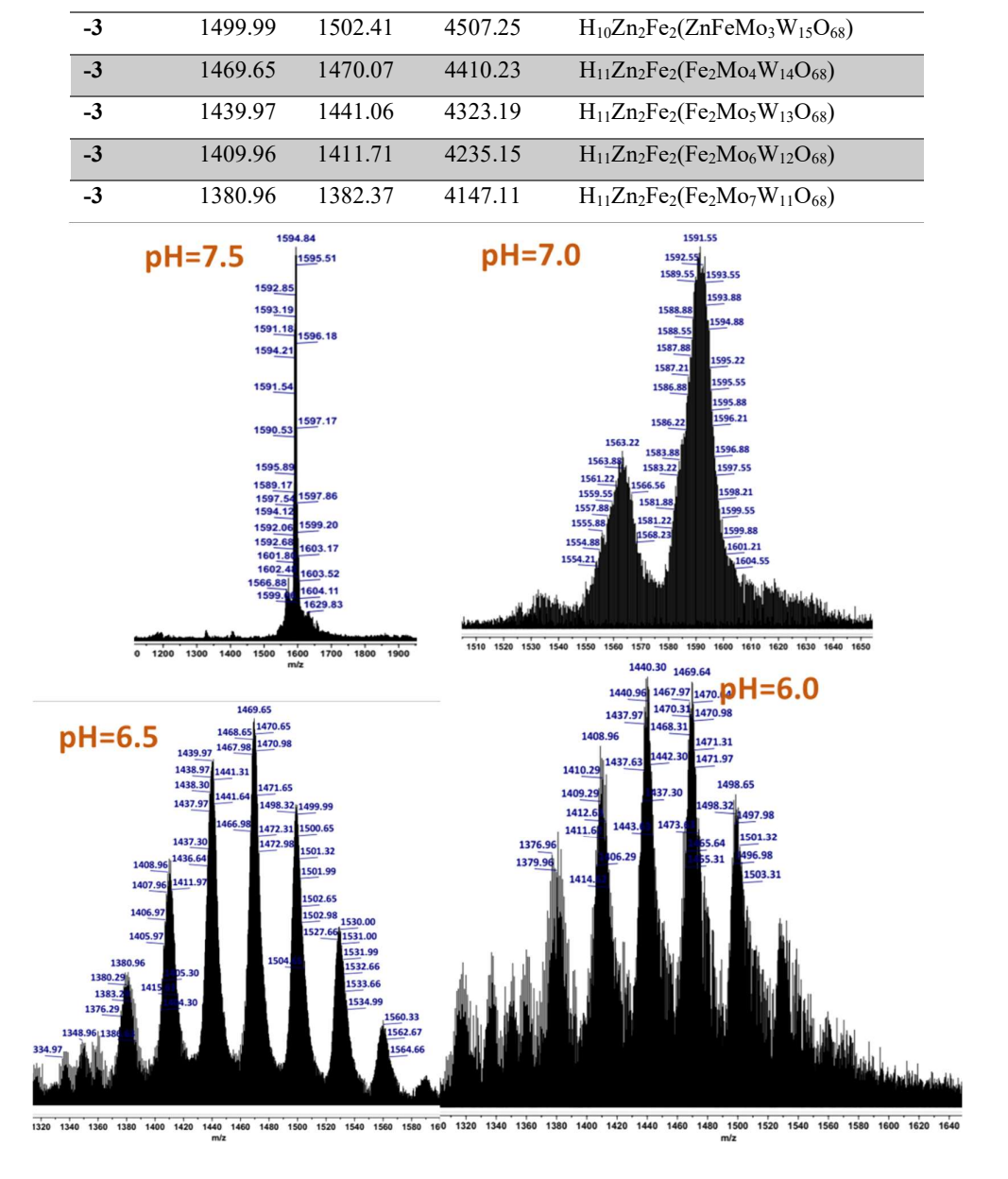


Figure 3A.S5 pH-dependent ESI-MS spectra of 2-M with charge (z)=-3

Table 3A.S8 Assignment of ESI-mass peaks of 2-M (pH-dependent study)					
Charge	m/z	m/z	Mol. Wt.	Assigned probable formula	
	(obs.)	(calc.)			
-3	1594.84	1593.79	4781.37	$H_{11}Zn_2Fe_2(Zn_2W_{18}O_{68})$	
-3	1563.22	1564.44	4693.33	$H_{11}Zn_2Fe_2(Zn_2MoW_{17}O_{68})$	
-3	1560.33	1560.77	4682.33	$H_{10}Zn_2Fe_2(ZnFeMoW_{17}O_{68})$	
-3	1530.00	1531.76	4595.29	$H_{10}Zn_2Fe_2(ZnFeMo_2W_{16}O_{68})$	
-3	1499.99	1502.41	4507.25	$H_{10}Zn_2Fe_2(ZnFeMo_3W_{15}O_{68})$	
-3	1469.65	1470.07	4410.23	$H_{11}Zn_{2}Fe_{2}(Fe_{2}Mo_{4}W_{14}O_{68})$	
-3	1439.97	1441.06	4323.19	$H_{11}Zn_2Fe_2(Fe_2Mo_5W_{13}O_{68})$	
-3	1409.96	1411.71	4235.15	$H_{11}Zn_2Fe_2(Fe_2Mo_6W_{12}O_{68})$	
-3	1380.96	1382.37	4147.11	$H_{11}Zn_{2}Fe_{2}(Fe_{2}Mo_{7}W_{11}O_{68})$	

	Bond valence param structure of 3 and 3-N		s calculated from
POMs	Transition metal	<b>Bond valence sum</b>	Oxidation state
		value	
	W	6.131	+6
	Fe	3.075	+3
3	Co1	2.362	+2
	Co2	2.059	+2
	Mo	6.106	+6
	W	6.059	+6
3-M	Fe	3.210	+3
	Co1	2.543	+2
	Co2	2.011	+2
Co 2p	W 46	Intensi	
800 600 Bind	400 200 ling energy (eV)	0 35 36 37 Binding	38 39 energy (eV)
Co 3d <sub>5/2</sub> (	782 5 eV)	Fe 3d <sub>5/2</sub> (713	/ 1\
	Co 3d <sub>3/2</sub> (797.8 eV)	Intensity (a.u.)	Fe 3d <sub>3/2</sub> (723.47 eV)
min	Comment Comment	Translate .	Communication

Figure 3A.S6 XP spectra of 3 showing (a) Survey spectra of 3, (b) W  $4f_{7/2}$  and  $4f_{5/2}$  (c) Co 3d, and (d) Fe 3d.

Table 3A.S10 Assignment of ESI-mass peaks of 3/3-M					
Charge	m/z (obs.)	m/z (calc.)	Mol. Wt.	Assigned probable formula	
-3	1585.18	1584.13	4752.39	$H_{10}Co_2Fe_2(FeCoMo_3W_{15}O_{68})$	
-3	1495.28	1495.75	4487.27	$H_{10}Co_2Fe_2(FeCoMo_3W_{15}O_{68})$	
-3	1466.94	1466.74	4400.23	$H_{10}Co_2Fe_2(FeCoMo_4W_{14}O_{68})$	
-3	1435.94	1436.06	4308.19	$H_9Co_2Fe_2(Fe_2Mo_5W_{13}O_{68})$	
-3	1406.26	1406.71	4220.15	$H_9Co_2Fe_2(Fe_2Mo_6W_{12}O_{68})$	
-3	1377.25	1377.37	4132.11	H <sub>9</sub> Co <sub>2</sub> Fe <sub>2</sub> (Fe <sub>2</sub> Mo <sub>7</sub> W <sub>11</sub> O <sub>68</sub> )	
-3	1347.57	1347.68	4043.06	$H_9Co_2Fe_2(Fe_2Mo_7W_{11}O_{68})$	

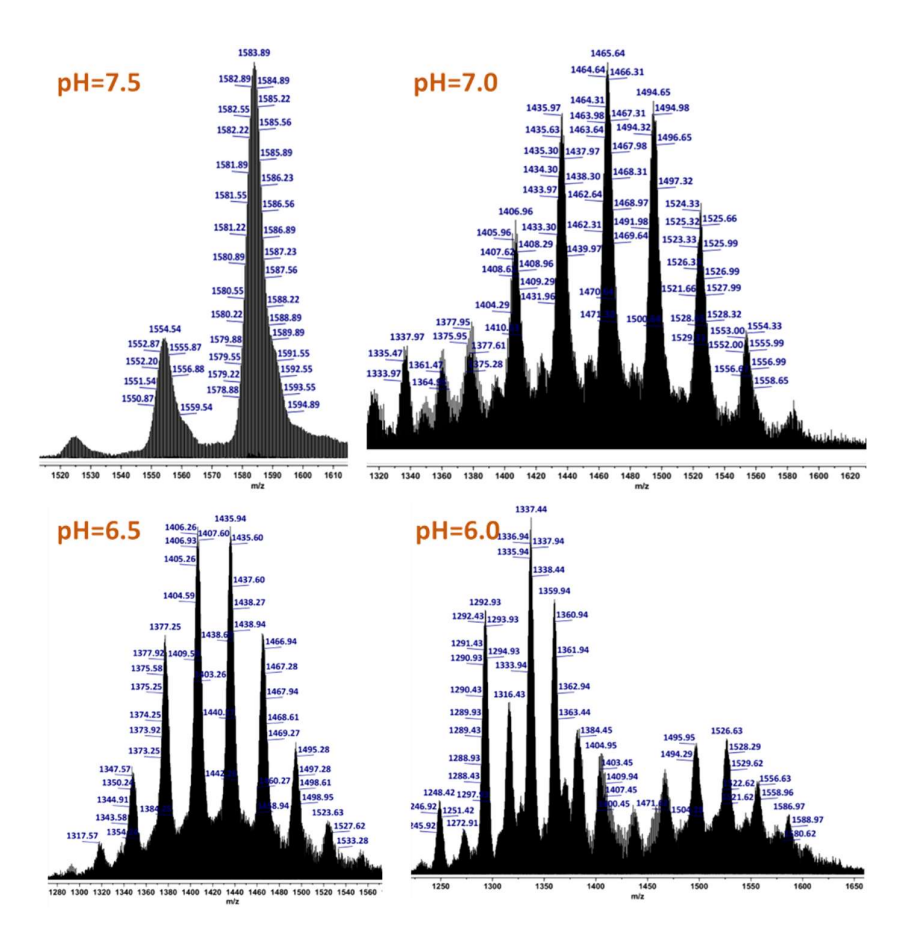
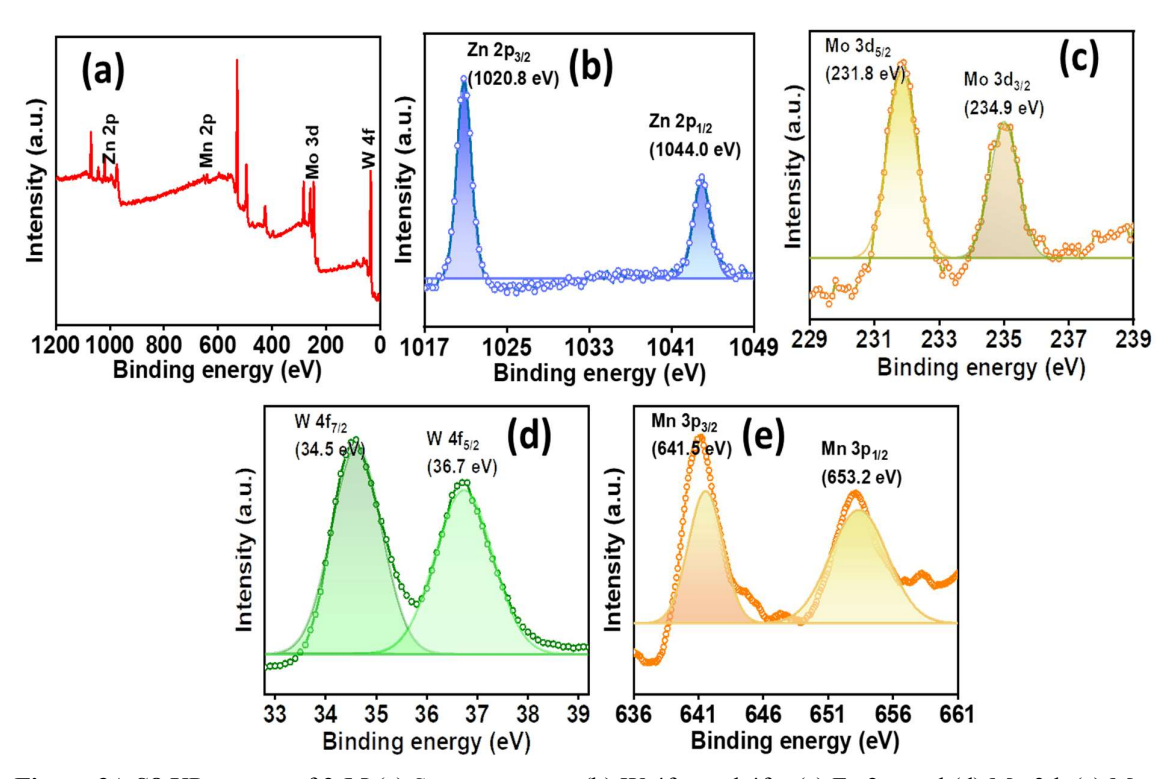


Figure 3A.S7 pH-dependent ESI-MS spectra of 3-M with charge (z)= -3

Table 3A.S11 Assignment of ESI-mass peaks of 3-M (pH dependent study)					
Charge	m/z	m/z	Mol. Wt.	Assigned probable formula	
	(obs.)	(calc.)			
-3	1554.54	1554.45	4663.35	$H_{10}Co_2Fe_2(FeCoMoW_{17}O_{68})$	
-3	1524.33	1525.10	4575.31	$H_{10}Co_2Fe_2(FeCoMo_2W_{16}O_{68})$	
-3	1494.65	1495.75	4487.27	$H_{10}Co_2Fe_2(FeCoMo_3W_{15}O_{68})$	
-3	1465.64	1466.74	4400.23	$H_{10}Co_2Fe_2(FeCoMo_4W_{14}O_{68})$	
-3	1435.97	1436.06	4308.19	$H_9Co_2Fe_2(Fe_2Mo_5W_{13}O_{68})$	
-3	1406.96	1406.71	4220.15	$H_9Co_2Fe_2(Fe_2Mo_6W_{12}O_{68})$	
-3	1377.25	1377.37	4132.11	$H_9Co_2Fe_2(Fe_2Mo_7W_{11}O_{68})$	
-3	1347.57	1348.02	4044.07	$H_9Co_2Fe_2(Fe_2Mo_8W_{10}O_{68})$	
-3	1317.57	1318.67	3956.03	H <sub>9</sub> Co <sub>2</sub> Fe <sub>2</sub> (Fe <sub>2</sub> Mo <sub>9</sub> W <sub>9</sub> O <sub>68</sub> )	

<b>Table 3A.S12</b> BVS parameter of selected atoms calculated from the SC-XRD structure of <b>4</b> and <b>4-M</b> .						
POMs	Transition metal	Bond valence sum value	Oxidation state			
	W	6.127	+6			
4	Mn	3.070	+3			
4	Zn1	2.246	+2			
	Zn2	2.108	+2			

	W	6.086	+6
	Mo	6.039	+6
4-M	Zn	2.313	+2
	Zn	2.260	+2
	Mn	3.104	+3



**Figure 3A.S8** XP spectra of **2-M** (a) Survey spectra, (b) W  $4f_{7/2}$  and  $4f_{5/2}$  (c) Fe 2p, and (d) Mo 3d, (e) Mn 3p.

Table 3A	Table 3A.S13 Assignment of ESI-mass peaks of 4/4-M					
Charge	m/z m/z Mol. Wt. Assigned probable form		Assigned probable formula			
	(obs.)	(calc.)				
-3	1592.75	1593.12	4779.37	$H_{11}Zn_2Mn_2(Zn_2W_{18}O_{68})$		
-3	1637.07	1635.11	4905.35	$H_{11}Zn_2MnW(Zn_2W_{18}O_{68})$		
-3	1635.73	1635.45	4906.36	$H_{11}MnWZn_2(Zn_2W_{18}O_{68})$		
-3	1607.73	1606.44	4819.32	$NaH_8WMn_3(Zn_2MoW_{17}O_{68})$		
-3	1590.74	1589.46	4768.38	$H_{11}ZnMn_3(Zn_2W_{18}O_{68})$		
-3	1576.71	1578.43	4735.29	$Na_2H_9Zn_2Mn_2(Zn_2MoW_{17}O_{68})$		

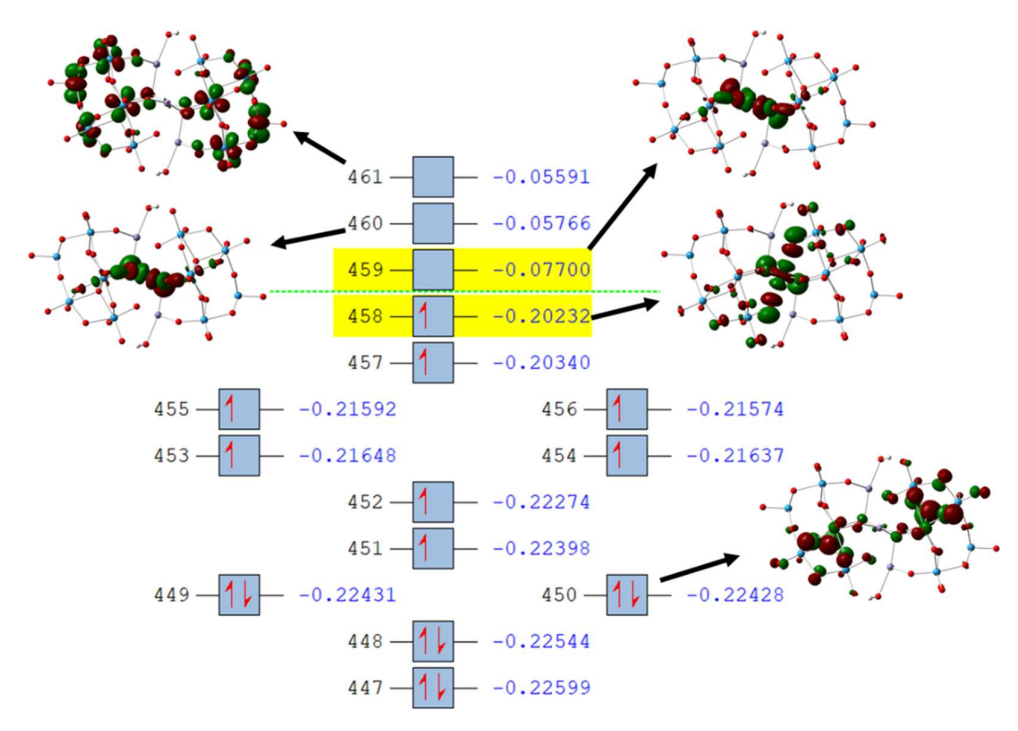


**Figure 3A.S9** Frontier molecular orbitals of tetrasubstituted sandwich POMs showing the effect of Mo doping on band gaps as well as shifting of electron density on addenda atoms in 4.

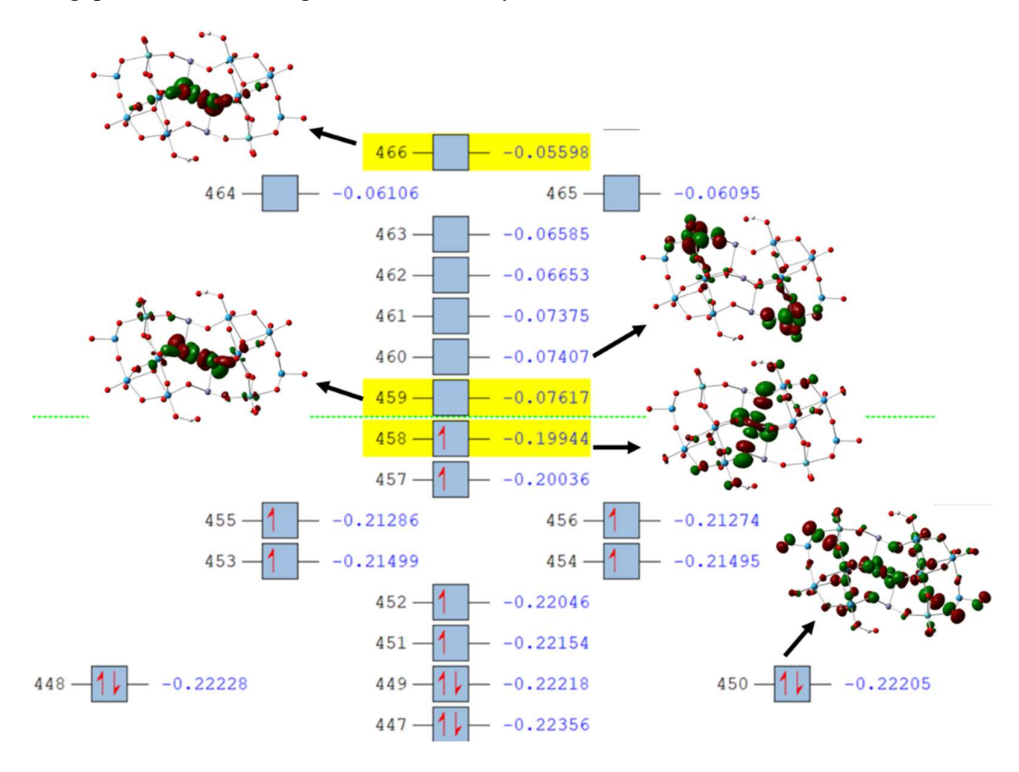


**Figure 3A.S10** Frontier molecular orbitals of tetrasubstituted sandwich POMs showing the effect of Mo doping on band gaps as well as shifting of electron density on addenda atoms in **4-M**.

Table 3A.S14 BVS of selected atoms calculated from the SC-XRD structure of 5 and 5-M						
POMs	Transition metal	Bond valence sum value	Oxidation state			
	W	6.054	+6			
5	Co1	2.111	+2			
3	Co2	2.018	+2			
	Mn1	3.001	+3			
	W	6.054	+6			
	Mo	6.109	+6			
5-M	Co1	2.125	+2			
	Co2	2.316	+2			

3.026

+3

Table 3A.S15 Assignment of ESI-mass peaks of 5/5-M

Mn1

Charge	m/z	m/z (calc.)	Mol. Wt.	Assigned probable formula
	(obs.)			
-3	1584.09	1584.46	4753.38	H <sub>11</sub> C02Mn <sub>2</sub> (C02W <sub>18</sub> O <sub>68</sub> )
-3	1554.74	1555.11	4665.34	H11C02Mn2(C02M0W17O68)
-3	1524.39	1525.77	4577.31	H <sub>11</sub> Co <sub>2</sub> Mn <sub>2</sub> (Co <sub>2</sub> Mo <sub>2</sub> W <sub>16</sub> O <sub>68</sub> )
-3	1600.41	1601.43	4804.31	H <sub>7</sub> NaMn <sub>3</sub> W(Co <sub>2</sub> MoW <sub>17</sub> O <sub>68</sub> )
-3	1631.42	1632.11	4896.35	H6NaCoWMn2(Co2W18O68)

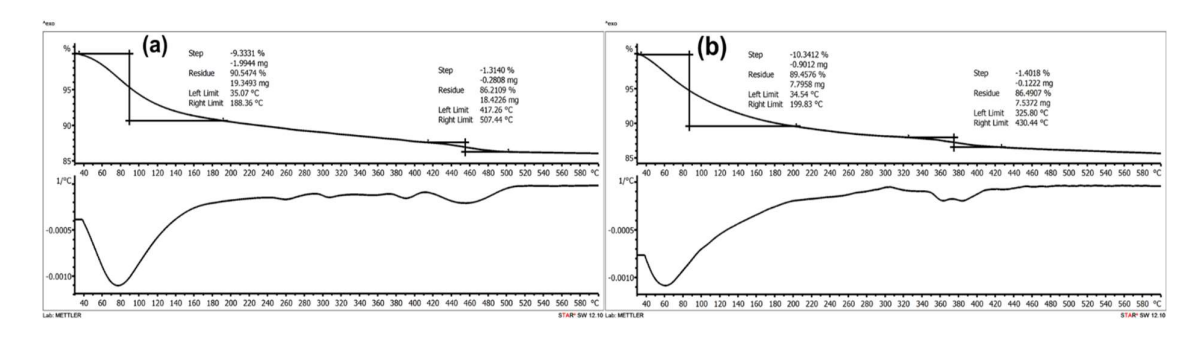


Figure 3A.S11 TGA curve along with corresponding first derivative of (a) 2 and (b) 2-M.

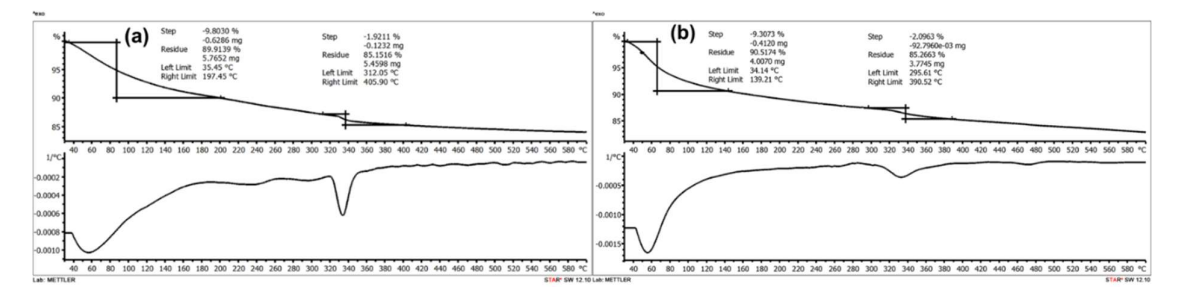
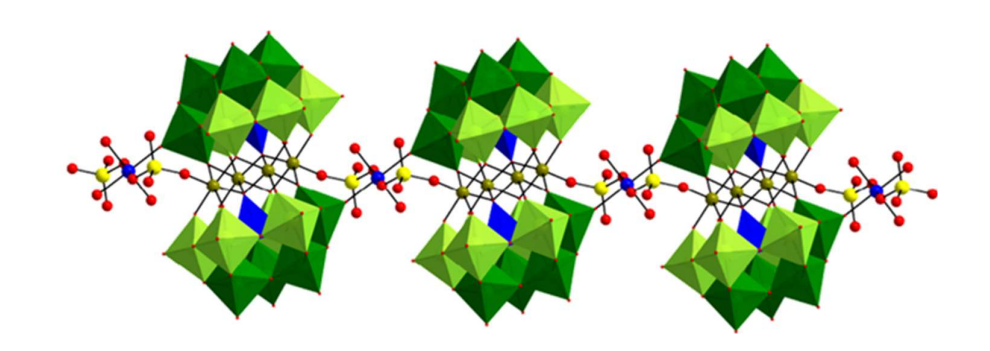


Figure 3A.S12 TGA curve along with corresponding first derivative of (a) 4 (b) 4-M.

## **Chapter 3**

## **Section B**

## Role of Charge Density towards formation of Framework Structures in Sandwich Polyoxometalates



#### **3B.1 Introduction**

The self-assembly of sandwich polyoxometalates (POMs) is significantly affected by the specific transition metal substitution and the overall cluster charge. Moreover, POMs feature oxygen atoms that exhibit flexibility in their coordination with transition or rare-earth metal ions.<sup>1, 2</sup> This characteristic enables POMs to construct one-, two-, or three-dimensional frameworks composed solely of inorganic components.<sup>3, 4</sup> These frameworks are known as POM-based coordination frameworks (POMCFs) and represent a substantial category of inorganic solid-state materials.<sup>1, 5</sup> However, the formation of entirely inorganic three-dimensional frameworks consisting exclusively of metal ions interconnected by POM building blocks remains relatively rare.

Recently, POMCFs consisting of mainly sandwich POMs have found applications in various fields such as catalysis, conductivity, and pollutant degradation. The formation of these POMCFs is highly dependent on charge/size ratio and the charge distribution on the covalently connected water molecule and its nearest terminal oxygens connected within the sandwich POM framework. The large difference in charge distribution on oxygen of water molecule and terminal oxygen of nearest addenda of framework in the DFT optimized structure directs the covalent attachment of the incoming transition metals at that position. Also, it is worth mentioning that POMs having higher charge/size ratio opt for the POMCPs, e.g., charge greater than -12 along with mix transition metals in Weakley type sandwich POMs favours the formation of POMCFs.

#### 3B.2. Results and Discussion

#### **3B.2.1 Synthetic Chemistry**

In mixed transition metals-based Weakley type sandwich POMs, the total charge can be tuned up to -16 using the transition metals in their lowest stable oxidation state (e.g. in formula  $[M_2M^2(H_2O)_2(MW_9O_{34})_2]$  (M=M'=transition metal with +2 oxidation state). Here, we build our efforts to use mix transition metals along with tuning the charge/size ratio (overall charge variation from -12 to -16 in the same framework). To further tuning the charge distribution on the oxygens participating in the formation of POMCPs, mixed addenda strategy was applied. Further, for charge/size ratio 0.174 (charge -16), in formula  $[M_2M^2(H_2O)_2(MW_9O_{34})_2]$  (M=M'=transition metal with +2 oxidation state) has higher tendency for the formation of POMCFs which leads fast crystallization and hence difficulty in isolating the single crystal of these POMs.

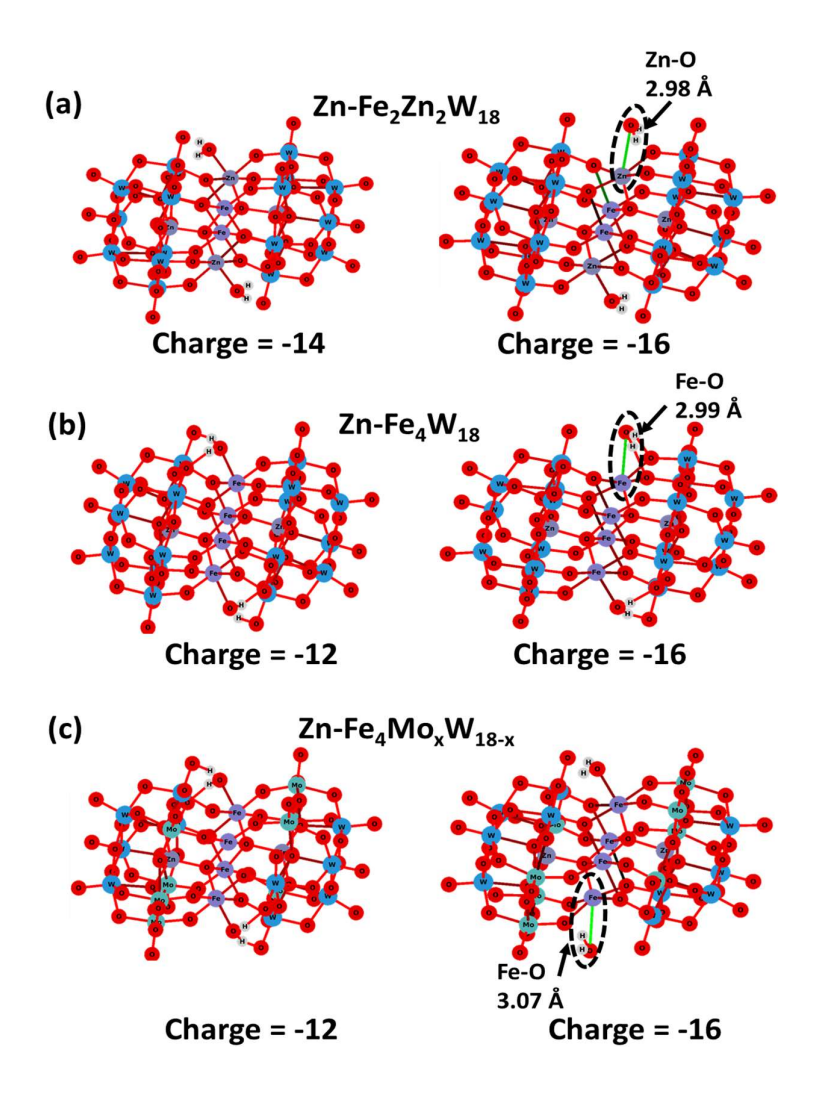


**Figure 3B.1** DFT optimized auxiliary structure of sandwich POMs with the general formula (a)  $[Zn_2Fe_2(H_2O)_2(ZnW_9O_{34})_2]^{n-}$  where n=14/16 (b)  $[Fe_4(H_2O)_2(ZnW_9O_{34})_2]^{n-}$  where n=12/16 (c)  $[Fe_4(H_2O)_2(ZnMo_xW_{9-x}O_{34})_2]^{n-}$  where n=12/16 showing elongated bond lengths (shown in green color).

To explore the influence of high negative charge density on the POM structure resulting from low oxidation state TM (+2), we conducted the DFT optimizations of the auxiliary structures  $[(TM_e)_2(TM_i)_2(H_2O)_2(ZnW_9O_{34})_2]^{16}$  ( $TM_e = Zn^{2+}$  or  $Fe^{2+}$ ,  $TM_i = Fe^{2+}$ ). The optimized structures of  $[Fe_4(H_2O)_2(ZnW_9O_{34})_2]^{16}$  ( $TM_e = TM_i = Fe^{2+}$ ,  $X = Zn^{2+}$ ) and  $[Zn_2Fe_2(H_2O)_2(ZnW_9O_{34})_2]^{16}$ , ( $TM_e = Zn^{2+}$ ,  $TM_i = Fe^{2+}$ ) revealed an elongation of the  $TM_e$ -H<sub>2</sub>O bond due to increased charge density (Fig. 3B.1). This elongation further increased in the case of mixed addenda POM ( $[Fe_4(H_2O)_2(ZnMo_4W_5O_{34})_2]^{16}$ , 3B.1c). These findings indicate the crucial role of precursors oxidation states in influencing the self-assembly towards POMCF. To understand the effect,  $Fe^{2+}/Zn^{2+}$  were taken as precursors instead of  $Fe^{3+}/Zn^{2+}$  in **2-M**. Strikingly, SC-XRD and ESI-MS reveal a much lower Mo:W ratio in the POM framework

compared to **2-M**. The SC-XRD structure in Fig 3B.2 confirms the formation of a POMCFs, Na<sub>2</sub>ZnMo<sub>2</sub>[Fe<sub>4</sub>(O)<sub>2</sub>(ZnMo<sub>x</sub>W<sub>9-x</sub>O<sub>34</sub>)<sub>2</sub>].19H<sub>2</sub>O **(6-M)**, where the oxygen linked to the external Fe<sub>e</sub> is bridged to a tetrahedral molybdate (MoO<sub>4</sub>), and further extending the link through a Zn atom to form POMCFs with ZnMo<sub>2</sub>O<sub>8</sub> linker (Fig. 3B.2a, 3B.S3).

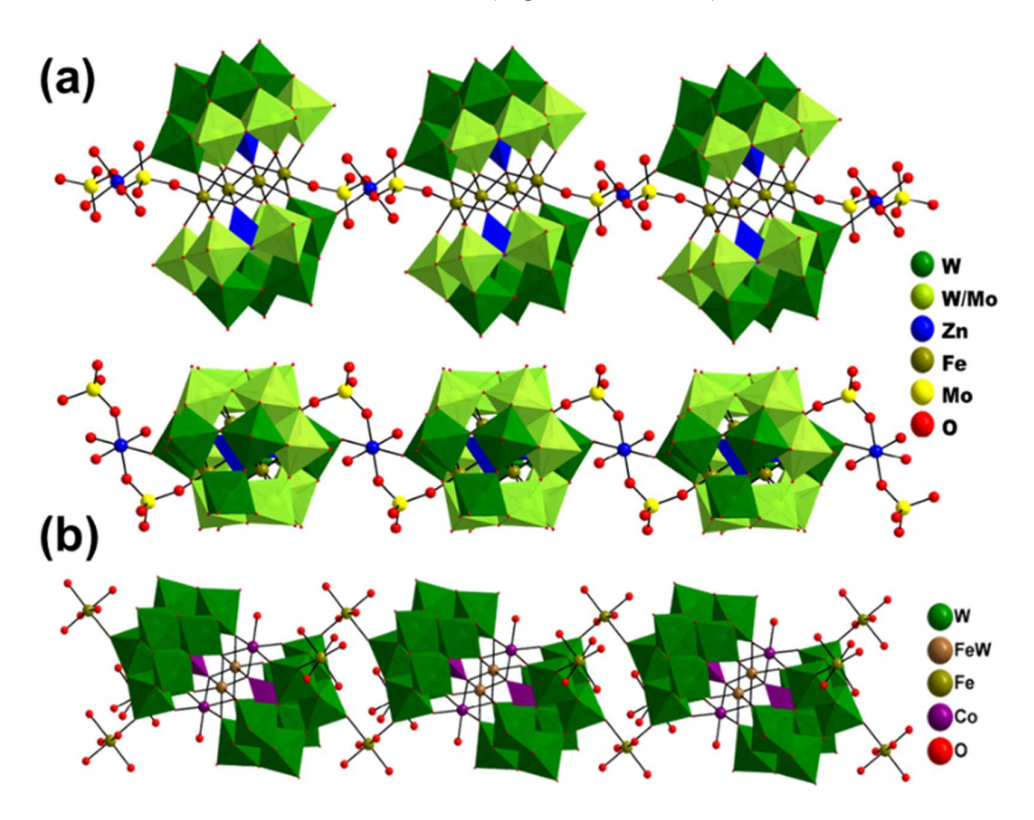


**Figure 3B.2** (a) Different views of 1D-framework of **6-M**; (b) 1D-framework of **7**; (counter cations and hydrogen atoms are omitted for clarity).

BVS calculations indicate all Fe in +3, Zn in +2 and Mo/W in +6 oxidation state. Using Fe<sup>2+</sup>/Zn<sup>2+</sup> precursor salts instead of Fe<sup>3+</sup>/Zn<sup>2+</sup> in W-only POM, **2**, resulted in rapid precipitation of microcrystalline POMCFs, which are difficult to characterize via SC-XRD. A similar POMCF formation was observed when Co<sup>2+</sup>/Fe<sup>2+</sup> precursor salts were used instead of Co<sup>2+</sup>/Fe<sup>3+</sup> in W-only POM, **3**, and when Zn<sup>2+</sup>/Mn<sup>2+</sup> salts replaced Zn<sup>2+</sup>/Mn<sup>3+</sup> in **4**. For example, 3D POMCFs was obtained for Na<sub>2</sub>Fe<sub>6</sub>[Co<sub>2</sub>Fe<sub>2</sub>(H<sub>2</sub>O)<sub>2</sub>(CoW<sub>9</sub>O<sub>34</sub>)<sub>2</sub>].21H<sub>2</sub>O (**7**) with Fe<sup>2+</sup> as a linker and ZnMn<sub>5</sub>[MnWZn<sub>2</sub>(H<sub>2</sub>O)<sub>2</sub>(ZnW<sub>9</sub>O<sub>34</sub>)<sub>2</sub>].22H<sub>2</sub>O (**8**) with Mn<sup>2+</sup> as a linker between two POM frameworks (details Fig. 3B.S1, Table 3B.S1-S2)). BVS calculations indicate Fe<sup>3+</sup> in sandwich position, Fe<sup>2+</sup> outside the POM framework, Co and Mn in +2, and W in +6 oxidation states. Additionally, the cation exchange of **3** with excess Fe<sup>2+</sup> led to the formation of insoluble crystalline powder with matching PXRD (Fig. 3B.S2) indicating POMCFs formation.

#### 3B.2.2 Structural Description

#### 3B-2.2a Structural Description and Characterizations of 6 and 6-M.

Compounds 6 and 6-M were characterized using SC-XRD, FT-IR, ESI-MS, PXRD, and UV-vis spectroscopy. The framework structure was confirmed by SC-XRD (CCDC 2330256, 2330257 and 2330261). All these crystallize in triclinic lattice with  $P\overline{1}$  space group (Table 3B.S1). The optical image of 6 and 6-M shows light yellow colored crystals with 3-D rectangular shape, however, it was observed that data collection at room temperature was not feasible for 6 as it gives poor diffractions (Figure 3B.S1). Compound 6 was characterized using FT-IR and ESI-MS. The crystal structure of 6-M shows that the trilacunary Keggin moiety contains a tetrahedrally bound Zn atom in the center as a templating agent to triads of addenda W/Mo atoms. The tetrasubstituted sandwich core consists of four Fe atoms (Figure 3B.3). The crystal structure of 6-M shows that it forms a three-dimensional network structure with POM frameworks connected using transition metal ligands with the formula ZnMo<sub>2</sub>O<sub>10</sub> (Figure 3B.2). Interstingly, the Mo atom of the ligand connects to the oxygen of the Fe atom in the sandwich position in a tetrahedral way thus making it coordinatively saturated. The two tetrahedrally bound Mo atoms further connect to the Zn atom (octahedrally connected between the two POM frameworks) thus forming the linker between the two POM frameworks.

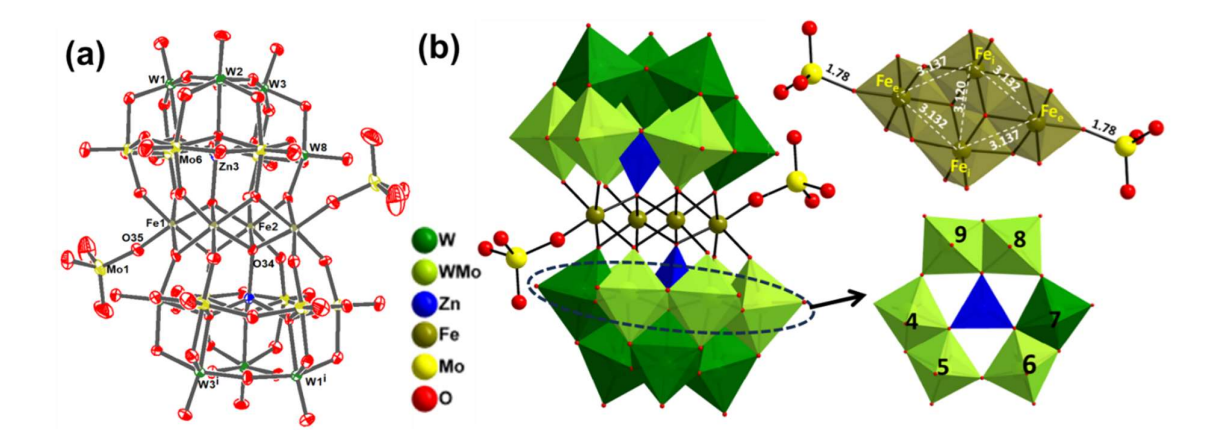


**Figure 3B.3** (a) ORTEP drawing (with 60% ellipsoid probability) (b) Cubane core showing the interatomic distance between transition metals in **6-M**; combined polyhedral/ball and stick representation of the single-crystal X-ray structure of polyoxometalate **6-M**; belt 2 depicting different ratios of molybdenum to tungsten in **6-M**, Countercations and hydrogen atoms are omitted for clarity.

The octahedrally bound Zn atom connects two sides with the Mo atom through oxygen, two water molecules, and two sides are directly connected to the W of the POM framework through oxygen atoms. From the comparison of **6-M** with the reference structure (Figure 2.2), Mo

incorporation is favorable at all belt positions except position 7 however, positional occupancy is very low (less than 15%) (Figure 3B.3b). The other positions in the cap are not favorable for Mo incorporation. The distance between Fe<sub>e</sub> and Fe<sub>i</sub> and between two Fe<sub>i</sub> is 3.13 Å. BVS indicates W/Mo in +6, Zn in +2, and Fe at internal as well as external position in +3 oxidation state (Table 3B.S2).

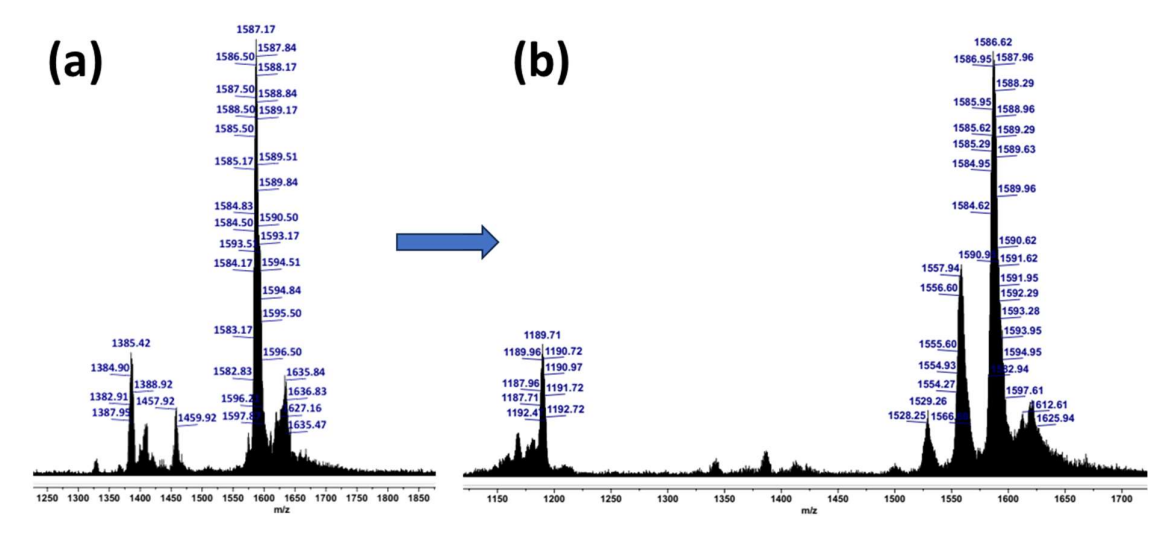
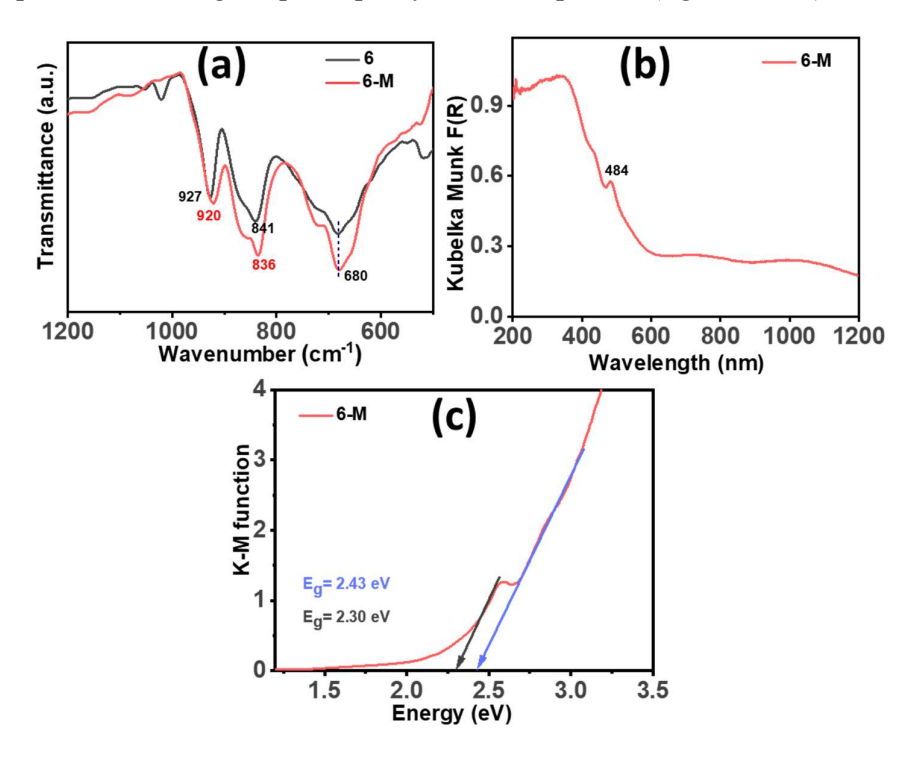


Figure 3B.4 ESI-MS spectra of (a) 6 (b) 6-M in the range of m/z 1100-1850 (z = -3).

ESI-mass spectrum of **6** in shows the envelope of peaks at m/z 1587.17 (z = -3) due to the presence of H<sub>9</sub>Fe<sub>4</sub>(Zn<sub>2</sub>W<sub>18</sub>O<sub>68</sub>) while ESI-mass spectrum of analog mixed addenda POMs **6-M** (Figure 3B.4, Table 3B.S3) shows the multiple envelopes of peaks attributed to varying ratios of Mo to W towards low m/z values. The **6-M** shows the envelopes of peaks in the range of m/z 1500-1630 for H<sub>9</sub>[{Fe<sub>4</sub>(H<sub>2</sub>O)<sub>2</sub>(ZnMo<sub>x</sub>W<sub>9-x</sub>)<sub>2</sub>}<sup>3-</sup>], and m/z 1150-1200 for H<sub>8</sub>[{Fe<sub>4</sub>(H<sub>2</sub>O)<sub>2</sub>(ZnMo<sub>x</sub>W<sub>9-x</sub>)<sub>2</sub>}<sup>4-</sup>]. The most abundant anion in [{Fe<sub>4</sub>(H<sub>2</sub>O)<sub>2</sub>(ZnMo<sub>x</sub>W<sub>9-x</sub>)<sub>2</sub>}<sup>12-</sup>], has the composition without Mo addenda in the formula i.e. formation of **6** dominates in the synthesis of **6-M**. However, the highest Mo/W ratio in **6-M** was found to be 2/16 with a constant charge of the cluster, i.e., -12. Further, in tuning the amount of Mo addenda incorporation, pH plays a crucial role. Hence, to understand the controlling of the Mo/W ratio in the **6-M**, a systematic synthetic study was performed at different pH. It was observed **6-M** forms only at a particular pH and lowering the pH does not incorporate more Mo addenda however it results in the formation of Keggin POMs as observed in ESI-MS.

The FT-IR spectra of **6** show the characteristics peaks at 927 cm<sup>-1</sup> (W=O<sub>term</sub>), 841, 680 cm<sup>-1</sup> (W-O-W) cm<sup>-1</sup> while **6-M** show the characteristics peaks at 920 cm<sup>-1</sup> (M=O<sub>term</sub>), 836, 680 cm<sup>-1</sup> (M-O-M) cm<sup>-1</sup> (Figure 3B.5a) with slight shifting due to Mo incorporation in the framework. **6-M** exhibit broad absorption bands in the UV-vis region due to ligand-to-metal charge transfer

(LMCT) (O2p → W5d) while very absorption in the visible region due to forbidden d-d transition. Moreover, a significant absorption peak at 484 was observed due to metal to POM framework charge transfer (MMCT) in 6-M (Figure 3B.5b). DRS indicates two different band gap in 6-M at 2.43 eV and 2.30 eV due to LMCT and MMCT (Figure 3B.5c). The phase purity of 6-M was obtained from PXRD. The experimental PXRD patterns are consistent with their simulated pattern indicating the phase purity of all compounds (figure 3B.S2).



**Figure 3B.5** (a) Effect of Mo incorporation in the framework of tetrasubstituted sandwich POMs in terms of shifting of characteristics peaks in FT-IR of **6-M** (b); solid-state UV-vis spectra and (c) optical band-gap derived from the Kubelka-Munk equation in **6-M**.

#### 3B.2.2b Structural Description and Characterizations of 7 and 8.

The SC-XRD structure of 7 (green colored rhombic crystals) and 8 (light yellow rhombic crystals) shows the formation of 3-D structure (Figure 3B.S1). The 3D SC-XRD structure of 7 shows that the trilacunary Keggin moiety contains a tetrahedrally bound Co atom in the center as a templating agent to triads of addenda W atoms. The tetrasubstituted sandwich core consists of Fe:W (85:15) at internal {TM<sub>i</sub>} position and Co as external atoms {TM<sub>e</sub>} and Fe atoms as a countercation coordinates to POMs structures to form 3-D network structure (Figure 3B.6b). BVS indicates W in +6, Co in +2 and Fe at internal in +3 while at countercation position in +2 oxidation state (Table 3B.S2). The 3D SC-XRD structure of 8 shows that the trilacunary Keggin moiety contains a tetrahedrally bound Zn atom in the center as a templating

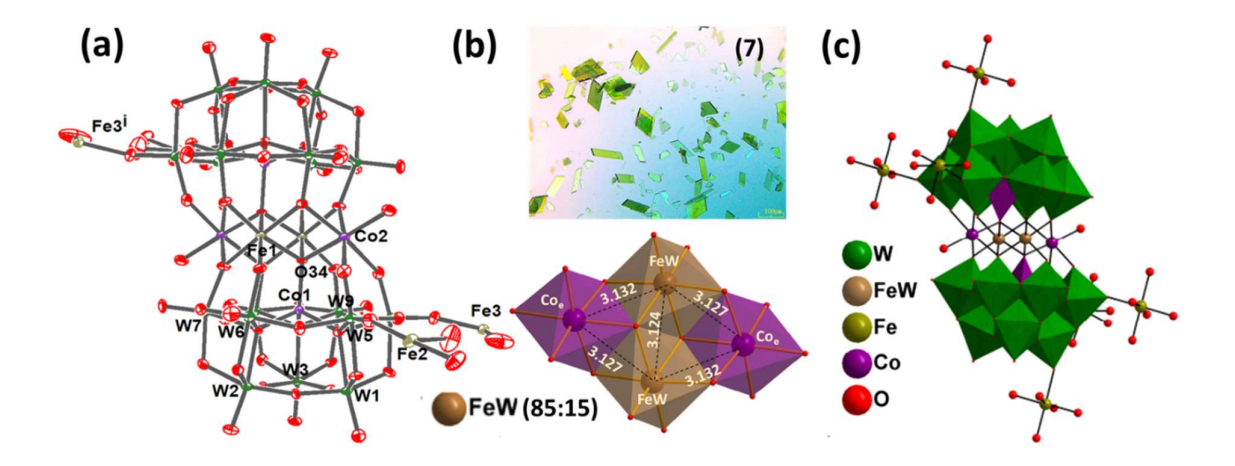


**Figure 3B.6** (a) ORTEP drawing (with 60% ellipsoid probability) (b) Optical images of sandwich POMs; 7 and Cubane core showing the interatomic distance between transition metals in 7; (c) combined polyhedral/ball and stick representation of the single-crystal X-ray structure of polyoxometalate 7 showing different coordination mode of POM framework; Countercations and hydrogen atoms are omitted for clarity.

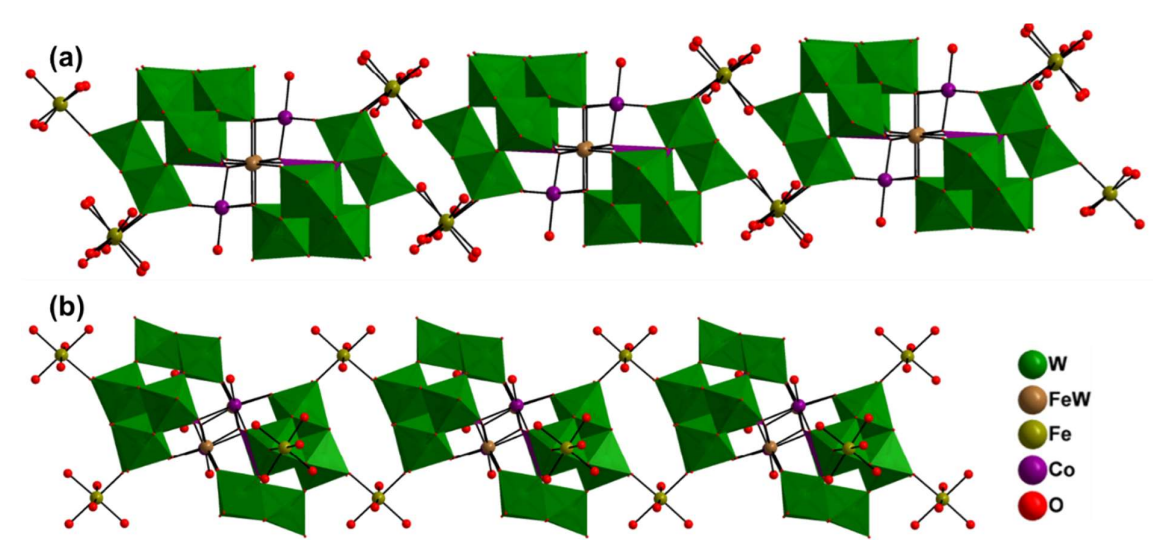


**Figure 3B.7** (a) Combined polyhedral/ball-and-stick representation of **7** with different views (c) Perspective view of the three-dimensional chain connected by linker Fe atoms; sodium and hydrogen are omitted for clarity.

agent to triads of addenda W atoms. The tetrasubstituted sandwich core consists of Zn:W (50:50) at internal  $\{TM_i\}$  position and Zn:Mn (50:50) as external atoms  $\{TM_e\}$  and Mn as well as Zn atoms acts as a countercation thus coordinating POMs structures to form 3-D network structure (Figure 3B.8). BVS indicates W in +6, Zn and Mn in +2 oxidation state (Table 3B.S2). The experimental PXRD patterns are consistent with their simulated pattern indicating the phase purity of 7 and 8 (Figure 3B.S2c).

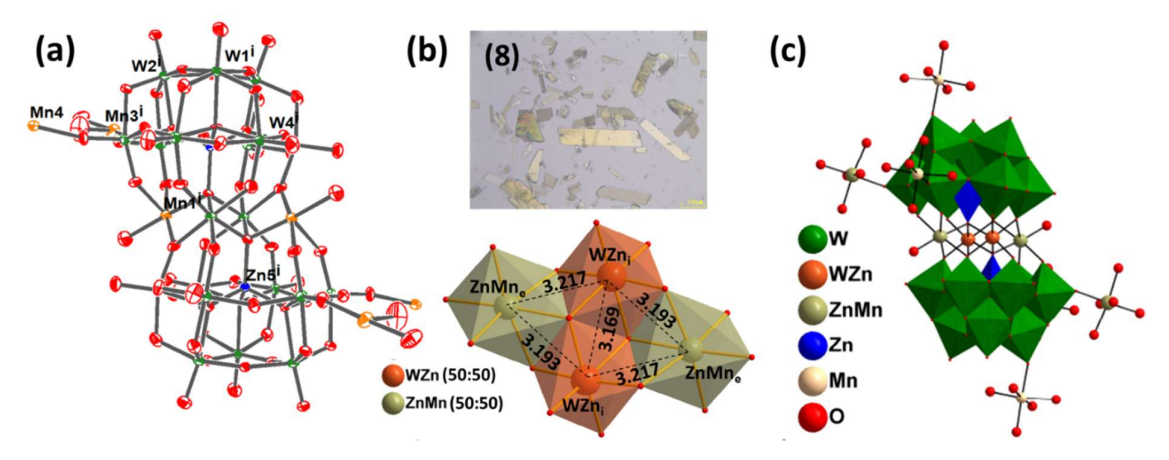


**Figure 3B.8** (a) ORTEP drawing (with 60% ellipsoid probability) (b) Optical images of sandwich POMs; **8** and Cubane core showing the interatomic distance between transition metals in **8**; (c) combined polyhedral/ball and stick representation of the single-crystal X-ray structure of polyoxometalate **8** showing different coordination mode of POM framework; Countercations and hydrogen atoms are omitted for clarity.

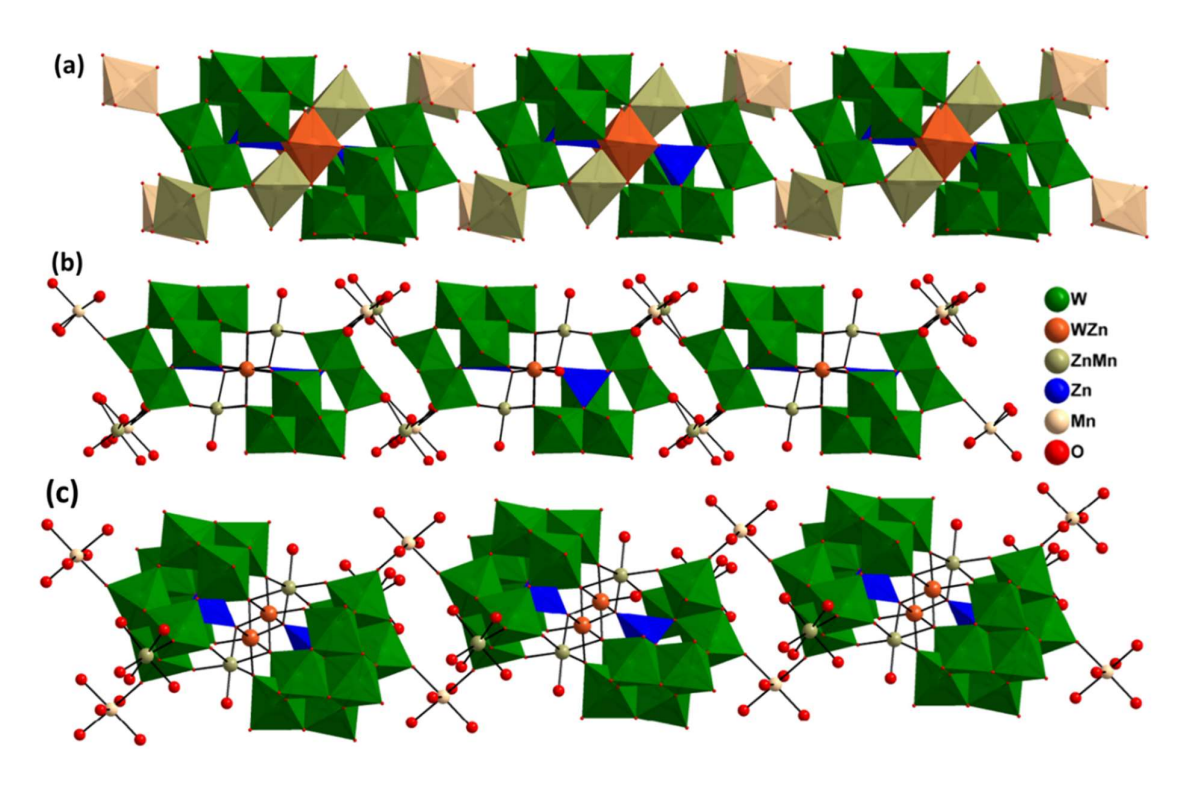


**Figure 3B.9** (a) Polyhedral and (b) Combined polyhedral/ball-and-stick representation of **8** anion with different views (c) Perspective view of the three-dimensional chain of **8** connected by linker Zn/Mn; sodium and hydrogen are omitted for clarity.

DFT study indicates the decrease in the band gap when we go from 6 to 6-M due to incorporation of Mo as addenda similar to 2/2-M. Apart from this. The overall charge of these

POMs significantly affects the properties of these POMs, e.g. in case of 6 and 6-M (Figure 3B.1), when we go from charge -12 to -16 within the same POM, the elogation of TM-O(H<sub>2</sub>O) bond take place due to increase in overall charge density of POM thus making it susceptible to substitution which was observed in 6-M experimentally also.

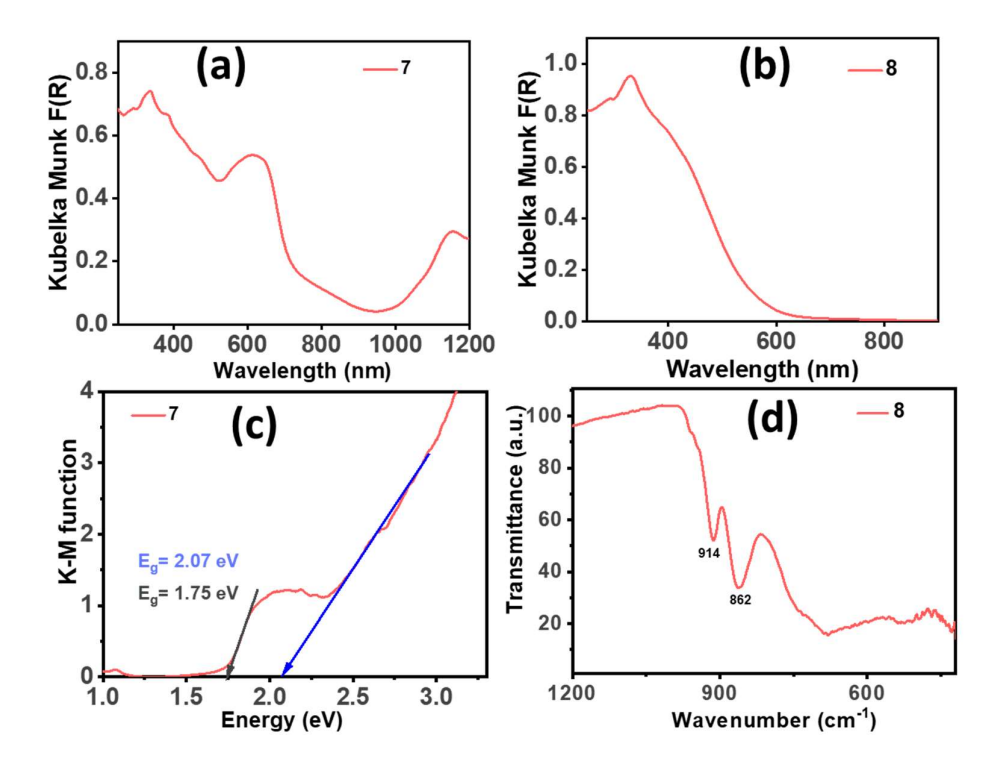


**Figure 3B.10** solid-state UV-vis spectra of (a) 7 (b) 8; (c) optical band-gap derived from the Kubelka-Munk equation in 7 and (d) FT-IR spectra of 8.

#### 3B.3 Conclusion

These findings indicate the crucial role of precursors oxidation states in influencing the self-assembly towards POMCF as well as Mo incorporation. Also, transition metals as heteroatom in high charge density lacunary POMs preferentially bind with transition metals of high oxidation state (e.g., W<sup>6+</sup>, Ru<sup>4+</sup>, Fe<sup>3+</sup>) at internal sandwich positions. However, using a transition metal of low oxidation state results in the formation of 1-D frameworks.

#### 3B.4 Experimental section

#### 3B.4.1 General Information and Instrumentation

**3B.4.1a Materials and Methods.** Deionized water used in the experiments was from the Millipore system (>18 M $\Omega$  cm-1). The transition metal salts used in synthesis were obtained from Alfa Aesar (purity > 99.9 %) and used without further purification. All polyoxometalates were recrystallized from an aqueous solution before characterization. All the synthetic

procedures were optimized in terms of pH and the different ratios of Mo to W salt as mentioned in our previously reported article. <sup>14</sup> The optimization in the case of mixed addenda POMs was done regarding the maximum Mo: W ratio in the final compound using pH dependent study.

#### 3B.4.1b Instrumentation

Already mentioned in section 2.4.1b (chapter 2)

Crystal data, data collection parameters, refinement statistics, and the Cambridge Crystallographic Data Centre; CCDC number (2330256, 2330257, 2330261).

#### 3B.4.1c Density Functional Theory (DFT) Calculation.

Already mentioned in section 2.4.1c (chapter 2)

#### 3B.4.2 Synthesis

#### $Na_{12}[Fe_4(H_2O)_2(ZnW_9O_{34})_2].23H_2O(6)$

Na<sub>2</sub>WO<sub>4</sub>.2H<sub>2</sub>O (2.67 g, 8.08 mmol) were dissolved in 15 mL DI water. Using 6M HCl, the pH of the solution was fixed at 7.2 and the resultant solution was put in Teflon microwave vials and irradiated under controlled pressure with a power ramp for 15 min and power hold for 30 min at 85 °C under 400 W maximum power. ZnCl<sub>2</sub> (0.36 g, 2.68 mmol) followed by FeCl<sub>2</sub>.2H<sub>2</sub>O (0.53 g, 2.68 mmol) was added to the above solution with vigorous stirring and irradiated again in the microwave for 30 min at 85 °C maintaining the previous parameter. The dark orange solution thus obtained was filtered hot and filtrate was kept for crystallization. After 1 day, orange-colored octahedral crystals appeared. These crystals were collected by filtration and dried at 60 °C under vacuum. Yield: 0.57 g (15.5%). FT-IR (cm<sup>-1</sup>): 927 (W=O<sub>t</sub>), 841 (W-O<sub>c</sub>-W), 680 (W-O<sub>e</sub>-W).

#### $Na_2ZnMo_2[Fe_4(O)_2(ZnMo_xW_{9-x}O_{34})_2].19H_2O(6-M)$

Na<sub>2</sub>WO<sub>4</sub>.2H<sub>2</sub>O (2.67 g, 8.08 mmol) and Na<sub>2</sub>MoO<sub>4</sub>.2H<sub>2</sub>O (0.97 g, 4.04 mmol) were dissolved in 15 mL DI water. Using 6M HCl, the pH of the solution was fixed at 6.8 and the resultant solution was put in Teflon microwave vials and microwave irradiated under controlled pressure with a power ramp for 15 min and power hold for 30 min at 85 °C under 400 W maximum power. ZnCl<sub>2</sub> (0.36 g, 2.68 mmol) followed by FeCl<sub>2</sub>.2H<sub>2</sub>O (0.53 g, 2.68 mmol) was added to the above solution with vigorous stirring and irradiated again in the microwave for 30 min at 85 °C maintaining the previous parameter. The dark orange solution thus obtained was filtered hot and filtrate was kept for crystallization. After 1 day, block-shaped orange-colored crystals appeared. These crystals were collected by filtration and dried at 60 °C under vacuum. Yield: 0.85 g (24.6%). FT-IR (cm<sup>-1</sup>): 920 (M=O<sub>t</sub>), 836 (M-O<sub>c</sub>-M), 680 (M-O<sub>c</sub>-M) (M=Mo/W)

#### $Na_2Fe_6[Co_2Fe_2(H_2O)_2(CoW_9O_{34})_2].21H_2O(7)$

Na<sub>2</sub>WO<sub>4</sub>.2H<sub>2</sub>O (4.00 g, 12.12 mmol) was dissolved in 15 mL DI water. Using 6M HCl, the pH of the solution was fixed at 7.25, the resultant solution was put in Teflon microwave vials and microwave irradiated under controlled pressure with a power ramp for 15 min and hold for 30 min at 85 °C under 400 W maximum power. CoCl<sub>2</sub>.6H<sub>2</sub>O (0.63 g, 2.68 mmol) followed by FeCl<sub>2</sub>.4H<sub>2</sub>O (0.51 g, 2.68 mmol) was added to the above solution with vigorous stirring and irradiated again in the microwave for 30 minutes at 85 °C maintaining the previous parameter. The dark green solution thus obtained was filtered hot and filtrate was kept for crystallization. After 2 h, block-shaped green colored crystals appeared which were collected by filtration and dried at 60 °C under vacuum. Yield: 0.58 g (15.6%). FT-IR (cm<sup>-1</sup>): 904 (W=O<sub>t</sub>), 838 (W-O<sub>c</sub>-W), 699 (W-O<sub>c</sub>-W).

#### $ZnMn_{5}[MnWZn_{2}(H_{2}O)_{2}(ZnW_{9}O_{34})_{2}].22H_{2}O$ (8)

Na<sub>2</sub>WO<sub>4</sub>.2H<sub>2</sub>O (4.00 g, 12.12 mmol) was dissolved in 15 mL DI water. Using 6M HCl, the pH of the solution was fixed at 7.25, the resultant solution was put in Teflon microwave vials and microwave irradiated under controlled pressure with a power ramp for 15 min and hold for 30 min at 85 °C under 400 W maximum power. ZnCl<sub>2</sub> (0.36 g, 2.68 mmol) followed by MnCl<sub>2</sub>.4H<sub>2</sub>O (0.53 g, 2.68 mmol) was added to the above solution with vigorous stirring and irradiated again in the microwave for 30 minutes at 85 °C maintaining the previous parameter. The orange solution thus obtained was filtered hot and filtrate was kept for crystallization. After 2 h, block-shaped purple-colored crystals appeared which were collected by filtration and dried at 60 °C under vacuum. Yield: 0.74 g (20.5%). FT-IR (cm<sup>-1</sup>): 914 (W=O<sub>t</sub>), 862 (W-O<sub>c</sub>-W), 682 (W-O<sub>c</sub>-W)

#### 3B.5 References

- 1. Long, D.-L.; Burkholder, E.; Cronin, L., Polyoxometalate clusters, nanostructures and materials: From self assembly to designer materials and devices. *Chem. Soc. Rev.* **2007**, *36* (1), 105-121.
- 2. Pang, H.; Zhang, C.; Shi, D.; Chen, Y., Synthesis of a purely inorganic three-dimensional porous framework based on polyoxometalates and 4d–4f heterometals. *Cryst. Growth Des.* **2008**, *8* (12), 4476-4480.
- 3. Liang, D.; Wang, Q.; Li, H.; Zhao, H.; Yu, Z.; Wu, C.; Sun, C.; Qian, S.; Ni, L.; Diao, G., 2D-architecture via self-assembly of the novel sandwich-type polyoxometalate [Zn3. 2Bi0.8(B-α-ZnW9O34)2]15–. *Polyhedron* **2017**, *133*, 343-347.
- 4. Shi, L.-X.; Zhao, W.-F.; Xu, X.; Tang, J.; Wu, C.-D., From 1D to 3D Single-Crystal-to-Single-Crystal Structural Transformations Based on Linear Polyanion [Mn4(H2O) 18WZnMn2(H2O)2(ZnW9O34)2]4—. *Inorg. Chem.* **2011**, *50* (24), 12387-12389.
- 5. Thiel, J.; Ritchie, C.; Streb, C.; Long, D.-L.; Cronin, L., Heteroatom-controlled kinetics of switchable polyoxometalate frameworks. *J. Am. Chem. Soc.* **2009**, *131* (12), 4180-4181.
- 6. Guo, K.-K.; Yang, Y.-L.; Dong, S.-M.; Li, F.-Y.; Jiang, X.-Y.; Xu, L., Decomposition—Reassembly Synthesis of a Silverton-Type Polyoxometalate 3D Framework: Semiconducting Properties and Photocatalytic Applications. *Inrog. Chem.* **2022**, *61* (17), 6411-6420.
- 7. Si, C.; Ma, P.; Han, Q.; Jiao, J.; Du, W.; Wu, J.; Li, M.; Niu, J., A Polyoxometalate-Based Inorganic Porous Material with both Proton and Electron Conductivity by Light Actuation:

- Photocatalysis for Baeyer-Villiger Oxidation and Cr (VI) Reduction. *Inorg. chem.* **2020**, *60* (2), 682-691.
- 8. Wang, J.-X.; Wang, Y.-D.; Wei, M.-J.; Tan, H.-Q.; Wang, Y.-H.; Zang, H.-Y.; Li, Y.-G., Inorganic open framework based on lanthanide ions and polyoxometalates with high proton conductivity. *Inorg. Chem. Front.* **2018**, *5* (5), 1213-1217.
- 9. Zhao, M.; Zhang, X.-W.; Wu, C.-D. J. A. C., Structural transformation of porous polyoxometalate frameworks and highly efficient biomimetic aerobic oxidation of aliphatic alcohols. *ACS Catal.* **2017**, *7* (10), 6573-6580.

### **Annexure-III**

Table 3B.S1 Cry	stal data, data collection	, and refinement paramete	rs for 6-M, 7 and 8.
	6-M	7	8
CCDC number	2330256	2330257	2330261
empirical formula	Fe <sub>4</sub> H <sub>4</sub> Mo <sub>2.7</sub> Na <sub>20</sub> O <sub>112</sub>	Co <sub>4</sub> Fe <sub>5.7</sub> H <sub>4</sub> Na <sub>14</sub> O <sub>108</sub> W <sub>18.3</sub>	$Mn_4Na_{13}O_{108}W_{19}Zn_5$
	$W_{17.3}Zn_3$		
formula weight	6114.98	5972.41	6066.63
temp (K)	273.15	298.15	273.15
crystal system	Triclinic	Triclinic	Triclinic
space group	$P\overline{1}$	$P\overline{1}$	$P\overline{1}$
unit cell dimension			
a (Å)	12.8944(4)	12.4815(10)	12.5610(10)
b (Å)	13.6975(5)	13.6112(12)	13.6814(10)
c (Å)	16.9682(6)	16.6742(15)	16.8388(11)
α (deg)	113.3020(10)	82.635(3)	82.312(2)
β (deg)	96.6120(10)	73.593(3)	73.528(2)
γ (deg)	94.7230(10)	64.249(2)	64.025(2)
$V(\mathring{\mathbf{A}}^3)$	2707.18(16)	2447.5(4)	2494.5(3)
Z	1	1	1
ho (calculated) (g/cm <sup>3</sup> )	3.751	4.052	4.038
μ/mm <sup>-1</sup>	19.961	23.062	23.644
F (000)	2708.0	2632.0	2663.0
crystal size (mm³)	$0.23 \times 0.18 \times 0.12$	$0.38 \times 0.25 \times 0.21$	$0.34 \times 0.23 \times 0.12$
20 range for data	4.25 to 52.854	4.174 to 52.908	4.186 to 52.89
collection/°			
index ranges	$-16 \le h \le 16, -17 \le k$	$-15 \le h \le 15, -17 \le k \le$	$-15 \le h \le 15, -17 \le k \le 17,$
	$\leq 17, -21 \leq 1 \leq 21$	$17, -20 \le 1 \le 20$	-21 ≤ 1 ≤ 21
no. of reflection	42474/	65901/10068	33266/10207
collected /unique	11074		
GOF on F <sup>2</sup>	1.099	1.127	1.067
final R indices	$R_1 = 0.033, wR_2 =$	$R_1 = 0.036, wR_2 = 0.087$	$R_1 = 0.042, wR_2 = 0.128$
$(I > 2\sigma(I))$	0.087		
R indices (all data)	$R_1 = 0.035, wR_2 =$	$R_1 = 0.039, wR_2 = 0.089$	$R_1 = 0.045, wR_2 = 0.132$
	0.088		

data/restraints/param	11074/0/738	10068/0/688	10207/0/674
Largest diff. peak/hole / e Å <sup>-3</sup>	3.81/-1.56	2.14/-1.62	3.84/-2.92

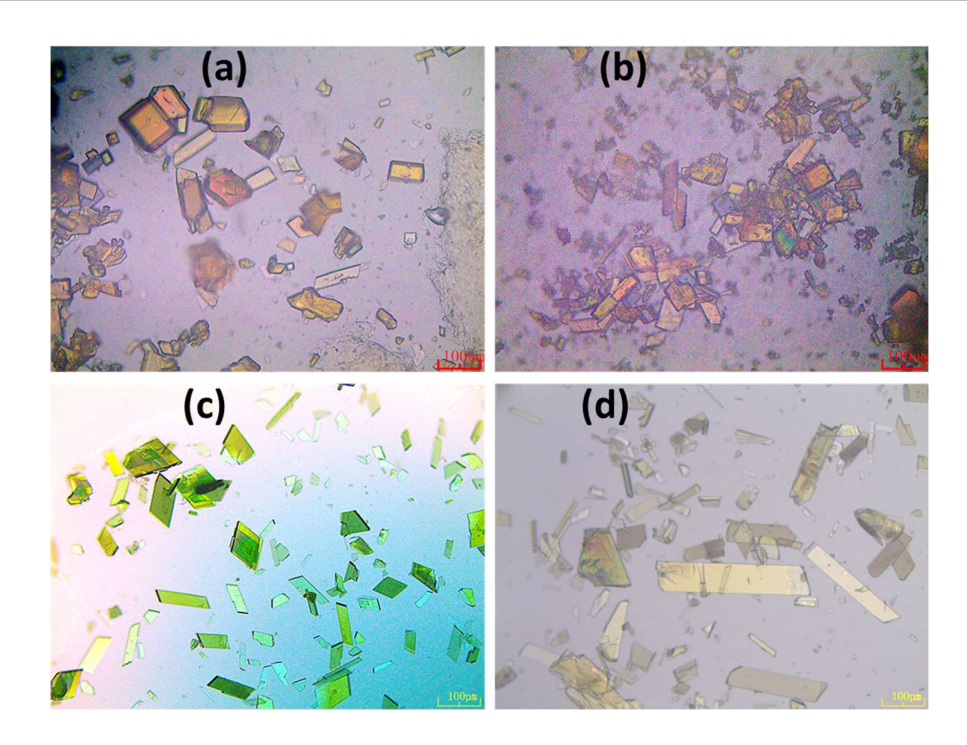


Figure 3B.S1 Optical images of sandwich POMs; (a) 6 (b) 6-M (c) 7 and (d) 8.

Table 3B.S2 Bond valence parameter of selected atoms calculated from	
the SC-XRD structure of framework structures <b>6-M</b> , <b>7</b> and <b>8</b>	

POMs	Transition metal	Bond valence sum	Oxidation state	
		value		
	W	6.031	+6	
	Mo	6.160	+6	
6-M	Zn1	2.343	+2	
	Zn3	2.310	+2	
	Fe1	3.037	+3	
	Fe2	3.015	+3	
	W	6.063	+6	
7	Fe1	3.052	+3	
	Fe2	2.234	+2	
	Fe3	2.329	+2	
	Co1	2.216	+2	

	Co2	2.041	+2
8	W	6.047	+6
	Zn2	2.591	+2
	Zn1	2.140	+2
	Zn3	2.067	+2
	Zn5	2.193	+2
	Mn3	2.438	+2
	Mn4	2.297	+2
	Mn1	2.346	+2

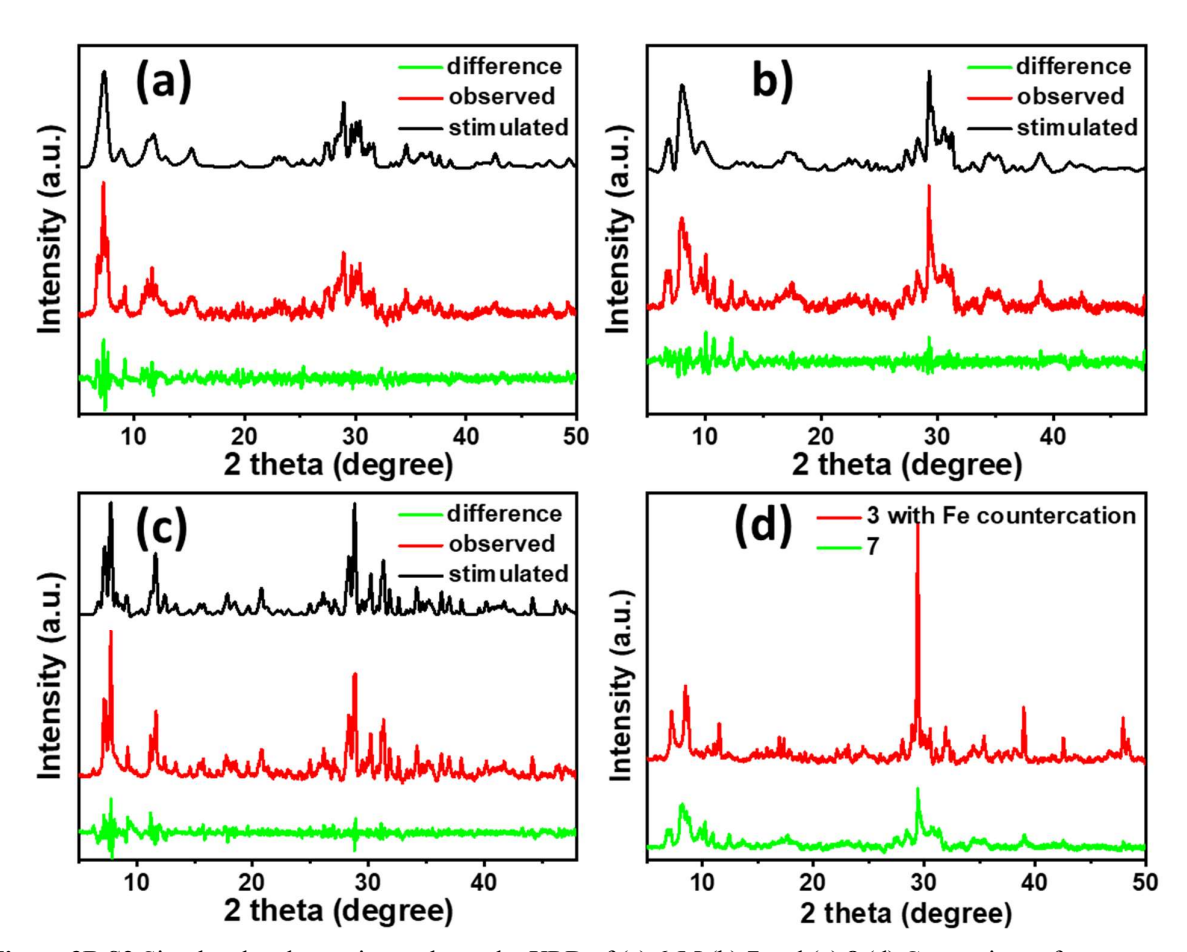
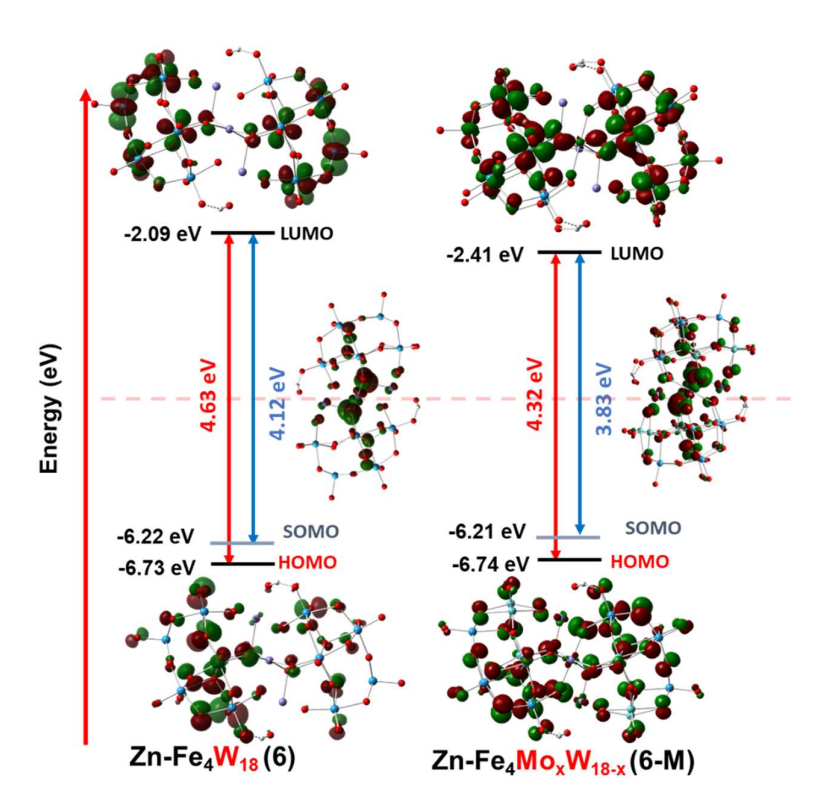


Figure 3B.S2 Simulated and experimental powder XRD of (a) 6-M (b) 7 and (c) 8 (d) Comparison of PXRD of 7 and 3 after countercation exchange with Fe.

Table 3B.S3 Assignment of ESI-mass peaks of 6/6-M

Charge	m/z (obs.)	m/z Mol. Wt.		Assigned probable	
		(calc.)		formula	
-3	1587.17/1586.62	1586.79	4760.38	$H_9Fe_4(Zn_2W_{18}O_{68})_2$	
-3	1557.94	1557.44	4672.34	$H_{11}Fe_4(Zn_2MoW_{17}O_{68})$	
-3	1529.26	1528.10	4584.30	$H_{11}Fe_4(Zn_2Mo_2W_{16}O_{68})$	
-4	1189.71	1189.84	4759.37	$H_8Fe_4(Zn_2W_{18}O_{68})_2$	



**Figure 3B.S3** Frontier molecular orbitals of tetrasubstituted sandwich POMs showing the effect of Mo doping on band gaps as well as shifting of electron density on addenda atoms in **6** and **6-M**.

## **Chapter 4**

# Modulation of Optoelectronic Properties and Framework in Trimetallic Sandwich Polyoxometalates

#### 4.1 Introduction

In Chapter 3, our cooperative mix-metal approach proves to be versatile synthetic strategy for mixed metal-mixed addenda POMs and also served as an effective tool for orbital engineering. It influences the overall band gap, charge transfer (especially metal to POM charge transfer - MPCT), modulation of electron density, and SOMO and HOMO-LUMO orbitals, which was further complemented by the DFT calculations. We believe that our cooperative mix metal approach presents a robust synthetic analogy, suitable for designing new POM and Hybrid POM complexes of tunable orbital for designing more active catalysts. This approach will help in substantial progress in developing novel heterogeneous materials based on POMs and opens access to a broader range of structural modifications with diverse functionalities.<sup>1-3</sup>

So far, we discussed cooperative mixed metal strategy in sandwich POMs containing only two types of metals. Nowadays, mixed metal oxides containing up to 5 metals are well known in the literature for efficient catalysis due to the synergistic behaviour of transition metals.<sup>4</sup> So, a multi-metallic concept in POMs chemistry can be beneficial not only for efficient catalysis but also for enhanced magnetic properties.<sup>5</sup> For the synthesis of multi-metallic sandwich POMs, a three-step sequential introduction of transition metals into trivacant lacunary polyoxometalate has been discussed.<sup>6</sup> Earlier, our group also performed side substitution in Zn-based sandwich POMs for different transition metals substituted sandwich POMs.<sup>7</sup>

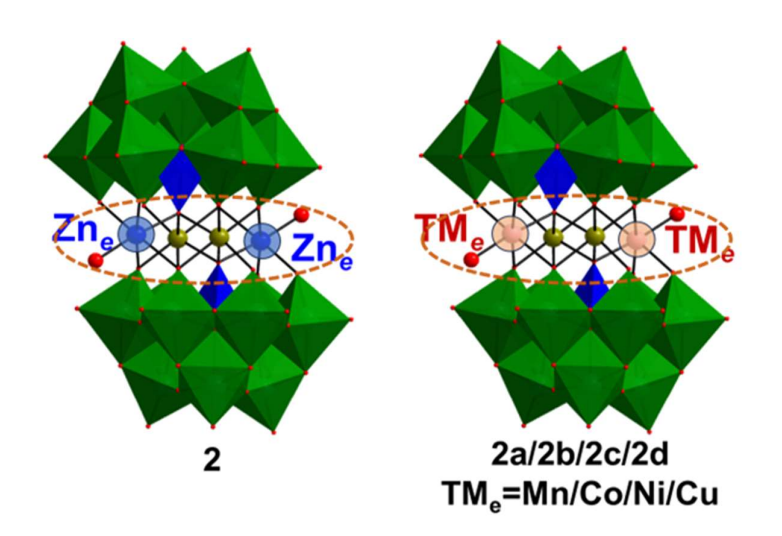
In section A of Chapter 4, we have extended our cooperative mixed metal approach for the one-pot synthesis of trimetallic sandwich **POMs** with the formula [(TM<sub>e</sub>)<sub>2</sub>(TM<sub>i</sub>)<sub>2</sub>(H<sub>2</sub>O)<sub>2</sub>(X<sub>TM</sub>W<sub>9</sub>O<sub>34</sub>)<sub>2</sub>]<sup>n</sup> and its orbital engineering has been studied using DFT study. Further, orbital engineering has been performed using a mixed addenda concept in these trimetallic sandwich POMs. In section B of Chapter 4, we have studied switching in frameworks by modulating heteroatoms and oxidation state of precursor transition metals. Also, mixed addenda in banana POMs and 1-D framework in Krebs POMs have been explored for the first time.8

#### 4.2 References

- 1. M. R.; Singh, A.; Alomari, S.; Goberna-Ferrón, S.; Benages-Vilau, R.; Chodankar, N.; Motta, N.; Ostrikov, K. K.; MacLeod, J.; Sonar, P., Polyoxometalates (POMs): from electroactive clusters to energy materials. *Energy Environ. Sci.* **2021**, *14* (4), 1652-1700.
- 2. Zeb, Z.; Huang, Y.; Chen, L.; Zhou, W.; Liao, M.; Jiang, Y.; Li, H.; Wang, L.; Wang, H., Comprehensive overview of polyoxometalates for electrocatalytic hydrogen evolution reaction. *Coord. Chem. Rev.* **2023**, *482*, 215058.
- 3. Singh, G.; Adhikary, S. D.; Mandal, D., Stabilization and activation of polyoxometalate over poly (vinyl butylimidazolium) cations towards electrocatalytic water oxidation in alkaline media. *Chem. Commun.* **2023**, *59* (32), 4774-4777.
- 4. Salley, D. S.; Keenan, G. A.; Long, D.-L.; Bell, N. L.; Cronin, L., A modular programmable inorganic cluster discovery robot for the discovery and synthesis of polyoxometalates. *ACS Cent. Sci.* **2020**, *6* (9), 1587-1593.
- 5. Minato, T.; Salley, D.; Mizuno, N.; Yamaguchi, K.; Cronin, L.; Suzuki, K., Robotic stepwise synthesis of hetero-multinuclear metal oxo clusters as single-molecule magnets. *J. Am. Chem. Soc.* **2021,** *143* (32), 12809-12816.
- 6. Gumerova, N. I.; Rompel, A., Polyoxometalates in solution: speciation under spotlight. *Chem. Soc. Rev.* **2020**, *49* (21), 7568-7601.
- 7. Singh, G.; Das Adhikary, S.; Mandal, D., Physico-and Electrochemical Properties of First-Row Transition-Metal-Substituted Sandwich Polyoxometalates. *Inorg. Chem.* **2023**, *62* (22), 8551-8564.
- 8. Zeng, B.; Zhang, Y.; Chen, Y.; Liu, G.; Li, Y.; Chen, L.; Zhao, J., 3-D antimonotung state framework based on 2, 6-H<sub>2</sub>pdca-connecting iron–cerium heterometallic Krebs-type polyoxotung states for detecting small biomolecules. *Inorg. Chem.* **2021**, *60* (4), 2663-2671.

## Chapter 4 Section A

## Modulation of Optoelectronic Properties in Trimetallic Sandwich Polyoxometalates via the Interplay of External Sandwich Position

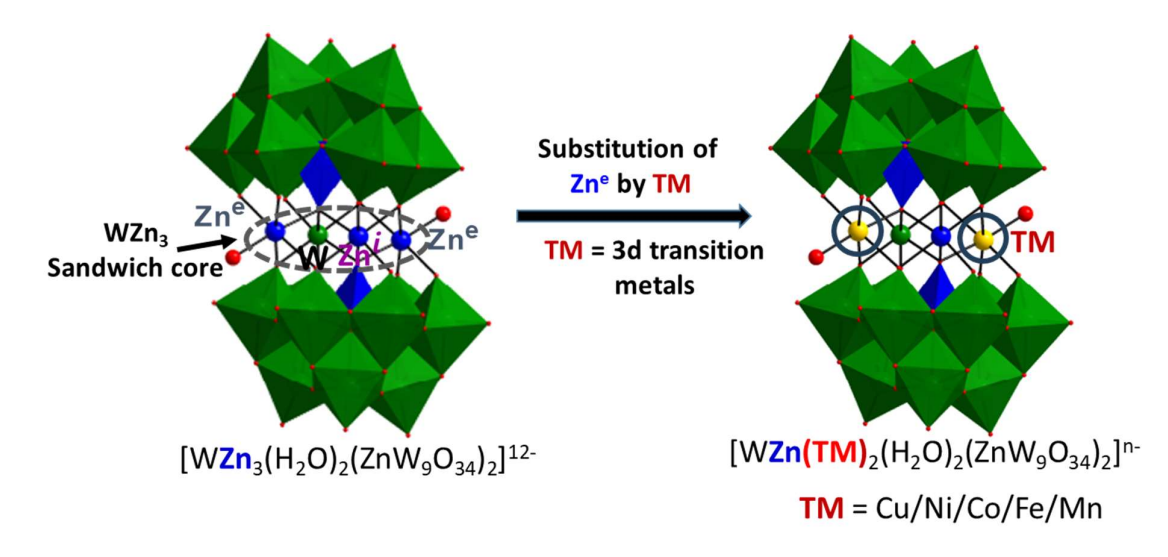


#### **4A.1 Introduction**

Recently, sandwich polyoxometalates with the general formula [M<sub>4</sub>(H<sub>2</sub>O)<sub>2</sub>(XW<sub>9</sub>O<sub>34</sub>)<sub>2</sub>]<sup>q-</sup> (where X = P, Si etc., M = transition metal) have attracted special attention because of their stability, fascinating electrochemical properties and wide range of potential applications. The tri-vacant Keggin subunits stabilize the transition metal core as an inorganic multidentate ligand and make these sandwich polyoxometalates robust against oxidative decomposition<sup>2</sup> (sandwich core, Scheme 4A.1). Sandwich polyoxometalates are efficient catalysts because of their multi-electron redox properties, robust nature and easily accessible active sites. The redox properties and the catalytic activities of such polyoxometalates depend on both the Keggin subunits and transition metals based 'sandwich core'. 3, 4 The electronic properties as well as reactivity of sandwich polyoxometalates are highly dependent on transition metal present in the sandwich core. For example,  $[Co_4(H_2O)_2(PW_9O_{34})_2]^{10}$  (P-Co<sub>4</sub>W<sub>18</sub>) (where Co<sub>4</sub> is sandwich highly active towards water oxidation, whereas, [WCo<sub>3</sub>(H<sub>2</sub>O)<sub>2</sub>(CoW<sub>9</sub>O<sub>34</sub>)<sub>2</sub>]<sup>10</sup>- (Co-WCo<sub>3</sub>W<sub>18</sub>) (where WCo<sub>3</sub> is sandwich core) is reported to be inactive under similar reaction condition.<sup>5</sup> Since the reactivities are highly dependent on the electronic properties of transition metals present in the sandwich core, the substitution of transition metals at the core would be highly important. Therefore, transition metals of the sandwich core can modulate the activity of sandwich POMs and the substitution at the sandwich core by various transition metals can be designed for 'task-specific' applications.

In the last few decades, several tetra-metal sandwich POMs are reported as efficient catalysts in organic transformation<sup>6</sup>, oxygen activation<sup>7</sup>, and oxygen evolution reactions.<sup>5,8-10</sup> Along with the p-block elements (P, Si etc.) as heteroatom and d-block elements as the sandwich core,<sup>5,8,11</sup> another set of sandwich polyoxometalates are also reported with d-block elements (Zn, Co) as heteroatom<sup>12</sup> as well as 'sandwich core' of general formula [W(TM)<sub>3</sub>(H<sub>2</sub>O)<sub>2</sub>(XW<sub>9</sub>O<sub>34</sub>)<sub>2</sub>]<sup>12-</sup> (X = Zn or Co; TM = transition metals; X-W(TM)<sub>3</sub>W<sub>18</sub>, where X=TM=Zn abbreviated as Zn-WZn<sub>3</sub> and X=TM=Co as Co-WCo<sub>3</sub>W<sub>18</sub>).<sup>13</sup> The structural beauty of these compounds is the presence of W atom in the sandwich position, which not only provides chirality to the structure but also paves the way for incoming transition metals at the external position by remaining intact in solution along with tri-vacant Keggin moiety. The size of the heteroatom also affects the overall redox potential of polyoxometalates e.g., the larger size of zinc increases reducing ability of the polyoxometalates.<sup>14</sup> The Zn-WZn<sub>3</sub>W<sub>18</sub> and transition metal substituted polyoxometalates (TMSPs) Zn-WZn(TM)<sub>2</sub>W<sub>18</sub>, are used in various organic transformation reactions, electrocatalysis, sensing, proton conductivity<sup>15</sup> and energy storage applications.<sup>16,17</sup> Neumann et al. reported Zn-WZn<sub>3</sub> as a recyclable catalyst for alcohol

oxidation and an attractive multi-purpose catalyst for oxidations in water with hydrogen peroxide.  $^{18}$ ,  $^{19}$  Zhang et al. studied the selective epoxidation of chiral allylic alcohols catalyzed by  $[WZn(TM)_2(ZnW_9O_{34})_2]^{q-}$  (where, M=Zn, Mn, Ru, Fe, Pd, Pt) using hydrogen peroxide.  $^{20}$  Neumann et al. reported  $[WZnMn_2(ZnW_9O_{34})_2]^{12-}$  catalyzed oxidation of secondary alcohols to ketones and epoxidation of alkenes with a high selectivity, where the selectivity is much higher for Mn substitution with respect to other first-row transition metal substituted analogues.  $^{21,22}$  The  $Bi^{III}$  substitution of transition metals in  $[WZn(TM)_2(H_2O)_2(ZnW_9O_{34})_2]^{q-1}$  has been reported to activate the peroxide and to change the chemoselectivity of the catalytic oxidation of alkene and  $\alpha,\beta$ -unsaturated alcohols.  $^{23}$ 



Scheme 4A.1 Substitution of external Zn-atoms  $(Zn^e)$  in  $[WZn_3(H_2O)_2(ZnW_9O_{34})_2]^{n-}$   $(Zn-WZn_3W_{18})$  by a series of first-row transition elements.

The effect of first-row transition metals in Keggin type heteropoly cobaltates was reported by Hill group.<sup>24</sup> However, the effect of various transition metals in the physico- and electrochemical behaviour of sandwich polyoxometalates are not yet explored. Moreover, a theoretical study on sandwich POM [Fe<sub>4</sub>(PW<sub>9</sub>O<sub>34</sub>)<sub>2</sub>]<sup>12-</sup> showed an interesting electronic configuration. Iron in the sandwich position (4 Fe) was reported to get reduced sequentially from the external positions to internal positions, and all the SOMO (Single occupied molecular orbitals) are from Fe<sup>+3</sup>, which is in between 'oxo band' and 'tungsten band'.<sup>25</sup> In Chapter 3, we have discussed the impact of transition metals at the internal sandwich position and their oxidation states towards modulation of optoelectronic properties. Here, we intend to introduce Fe<sup>+3</sup> at the external position of the sandwich core where Fe<sup>+3</sup> can easily switch the oxidation state from Fe<sup>+3</sup> to Fe<sup>+4</sup>, similar to isostructural Ru<sup>+3</sup> substituted TMSP, which are highly active

for various reactions like hydroxylation reactions, epoxidation, and dioxygen activation. <sup>26,27</sup> This finding encourages us to study Fe<sup>+3</sup> substitution at the external position of the 'sandwich core' thus forming the trimetallic sandwich POMs and its effect on the physico- and electrochemical properties of [WZn<sub>3</sub>(H<sub>2</sub>O)<sub>2</sub>(ZnW<sub>9</sub>O<sub>34</sub>)<sub>2</sub>]<sup>12-</sup> (Zn-WZn<sub>3</sub>W<sub>18</sub>). As we see, the presence of high oxidation state transition metal i.e. W<sup>+6</sup> at the internal sandwich position makes these POMs susceptible to substitution at external sandwich position. Similarly, we have explored transition metal substitution at external sandwich position when high oxidation state transition metal is present at internal sandwich position e.g. Fe<sup>+3</sup>/Mn<sup>+3</sup> etc.

#### **4A.2 Results and Discussion**

#### **4A.2.1 Reaction chemistry**

Our interest was to further extend the mixed addenda scope with trimetallic mixed metal sandwich POMs. We explored the substitution of transition metals at external sandwich positions in [WZn<sub>3</sub>(H<sub>2</sub>O)<sub>2</sub>(ZnW<sub>9</sub>O<sub>34</sub>)<sub>2</sub>]<sup>12</sup>- since the presence of W<sup>+6</sup> at the sandwich core WZn<sub>3</sub> renders the external TMs susceptible for substitution with 3d TM resulting in the formation of $[(TM_e)_2WZn(H_2O)_2(ZnW_9O_{34})_2]^{12}$   $TM_e = Mn/Fe/Co/Ni/Cu)$ . 28, 29 While analogous mixed addenda with WZn<sub>3</sub> at the sandwich [WZn<sub>3</sub>(H<sub>2</sub>O)<sub>2</sub>{ZnMo<sub>x</sub>W<sub>9-x</sub>O<sub>34</sub>}<sub>2</sub>]<sup>12</sup> were DFT optimized, however, the mixed addenda POM synthesis was unsuccessful. Even, side substitution in Fe<sup>3+</sup>based sandwich POMs [Zn<sub>2</sub>Fe<sub>2</sub>(H<sub>2</sub>O)<sub>2</sub>(ZnW<sub>9</sub>O<sub>34</sub>)<sub>2</sub>]<sup>14</sup> (2) results in a mixture of products as characterized by ESI-MS (Fig. 4A.S1, Table 4A.S1). Hence, side substitution in  $[Zn_2(TM_i)_2(H_2O)_2(ZnW_9O_{34})_2]^{14}$  (2 for  $TM_i = Fe^{+3}$  / 4 for  $TM_i = Mn^{+3}$ ) and  $[Co_2(TM_i)_2(H_2O)_2(CoW_9O_{34})_2]^{14} \text{ (3 for } TM_i = Fe^{+3} \text{ / 5 for } TM_i = Mn^{+3} \text{) could not achieved.}$ However, using mixed transition metals (Zn/Fe<sup>3+</sup>/TM<sub>e</sub> and Co/Fe<sup>3+</sup>/TM<sub>e</sub>) precursors in stochiometric ratios we could successfully synthesize trimetallic sandwich POMs with the general formula  $[(TM_e)_2Fe_2(H_2O)_2(X_{TM}W_9O_{34})_2]^{14}$   $(TM_e = Mn/Co/Ni/Cu/Zn; 2a/2b/2c/2d/2,$ respectively (Fig. 4A.S8) when  $X_{TM} = Zn^{2+}$ , and 3a/3/3b/3c/3d when  $X_{TM} = Co^{2+}$ ), which were characterized by SC-XRD, FT-IR, XPS, Raman and ESI-MS (Section 4A.2.3). ESI-MS for Zn/Fe<sup>3+</sup>/TM based POMs exhibited peaks at m/z 1586.41, 1589.48, 1589.52, 1591.52, and 1593.43 due to fragment  $H_{11}[(TM_e)_2Fe_2(H_2O)_2(ZnW_9O_{34})_2]^{3-}$ , where  $TM_e = Mn/Co/Ni/Cu/Zn$ ; (2a/2b/2c/2d/2), (Fig. 4A.S5, Table 4A.S8), respectively. A similar trend of m/z value at 1583.51, 1585.17, 1585.14, 1587.51, and 1589.48 was observed for Co-hetero atom-based POMs due to fragment  $H_{11}[(TM_e)_2Fe_2(H_2O)_2(CoW_9O_{34})_2]^{3-}$  (Fig. 4A.S7, Table 4A.S10).

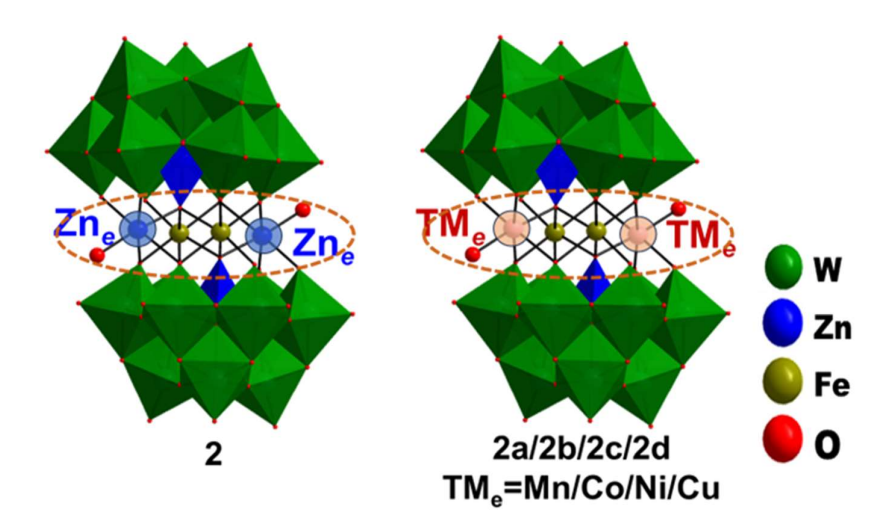


Figure 4A.1 (a) SC-XRD structure of 2 (left) and representative trimetallic sandwich POMs 2a/2b/2c/2d (right); (counter cations and hydrogen atoms are omitted for clarity).

The mixed addenda of these trimetallic sandwich POMs were also synthesized in situ directly from its precursors, e.g.  $[Ni_2Fe_2^{III}(H_2O)_2(ZnMo_xW_{9-x}O_{34})_2]^{14-}$  (2c-M) and  $[Ni_2Fe_2^{III}(H_2O)_2(CoMo_xW_{9-x}O_{34})_2]^{14-}$  (3b-M) were synthesized from Ni/Fe/TM (TM=Zn/Co) and Mo/W salts. The Mo:W ratio was observed to be 5:13 in the most abundant peak of 3b-M (ESI-MS), which is similar to 3-M, thus indicating the transition metal at external positions has a negligible effect on mixed addenda in these trimetallic sandwich POMs. This trimetallic sandwich POM approach was also applied to  $Mn^{3+}$  (Zn/Mn<sup>3+</sup>/TM) for the synthesis of  $[(Fe_e)_2(Mn_i)_2(H_2O)_2(ZnW_9O_{34})_2]^{14-}$  (4a) (Section 4A.2.4) and its mixed addenda analogue  $[(Fe_e)_2(Mn_i)_2(H_2O)_2(ZnMo_xW_{9-x}O_{34})_2]^{14-}$  (4a-M), where only a negligible Mo:W ratio (1:17) was observed in ESI-MS (Fig. 4A.19, Table 4A.S13).

#### 4A.2.2 When W(VI) is present at internal sandwich position

The substitution at external sandwich position in The ESI-mass spectra of Zn-WZnFe<sub>2</sub> show one envelope of peaks at m/z of 1634 assigned for {[WZnFe<sub>2</sub>(ZnW<sub>9</sub>O<sub>34</sub>)<sub>2</sub>]+9H}<sup>3-</sup> cluster anion (Figure 4A.S3 and Table 4A.S1). The oxidation states of all the atoms were calculated from BVS calculation in SC-XRD structure except Zn-WZnFe<sub>2</sub> for which the oxidation state of Fe atoms was determined form XPS analysis. The XP spectrum of Zn-WZnFe<sub>2</sub> POM revealed the presence of tungsten (W), iron (Fe), zinc (Zn) and oxygen. (Figure 4A.S2) The Zn 2p in Figure 4A.S2a shows doublet peaks originating from Zn-WZnFe<sub>2</sub> POM consisting of Zn 2p<sub>1/2</sub> (1045.4 eV) and Zn 2p<sub>3/2</sub> (1022.3 eV). The two peaks at 711.4 and 724.6 eV in Figure 4A.S2b can be attributed to the presence of iron in +3 oxidation state. In comparison, the XPS of Zn-WZn<sub>3</sub>

POM shows the peaks of W 4f (35.8 and 37.9 eV), Zn 2p (1021.7 and 1044.8 eV), and oxygen 2p (530.6 and 533.0 eV). The shift to higher values in Zn-WZnFe<sub>2</sub> POM compared to parent Zn-WZn<sub>3</sub> POM can be attributed to strong anion-anion interaction in Zn-WZnFe<sub>2</sub> POM due to less overall negative charge.

#### **Density Functional Theory (DFT)**

Geometries of the sandwich polyoxometalates anions were fully optimized in Density Functional Theory (DFT) method using B3LYP functional in CPCM model, taking water as solvent and considering different spin states without magnetic coupling using unrestricted hybrid functional. In Zn-WZn<sub>3</sub>, the oxo band (appears at –6.46 eV) is defined as the highest occupied molecular orbital (HOMO) with doubly occupied oxygen orbital contribution and the tungsten band (appears at -2.30 eV) is defined as the lowest unoccupied molecular orbital (LUMO) with a large contribution from W 5d orbitals. The energy gap between the tungsten and oxo bands was found to be 4.16 eV (Table 4A.1). In the frontier orbitals of oxo band, the electron density is mostly localized on oxygen orbitals, and the tungsten band is mostly localized on the overlapping orbitals of oxygen and tungsten. While for the TMSP complexes, in between oxo and tungsten band, a series of single occupied molecular orbitals (SOMO) are contributed from the sandwich core where the number of unpaired electrons depends on the nature of the transition metal core (Fig. 4A.2). The energy gaps between the tungsten and oxo bands in TMSP complexes are found to be 4.16-4.30 eV, which is independent of the framework structure, but may depend on the functional and the spin multiplicity.<sup>25</sup>

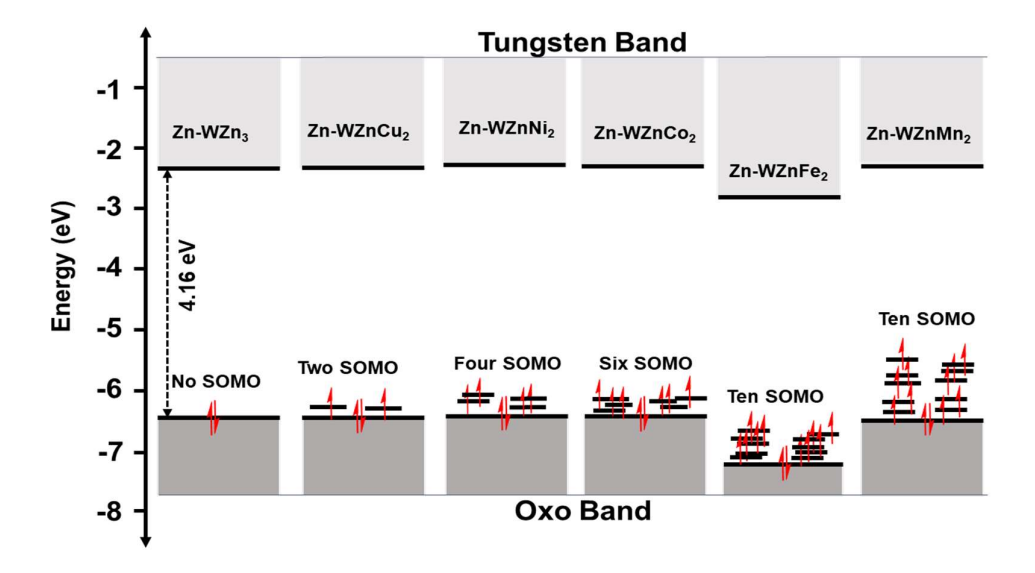


Figure 4A.2 Representation of the electronic arrangements in Zn-WZn<sub>3</sub> and TMSP complexes.

Table 4A.1 Band gap of Zn-WZn <sub>3</sub> and TMSP complexes calculated from DFT						
	Oxo	Band	Tungsten	Band	Bandgap	SOMO
	(eV)		(eV)		[HOMO-LUMO] (eV)	
Zn-WZn <sup>i</sup> Zn <sup>e</sup> <sub>2</sub>	-6.46		-2.30		4.16	
Zn-WZn <sup>i</sup> Cu <sup>e</sup> <sub>2</sub>	-6.48		-2.31		4.17	Two
Zn-WZn <sup>i</sup> Ni <sup>e</sup> <sub>2</sub>	-6.47		-2.25		4.22	Four
Zn-WZn <sup>i</sup> Co <sup>e</sup> <sub>2</sub>	-6.49		-2.29		4.20	Six
Zn-WZn <sup>i</sup> Fe(III) <sup>e</sup> <sub>2</sub>	-7.12		-2.84		4.28	Ten
Zn-WZn <sup>i</sup> Mn <sup>e</sup> <sub>2</sub>	-6.59		-2.31		4.30	Ten

As observed from Figure 4A.2, among the TMSP complexes, Zn-WZn $^{\dot{1}}$ Fe(III) $^{e}_{2}$  gave a bandgap of 4.30 eV with the lowest energy HOMO as well as LUMO among all the TMSP studied, probably due to the Fe(III) and overall charge of the complex. HOMO orbitals are localized purely on the oxygen atoms. All the LUMOs are localized on W orbitals as W-band and on the overlapping orbitals of oxygen and tungsten bonds; of which LUMO is mostly from the contribution of W  $d_z^2$  and LUMO+1 from W  $d_{xz}$  orbital of WZnFe<sub>2</sub> core. SOMO orbitals are contributions from two Fe and oxygen atoms.

#### **Charge Distribution and Spin Coupling effect**

To identify the role of Zn-WZn<sub>3</sub> and TMSPs in various oxidative and acid/base reactions, charge distribution on oxygen was determined (Table 4A.S2). The NBO (natural bond orbital) charge analysis reveals that transition metal substitutions do not affect the negative charge on μ4 oxygen (oxygen attached to Zn-heteroatom). The higher negative charges of corner (O<sub>c</sub>) and edge (O<sub>e</sub>) sharing oxygen atoms, than the terminal oxygens (O<sub>t</sub>) revealed the higher basicity of these oxygens. Also, the corner-sharing oxygen of Zn-WZn<sub>3</sub> and its Fe-substituted analogue (Zn-WZnFe<sub>2</sub>) has higher charges compared to other TMSPs, which imparts its highest activity in catalytic imine synthesis compared to other TMSPs (Table 4A.S4).<sup>30</sup> More importantly, the variation of charge on TMs following the O<sub>2</sub> binding ability of the TMs. Also, the free energy in different spin states was calculated to identify the effect of the environment on the spin states of these substituted transition metals. As can be seen from Table 4A.2, the high spin states for all the compounds are found to be the lowest energy state, i.e., undecitet for Zn-WZnMn<sub>2</sub> & Zn-WZnFe<sub>2</sub>, septet for Zn-WZnCo<sub>2</sub>, quintet for Zn-WZnNi<sub>2</sub>, triplet for Zn-WZnCu<sub>2</sub> and singlet

for Zn-WZn<sub>3</sub> i.e., tri-lacunary POM framework does not affect the properties of transition metal oxides.

<b>Table 4A.2</b> Energy difference ( $\Delta E$ , in kcal/mol) between the lower lying spin states (high spin, lower free									
energy) and hig	energy) and higher energy spin states (after coupling).								
Structure	States	ΔΕ	Structure	States	ΔΕ	Structure	States	ΔΕ	
	(2S+1)			(2S+1)			(2S+1)		
Zn-WZnMn <sub>2</sub>	Undecitet	0.0	Zn-WZnFe <sub>2</sub>	Undecitet	0.0	Zn-WZnCo <sub>2</sub>	Septet	0.0	
	Singlet	192.32		Nonet	15.79		Singlet	114.3	
				Septet	34.88				
				Singlet	94.81				
Zn-WZnNi <sub>2</sub>	Quintet	0.0	Zn-WZnCu <sub>2</sub>	Triplet	0.0	Zn-WZn <sub>3</sub>	Singlet	0.0	
	Singlet	94.09		Singlet	44.53				

For better understanding of the charge distribution on transition metals (Table 4A.S2) and the dioxygen activation ability of the TMSPs, catalytic activity towards imine synthesis using oxidative coupling of benzyl alcohol and aniline was performed using 2 mol% Zn-WZn<sub>3</sub> and other TMSPs in the presence of dioxygen and t-BuOK according to our previously reported procedure.<sup>35</sup> As expected Zn-WZnMn<sub>2</sub> and Zn-WZnFe<sub>2</sub> show highest activity and selectivity toward imine synthesis similar to Zn-WZn<sub>3</sub>, which justifies the higher charge distribution on Mn, Fe and Zn as well as their higher dioxygen activation ability compared to others.

# 4A.2.3 When Fe(III) is present at internal sandwich position

# 4A.2.3a With Zn as heteroatom and TM<sub>e</sub>=Mn/Co/Ni/Cu/Zn

Compounds 2a/2b/2c/2d and 2c-M were characterized using SC-XRD, FT-IR, ESI-MS, XPS, and UV-visible spectroscopy (Figure 4A.3-4A.8). The framework structure of 2c/2d/2c-M was confirmed by SC-XRD (CCDC 2330244, 2330254 and 2330258). 2c crystallizes in a triclinic

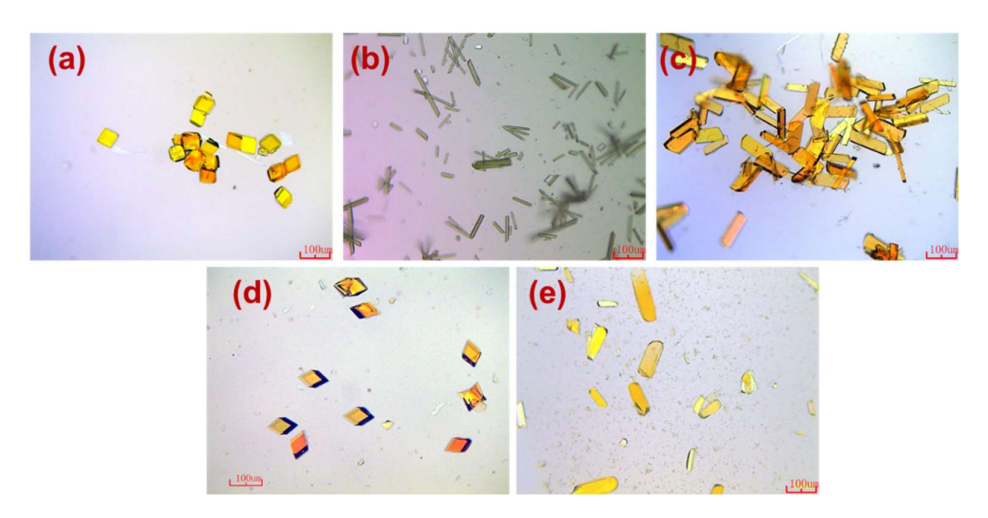
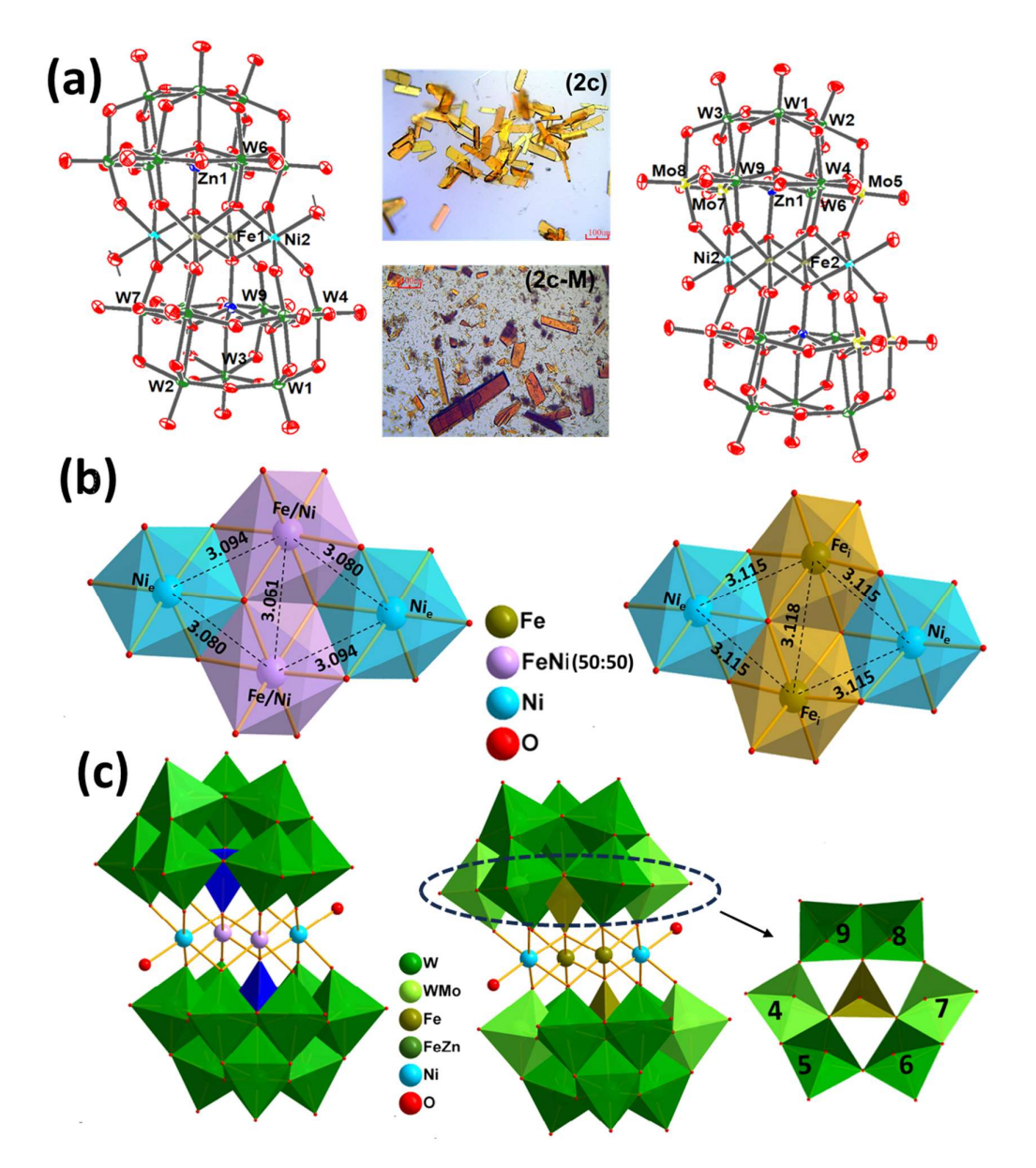


Figure 4A.3 Optical images of sandwich POMs; (a) 2a (b) 2b (c) 2c (d) 2d (e) 2.

lattice with  $P\overline{1}$  space group while its analogue mixed addenda **2c-M** and **2d** crystallizes in a monoclinic lattice with a P2<sub>1</sub>/n space group (Table 4A.S5).

The 3D SC-XRD structure of 2c/2d and 2c-M shows that the tri lacunary Keggin moiety contains a tetrahedrally bound zinc atom in the center as a templating agent to triads of addenda W/Mo atoms. The tetrasubstituted sandwich core consists of Fe at the internal  $\{TM_i\}$  position



**Figure 4A.4** (a) ORTEP drawing (with 60% ellipsoid probability) and Optical images of sandwich POMs; **2c** (left) and **2c-M** (right); (b) Cubane core showing the interatomic distance between transition metals in **2c** (left) and **2c-M** (right); (c) combined polyhedral/ball and stick representation of the single-crystal X-ray structure of polyoxometalate **2c** (left) and **2c-M** (right), belt 2 depicting different ratios of molybdenum to tungsten in **2c-M**; Countercations and hydrogen atoms are omitted for clarity.

184

and Ni as external atoms  $\{TM_e\}$  in 2c/2c-M while in 2d, Cu is at the external transition position (Figure 4A.4b). The optical image shows that the substitution of external transition metals in 2 completely changes the size and shape of the crystals (Figure 4A.3). The ESI-MS spectrum of parent 2 shows one envelope of peaks at a m/z of 1593.43 assigned for a  $\{H_{11}[Zn_2Fe_2(ZnW_9O_{34})_2]^{3-}$  cluster anion. Transition metal substitutes analog of 2 shows the envelope of peaks at m/z 1591.52 for  $\{H_{11}[Cu_2Fe_2(ZnW_9O_{34})_2]^{3-}$ , 1589.52 for  $\{H_{11}[Ni_2Fe_2(ZnW_9O_{34})_2]^{3-}$ , 1589.46 for  $\{H_{11}[Co_2Fe_2(ZnW_9O_{34})_2]^{3-}$  and 1586.91 for  $\{H_{11}[Mn_2Fe_2(ZnW_9O_{34})_2]^{3-}$  thus indicating that these POMs cluster anions have high hydrolytic stability in the solution (Figure 4A.5, Table 4A.S8). The 2c-M shows the envelopes of peaks (Figure 4A.6, Table 4A.S6) in the range of m/z 1490-1630 for  $H_{11}[\{Ni_2Fe_2(H_2O)_2(ZnMo_xW_{9-x})_2\}^{3-}]$ .

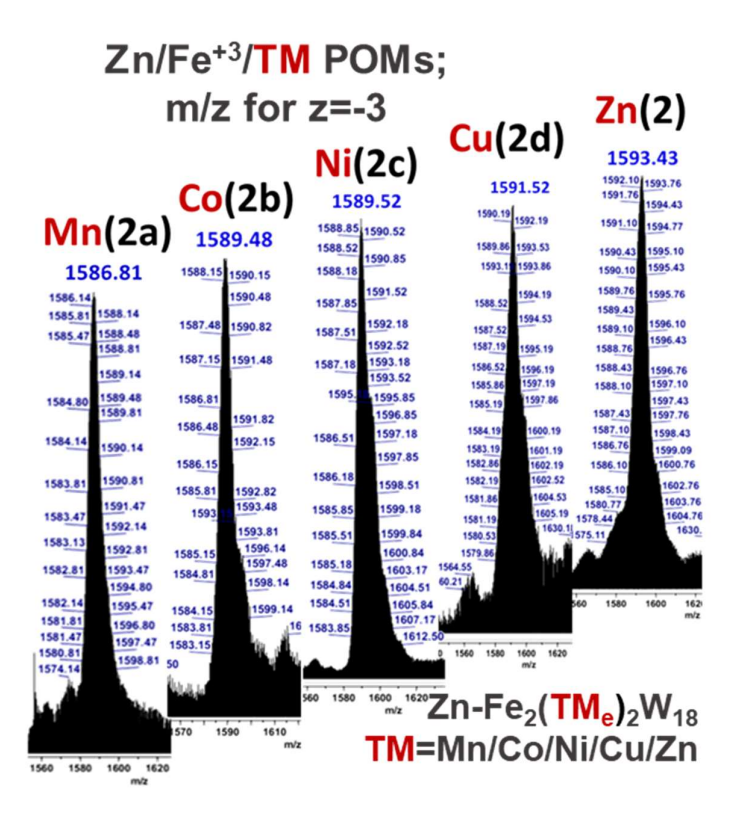


Figure 4A.5 ESI-MS spectra of 2c-M in the range of m/z 1200-1900 (z=-3).

The most abundant anion in 2c-M has the composition without Mo addenda in the formula i.e. formation of 2c dominates in the synthesis of 2c-M. However, the highest Mo/W ratio in 2c-M was found to be 3:15 with a constant -14 charge of

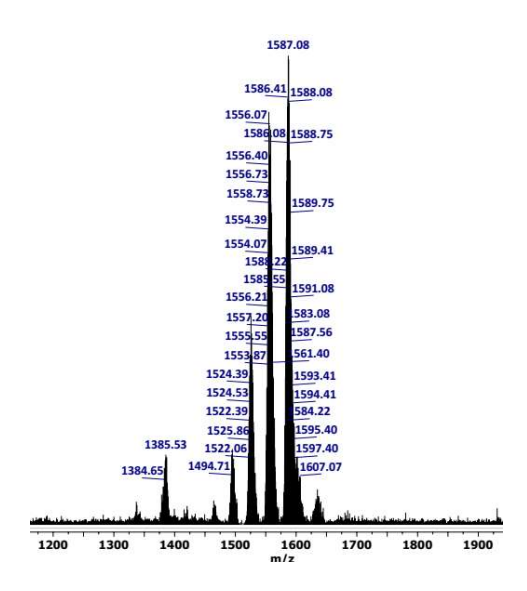


Figure 4A.6 ESI-MS spectra of 2c-M in the range of m/z 1200-1900 (z=-3).

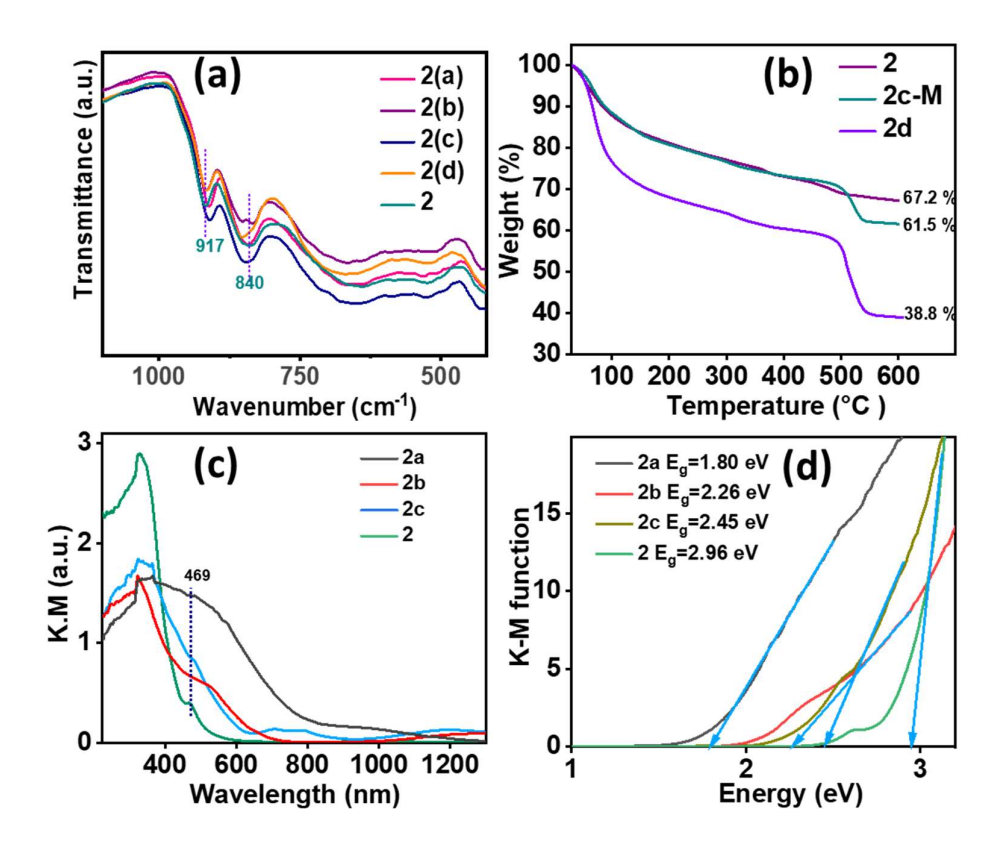


Figure 4A.7 (a) FT-IR spectra of 2a/2b/2c/2d/2 showing the impact of external transition metal substitution in terms of shifting from parent 2; (c) TGA curves of 2/2d/2c-M. (a) solid-state UV-visible spectra and (b) corresponding optical band-gap shifting derived from the Kubelka-Munk equation in 2a/2b/2c/2.

the cluster. From the comparison of **2c-M** with the reference (Figure 1.10, chapter 1) structure, a small amount of Mo incorporation is favorable at 4/7 positions of the belt, while other

positions in the belt as well as in the cap are less favorable for the incorporation of Mo addenda in the tetrasubstituted framework (Figure 4A.4c).

The distance between Ni atoms at the external and Ni/Fe (50:50) at the internal positions is 3.08-3.09 Å, however, the distance between Ni/Fe atoms in the internal positions is 3.06 Å in **2c.** The distance between Ni atoms at the external and Fe at the internal positions is 3.11 Å, and, the distance between internal Fe atoms is 3.11 Å in **2c-M** (Figure 4A.4b). The FT-IR spectra of all these POMs show the characteristics peaks in the region 650-920 cm<sup>-1</sup> e.g. the FT-IR spectra of **2c** show characteristics peaks at 910 cm<sup>-1</sup> (W=O<sub>term</sub>), 845, 679 cm<sup>-1</sup> (W-O-W) cm<sup>-1</sup> (Figure 4A.7A) while the FT-IR spectra of **2c-M** show characteristics peak similar to **2c** in the region 650-920 cm<sup>-1</sup> with slight shifting due to Mo incorporation in the framework. TGA Thermal stability was determined by thermogravimetric analysis from 25 to 600 °C (Figure 4A.S9). The TGA curve of **2** shows high thermal stability even up to 600 °C. The first weight loss of ~15% was observed in the range of 30-200 °C attributed to the release of hydrated water molecules. However, the weight loss is more in mixed addenda **2-M** and TMSP **2d** compared to parent **2**. This shows that transition metal substitution in these POMs decreases thermal stability of these POMs.

BVS calculation indicates that all addenda atoms are in their highest oxidation state (+6) and Fe, Ni, Cu, Zn in +3, +2, +2 and +2 oxidation states respectively (Table 4A.S7). Apart from the BVS, the oxidation states of all of the atoms in **2c-M** were determined from XPS analysis. The two peaks at 713.4 and 719.6 eV in **2c-M** can be attributed to the presence of Fe in a +3

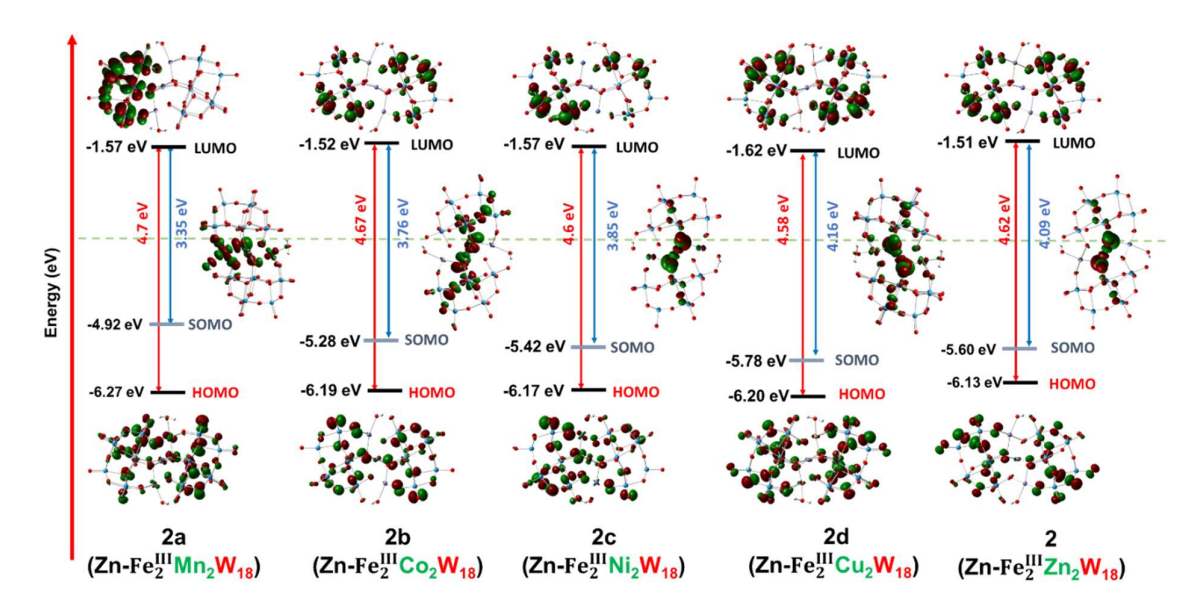


Figure 4A.8 Frontier molecular orbitals of tetrasubstituted sandwich POMs showing band gaps as well as electron density on addenda atoms in 2a/2b/2c/2d/2.

oxidation state. The W 4f doublet appears between 36.3 and 38.4 eV, corresponding to W  $4f_{7/2}$  and  $4f_{5/2}$  in +6 oxidation state. In UV-visible spectroscopy, all these POMs show a strong and broad absorption band between 280-350 nm, as expected, due LMCT) ( $O_{2p}$  to  $W_{5d}$ ) transitions for ZnW<sub>9</sub>O<sub>34</sub> units. Apart from this, all these POMs show a feeble peak due to MPCT around 469 nm. The absorbance spectra as well as the band gap of these TMSP are highly influenced by the substituted transition metals and show shifts in the absorption band e.g. the LMCT band shifts to a lower wavelength for 2a/2b/2c/2d than parent 2. Similarly, HOMO-LUMO gap increases with the increase in the atomic number of transition metals except for 3d. The trend of the band gap is 2c > 2b > 2a > 2 (Figure 4A.7b). This increase in band gap was further supported by the DFT study, which indicates that the band gap (highest SOMO to LUMO) increases when we go from 2a to 2d. Interestingly, the LUMO of all these POMs lies at the internal transition atom i.e. Fe(III) (Fig. 4A.S8)

# 4A.2.3b With Co as heteroatom and TM<sub>e</sub>=Mn/Co/Ni/Cu/Zn

Compounds 3a/3b/3c/3d and 3b-M were characterized using SC-XRD, FT-IR, ESI-MS, XPS, and UV-visible spectroscopy (Figure 4A.9-4A.16). The framework structure was confirmed by SC-XRD (CCDC 2330249, 2330250) for 3b, 3c and 3b-M.

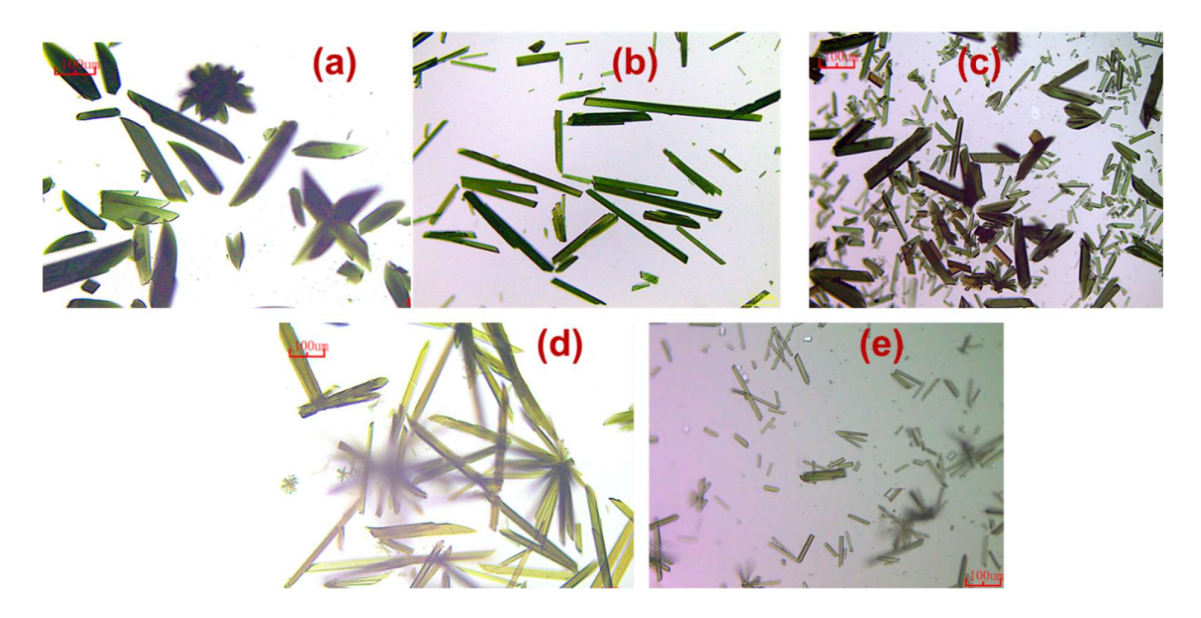
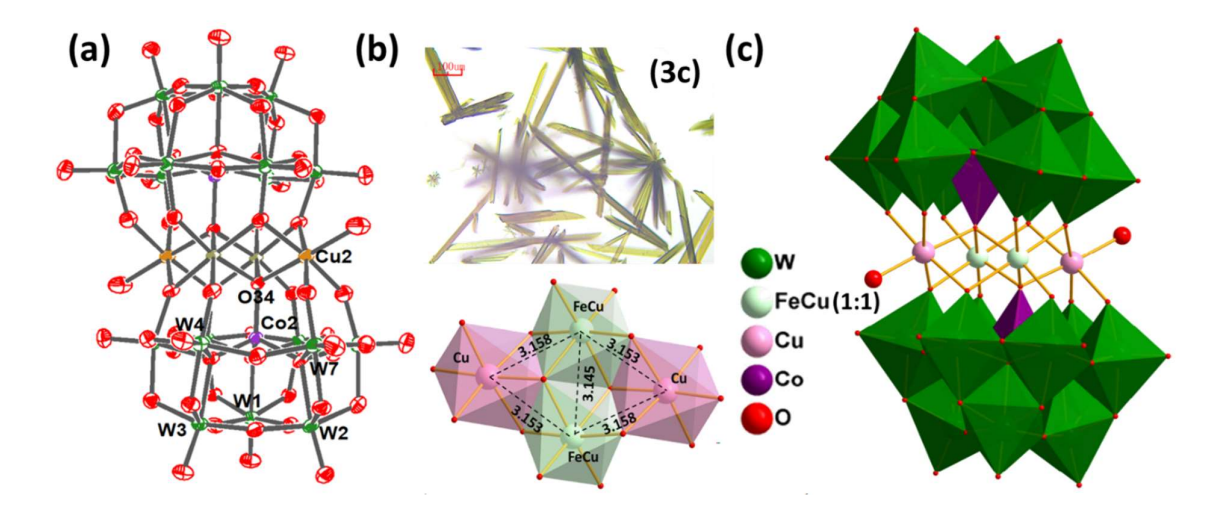
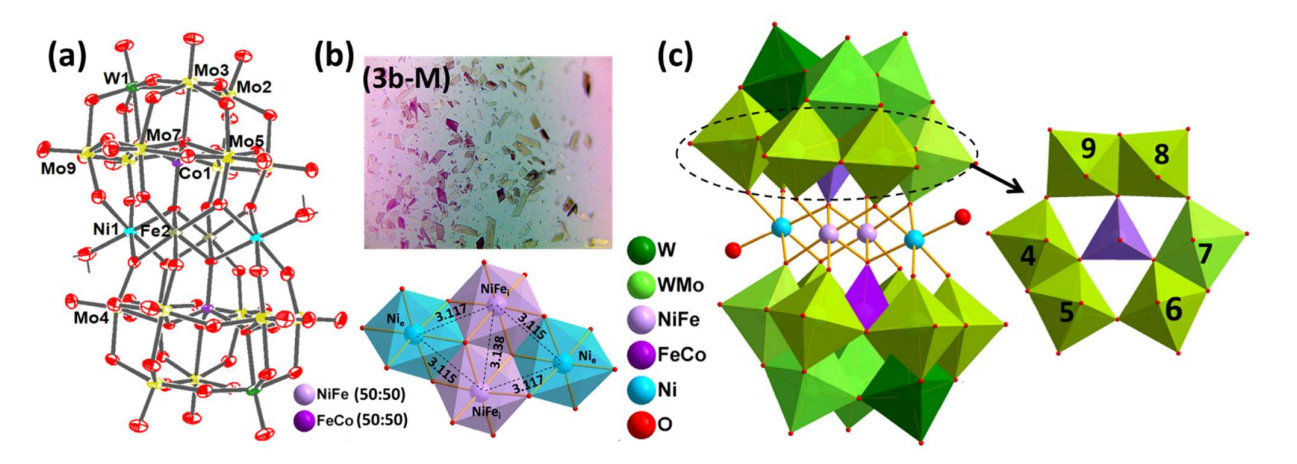


Figure 4A.9 Optical images of sandwich POMs; (a) 3a (b) 3 (c) 3b (d) 3c (e) 3d.



**Figure 4A.10** (a) ORTEP drawing (with 60% ellipsoid probability) (b) Optical images and Cubane core showing the interatomic distance between transition metals in **3c** (c) combined polyhedral/ball and stick representation of the single-crystal X-ray structure of polyoxometalate **3c.** Countercations and hydrogen atoms are omitted for clarity.

3b crystallize in triclinic lattice with  $P\overline{1}$  space group while its analog mixed addenda 3b-M crystallize in monoclinic lattice with P2<sub>1</sub>/n space group (Table 4A.S5). The 3D SC-XRD structure of **3b**, **3c** and **3b-M** shows that the trilacunary Keggin moiety contains a tetrahedrally bound Co atom in the center as a templating agent to triads of addenda W/Mo atoms. The tetrasubstituted sandwich core consists of Fe at internal  $\{TM_i\}$  position and Ni as external



**Figure 4A.11** (a) ORTEP drawing (with 60% ellipsoid probability) (b) Optical images and Cubane core showing the interatomic distance between transition metals in **3b-M** (c) combined polyhedral/ball and stick representation of the single-crystal X-ray structure of polyoxometalate **3b-M**. Countercations and hydrogen atoms are omitted for clarity; belt 2 depicting different ratios of molybdenum to tungsten in **3b-M**. Countercations and hydrogen atoms are omitted for clarity.

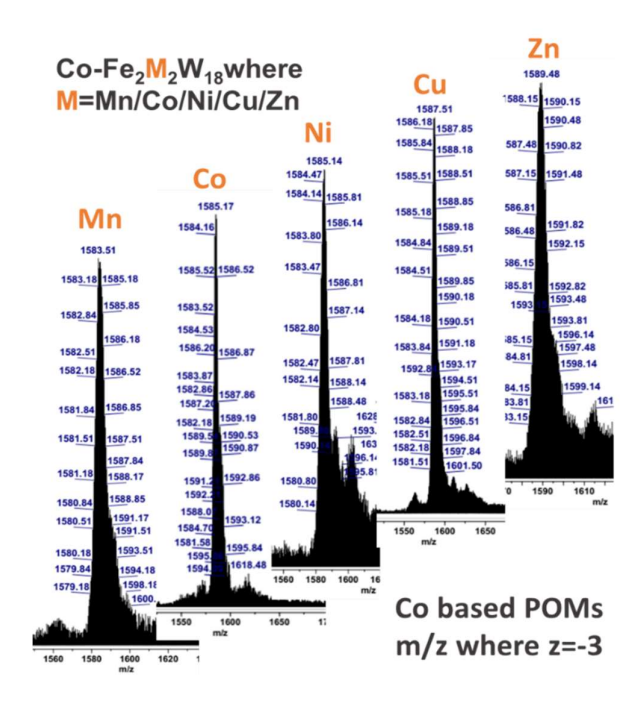


Figure 4A.12 ESI-MS spectra of 3a/3/3b/3c/3d in the range of m/z 1500-1650 (z=-3).

atoms {TM<sub>e</sub>} in **3b, 3b-M** while in **3c,** Fe at internal position and Cu as external atoms (Figure 4A.10/11). The optical image shows that substitution of external transition metals in **3** completely changes the size and shape of the crystals (Figure 4A.9). The ESI-MS spectrum of the parent **3** shows one envelope of peaks at a m/z of 1585.17 assigned for a {H<sub>11</sub>[Co<sub>2</sub>Fe<sub>2</sub>(CoW<sub>9</sub>O<sub>34</sub>)<sub>2</sub>]<sup>3-</sup> cluster anion. Transition metal substitutes analogs of **3** shows the envelope of peaks at m/z 1587.51 for {H<sub>11</sub>[Cu<sub>2</sub>Fe<sub>2</sub>(CoW<sub>9</sub>O<sub>34</sub>)<sub>2</sub>]<sup>3-</sup>, 1585.14 for

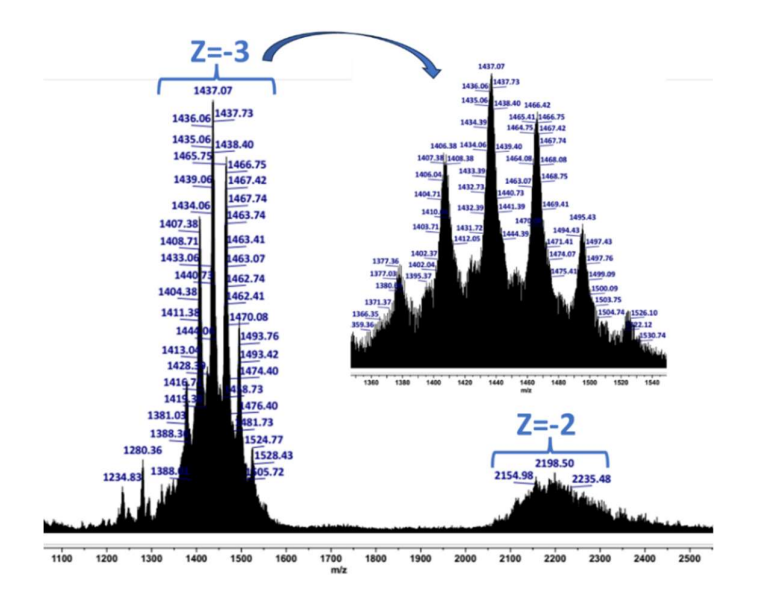


Figure 4A.13 ESI-MS spectra of 3b-M in the range of m/z 1100-2500 (z=-3).

 $\{H_{11}[Ni_2Fe_2(ZnW_9O_{34})_2]^{3-}$ , and 1583.51 for  $\{H_{11}[Mn_2Fe_2(ZnW_9O_{34})_2]^{3-}$  thus indicating that these POMs cluster anions have high hydrolytic stability in the solution (Figure 4A.12, Table 4A.S10).

The **3b-M** shows the envelopes of peaks (Figure 4A.13) in the range of m/z 1370-1490 for H11[ $\{Ni_2Fe_2(H_2O)_2(CoMo_xW_{9-x})_2\}^{3-}$ ]. The most abundant anion in **3b-M** has the composition without Mo addenda in the formula i.e. formation of 2c dominates in the synthesis of 2c-M. ESI-mass spectrum of 3 in shows the envelope of peaks at m/z 1585 (z=-3) while the analog mixed addenda POMs structure show the isotopic multiple envelopes of peaks attributed to varying ratios of molybdenum to tungsten. The mixed addenda sandwich POMs 3b-M show the envelopes of peaks (Figure 4A.13, Table 4A.S11) in the range of m/z 1370-1490 for  $[H_{11}{Ni_2Fe_2(H_2O)_2(CoMo_xW_{9-x})_2}^{3-}]$ for z=-3and m/z2100-2300  $[H_{12}{Ni_2Fe_2(H_2O)_2(CoMo_xW_{9-x})_2}^{2-}]$  for z=-2. The most abundant anion in **3-M** has the composition of Mo/W (5:13) with the formula  $[H_{10}\{Ni_2Fe_2(H_2O)_2(CoFeMo_5W_{13}O_{68}\}^3]$ , while the Mo/W ratio varies from 1:5 to 7:11 with a constant charge of the cluster, i.e., -14. From the

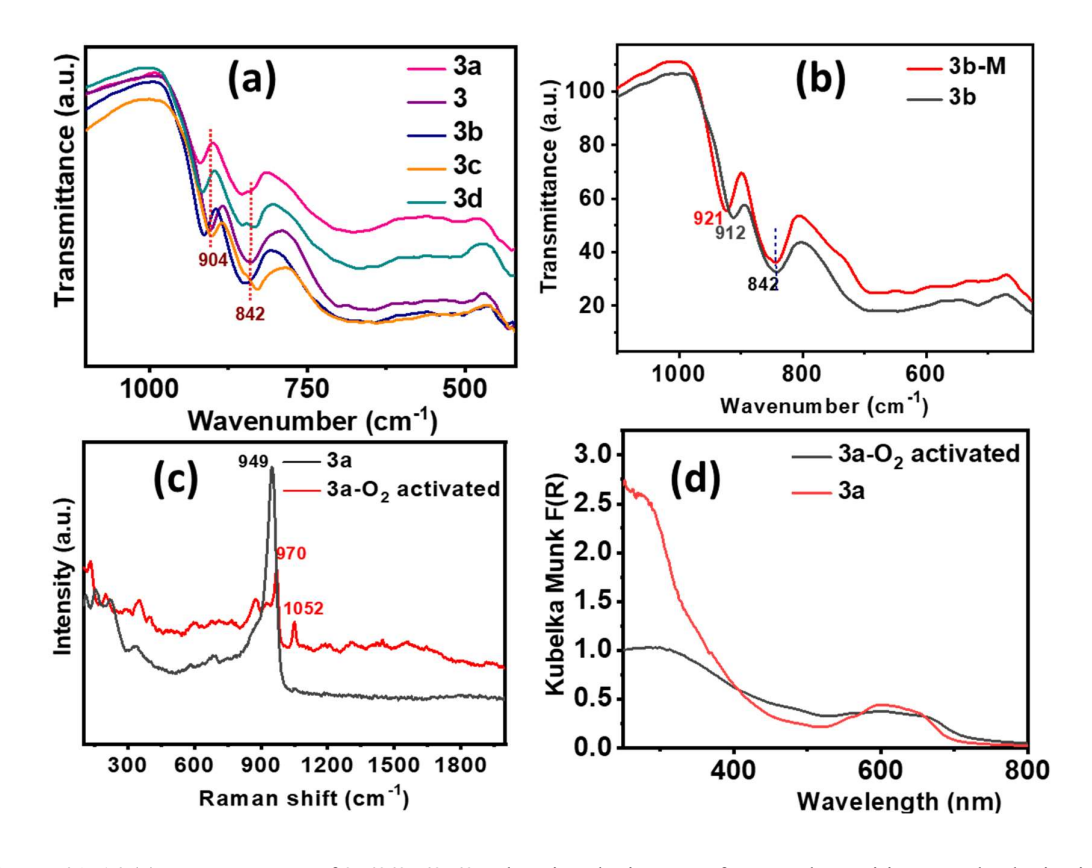
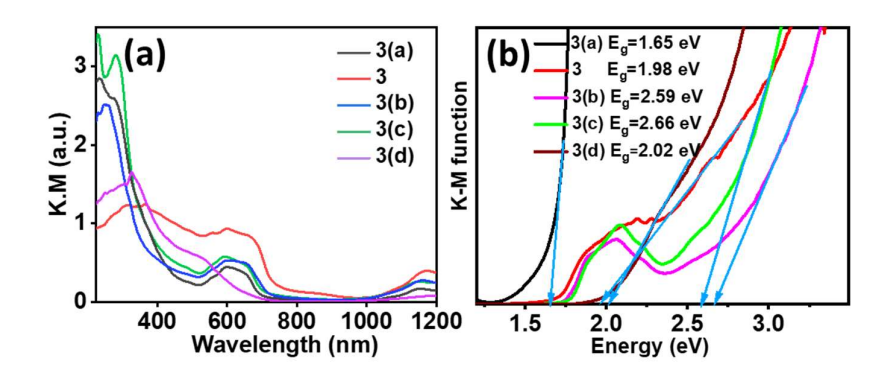


Figure 4A.14 (a) FT-IR spectra of 3a/3/3b/3c/3d showing the impact of external transition metal substitution in terms of shifting from parent 3; (b) shift in FT-IR indicating Mo-doping in 3b and 3b-M and (c) Raman spectra and (d) corresponding UV spectra of 3a before and after dioxygen activation.

comparison of **3b-M** with the reference structure (Figure 1.10), it is clear that only a small amount of Mo incorporation is favorable at all belt position, while other positions in the cap do not favor the incorporation of Mo addenda in the tetrasubstituted framework (Figure 4A.11).

All these POMs (3a/3b/3c/3d) show similar IR patterns to the parent 3 because of their similar structural geometry. The characteristic W = O<sub>t</sub> ( $904 \text{ cm}^{-1}$ ), and W-O<sub>c</sub>-W ( $842 \text{ cm}^{-1}$ ), bond stretching frequencies of 3 remain almost identical even after substitution of first-row transition-metal atoms, as shown in Figure 4A.14. TGA Thermal stability was determined by thermogravimetric analysis from 25 to 600 °C (Figure 4A.S10). The TGA curve of 3 shows high thermal stability even up to 600 °C. The first weight loss of  $\sim 7\%$  was observed in the range of 30-200 °C attributed to the release of hydrated water molecules. However, the weight loss is more in mixed addenda 3-M and TMSP 3c compared to parent 3. This shows that transition metal substitution in these POMs decreases the thermal stability of these POMs. However, the thermal stability of these Co/Fe based POMs (3/3-M/3c) is higher than their corresponding Zn/Fe based POMs (2/2-M/2d).

BVS indicates W/Mo in +6, Co, Ni, Cu in +2 and Fe in +3 oxidation state in **3b**, **3c** and **3b-M** (Table 4A.S9). Apart from the BVS, the oxidation states of all of the atoms in **3b-M** were determined from XPS analysis. The XP spectra of **3b-M** revealed the presence W, Mo, Fe, Ni, Co and oxygen (Figures 4A.S8). The two peaks at 712.4 and 726.7 eV in **3b-M** can be attributed to the presence of Fe in a +3 oxidation state. The W 4f doublet appears between 35.4 and 37.5 eV, corresponding to W  $4f_{7/2}$  and  $4f_{5/2}$  and Mo 3d doublet appears between 232.5 and 235.6 eV, corresponding to Mo  $3d_{5/2}$  and  $3d_{3/2}$  indicating the presence of W/Mo in +6 oxidation state.



**Figure 4A.15** (a) solid-state UV-visible spectra and (b) optical band-gap shifting derived from the Kubelka-Munk equation in **3a/3/3b/3c/3d**.

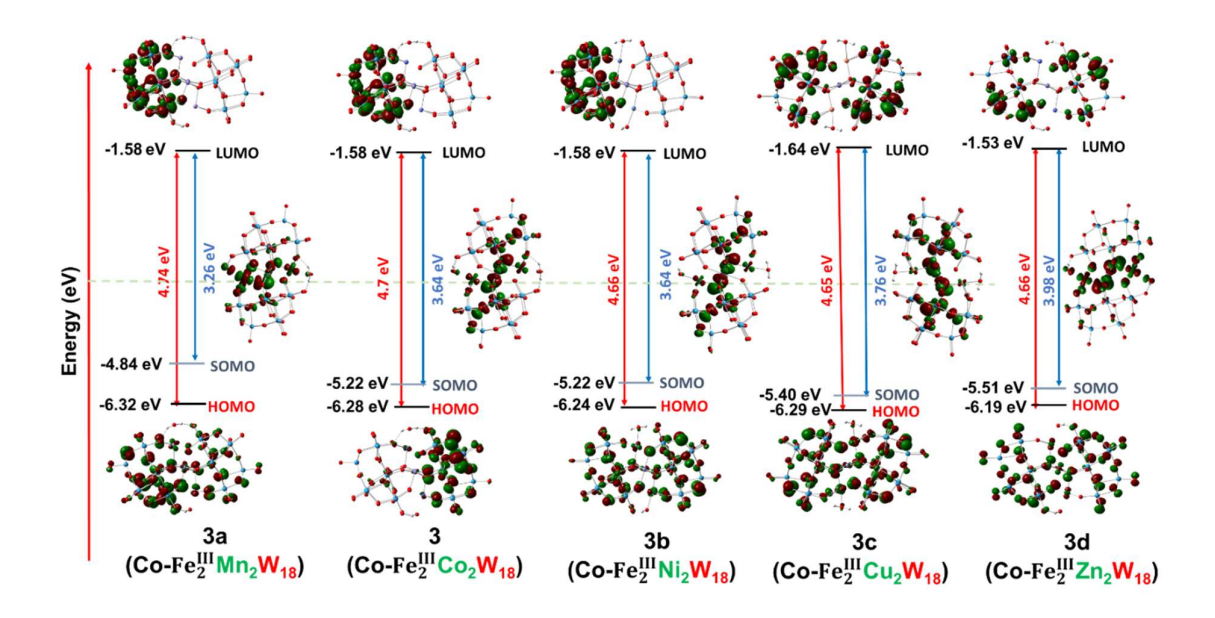


Figure 4A.16 FMOs of tetrasubstituted sandwich POMs showing band gaps as well as electron density on addenda atoms in 3a/3/3b/3c/3d.

In UV-visible spectroscopy, all these POMs show a strong and broad absorption band between 280-350 nm, as expected, due LMCT) (O2p to W5d) transitions for  $CoW_9O_{34}$  units (Figure 4A.15). The HOMO-LUMO energy gaps of these TMSP are highly influenced by the substituted transition metals and show shifts in the absorption band e.g. the LMCT band shifts to a lower wavelength for 3a/3b/3c/3d than parent 3. Similarly, the band gap of 3 and its TM-substituted POMs is remarkably influenced by the substituted TM, and HOMO-LUMO gap increases with the increase in the atomic number of transition metals except for 3d. The trend of the band gap is 3c > 3b > 3 > 3a (Figure 4A.15b). The anomalous behavior of 3d might be due to competition between Zn and Co to the heteroposition. This increse in band gap was further supported by the DFT study, which indicates that band gap (highest SOMO to LUMO) increses when we go form 3a to 3d (Figure 4A.16).

# 4A.2.4 When Mn(III) is present at the internal sandwich position

# 4A.2.4a With Zn as heteroatom and TM<sub>e</sub>=Fe

Compounds **4a** and **4a-M** were characterized using SC-XRD, FT-IR, and ESI-MS (Figure 4A.17-20). The framework structure of **4a** was confirmed by SC-XRD (**CCDC 2330246**) (Table 4A.S5) however crystals of **4a-M** give poor diffractions. The dark orange-colored octahedral crystals (Figure 4A.18) of **4a** crystallize in monoclinic with P2<sub>1</sub>/n space group. The 3D SC-XRD structure of **4a** shows that the trilacunary Keggin moiety contains a tetrahedrally bound zinc atom in the center as a templating agent to triads of addenda W atoms.

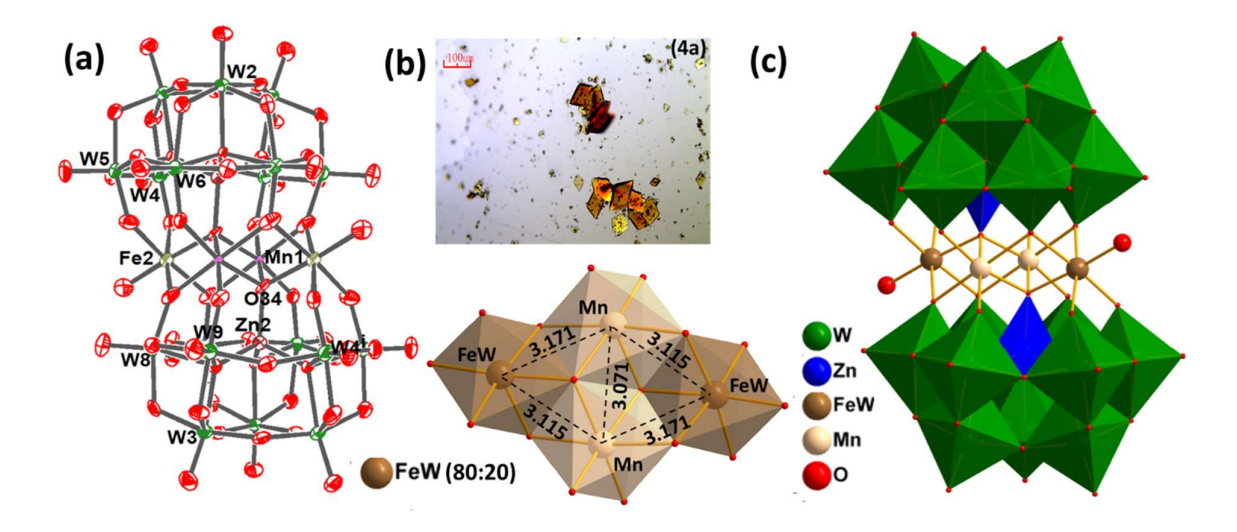


**Figure 4A.17** (a) ORTEP drawing (with 60% ellipsoid probability) (b) Optical images and Cubane core showing the interatomic distance between transition metals in **4a** (c) combined polyhedral/ball and stick representation of the single-crystal X-ray structure of polyoxometalate **4a.** Countercations and hydrogen atoms are omitted for clarity.

The tetrasubstituted sandwich core consists of Mn at the internal  $\{TM_i\}$  position and Fe/W (80:20) as external atoms  $\{TM_e\}$ . The distance between Fe/W atoms at the external and Mn at the internal positions is 3.11-3.17 Å, however, the distance between Mn atoms in the internal positions is 3.07 Å in **4**a (Fig. 4A.17). BVS calculation indicates that all addenda atoms are in their highest oxidation state (+6) and Zn, Fe, Mn in +2, +2 and +3 oxidation state respectively (Table 4A.S12). The FT-IR spectra of **4a** show the characteristics peaks at 921 cm<sup>-1</sup> (W=O<sub>term</sub>), 842, 681 cm<sup>-1</sup>

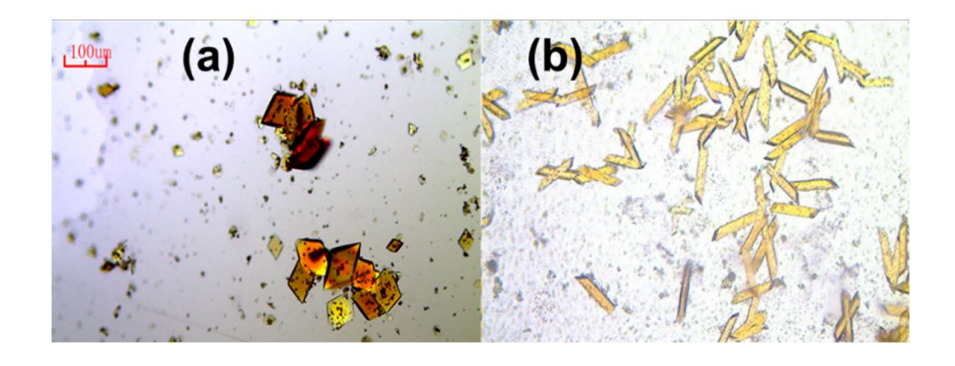


Figure 4A.18 Optical images of sandwich POMs; (a) 4a and (b) 4a-M.

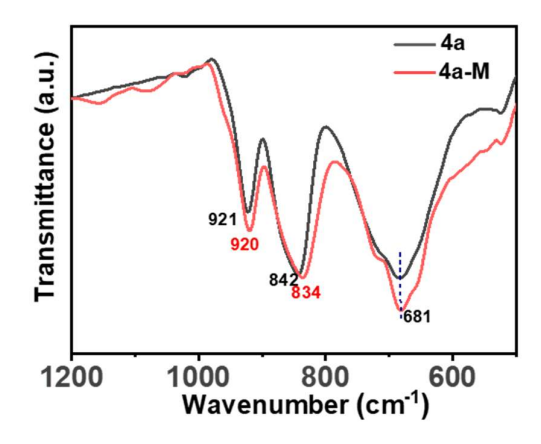


Figure 4A.19 Effect of molybdenum incorporation in the framework of tetrasubstituted sandwich POMs in terms of shifting of characteristics peaks in FT-IR of 4a and 4a-M.

(W-O-W) cm<sup>-1</sup> while **4a-M** show the characteristics peaks at 920 cm<sup>-1</sup> (M=O<sub>term</sub>), 834, 681 cm<sup>-1</sup> (M-O-M) cm<sup>-1</sup> (Figure 4A.19) with slight shifting thus indicating very less Mo incorporation in the framework which was further confirmed in ESI-MS.

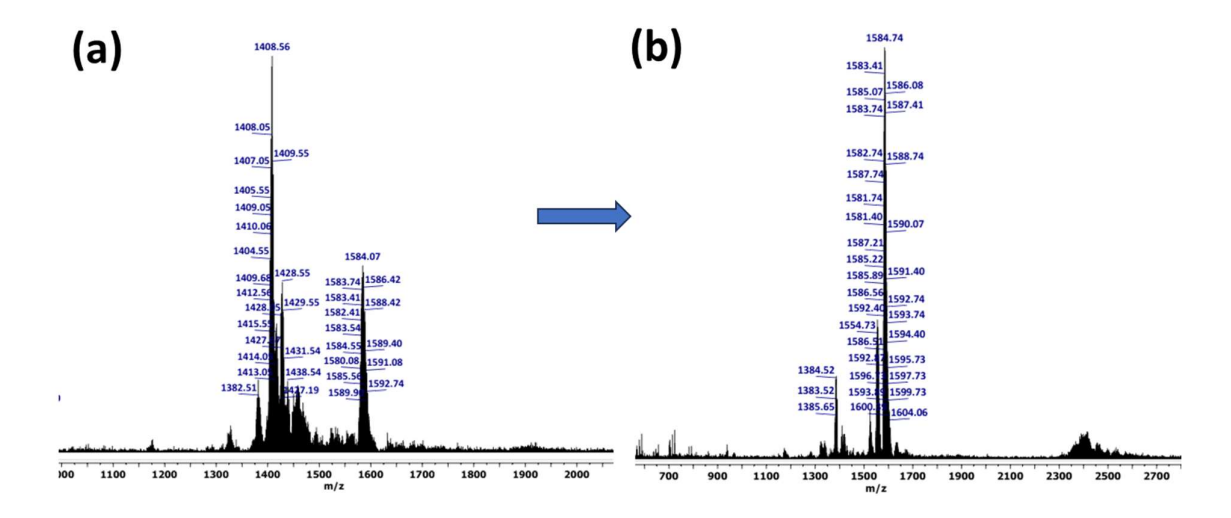


Figure 4A.20 ESI-MS spectra of (a) 4a (b) 4a-M in the range of m/z 1000-2700 (z=-3).

The ESI-MS spectrum of the parent 4a shows one envelope of peaks at a m/z of 1584.07 assigned for a  $\{H_{11}[Fe_2Mn_2(ZnW_9O_{34})_2]^{3-}$  cluster anion. The analog mixed addenda 4a-M show the envelopes of peaks (Figure 4A.20, Table 4A.S13) for the most abundant anion at m/z 1584.74 for  $\{H_{11}[Fe_2Mn_2(ZnFeW_{18}O_{68})]^{3-}$  cluster anion thus indicating equal probability for Zn and Fe at heteroposition which was also observed in 2-M and 3-M. The highest Mo/W ratio in 4a-M was found to be 2:16 with z=-3 and further pH variation does not improve the Mo/W ratio.

<b>Table 4A.3</b> Effect of Mo incorporation and position towards optical band gap, Mo/W Ratio.								
POMs	Optical Band gap from DRS	Mo:W ratio						
(Reference Code)	(eV)	Abundant Mo:W	Maximum Mo:W					
A. Effect of changing transition metal at external sandwich positions								
$2a \rightarrow 2b \rightarrow 2c$	1.80 → 2.26 → 2.41							
$3a \rightarrow 3 \rightarrow 3b \rightarrow 3c$	$1.65 \rightarrow 1.98 \rightarrow$ $2.59 \rightarrow 2.66$							
B. Effect of change	e in heteroatoms							
2 vs 3d	3.03 vs 2.02							
2b vs 3	2.26 vs 1.98							
C. Effect of Mo in	corporation in fr	amework						
2c vs 2c-M								

<b>Table 4A.4</b> Effect of Mo incorporation and position towards optical band gap, Mo/W Ratio (From DFT)							
POMs	Band gap (eV) LMCT (O →	Atom/grou atoms at w	-	LUMO position (eV)			
	W/Mo) / <b>MPCT</b> (SOMO → W/Mo)	Highest SOMO	LUMO				
A. Effect of MPCT	transition metal	at external	sandwich	position towards			
$2a \rightarrow 2b \rightarrow 2c \rightarrow 2d$	3.35 < 3.76 < 3.85 < 4.16	Mn/Fe <sup>3+</sup> ; Fe <sup>3+</sup> /Zn; Fe <sup>3+</sup> ; Fe <sup>3+</sup>	W only for all	-1.57 → -1.52 → -1.57 → -1.62			
$3a \rightarrow 3 \rightarrow 3b \rightarrow 3c \rightarrow 3d$	3.26 < 3.64 = 3.64 < 3.76 < 3.98	Mn/Fe <sup>3+</sup> ; Fe <sup>3+</sup> /Co; Fe <sup>3+</sup> /Co; Fe <sup>3+</sup> /Co; Fe <sup>3+</sup> /Zn	W only for all	-1.58 → -1.58 → -1.58 → -1.64 → -1.53			
B. Effect of c	B. Effect of change in heteroatom towards MPCT						
2 vs 3d	4.09 vs 3.98	Fe <sup>3+</sup> ; Fe <sup>3+</sup> /Zn	W only	-1.51 vs -1.53			

<b>3</b> vs <b>2b</b> 3.64 vs	3.76 Fe <sup>3+</sup> /Co; Fe <sup>3+</sup> /Zn	W only	-1.58 vs -1.52
-------------------------------	--	--------	----------------

### **4A.3 Conclusion**

Following the synthesis of various mixed-metal, mixed-addenda TMSPs and theoretical analysis of these POMs using DFT, it is evident that orbital engineering and electronic bandgap align with the optical bandgap, as summarized in Table 4A.3 and 4A.4. The data in these Table indicate that modifying a transition metal at external sandwich or heteroatom positions within these TMSPs or incorporating Mo addenda significantly impacts bandgap modulation. For example, when moving from right to left across a row of 3d transition metals (Zn to Mn), altering the transition metal at the external sandwich or heteroatom position decreases the band gap, a trend also supported by theoretical calculations. From this, we observed that transition metal at external position impacts the optical band gap, however effect is comparatively less than internal sandwich position.

# **4A.4 Experimental Section**

### 4A.4.1 General Information and Instrumentation

# 4A.4.1a Materials and Methods

Already mentioned in section 2.4.1a (chapter 2)

### 4A.4.1b Instrumentation

Already mentioned in section 2.4.1b (chapter 2)

Crystal data, data collection parameters, refinement statistics, and the Cambridge Crystallographic Data Centre; CCDC number (2330244, 2330246, 2330249, 2330250, 2330254, 2330258).

# 4A.4.1c Density Functional Theory (DFT) Calculation.

Already mentioned in section 2.4.1c (chapter 2)

# 4A.4.2 Synthesis

Na<sub>12</sub>[WZn<sub>3</sub>(H<sub>2</sub>O)<sub>2</sub>(ZnW<sub>9</sub>O<sub>34</sub>)<sub>2</sub>]•13H<sub>2</sub>O (Zn-WZn<sub>3</sub>). A mixture of Na<sub>2</sub>WO<sub>4</sub>.2H<sub>2</sub>O (16.000 g, 48.48 mmol), H<sub>2</sub>O (60 mL) and conc. HNO<sub>3</sub> (2 mL) was transferred into Teflon microwave vials. The sample mixture was microwave irradiated by controlled pressure programming with a power ramp for 5 min. and holding for 30 min. at 85 °C, under 300 W maximum power (table S1, SI). After cooling to room temperature, the resultant solution was charged with Zn(NO<sub>3</sub>)<sub>2</sub>.6H<sub>2</sub>O (3.748 g, 12.56 mmol) and further microwave irradiated for 30 min at 85 °C, maintaining the previous parameters. The obtained hot solution was filtered and the filtrate was

allowed for crystallization. After standing for 3 days colourless needle shaped crystals were collected by filtration, recrystallized from water, and dried at ~80 °C under vacuum to get the title compound Zn-WZn<sub>3</sub> (6.159 g, 47.2%). FT-IR (cm<sup>-1</sup>): 1624, 1386, 916, 865, 686, 521. Raman (solid), cm<sup>-1</sup>: 230, 313, 644, 706, 787, 872, 911, 950, 2622, 2647, 3463, 3476.

Na<sub>10</sub>[WZnFe<sub>2</sub>(H<sub>2</sub>O)<sub>2</sub>(ZnW<sub>9</sub>O<sub>34</sub>)<sub>2</sub>]•31H<sub>2</sub>O (Zn-WZnFe<sub>2</sub>). A 0.5 mL aq. solution of Fe(NO<sub>3</sub>)<sub>3</sub>.9H<sub>2</sub>O ( 0.436 g, 1.80 mmol) was added dropwise to the 5 mL aq. solution of Zn-WZn<sub>3</sub> (0.640 g, 0.12 mmol) in a round bottom flask with stirring and continued stirring for 1 h. Upon addition of 0.5 g of sodium acetate, the light yellow solution became turbid. This turbid solution was kept at 0 °C which appeared as microcrystalline powder after 2 h, which was filtered off. The microcrystalline powder was washed with cold methanol/water (3:1) and dried at room temperature under vacuum to obtain Zn-WZnFe<sub>2</sub> (0.473 g, 74.3 %). FT-IR (cm<sup>-1</sup>): 1625, 1358, 917, 860, 685, 530. Raman (solid, cm<sup>-1</sup>): 492, 668, 799, 882, 911, 944.

# $Na_{14}[(TM_{e})_{2}Fe_{2}^{III}(H_{2}O)_{2}(ZnW_{9}O_{34})_{2}] \ (2a/2b/2c/2d \ for \ TM_{e} = Mn/Co/Ni/Cu, \ n=42/78 \ for \ 2c/2d)$

Na<sub>2</sub>WO<sub>4</sub>.2H<sub>2</sub>O (4.00 g, 12.12 mmol) was dissolved in 15 mL DI water to which 0.5 mL nitric acid was added dropwise (precipitates formed during HNO<sub>3</sub> addition were dissolved with vigorous stirring). The resultant solution was put in Teflon microwave vials and microwave irradiated under controlled pressure with a power ramp for 15 min and hold for 45 min at 85 °C under 400 W maximum power. Zn(NO<sub>3</sub>)<sub>2</sub>.6H<sub>2</sub>O (0.39 g, 1.34 mmol) was added to the vial with stirring followed by a mixture of Fe(NO<sub>3</sub>)<sub>3</sub>.9H<sub>2</sub>O (0.54 g, 1.34 mmol) and (TM)Cl<sub>2</sub>.xH<sub>2</sub>O(1.34 mmol) (TM=Mn/Co/Ni/Cu) was added to the above solution with vigorous stirring and irradiated again in the microwave for 1 h at 85 °C maintaining the previous parameter. The solution thus obtained was filtered hot and the filtrate was kept for crystallization. After one day, crystals appeared which were collected by filtration and dried at 60 °C under vacuum. Yield: 0.74 g (22.2%) when TM=Mn (2a); FT-IR (cm<sup>-1</sup>): 912 (W=O<sub>t</sub>), 842 (W-O<sub>c</sub>-W), 688 (W-O<sub>c</sub>-W)

 $0.81 \text{ g } (23.5\%) \text{ when TM=Co } (2b); \text{ FT-IR } (\text{cm}^{-1}): 915 \text{ (W=O_t)}, 854, 832 \text{ (W-O_c-W)}, 636 \text{ (W-O_c-W)}$ 

 $0.77~g~(19.7\%)~when~TM=Ni~(2c);~FT-IR~(cm^{-1}):~910~(W=O_t),~845~(W-O_c-W),~679~(W-O_e-W)\\ 0.74~g~(17.1\%)~when~TM=Cu~(2d);~FT-IR~(cm^{-1}):~915~(W=O_t),~852~(W-O_c-W),~672~(W-O_e-W)\\ 0.74~g~(17.1\%)~when~TM=Cu~(2d);~FT-IR~(cm^{-1}):~915~(W=O_t),~852~(W-O_c-W),~672~(W-O_e-W)\\ 0.74~g~(17.1\%)~when~TM=Cu~(2d);~FT-IR~(cm^{-1}):~915~(W=O_t),~852~(W-O_c-W),~672~(W-O_e-W)\\ 0.74~g~(17.1\%)~when~TM=Cu~(2d);~FT-IR~(cm^{-1}):~915~(W=O_t),~852~(W-O_c-W),~672~(W-O_e-W)\\ 0.74~g~(17.1\%)~when~TM=Cu~(2d);~FT-IR~(cm^{-1}):~915~(W=O_t),~852~(W-O_c-W),~672~(W-O_e-W)\\ 0.74~g~(17.1\%)~when~TM=Cu~(2d);~FT-IR~(cm^{-1}):~915~(W=O_t),~852~(W-O_c-W),~672~(W-O_e-W)\\ 0.74~g~(W-O_e-W)~(W-O_e-W),~672~(W-O_e-W)\\ 0.74~g~(W-O_e-W)~(W-O_e-W)\\ 0.74~g~(W-O_e-W)\\ 0.74~g~(W-O_e-W$ 

# $Na_{14}[Ni_{2}Fe_{2}^{III}(H_{2}O)_{2}(ZnMo_{x}W_{9-x}O_{34})_{2}].46H_{2}O\ (2c\text{-}M)$

A mixture of Na<sub>2</sub>WO<sub>4</sub>.2H<sub>2</sub>O (2.67 g, 8.08 mmol) and Na<sub>2</sub>MoO<sub>4</sub>.2H<sub>2</sub>O (0.97 g, 4.04 mmol) was dissolved in 15 mL DI water completely. The pH of the solution was fixed at 6.5 using glacial

acetic acid. The resultant solution was put in Teflon microwave vials and microwave irradiated under controlled pressure with a power ramp for 15 min and hold for 45 min at 85 °C under 400 W maximum power. Zn(NO<sub>3</sub>)<sub>2</sub>.6H<sub>2</sub>O (0.39 g, 1.34 mmol) was added to the vial with stirring followed by a mixture of Fe(NO<sub>3</sub>)<sub>3</sub>.9H<sub>2</sub>O (0.54 g, 1.34 mmol) and NiCl<sub>2</sub>.6H<sub>2</sub>O (0.31 g, 1.34 mmol) was added to the above solution with vigorous stirring and irradiated again in the microwave for 1 h at 85 °C maintaining the previous parameter. The dark red solution thus obtained was filtered hot and the filtrate was kept for crystallization. After one day, red colored block crystals appeared which were collected by filtration and dried at 60 °C under vacuum. Yield: 0.74 g (19.3%). FT-IR (cm<sup>-1</sup>): 920 (M=O<sub>t</sub>), 836 (M-O<sub>c</sub>-M), 680 (M-O<sub>c</sub>-M) (M=Mo/W) Na<sub>14</sub>[(TM<sub>e</sub>)<sub>2</sub>Fe<sup>III</sup><sub>2</sub>(H<sub>2</sub>O)<sub>2</sub>(CoW<sub>9</sub>O<sub>34</sub>)<sub>2</sub>].nH<sub>2</sub>O (3a/3b/3c/3d for TM<sub>e</sub> = Mn/Ni/Cu/Zn, n=21 for 3c)

The synthetic procedure of compound (2a) was followed with slight modification. In place of Zn(NO<sub>3</sub>)<sub>2</sub>.6H<sub>2</sub>O, Co(NO<sub>3</sub>)<sub>2</sub>.6H<sub>2</sub>O (0.38 g, 1.34 mmol) was used. The solution thus obtained was filtered hot and the filtrate was kept for crystallization. After one day, crystals appeared which were collected by filtration and dried at 60 °C under vacuum. Yield: 0.84 g (25.0%) when TM=Mn (3a), FT-IR (cm<sup>-1</sup>): 918 (W=O<sub>t</sub>), 853, 838 (W-O<sub>c</sub>-W), 676 (W-O<sub>e</sub>-W)

0.82 g (24.5%) when TM=Ni (3b), FT-IR (cm<sup>-1</sup>): 914 (W=O<sub>t</sub>), 849 (W-O<sub>c</sub>-W), 699, 644 (W-O<sub>c</sub>-W)

0.87~g~(23.7%) when TM=Cu (3c), FT-IR (cm<sup>-1</sup>): 901 (W=O<sub>t</sub>), 849, 828 (W-O<sub>c</sub>-W), 638 (W-O<sub>e</sub>-W)

0.74~g~(22.0%) when TM=Zn (3d). FT-IR (cm<sup>-1</sup>): 915 (W=O<sub>t</sub>), 852, 832 (W-O<sub>c</sub>-W), 663 (W-O<sub>c</sub>-W)

# Na14[Ni2Fe2III(H2O)2(CoMoxW9-xO34)2].28H2O (3b-M)

A mixture of Na<sub>2</sub>WO<sub>4</sub>.2H<sub>2</sub>O (2.67 g, 8.08 mmol) and Na<sub>2</sub>MoO<sub>4</sub>.2H<sub>2</sub>O (0.97 g, 4.04 mmol) was dissolved in 15 mL DI water completely. The pH of the solution was fixed at 6.5 using nitric acid. The resultant solution was put in Teflon microwave vials and microwave irradiated under controlled pressure with a power ramp for 15 min and hold for 45 min at 85 °C under 400 W maximum power. Co(NO<sub>3</sub>)<sub>2</sub>.6H<sub>2</sub>O (0.39 g, 1.34 mmol) was added to the vial with stirring followed by a mixture of Fe(NO<sub>3</sub>)<sub>3</sub>.9H<sub>2</sub>O (0.54 g, 1.34 mmol) and NiCl<sub>2</sub>.6H<sub>2</sub>O (0.31g, 1.34 mmol) was added to the above solution with vigorous stirring and irradiated again in the microwave for 1 h at 85 °C maintaining the previous parameter. The dark colored solution thus obtained was filtered hot and the filtrate was kept for crystallization. After one day, light green colored block crystals appeared which were collected by filtration and dried at 60 °C under

vacuum. Yield: 0.48 g (13.7%). FT-IR (cm<sup>-1</sup>): 910 (M=O<sub>t</sub>), 842 (M-O<sub>c</sub>-M), 682 (M-O<sub>c</sub>-M) (M=Mo/W).

# $Na_{14}[Fe_2Mn_2^{III}(H_2O)_2(ZnW_9O_{34})_2].25H_2O$ (4a)

A mixture of Na<sub>2</sub>WO<sub>4</sub>.2H<sub>2</sub>O (4.00 g, 12.12 mmol) was dissolved in 15 mL DI water. The pH of the solution was fixed at 6.5 using glacial acetic acid. The resultant solution was put in Teflon microwave vials and microwave irradiated under controlled pressure with a power ramp for 15 min and hold for 45 min at 85 °C under 400 W maximum power. Zn(NO<sub>3</sub>)<sub>2</sub>.6H<sub>2</sub>O (0.39 g, 1.34 mmol) was added to the vial with stirring followed by a mixture of Mn(OAc)<sub>3</sub>.2H<sub>2</sub>O (0.35 g, 1.34 mmol) and FeCl<sub>2</sub>.4H<sub>2</sub>O (0.26 g, 1.34 mmol) was added to the above solution with vigorous stirring and irradiated again in the microwave for 1 h at 85 °C maintaining the previous parameter. The dark red solution thus obtained was filtered hot and the filtrate was kept for crystallization. After one day, red colored block crystals appeared which were collected by filtration and dried at 60 °C under vacuum. Yield: 0.48 g (12.9%). FT-IR (cm<sup>-1</sup>): 921 (W=O<sub>1</sub>), 842 (W-O<sub>c</sub>-W), 681 (W-O<sub>c</sub>-W).

# $Na_{14}[Fe_2Mn_2^{III}(H_2O)_2(ZnMo_xW_{9-x}O_{34})_2]$ (4a-M)

A mixture of Na<sub>2</sub>WO<sub>4</sub>.2H<sub>2</sub>O (2.67 g, 8.08 mmol) and Na<sub>2</sub>MoO<sub>4</sub>.2H<sub>2</sub>O (0.97 g, 4.04 mmol) was dissolved in 15 mL DI water completely. The pH of the solution was fixed at 6.5 using glacial acetic acid. The resultant solution was put in Teflon microwave vials and microwave irradiated under controlled pressure with a power ramp for 15 min and hold for 45 min at 85 °C under 400 W maximum power. Zn(NO<sub>3</sub>)<sub>2</sub>.6H<sub>2</sub>O (0.39 g, 1.34 mmol) was added to the vial with stirring followed by a mixture of Mn(OAc)<sub>3</sub>.2H<sub>2</sub>O (0.35 g, 1.34 mmol) and FeCl<sub>2</sub>.4H<sub>2</sub>O (0.26 g, 1.34 mmol) was added to the above solution with vigorous stirring and irradiated again in the microwave for 1 h at 85 °C maintaining the previous parameter. The dark red solution thus obtained was filtered hot and the filtrate was kept for crystallization. After one day, red colored block crystals appeared which were collected by filtration and dried at 60 °C under vacuum. Yield: 0.44 g (14.3%). FT-IR (cm<sup>-1</sup>): 920 (M=O<sub>1</sub>), 834 (M-O<sub>c</sub>-M), 681 (M-O<sub>c</sub>-M) (M=Mo/W).

# **4A.5 References**

- 1. Singh, V.; Chen, Z.; Ma, P.; Zhang, D.; Drew, M. G. B.; Niu, J.; Wang, J., Unprecedented {Fe14}/{Fe10} Polyoxotungstate-Based Nanoclusters with Efficient Photocatalytic H2 Evolution Activity: Synthesis, Structure, Magnetism, and Electrochemistry. *Chemistry A European Journal* **2016**, *22* (31), 10983-10989.
- 2. Ruhlmann, L.; Nadjo, L.; Canny, J.; Contant, R.; Thouvenot, R., Di- and Tetranuclear Dawson-Derived Sandwich Complexes: Synthesis, Spectroscopic Characterization, and Electrochemical Behavior. *European Journal of Inorganic Chemistry* **2002**, *2002* (4), 975-986.

- 3. Lv, H.; Song, J.; Geletii, Y. V.; Vickers, J. W.; Sumliner, J. M.; Musaev, D. G.; Kögerler, P.; Zhuk, P. F.; Bacsa, J.; Zhu, G.; Hill, C. L., An Exceptionally Fast Homogeneous Carbon-Free Cobalt-Based Water Oxidation Catalyst. *Journal of the American Chemical Society* **2014**, *136* (26), 9268-9271.
- 4. Martin-Sabi, M.; Soriano-López, J.; Winter, R. S.; Chen, J.-J.; Vilà-Nadal, L.; Long, D.-L.; Galán-Mascarós, J. R.; Cronin, L., Redox tuning the Weakley-type polyoxometalate archetype for the oxygen evolution reaction. *Nature Catalysis* **2018**, *1* (3), 208-213.
- 5. Yin, Q.; Tan, J. M.; Besson, C.; Geletii, Y. V.; Musaev, D. G.; Kuznetsov, A. E.; Luo, Z.; Hardcastle, K. I.; Hill, C. L., A Fast Soluble Carbon-Free Molecular Water Oxidation Catalyst Based on Abundant Metals. *Science* **2010**, *328* (5976), 342.
- 6. Rubinstein, A.; Jiménez-Lozanao, P.; Carbó, J. J.; Poblet, J. M.; Neumann, R., Aerobic Carbon–Carbon Bond Cleavage of Alkenes to Aldehydes Catalyzed by First-Row Transition-Metal-Substituted Polyoxometalates in the Presence of Nitrogen Dioxide. *Journal of the American Chemical Society* **2014**, *136* (31), 10941-10948.
- 7. Neumann, R.; Dahan, M., Molecular Oxygen Activation by a Ruthenium-Substituted "Sandwich" Type Polyoxometalate. *Journal of the American Chemical Society* **1998**, *120* (46), 11969-11976.
- 8. Guo, S.-X.; Liu, Y.; Lee, C.-Y.; Bond, A. M.; Zhang, J.; Geletii, Y. V.; Hill, C. L., Graphene-supported [{Ru4O4(OH)2(H2O)4}(γ-SiW10O36)2]10– for highly efficient electrocatalytic water oxidation. *Energy & Environmental Science* **2013**, *6* (9), 2654-2663.
- 9. Besson, C.; Huang, Z.; Geletii, Y. V.; Lense, S.; Hardcastle, K. I.; Musaev, D. G.; Lian, T.; Proust, A.; Hill, C. L., Cs9[(γ-PW10O36)2Ru4O5(OH)(H2O)4], a new all-inorganic, soluble catalyst for the efficient visible-light-driven oxidation of water. *Chemical Communications* **2010**, *46* (16), 2784-2786.
- 10. Adhikary, S. D.; Tiwari, A.; Nagaiah, T. C.; Mandal, D., Stabilization of Cobalt-Polyoxometalate over Poly(ionic liquid) Composites for Efficient Electrocatalytic Water Oxidation. ACS Applied Materials & Interfaces 2018, 10 (45), 38872-38879.
- 11. Lv, H.; Gao, Y.; Guo, W.; Lauinger, S. M.; Chi, Y.; Bacsa, J.; Sullivan, K. P.; Wieliczko, M.; Musaev, D. G.; Hill, C. L., Cu-based Polyoxometalate Catalyst for Efficient Catalytic Hydrogen Evolution. *Inorganic Chemistry* **2016**, *55* (13), 6750-6758.
- 12. Guo, K.-K.; Xu, M.; Zheng, Y.; Wang, X.-X.; Li, F.-Y.; Xu, W.-J.; Xu, L. J. I. C., Exploring the Coordination Modes of a Keggin-Type [ZnW12O40] 6–Anionic Cluster: Bonding Patterns, Crystal Structure, and Semiconducting Properties. *Inorg. Chem.* **2021**, *60*, 9097–9109.
- 13. Tourné, C. M.; Tourné, G. F.; Zonnevijlle, F., Chiral polytungstometalates [WM3(H2O)2(XW9O34)2]12–(X = M = Zn or Co) and their M-substituted derivatives. Syntheses, chemical, structural and spectroscopic study of some D,L sodium and potassium salts. *Journal of the Chemical Society, Dalton Transactions* 1991, (1), 143-155.
- 14. Mbomekallé, I.-M.; López, X.; Poblet, J. M.; Sécheresse, F.; Keita, B.; Nadjo, L. J. I. c., Influence of the heteroatom size on the redox potentials of selected polyoxoanions. *Inorg. Chem.* **2010**, *49* (15), 7001-7006.
- 15. Si, C.; Ma, P.; Han, Q.; Jiao, J.; Du, W.; Wu, J.; Li, M.; Niu, J. J. I. C., A Polyoxometalate-Based Inorganic Porous Material with both Proton and Electron Conductivity by Light Actuation: Photocatalysis for Baeyer–Villiger Oxidation and Cr (VI) Reduction. *Inorg. Chem.* **2020**, *60* (2), 682-691.
- Thakur, N.; Das Adhikary, S.; Kumar, M.; Mehta, D.; Padhan, A. K.; Mandal, D.; Nagaiah, T. C., Ultrasensitive and Highly Selective Electrochemical Detection of Dopamine Using Poly(ionic liquids)—Cobalt Polyoxometalate/CNT Composite. ACS Omega 2018, 3 (3), 2966-2973.
- 17. Thakur, N.; Kumar, M.; Das Adhikary, S.; Mandal, D.; Nagaiah, T. C., PVIM-Co5POM/MNC composite as a flexible electrode for the ultrasensitive and highly selective non-enzymatic electrochemical detection of cholesterol. *Chemical Communications* **2019**, *55* (34), 5021-5024.
- 18. Sloboda-Rozner, D.; Alsters, P. L.; Neumann, R., A Water-Soluble and "Self-Assembled" Polyoxometalate as a Recyclable Catalyst for Oxidation of Alcohols in Water with Hydrogen Peroxide. *Journal of the American Chemical Society* **2003**, *125* (18), 5280-5281.

- 19. Witte, P. T.; Alsters, P. L.; Jary, W.; Müllner, R.; Pöchlauer, P.; Sloboda-Rozner, D.; Neumann, R., Self-Assembled Na12[WZn3(ZnW9O34)2] as an Industrially Attractive Multi-Purpose Catalyst for Oxidations with Aqueous Hydrogen Peroxide. *Organic Process Research & Development* **2004**, *8* (3), 524-531.
- 20. Adam, W.; Alsters, P. L.; Neumann, R.; Saha-Möller, C. R.; Sloboda-Rozner, D.; Zhang, R., A Highly Chemoselective, Diastereoselective, and Regioselective Epoxidation of Chiral Allylic Alcohols with Hydrogen Peroxide, Catalyzed by Sandwich-Type Polyoxometalates: Enhancement of Reactivity and Control of Selectivity by the Hydroxy Group through Metal-Alcoholate Bonding. *The Journal of Organic Chemistry* 2003, 68 (5), 1721-1728.
- 21. Neumann, R.; Gara, M., The Manganese-Containing Polyoxometalate, [WZnMnII2(ZnW9O34)2]12-, as a Remarkably Effective Catalyst for Hydrogen Peroxide Mediated Oxidations. *Journal of the American Chemical Society* **1995**, *117* (18), 5066-5074.
- 22. Neumann, R.; Gara, M., Highly Active Manganese-Containing Polyoxometalate as Catalyst for Epoxidation of Alkenes with Hydrogen Peroxide. *Journal of the American Chemical Society* **1994**, *116* (12), 5509-5510.
- 23. Amanchi, S. R.; Khenkin, A. M.; Diskin-Posner, Y.; Neumann, R. J. A. C., Bismuth-substituted "sandwich" type polyoxometalate catalyst for activation of peroxide: umpolung of the peroxo intermediate and change of chemoselectivity. *ACS Catal.* **2015**, *5* (6), 3336-3341.
- 24. Glass, E. N.; Fielden, J.; Huang, Z.; Xiang, X.; Musaev, D. G.; Lian, T.; Hill, C. L., Transition Metal Substitution Effects on Metal-to-Polyoxometalate Charge Transfer. *Inorganic Chemistry* **2016**, *55* (9), 4308-4319.
- 25. Romo, S.; Fernández, J. A.; Maestre, J. M.; Keita, B.; Nadjo, L.; de Graaf, C.; Poblet, J. M., Density Functional Theory and ab Initio Study of Electronic and Electrochemistry Properties of the Tetranuclear Sandwich Complex [FeIII4(H2O)2(PW9O34)2]6. *Inorganic Chemistry* **2007**, 46 (10), 4022-4027.
- 26. Neumann, R.; Khenkin, A. M.; Dahan, M. J. A. C. I. E. i. E., Hydroxylation of Alkanes with Molecular Oxygen Catalyzed by a New Ruthenium-Substituted Polyoxometalate, [WZnRu (OH)(H2O)(ZnW9O34) 2] 11–. *Angew. Chem. Int. Ed.* 1995, 34 (15), 1587-1589.
- 27. Neumann, R.; Dahan, M. J. J. o. t. A. C. S., Molecular oxygen activation by a ruthenium-substituted "sandwich" type polyoxometalate. *J. Am. Chem. Soc.* **1998**, *120* (46), 11969-11976.
- 28. Singh, G.; Das Adhikary, S.; Mandal, D., Physico-and Electrochemical Properties of First-Row Transition-Metal-Substituted Sandwich Polyoxometalates. *Inorg. Chem* **2023**, *62* (48), 8551–8564.
- 29. Neumann, R.; Khenkin, A. M., Noble Metal (RuIII, PdII, PtII) Substituted" Sandwich" Type Polyoxometalates: Preparation, Characterization, and Catalytic Activity in Oxidations of Alkanes and Alkenes by Peroxides. *Inorg. Chem* **1995**, *34* (23), 5753-5760.
- 30. Adhikary, S. D.; Mandal, D. J. T., Polyoxometalate catalyzed imine synthesis: Investigation of mechanistic pathways. *Tetrahedron* **2020**, *76* (25), 131245.

# **Annexure-IV**

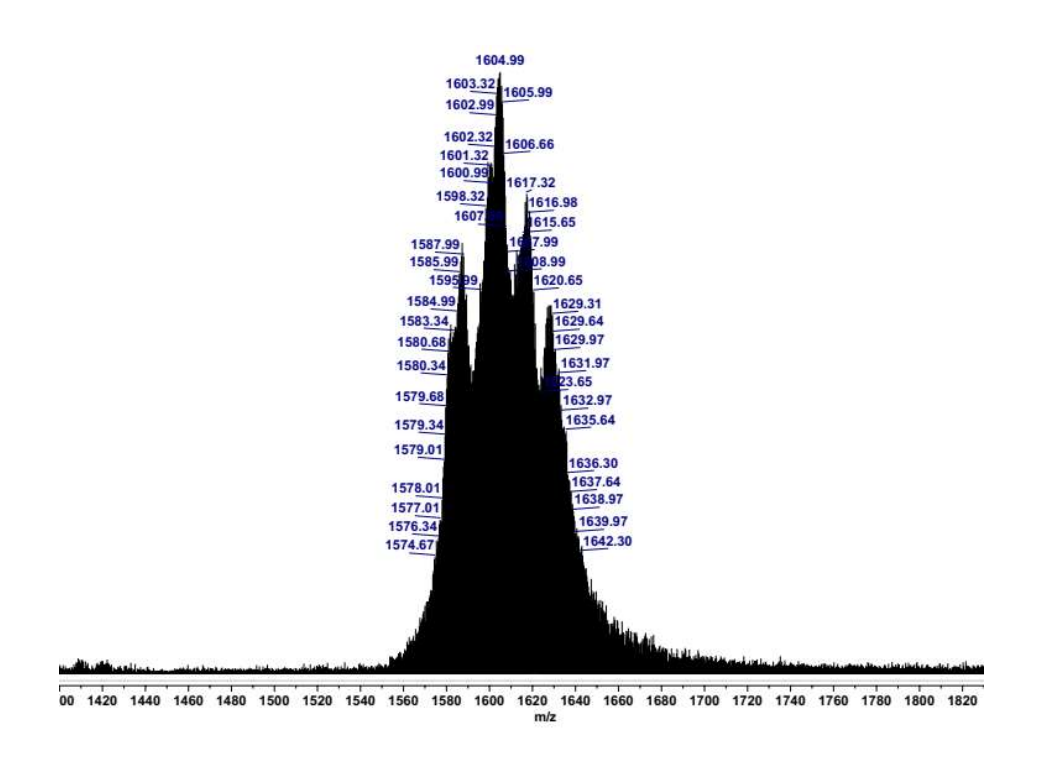


**Figure 4A.S1** ESI-MS spectra of crystals obtained after side substitution of **2** showing multiple peaks in the range of m/z 1400-1820 (z=-3).

Table 44 S1	Assignment	of ESI-mass pea	ks (side sul	hstitution of 2)
I adde 4A.SI	ASSIZHIIICHU	UL PASI-IIIASS DEA	KS ISIUC SUI	OSULULION OL 41

Charge	m/z	m/z (calc.)	Mol. Wt.	Assigned probable
	(obs.)			formula
-3	1629.31	1586.79	4760.39	$H_{11}Mn_2Fe_2(Zn_2W_{18}O_{68})$
-3	1617.32	1604.78	4814.34	$Na_2H_9Zn_2Fe_2(ZnFeW_{18}O_{68})$
-3	1604.99	1616.10	4848.30	$H_5Na_4Fe_4(Zn_2W_{18}O_{68})$
-3	1587.99	1628.79	4886.38	$H_{11}Mn_2FeW(Zn_2W_{18}O_{68})$

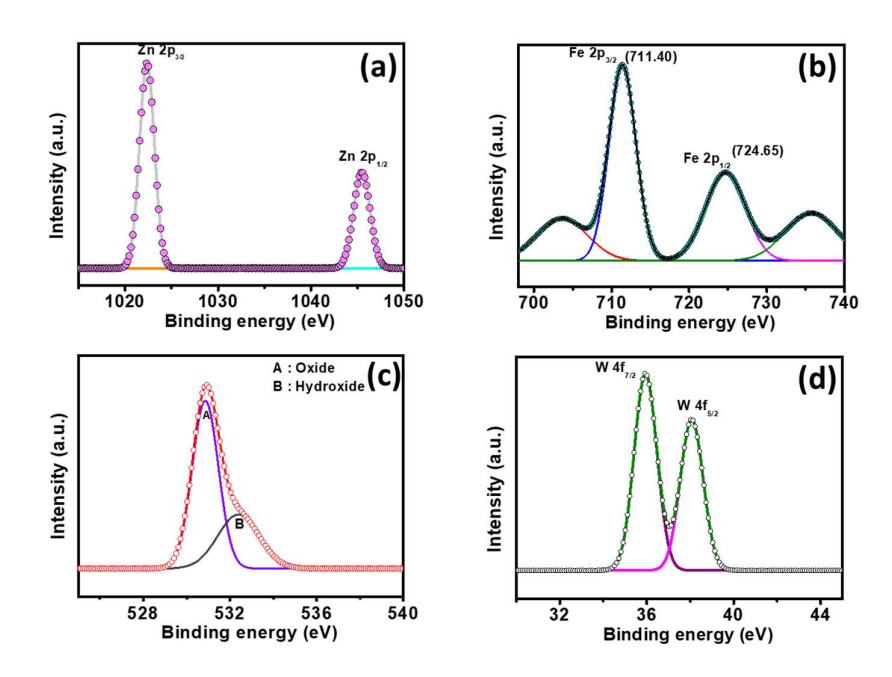


**Figure 4A.S2** XP spectra of Zn-WZnFe<sub>2</sub> POM showing (a) Zn  $2p_{1/2}$  and  $2p_{3/2}$ , (b) Fe  $2p_{1/2}$ , (c) Oxygen and (d) W  $4f_{7/2}$  and  $4f_{5/2}$ .

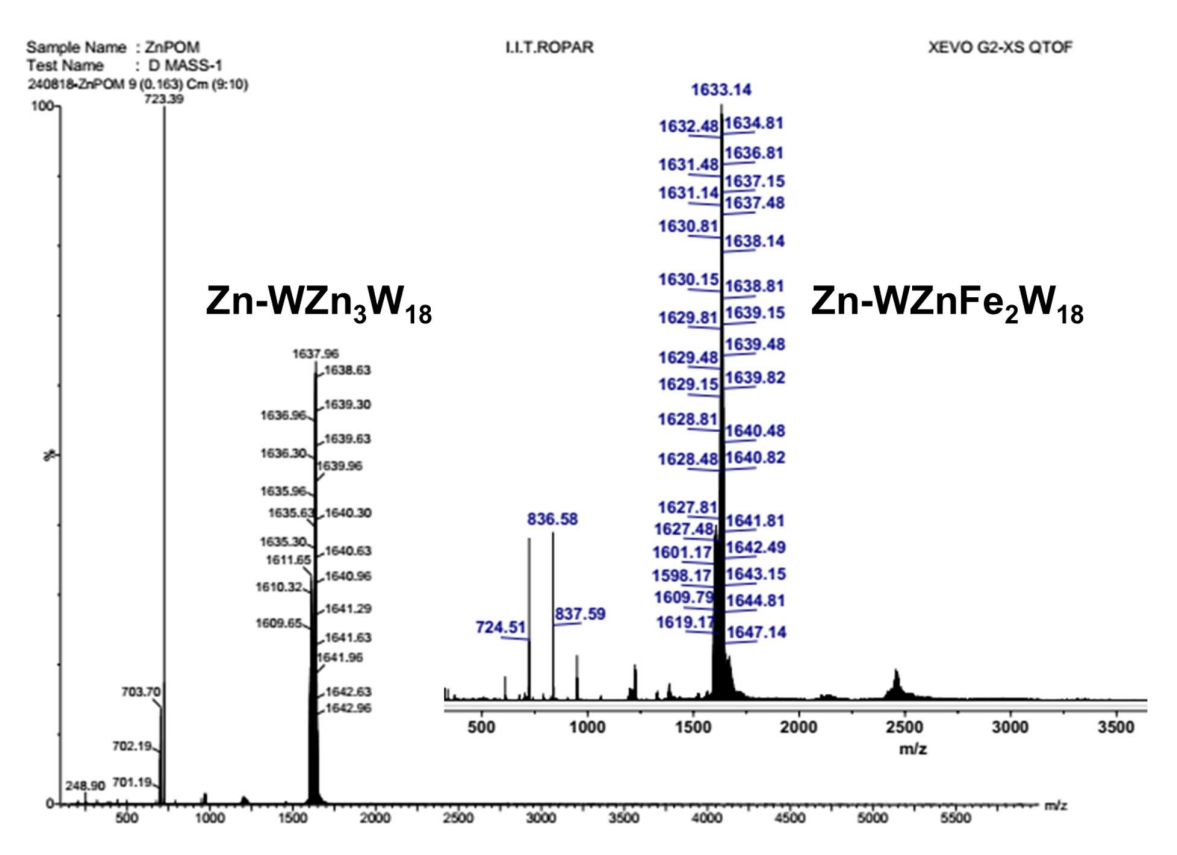


Figure 4A.S3 ESI-MS spectra of Zn-WZn $_3$ W $_{18}$  and Zn-WZnFe $_2$ W $_{18}$ .

Table 4A.S2 Assignment of ESI-mass peaks of Zn-WZnFe <sub>2</sub> .								
Fragment	Mol. Wt.	Cal. Mass	Z	m/z(cal.)	m/z (obs.)			
	(calculated)							
$\{[WZn_3(ZnW_9O_{34})_2]+9H\}^{3-}$	4916.86	4911.44	-3	1637.1467	1637.96			
$\{[WZnFe_2(ZnW_9O_{34})_2]+7H\}^{3-}$	4895.80	4895.36	-3	1631.79	1633.14			

Charge distribution on different types of oxygen atoms in the framework was calculated from the optimized structures in their most stable spin state, here,  $Zn_h$  - heteroatom zinc in the trilacunary framework,  $O\mu_4$  – tetra-coordinated oxygen atom, W-O-TM<sup>e</sup> – oxygen attached to terminal W and external substituted transition metal,  $Zn_h$ -O- $Zn^i/W$  – oxygen attached to heteroatom Zn and internal Zn/W,  $O(H_2O)$  – oxygen attached to aqua ligand, W=O<sub>t</sub> – oxygen attached to the terminal W atom.

Table 4A.S3 Charge distribution on oxygen atoms at different positions in Zn-W $Zn_3$  and other TMSP complexes along with at substituted transition metal

Atom/Group	Zn-WZnMn <sub>2</sub>	Zn-WZnFe <sub>2</sub>	Zn-WZnCo <sub>2</sub>	Zn-WZnNi <sub>2</sub>	Zn-WZnCu <sub>2</sub>	Zn-WZn <sub>3</sub>
Znh	1.22	1.22	1.23	1.23	1.23	1.24
Ομ4	-1.01	-1.03	-1.02	-1.02	-1.01	-1.01
W-O-TM <sup>e</sup>	-0.73	-0.70	-0.70	-0.71	-0.71	-0.78
Zn <sub>h</sub> -O-Zn <sup>i</sup> /W	-1.05	-1.02	-1.05	-1.04	-1.05	-1.10
<b>O</b> (H <sub>2</sub> O)	-1.00	-0.95	-0.99	-0.97	-0.99	-1.03
$W=O_t$	-0.59	-0.59	-0.63	-0.64	-0.64	-0.63
W-O <sub>c</sub> -W	-0.72	-0.71	-0.72	-0.72	-0.71	-0.72
W-O <sub>e</sub> -W	-0.73	-0.70	-0.73	-0.73	-0.73	-0.73
Transition metal	1.27	1.39	1.16	1.10	1.09	1.43

Table 4	Table 4A.S4 Screening of catalysts. [a]							
OH + OH2 Zn-WZn3 + OH H  tBuOK/toluene (1) (2)								
Entry	Catalyst (mol%)	Conv. (%)	Yield (%)[	Yield (%) <sup>[b]</sup>				
	(1110176)	, ,	(1)	(2)				
1	Zn-WZn <sub>3</sub>	99	98	1				
2	Zn-WZnCu2	27	27	0				
3	Zn-WZnNi <sub>2</sub>	83	72	0 11 <sup>[b]</sup>				
4	Zn-WZnCo <sub>2</sub>	84	74	0 10 <sup>[b]</sup>				
5	Zn-WZnFe <sub>2</sub>	>99	98	2				

$\begin{array}{ c c c c c c c c c c c c c c c c c c c$	6	Zn-WZnMn <sub>2</sub>	99	89	0
--	---	-----------------------	----	----	---

[a] Reaction conditions: benzyl alcohol (0.5 mmol), aniline (0.5 mmol), catalyst (2 mol%), *t*-BuOK (0.6 equiv.), toluene (0.5 mL), 110 °C, O<sub>2</sub> atmosphere, 15 h. Products are confirmed by GC-MS and yields are determined based on reactant to imine ratio. [b] aldehyde yield.

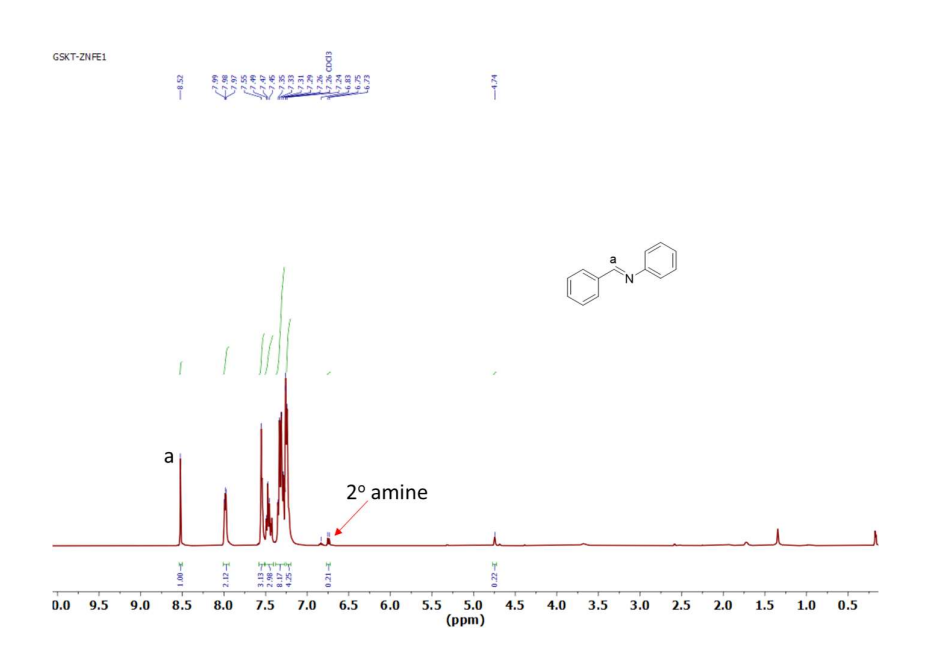


Figure 4A.S4 <sup>1</sup>H NMR showing imine synthesis using Zn-WZnFe<sub>2</sub> as a catalyst.

Table 4A.S5	Table 4A.S5 Crystal data, data collection, and refinement parameters for 2c, 2c-M, 2d, 3c, 3b-M and 4a							
	2c	2c-M	2d	3c	3b-M	4a		
CCDC no.	2330244	2330254	2330258	2330250	2330249	2330246		
empirical	FeH <sub>4</sub> Na <sub>20</sub> Ni <sub>3</sub>	Fe <sub>5.6</sub> H <sub>36</sub> Mo <sub>0.6</sub>	H <sub>1.2</sub> Cu <sub>2</sub> Fe <sub>2</sub> Na	Co <sub>2</sub> Cu <sub>3</sub> FeH <sub>16</sub>	H <sub>18.4</sub> CoFe <sub>2</sub> M	H <sub>51.2</sub> Fe <sub>3.2</sub> Na <sub>24</sub>		
formula	$O_{105}W_{18}Zn_2$	Na <sub>26</sub> Ni <sub>4</sub> O <sub>213.3</sub>	$_{13}O_{109.6}W_{18}Zn$	Na <sub>11</sub> O <sub>108</sub> W <sub>18</sub>	o <sub>3.2</sub> Na <sub>9</sub> Ni <sub>3</sub> O <sub>10</sub>	$O_{217.6}W_{36.8}Zn$		
		$_{3}W_{35.4}Zn_{2.4}$	2		9.2W <sub>14.8</sub>	<sub>8</sub> Mn		
formula	5815.85	11317.65	5732.50	5670.65	5347.40	11607.27		
wt								
temp (K)	273.15	273.15	273.15	273.15	293.15	273.15		
crystal	triclinic	monoclinic	Monoclinic	Monoclinic	monoclinic	monoclinic		
space	$P\overline{1}$	P2 <sub>1</sub> /n	P2 <sub>1</sub> /n	P2 <sub>1</sub> /n	P2 <sub>1</sub> /n	P2 <sub>1</sub> /n		
group								
dimension								
a (Å)	12.3582(8)	13.1369(3)	13.158(3)	13.203(7)	13.1444(8)	13.1455(17)		
<b>b</b> (Å)	13.7895(9)	17.7170(4)	17.730(3)	17.793(9)	17.7309(10)			
						17.670(3)		
c (Å)	14.8800(10)	21.0769(4)	21.116(5)	21.113(11)	20.9862(13)	21.115(4)		

α (deg)	99.217(2)	90	90	90	90	90
β (deg)	104.045(2)	93.5160(10)	93.834(8)	93.335(18)	93.532(2)	93.528(5)
γ (deg)	102.158(2)	90	90	90	90	90
$V(\mathring{A}^3)$	2344.3(3)	4896.34(18)	4915.4(17)	4951(4)	4881.8(5)	4895.2(13)
Z	1	1	2	2	2	1
$\rho$ (g/cm <sup>3</sup> )	4.119	3.838	3.873	3.803	3.638	3.937
,						
μ/mm <sup>-1</sup>	23.438	21.978	22.335	22.080	18.935	22.950
F (000)	2566.0	500	5046.0	5000.0	4767.0	5127.0
		3.0				
crystal	0.33 × 0.27 ×	0.24 × 0.18 ×	0.22 × 0.15 ×	0.44 × 0.25 ×	0.34 × 0.28 ×	0.24 × 0.13 ×
size (mm³)	0.11	0.11	0.12	0.18	0.28	0.05
2Θ range	4.038 to	3.864 to	3.866 to	3.864 to	3.862 to	3.866 to
for data	52.918	52.872	55.074	51.354	52.922	52.89
collection/						
0						
index	$-15 \le h \le 15$ ,	-16≤h≤16,-	-17≤h≤17,-	-16 ≤ h ≤ 16, -	-16≤h≤16, -	-16≤h≤16, -
ranges	$-17 \le k \le 17$ ,	$22 \le k \le 22$ , -	$22 \le k \le 18$ , -	$21 \le k \le 21$ , -	$22 \le k \le 22$ , -	$22 \le k \le 22$ , -
	-18 ≤ 1 ≤ 18	$26 \le l \le 26$	$27 \le l \le 27$	25 ≤ 1 ≤ 25	26 ≤ 1 ≤ 26	$26 \le l \le 26$
Collected	40286/9629	57170/10056	39049/ 11220	45120/9378	58526/10053	45968/10054
refl						
/unique						
GOF on	1.020	1.069	1.073	1.075	1.047	1.051
$F^2$						
final R	$R_1 = 0.036,$	$R_1 = 0.030,$	$R_1 = 0.054,$	$R_1 = 0.033,$	$R_1 = 0.035,$	$R_1 = 0.044,$
indices	$wR_2 = 0.078$	$wR_2 = 0.075$	$wR_2 = 0.151$	$wR_2 = 0.075$	$wR_2 = 0.089$	$wR_2 = 0.099$
$(I \geq 2\sigma(I))$						
R indices	$R_1 = 0.049,$	$R_1 = 0.033,$	$R_1 = 0.063,$	$R_1 = 0.040,$	$R_1 = 0.044,$	$R_1 = 0.068,$
(all data)	$wR_2 = 0.084$	$wR_2 = 0.077$	$wR_2 = 0.157$	$wR_2 = 0.079$	$wR_2 = 0.095$	$wR_2 = 0.112$
data/restr	9629/0/705	10056/0/682	11220/0/665	9378/0/663	10053/0/640	10054/1/668
aints/para						
m						
Largest	1.64/-1.57	3.02/-2.31	4.21/-3.63	1.97/-1.75	2.20/-1.24	2.92/-1.76
diff.						
peak/hole						
/ e Å-3						

Table 4A.S6 Assignment of ESI-mass peaks of 2c-M

Charge	m/z	m/z	Mol.	Assigned probable formula
	(obs.)	(calc.)	Wt.	

-3	1587.08	1587.13	4761.39	H <sub>11</sub> Ni <sub>3</sub> Fe(ZnFeW <sub>18</sub> O <sub>68</sub> )
-3	1556.07	1556.45	4669.35	H <sub>10</sub> Ni <sub>2</sub> Fe <sub>2</sub> (ZnFeMoW <sub>17</sub> O <sub>68</sub> )
-3	1525.72	1527.10	4581.31	$H_{10}Ni_2Fe_2(ZnFeMo_2W_{16}O_{68})$
-3	1495.03	1496.75	4490.26	H <sub>9</sub> NiFe <sub>3</sub> (ZnFeMo <sub>3</sub> W <sub>15</sub> O <sub>68</sub> )

Table 4A.S7	Bond valence para	meter of selected a	toms calculated			
from the SC-XRD structure of 2c/2d and 2c-M						
POMs	Transition	tion Bond valence Oxidation				
	metal	sum value	state			
	Mo	6.130	+6			
	W	6.059	+6			
2c-M	Zn	2.475	+2			
	Fe	3.144	+3			
	Ni	2.057	+2			
	W	6.048	+6			
2c	Zn1	2.312	+2			
20	Fe1	3.090	+3			
	Ni2	2.065	+2			
	W	6.105	+6			
2d	Zn1	2.407	+2			
2u	Fe1	3.068	+3			
	Cu1	2.030	+2			

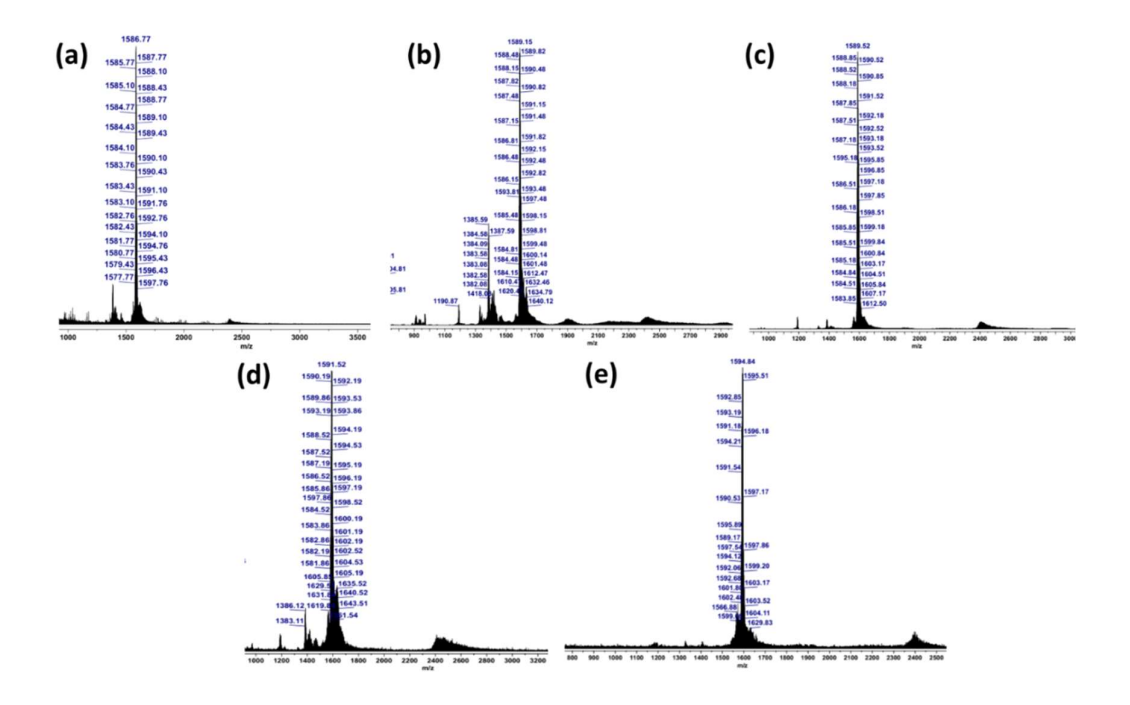
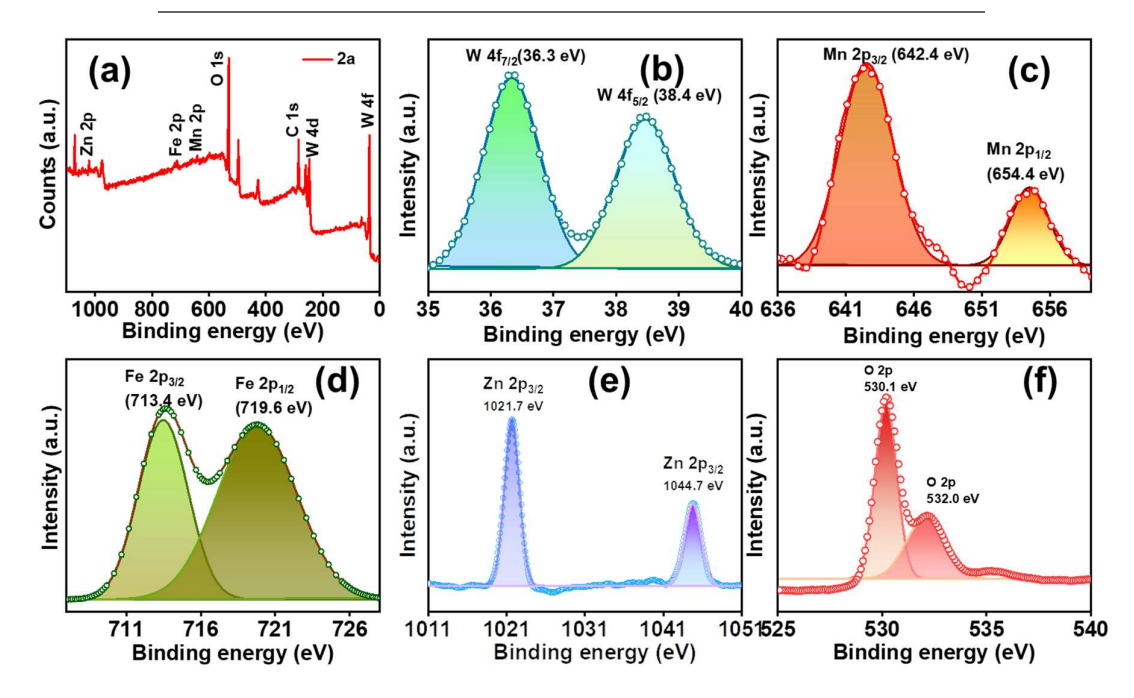


Figure 4A.S5 ESI-MS spectra of a series of POMs (z=-3) for 2a/2b/2c/2d/2.

Table 4A.S8 Assignment of ESI-mass peaks of Zn-Fe<sub>2</sub>M<sub>2</sub> POMs where M=Mn/Co/Ni/Cu/Zn

Charge	m/z	m/z	Mol. Wt.	Assigned probable
	(obs.)	(calc.)		formula
-3	1586.81	1586.79	4760.39	$H_{11}Mn_2Fe_2(ZnW_9O_{34})_2$
-3	1589.48	1589.46	4768.38	$H_{11}Co_2Fe_2(ZnW_9O_{34})_2$
-3	1589.52	1589.12	4767.38	$H_{11}Ni_2Fe_2(ZnW_9O_{34})_2$
-3	1591.52	1592.46	4777.39	$H_{11}Cu_2Fe_2(ZnW_9O_{34})_2$
-3	1593.43	1593.79	4781.37	$H_{11}Zn_2Fe_2(ZnW_9O_{34})_2$



**Figure 4A.S6** XP spectra of **2a** (a) Survey spectra, (b) W  $4f_{7/2}$  and  $4f_{5/2}$  (c) Mn 2p (d) Fe 2p (e) Zn 2p and (f) O 2p.

<b>Table 4A.S9</b> Bond valence parameter calculated from the SC-XRD structure of sandwich POMs in <b>3c</b> and <b>3b-M</b>					
POMs	Transition metal	Bond valence sum value	Oxidation state		
3b-M	W Mo Ni1 Ni2 Fe1 Co2	6.067 6.794 3.188 2.031 3.119 2.608	+6 +6 +3 +2 +3 +2		

	W	6.073	+6
	Fe1	3.073	+3
3c	Cu1	3.257	+3
	Cu2	2.075	+2
	Co2	2.321	+2

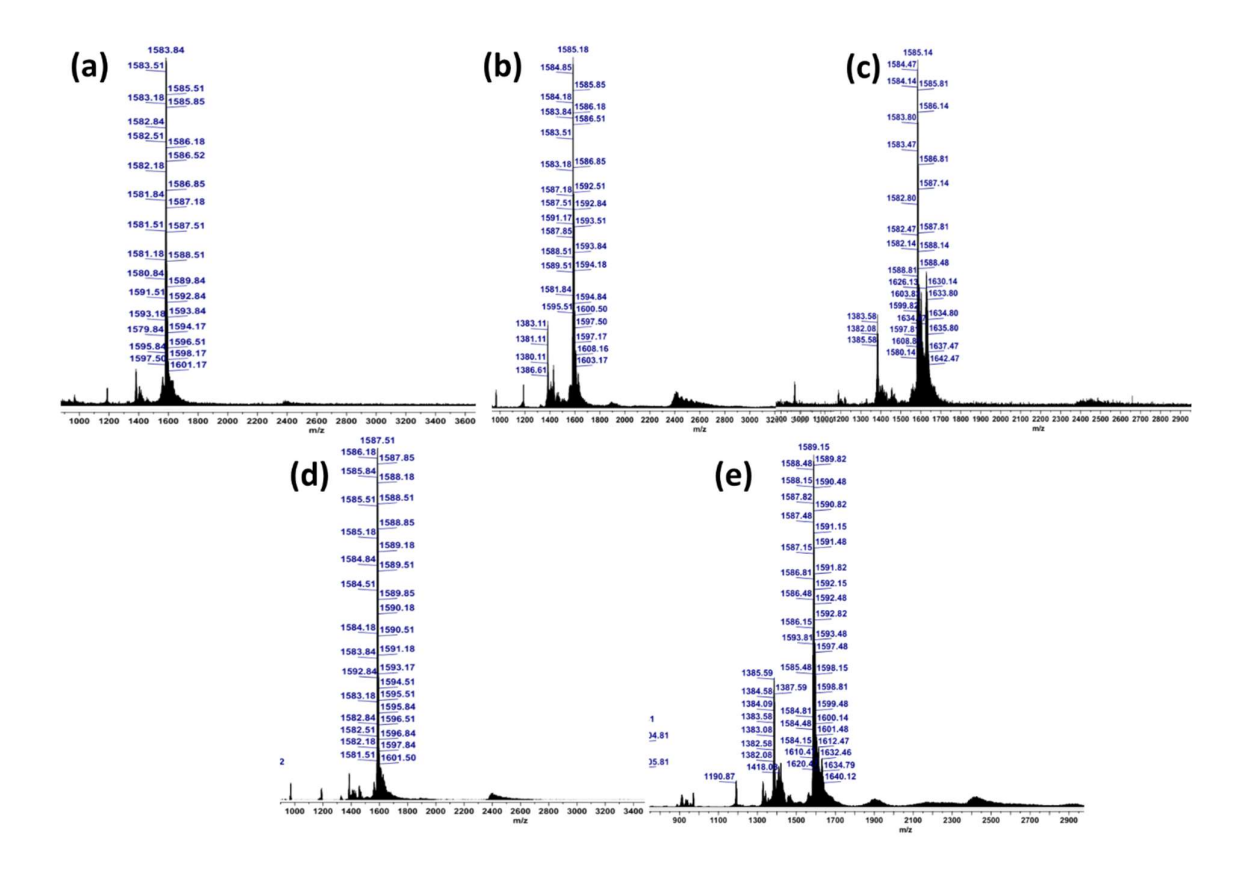
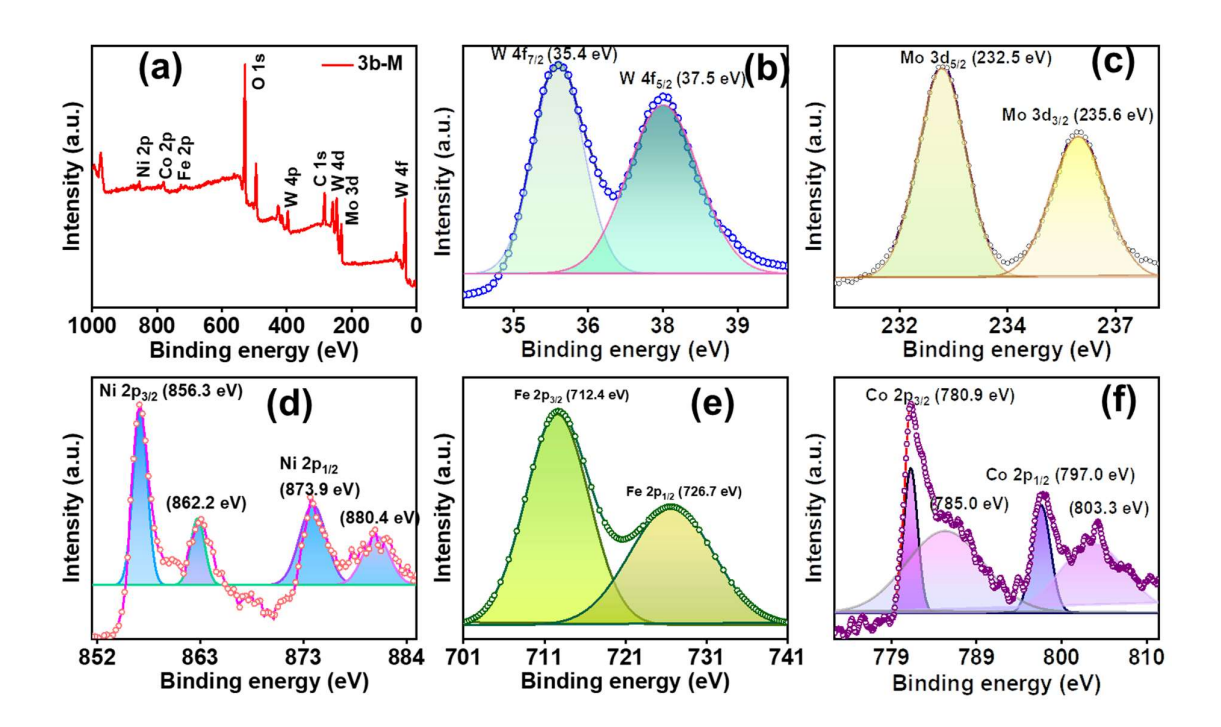


Figure 4A.S7 ESI-MS spectra of 3a/3/3b/3c/3d in the full range of m/z 1000-3000 (z=-3).

Table 4A	Table 4A.S10 Assignment of ESI-mass peaks of 3a/3/3b/3c/3d					
Charge	m/z	m/z (calc.)	Mol. Wt.	Assigned probable		
	(obs.)			formula		
-3	1583.51	1582.46	4747.40	H <sub>11</sub> Mn <sub>2</sub> Fe <sub>2</sub> (CoW <sub>9</sub> O <sub>34</sub> ) <sub>2</sub>		
-3	1585.17	1585.13	4755.39	$H_{11}Co_{2}Fe_{2}(CoW_{9}O_{34})_{2}$		
-3	1585.14	1585.13	4755.39	$H_{11}Ni_2Fe_2(CoW_9O_{34})_2$		
-3	1587.51	1588.13	4764.40	$H_{11}Cu_2Fe_2(CoW_9O_{34})_2$		
-3	1589.48	1589.46	4768.38	$H_{11}Zn_{2}Fe_{2}(CoW_{9}O_{34})_{2}$		

Table 4A.S11 Assignment of ESI-mass peaks of 3b-M					
Charge	m/z	m/z	Mol. Wt.	Assigned probable formula	
	(obs.)	(calc.)			
-3	1495.43	1495.75	4487.27	H <sub>10</sub> Ni <sub>2</sub> Fe <sub>2</sub> (FeCoMo <sub>3</sub> W <sub>15</sub> O <sub>68</sub> )	
-3	1466.42	1466.41	4399.23	H <sub>10</sub> Ni <sub>2</sub> Fe <sub>2</sub> (FeCoMo <sub>4</sub> W <sub>14</sub> O <sub>68</sub> )	
-3	1437.07	1437.06	4311.19	H <sub>10</sub> Ni <sub>2</sub> Fe <sub>2</sub> (FeCoMo <sub>5</sub> W <sub>13</sub> O <sub>68</sub> )	
-3	1406.38	1407.71	4222.16	H <sub>10</sub> Ni <sub>2</sub> Fe <sub>2</sub> (FeCoMo <sub>6</sub> W <sub>12</sub> O <sub>68</sub> )	
-3	1377.36	1378.70	4136.11	H <sub>10</sub> Ni <sub>2</sub> Fe <sub>2</sub> (FeCoMo <sub>7</sub> W <sub>11</sub> O <sub>68</sub> )	



**Figure 4A.S8** XP spectra of **3b-M** (a) Survey spectra, (b) W  $4f_{7/2}$  and  $4f_{5/2}$  (c) Mo 3d (d) Ni 2p (e) Fe 2p and (f) Co 2p.

<b>Table 4A.S12</b> BVS calculated from the SC-XRD structure of sandwich POMs in 4a					
POMs	Transition metal	Bond valence sum value	Oxidation state		
	W	6.175	+6		
4a	Mn1	3.247	+3		
4a	Fe2	2.371	+2		
	Zn1	2.355	+2		

Table 4A.S13 Assignment of ESI-mass peaks of 4a/4a-M

Charge	m/z	m/z	Mol. Wt.	Assigned probable formula
	(obs.)	(calc.)		
-3	1584.07	1583.46	4750.40	$H_{11}Mn_2Fe_2(ZnFeW_{18}O_{68})$
-3	1554.73	1554.45	4663.36	$H_{11}Mn_2Fe_2(ZnFeMoW_{17}O_{68})$

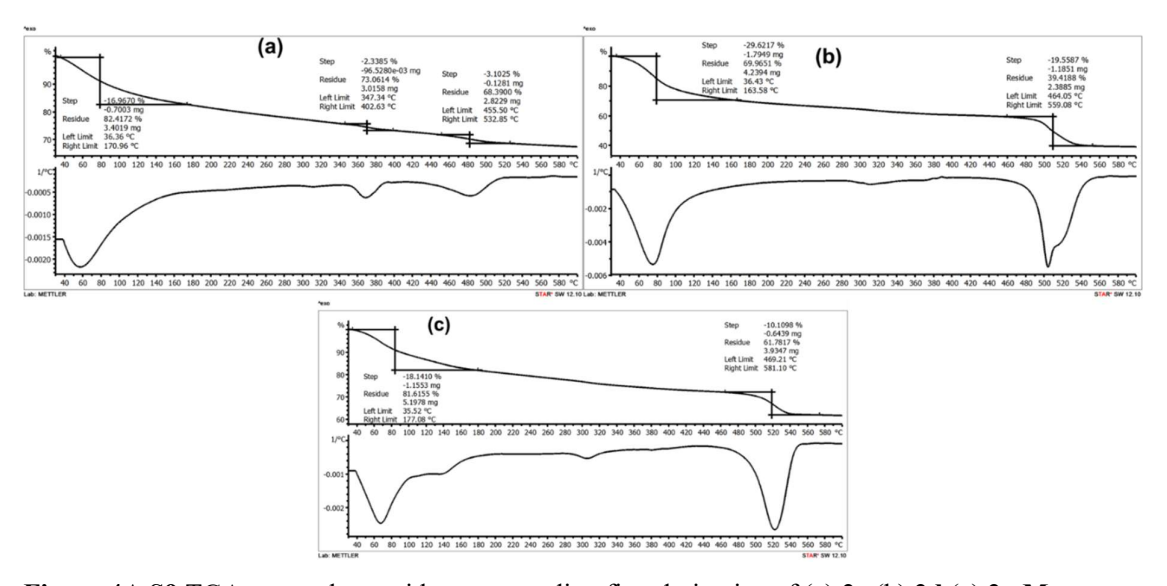


Figure 4A.S9 TGA curve along with corresponding first derivative of (a) 2c (b) 2d (c) 2c-M.

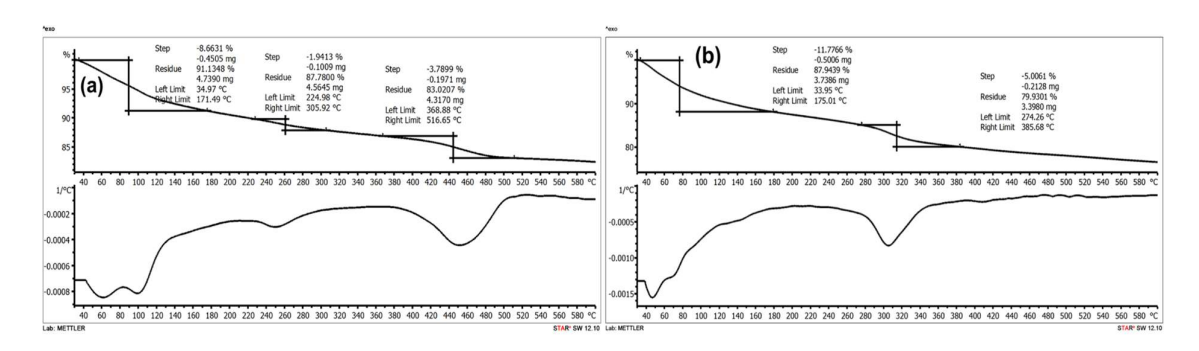
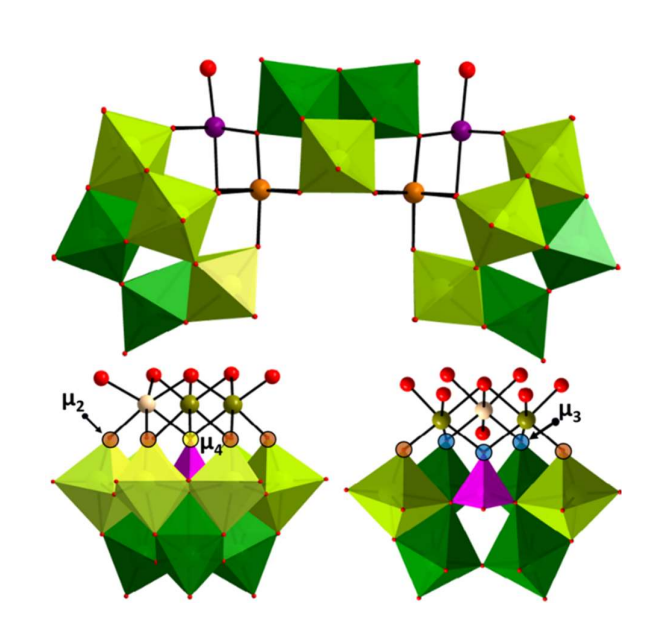


Figure 4A.S10 TGA curve along with corresponding first derivative of (a) 3c (b) 3b-M.

# Chapter 4 Section B

Framework Switch in Trimetallic Sandwich
Polyoxometalates Control by Heteroatom and
Oxidation State



### 4B.1 Introduction

Transition metals at sandwich core play an important role in the self-assembly of tetrasubstituted sandwich POMs. In Chapter 3, we examined the role of 3d transition metals at the internal sandwich position, while in Chapter 4A, we focused on the significance of transition metals at external sandwich position and their cooperative effect on the self-assembly of these POMs. Here in Chapter 4B; we emphasize the impact of different heteroatoms along with varying oxidation state of transition metals, leading to switching of framework and impact towards incorporation of mixed addenda in the framework. We explored the role of different heteroatoms (top to bottom in a column e.g. P to Bi) along with the cooperative effect of mixed-metals in different oxidation states at the sandwich position on the self-assembly of transition metal substituted sandwich POMs. The applicability of the cooperative effect of transition metals is also extended towards the incorporation of mixed addenda in other frameworks such as Sandwich, Banana, and Krebs POMs. <sup>1-3</sup>

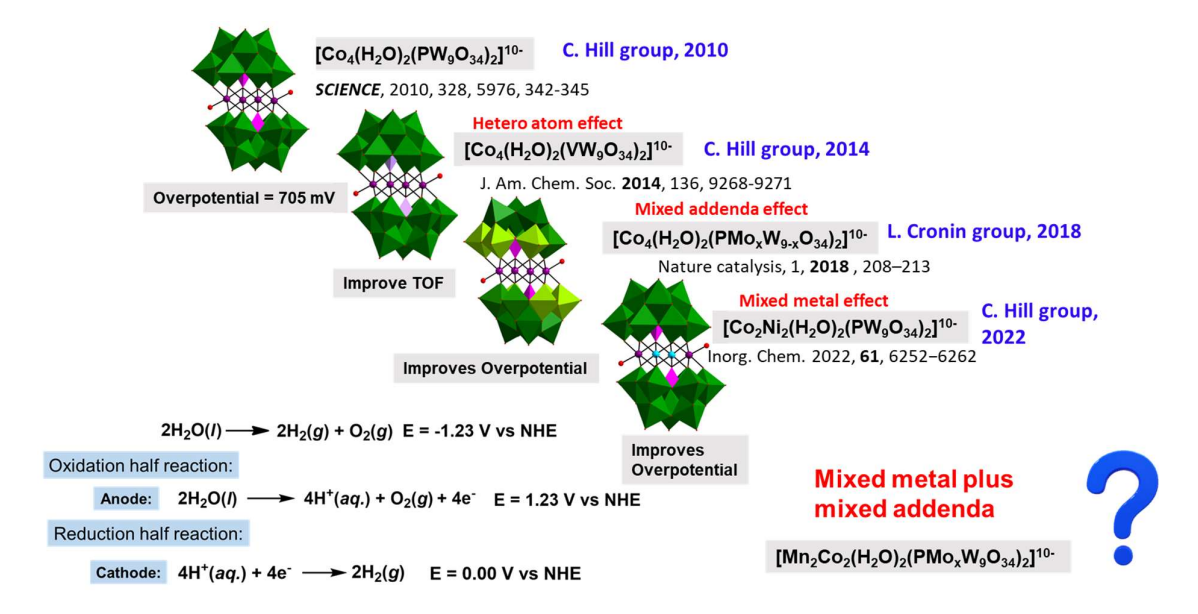
The potential applications of heteroatom and redox-controlled switchable frameworks are highly appealing.<sup>4</sup> Different POM frameworks, built from various building blocks, exhibit distinct optoelectronic properties and can even realize "emergent" properties as the framework evolves.<sup>5, 6</sup> As discussed in Chapter 2A, a mono-substituted Keggin structure was achieved using P as the heteroatom and Fe as a substituent at one of the addenda positions, when Fe was employed as the transition metal. This provides valuable insights into studying the cooperative effect of mixed transition metals with Mn or Fe as one of the elements in different oxidation states, alongside the effects of heteroatom (P to Bi). Other important factors contributing to the extensive structural diversity of these transition metal substituted sandwich POMs include: (a) the sequence in which transition metals are added, (b) the use of cooperative effect of mixed metal that promote selective binding, (c) the impact of oxidation states of transition metals, (d) the effect of Jahn-Teller distortion leading to elongated axial bonds, and (e) the size of incorporated transition metal ions within a group/period. Additionally, the cooperative role of substituting transition metals in the functionalization of amino acids in Krebs POMs have been explored, which can have potential application in medicinal chemistry.

### 4B.2 Results and Discussion

# 4B.2.1 Cooperative Effects of Mixed Metals with Phosphorus as the heteroatom

Non-noble metal-based, robust POMs as a water oxidation catalysts (WOC) are reported as a breakthrough in this field. Several POM-based WOCs have been reported with quasi-cubane

or cubane cores, stabilized by lacunary POM. Hill et al., reported the P-centered tetracobalt sandwich POM  $[Co_4(H_2O)_2(PW_9O_{34})_2]^{10-}$  in 2010, and  $[Co_4(H_2O)_2(VW_9O_{34})_2]^{10-}$  as an efficient homogeneous WOC.<sup>7,8</sup> Mixed 3d metal oxides as well as POMs containing mixed metals at the sandwich position such as  $[Co_2Ni_2(H_2O)_2(PW_9O_{34})_2]^{10}$  have shown promising WOC especially when P as heteroatom based sandwich POMs. 9 Also, the water oxidation activity enhances using mixed Mo/W addenda atoms in sandwich POMs by lowering the overpotential (Scheme 4B.1). Thus, the choice of transition metal in combinations greatly influences the catalytic activity of these POMs. However, the cooperative effect of these transition metals towards the self-assembly of these POMs as well as incorporation of mixed addenda in framework and their effect on the optoelectronic properties, is still unexplored. In this direction, we have synthesized various mixed-metal based mixed-addenda sandwich POMs based on P as hetetroatom and investigated their optoelectronic properties to understand their HOMO-LUMO positions, which can be helpful for the prediction of their catalytic activities. POMs like  $Na_{10}[Mn_2Co_2(H_2O)_2(PMo_xW_{9-x}O_{34})_2].nH_2O$  $(P-Mn_2Co_2Mo_xW_{18-x})$  $Na_{10}[Ni_2Zn_2(H_2O)_2(PMo_xW_{9-x}O_{34})_2].nH_2O~\textbf{(P-Ni_2Zn_2Mo_xW_{18-x})}~have~been~synthesized~under~also and also also been synthesized and also also been synthesized and also been synthes$ microwave heating using the previously employed method for P-based sandwich POMs (section 2.4, Chapter 2). Following the synthesis under microwave heating, these POMs shows relatively faster crystallization. These POMs are characterised using SC-XRD, ESI-mass, FT-IR and their optoelectronic properties have been studied using UV-vis spectroscopy and complimented by theoretical study.



Scheme 4B.1 Evoltution in structural chemistry of P-based sandwich POMs for oxygen evolution reaction.

# 4B.2.1a Characterization of P-Mn<sub>2</sub>Co<sub>2</sub>Mo<sub>x</sub>W<sub>18-x</sub> and P-Ni<sub>2</sub>Zn<sub>2</sub>Mo<sub>x</sub>W<sub>18-x</sub>

POMs P-Mn<sub>2</sub>Co<sub>2</sub>Mo<sub>x</sub>W<sub>18-x</sub> and P-Ni<sub>2</sub>Zn<sub>2</sub>Mo<sub>x</sub>W<sub>18-x</sub> were synthesized and characterized using SC-XRD, FT-IR, ESI-MS, and UV-visible spectroscopy (Figure 4B.1-4B.3, Table 4B.S1). The framework structure was confirmed by SC-XRD (CCDC 2330241 and 2330260). The dark brown crystals (Figure 4B.1b) of P-Mn<sub>2</sub>Co<sub>2</sub>Mo<sub>x</sub>W<sub>18-x</sub> crystallize in triclinic ( $P\overline{1}$  space group) and the light yellow crystals (Figure 4B.2b) of P-Ni<sub>2</sub>Zn<sub>2</sub>Mo<sub>x</sub>W<sub>18-x</sub> crystallize in monoclinic (P2<sub>1</sub>/n space group) (Table S37). BVS calculation indicates that all addenda atoms (Mo, W) are in their highest oxidation state (+6), P in +5 and all 3d transition metals (Mn, Co, Ni, Zn) in +2 oxidation states (Table S38). Oxidation states of all of the atoms in P- $Mn_2Co_2Mo_xW_{18-x}/P-Ni_2Zn_2Mo_xW_{18-x}$  were determined from XPS analysis. The XP spectra of P-Mn<sub>2</sub>Co<sub>2</sub>Mo<sub>x</sub>W<sub>18-x</sub> revealed the presence of W, Mo, Mn, Co, P, and oxygen (Figures 4B.S1). The W 4f doublet appears between 35.3 and 37.4 eV, corresponding to W  $4f_{7/2}$  and  $4f_{5/2}$ , Mo 3d doublet appears between 232.3 and 235.7 eV, corresponding to Mo 3d<sub>5/2</sub> and 3d<sub>3/2</sub> indicating the presence of W/Mo in +6 oxidation state. The doublet at 641.2 eV and 653.2 eV corresponding to Mn  $2p_{3/2}$  and  $2p_{1/2}$  can be attributed to +2 oxidation state of Mn. The doublet at 780.9 eV and 797.0 eV corresponding to Co 2p<sub>3/2</sub> and 2p<sub>1/2</sub> can be attributed to +2 oxidation state of Co. Similarly, the XP spectra of P-Ni<sub>2</sub>Zn<sub>2</sub>Mo<sub>x</sub>W<sub>18-x</sub> revealed the presence of W, Mo, Ni, Zn, P, and oxygen (Figures 4B.S2).

The crystal structure of **P-Mn<sub>2</sub>Co<sub>2</sub>Mo<sub>x</sub>W<sub>18-x</sub>** and **P-Ni<sub>2</sub>Zn<sub>2</sub>Mo<sub>x</sub>W<sub>18-x</sub>** shows that the tri-lacunary Keggin moiety contains a tetrahedrally bound P atom at the center as a templating agent to triads of addenda W/Mo atoms. The tetrasubstituted sandwich core of **P-Mn<sub>2</sub>Co<sub>2</sub>Mo<sub>x</sub>W<sub>18-x</sub>** and **P-Ni<sub>2</sub>Zn<sub>2</sub>Mo<sub>x</sub>W<sub>18-x</sub>** consists of Mn/Co and Ni/Zn with equal occupancy (50/50). From the comparison of **P-Mn<sub>2</sub>Co<sub>2</sub>Mo<sub>x</sub>W<sub>18-x</sub>/P-Ni<sub>2</sub>Zn<sub>2</sub>Mo<sub>x</sub>W<sub>18-x</sub>** with the reference structure (Figure 1.10, Chapter 1), it is clear that Mo incorporation is favorable at the 4/5/6/9 belt position, and most favorable at 4/5, which are connected to transition metals in the sandwich position through μ<sub>2</sub> oxygens. (Figure 4B.1c/4B.2c). The other positions in the belt and cap are comparatively less favorable for Mo incorporation, as also observed in our previously reported P-based POMs.<sup>11</sup> The distance between TM<sub>c</sub> and TM<sub>i</sub> atoms in **P-Mn<sub>2</sub>Co<sub>2</sub>Mo<sub>x</sub>W<sub>18-x</sub>** and **P-Ni<sub>2</sub>Zn<sub>2</sub>Mo<sub>x</sub>W<sub>18-x</sub>** was found to be 3.25 and 3.16 Å,and the distance between TM<sub>i</sub> is 3.35 and 3.29 Å, respectively (Figure 4B.2b), which are in between single TM substituted sandwich POMs.

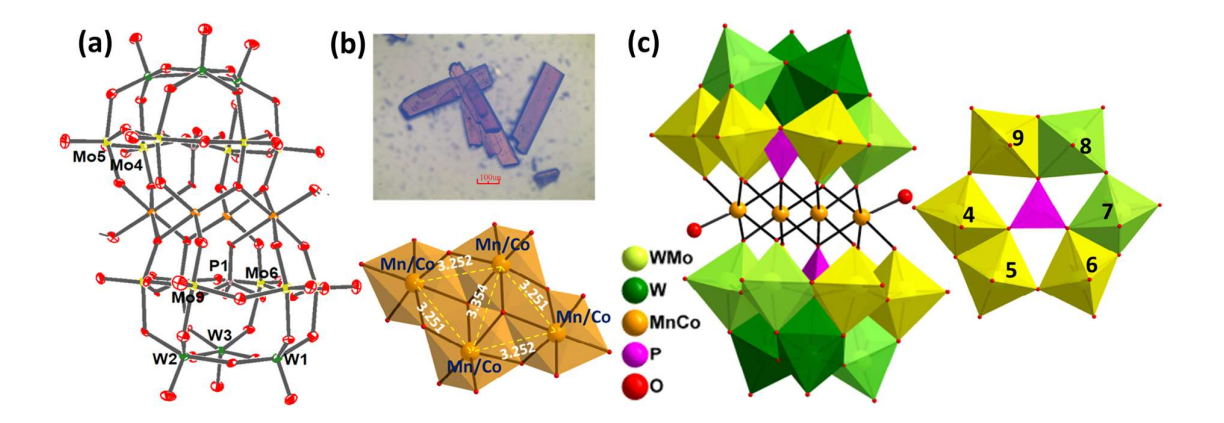


**Figure 4B.1** (a) ORTEP drawing (60% ellipsoid probability), (b) optical images and Cubane core showing the interatomic distance between transition metals in **P-Mn<sub>2</sub>Co<sub>2</sub>Mo<sub>x</sub>W<sub>18-x</sub>** (c) combined polyhedral/ball and stick representation of the single-crystal X-ray structure of polyoxometalate **P-Mn<sub>2</sub>Co<sub>2</sub>Mo<sub>x</sub>W<sub>18-x</sub>** belt 2 depicting different ratios of Mo to W in **P-Mn<sub>2</sub>Co<sub>2</sub>Mo<sub>x</sub>W<sub>18-x</sub>**. (Countercations and hydrogen atoms are omitted for clarity.)

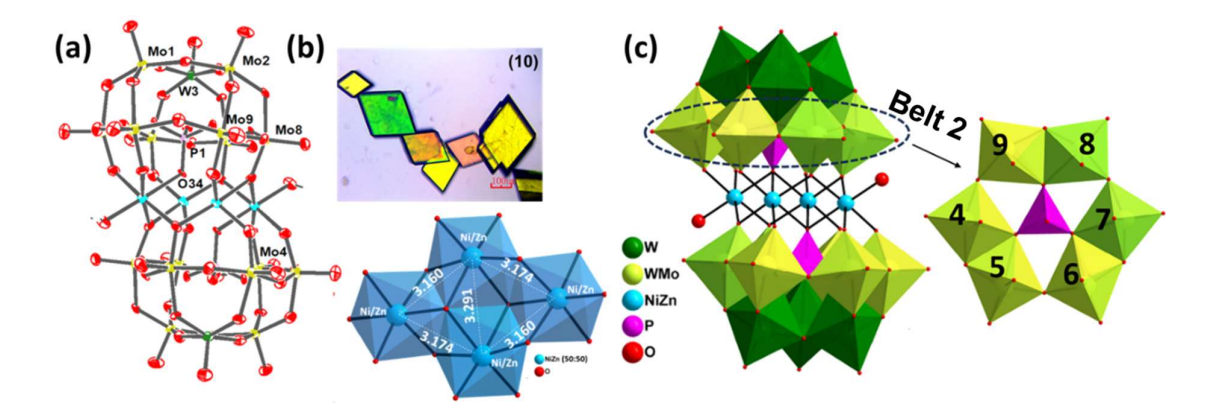


Figure 4B.2 (a) ORTEP drawing (with 60% ellipsoid probability), (b) optical images and Cubane core showing the interatomic distance between transition metals in P-Ni<sub>2</sub>Zn<sub>2</sub>Mo<sub>x</sub>W<sub>18-x</sub> (c) combined polyhedral/ball and stick representation of the single-crystal X-ray structure of polyoxometalate P-Ni<sub>2</sub>Zn<sub>2</sub>Mo<sub>x</sub>W<sub>18-x</sub>. belt 2 depicting different ratios of Mo to W in P-Ni<sub>2</sub>Zn<sub>2</sub>Mo<sub>x</sub>W<sub>18-x</sub>. (Countercations and hydrogen atoms are omitted for clarity.)

The ESI-mass spectrum of **P-Mn<sub>2</sub>Co<sub>2</sub>Mo<sub>x</sub>W<sub>18-x</sub>/P-Ni<sub>2</sub>Zn<sub>2</sub>Mo<sub>x</sub>W<sub>18-x</sub>** shows isotopic multiple envelopes of peaks attributed to varying ratios of Mo to W. The ESI-mass spectrum of **P-Mn<sub>2</sub>Co<sub>2</sub>Mo<sub>x</sub>W<sub>18-x</sub>** show the envelopes of peaks (Figure 4B.S3, Table 4B.S2) in the range of m/z 1050-1200 for [{H<sub>6</sub>Mn<sub>2</sub>Co<sub>2</sub>(H<sub>2</sub>O)<sub>2</sub>(PMo<sub>x</sub>W<sub>9-x</sub>)<sub>2</sub>}<sup>4-</sup>], 1400-1570 for [{H<sub>7</sub>Mn<sub>2</sub>Co<sub>2</sub>(H<sub>2</sub>O)<sub>2</sub>(PMo<sub>x</sub>W<sub>9-x</sub>)<sub>2</sub>}<sup>3-</sup>], and m/z 2100-2400 for [{H<sub>8</sub>Mn<sub>2</sub>Co<sub>2</sub>(H<sub>2</sub>O)<sub>2</sub>(PMo<sub>x</sub>W<sub>9-x</sub>)<sub>2</sub>}<sup>3-</sup>]. The most abundant anion in **P-Mn<sub>2</sub>Co<sub>2</sub>Mo<sub>x</sub>W<sub>18-x</sub>** has the composition of Mo/W (2:7) with the formula [{Mn<sub>2</sub>Co<sub>2</sub>(H<sub>2</sub>O)<sub>2</sub>(PMo<sub>2</sub>W<sub>7</sub>O<sub>34</sub>)<sub>2</sub>}<sup>14-</sup>], while the Mo/W ratio varies from 1:8 to

1:2 with a constant charge of the cluster, i.e., -14. Similarly, ESI-mass spectrum of **P-Ni<sub>2</sub>Zn<sub>2</sub>Mo<sub>x</sub>W<sub>18-x</sub>** shows the envelopes of peaks (Figure 4B.S4) in the range of m/z 1050-1200 for [{H<sub>6</sub>Ni<sub>2</sub>Zn<sub>2</sub>(H<sub>2</sub>O)<sub>2</sub>(PMo<sub>x</sub>W<sub>9-x</sub>)<sub>2</sub>}<sup>4-</sup>], 1400-1570 for [{H<sub>7</sub>Ni<sub>2</sub>Zn<sub>2</sub>(H<sub>2</sub>O)<sub>2</sub>(PMo<sub>x</sub>W<sub>9-x</sub>)<sub>2</sub>}<sup>3-</sup>], and m/z 2100-2400 for [{H<sub>8</sub>Ni<sub>2</sub>Zn<sub>2</sub>(H<sub>2</sub>O)<sub>2</sub>(PMo<sub>x</sub>W<sub>9-x</sub>)<sub>2</sub>}<sup>2-</sup>]. The most abundant anion in **P-Ni<sub>2</sub>Zn<sub>2</sub>Mo<sub>x</sub>W<sub>18-x</sub>** has the composition of Mo/W (5:13) with the formula [{Ni<sub>2</sub>Zn<sub>2</sub>(H<sub>2</sub>O)<sub>2</sub>(PMo<sub>2.5</sub>W<sub>6.5</sub>O<sub>34</sub>)<sub>2</sub>}<sup>14-</sup>], while the Mo/W ratio varies from 1:8 to 4:5 with a constant charge of the cluster, i.e., -14 (Figure 4B.S4, Table 4B.S3).

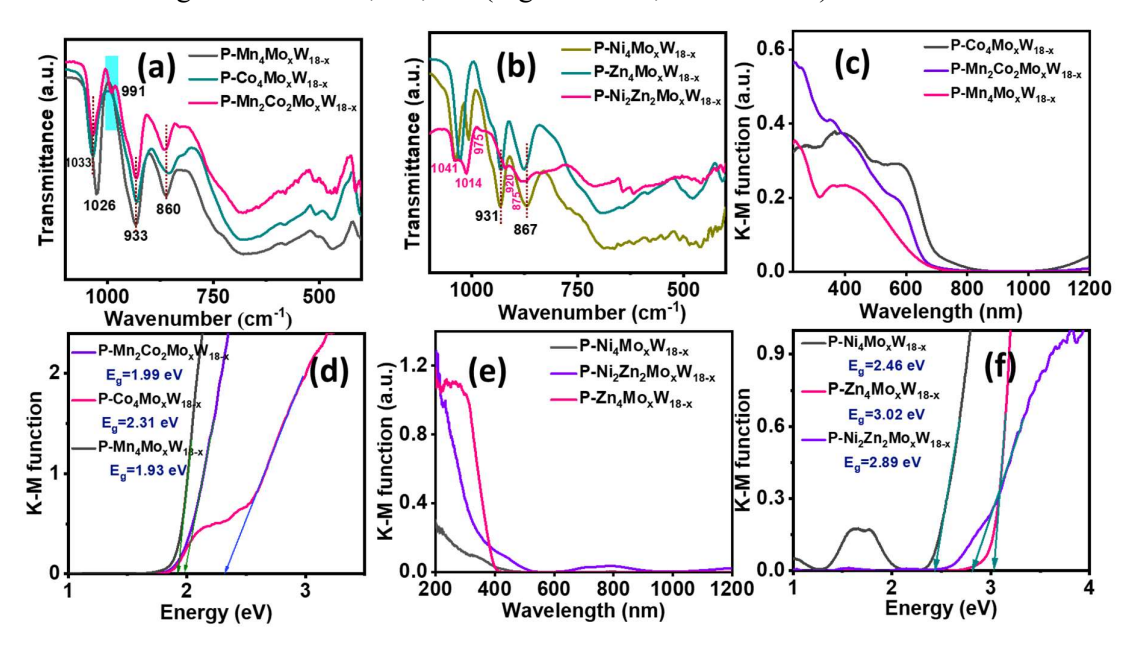


Figure 4B.3 (a) Shifting in FT-IR spectra of  $P-Mn_2Co_2Mo_xW_{18-x}$  from earlier reported  $[Mn_4(H_2O)_2(PMo_xW_{18-x}O_{34})_2]^{10-}$  ( $P-Mn_4Mo_xW_{18-x}$ ) and  $[Co_4(H_2O)_2(PMo_xW_{18-x}O_{34})_2]^{10-}$  ( $P-Co_4Mo_xW_{18-x}$ ); (b) Shifting in FT-IR spectra of  $P-Ni_2Zn_2Mo_xW_{18-x}$  from  $[Ni_4(H_2O)_2(PMo_xW_{18-x}O_{34})_2]^{10-}$  ( $P-Ni_4Mo_xW_{18-x}$ ) and  $[Zn_4(H_2O)_2(PMo_xW_{18-x}O_{34})_2]^{10-}$  ( $P-Zn_4Mo_xW_{18-x}$ ); and (c) UV-vis spectra of  $P-Mn_2Co_2Mo_xW_{18-x}$  and (d) its corresponding band gap; (e) UV-vis spectra of  $P-Ni_2Zn_2Mo_xW_{18-x}$  and(d) its corresponding band gap derived from K-M equation.

Comparing the stretching frequencies of P-based mixed metal P-Mn<sub>2</sub>Co<sub>2</sub>Mo<sub>x</sub>W<sub>18-x</sub>/P-Ni<sub>2</sub>Zn<sub>2</sub>Mo<sub>x</sub>W<sub>18-x</sub> with corresponding reported mixed addenda sandwich POMs, there is a subtle variation in the characteristic peaks. The FT-IR spectra of P-Mn<sub>2</sub>Co<sub>2</sub>Mo<sub>x</sub>W<sub>18-x</sub> show the characteristics peaks in the region 850-1050 cm<sup>-1</sup> with characteristics peaks at 1033 cm<sup>-1</sup> (P-O), 991 cm<sup>-1</sup> (M=O<sub>term</sub>, M=Mo/W), 933, 860 cm<sup>-1</sup> (M-O-M, M=Mo/W) (Figure 4B.3a). The FT-IR spectra of P-Ni<sub>2</sub>Zn<sub>2</sub>Mo<sub>x</sub>W<sub>18-x</sub> show characteristics peaks similar to P-Mn<sub>2</sub>Co<sub>2</sub>Mo<sub>x</sub>W<sub>18-x</sub> in the region 850-1050 cm<sup>-1</sup> with characteristics peaks at 1041 cm<sup>-1</sup> (P-O), 1014, 975 cm<sup>-1</sup> (M=O<sub>term</sub>, M=Mo/W), 920, 875 cm<sup>-1</sup> (M-O-M, M=Mo/W) (Figure 4B.3b). Both P-Mn<sub>2</sub>Co<sub>2</sub>Mo<sub>x</sub>W<sub>18-x</sub> and P-Ni<sub>2</sub>Zn<sub>2</sub>Mo<sub>x</sub>W<sub>18-x</sub> exhibit broad absorption bands in the UV-vis

region due to ligand-to-metal charge transfer (LMCT) ( $O_{2p} \rightarrow W_{5d}$ ) and d-d transitions. Moreover, a significant contribution of Mo is evident in mixed addenda sandwich POMs through a red shift in the visible region (Figure 4B.3c/4B.3e). This red shift can be explained by the changes in the band gap of these POMs, which were investigated using DRS. The band gap calculated from DRS is found to be 1.99 eV in P-Mn<sub>2</sub>Co<sub>2</sub>Mo<sub>x</sub>W<sub>18-x</sub> and 2.89 eV in P-Ni<sub>2</sub>Zn<sub>2</sub>Mo<sub>x</sub>W<sub>18-x</sub>, which is found to be in between the corresponding reported mixed addenda sandwich POMs (Figure 4B.3d/4B.3f). These results were further supported with DFT study, where the HOMO-LUMO band gap in  $P-Mn_2Co_2Mo_xW_{18-x}/P-Ni_2Zn_2Mo_xW_{18-x}$ (representative structure of P-Mn<sub>2</sub>Co<sub>2</sub>Mo<sub>x</sub>W<sub>18-x</sub> is taken with the  $[Mn_2Co_2(H_2O)_2(PMo_4W_5O_{34})_2]^{10-}$  and for  $P-Ni_2Zn_2Mo_xW_{18-x}$  the formula is taken with  $[Ni_2Zn_2(H_2O)_2(PMo_4W_5O_{34})_2\}^{10-})$  was calculated (Figure 4B.S5).

## 4B.2.1b Effect of oxidation state of precursor transition metals: Synthesis and Characterisation of mixed addenda Banana Polyoxometalates

In literature, Kortz group reported a W-based mixed Ni/Mn banana-type POM,  $Na_{17}[Ni_4Mn_2P_3W_{24}O_{94}(H_2O)_2]$  ( $Ni_4Mn_2W_{24}$ ). Xue and colleagues synthesized a series of Mobased mixed-metal-substituted banana-type POMs using a one-pot synthesis approach, including  $[As_2MFe_5Mo_{22}O_{85}(H_2O)]^{n-}$  (where  $M = Fe^{3+}$  (Fe<sub>6</sub>),  $Ni^{2+}$  ( $NiFe_5$ ),  $Mn^{2+}$  ( $MnFe_5$ ) and  $Co^{2+}$  ( $CoFe_5$ ).  $^{1,12,13}$  While several banana-type sandwich POMs have been reported, either W-based or Mo-based, none explored (W/Mo) mixed addenda.  $^{14}$  In our study, we found that the cooperative effect of mixed metals plays a crucial role in the self-assembly of mixed-addenda to form banana-type sandwich POMs.  $^{15-17}$ 

We have previously demonstrated, both experimentally and theoretically, that the denticity of bridging oxygen atoms plays an important role in dictating the positioning of Mo in tetrasubstituted sandwich POMs. This is probably due to the lower charge density of  $\mu_2$  oxygen compared to  $\mu_3$  oxygen.  $\mu_2$  oxygen preferentially binds with Mo owing to lower effective nuclear charge and better  $\pi$ -acceptor ability. To further explore the effect of  $\mu_2$  oxygen denticity and its influence on electronic properties, we extended this mixed-addenda concept to bananatype sandwich POMs. In these structures, all six belt addenda atoms bind to the sandwich metals via  $\mu_2$  oxygens, whereas in tetrasubstituted sandwich POMs, only four belt addenda atoms using  $\mu_2$  oxygens to bind sandwich metals (Figure 1.10).

In Chapter 2, we were unable to get the crystals of tetrasubstituted sandwich POMs using Fe as a precursor, instead, we obtained mixed-addenda Keggin POMs with the formula PFeMo<sub>x</sub>W<sub>11-x</sub>O<sub>39</sub>, as confirmed from mass spectrometry. To further investigate the possible role of transition metals, here we focused on the oxidation state of precursor metals along with

mixed-metals in P-based sandwich POMs. Interestingly, by using Mn<sup>3+</sup>/Fe<sup>2+</sup> along with other transition metals in low oxidation states (i.e. +2 for Mn/Co), we obtained a structural transformation into mixed-addenda banana POMs, which have not been explored so far.

Under microwave heating with controlled pH, temperature, and suitable mixed transition metal salts along with Fe precursors, we have synthesized two new mixed addenda banana POMs with the formula [Mn<sub>2</sub>Fe<sub>4</sub>(PMo<sub>x</sub>W<sub>6-x</sub>O<sub>26</sub>)(PMo<sub>x</sub>W<sub>9-x</sub>O<sub>34</sub>)<sub>2</sub>(H<sub>2</sub>O)<sub>2</sub>]<sup>17-</sup> (P-Mn<sub>2</sub>Fe<sub>4</sub>Mo<sub>x</sub>W<sub>24-x</sub>) and [Co<sub>5</sub>Fe(PMo<sub>x</sub>W<sub>6-x</sub>O<sub>26</sub>)(PMo<sub>x</sub>W<sub>9-x</sub>O<sub>34</sub>)<sub>2</sub>(H<sub>2</sub>O)<sub>2</sub>]<sup>17-</sup> (P-Co<sub>5</sub>FeMo<sub>x</sub>W<sub>24-x</sub>). Dark brown hexagonal flake crystals of P-Mn<sub>2</sub>Fe<sub>4</sub>Mo<sub>x</sub>W<sub>24-x</sub> and P-Co<sub>5</sub>FeMo<sub>x</sub>W<sub>24-x</sub> were obtained after 4 days and were characterized using FT-IR, SC-XRD and UV-vis spectra (Figure 4B.4/4B.S6-4B.S10). The BVS calculations indicates +2 oxidation states for Mn/Co/Fe, +5 for P, and +6 for Mo/W.

Synthesis optimization revealed crucial factors governing the self-assembly to form mixed addenda of this banana-type architecture. The mixed addenda banana archetype formed from a mixture of 3d TMs in the solution of P, W, and Mo salts, in contrast, Weakley-type sandwich/Keggin POMs formed when only a single 3d TMs was used. We observed that the presence of Fe<sup>2+</sup> has a significant influence on directing the self-assembly. Banana architecture formed by adding mixed metals salts like Mn/Fe or Co/Fe into a solution of P, W, and Mo salts under suitable pH. Alternatively, tetrasubstituted sandwich POMs were obtained from Mn/Co salts without Fe. The sequence of adding transition metal salts also influence the outcome. For instance, adding Fe salt first, followed by Co/Mn(+2) salts, led to the formation of Banana structure, whereas adding Co/Mn salts first, followed by Fe salt to the solution of P, W, and Mo salts resulted in tetrasubstituted sandwich structure at pH 6.5. DFT optimizations of these Banana architecture reveal that LUMO is predominantly associated with the Mo addenda atoms, which suggests a change in the directionality of the incoming electron towards Mo in mixed addenda compared to W-based banana POMs.

Compounds P-Mn<sub>2</sub>Fe<sub>4</sub>Mo<sub>x</sub>W<sub>24-x</sub> and P-Co<sub>5</sub>FeMo<sub>x</sub>W<sub>24-x</sub> were characterised using SC-XRD, FT-IR, XPS and UV-visible spectroscopy (Figure 4B.5-4B.7 and 4B.S6-4B.S10). The banana framework structure was confirmed from SC-XRD (CCDC 2330251 and 2330259). The hexagonal-shaped orange crystals (Figure 4B.S6) of these banana POMs crystallize in monoclinic (P2<sub>1</sub>/c space group) (Table 4B.S1). BVS calculation indicates that all addenda atoms (Mo, W) are in their highest oxidation state (+6), P in +5 and all 3d transition metals

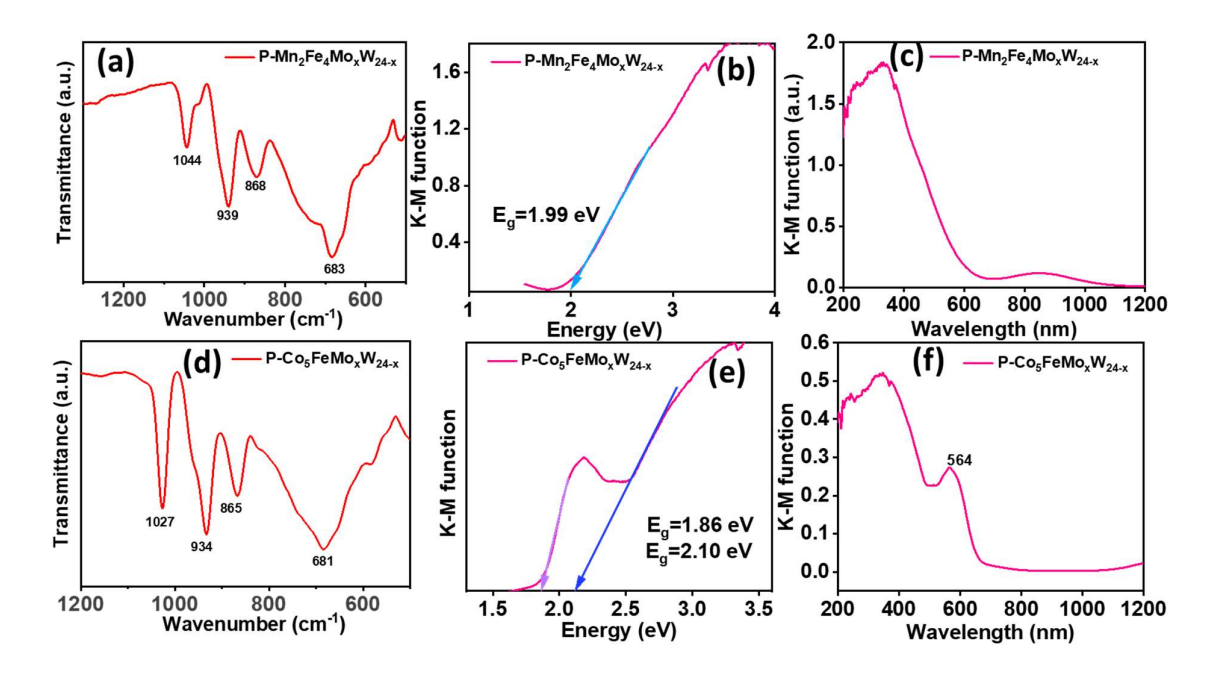
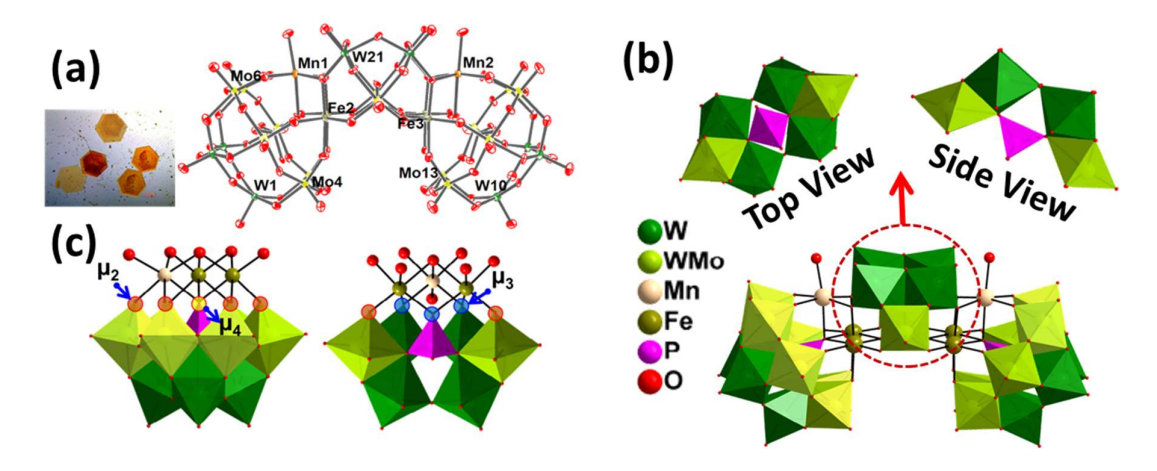


Figure 4B.4 (a) FT-IR spectra (b) optical band gap (c) UV-visible spectra of P-Mn<sub>2</sub>Fe<sub>4</sub>Mo<sub>x</sub>W<sub>24-x</sub> and (d) FT-IR spectra (e) optical band gap (f) UV-visible spectra of P-Co<sub>5</sub>FeMo<sub>x</sub>W<sub>24-x</sub>.



**Figure 4B.5** Mixed addenda Banana POM, **P-Mn<sub>2</sub>Fe<sub>4</sub>Mo<sub>x</sub>W<sub>24-x</sub>** (a) optical images (hexagonal flakes) and ORTEP representation, (b) combined polyhedral/ball and stick representation with different views of fragments, and (c) Keggin fragments showing different binding mode of oxygens with transition metals.

(Mn, Co, Fe) in +2 oxidation states, respectively (Table S42). Apart from the BVS, the oxidation states of all of the atoms in these POMs were determined from XPS analysis. The XP spectra of **P-Mn<sub>2</sub>Fe<sub>4</sub>Mo<sub>x</sub>W<sub>24-x</sub>** revealed the presence of W, Mo, Mn, Fe, P, and oxygen (Figure 4B.S7). The W 4f doublet appears between 34.5 and 36.8 eV, corresponding to W 4f<sub>7/2</sub> and 4f<sub>5/2</sub>, Mo 3d doublet appears between 231.0 and 234.1 eV, corresponding to Mo 3d<sub>5/2</sub> and 3d<sub>3/2</sub> indicating the presence of W/Mo in +6 oxidation state. The doublet at 640.6 eV and 652.9

eV corresponding to Mn 2p<sub>3/2</sub> and 2p<sub>1/2</sub> can be attributed to +2 oxidation state of Mn. The doublet at 713.1 eV and 723.6 eV corresponding to Fe 2p<sub>3/2</sub> and 2p<sub>1/2</sub> can be attributed to +3 oxidation state of Fe. Similarly, the XP spectra of **P-CosFeMoxW24-x** revealed the presence of W, Mo, Fe, Co, P, and oxygen (Figure 4B.S8). The 3D SC-XRD structure of **P-Mn2Fe4MoxW24-x** and **P-CosFeMoxW24-x** shows that the tri lacunary Keggin moiety contains a tetrahedrally bound P atom in the center as a templating agent to triads of addenda W/Mo atoms (Figure 4B.5b). The FT-IR spectra of **P-Mn2Fe4MoxW24-x** show the characteristics peaks in the region 650-1050 cm<sup>-1</sup> with characteristics peaks at 1044 cm<sup>-1</sup> (P-O), 939 cm<sup>-1</sup> (M=O<sub>term</sub>, M=Mo/W), 868, 683 cm<sup>-1</sup> (M-O-M, M=Mo/W) (Figure 4B.4a). The FT-IR spectra of **P-CosFeMoxW24-x** show characteristics peaks similar to **P-Mn2Fe4MoxW24-x** in the region 650-1050 cm<sup>-1</sup> with characteristics peaks at 1027 cm<sup>-1</sup> (P-O), 934 cm<sup>-1</sup> (M=O<sub>term</sub>, M=Mo/W), 865, 681 cm<sup>-1</sup> (M-O-M, M=Mo/W) (Figure 4B.5d).

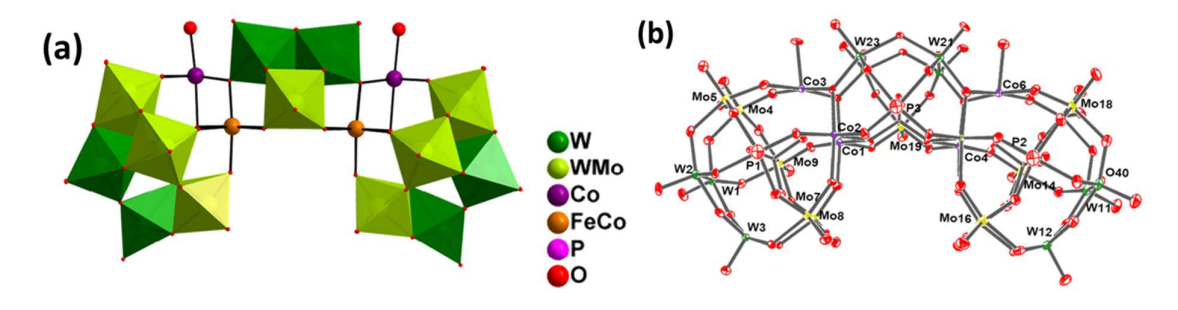


**Figure 4B.6** (a) combined polyhedral/ball and stick and (b) ORTEP drawing (with 60% ellipsoid probability) SC-XRD of **P-Co<sub>5</sub>FeMo<sub>x</sub>W<sub>24-x</sub>**.

Both **P-Mn<sub>2</sub>Fe<sub>4</sub>Mo<sub>x</sub>W**<sub>24-x</sub> and **P-Co<sub>5</sub>FeMo<sub>x</sub>W**<sub>24-x</sub> exhibit broad absorption bands in the UV-vis region due to ligand-to-metal charge transfer (LMCT) ( $O_{2p} \rightarrow W_{5d}$ ) and d-d transitions. A significant contribution of Mo is evident in mixed addenda sandwich POMs through a red shift of LMCT (Figure 4B.4/4B.5). This red shift can be explained from the changes in the band gap of these POMs, which were investigated using DRS. The band gap calculated from DRS is found to be 2.0 eV in **P-Mn<sub>2</sub>Fe<sub>4</sub>Mo<sub>x</sub>W**<sub>24-x</sub> and 2.1 eV in **P-Co<sub>5</sub>FeMo<sub>x</sub>W**<sub>24-x</sub> (Figure 4B.4). DFT study indicates a similar effect of Mo as observed in TMSPs where the HOMO-LUMO band gap in **P-Mn<sub>2</sub>Fe<sub>4</sub>Mo<sub>x</sub>W**<sub>24-x</sub> (representative structure of **P-Mn<sub>2</sub>Fe<sub>4</sub>Mo<sub>x</sub>W**<sub>24-x</sub> is taken with the formula [Mn<sub>6</sub>(PMo<sub>2</sub>W<sub>4</sub>O<sub>26</sub>)(PMo<sub>6</sub>W<sub>3</sub>O<sub>34</sub>)<sub>2</sub>(H<sub>2</sub>O)<sub>2</sub>] and its corresponding W-based auxiliary structure) decreases when moving from W-only to mixed addenda (W/Mo) in this banana architecture with complete shift of electron density on Mo addenda at the belt region (Figure 4B.S10). Thermal stability of these POMs was determined by TGA analysis from 30 to 600 °C (Figure 4B.9). The TGA curve of these POMs shows high thermal stability

even up to 480 °C. The first weight loss was observed in the range of 30-170 °C, attributed to the release of water of crystallisation.

While using Mn(+3) along with Co(+2) results in the formation of [Mn<sub>2</sub>Fe<sub>4</sub>(PMo<sub>x</sub>W<sub>6</sub><sub>x</sub>O<sub>26</sub>)(PMo<sub>x</sub>W<sub>9-x</sub>O<sub>34</sub>)<sub>2</sub>(H<sub>2</sub>O)<sub>2</sub>]<sup>17-</sup> (**P-Mn<sub>2</sub>Co<sub>4</sub>Mo<sub>x</sub>W<sub>24-x</sub>**), which was characterised using SC-XRD (Figure 4B.7). The 3D structure of **P-Mn<sub>2</sub>Co<sub>4</sub>Mo<sub>x</sub>W<sub>24-x</sub>** was confirmed by SC-XRD. The long needle-shaped dark brown crystals in monoclinic (P2<sub>1</sub>/c space group) (Table S41). FT-IR comparison of **P-Mn<sub>2</sub>Co<sub>4</sub>Mo<sub>x</sub>W<sub>24-x</sub>** to **P-Mn<sub>2</sub>Co<sub>2</sub>Mo<sub>x</sub>W<sub>18-x</sub>** indicates the shift in the characteristic peaks of POMs due to the switching of framework from sandwich to banana (Figure 4B.7b). Interestingly, the incorporation of Mn<sup>+3</sup> in the framework not only switches the framework but also decreases the Mo incorporation at the addenda positions. Now, only two positions of hexa-lacunary Keggin POMs are favorable for Mo incorporation, whether it is connected to µ<sub>2</sub> oxygen or not. This is due to Jahn-Teller distortions (z-out) present in Mn<sup>+3</sup> (d<sup>4</sup> configurations).

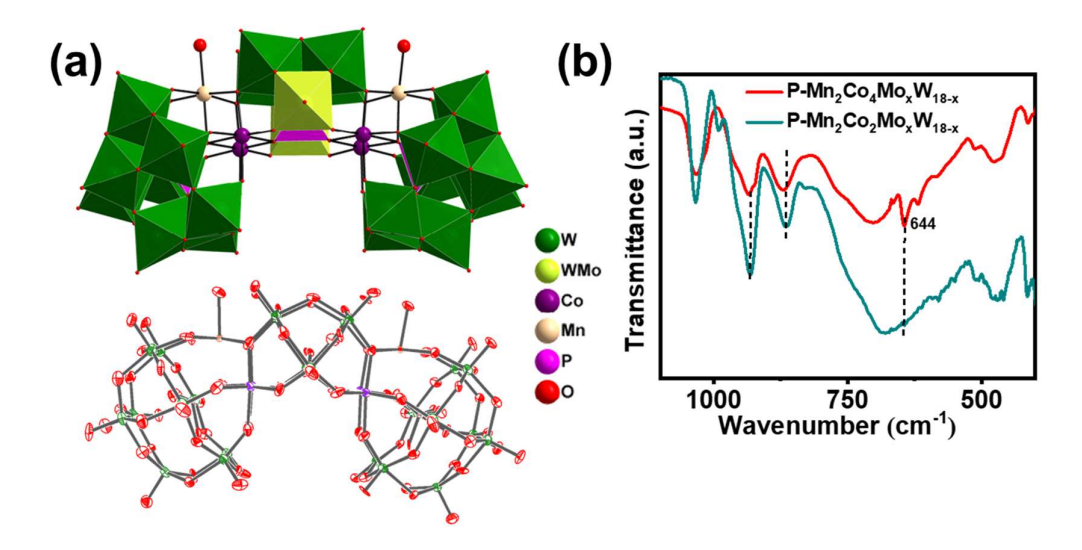


**Figure 4B.7** (a) combined polyhedral/ball and stick and ORTEP drawing (with 60% ellipsoid probability) of single crystal structure of **P-Co<sub>4</sub>Mn<sub>2</sub>Mo<sub>x</sub>W<sub>24-x</sub>**. (b) Shift in FTIR spectra due to framework switching from sandwich to banana.

#### 4B.2.2 Cooperative Effects of Mixed Metals using Bismuth as the heteroatom

The repulsive forces between the lone pairs on heteroatom (Sb<sup>3+</sup> or Bi<sup>3+</sup>) in Krebs-type POMs cause a distortion resulting in two tri-lacunary subunits moving away from their perpendicular alignment. Krebs-type POMs are formed when transition metal ions are substituted into the equatorial positions of trivacant lacunary POMs, allowing up to 4 transition

metals to be incorporated in these POMs. 18, 19 Interestingly, the POMs scaffold does not shield the 3d-metal ions in these structures. The biological activity, molecular magnetism, and catalytic activity of the Krebs-type POMs are all impacted by incorporated transition metals.<sup>20</sup>, <sup>21</sup> However, it was observed that when Bi is present at heteroatom, W occupies one of the sandwich positions along with 3d transition metals. Additionally, all transition metals incorporated so far have been in the +2 oxidation state. Krebs et al. have shown that in the parent  $[\{(TM)O_2(OH)\}_2((TM)WO_4)(BiW_9O_{33})_2]^{n-}$  POMs, the two outer fac- $\{(TM)O_2(OH)\}_2$ octahedral groups are labile, whereas the two inner cis-{(TM)WO<sub>4</sub>} units are non-labile or inert. 20 This lability leads to the formation of defected intermediates [(TM)WO<sub>4</sub>)(BiW<sub>9</sub>O<sub>33</sub>)<sub>2</sub>]<sup>n+2</sup> in solution, which facilitates replacement of external sites by the incoming transition metals.<sup>22</sup>, <sup>23</sup> The interchange of the outer {(TM)MO<sub>2</sub>(OH)} groups with the different transition metals (TM = Mn/Fe/Co/Ni/Zn) in these POMs has been extensively studied. Nevertheless, there has been only little research on why {WO<sub>2</sub>} occupies the inner positions or why there are no reports of transition metals being present only at the sandwich position without any W. So, our target was to explore a cooperative mixed metal strategy, investigating the role of different oxidation states of transition metals in the self-assembly of Krebs-type POMs. Additionally, the size of metal ions at the inner and outer sandwich positions can play an impactful role along with oxidation states of transition metals towards the self-assembly of Krebs POMs.

## 4B.2.2a Synthesis and characterisation of Krebs Polyoxometalates using cooperative mixed metals strategy

cooperative Using mixed metal strategy, we have synthesized  $[{Zn(OH_2)_2}_2(FeO_3)_2(BiW_9O_{33})_2]^{n-}$  (Bi-Zn<sub>2</sub>Fe<sub>2</sub>W<sub>18</sub>) (Figure 4B.8), and characterised using SC-XRD and ESI-MS. Bi-Zn<sub>2</sub>Fe<sub>2</sub>W<sub>18</sub> crystallizes in monoclinic (C2/m space group) (Table 4B.S5). The ESI-mass spectrum of Bi-Zn<sub>2</sub>Fe<sub>2</sub>W<sub>18</sub> shows the envelopes of peaks at m/z 1692.03  $\{H_5Fe_2Zn_2(BiW_9O_{34})_2(H_2O)\}^{3-}$ for the fragments (Figure 4B.10a, Table 4B.S6). Functionalisation of POMs with organic moieties improves their usefulness in various applications, e.g. medicinal chemistry, materials science, and catalysis, especially with regard to their antibacterial and anticancer qualities. Amino acid-based organic ligand functionalisation of Krebs-type POMs can be possible, where amino acids can bind directly to the transition metal ions at equatorial positions by replacing labile water molecules. Only a few examples of amino acid-functionalized inorganic-organic hybrid POMs have been reported so far.

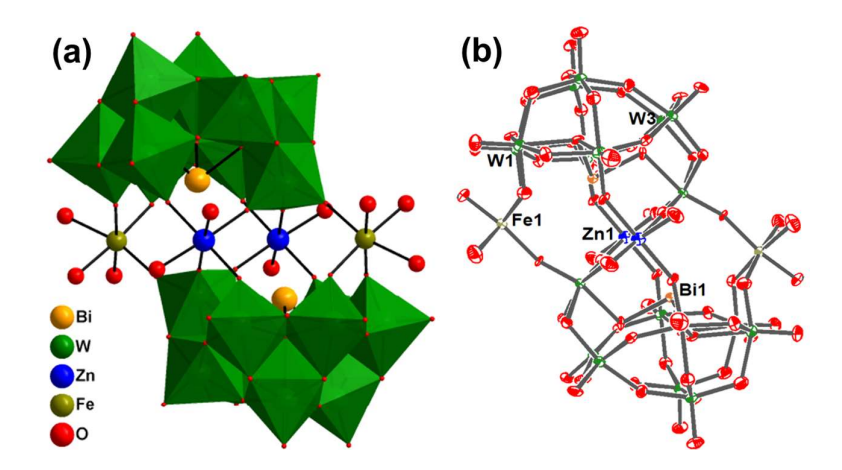


Figure 4B.8 (a) combined polyhedral/ball and stick and (b) ORTEP drawing (with 60% ellipsoid probability) of single crystal structure of Bi-Zn<sub>2</sub>Fe<sub>2</sub>W<sub>18</sub>.

Here using cooperative mixed metals strategy, we have functionalise Bi-Zn<sub>2</sub>Fe<sub>2</sub>W<sub>18</sub> with glycine to isolate  $[{Zn(OH_2)_2}_2(FeO_3)_2(BiW_9O_{33})_2(Gly)_2]^{n-}$  (Bi-Zn<sub>2</sub>Fe<sub>2</sub>W<sub>18</sub>{Gly}) (Figure 4B.9) which have been characterised using SC-XRD. Bi-Zn<sub>2</sub>Fe<sub>2</sub>W<sub>18</sub>{Gly} crystallize in monoclinic (C2/m space group) (Table S41). The ESI-mass spectrum of Bi-Zn<sub>2</sub>Fe<sub>2</sub>W<sub>18</sub>{Gly} 1742.46 shows the envelopes of peaks at m/zfor the fragments H<sub>3</sub>Fe<sub>2</sub>Zn<sub>2</sub>(BiW<sub>9</sub>O<sub>34</sub>)<sub>2</sub>(Gly)<sub>2</sub>(H<sub>2</sub>O)<sub>3</sub> (Figure 4B.10b, Table 4B.S7) Another crucial factor is the sequence in which transition metals are added. For example, after synthesizing the tri-lacunary BiW<sub>9</sub>O<sub>34</sub>, addition of Zn followed by Mn results in the formation of Krebs POMs with the formula  $[{ZnMn(OH_2)_4}{{ZnW(OH_2)_6}(BiW_9O_{33})_2}]^{n-}$  (**Bi-MnWZn<sub>2</sub>W<sub>18</sub>**) (Figure 4B.11).

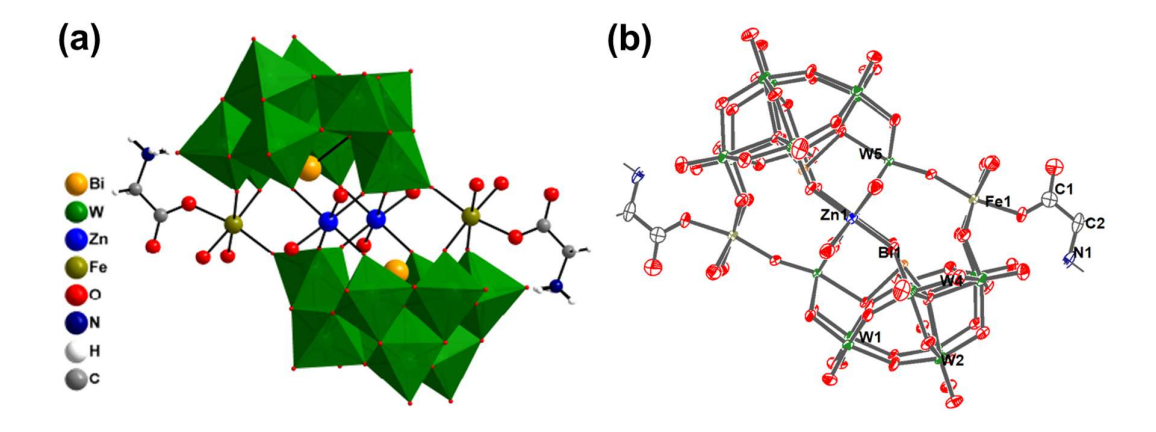


Figure 4B.9 (a) combined polyhedral/ball and stick and (b) ORTEP drawing (with 60% ellipsoid probability) representation of Bi-Zn<sub>2</sub>Fe<sub>2</sub>W<sub>18</sub>{Gly}.

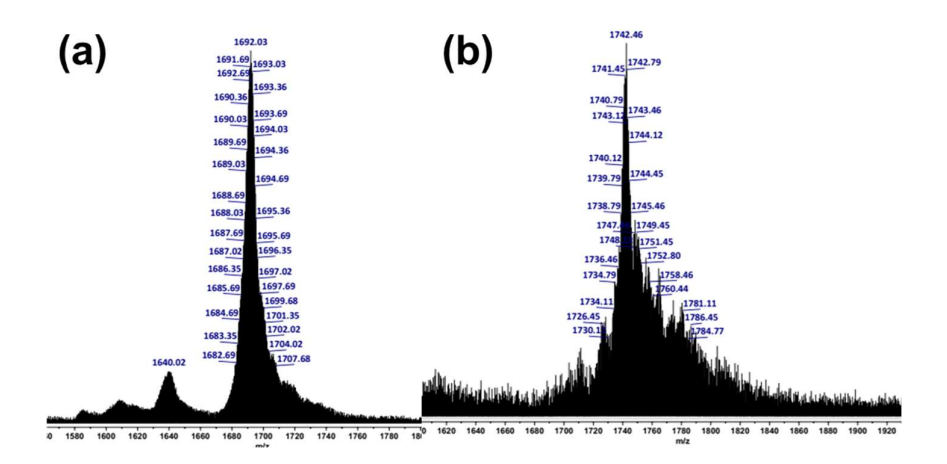


Figure 4B.10 ESI-MS spectra of (a) Bi- $Zn_2Fe_2W_{18}$  and (b) Bi- $Zn_2Fe_2W_{18}$ {Gly} in the range of m/z 1500-1800 with z= -3.

Conversely, addition of Mn first followed by Zn results in the formation of a 1-D framework in Krebs POMs with the general formula [{ZnMn(OH<sub>2</sub>)<sub>4</sub>} {ZnW(OH<sub>2</sub>)<sub>6</sub>}(BiW<sub>9</sub>O<sub>33</sub>)<sub>2</sub>]<sup>n-</sup> (**Bi-ZnWMn<sub>2</sub>W<sub>18</sub>**) (Figure 4B.12). Interestingly, in **Bi-ZnWMn<sub>2</sub>W<sub>18</sub>**, Mn was found to be in +3 oxidation states. Octahedral Mn(III) centres produce pronounced Jahn-Teller distortion, leading to elongated axial O-Mn-O bonds. The configurational flexibility provided by the Jahn-Teller distortion reduces the steric hindrance and allows the Mn(III) centres to link with one another and other polyanions, thus forming the 1D structure. For instance, elongated Mn-O-W bonds create 1D chains in **Bi-ZnWMn<sub>2</sub>W<sub>18</sub>**. Thus, substantial structural changes result from changing the reaction conditions.

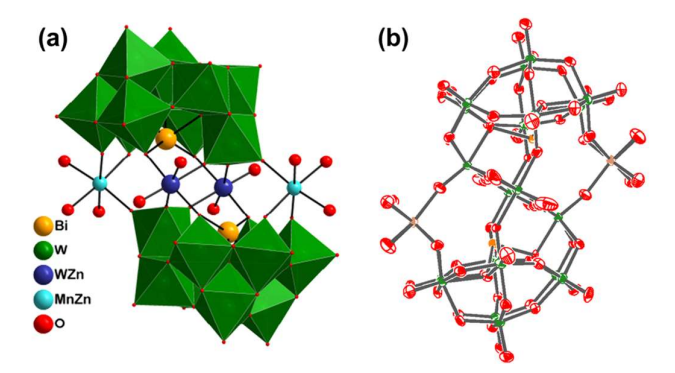


Figure 4B.11 (a) combined polyhedral/ball and stick and (b) ORTEP drawing (with 60% ellipsoid probability) of SC-XRD of Bi-MnWZn<sub>2</sub>W<sub>18</sub>.

Compounds **Bi-MnWZn<sub>2</sub>W<sub>18</sub>** and **Bi-ZnWMn<sub>2</sub>W<sub>18</sub>** were characterized using SC-XRD. The framework structure was confirmed by SC-XRD, **Bi-MnWZn<sub>2</sub>W<sub>18</sub>** crystallize in monoclinic (P2<sub>1</sub>/c space group) (Table 4B.S5) while **Bi-ZnWMn<sub>2</sub>W<sub>18</sub>** crystallize in triclinic (P\overline{1}\) space

group). It was observed from the detailed crystal structure analysis that all countercations and crystal water molecules show disorder.

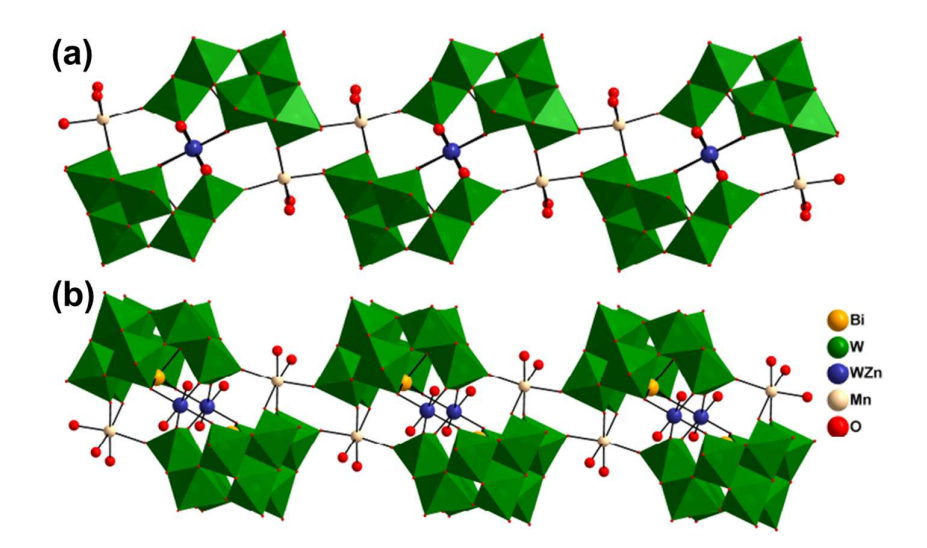


Figure 4B.12 (a) combined polyhedral/ball and stick and (b) ORTEP drawing (with 60% ellipsoid probability) representation of  $Bi\text{-}ZnWMn_2W_{18}$ .

#### **4B.3 Conclusion**

Apart from cooperative mixed metal strategy, several other factors contribute to the self-assembly of transition metals based tetrasubstituted sandwich POMs. The oxidation state of transition metals as well as the size of heteroatom, play an important role towards the switching of framework from sandwich to banana or Keggin to banana POMs. The sequence of transition metals addition results in the switching of frameworks as Jahn-Teller distortion in Bi-based Krebs POMs leads to the elongation of equatorial bonds, forming 1D frameworks. A cooperative mixed-metal strategy enables the incorporation of amino acids in Krebs POMs, which can be a possible route for post-functionalization in these POMs.

#### 4B.4 Materials and Instrumentation

#### 4B.4.1 General information and Instrumentation

#### 4B.4.1a Materials and Methods

Already mentioned in section 2.4.1a (chapter 2)

#### 4B.4.1b Instrumentation

Already mentioned in section 2.4.1b (chapter 2)

#### 4B.4.1c Density Functional Theory (DFT) Calculation.

Already mentioned in section 2.4.1c (chapter 2)

#### 4B.4.2 Synthesis

#### $Na_{10}[Mn_2Co_2(H_2O)_2(PMo_xW_{9-x}O_{34})_2].nH_2O (P-Mn_2Co_2Mo_xW_{18-x})$

A mixture of of Na<sub>2</sub>WO<sub>4</sub>.2H<sub>2</sub>O (2.00 g, 6.06 mmol), Na<sub>2</sub>MoO<sub>4</sub>.2H<sub>2</sub>O (1.4 g, 6.06 mmol), Na<sub>2</sub>HPO<sub>4</sub>.2H<sub>2</sub>O (0.190 g, 1.34 mmol) dissolved in 12 mL of DI water and pH was fixed at 6.5 using glacial acetic acid. The resultant solution was put in Teflon microwave vials and microwave irradiated under control pressure at 85 °C with a power ramp for 15 min and hold for 45 min under 400W maximum power. In the resultant solution, a mixture of Mn(OAc)<sub>2</sub>.4H<sub>2</sub>O (0.32 g, 1.34 mmol) and Co(OAc)<sub>2</sub>.4H<sub>2</sub>O (0.33 g, 1.34 mmol) was added to the above solution with vigorous stirring and irradiated again in the microwave for 1 h at 85 °C maintaining the previous parameter. The resultant solution was filtered hot and filtrate was kept for crystallization. After 2 days brown colored block crystals appeared which then collected and dried at 60 °C under vacuum. Yield: 0.98 g (35.2%). FT-IR (cm<sup>-1</sup>): 1033 (P-O), 991, 933 (M=O<sub>t</sub>), 860 (M-O<sub>c</sub>-M), 683 (M-O<sub>c</sub>-M) (M=Mo/W).

#### $Na_{10}[Ni_2Zn_2(H_2O)_2(PMo_xW_{9-x}O_{34})_2].nH_2O (P-Ni_2Zn_2Mo_xW_{18-x})$

The synthetic procedure of compound **P-Mn<sub>2</sub>Co<sub>2</sub>Mo<sub>x</sub>W<sub>18-x</sub>** was followed with slight modification. Typically, a mixture of Na<sub>2</sub>WO<sub>4</sub>.2H<sub>2</sub>O (2.00 g, 6.06 mmol), Na<sub>2</sub>MoO<sub>4</sub>.2H<sub>2</sub>O (1.40 g, 6.06 mmol), Na<sub>2</sub>HPO<sub>4</sub>.2H<sub>2</sub>O (0.19 g, 1.34 mmol), 12 mL H<sub>2</sub>O, and pH of solution was maintained to 7.15 using glacial acetic acid. The resultant solution was put in Teflon microwave vials and microwave irradiated under control pressure at 85 °C with a power ramp for 15 min and hold for 45 min under 400W maximum power. The resultant solution cooled to room temperature then solution of Zn(OAc)<sub>2</sub> .6H<sub>2</sub>O (0.35 g, 1.34 mmol) and Ni(OAc)<sub>2</sub>.6H<sub>2</sub>O (0.34 g, 1.34 mmol) added and again microwave-irradiated for 30 min at 85 °C, following previous parameters. The resultant solution was filtered hot and filtrate was kept for crystallization. Yield: 0.73 g (27.8%). FT-IR (cm<sup>-1</sup>): 1041 (P-O), 1014, 975 (M=O<sub>t</sub>), 920 (M-O<sub>c</sub>-M), 875 (M-O<sub>c</sub>-M) (M=Mo/W).

#### $Na_{17}[Mn_{2}Fe_{4}(PMo_{x}W_{6-x}O_{26})(PMo_{x}W_{9-x}O_{34})_{2}(H_{2}O)_{2}].nH_{2}O(P-Mn_{2}Fe_{4}Mo_{x}W_{24-x})$

A mixture of Na<sub>2</sub>WO<sub>4</sub>.2H<sub>2</sub>O (2.00 g, 6.06 mmol), Na<sub>2</sub>MoO<sub>4</sub>.2H<sub>2</sub>O (1.46 g, 6.06 mmol), and Na<sub>2</sub>HPO<sub>4</sub>.2H<sub>2</sub>O (0.23 g, 1.34 mmol) dissolved in 15 mL of DI water. Using glacial acetic acid, pH of the solution was adjusted to 6.5. The resultant solution was put in Teflon microwave vials having 100 mL volume and microwave irradiated under controlled pressure with a power ramp for 15 min, and power hold for 30 min at 85 °C under 400 W maximum power (step 1). After that, FeCl<sub>2</sub>.4H<sub>2</sub>O (0.26 g, 1.34 mmol) was added to the vial and irradiated in the microwave for 15 min at 85 °C, maintaining the previous parameters (step 2). Then

Mn(OAc)<sub>2</sub>.4H<sub>2</sub>O (0.32 g, 1.34 mmol) was added in the Teflon vial and irradiated again in the microwave for 15 min at 85 °C, maintaining the previous parameters (step 3). The resultant solution was filtered hot, and the filtrate was allowed to crystallization. The final pH was found to be 5.9. After 2-3 days, yellowish-brown hexagonal shape crystals appeared, which were collected and dried at 60 °C under vacuum. Yield: 0.97 g (23.8%). FT-IR (cm<sup>-1</sup>): 1044 (P-O), 939 (M=O<sub>t</sub>), 868 (M-O<sub>c</sub>-M), 683 (M-O<sub>e</sub>-M) (M=Mo/W).

#### $Na_{17}[Co_5Fe(PMo_xW_{6-x}O_{26})(PMo_xW_{9-x}O_{34})_2(H_2O)_2].nH_2O(P-Co_5FeMo_xW_{24-x})$

The synthetic procedure of compound **P-Mn<sub>2</sub>Fe<sub>4</sub>Mo<sub>x</sub>W<sub>24-x</sub>** was followed with slight modification. In place of Mn(OAc)<sub>2</sub>.4H<sub>2</sub>O, Co(OAc)<sub>2</sub>.4H<sub>2</sub>O (0.33 g, 1.34 mmol) was used. Thus, the dark orange solution was filtered hot, and the filtrate was kept for crystallization. After 6 h, light orange crystals were obtained, collected by filtration, and dried at 60 °C under vacuum. Yield: 0.44 g (10.8%). FT-IR (cm<sup>-1</sup>): 1027 (P-O), 934 (M=O<sub>t</sub>), 865 (M-O<sub>c</sub>-M), 681 (M-O<sub>c</sub>-M) (M=Mo/W).

Na<sub>14</sub>[{Zn(OH<sub>2</sub>)<sub>2</sub>}<sub>2</sub>(FeO<sub>3</sub>)<sub>2</sub>(BiW<sub>9</sub>O<sub>33</sub>)<sub>2</sub>].nH<sub>2</sub>O (Bi-Zn<sub>2</sub>Fe<sub>2</sub>W<sub>18</sub>) - Na<sub>2</sub>WO<sub>4</sub>.2H<sub>2</sub>O (4.00 g, 12.12 mmol) salt was added to a 100 mL beaker with 15 mL DI water and stirred for 10 min until it got completely dissolved. Then pH of the solution was fixed to 7.2 using HNO<sub>3</sub>. The reaction mixture was microwave irradiated for 1 h at 80 °C. After that BiCl<sub>3</sub> (0.42 g, 1.34 mmol) was added, followed by FeCl<sub>2</sub> (0.16 g, 1.34 mmol), and Zn(NO<sub>3</sub>)<sub>2</sub> (0.39 g, 1.34 mmol) to the solution and again microwave irradiated for 1 h at 80 °C. The resultant solution was filtered into a 100 mL beaker and kept for crystallization at room temperature. After one day, crystals started forming at the bottom of the beaker, which were analysed using SC-XRD and mass spectrometry. Yield (2.38 g, 45.7 %) mass spectra: m/z observed =1692.03, m/z calculated = 1693.46

Na<sub>14</sub>[{Zn(OH<sub>2</sub>)<sub>2</sub>}<sub>2</sub>(FeO<sub>3</sub>)<sub>2</sub>(BiW<sub>9</sub>O<sub>33</sub>)<sub>2</sub>(Gly)<sub>2</sub>].nH<sub>2</sub>O (Bi-Zn<sub>2</sub>Fe<sub>2</sub>W<sub>18</sub>{Gly})- Na<sub>2</sub>WO<sub>4</sub>.2H<sub>2</sub>O (4.00 g, 12.12 mmol) salt was added to a 100 mL beaker with 15 mL DI water and stirred for 10 min until it got completely dissolved. Then pH of the solution was fixed to 7.0 using HNO<sub>3</sub>. The reaction mixture was microwave irradiated for 1 h at 80 °C. After that BiCl<sub>3</sub> (0.42 g, 1.34 mmol) was added, followed by FeCl<sub>2</sub> (0.16 g, 1.34 mmol), and Zn(NO<sub>3</sub>)<sub>2</sub> (0.39 g, 1.34 mmol) along with Glycine (1.88 g) to the solution and again microwave irradiated for 1 h at 80 °C. The resultant solution was filtered into a 100 mL beaker and kept for crystallization at room temperature. After one week, crystals started forming at the bottom of the beaker, which were analysed using SC-XRD and mass spectrometry. Yield (2.73 g, 43.4 %) mass spectra: m/z observed =1742.46, m/z calculated = 1742.83

Na<sub>14</sub>[{ZnMn(OH<sub>2</sub>)<sub>4</sub>}{ZnW(OH<sub>2</sub>)<sub>6</sub>}(BiW<sub>9</sub>O<sub>33</sub>)<sub>2</sub>].nH<sub>2</sub>O (Bi-MnWZn<sub>2</sub>W<sub>18</sub>) - Na<sub>2</sub>WO<sub>4</sub>2H<sub>2</sub>O (4.00 g, 12.12 mmol) salt was added to a 100 mL beaker with 15 mL DI water and stirred for 10 min until it got completely dissolved. Then pH of the solution was fixed to 7.0 using concentrated HNO<sub>3</sub>. The reaction mixture was irradiated using microwave for 1 h at 80 °C. After that BiCl<sub>3</sub> (0.42 g, 1.34 mmol) was added, followed by Zn(NO<sub>3</sub>)<sub>2</sub> (0.25 g, 1.34 mmol) and MnCl<sub>2</sub> (0.17 g, 1.34 mmol) to the solution and again microwave irradiated for 1 h at 80 °C. The resultant solution was filtered into a 100 mL beaker and kept for crystallization at room temperature. After two days, crystals thus formed were analysed using SC-XRD. Yield (1.47 g, 28.3%).

Na<sub>14</sub>[{ZnMn(OH<sub>2</sub>)<sub>4</sub>}{ZnW(OH<sub>2</sub>)<sub>6</sub>}(BiW<sub>9</sub>O<sub>33</sub>)<sub>2</sub>].nH<sub>2</sub>O (Bi-ZnWMn<sub>2</sub>W<sub>18</sub>) The synthetic procedure of compound Bi-MnWZn<sub>2</sub>W<sub>18</sub> was followed with slight modification in the sequence of addition of transition metals. Na<sub>2</sub>WO<sub>4</sub>.2H<sub>2</sub>O (4.00 g, 12.12 mmol) salt was added to a 100 mL beaker with 15 mL DI water and stirred for 10 min until completely dissolved. Then pH of the solution was fixed to 7.0 using concentrated HNO<sub>3</sub>. The reaction mixture was microwave irradiated for 1 h at 80 °C. After that BiCl<sub>3</sub> (0.42 g, 1.34 mmol) was added, followed by MnCl<sub>2</sub> (0.17 g, 1.34 mmol) and Zn(NO<sub>3</sub>)<sub>2</sub> (0.25 g, 1.34 mmol) to the solution and again microwave irradiated for 1 h at 80 °C. The resultant solution was filtered into a 100 mL beaker and kept for crystallization at room temperature. After two days, crystals thus formed were analysed using SC-XRD. Yield (1.78 g, 34.2%)

#### **4B.5 References**

- 1. Mbomekalle, I. M.; Keita, B.; Nierlich, M.; Kortz, U.; Berthet, P.; Nadjo, L., Structure, magnetism, and electrochemistry of the multinickel polyoxoanions [Ni6As3W24O94(H2O)2]17-, [Ni3Na(H2O)2(AsW9O34)2]11-, and [Ni4Mn2P3W24O94(H2O)2]17-, Inorg. Chem. 2003, 42 (17), 5143-5152.
- 2. Yang, L.; Zhao, J.; Zhao, J.; Niu, J., Syntheses, crystal structures, and magnetic properties of the banana-shaped tungstophosphates:[M6(H2O)2(PW9O34)2 (PW6O26)]17– (MII= NiII, CoII). *J Coord Chem* **2012**, *65* (19), 3363-3371.
- 3. Niu, J.-Q.; Zhao, Q.; Xin, X.; Zhang, Y.-Q.; Hu, N.; Ma, Y.-Y.; Han, Z.-G., Krebs-type polyoxometalate-based crystalline materials: synthesis, characterization and catalytic performance. *J Coord Chem* **2020**, *73* (17-19), 2391-2401.
- 4. Thiel, J.; Ritchie, C.; Streb, C.; Long, D.-L.; Cronin, L., Heteroatom-controlled kinetics of switchable polyoxometalate frameworks. *J. Am. Chem. Soc.* **2009**, *131* (12), 4180-4181.
- 5. Evangelisti, F.; Car, P.-E.; Blacque, O.; Patzke, G. R., Photocatalytic water oxidation with cobalt-containing tungstobismutates: tuning the metal core. *Catal. Sci. Technol.* **2013**, *3* (12), 3117-3129.
- 6. Liu, Y.; Liu, B.; Xue, G.; Hu, H.; Fu, F.; Wang, J., The novel sandwich-type heteropolyoxotungstates [M2Bi2(β-B-MW9O34)2]14– (M= Co , Zn): β-type dimeric heteropolyanions with a transition metal as the central heteroatom and Bi III and M as linking atoms. *Dalton Trans.* **2007**, (33), 3634-3639.

- 7. Lv, H.; Song, J.; Geletii, Y. V.; Vickers, J. W.; Sumliner, J. M.; Musaev, D. G.; Kögerler, P.; Zhuk, P. F.; Bacsa, J.; Zhu, G., An exceptionally fast homogeneous carbon-free cobalt-based water oxidation catalyst. *J. Am. Chem. Soc.* **2014**, *136* (26), 9268-9271.
- 8. Yin, Q.; Tan, J. M.; Besson, C.; Geletii, Y. V.; Musaev, D. G.; Kuznetsov, A. E.; Luo, Z.; Hardcastle, K. I.; Hill, C. L., A fast soluble carbon-free molecular water oxidation catalyst based on abundant metals. *Science* **2010**, *328* (5976), 342-345.
- 9. Tao, M.; Yin, Q.; Kaledin, A. L.; Uhlikova, N.; Lu, X.; Cheng, T.; Chen, Y.-S.; Lian, T.; Geletii, Y. V.; Musaev, D. G., Structurally Precise Two-Transition-Metal Water Oxidation Catalysts: Quantifying Adjacent 3d Metals by Synchrotron X-Radiation Anomalous Dispersion Scattering. *Inorg. Chem.* **2022**, *61* (16), 6252-6262.
- Martin-Sabi, M.; Soriano-López, J.; Winter, R. S.; Chen, J.-J.; Vilà-Nadal, L.; Long, D.-L.; Galán-Mascarós, J. R.; Cronin, L., Redox tuning the Weakley-type polyoxometalate archetype for the oxygen evolution reaction. *Nat. Catal.* 2018, 1 (3), 208-213.
- 11. Singh, G.; Mandal, D., Modulation of the Band Gap and Redox Properties by Mixed Addenda in Sandwich Polyoxometalates. *Inorg. Chem* **2023**, *62* (48), 19648-19663.
- 12. Gu, Y.-N.; Chen, Y.; Wu, Y.-L.; Zheng, S.-T.; Li, X.-X., A series of banana-shaped 3d-4f heterometallic cluster substituted polyoxometalates: syntheses, crystal structures, and magnetic properties. *Inorg. Chem.* **2018**, *57* (5), 2472-2479.
- 13. Martin-Sabi, M.; Winter, R. S.; Lydon, C.; Cameron, J. M.; Long, D.-L.; Cronin, L., Rearrangement of {α-P2W15} to {PW6} moieties during the assembly of transition-metal-linked polyoxometalate clusters. *Chem. Commun.* **2016**, *52* (5), 919-921.
- 14. Liu, B.; Li, L.; Zhang, Y.; Ma, Y.; Hu, H.; Xue, G., Three banana-shaped arsenomolybdates encapsulating a hexanuclear transition-metal central magnetic cluster:[AsIII2FeIII5MMo22O85(H2O)]n- (M= Fe3+, n= 14; M= Ni2+ and Mn2+, n= 15). *Inorg. Chem.* **2011**, *50* (18), 9172-9177.
- 15. Clemente-Juan, J. M.; Coronado, E.; Forment-Aliaga, A.; Galán-Mascarós, J. R.; Giménez-Saiz, C.; Gómez-García, C. J., A new heptanuclear cobalt (II) cluster encapsulated in a novel heteropolyoxometalate topology: synthesis, structure, and magnetic properties of [Co7(H2O)2(OH)2P2W25O94]16- *Inorg. Chem.* **2004**, *43* (8), 2689-2694.
- 16. Dong, X.; Zhang, Y.; Liu, B.; Zhen, Y.; Hu, H.; Xue, G., Double Sandwich Polyoxometalate and Its Fe (III) Substituted Derivative,[As2Fe5Mo21O82]17— and [As2Fe6Mo20O8(H2O)2]16— *Inorg. Chem.* **2012**, *51* (4), 2318-2324.
- 17. Li, B.; Zhao, J.-W.; Zheng, S.-T.; Yang, G.-Y., A banana-shaped iron (III)-substituted tungstogermanate containing two types of lacunary polyoxometalate units. *Inorg. Chem. Commun.* **2009**, *12* (2), 69-71.
- 18. von Allmen, K. D.; Grundmann, H.; Linden, A.; Patzke, G. R., Synthesis and characterization of 0D–3D copper-containing tungstobismuthates obtained from the lacunary precursor Na9[B-α-BiW9O33]. *Inorg. Chem.* **2017**, *56* (1), 327-335.
- 19. Yang, S.; Gong, T.; Dai, Y.; Xiao, X.; Liu, J.; Chen, L.; Zhao, J., An Unusual Bismuth–Antimony–Europium Cluster-Imbedded Polyoxotungstate and Its Bidirectional Luminescence Detection. *Inorg. Chem.* **2023**, *62* (43), 17861-17869.
- Rafieeshad, M.; Gumerova, N. I.; Tanuhadi, E.; Giester, G.; Čipčić-Paljetak, H.; Verbanac, D.; Rompel, A., Synthesis, Characterization, and Antibacterial Activity of Ni-Substituted Krebs-type Sandwich-Tungstobismuthates Functionalized with Amino Acids. *Inorg. Chem.* 2023, 62 (24), 9484-9490.
- 21. Wang, L.; Zhou, B.-B.; Yu, K.; Su, Z.-H.; Gao, S.; Chu, L.-L.; Liu, J.-R.; Yang, G.-Y., Novel antitumor agent, trilacunary Keggin-type tungstobismuthate, inhibits proliferation and induces apoptosis in human gastric cancer SGC-7901 cells. *Inorg. Chem.* **2013**, *52* (9), 5119-5127
- 22. Artetxe, B.; Reinoso, S.; San Felices, L.; Lezama, L.; Pache, A.; Vicent, C.; Gutierrez-Zorrilla, J. M., Rearrangement of a Krebs-type polyoxometalate upon coordination of N, O-bis (bidentate) ligands. *Inorg. Chem.* **2015**, *54* (2), 409-411.
- 23. Artetxe, B.; Reinoso, S.; San Felices, L.; Vitoria, P.; Pache, A.; Martín-Caballero, J.; Gutiérrez-Zorrilla, J. M., Functionalization of Krebs-type polyoxometalates with N, Ochelating ligands: a systematic study. *Inorg. Chem.* **2015**, *54* (1), 241-252.

### **Annexure-V**

Table 4B.S1 Crystal data, data collection, and refinement parameters for P-M <sub>4</sub> W <sub>18</sub>						
	P-Mn <sub>2</sub> Co <sub>2</sub> Mo <sub>x</sub> W <sub>18-x</sub>	P-Ni <sub>2</sub> Zn <sub>2</sub> Mo <sub>x</sub> W <sub>18-x</sub>	P-Mn <sub>2</sub> Fe <sub>4</sub> Mo <sub>x</sub> W <sub>24-x</sub>	P-Co <sub>5</sub> FeMo <sub>x</sub> W <sub>24-x</sub>		
CCDC number	2330241	2330260	2330251	2330259		
empirical formula	$Co_2Mn_2Mo_{3.9}Na_{15}O \\ 98P_2W_{14.1}$	$\begin{array}{c} H_{40}K_8Mo_{4.2}Na_{15}Ni \\ {}_{4}O_{200}P_4W_{31.8}Zn_4 \end{array}$	$Fe_{16}Mn_8Mo_{16.6}Na_{78}\\O_{515}P_{12}W_{79.4}$	$\begin{array}{c} Co_5FeMo_{4.15}Na_{20.9}O_1 \\ _{26.33}P_3W_{19.85} \end{array}$		
formula weight	5168.98	10767.55	27928.27	6992.71		
temp (K)	273.15	273.15	293.15	273.15		
crystal system	triclinic	monoclinic	monoclinic	monoclinic		
space group	$P\overline{1}$	P2 <sub>1</sub> /n	P2 <sub>1</sub> /c	P2 <sub>1</sub> /c		
unit cell dimension						
a (Å)	11.595(3)	12.8923(10)	15.8332(19)	15.7812(15)		
b (Å)	12.933(3)	16.5101(11)	22.101(3)	22.134(2)		
c (Å)	17.322(5)	21.5306(14)	35.281(4)	35.138(4)		
α (deg)	97.469(8)	90	90	90		
$\beta$ (deg)	107.033(7)	104.045(2)	97.686(4)	97.802(3)		
γ (deg)	111.262(6)	90	90	90		
$V(\mathring{\mathbf{A}}^3)$	2231.7(10)	4445.9(5)	12235(2)	12160(2)		
Z	1	1	1	4		
ρ (calculated) (g/cm³)	3.846	4.022	3.791	3.820		
F (000)	2290.0	4779.0	12347.0	12359.0		
crystal size (mm³)	$0.32 \times 0.22 \times 0.14$	$0.32 \times 0.23 \times 0.22$	$0.23 \times 0.22 \times 0.11$	0.33 ×0.26 × 0.23		
index ranges	$-14 \le h \le 14, -15 \le 16, -21 \le 1 \le 21$	$   -16 \le h \le 16, -20 \le k \le 20, -26 \le l \le 26 $	$-19 \le h \le 19, -27 \le k \le 27, -42 \le l \le 44$	$ \begin{vmatrix} -19 \le h \le 19, -27 \le k \\ \le 27, -43 \le l \le 43 \end{vmatrix} $		
no. of reflection collected /unique	26992/9027	50732/9070	117211/ 25131	136406/24933		
GOF on $F^2$	1.024	1.130	1.017	1.059		
final $R$ indices $(I > 2\sigma(I))$	$R_1 = 0.031, wR_2 = 0.086$	$R_1 = 0.046, wR_2 = 0.124$	$R_1 = 0.053, wR_2 = 0.132$	$R_1 = 0.040, wR_2 = 0.102$		
R indices (all data)	$R_1 = 0.033, wR_2 = 0.088$	$R_1 = 0.047, wR_2 = 0.125$	$R_1 = 0.073, wR_2 = 0.146$	$R_1 = 0.050, wR_2 = 0.109$		
data/restraints/par am	9027/0/629	9070/1/618	25131/0/1654	24933/0/1638		

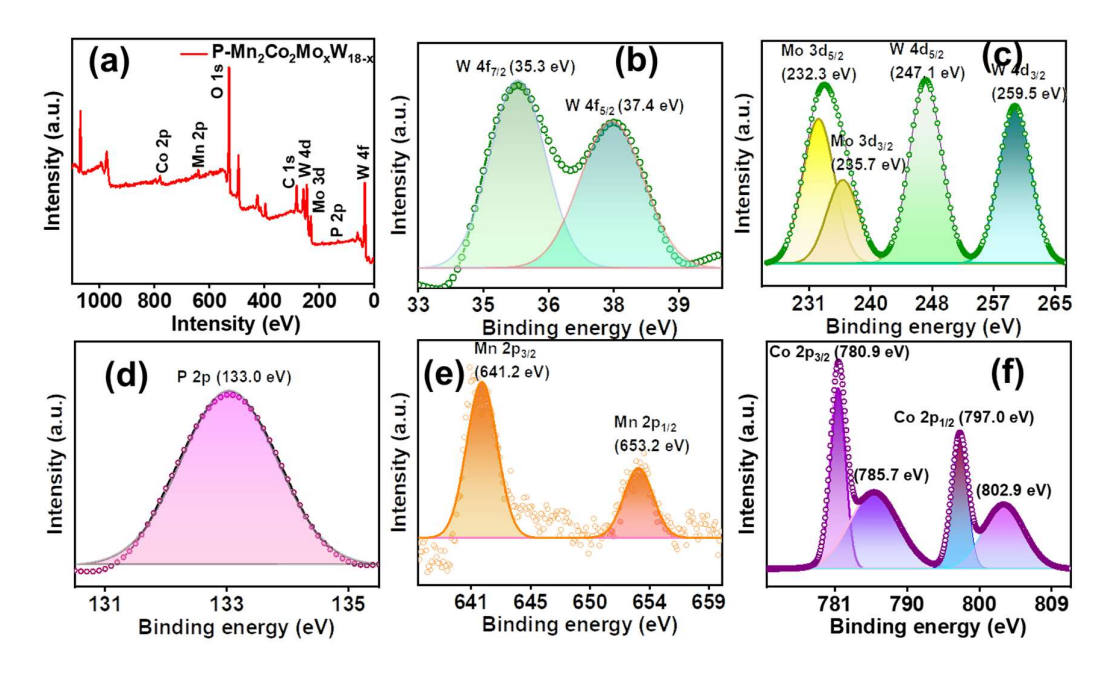


**Figure 4B.S1** XP spectra of P-Mn<sub>2</sub>Co<sub>2</sub>Mo<sub>x</sub>W<sub>18-x</sub> (a) Survey spectra, (b) W  $4f_{7/2}$  and  $4f_{5/2}$  (c) Mo 3d and W 4d (d) P 2p (e) Mn 2p and (f) Co 2p.

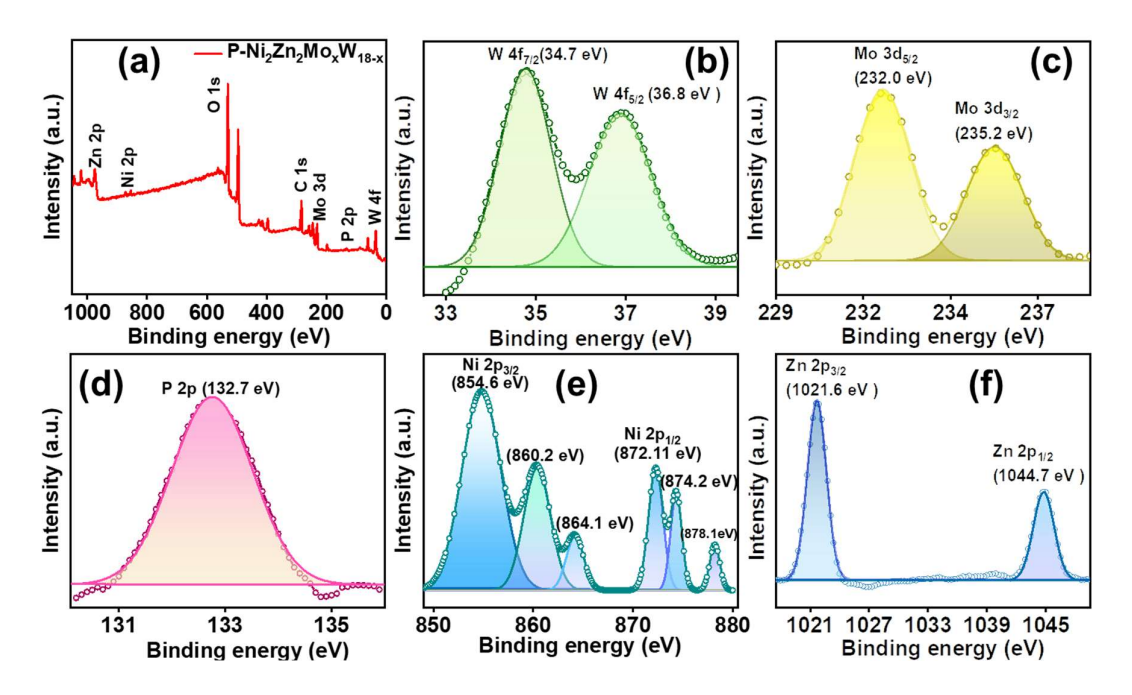


**Figure 4B.S2** XP spectra of  $P-Ni_2Zn_2Mo_xW_{18-x}$  (a) Survey spectra, (b) W  $4f_{7/2}$  and  $4f_{5/2}$  (c) Mo 3d (d) P 2p (e) Ni 2p and (f) Zn 2p.

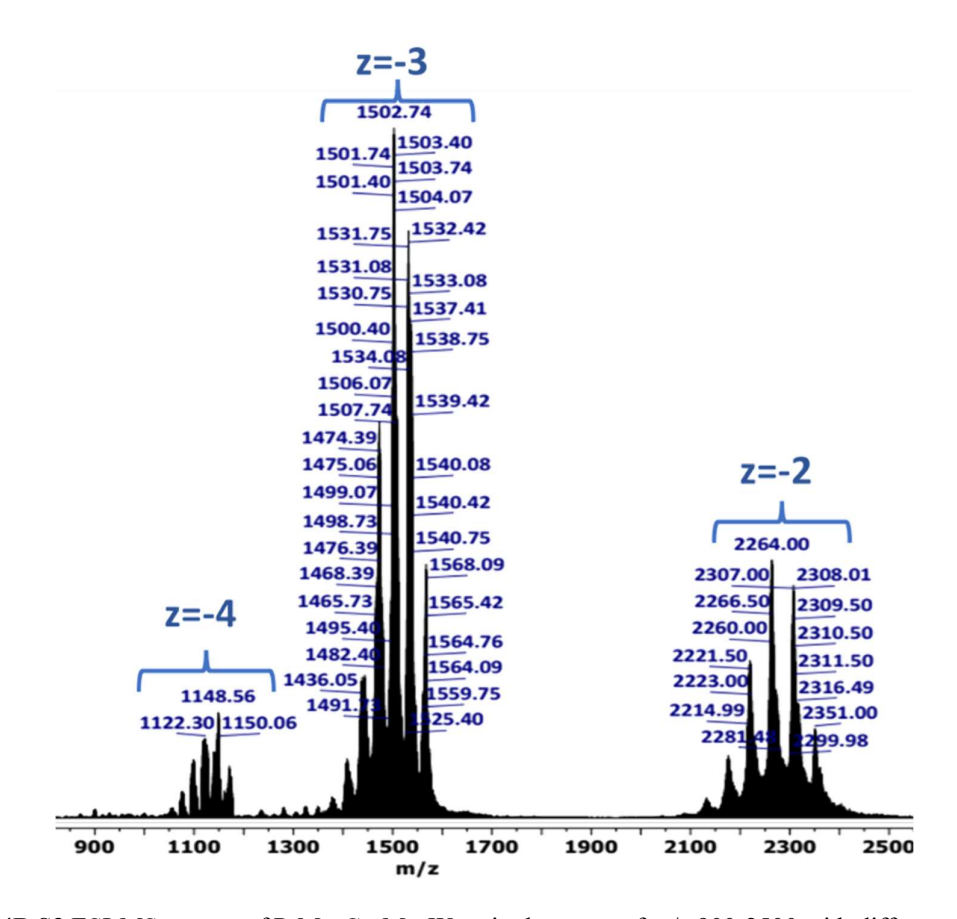
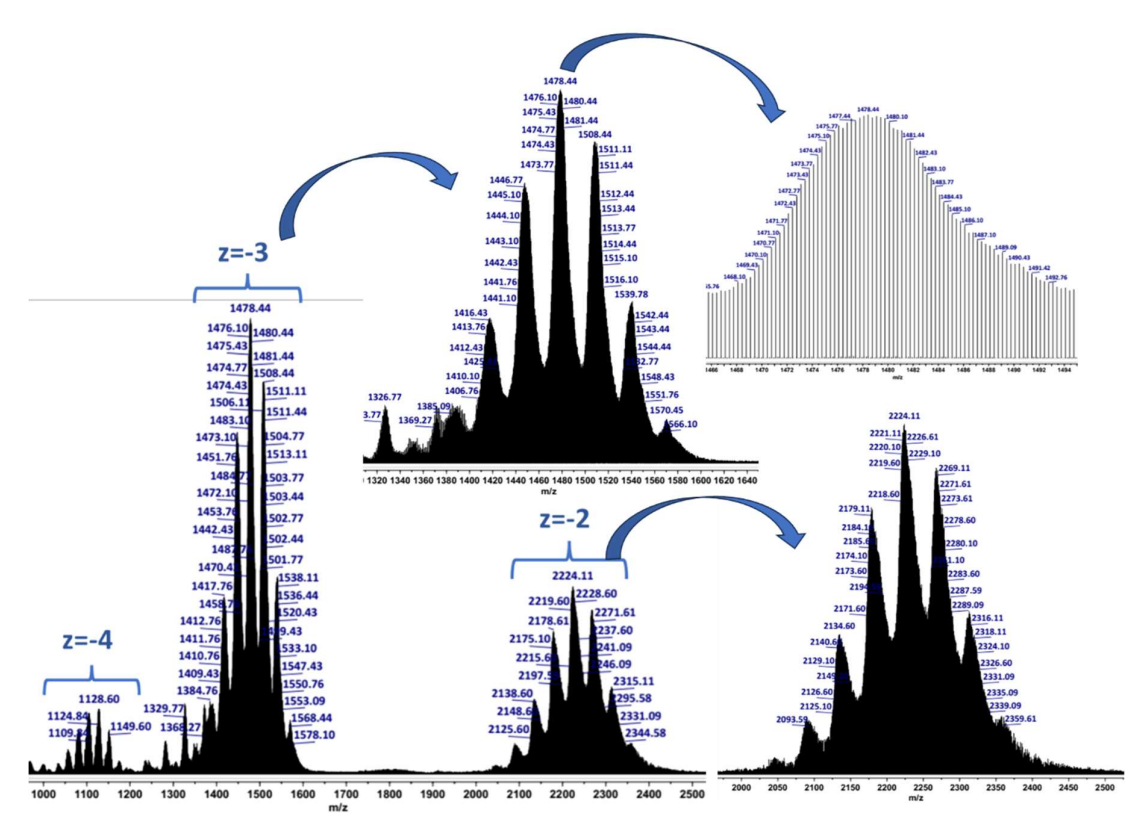


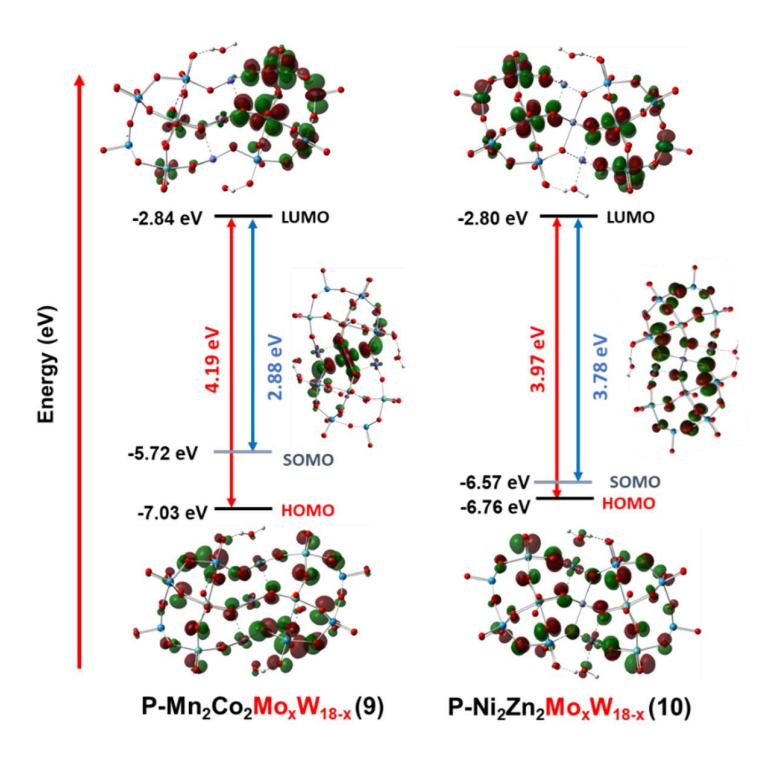
Figure 4B.S3 ESI-MS spectra of P-Mn<sub>2</sub>Co<sub>2</sub>Mo<sub>x</sub>W<sub>18-x</sub> in the range of m/z 900-2500 with different z values.

Table 4B.S2	Table 4B.S2 Assignment of ESI-mass peaks of P-Mn <sub>2</sub> Co <sub>2</sub> Mo <sub>x</sub> W <sub>18-x</sub>					
Charge	m/z (obs.)	m/z (calc.)	Mol. Wt.	Assigned probable formula		
-3	1568.09	1568.06	4704.18	$K_2Na_5Mn_2Co_2P_2Mo_2W_{16}O_{68}$		
-3	1532.42	1533.38	4600.16	$KNa_6Mn_2Co_2P_2Mo_3W_{15}O_{68}$		
-3	1502.74	1504.04	4512.12	KNa <sub>6</sub> Mn <sub>2</sub> Co <sub>2</sub> P <sub>2</sub> Mo <sub>4</sub> W <sub>14</sub> O <sub>68</sub>		
-3	1474.39	1474.69	4424.08	$KNa_6Mn_2Co_2P_2Mo_5W_{13}O_{68}$		
-3	1439.75	1440.02	4320.07	Na <sub>7</sub> Mn <sub>2</sub> Co <sub>2</sub> P <sub>2</sub> Mo <sub>6</sub> W <sub>12</sub> O <sub>68</sub>		
-2	2308.01	2308.57	4617.14	$HK_2Na_5Mn_2Co_2P_2Mo_3W_{15}O_{68}$		
-2	2264.00	2264.55	4529.10	HK <sub>2</sub> Na <sub>5</sub> Mn <sub>2</sub> Co <sub>2</sub> P <sub>2</sub> Mo <sub>4</sub> W <sub>14</sub> O <sub>68</sub>		
-2	2221.50	2220.53	4441.06	$HK_2Na_5Mn_2Co_2P_2Mo_5W_{13}O_{68}$		
-4	1148.56	1148.28	4593.15	$K_2Na_4Mn_2Co_2P_2Mo_3W_{15}O_{68}$		
-4	1122.30	1122.28	4489.13	$K_2Na_4Mn_2Co_2P_2Mo_4W_{14}O_{68}$		



 $\textbf{Figure 4B.S4} \ \text{ESI-MS spectra of } P\text{-Ni}_2Zn_2Mo_xW_{18\text{-x}} \text{ in range of } m/z \ 1000\text{-}2500 \text{ for different } z \text{ values}.$ 

Table 4B.S3 Assignment of ESI-mass peaks of P-Ni <sub>2</sub> Zn <sub>2</sub> Mo <sub>x</sub> W <sub>18-x</sub>					
Charge	m/z	m/z	Mol. Wt.	Assigned probable formula	
	(obs.)	(calc.)			
-3	1385.09	1384.65	4152.96	$K_2H_2Na_3Ni_2Zn_2P_2Mo_8W_{10}O_{68}$	
-3	1416.43	1418.99	4256.97	$H_2K_3Na_2Ni_2Zn_2P_2Mo_7W_{11}O_{68}$	
-3	1446.77	1448.33	4345.01	$H_2K_3Na_2Ni_2Zn_2P_2Mo_6W_{12}O_{68}$	
-3	1478.44	1477.68	4433.05	$H_2K_3Na_2Ni_2Zn_2P_2Mo_5W_{13}O_{68}$	
-3	1508.11	1507.03	4521.09	$K_3H_2Na_2Ni_2Zn_2P_2Mo_4W_{14}O_{68}$	
-3	1539.78	1538.04	4614.14	K <sub>2</sub> HNa <sub>4</sub> Ni <sub>2</sub> Zn <sub>2</sub> P <sub>2</sub> Mo <sub>3</sub> W <sub>15</sub> O <sub>68</sub>	
-3	1568.44	1567.39	4702.18	K <sub>2</sub> HNa <sub>4</sub> Ni <sub>2</sub> Zn <sub>2</sub> P <sub>2</sub> Mo <sub>2</sub> W <sub>16</sub> O <sub>68</sub>	
-2	2134.40	2135.00	4270.00	KHNa <sub>6</sub> Ni <sub>2</sub> Zn <sub>2</sub> P <sub>2</sub> Mo <sub>7</sub> W <sub>11</sub> O <sub>68</sub>	
-2	2179.11	2179.02	4358.04	$KHNa_6Ni_2Zn_2P_2Mo_6W_{12}O_{68}$	
-2	2224.11	2225.01	4450.03	$K_4H_3NaNi_2Zn_2P_2Mo_5W_{13}O_{68}$	
-2	2269.11	2269.03	4538.07	$K_4H_3NaNi_2Zn_2P_2Mo_4W_{14}O_{68}$	
-2	2316.11	2316.06	4632.12	K <sub>3</sub> H <sub>2</sub> Na <sub>3</sub> Ni <sub>2</sub> Zn <sub>2</sub> P <sub>2</sub> Mo <sub>3</sub> W <sub>15</sub> O <sub>68</sub>	
-4	1128.60	1127.78	4511.13	$KH_2Na_5Ni_2Zn_2P_2Mo_4W_{14}O_{68}$	



 $\label{eq:Figure 4B.S5} FMO \ of \ tetrasubstituted \ sandwich \ POMs \ showing \ the \ effect \ of \ Mo \ doping \ on \ band \ gaps \ as \ well \ as \ shifting \ of \ electron \ density \ on \ addenda \ atoms \ in \ P-Mn_2Co_2Mo_xW_{18-x} \ and \ P-Ni_2Zn_2Mo_xW_{18-x}.$ 

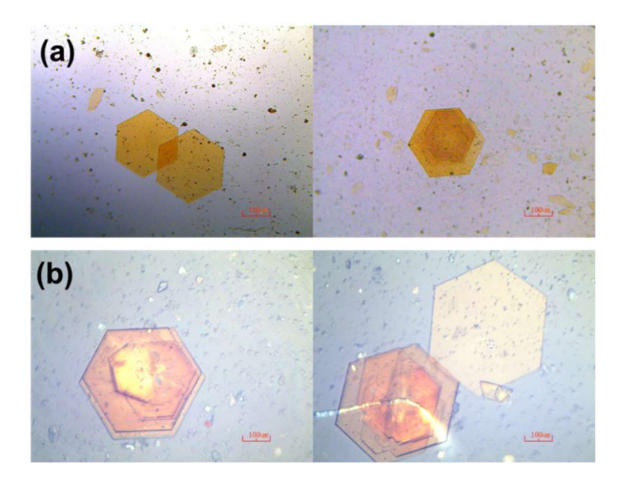


Figure 4B.S6 Optical images of sandwich POMs; (a) P-Mn<sub>2</sub>Fe<sub>4</sub>Mo<sub>x</sub>W<sub>24-x</sub> and (b) P-Co<sub>5</sub>FeMo<sub>x</sub>W<sub>24-x</sub>.

Table 4B.S4 BVS parameter calculated from the SC-XRD structure of mixed addenda sandwich POMs P-Mn <sub>2</sub> Fe <sub>4</sub> Mo <sub>x</sub> W <sub>24-x</sub> and P-Co <sub>5</sub> FeMo <sub>x</sub> W <sub>24-x</sub>					
POMs	Transition metal	Bond valence sum value	Oxidation state		
	W	6.115	+6		
	Mo	6.082	+6		
P-Mn <sub>2</sub> Fe <sub>4</sub> Mo <sub>x</sub> W <sub>24-x</sub>	P1	5.071	+5		
	P2	5.236	+5		
	Р3	5.031	+5		

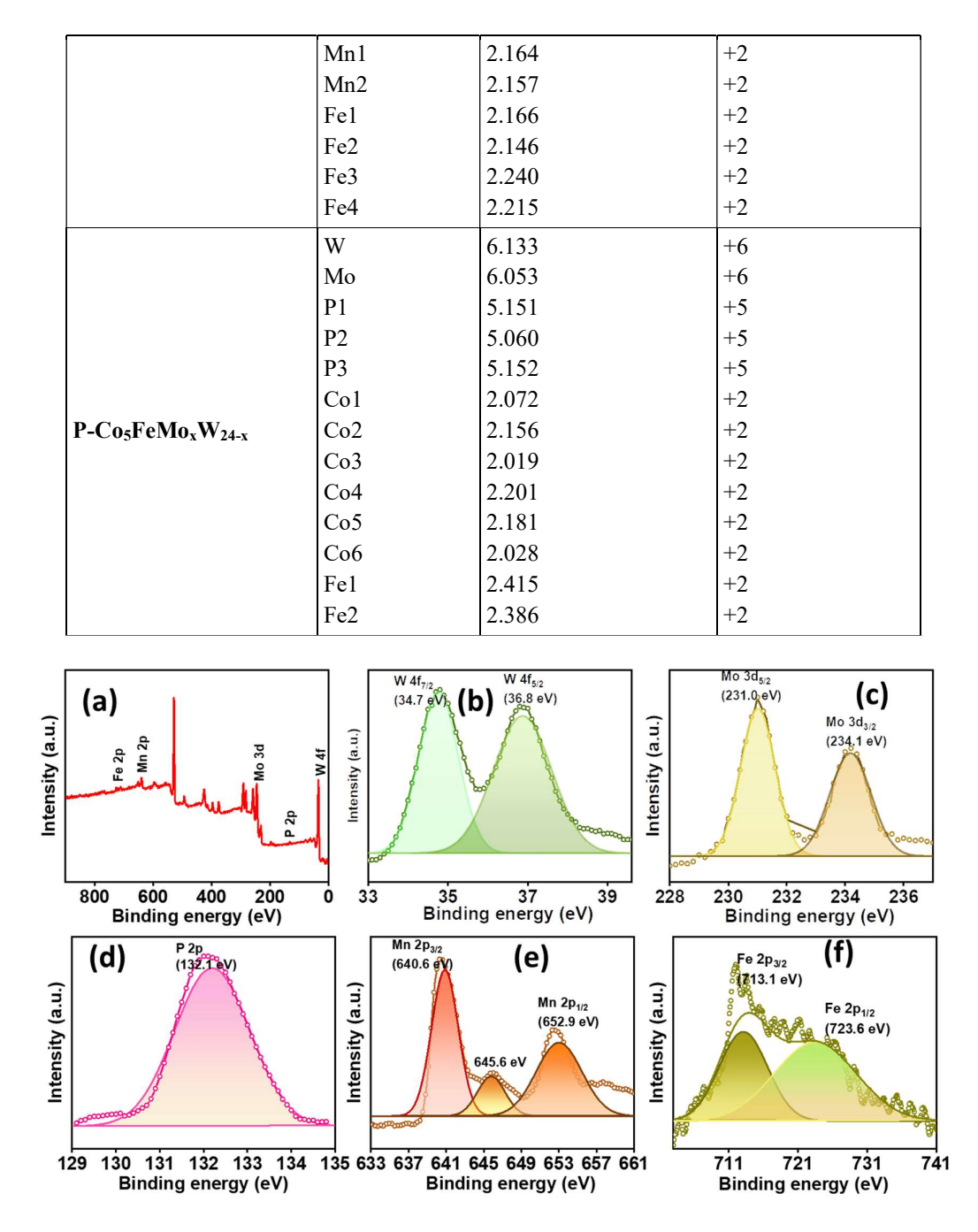
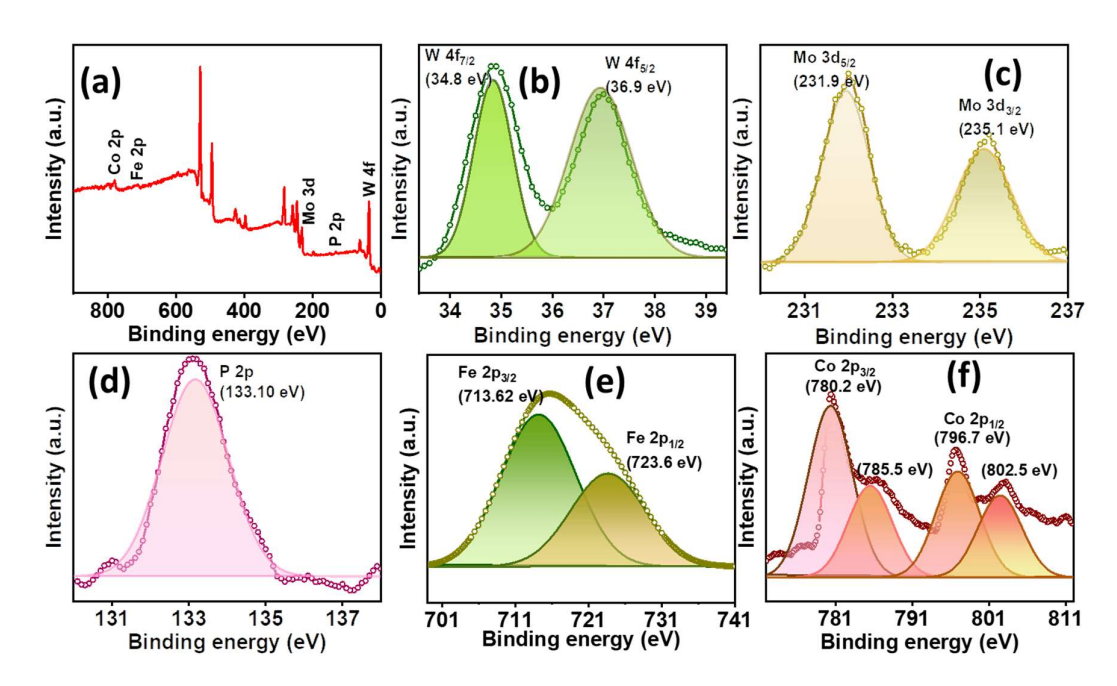


Figure 4B.S7 XP spectra of  $P-Mn_2Fe_4Mo_xW_{24-x}$  (a) Survey spectra, (b) W  $4f_{7/2}$  and  $4f_{5/2}$  (c) Mo  $3d_{5/2}$  and  $3d_{3/2}$  (d) P 2p (e) Mn 2p and (f) Fe 2p.



**Figure 4B.S8** XP spectra of **P-Co<sub>5</sub>FeMo<sub>x</sub>W<sub>24-x</sub>** (a) Survey spectra, (b) W  $4f_{7/2}$  and  $4f_{5/2}$  (c) Mo  $3d_{5/2}$  and  $3d_{3/2}$  (d) P 2p (e) Fe 2p and (f) Co 2p.

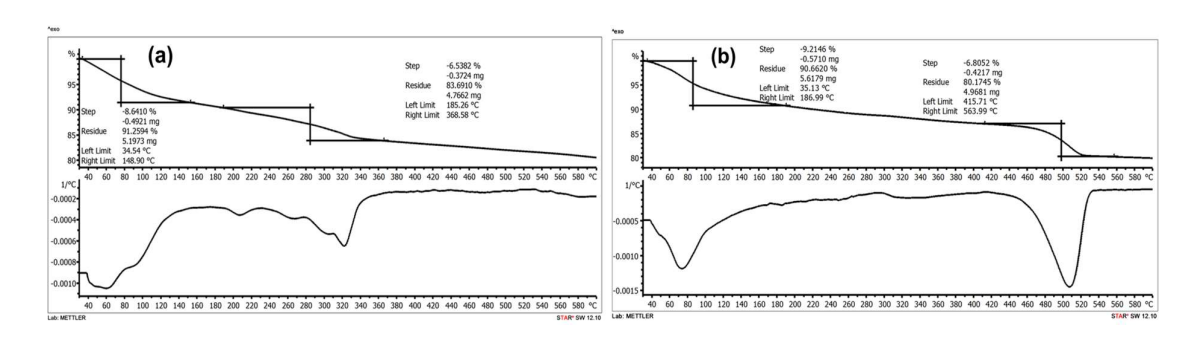


Figure 4B.S9 TGA curve along with corresponding first derivative of (a)  $P-Mn_2Fe_4Mo_xW_{24-x}$  and (b)  $P-Co_5FeMo_xW_{24-x}$ .

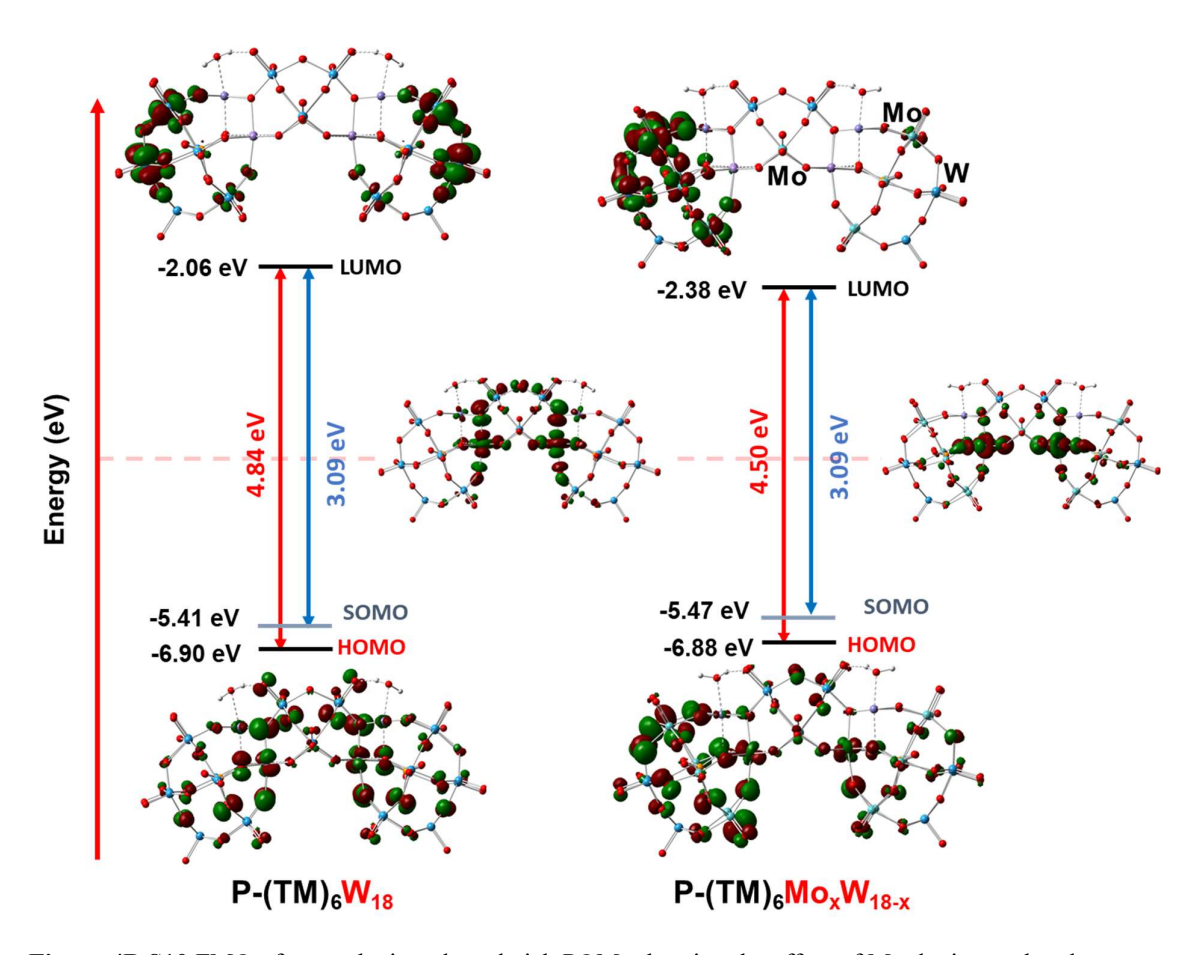


Figure 4B.S10 FMO of tetrasubstituted sandwich POMs showing the effect of Mo doping on band gaps as well as shifting of electron density on addenda atoms in the representative structure of  $P-Mn_2Fe_4Mo_xW_{24-x}$  (right) and its W-based analogous structure (left) (TM=Mn/Fe).

Table 4B.S5 Crystal data, data collection, and refinement parameters for Bi based Krebs POMs					
	Bi-Zn <sub>2</sub> Fe <sub>2</sub> W <sub>18</sub>	$Bi\text{-}Zn_2Fe_2W_{18}\{Gly\}$	Bi-MnWZn <sub>2</sub> W <sub>18</sub>	Bi-ZnWMn <sub>2</sub> W <sub>18</sub>	
empirical formula	Bi <sub>2</sub> Fe <sub>2</sub> Na <sub>15</sub> O <sub>92</sub>	C <sub>4</sub> H <sub>42</sub> Bi <sub>2</sub> Fe <sub>2</sub> N <sub>2</sub> Na <sub>12</sub>	BiMn <sub>0.8</sub> Na <sub>8.5</sub> O <sub>50</sub>	BiMnNa <sub>7.5</sub> O <sub>45</sub> W <sub>9.5</sub>	
	$W_{18}Zn_2$	$O_{104}W_{18}Zn_2$	$W_{9.5}Zn_{0.7}$	Zn <sub>0.5</sub>	
formula weight	5786.55	6027.97	3040.68	2935.60	
temp (K)	273.15	273.15	273.15	273.15	
crystal system	monoclinic	Monoclinic	Monoclinic	triclinic	
space group	C2/m	C2/m	P2 <sub>1</sub> /n	P <del>1</del>	
unit cell					
dimension					
a (Å)	20.117(3)	20.0716(9)	12.9396(16)	13.3749(19)	
<b>b</b> (Å)	15.380(3)	15.3753(6)	25.247(3)	13.5233(19)	
c (Å)	16.172(2)	17.2140(8)	16.1667(19)	14.036(2)	
α (deg)	90	90	90	93.599(4)	

β (deg)	95.062(7)	99.5370(10)	94.079(4)	105.109(4)
γ (deg)	90	90	90	106.378(4)
V (Å <sup>3</sup> )	4984(13)	5238.9(4)	5268.1(11)	2326.0(6)
Z	2	2	4	2
ρ (calculated)	3.856	3.821	3.834	4.192
(g/cm <sup>3</sup> )				
μ/mm <sup>-1</sup>	25.114	23.897	24.649	27.841
F (000)	5022.0	5308.0	5282.0	2537.0
crystal size (mm <sup>3</sup> )	0.28 × 0.24 ×	$0.32 \times 0.24 \times 0.14$	$0.32 \times 0.19 \times 0.12$	$0.28 \times 0.21 \times 0.14$
	0.14			
2Θ range for data	4.066 to 51.368	3.92 to 52.784	3.9 to 53.008	4.058 to 50.052
collection/°				
index ranges	$-24 \le h \le 24, -18$	$-22 \le h \le 25, -17 \le k$	$-16 \le h \le 16, -31 \le$	$-15 \le h \le 15, -16 \le$
	$\leq$ k $\leq$ 18, -19 $\leq$ 1	$\leq 19, -21 \leq 1 \leq 15$	$k \le 31, -19 \le 1 \le 20$	$k \le 16, -16 \le l \le 16$
	≤ 19			
no. of reflection	28030/4915	17916/	10855/ 75843	8138/25165
collected /unique		5552		
GOF on F <sup>2</sup>	1.137	1.048	1.112	1.103
final R indices	$R_1 = 0.056,$	$R_1 = 0.032, wR_2 =$	$R_1 = 0.052, wR_2 =$	$R_1 = 0.090, \text{ wR}_2 =$
$(I \geq 2\sigma(I))$	$wR_2 = 0.137$	0.087	0.123	0.216
R indices (all data)	$R_1 = 0.072,$	$R_1 = 0.034, WR_2 =$	$R_1 = 0.064, wR_2 =$	$R_1 = 0.117, \text{ wR}_2 =$
	$wR_2 = 0.145$	0.088	0.129	0.235
data/restraints/pa	4915/0/322	5552/0/323	10855/0/650	8138/0/587
ram				
Largest diff.	4.18/-3.24	2.30/-2.14	2.77/-2.92	6.23/-4.74
peak/hole / e Å-3				

Table 4B.S6. Assignment of ESI-mass peaks of Bi-Zn<sub>2</sub>Fe<sub>2</sub>W<sub>18</sub>

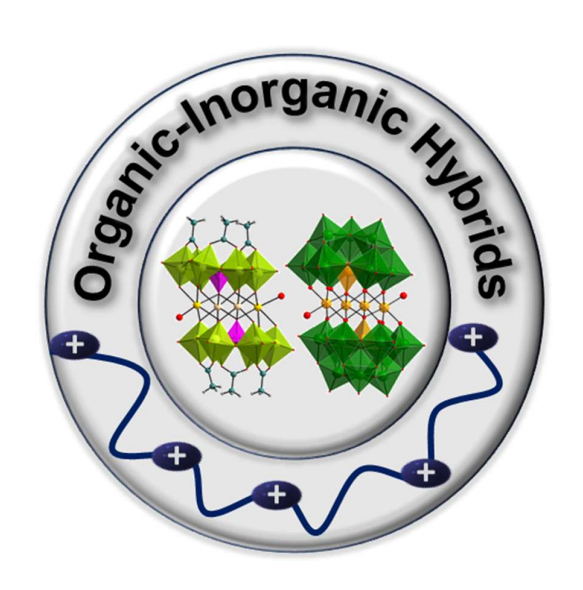
Charge	m/z	m/z	Mol. Wt.	Assigned probable formula
	(obs.)	`(calc.)		
-3	1692.03	1693.48	5080.44	$H_5Fe_2Zn_2(BiW_9O_{34})_2(H_2O)$

Table 4B.S7 Assignment of ESI-mass peaks of Bi-Zn<sub>2</sub>Fe<sub>2</sub>W<sub>18</sub>{Gly}

Charge	m/z	m/z	Mol. Wt.	Assigned probable formula
	(obs.)	(calc.)		
-3	1742.46	1742.83	5228.49	$H_3Fe_2Zn_2(BiW_9O_{34})_2(Gly)_2(H_2O)_3$

### **Chapter 5**

Design of Polyoxometalates-based inorganicorganic hybrids for task-specific application



#### **5.1 Introduction**

Inorganic-organic hybrids represent the interface between two chemical domains that significantly contribute to material science. The synergy between inorganic and organic components of these hybrid materials results in new and enhanced properties and functions. Inorganic-organic hybrids can be categorized into two types based on the nature of chemical interactions between components. In Type-I hybrids, stronger interactions such as covalent bonds dominate, while Type-II hybrids are characterized by weak supramolecular interactions such as electrostatic forces or hydrogen bonding (Figure 5.1). In the context of forming organic-inorganic hybrids with POMs, electrostatic interactions with cationic organic groups are widely utilized due to the high negative charge of POMs. Another approach involves directly incorporating organic moieties as ligands, either with addenda atoms (such as W or Mo) or with transition metal complexes positioned at the addenda sites (Figure 5.1a).

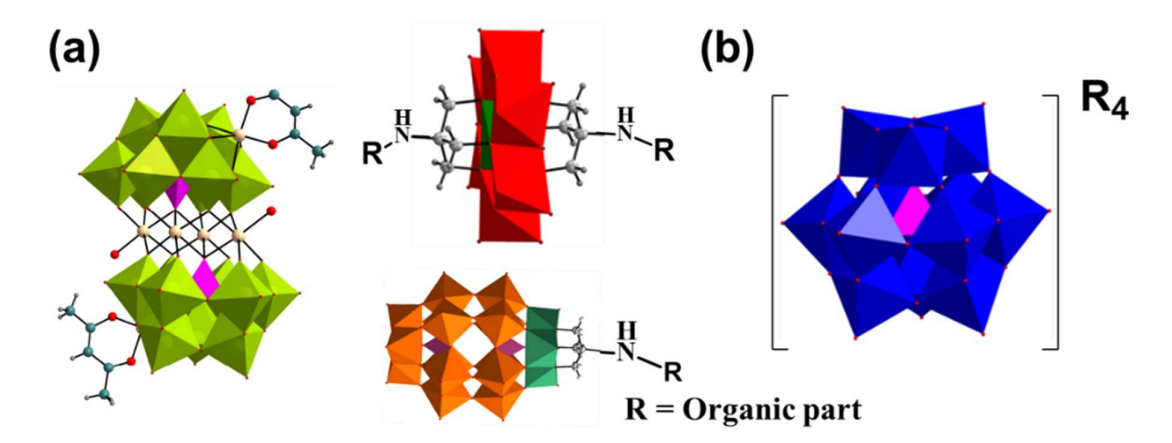


Figure 5.1 (a) Type-I and (b) Type-II inorganic organic hybrids based on POMs.

In section A of Chapter 5, the cooperative effect of transition metals along with organic ligands such as acetate, and glycinate have been explored for the synthesis of sandwich POMs based on phosphomolybdates, which is still unexplored area. Section B of Chapter 5 deals with the POM-based type II inorganic-organic hybrids for anti-corrosive underwater adhesive applications.

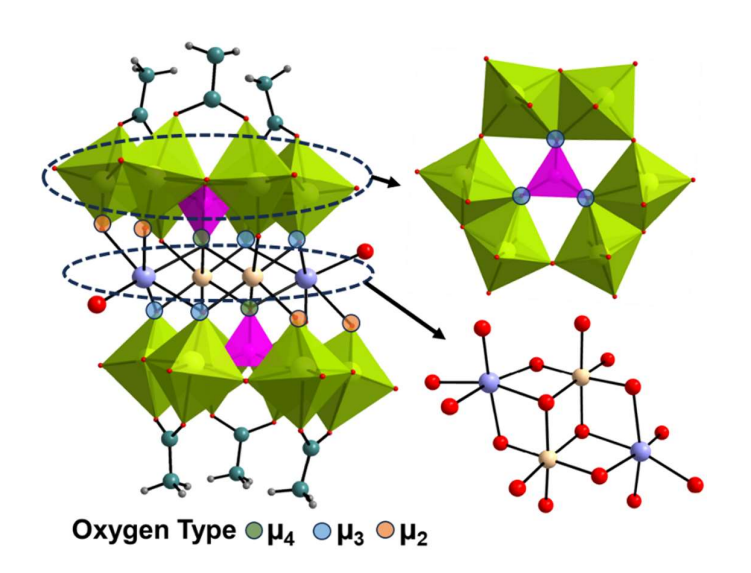
#### 5.2 References

- 1. Dolbecq, A.; Dumas, E.; Mayer, C. R.; Mialane, P., Hybrid organic inorganic polyoxometalate compounds: from structural diversity to applications. *Chem. Rev.* **2010**, *110* (10), 6009-6048.
- 2. Santoni, M.-P.; Hanan, G. S.; Hasenknopf, B., Covalent multi-component systems of polyoxometalates and metal complexes: Toward multi-functional organic—inorganic hybrids in molecular and material sciences. *Coord. Chem. Rev.* **2014**, *281*, 64-85.

- 3. Taleghani, S.; Mirzaei, M.; Eshtiagh-Hosseini, H.; Frontera, A., Tuning the topology of hybrid inorganic—organic materials based on the study of flexible ligands and negative charge of polyoxometalates: A crystal engineering perspective. *Coord. Chem. Rev.* **2016**, *309*, 84-106.
- 4. Li, C.; Jimbo, A.; Yamaguchi, K.; Suzuki, K., A protecting group strategy to access stable lacunary polyoxomolybdates for introducing multinuclear metal clusters. *Chem. Sci.* **2021**, *12* (4), 1240-1244.

# Chapter 5 Section A

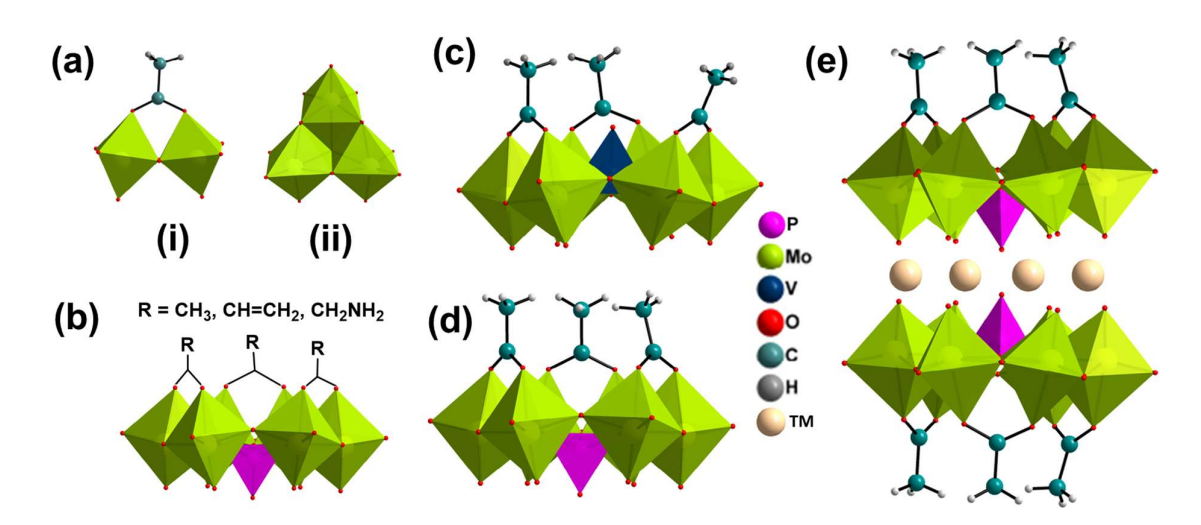
# Microwave-assisted synthesis of transition metals substituted sandwich Phosphomolybdates



#### **5A.1 Introduction**

The self-assembly of inorganic-organic hybrid materials based on polyoxometalates (POMs) has gained increasing attention, not only for extending their intriguing, diverse architectures but also for exploring their potential applications in catalysis, medicine, biology, magnetism, and materials science.<sup>1-3</sup> Polyoxometalates have continued to fascinate in developing novel structures in pursuit of their unexplored applications and properties.<sup>4, 5</sup>

Weakley-type sandwich POMs, especially with the formula [M<sub>4</sub>(H<sub>2</sub>O)<sub>2</sub>(PW<sub>9</sub>O<sub>34</sub>)<sub>2</sub>]<sup>n-</sup>, have found applications in a wide range of areas such as catalysis, magnetism, energy storage, and electrochemical applications.<sup>6, 7</sup> These sandwich motifs have two trivacant Keggin subunits (PW<sub>9</sub>O<sub>34</sub>) joining tetrasubstituted transition metal core at the center. While these trivacant subunits are typically made of tungstates, molybdates are less common due to their higher kinetic lability of molybdates in aqueous solution compared to tungstates. Recently, one molybdate-based tetrasubstituted sandwich POM was isolated in acetonitrile using a protecting group strategy, however, its solubility in organic solvent limits its use in aqueous media.<sup>8</sup> Theoretically, Mo in the POM framework not only increases its basicity but also has the advantage of higher electron storage capacity compared to isostructural W-based POMs.<sup>9, 10</sup>



**Scheme 5A.1** Hexamolybdate with (a) vanadium as a heteroatom, (b) phosphorous as a heteroatom and (c) phosphorus as heteroatom with different functional groups, R (d) when  $R = -CH_3$  (e) representative structure of molybdate based sandwich POMs (TM represents transition metal).

In Chapter 2, we have used a mixed addenda strategy, which proves particularly useful in stabilizing Mo-based tetrasubstituted sandwich POMs in an aqueous solution, enabling band gap tuning to such an extent that these POMs exhibit shifting the absorption band towards

visible light and improved optoelectronic properties.<sup>11</sup> Consequently, the design and synthesis of novel tetrasubstituted POMs based on pure Mo will have significant and promising pursuits, offering unprecedented performance.

In the past decade, much attention has been paid to modifying the basic unit of Keggin POM frameworks, i.e. triads have been modified with carboxylate as organic groups as well as phosphate as inorganic groups (Scheme 5A.1a). This triad in the presence of templating agent forms lacunary POMs, which forms the structure directing unit for various POMs. Also, triads of amino acids or carboxylate ligands have been used for synthesis of covalently modified hexanuclear heteromolybdates units,  $[XMo_6O_{21}]^{n-}$  (XMo<sub>6</sub>) (X = P, Se, As, Bi) (Scheme 5A.1b). This strategy has also been used in synthesis of functionalized ring-shaped POMs, sulphur POMs etc. using bonding with various multifunctional groups to the terminal of three pairs of  $\{Mo_2O_{10}\}$  fragments on the same side. 18-20

Inspired by the fact that covalently attached carboxylate can be used to construct the monomeric arrangement from {XMo<sub>6</sub>} where X=V/P.<sup>21</sup> Hence, it is worth noting that (a) As a heteroatom, the orientation of vanadium is opposite to that of phosphorus thus making vanadium less susceptible to transition metal substitution {Scheme 5A.1(c/d)} (b) using three monocarboxylate ligands along with XMo<sub>6</sub>, it is reasonable to assume that sandwich POMs can be formed using transition metals (Scheme 5A.1e) (c) using acrylic acid as functional ligands could result in the formation of polymeric forms by connecting two or more {XMo<sub>6</sub>} subunits. Also, replacing the acetate group with acrylates possesses the opportunity for constructing these POMs-based copolymers, which can enhance the properties for their use in various applications such as gelation, photochromism, catalyst and non-linear optical properties (Scheme 5A.1c). 22-24 Here, we report a simple and efficient microwave-assisted approach to incorporate organic groups as well as transition metals simultaneously into phosphomolybdates in an aqueous medium. Through rational structural design, employing ligand and transition metal controlled self-assembly, which is rare in traditional "one-pot" POM synthesis, we could produce a range of Inorganic-organic hybrids using microwave assisted rapid synthesis in 30 minutes and fast crystallization with a yield of up to 80 %. Such approach gives dimensionality to incorporate different carboxylate-based monomers and amino acids as covalent ligands as well as tuning of transition metals (3d/4d/5d series), paving the way for post-functionalization on the other ligands, like nitrogen-based ligands.

#### **5A.2 Results and Discussion**

#### 5A.2.1 Synthesis of Inorganic-organic Hybrids

Here, we build upon our recent efforts towards synthesizing tetrasubstituted sandwich POMs based on phosphomolybdates by microwave-assisted synthesis. First, we synthesized monocarboxylate ligands-based sodium salt of [Na<sub>7</sub>(PMo<sub>6</sub>O<sub>22</sub>)<sub>2</sub>(OAc)<sub>6</sub>].nH<sub>2</sub>O (1) by one-pot reactions of Na<sub>2</sub>MoO<sub>4</sub>.2H<sub>2</sub>O and Na<sub>2</sub>HPO<sub>4</sub>.2H<sub>2</sub>O in aqueous solution at pH=3.0 using acetic acid under microwave heating for 30 minutes. The sandwich structure thus obtained has seven sodium atoms present at the sandwich position, forming a double cubane structure (Figure 5A.1). All these POMs have the common PMo<sub>6</sub>O<sub>22</sub><sup>3-</sup> polyoxoanion, which is made up of six MoO<sub>6</sub> octahedra that share their edges and corners alternatively to form a ring with a central phosphate group. An acetate group decorates each of these {Mo<sub>2</sub>O<sub>8</sub>} units through a single μ<sub>2</sub>oxo to each Mo centre with a total six Mo–O bonds lying perpendicular to the plane of hexamolybdate (Figure 5A.1a).

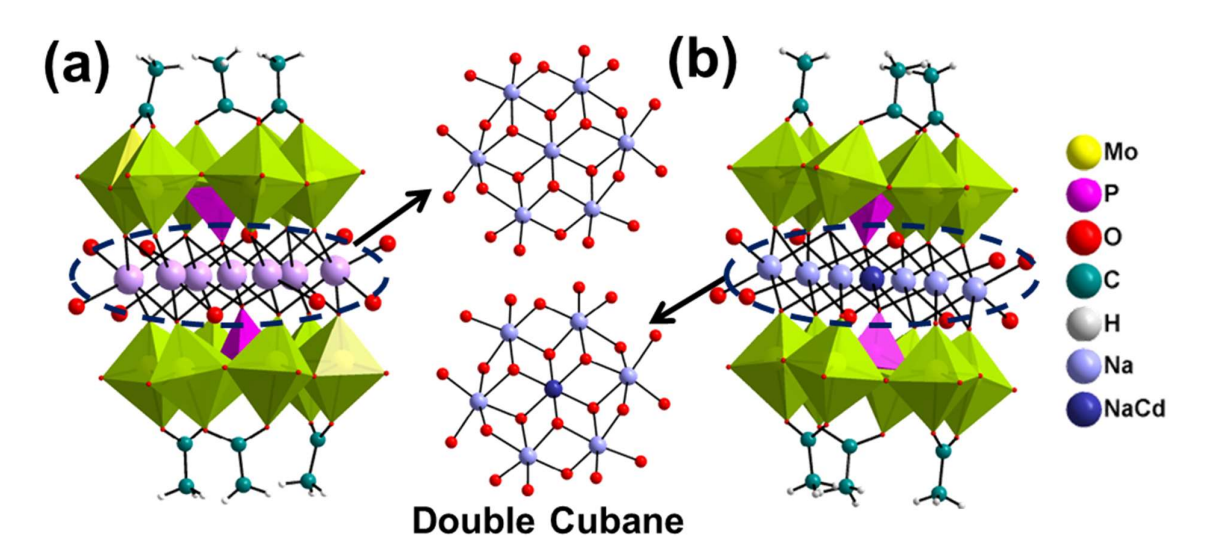


Figure 5A.1 Combined polyhedral/ball and stick representation of pure Mo-based sandwich POM anion with double cubane structure at sandwich position for (a) 1 and (b) 2.

As the crystal radius of Na-O (2.30 Å) is almost equal to crystal radius of Cd-O (2.33 Å), adding Cd(OAc)<sub>2</sub> in solution of one-pot reactions containing Na<sub>2</sub>MoO<sub>4</sub>.2H<sub>2</sub>O and Na<sub>2</sub>HPO<sub>4</sub>.2H<sub>2</sub>O at the similar condition results in the formation of sodium salt of [Na<sub>6.5</sub>Cd<sub>0.5</sub>(PMo<sub>6</sub>O<sub>22</sub>)<sub>2</sub>(OAc)<sub>6</sub>].nH<sub>2</sub>O (2) where disordered Cd is found at the centre of double cubane (Figure 5A.1b). Extending structures 1 and 2 at sandwich position leads to the formation of a 1-D network structure (Figure 5A.S1). However, using 3d transition metals such as Zn instead of Cd results in the formation of tetrasubstituted sandwich POM Na<sub>6</sub>[Na<sub>2</sub>Zn<sub>2</sub>(H<sub>2</sub>O)<sub>2</sub>(PMo<sub>6</sub>O<sub>22</sub>)<sub>2</sub>(OAc)<sub>6</sub>].nH<sub>2</sub>O (3) with cubane structure at the sandwich

position (Figure 5A.2). It was found that the cubane core consists of two zinc shared with sodium (Zn/Na 50:50) at the internal sandwich position while the external position consists of same sodium atoms only. The behavior was observed in the Na<sub>6</sub>[Na<sub>2</sub>Ni<sub>2</sub>(H<sub>2</sub>O)<sub>2</sub>(PMo<sub>6</sub>O<sub>22</sub>)<sub>2</sub>(OAc)<sub>6</sub>].nH<sub>2</sub>O (4) where Ni also share an internal sandwich position with sodium (Ni/Na 50:50). Interestingly, the precursors play a crucial role towards the self-assembly of these sandwich POMs, e.g. employing Co/Mn salts as a precursor leads to the formation of  $Na_6[Na_2Co_2(H_2O)_2(PMo_6O_{22})_2(OAc)_6].nH_2O$ **(5)** and Na<sub>6</sub>[Na<sub>2</sub>Mn<sub>2</sub>(H<sub>2</sub>O)<sub>2</sub>(PMo<sub>6</sub>O<sub>22</sub>)<sub>2</sub>(OAc)<sub>6</sub>].nH<sub>2</sub>O (6), where cubane core has transition metals Co/Mn at the internal sandwich position and Na atoms at the external position. However, Fe/Cu are unable to form these sandwich POMs as Cu prefers to form acetate complex in such conditions, and Fe(II) is oxidized in situ to Fe(III), thus changing the solution pH.

The pH of the solution containing Na<sub>2</sub>MoO<sub>4</sub>,2H<sub>2</sub>O and Na<sub>2</sub>HPO<sub>4</sub>,2H<sub>2</sub>O was adjusted to 3.0 using glacial acetic acid in all these POMs (1-6) syntheses, followed by the addition of 3d transition metals. All synthesized POMs are characterized by single crystal X-ray diffraction (SC-XRD), Powder XRD, FT-IR, TGA, Raman spectroscopy in the solid state and <sup>1</sup>H, <sup>13</sup>C, <sup>31</sup>P-NMR, UV-visible spectroscopy in the solution state. The optical images show different sizes and shapes of single crystals due to the presence of different transition metals at sandwich positions (Figure 5A.S2). With its three µ<sub>3</sub> oxygens, the central phosphorus acts as a templating agent for molybdate octahedra in the plane of Mo<sub>6</sub>O<sub>22</sub> while its μ<sub>4</sub> oxygen binds transition metals in the sandwich position (Figure 5A.3b). The hexamolybdate ring  $\{Mo_6O_{22}\}\$  of these POMs comprises three edge-sharing {Mo<sub>2</sub>O<sub>8</sub>} units connected through corner-sharing oxygen atoms. The methyl group of carboxylate ligand points away from the cluster. A {Mo<sub>2</sub>O<sub>8</sub>(OCOCH<sub>3</sub>)} triad is formed with this kind of coordination, which is similar to the {Mo<sub>3</sub>O<sub>13</sub>} triads that are a common component of most polyoxoanion clusters. Comparison of these triads gives structural changes, e.g. two of the {Mo<sub>2</sub>O<sub>10</sub>(OAc)}<sup>x-</sup> unit were found to be in a plane while in the third {Mo<sub>2</sub>O<sub>10</sub>(OAc)}<sup>x-</sup> unit, -CCH<sub>3</sub> group is slightly bent inwards possibly due to the presence of sodium close to the two acetate groups making them to be planar.

Three of these  $\{Mo_2O_{10}(OAc)\}^{x-}$  triads then combine through a central phosphate to form the lacunary species,  $[PMo_6O_{23}(OAc)_3]^{x-}$  which then coordinate to additional  $\{Na_7\}$  in 1,  $\{CdNa_6\}$  in 2 and  $\{M_2Na_2\}$  in 3/4/5/6 with M = Zn/Ni/Co/Mn fragment through the seven oxygens (six Mo-O and one P-O) from both side through the lacunary species resulting in

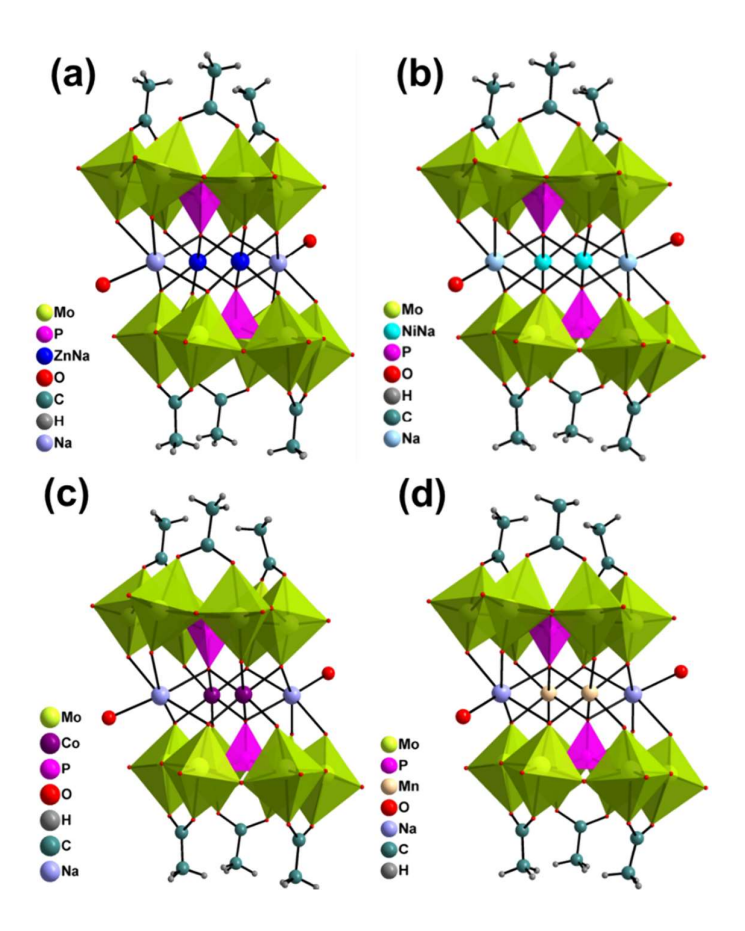


**Figure 5A.2** Combined polyhedral/ball and stick representation of pure Mo-based sandwich POM anion for (a) **3**, (b) **4**, (c) **5** and (d) **6**.

the formation of a sandwich POMs. Structural parameters such as bond lengths and bond angles indicate that each half of the sandwich POMs are crystallographically inequivalent.

It was observed that POMs 5 and 6 crystallize from mother liquor within 5 minutes with yield more than 50%, which gradually increases up to 95% over one month with no side crystals observed. Further, when comparing these structures with the corresponding tetrasubstituted sandwich polyoxomolybdates (Figure 5A.3c) having Mn at the sandwich position, some key structural changes were observed. Firstly, Na ions replace Mn at the external sandwich position when the belt-1 triad of molybdate is substituted with acetate ions. Secondly, one Mn atom at belt-1 stabilizes the molybdate framework, which also binds to the bridging oxygen of belt-2 (Figure 5A.3c). In contrast in the case of 6, the Na atom near the acetate group, stabilizes the framework (Figure 5A.3a, 5A.S17a). Thirdly, Mn provides stabilization from the side of  $\mu_3$  oxygen, while Na stabilizes the framework from the side of  $\mu_2$  oxygen (Figure 5A.3c, 5A.S17a). Thus, the crystal structure of these POMs reveals the presence of two types of Na very close to

the framework, (i) first type located within the cubane core at sandwich position, stabilizing the framework, linked octahedrally to the framework through two  $\mu_2$  oxygens, two  $\mu_3$  oxygens, one  $\mu_4$  oxygen and sixth coordination site is linked to a water molecule; (ii) other type is positioned outside the framework near the acetate groups, binding to molybdate of another molecule and extending these clusters into 1D chains through sodium ions (Figure. 5A.S17a).

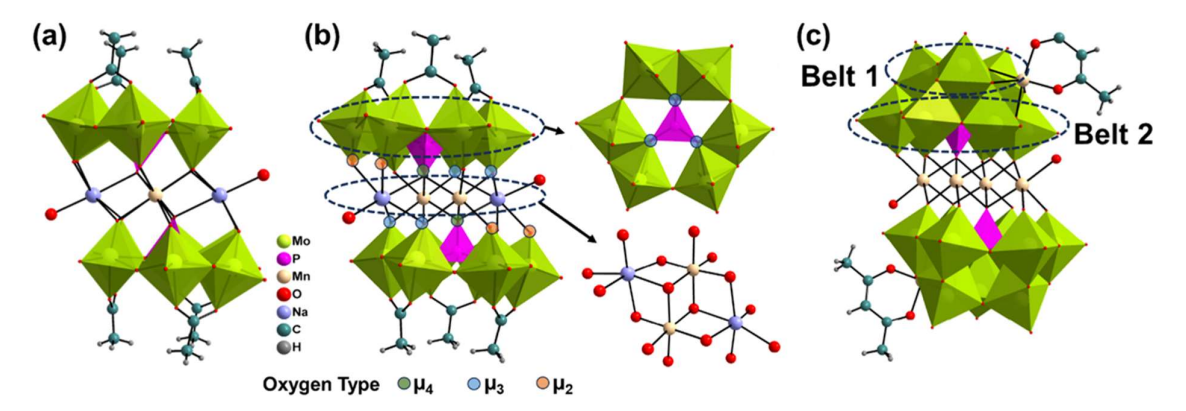


**Figure 5A.3** Combined polyhedral/ball and stick representation of (a) pure Mo-based sandwich POM anion **6** (side view), (b) structural views of hexamolybdate and cubane core along with different types of oxygen and (c) Mo-based Weakley type sandwich POMs highlighted with its belt-1 and belt-2 (ref).

The structural features of compounds 3-6 were investigated using FT-IR and Raman spectroscopy, which showed nearly identical peaks across all compounds, indicating the fundamental structure similarities of these polyanions (Figure 5A.S3). This is in good agreement with the SC-XRD studies. Strong vibrational peaks in the 800-1060 cm<sup>-1</sup> region can be attributed to the characteristic peaks of the molybdate frameworks. Peaks between 680 and 635 cm<sup>-1</sup> are linked to the Mo-O<sub>e</sub>-Mo group's vibrations, whereas those between 800 and 980 cm<sup>-1</sup> are Mo-O<sub>c</sub>-Mo group vibrations, where e and c represent edge and corner, respectively. The characteristic peak of P-O in compounds 1-6 is found to be in the range of 1045 to 1060 cm<sup>-1</sup>. Further, the bulk purity and composition of these POMs were determined by comparing simulated PXRD with experimentally observed PXRD data and EDAX data (Figure 5A.S4/S11). The optoelectronic property was studied using solid-state UV-Vis spectroscopy, which indicates that all these show the characteristic absorption in the UV region extending to the visible region due to ligand to metal charge transfer (LMCT) spectra and in the visible region due to d-d transitions (Figure 5A.S7). The band gap of these POMs was determined from diffuse reflectance spectroscopy (DRS) using Kubelka-Munk equation (Figure 5A.S8), which was then correlated with DFT study (Figure 5A.S10). DFT study of these POMs shows the highest occupied molecular orbitals (HOMO) at oxygen atoms while the lowest unoccupied

molecular orbitals (LUMO) at Mo atoms. In solution state, the methyl group of acetyl appears at  $\delta = 2.0$  ppm in  $^1$ H NMR, and at 22 and 178 ppm in  $^{13}$ C NMR, indicating the solution state stability of these POMs (Figure 5A.S5/S6). TGA reveals the thermal stability up to 220 °C, with the weight loss for the loss of water molecules below 220 °C. However, all these POMs are typically isolated with Na-ions in the POM framework at the external sandwich positions, which are labile and can be easily exchanged in aqueous solution. Therefore, we have employed the mixed metals strategy and various organic ligands to replace the labile Na-ions at the external sandwich positions.

In chapter 3A, the cooperative effects of transition metals play a significant role in selfassembly, we explored the cooperative effect of transition metals in 6 by taking Mn in combination with various transition metals for substituting the Na at external sandwich positions. Despite variations in crystal shape and size, using combinations like Mn/Zn, Mn/Ag, Mn/Hg and Mn/N<sub>2</sub>H<sub>4</sub> (Figure 5A.S12), only Mn/Ag was found to be effective in replacing Na. cooperative effect of Mn/Ag, we targeted the synthesis  $[Ag_2Mn_2(H_2O)_2(PMo_6O_{22})_2(OAc)_6]^{n-}$ . However, the success of Mn/Ag substitution dependent on the sequence of metal addition. When Mn was added first followed by Ag, to a reaction mixture of Na<sub>2</sub>MoO<sub>4</sub>,2H<sub>2</sub>O and Na<sub>2</sub>HPO<sub>4</sub>,2H<sub>2</sub>O at pH 3, we obtained the sodium salt of  $[Ag_{0.75}Na_{1.25}Mn_2(H_2O)_2(PMo_6O_{22})_2(OAc)_6].nH_2O$  (7) (Figure 5A.4a). Reversing the order (Ag first, then Mn) led to the formation of  $[Ag_{0.85}Na_{1.15}Mn_2(H_2O)_2(PMo_6O_{22})_2(OAc)_6].nH_2O$  (7a) (Figure 5A.4b), characterized with a disordered external sandwich position. Although the compositions of 7 and 7a appear similar, the Ag uptake varied at the disordered positions (Figure 5A.4a/4b). We further explored the cooperative effect by using Co/Ag in 5 (Figure of of 5A.2c), resulting in the formation sodium salt  $[Ag_{0.65}Na_{1.35}Co_2(H_2O)_2(PMo_6O_{22})_2(OAc)_6].nH_2O$  (8), with Ag/Na (0.65/0.35) substitutional disorder at the external sandwich position. The presence of disordered Ag/Na along with Mn, was further confirmed by XPS analysis of 7 along with a slight shift observed in FT-IR spectra (Figure 5A.S13/S14). Furthermore, as the geometry and connectivity of organic moiety also influence these POM structures, different organic ligands were employed instead of acetate. The choice of organic ligands is critical, as they must bind symmetrically to the polyoxoanion unit. Careful control of synthesis conditions, like concentrations and pH, facilitate the formation of precursor molecules suitable for the developing new structures through covalent grafting or post-functionalization. However, post-functionalization of phosphate,

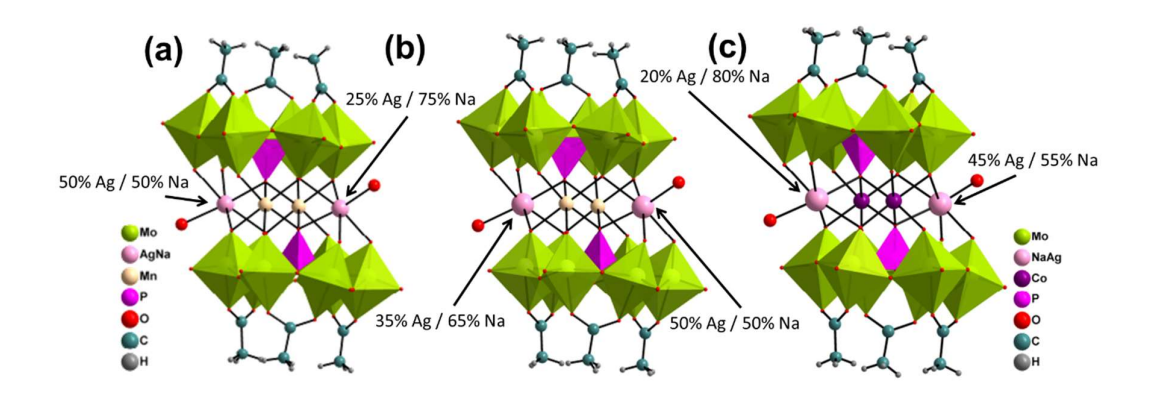
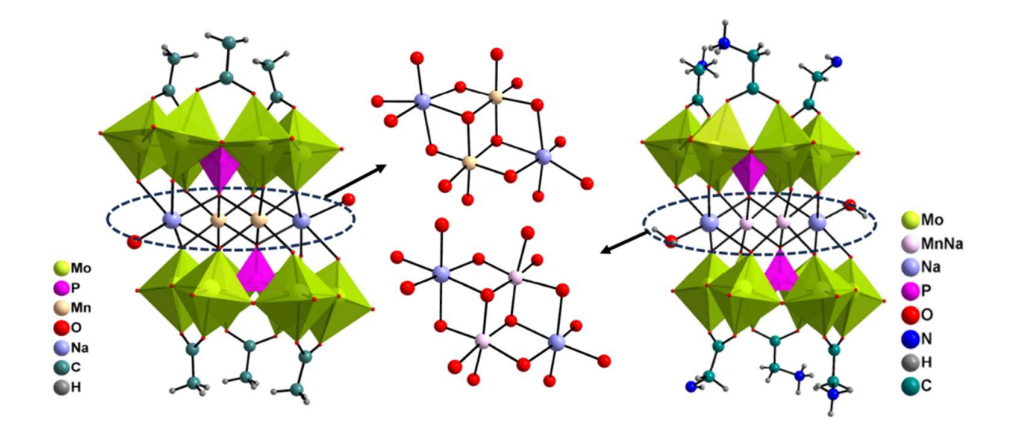


Figure 5A.4 Combined polyhedral/ball and stick representation of sandwich POMs showing the disordered external sandwich position (a) 7 (b) 7a and (c) 8.

arsenate, and acetate groups grafted on these polyanions is challenging. On the other hand, grafting these polyanions with amino acids offers post-functionalization and can enable various POM-protein interactions. To explore this, we aimed to replace the acetate group in 6 with different amino acids. While crude crystalline powder were obtained with few amino acids such as glycine, lysine, glutamic acid, only glycine yielded well-diffracting crystals. SC-XRD analysis revealed six glycine functionlized resulting structure as the sodium salt of [Na<sub>2</sub>Mn<sub>2</sub>(H<sub>2</sub>O)<sub>2</sub>(PMo<sub>6</sub>O<sub>22</sub>)<sub>2</sub>(OGly)<sub>6</sub>].nH<sub>2</sub>O (9) at pH 2.5. Polyanions 9 contains the heteroatom P, surrounded by a ring of six MoO<sub>6</sub> octahedra, which alternately connect edges and corners sharing. Instead of acetate, three glycine molecules are each bound to two edge-sharing Mo centers through their carboxylate groups on the same side of the ring (Figures 5A.5). These glycine molecules bind symmetrically to the polyoxomolybdate framework via their



**Figure 5A.5** Combined polyhedral/ball and stick representation of single cubane-based sandwich POMs with acetate (left) and glycinate (right) as organic functional group.

carboxylate (COO) group through six  $\mu_2$  oxygen on each side to form a sandwich structure similar to acetate. Considering the pH 2.5 of the reaction mixture, which is below the isoelectric point (~6) and glycine exists in its cationic form. However, the crystal structure of the polyanion 9 revealed that four out of six pendant amino groups had protonation and the remaining two pendant amino groups were very close to the Na atom. Comparing the belt-1 triad group  $\{Mo_2O_{10}(Gly)\}\$  of 9 with  $\{Mo_2O_{10}(OAc)\}\$  of 5, it was observed that the two apical oxo ligands of the {Mo<sub>2</sub>} units bound to glycine are pulled apart compared to the corresponding positions in the acetate units (Figure 5A.6c). This results in greater relaxation within the triad; however, the overall {Mo<sub>2</sub>O<sub>10</sub>(Gly)} unit slightly bents outwards and out of plane possibly due to lone pair/H-bonding at amino group. Also, the presence of glycinate group introduces disorder at the internal sandwich position and causes the cubane core to bend inwards. In addition, one water molecule is positioned in polyanion 9 just above the central phosphorus, at a distance of 3.15-3.29 Å from the cavity of glycine carbonyl carbon (Figure 5A.S17b). POM 9 was further characterized by Powder XRD, XPS in the solid state, and NMR in the solution state. The bulk purity of 9 was determined by comparing simulated PXRD with experimentally observed data, while XPS indicates the presence of Mo, P, N, C and O (Figure 5A.S16). Solution-state stability of 9 was confirmed using NMR, where <sup>1</sup>H NMR indicates the presence of methylene group at 3.47 ppm while  $^{31}P$  NMR shows two peaks at = -0.55 and -1.27 ppm (Figure 5A.S18/S19). DFT analysis of 9 indicates the shifting of HOMO towards nitrogen which was situated at oxygen in 6, while LUMO remains localized on Mo in both 6 and 9, resulting in a decrease in the band gap for the glycine functionalized POM (Figure 5A.S15).

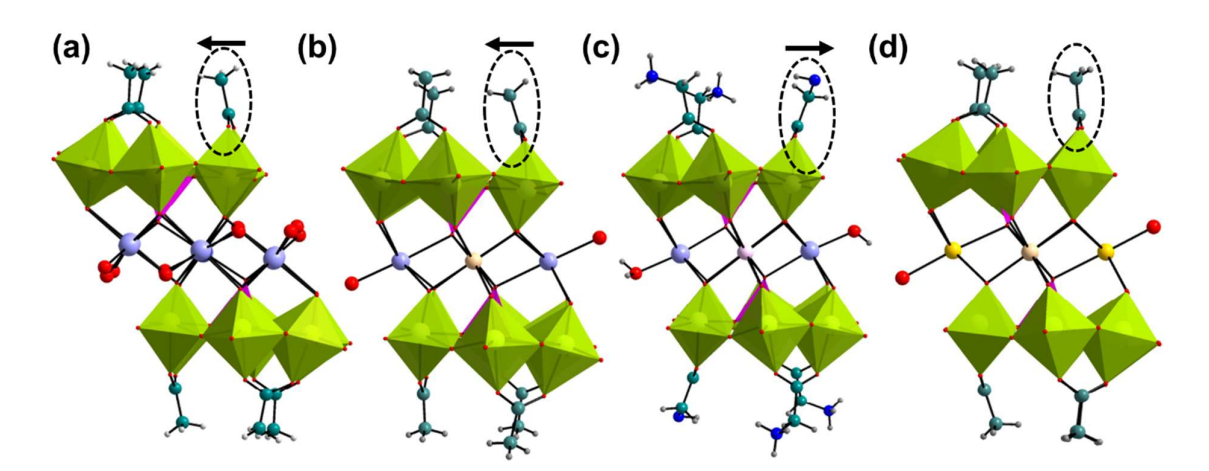


Figure 5A.6 Combined polyhedral/ball and stick representation of sandwich POMs showing the orientation of organic group in (a) 1 (b) 5 (c) 9 and (d) 7.

In addition to glycine, we investigated acrylic acid and itaconic acid. While these acids appear to form the desired structure, we have not yet been able to isolate pure products. For example, with acrylic acid, we obtained the acrylate-based POM, which was further polymerized and characterized by <sup>1</sup>H and <sup>13</sup>C NMR analysis (Fig 5A.S20-S21). Our studies on carboxylate ligands -with long chain or bulky groups suggest challenges from such POMs, highlighting the crucial role of pH and countercations in the process. Overall, the orientation and nature of functional groups at hexamolybdate framework significantly influence the cubane composition at sandwich position (Figure 5A.6)

#### **5A.3 Conclusion**

In summary, the successful isolation of the Mo-based sandwich POM framework using the cooperative effect of transition metals and organic ligands highlights the critical role of these effects in the formation and isolation new inorganic-organic hybrid architecture. This study emphasizes that the self-assembly of Mo-based sandwich POMs is largely influenced by the choice of transition metals, as well as the nature of organic ligands, which ultimately determine the size and shape of the final product. This work not only establishes a new pathway for creating complex POM structures but also paves the way for future advancements in copolymerization and post-functionalization of these POMs, potentially leading to the development of POM-based novel materials with diverse applications.

## **4A.4 Experimental Section**

#### 4A.4.1 General Information and Instrumentation

#### 5A.4.1a Materials and Methods

Already mentioned in section 2.4.1a (chapter 2)

## 5A.4.1b Instrumentation

Already mentioned in section 2.4.1b (chapter 2)

## 5A.4.1c Density Functional Theory (DFT) Calculation.

Already mentioned in section 2.4.1c (chapter 2)

## 5A.4.2 Synthesis

Na salt of [Na<sub>7</sub>(PMo<sub>6</sub>O<sub>22</sub>)<sub>2</sub>(OAc)<sub>6</sub>].nH<sub>2</sub>O (1) Na<sub>2</sub>MoO<sub>4</sub>.2H<sub>2</sub>O (2.00 g, 8.26 mmol) and NaH<sub>2</sub>PO<sub>4</sub>.2H<sub>2</sub>O (0.245 g, 1.37 mmol) was dissolved in 5 mL DI water completely. The pH of the solution was fixed at 3.0 using glacial acetic acid. The resultant solution was put in Teflon microwave vials of 100 mL volume and microwave irradiated under controlled pressure with

a power ramp for 15 min, and power hold for 45 min at 85 °C under 400 W maximum power. The solution thus obtained was filtered hot, and the filtrate was kept for crystallization. After one day, glassy square crystals appeared, which were collected by filtration and dried at 60 °C under vacuum. Yield = 0.95 g (54.8 %)

Na salt of [Na<sub>6.5</sub>Cd<sub>0.5</sub>(H<sub>2</sub>O)<sub>2</sub>(PMo<sub>6</sub>O<sub>22</sub>)<sub>2</sub>(OAc)<sub>6</sub>].nH<sub>2</sub>O (2): The above-mentioned microwave synthesis method for 1 was repeated using CdCl<sub>2</sub> (0.251 g, 1.37 mmol). The obtained solution was filtered, and the filtrate was left for crystallization. After two days, colourless crystals of 2 formed. The crystals are characterized using single-crystal XRD. Yield = 0.76 g (42.7 %)

Na salt of [Na<sub>2</sub>Zn<sub>2</sub>(H<sub>2</sub>O)<sub>2</sub>(PMo<sub>6</sub>O<sub>22</sub>)<sub>2</sub>(OAc)<sub>6</sub>].nH<sub>2</sub>O (3): In a typical procedure, the pH of the final mixture of Na<sub>2</sub>MoO<sub>4</sub>.2H<sub>2</sub>O (2.00 g, 8.26 mmol), and NaH<sub>2</sub>PO<sub>4</sub>.2H<sub>2</sub>O (0.245 g, 1.37 mmol), in 5 mL of water was fixed to 3.0 using glacial acetic acid. The final solution was transferred to a microwave vial and microwave-irradiated by controlled pressure programming with a power ramp for 5 min, and power hold for 15 min at 85 °C, under a 400 W maximum power. After cooling, solid Zn(OAc)<sub>2</sub>.4H<sub>2</sub>O (0.684 g, 1.37 mmol) was added to the resultant solution and further microwave irradiated with the above-mentioned reaction parameters. The obtained solution was filtered hot, and the filtrate was left for crystallization. After four days, Colourless crystals of 3 formed, which were characterized using single-crystal XRD. The crystals were collected by filtration and dried at ~60 °C under a vacuum to get the title compound. Yield = 0.81 g (46.1 %)

Na salt of  $[Na_2Ni_2(H_2O)_2(PMo_6O_{22})_2(OAc)_6]$ . The above-mentioned microwave synthesis method for 3 was repeated using Ni $(OAc)_2$ .4H<sub>2</sub>O (0.342 g, 1.37 mmol). The obtained solution was filtered, and the filtrate was left for crystallization. After two days, yellow crystals of 4 formed. The crystals were characterized using single-crystal XRD. Yield = 0.57 g (32.6%)

Na salt of  $[Na_2Co_2(H_2O)_2(PMo_6O_{22})_2(OAc)_6]$ .nH<sub>2</sub>O (5): The above-mentioned microwave synthesis method for 3 was repeated using  $Co(OAc)_2.4H_2O$  (0.335 g, 1.37 mmol). The obtained solution was filtered, and the filtrate was left for crystallization. After one day, dark green-colored one-corner truncated cubic crystals of 5 were formed. The crystals keep growing till the solution becomes almost colorless for ca. 2 weeks. Yield = 1.13 g (64.6%)

Na salt of [Na<sub>2</sub>Mn<sub>2</sub>(H<sub>2</sub>O)<sub>2</sub>(PMo<sub>6</sub>O<sub>22</sub>)<sub>2</sub>(OAc)<sub>6</sub>].nH<sub>2</sub>O (6): The above-mentioned microwave synthesis method for 3 was repeated using Mn(OAc)<sub>2</sub>.4H<sub>2</sub>O (0.335 g, 1.37 mmol). The obtained solution was filtered, and the filtrate was left for crystallization. After 2 h, red-colored one-corner truncated cubic crystals of 6 were formed. The crystals keep growing from the red-colored solution till the solution becomes almost colourless for ca. 2 weeks. The crystals were

collected by filtration and dried at  $\sim$ 60 °C under a vacuum to get the title compound. Yield = 1.42 g (81.4%)

Na salt of [Ago.75Na1.25Mn2(H2O)2(PMo6O22)2(OAc)6].nH2O (7): Na2MoO4.2H2O (2.00 g, 8.26 mmol) and NaH2PO4.2H2O (0.245 g, 1.37 mmol) were dissolved in 5 mL DI water completely. The pH of the solution was fixed at 3.0 using glacial acetic acid, the resultant solution was put in Teflon microwave vials of 100 mL volume and microwave irradiated under controlled pressure with a power ramp for 15 min, and power hold for 45 min at 85 °C under 400 W maximum power. To this solution, Mn(OAc)2.4H2O (0.335 g, 1.37 mmol) was added and vigorously stirred for 30 min, followed by addition of AgNO3(0.28 g, 1.37 mmol), which was irradiated again in microwave for 1 hour at 85 °C following the previous parameter. The orange solution thus obtained was filtered hot, and filtrate was kept for crystallization. After one day, block orange-colored crystals appeared, which were collected by filtration and dried at 60 °C under vacuum. Yield = 0.98 g (52.7%)

Na salt of [Ag<sub>0.85</sub>Na<sub>1.15</sub>Mn<sub>2</sub>(H<sub>2</sub>O)<sub>2</sub>(PMo<sub>6</sub>O<sub>22</sub>)<sub>2</sub>(OAc)<sub>6</sub>].nH<sub>2</sub>O (7a): Na<sub>2</sub>MoO<sub>4</sub>.2H<sub>2</sub>O (2.00 g, 8.26 mmol) and NaH<sub>2</sub>PO<sub>4</sub>.2H<sub>2</sub>O (0.245 g, 1.37 mmol) was dissolved in 5 mL DI water completely. The pH of the solution was fixed at 3.0Using glacial acetic acid, the resultant solution was put in Teflon microwave vials of 100 mL volume and microwave irradiated under controlled pressure with a power ramp for 15 min, and power hold for 45 min at 85 °C under 400 W maximum power. To this solution, AgNO<sub>3</sub> (0.28 g, 1.37 mmol) was added and vigorously stirred for 30 min, followed by addition of Mn(OAc)<sub>2</sub>.4H<sub>2</sub>O (0.335 g, 1.37 mmol), which was again irradiated in microwave for 1 hour at 85 °C following the previous parameter. The orange solution thus obtained was filtered hot, and filtrate was kept for crystallization. After one day, block orange-colored crystals appeared, which were collected by filtration and dried at 60 °C under vacuum. Yield = 0.88 g (47.3%)

Na salt of [Ago.65Na1.35Co2(H2O)2(PMo6O22)2(OAc)6].nH2O (8): Na2MoO4.2H2O (2.00 g, 8.26 mmol) and NaH2PO4.2H2O (0.245 g, 1.37 mmol) were dissolved in 5 mL DI water completely. The pH of the solution was fixed at 3.0 using glacial acetic acid. The resultant solution was put in Teflon microwave vials of 100 mL volume and microwave irradiated under controlled pressure with a power ramp for 15 min, and power hold for 45 min at 85 °C under 400 W maximum power. To this solution, Co(OAc)2.2H2O (0.66 g, 1.37 mmol) was added and vigorously stirred for 30 min, followed by the addition of AgNO3(0.28 g, 1.37 mmol), which was again irradiated in the microwave for 1 hour at 85 °C following the previous parameter. The orange solution thus obtained was filtered hot, and filtrate was kept for crystallization.

After one day, block orange-colored crystals appeared, which were collected by filtration and dried at 60  $^{\circ}$ C under vacuum. Yield = 0.95 g (50.9 %)

## Na salt of $[Na_2Mn_2(H_2O)_2(PMo_6O_{22})_2(Gly)_6].nH_2O$ (9)

Na<sub>2</sub>MoO<sub>4</sub>.2H<sub>2</sub>O (2.00 g, 8.27 mmol) and NaH<sub>2</sub>PO<sub>4</sub>.2H<sub>2</sub>O (0.245 g, 1.37 mmol) were dissolved in 5 ml DI water. After dissolving the salts, glycine (0.31 g, 4.13 mmol) was added to the solution and stirred for 15 mins. After making a completely dissolved solution, the pH of the solution was fixed at 2.5 with 4M HCl, and the solution was stirred vigorously for 1 h at RT. MnCl<sub>2</sub> (0.27 g, 1.37 mmol) was added to the above solution and microwave irradiated by controlled pressure programming with a power ramp for 5 min and power hold for 30 min at 85 °C, under a 400 W maximum power. The reaction solution was filtered and kept at room temperature for crystallization. After two days, light yellow-colored cubic crystals were obtained. Yield = 0.85 g (48.9 %)

Na salt of [(PMo<sub>6</sub>O<sub>22</sub>)<sub>2</sub>(Acrylate)<sub>6</sub>].nH<sub>2</sub>O (10) Na<sub>2</sub>MoO<sub>4</sub>.2H<sub>2</sub>O (2.00 g, 8.26 mmol) and NaH<sub>2</sub>PO<sub>4</sub>.2H<sub>2</sub>O (0.245 g, 1.37 mmol) was dissolved in 5 mL DI water completely. The pH of the solution was fixed at 3.5 using acrylic acid. The resultant solution was put in Teflon microwave vials of 100 mL volume and microwave irradiated under controlled pressure with a power ramp for 15 min, and power hold for 45 min at 85 °C under 400 W maximum power. The blue solution was obtained with dark blue precipitate in it. The precipitate was filtered out and washed 3-4 times with acetone. Collect the precipitate.

## **4A.5 References**

- 1. An, H.; Hou, Y.; Chang, S.; Zhang, J.; Zhu, Q., Highly efficient oxidation of various thioethers catalyzed by organic ligand-modified polyoxomolybdates. *Inorg. Chem. Front.* **2020,** *7* (1), 169-176.
- 2. Hou, Y.; An, H.; Zhang, Y.; Hu, T.; Yang, W.; Chang, S., Rapid destruction of two types of chemical warfare agent simulants by hybrid polyoxomolybdates modified by carboxylic acid ligands. *ACS Catal.* **2018**, *8* (7), 6062-6069.
- 3. Sun, X.; Yang, D.; Wang, G.; Liang, Z.; Ma, P.; Wang, J.; Niu, J., Controlled assembly of hybrid architectures based on carboxylic acid ligands and [(O 3 PCH 2 PO 3) Mo 6 O 22] 12–. *RSC Adv* **2015**, *5* (40), 31392-31398.
- 4. Kortz, U., Polyoxometalate— diphosphate complexes. 6.1 Possible intermediates in the molybdate-catalyzed hydrolysis of pyrophosphate: Structure of hexamolybdopyrophosphate [(O3POPO3) Mo6O18 (H2O) 4] 4. *Inorg. Chem.* **2000**, *39* (3), 625-626.
- 5. Wang, J.; Liang, Y.; Ma, P.; Zhang, D.; Niu, J.; Wang, J., Ligand-controlled formation of covalently modified antimoniomolybdates and their photochromic properties. *CrystEngComm* **2017**, *19* (2), 207-213.

- Gomez-Garcia, C. J.; Coronado, E.; Gómez-Romero, P.; Casan-Pastor, N., A tetranuclear rhomblike cluster of manganese (II). Crystal structure and magnetic properties of the heteropoly complex K10 [Mn4 (H2O) 2 (PW9O34) 2]. cntdot. 20H2O. *Inorg. Chem.* 1993, 32 (15), 3378-3381.
- 7. Martin-Sabi, M.; Soriano-López, J.; Winter, R. S.; Chen, J.-J.; Vilà-Nadal, L.; Long, D.-L.; Galán-Mascarós, J. R.; Cronin, L., Redox tuning the Weakley-type polyoxometalate archetype for the oxygen evolution reaction. *Nat. Catal* **2018**, *1* (3), 208-213.
- 8. Li, C.; Jimbo, A.; Yamaguchi, K.; Suzuki, K., A protecting group strategy to access stable lacunary polyoxomolybdates for introducing multinuclear metal clusters. *Chem. Sci.* **2021**, *12* (4), 1240-1244.
- 9. López, X.; Bo, C.; Poblet, J. M., Electronic properties of polyoxometalates: Electron and proton affinity of mixed-addenda Keggin and Wells–Dawson anions. *J. Am. Chem. Soc.* **2002**, *124* (42), 12574-12582.
- 10. Lopez, X.; Maestre, J. M.; Bo, C.; Poblet, J.-M., Electronic properties of polyoxometalates: A DFT study of α/β-[XM12O40] n-relative stability (M= W, Mo and X a main group element). *J. Am. Chem. Soc.* **2001**, *123* (39), 9571-9576.
- 11. Singh, G.; Mandal, D., Modulation of the Band Gap and Redox Properties by Mixed Addenda in Sandwich Polyoxometalates. *Inorg. Chem.* **2023**, *62* (48), 19648-19663.
- 12. Kong, H.; Liu, S.; Wang, Y.; Xu, Q.; Li, K.; Ma, P.; Wang, J.; Niu, J., Assembly of a Hexameric Cluster of Polyoxomolybdotriphosphonate Builts from [Zn (H2O){TeMo6O21}{N (CH2PO3) 3}] 6–Subunits and Its Optical and Catalytic Properties. *Inorg. Chem.* **2021**, *60* (20), 15759-15767.
- 13. Ma, P.; Hu, F.; Wang, J.; Niu, J., Carboxylate covalently modified polyoxometalates: From synthesis, structural diversity to applications. *Coord. Chem. Rev.* **2019**, *378*, 281-309.
- 14. Yang, D.; Li, S.; Ma, P.; Wang, J.; Niu, J., Carboxylate-functionalized phosphomolybdates: ligand-directed conformations. *Inorg. Chem.* **2013**, *52* (15), 8987-8992.
- 15. Wang, J.; Shi, W.; Li, S.; Mao, Q.; Ma, P.; Niu, J.; Wang, J., Construction of a new binding manner in carboxylic acid-functionalized phosphomolybdates. *Dalton Trans.* **2018**, *47* (24), 7949-7955.
- 16. Yang, D.; Liang, Y.; Ma, P.; Li, S.; Wang, J.; Niu, J., Self assembly of carboxylate/alcoholate functionalized ring-shape phosphomolybdates. *CrystEngComm* **2014**, *16* (34), 8041-8046.
- 17. Kortz, U.; Savelieff, M. G.; Ghali, F. Y. A.; Khalil, L. M.; Maalouf, S. A.; Sinno, D. I., Heteropolymolybdates of AsIII, SbIII, BiIII, SeIV, and TeIV functionalized by amino acids. *Angew. Chem. Int. Ed.* **2002**, *41* (21), 4070-4073.
- 18. Li, F.; Xu, L., Coordination assemblies of polyoxomolybdate cluster framework: From labile building blocks to stable functional materials. *Dalton Trans.* **2011,** *40* (16), 4024-4034.
- 19. Liang, Y.; Li, S.; Yang, D.; Ma, P.; Niu, J.; Wang, J., Controllable assembly of multicarboxylic acids functionalized heteropolyoxomolybdates and allochroic properties. *J. Mater. Chem. C* **2015**, *3* (18), 4632-4639.
- 20. Liu, J.; Yu, J.; Han, Q.; Shao, B.; Wen, Y.; Chen, L.; Zhao, J., Syntheses, structures and properties of four inorganic-organic hybrid heteropolymolybdates functionalized by chiral serine ligands. *Inorg. Chem. Commun* **2016**, *70*, 136-139.
- 21. Qu, D.; Liu, X.; Duan, F.; Xue, R.; Li, B.; Wu, L., {VMo 9 O 31 [RC (CH 2 O) 3]} 6-: the first class of triol ligand covalently-decorated Keggin-type polyoxomolybdates. *Dalton Trans.* **2020**, *49* (37), 12950-12954.
- 22. Liu, W.; Kinyon, J. S.; Bassil, B. S.; Lin, Z.; Bindra, J. K.; Dalal, N. S.; Kortz, U., Arsenic (III)-Capped 12-Tungsto-2-Arsenates (III)[M2 (AsIIIW6O25) 2 (AsIIIOH) x] n-(M= CrIII, FeIII, ScIII, InIII, TilV, MnII) and Their Magnetic Properties. *Inorg. Chem.* **2021**, *60* (11), 8267-8275.
- 23. Manna, P.; Bhattacharya, S.; Kortz, U., Arylarsonate-and Phosphonate-Capped Polyoxomolybdates,[(RC6H4As) 2Mo6O24] n- and [(R' C6H4P) 2Mo5O21] n-. *Inorg. Chem.* **2021**, *60* (10), 7161-7167.
- 24. Yu, H.; Ying, J.; Sun, C.; Jin, L.; Tian, A.; Wang, X., {PMo 6 O 24 N 4} subunit functionalized by organonitrogen through Mo–N bonds: hydrothermal synthesis, structure, photocatalytic, and fluorescence sensing properties. *New J. Chem.* **2021**, *45* (18), 7942-7945.

## **Annexure-VI**

Table 5A.S1 Crystal data, data collection and refinement parameters for Mo-based sandwich POMs (1 to 5 6  $C_{28}H_{82}Co_4Mo$   $C_{56}H_{84}Mn_8Mo_4$ C6H9M06Na6O38P  $C_6H_9Cd_{0.2}Mo_6N|C_{28}H_{42}Mo_{24}N|C_{14}H_{25.5}Mo_{12}$ empirical a<sub>21.4</sub>O<sub>146.72</sub>P<sub>4</sub>Z | Na<sub>9.7</sub>Ni<sub>1.3</sub>O<sub>76.2</sub> | <sub>24</sub>Na<sub>19</sub>O<sub>150</sub>P<sub>4</sub> formula a5.55O38P <sub>8</sub>Na<sub>45</sub>O<sub>295</sub>P<sub>8</sub>  $_{5}P_{2}$ formula 1433.68 1445.82 5814.44 2926.39 5917.90 11804.18 weight 293.15 293.15 293.15 293.15 293.15 293.15 temp (K) crystal triclinic monoclinic monoclinic monoclinic monoclinic triclinic system  $P2_1/c$  $P2_1/c$  $P2_1/c$  $P2_1/c$ space group  $P\overline{1}$  $P\overline{1}$ unit cell dimension a (Å) 10.4459(16) 10.4473(6) 22.497(3) 22.5353(7) 22.444(14) 22.4850(13) b (Å) 11.3015(16) 11.3379(7) 16.325(2) 16.3551(7) 16.296(14) 16.4192(8) c (Å) 16.971(3) 16.9336(11) 20.778(3) 20.805(15) 20.842(18) 20.7850(10) 90 90 90  $\alpha$  (deg) 96.166(5) 96.323(2) 90 90.139(4) 90  $\beta$  (deg) 98.204(5) 98.010(2) 90.250(3) 90.205(2) 90 y (deg) 104.190(4) 103.927(2) 90 90 90  $V(Å^3)$ 1901.2(5) 7668.3(7) 1906.2(2) 7631.3(17) 7623.4(10) 7673.5(7) 2.504 2.530 2.535  $\rho$  (g/cm<sup>3</sup>) 2.519 2.578 2.554 (calculated) F(000)1364.0 1373.0 5530.0 5586.0 5670.0 5611.0  $0.23 \times 0.19 \times 0.17 | 0.34 \times 0.15 \times$ crystal size  $0.24 \times 0.22 \times |0.23 \times 0.16 \times |0.25 \times 0.16 \times |$  $(mm^3)$ 0.13 0.17 0.13 0.12 index ranges -13≤h≤13, -14≤k≤  $-13 \le h \le 13$ ,  $-14 \le |-27 < h < 26$ , -20|-27 < h < 28, -20|-28 < h < 28, -20|-28 < h < 28, -20 < h < 28k ≤ 14, -22 ≤ 1 ≤ 22 | < k < 20, -25 < 1 | < k < 20, -25 < 1 | < k < 20, -26 < 1 | k < 20, -26 < 1 < 14, -21≤1≤21 < 25 <25 < 26 3.744 to 4.172 to 54.688 4.312 to 52.86 2Θ range 55.136 no. of 47255/8478 27195/8783 64516/ 52117/ 98497/ 128797/ reflection 15441 15698 15636 15745 collected /unique GOF on  $F^2$ 1.052 1.035 1.051 1.059 1.043 1.038 final R  $R_1 = 0.027$ ,  $wR_2 =$  $R_1 = 0.039$ .  $R_1 = 0.047$  $R_1 = 0.045$  $R_1 = 0.049$  $R_1 = 0.034$ . indices 0.077  $wR_2 = 0.096$  $wR_2 = 0.117$  $wR_2 = 0.119$  $wR_2 = 0.093$  $wR_2 = 0.079$  $|(I > 2\sigma(I))|$ R indices (all  $|R_1 = 0.030, wR_2 =$  $R_1 = 0.049$  $R_1 = 0.074$  $R_1 = 0.050$ ,  $R_1 = 0.083$ ,  $R_1 = 0.046$ , data) 0.080  $wR_2 = 0.103$  $wR_2 = 0.135$  $wR_2 = 0.123$  $wR_2 = 0.104$  $wR_2 = 0.086$ 

data/restraint

s/ param

8478/0/521

8783/0/516

15441/0/103

15698/1/102

15636/2/106

15745/0/1078

<b>Table 5A.S2</b> Crystal data, data collection and refinement parameters for Mo-based sandwich POMs (7 to 9)							
	7	7A	8	9			
empirical formula	$C_{14}H_{21}Ag_{0.75}Mn_2Mo$ $_{12}Na_{10.5}O_{74}P_2$	$\begin{array}{c} C_{14}H_{21}Ag_{0.85}Mn_2 \\ Mo_{12}Na_{10.15}O_{74}P_2 \end{array}$	$\begin{array}{c} C_{14}H_{21}Ag_{0.65}Co_2\\ Mo_{12}Na_{10.1}O_{74}P_2 \end{array}$	$C_{12}H_{44.87}Mn_{1.1}Mo_{1}\\ {_{2}N_{6}Na_{8.9}O_{69.44}P_{2}}$			
formula weight	3018.70	3021.44	3006.70	2862.63			
temp (K)	293.15	293.15	293.15	293.15			
crystal system	monoclinic	monoclinic	monoclinic	monoclinic			
space group	P2 <sub>1</sub> /c	P2 <sub>1</sub> /c	P2 <sub>1</sub> /c	P2 <sub>1</sub> /n			
unit cell dimension							
a (Å)	22.475(2)	22.5200(18)	22.5101(9)	12.553(2)			
b (Å)	16.4610(12)	16.4875(13)	16.3942(8)	14.996(2)			
c (Å)	20.7305(18)	20.6989(17)	20.7285(9)	20.667(3)			
α (deg)	90	90	90	90			
$\beta$ (deg)	90.316(3)	90.554(3)	90.174(2)	101.962(5)			
γ (deg)	90	90	90	90			
$V(Å^3)$	7669.4(11)	7685.1(11)	7649.5(6)	3806.2(10)			
Z	4	4	4	2			
$\rho$ (calculated) (g/cm <sup>3</sup> )	2.614	2.611	2.611	2.498			
F (000)	5727.0	5730.0	5707.0	2747.0			
crystal size (mm³)	$0.18 \times 0.14 \times 0.11$	0.26 × 0.17 × 0.11	0.18 × 0.16 × 0.16	$0.24 \times 0.18 \times 0.13$			
index ranges	$-26 \le h \le 27, -19 \le k \le 14, -19 \le l \le 24$	$-27 \le h \le 28, -20$ $\le k \le 20, -25 \le l \le$ 25	$-27 \le h \le 28$ , $-20 \le k \le 20$ , $-25$ $\le 1 \le 25$	$-15 \le h \le 15, -18 \le k \le 18, -25 \le l \le 24$			
2Θ range	1.812 to 50.698	3.936 to 52.898	4.322 to 52.818	4.03 to 52.826			
no. of reflection collected /unique	34812/13516	76048/15743	116086/15653	86865/ 7808			
GOF on $F^2$	1.019	1.076	1.076	1.124			
final $R$ indices $(I > 2\sigma(I))$	$R_1 = 0.067, wR_2 = 0.154$	$R_1 = 0.049,$ $wR_2 = 0.119$	$R_1 = 0.034,$ $wR_2 = 0.088$	$R_1 = 0.055, wR_2 = 0.142$			
R indices (all data)	$R_1 = 0.147, wR_2 = 0.210$	$R_1 = 0.062,$ $wR_2 = 0.129$	$R_1 = 0.037,$ $wR_2 = 0.090$	$R_1 = 0.070, wR_2 = 0.151$			
data/restraints/ param	13516/1/1059	15743/0/1044	15653/0/1068	7808/0/51			

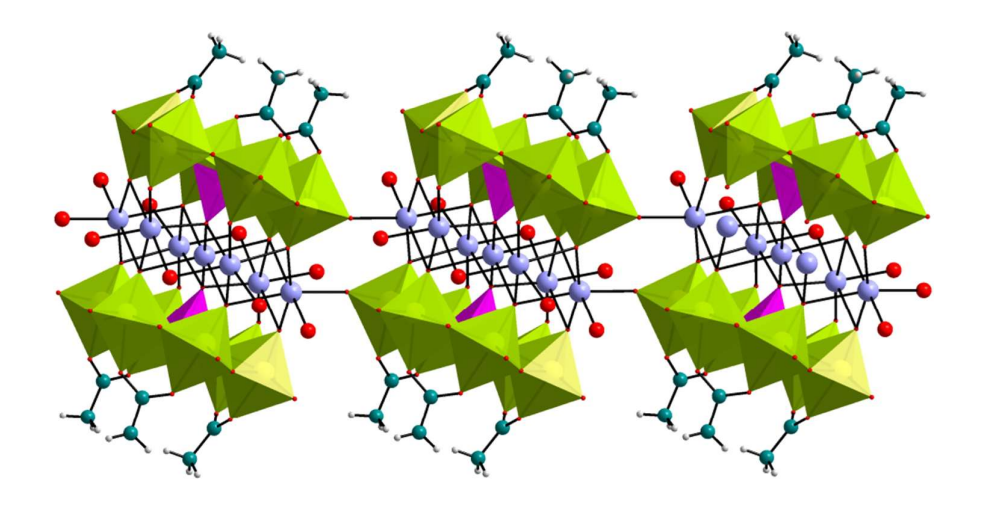


**Figure 5A.S1** Combined polyhedral/ball and stick representation of Mo-based sandwich POMs showing 1-D chain structure.

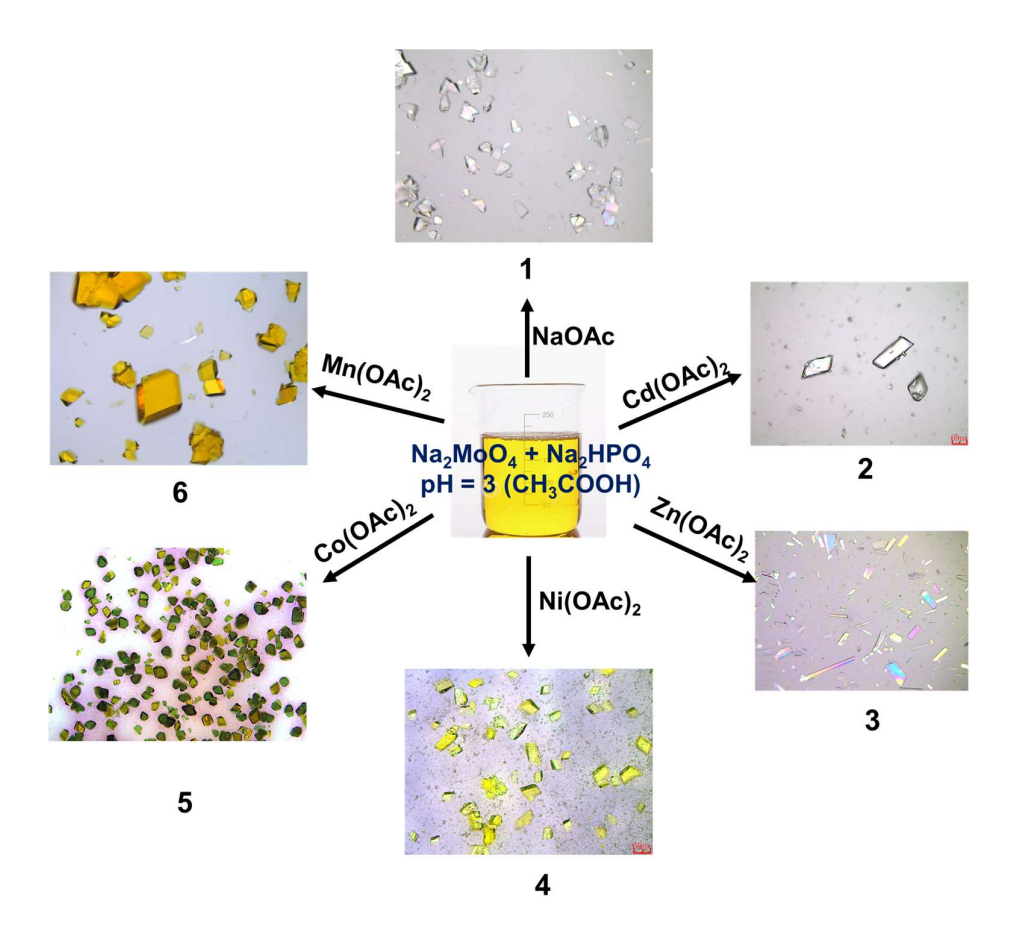


Figure 5A.S2 Optical images of Mo-based tetrasubstituted sandwich POMs.

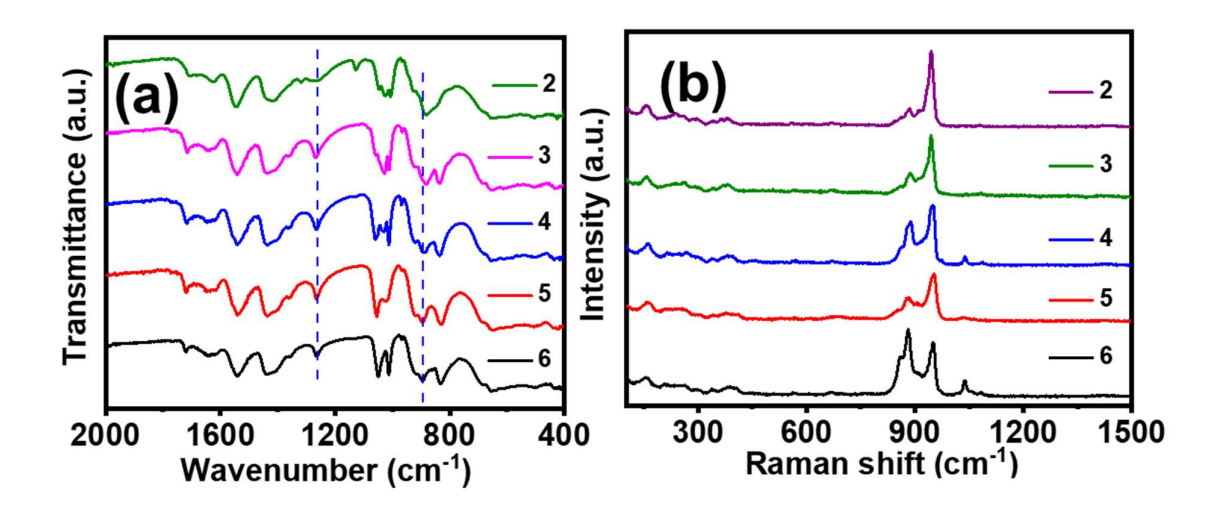


Figure 5A.S3 Comparison of FT-IR spectra of Mo based tetrasubstituted sandwich POMs.

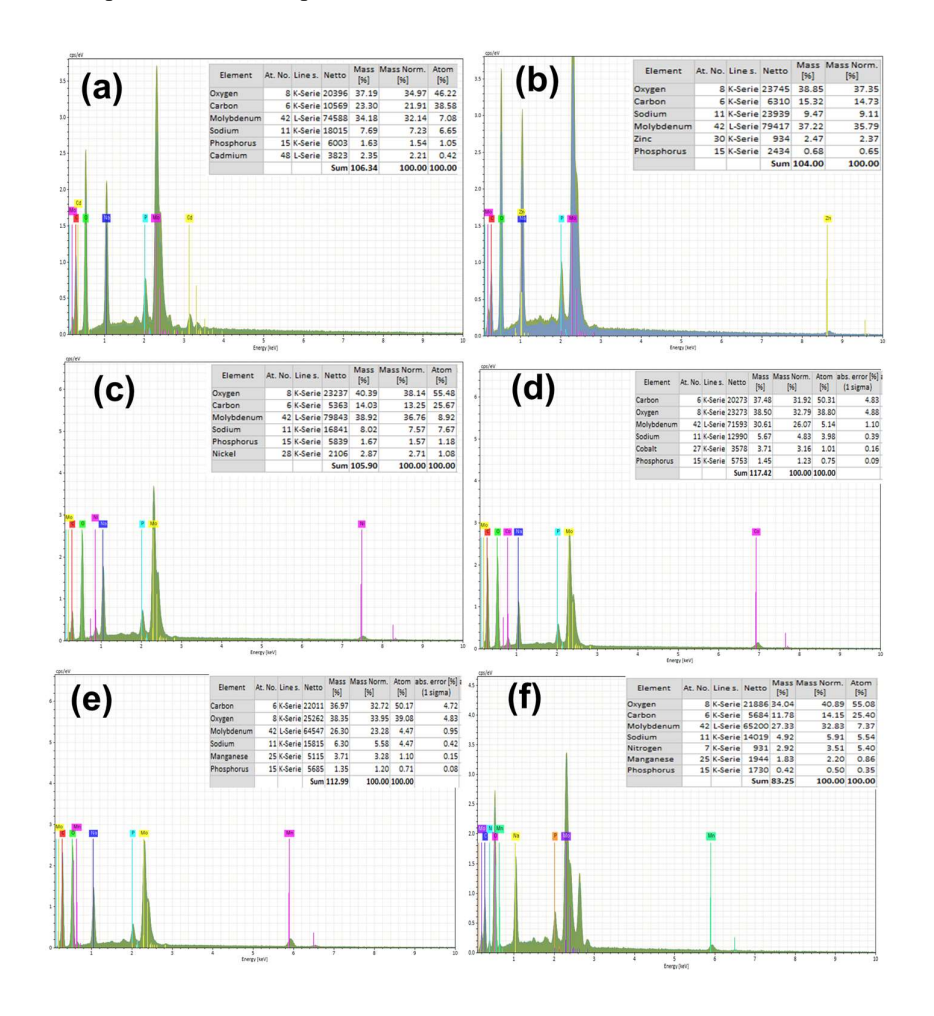


Figure 5A.S4 EDX mapping for Mo-based sandwich POMs (a) 2 (b) 3 (c) 4 (d) 5 (e) 6 and (f) 9.

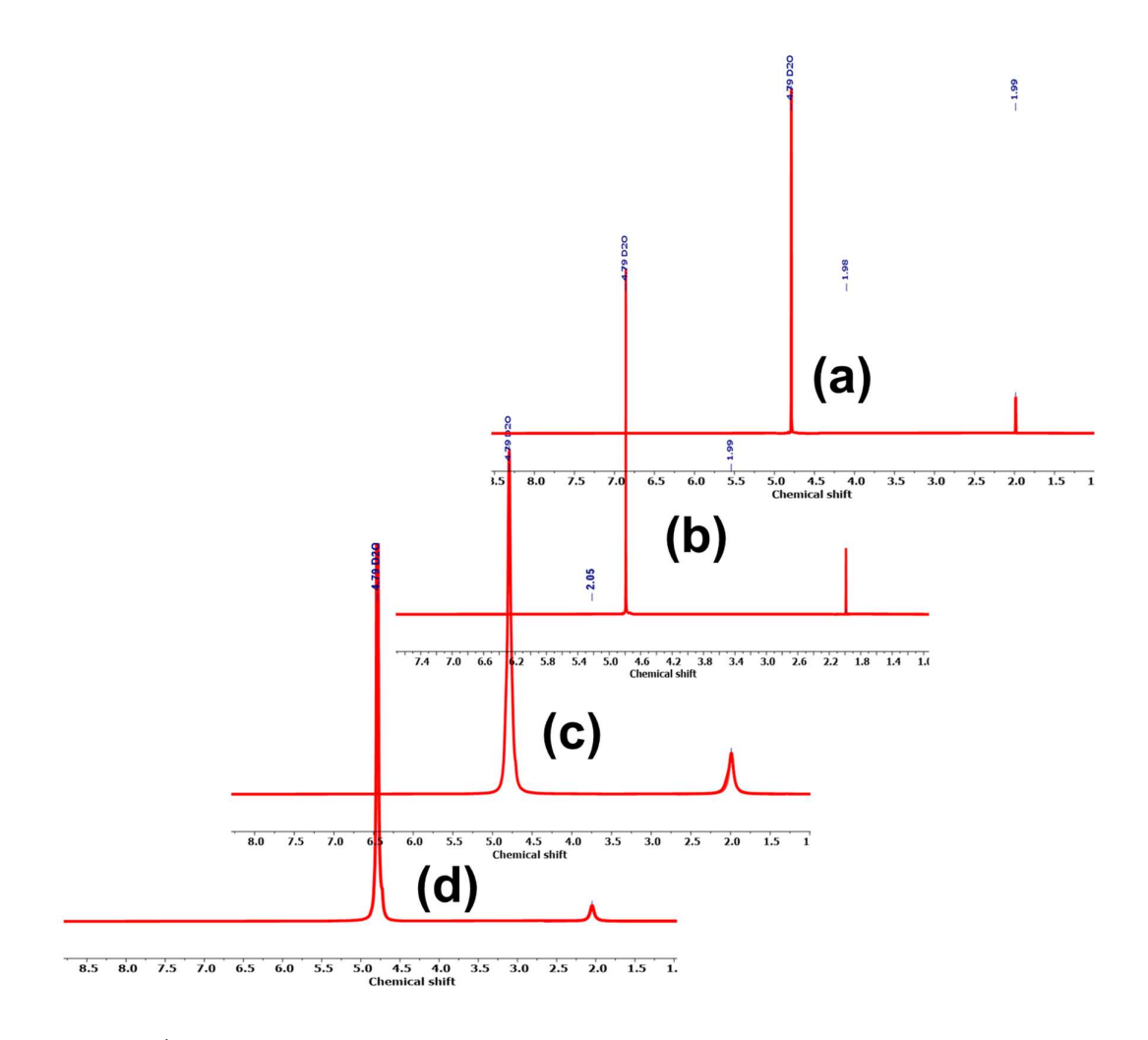


Figure 5A.S5 <sup>1</sup>H NMR Mo-based sandwich POMs (a) 2 (b) 3 (c) 4 and (d) 5.

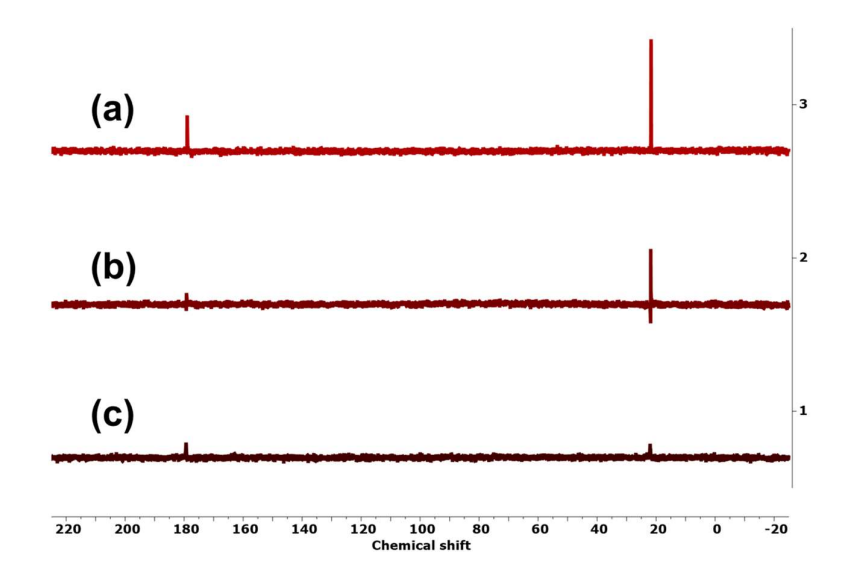


Figure 5A.S6 <sup>13</sup>C NMR for Mo-based sandwich POMs (a) 2 (b) 3 and (c) 4.

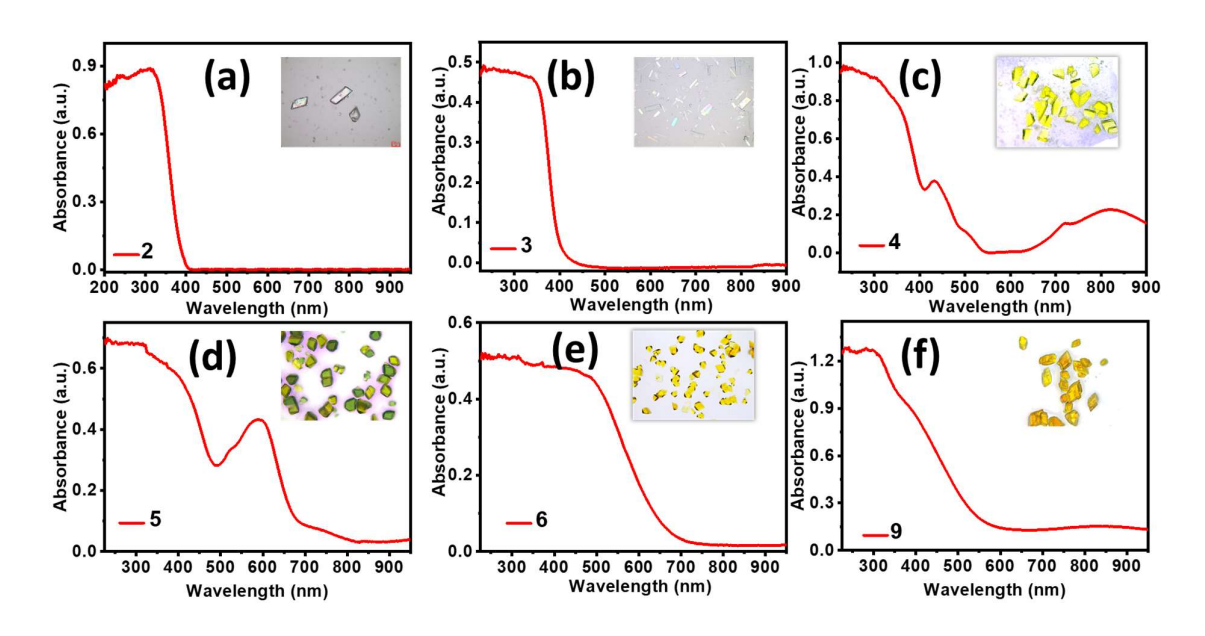


Figure 5A.S7 Solid state UV-visible absorbance spectra of (a) 1 (b) 3 (c) 4 (d) 5 (e) 6 and (f) 9.

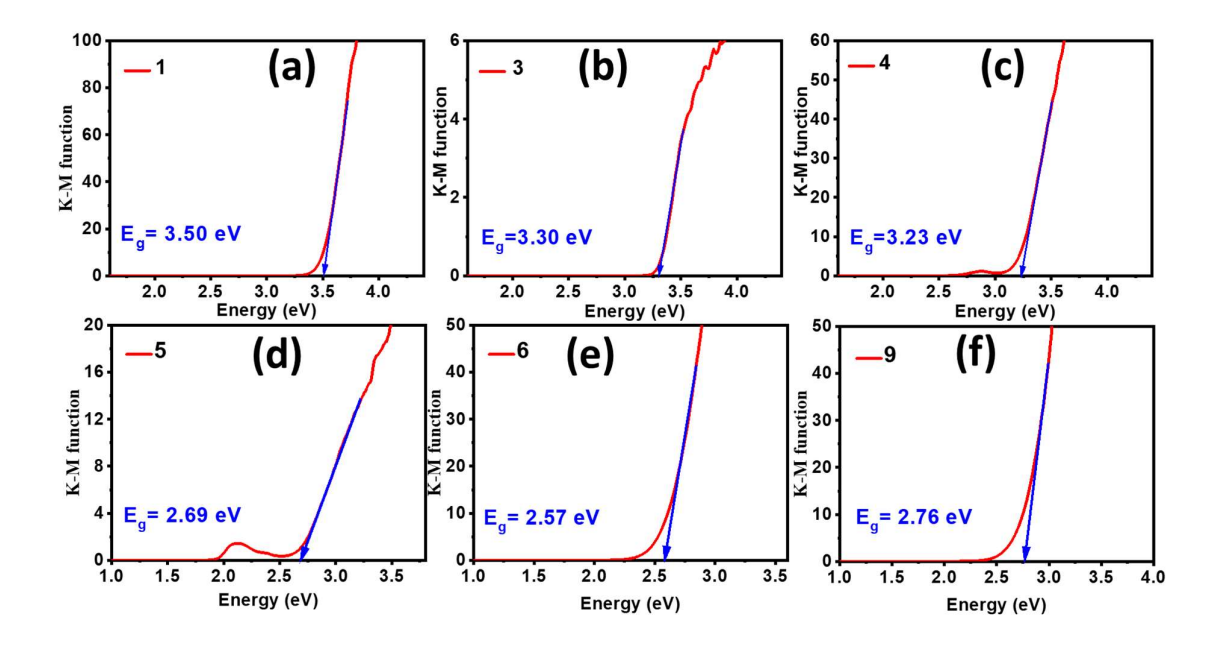


Figure 5A.S8 Band gap calculation from reflectance using K-M equation in (a) 1 (b) 3 (c) 4 (d) 5 (e) 6 and (f) 9.

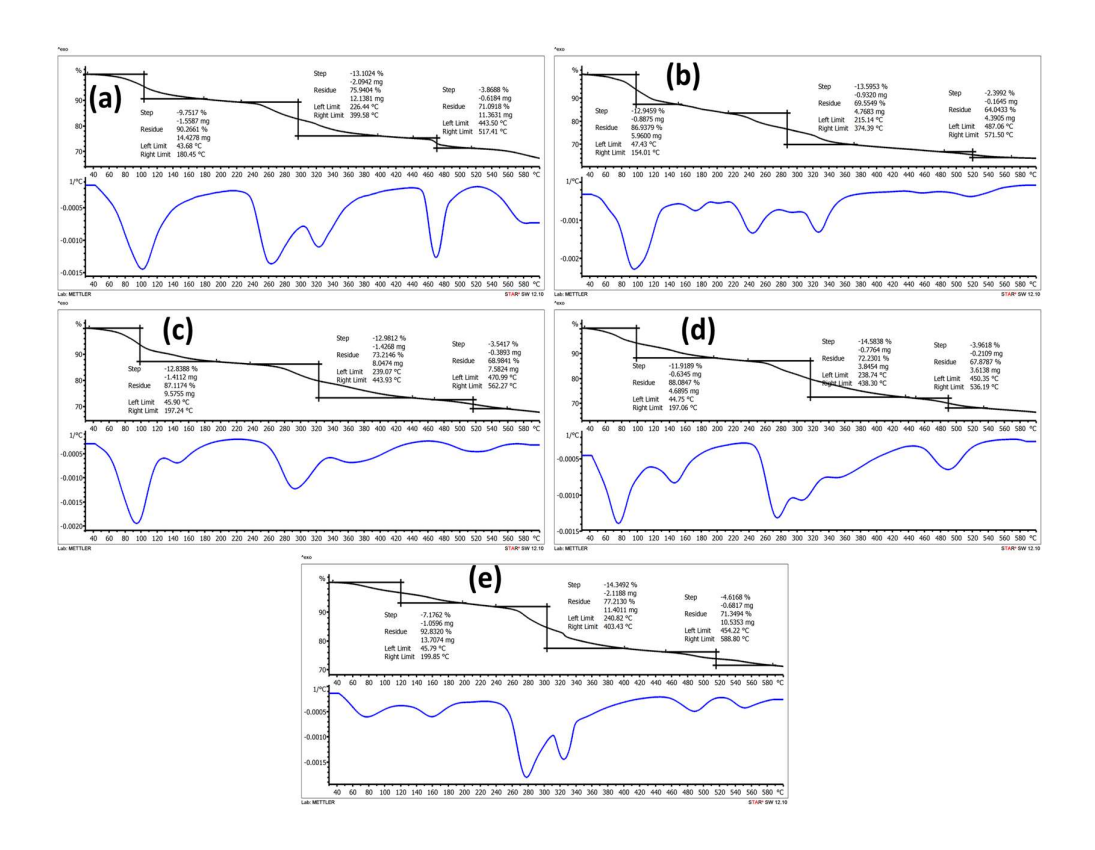


Figure 5A.S9 TGA curves of Mo-based sandwich POMs (a) 3 (b) 4 (c) 5 (d) 6 and (e) 9.

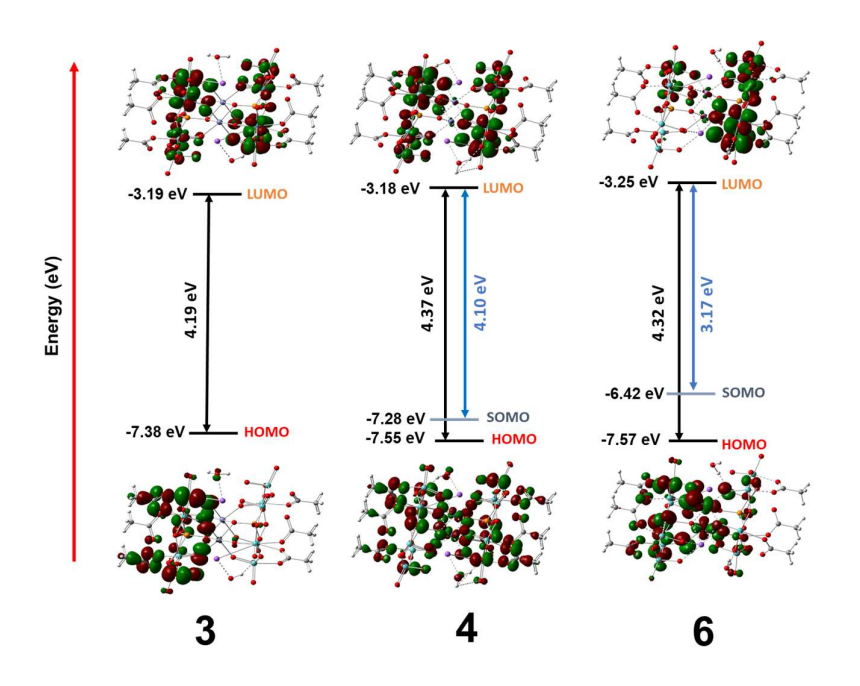


Figure 5A.10 Frontier molecular orbitals (HOMO, LUMO) for Mo-based tetrasubstituted sandwich POMs.

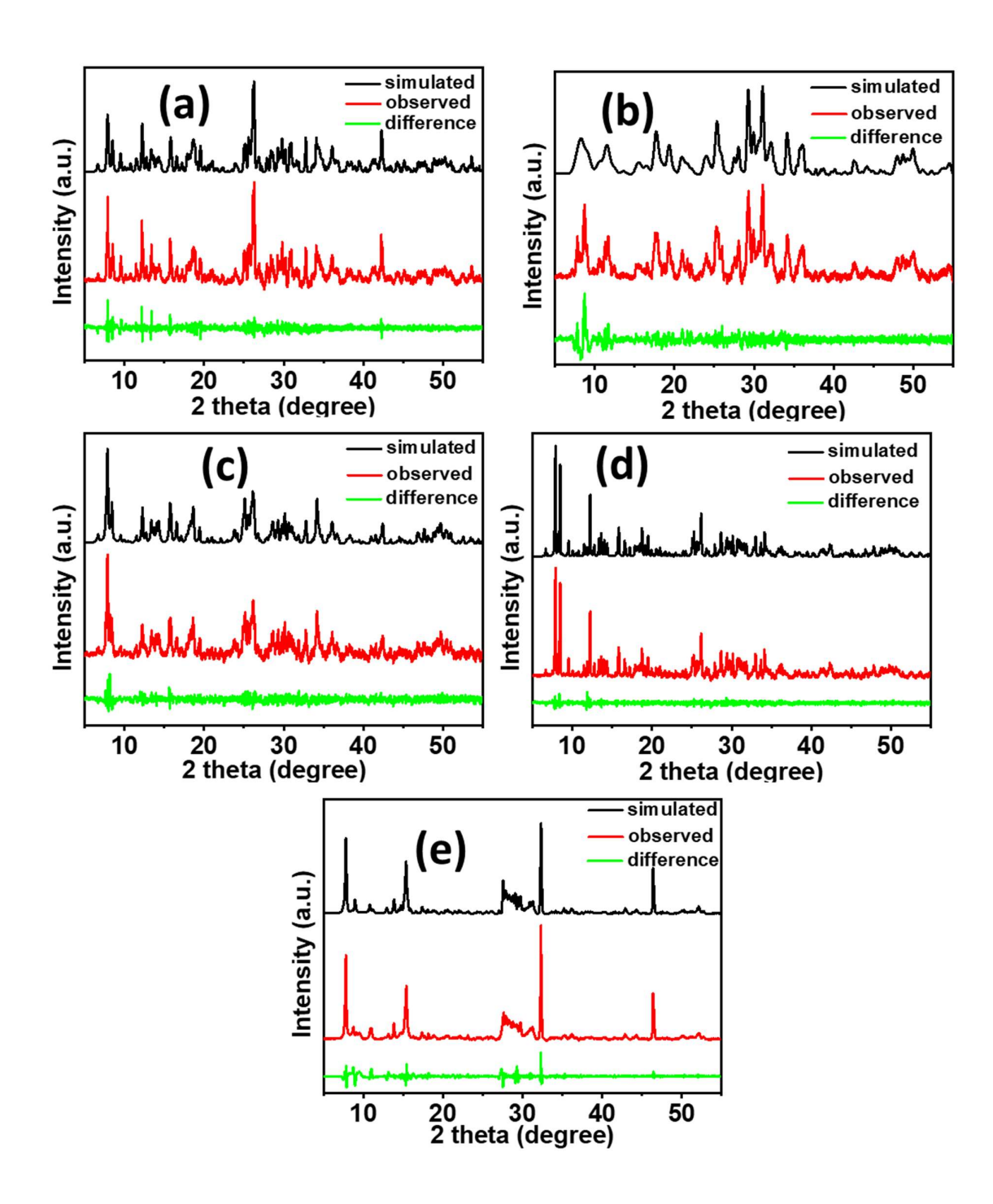
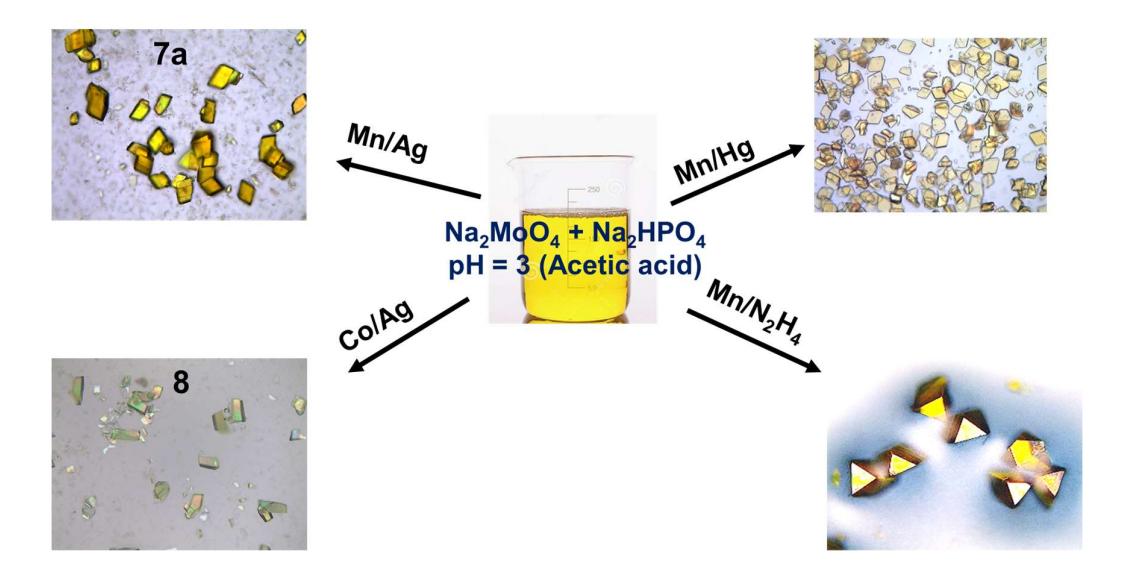
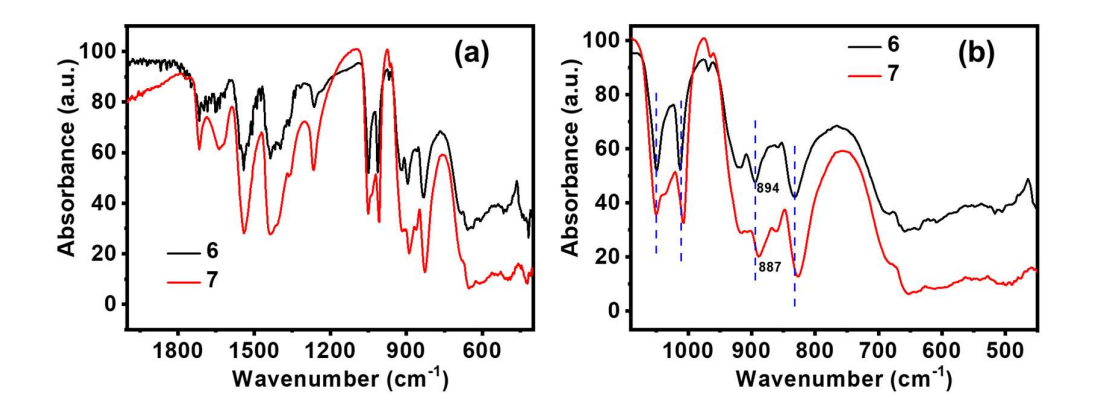


Figure 5A.S11 PXRD pattern and comparison with the simulated data from single crystal XRD for (a) 3 (b) 4 (c) 5 (d) 6 and (e) 9.



**Figure 5A.S12** Optical images of Mo-based tetrasubstituted sandwich POMs showing the cooperative effect of transition metals.



**Figure 5A.S13** Comparison of FT-IR spectra of Mo based tetrasubstituted sandwich POMs in **6** and **7** (a) in the range 400-2000 cm<sup>-1</sup> (b) zoom area in the range 400-1100 cm<sup>-1</sup>.

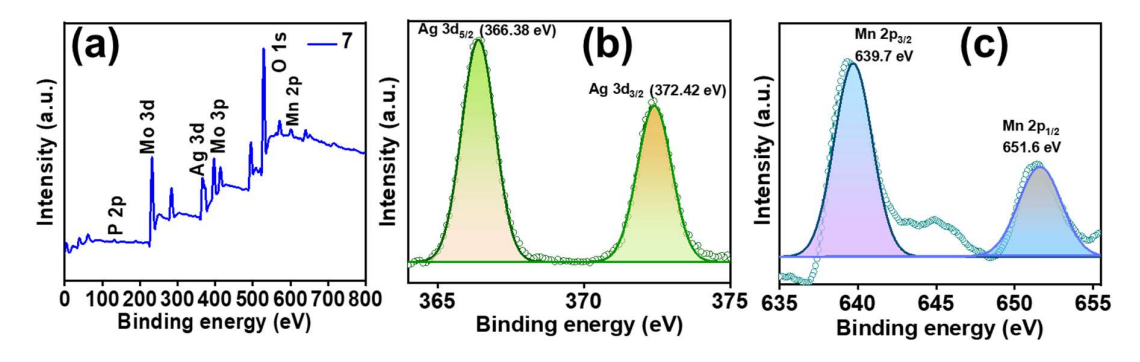
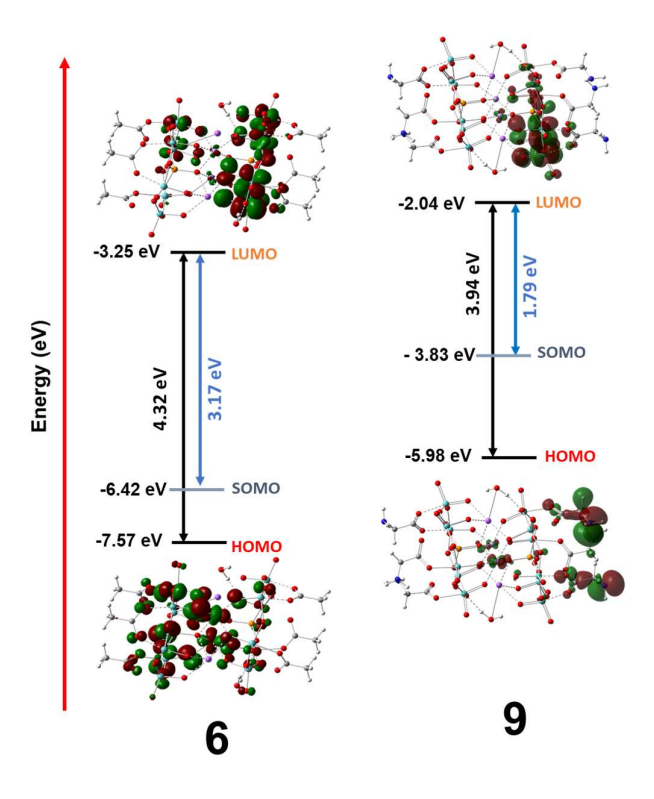
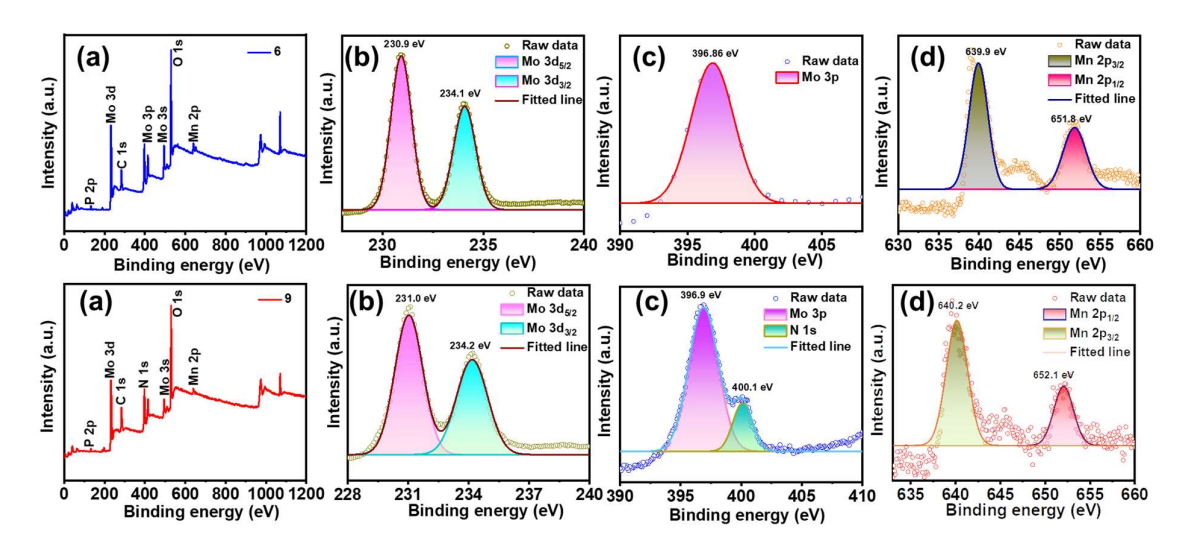


Figure 5A.S14 XPS of 7 (a) Survey spectra (b) Ag 3d spectra (c) Mn 2p spectra.



**Figure 5A.S15** Frontier molecular orbitals (HOMO, LUMO) for Mo-based tetrasubstituted sandwich POMs 6 and 9.



**Figure 5A.S16** (above) XPS spectra of **6** (a) Survey spectra, (b) Mo 3d, (c) Mo 3p, (d) Mn 2p; and (below) XPS spectra of **9** (a) Survey spectra, (b) Mo 3d, (c) Mo 3p and N 1s, (d) Mn 2p.

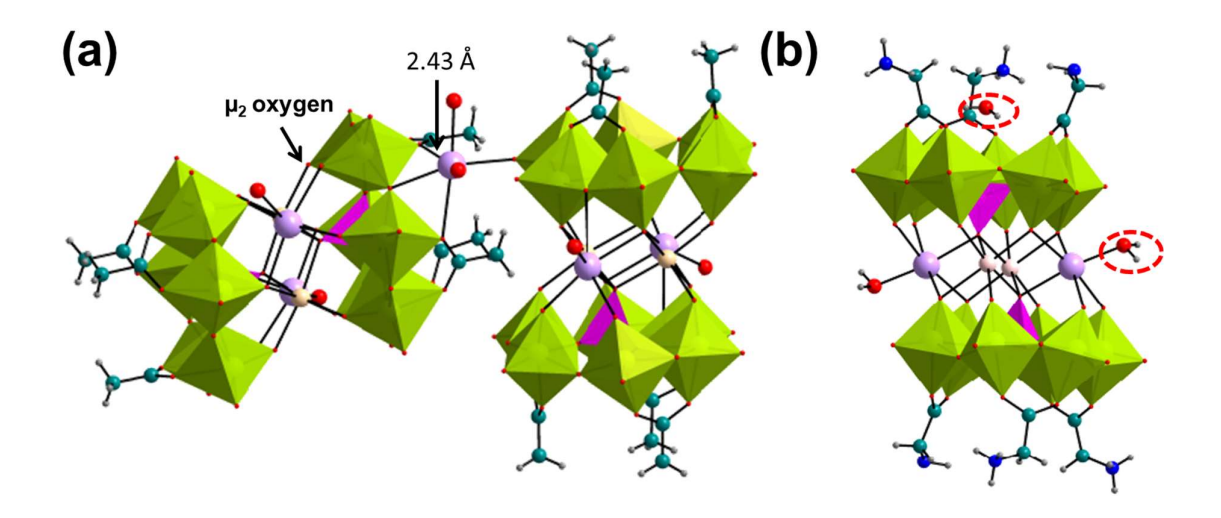


Figure 5A.S17 Combined polyhedral/ball and stick representation of Mo-based sandwich POMs showing the 1-D chain through sodium atoms in 6 (b) closest/covalently bound water molecule (highlighted) in 9.

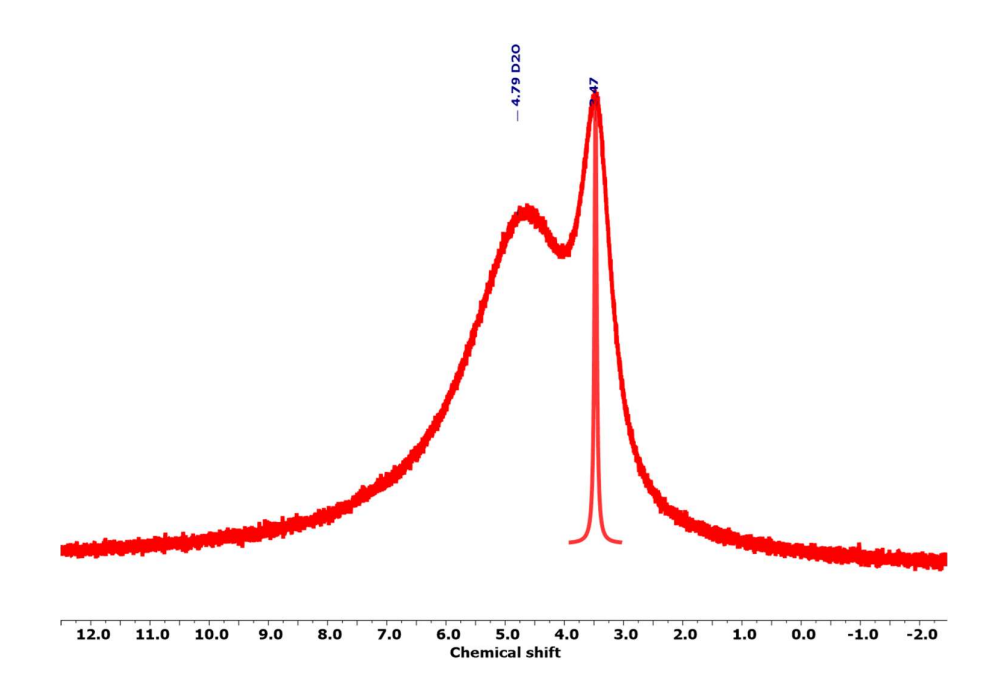


Figure 5A.S18 <sup>1</sup>H NMR spectrum of 9.

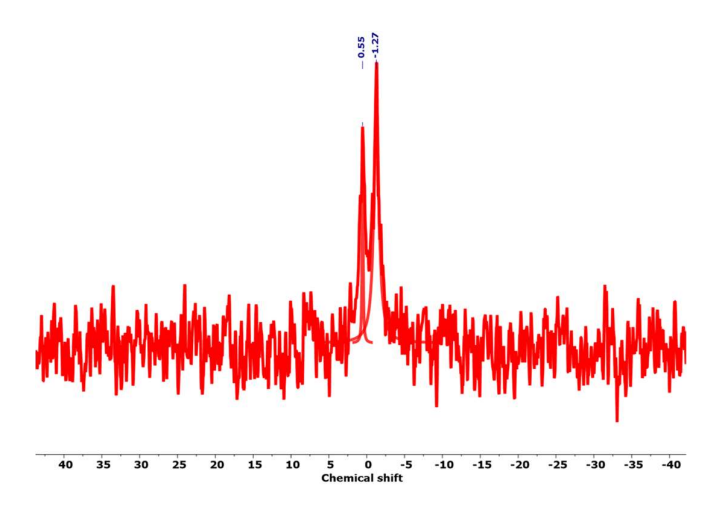


Figure 5A.S19 <sup>31</sup>P NMR spectrum of 9.

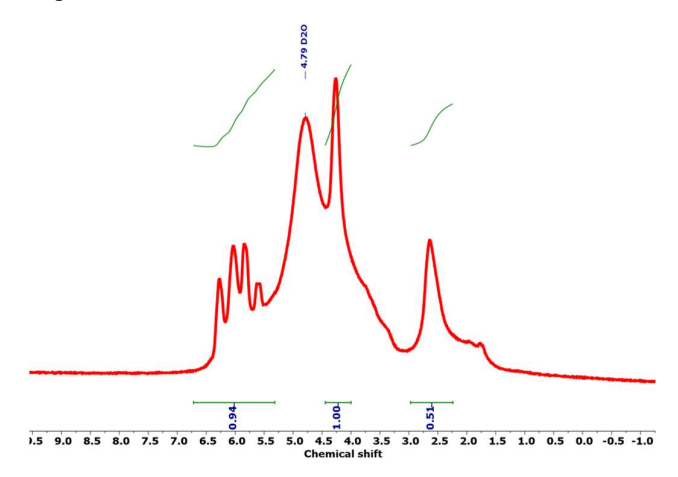


Figure 5A.S20 <sup>1</sup>H NMR spectra of 10 after polymerisation.

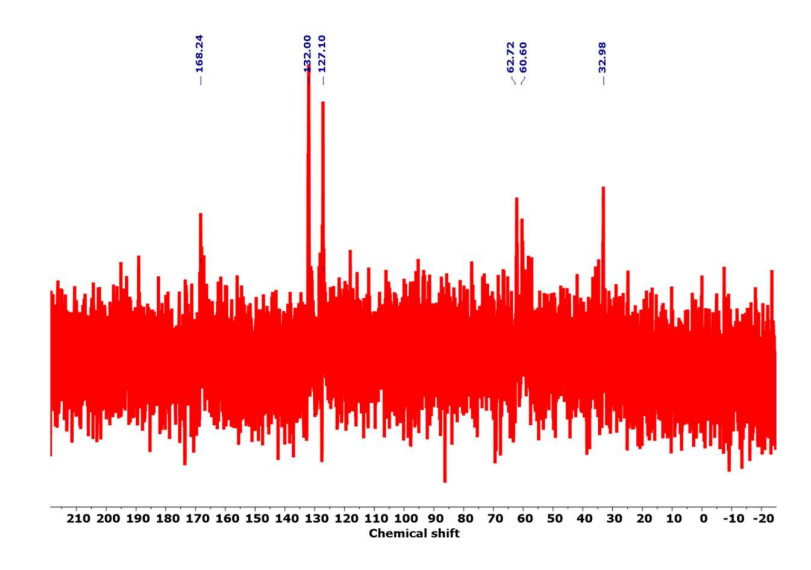
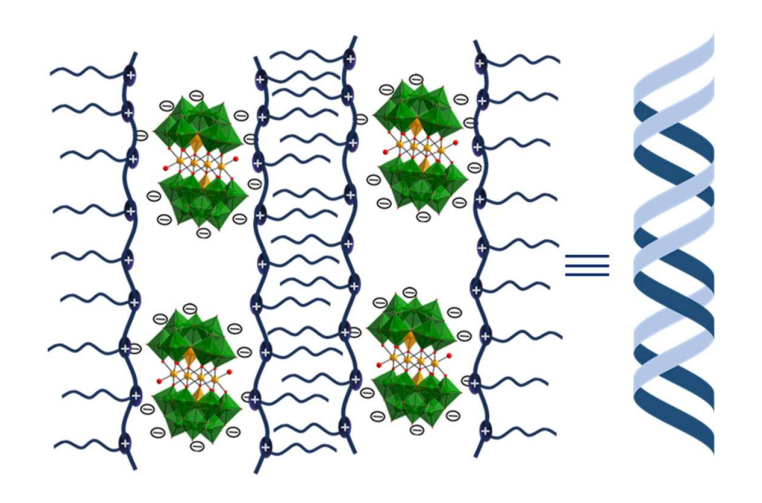


Figure 5A.S21 <sup>13</sup>C NMR spectra of 10 after polymerisation.

# Chapter 5 Section B

Self-assembled Polyoxometalate-based Nanohybrids for Corrosion-Resistant Underwater Adhesive



#### **5B.1 Introduction**

Underwater adhesives have emerged as essential tools across diverse fields such as modern surgery, biomedical development, soft robotics, architecture and art restoration, and highperformance coatings. Inspiration from natural underwater adhesives, pioneer studies have provided valuable guidelines for synthetic chemists aiming to engineer such underwater adhesive materials.<sup>2, 3</sup> Varieties of bioinspired adhesives have been developed based on 3,4dihydroxyphenylalanine (DOPA), a key component in mussels and sandcastle worms. 4-6 By integrating DOPA units into various oligomers and polymers, these adhesives can achieve adhesive strengths of up to 2 MPa in dry conditions while less than 1 MPa when submerged. However, many of these underwater adhesives suffer from impractically long curing times (exceeding 1 h curing time in some studies) and difficulties in performing all essential steps while underwater, such as spreading, bonding, and curing. Conversely, most synthetic underwater adhesives in the literature are made up of polymers with high storage moduli (>1 MPa) and glass transition temperatures (Tg) above room temperature. Therefore, a major challenge in the advancement of underwater adhesives lies in transforming low-viscosity polymers into those with high Young's moduli while preserving effective surface wetting for optimal adhesion. The development of versatile adhesives combining high strength, reversibility, corrosion resistance, suitability for underwater usage, and tolerance to extreme temperatures is urgently needed. In recent time, emphasis has shifted towards supramolecular underwater adhesives that do not mimic biological adhesives but instead rely on combinations of non-covalent interactions.<sup>9, 10</sup> These supramolecular underwater adhesives have shown promising lap shear strengths of up to 3 MPa when applied to steel plates underwater. <sup>11</sup> Notable examples include nucleobase-containing organo-gels, crown-based building blocks, and amino acid-incorporating polyoxometalates (POMs), which form robust 3D network structures and significantly enhances bulk mechanical strength. 12-14 Multivalent interactions between amino acids and polyoxometalates create robust 3D networks via supramolecular contacts, resulting in gel-like behaviour capable of adhering to a wide range of surfaces underwater. 15-18

S. Zhang et al. recently developed a simple process to create an inorganic subnanometer nanowire adhesive using polyanions in aqueous conditions.<sup>19</sup> This adhesive exhibit enhanced adhesion strengths of up to 3 MPa on stainless steel.<sup>20, 21</sup> Also, coacervate-based adhesives utilizing hydrogen bonding and electrostatic interactions involving polyethyleneimine (PEI) and Keggin-type polyoxometalate H<sub>3</sub>PW<sub>12</sub>O<sub>40</sub> (PW<sub>12</sub>) have shown promising in wound healing and other biomedical applications.<sup>22</sup> Furthermore, sandwich POMs have more total negative

charge and oxygen atoms than in simple Keggin POMs. Especially, tetrasubstituted sandwich POMs, derived from the trivacant Keggin lacunary POMs possess high negative charge density. Towards this, here we have synthesized sodium salt of 'cobalt'-centered penta-cobalt POM [WCo<sub>3</sub>(H<sub>2</sub>O)<sub>2</sub>(CoW<sub>9</sub>O<sub>34</sub>)<sub>2</sub>]<sup>12-</sup> (Co-WCo<sub>3</sub>).<sup>23</sup> The presence of Co(+2) as heteroatom in place of P(+5), results in an increased total charge (-12), and smaller size of this POM raises the charge-to-size (q/m) ratio. Conversely, quaternization of PEI with hexyl bromide results in the formation of a positively charged polymer, [q-PEI-hexyl][Br] can render good adhesive properties apart from hydrophobicity.<sup>24</sup>

Further, organic-inorganic hybrids based on electrostatic and van der Waal interactions, such as highly versatile and stable POM-ionic liquid; [C<sub>25</sub>H<sub>54</sub>N][Co-WCo<sub>3</sub>] and POM-polymer; [q-PEI-hexyl][Co-WCo<sub>3</sub>] have been synthesized. These POM-polymer hybrids show superior underwater adhesion properties and show corrosion-resistant behaviour at stainless steel (SS) substrate. These can be applied to stainless steel, aluminium, and glass, demonstrating adaptability to underwater and ultra-low temperature conditions. With addition of small amount solvent, these adhesives could be easily removed without leaving any residue or damage, allowing for recycling over 10 times. Interestingly, the adhesives [q-PEI-hexyl][Co-WCo<sub>3</sub>] adopt micro rope-like structures upon grinding with a small amount of MeOH/H<sub>2</sub>O.

## 5B.2 Results and Discussion

## 5B. 2.1 Synthesis of [C<sub>25</sub>H<sub>54</sub>N][Co-WCo<sub>3</sub>] hybrids for Underwater adhesion

The hybrid [ $C_{25}H_{54}N$ ][Co-WCo<sub>3</sub>] was synthesized via the ion exchange metathesis, which includes exchanging the chloride of the ionic liquid, aliquat–336 ( $C_{25}H_{54}N^+$  Cl<sup>-</sup>) with the Na<sub>12</sub>[Co-WCo<sub>3</sub>] POM moiety. Na<sub>12</sub>[Co-WCo<sub>3</sub>] POM was synthesized and characterized using our reported procedure.<sup>23</sup> The molecular structure of Na<sub>12</sub>[Co-WCo<sub>3</sub>] was analyzed by single crystal X-ray diffraction (SC-XRD) and ESI-mass analysis. The crystal data of Na<sub>12</sub>[Co-WCo<sub>3</sub>] was matched with our previously reported data (CCDC 1558372). As observed from the crystal structure, the WCo<sub>3</sub> core was sandwiched between two [CoW<sub>9</sub>O<sub>34</sub>]<sup>12-</sup> (Co as heteroatom) units. The ESI-mass spectrum of Co-WCo<sub>3</sub> POM (negative mode) in Figure 5B.S2 shows the m/z value of 2461.79 for z = -2, 1628.54 for z = -3 and 1221.63 for z = -4 (Table 5B.S1).

The hybrid is insoluble in water and soluble in organic solvents, e.g., DCM, THF. FT-IR spectra of [Co-WCo<sub>3</sub>](C<sub>25</sub>H<sub>54</sub>N) show the characteristic peaks of Co-WCo<sub>3</sub> POM and C<sub>25</sub>H<sub>54</sub>N with slight shifting due to strong electrostatic interactions as well as hydrogen bonding (Fig 5B.1c/1d). Apart from H-bonding, distinctive absorption bands at 928 (W=O), 868 (W-O-W),

and 2920, 2850 cm<sup>-1</sup> indicates the interactions between quaternary ammonium groups of C<sub>25</sub>H<sub>54</sub>N with anionic Co-WCo<sub>3</sub> POM.

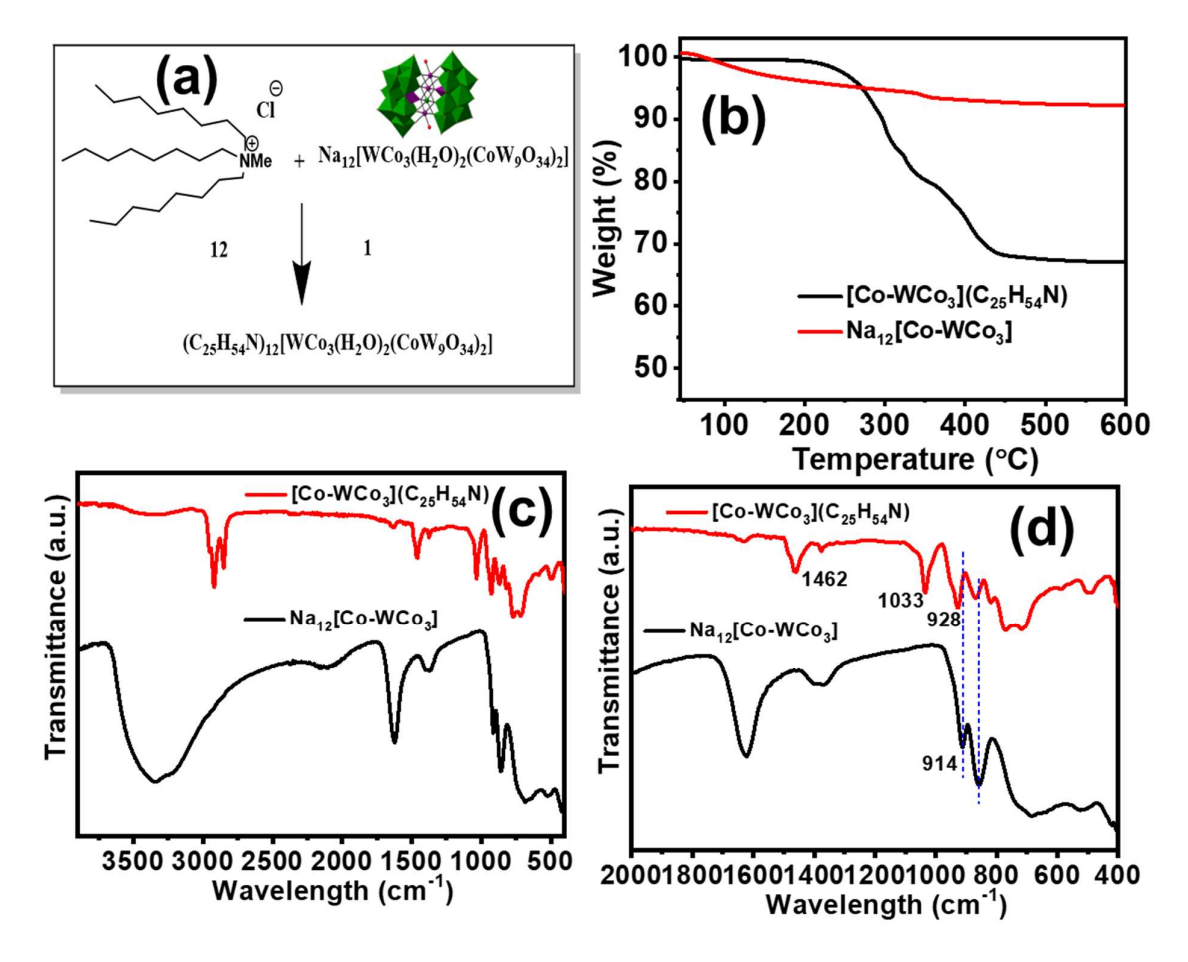


**Figure 5B.1** (a) Synthesis of  $[C_{25}H_{54}N][Co-WCo_3]$  by ion-exchange method. (b) TGA curve of  $[Co-WCo_3]$  POM and  $[C_{25}H_{54}N][Co-WCo_3]$  (c) Comparison of FT-IR spectra in the range of 400-4000 cm<sup>-1</sup> (d) FT-IR spectra showing shifting in  $[Co-WCo_3][C_{25}H_{54}N]$  from  $[Co-WCo_3]$  POM (400-2000 cm<sup>-1</sup>).

TGA suggests the thermal stability of [C<sub>25</sub>H<sub>54</sub>N][Co-WCo<sub>3</sub>] up to 230 °C and a total weight loss of ~32% was observed up to 600 °C. The composition of [Co-WCo<sub>3</sub>] is ~24 wt.% in [C<sub>25</sub>H<sub>54</sub>N][Co-WCo<sub>3</sub>] obtained from the comparison of TGA of [C<sub>25</sub>H<sub>54</sub>N] and [Co-WCo<sub>3</sub>] POM. Furthermore, coating at the glass surface revealed that the water contact angle of [C<sub>25</sub>H<sub>54</sub>N][Co-WCo<sub>3</sub>] was 92.5° (Fig. 5B.2a). Also, DLS study in Figure 5B.2 shows the self-assembly of [C<sub>25</sub>H<sub>54</sub>N][Co-WCo<sub>3</sub>], as hybrid with 987 nm size in IPA gets assembled to 180 nm in water and 212 nm in hexane due to hydrophobic (alkyl chain) as well as hydrophilic (POM) constituents thus indicating polarity reversal affecting self-assembly. The optical images of [C<sub>25</sub>H<sub>54</sub>N][Co-WCo<sub>3</sub>] show gel

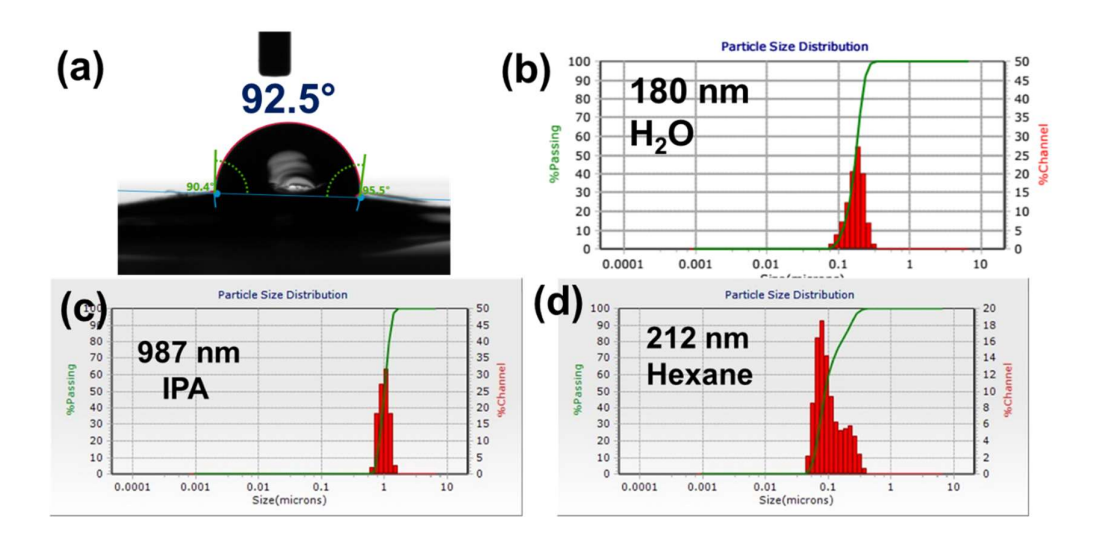


**Figure 5B.2** (a) Water contact angle of [C<sub>25</sub>H<sub>54</sub>N][Co-WCo<sub>3</sub>] (b, c, d) DLS study of [C<sub>25</sub>H<sub>54</sub>N][Co-WCo<sub>3</sub>] in different solvents.

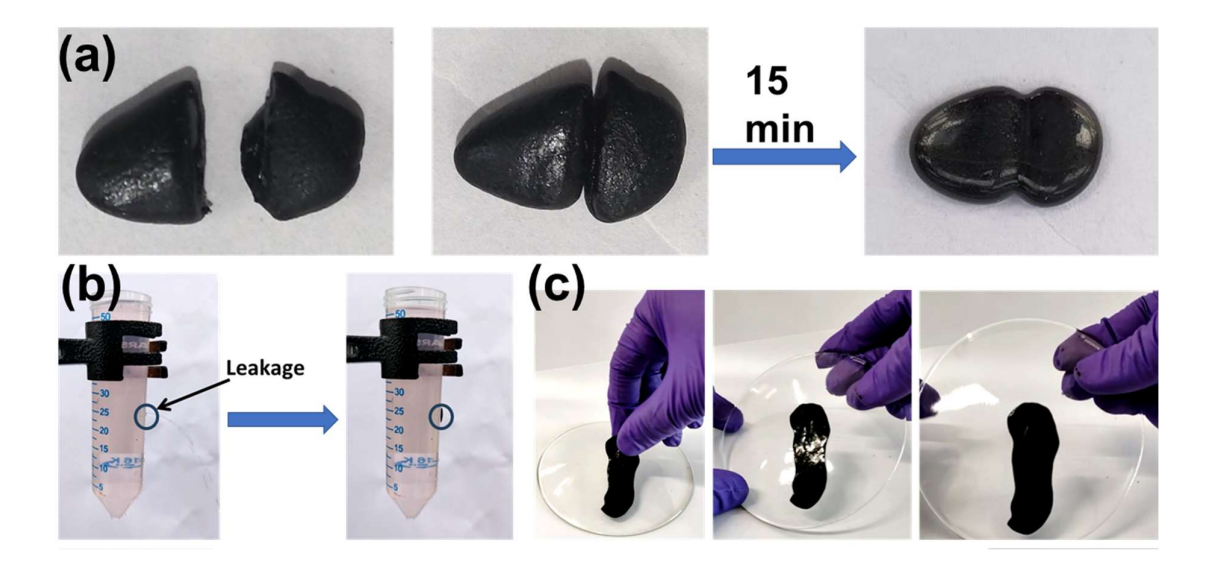


**Figure 5B.3** (a) Images of  $[C_{25}H_{54}N][Co-WCo_3]$  showing the gel behaviour (b) blockage of the water leakage using  $[C_{25}H_{54}N][Co-WCo_3]$  and (c) adhesion behaviour of  $[C_{25}H_{54}N][Co-WCo_3]$  at glass surface.

nature complimented by the strong adhesion behaviour, which can be used to block water leakage (Fig. 5B.3). These findings indicate that [Co-WCo<sub>3</sub>][C<sub>25</sub>H<sub>54</sub>N] is good for underwater adhesion. However, the adhesion strength is poor due to its permanent gel nature. So, to get strong underwater adhesion, we sought the material, which gives good adhesion in gel form and can be dried after adhesion thus making it strong adhesion.

## 5B.2.2 Synthesis [q-PEI-hexyl][Co-WCo<sub>3</sub>] hybrids for Underwater adhesion

Branched PEI can be produced on an industrial scale and depending on its polycationic character, its hydrophobicity can be modulated via quaternization of its different amino groups. As a shotgun approach, we hypothesize that the quaternization of PEI with alkyl chains and ion exchange with ultrasmall POM clusters may increase the positive surface charge density of hybrid material, and facilitate the formation of hydrophobic complex coacervation with solid phase separation. Here, as Br can be easily replaced with POM anions than Cl, we have quaternized high molecular weight (M<sub>w</sub>=25,000) branched PEI with n-hexyl bromide to obtain water insoluble quaternized PEI hexyl bromide or [q-PEI-hexyl]Br. The [q-PEI-hexyl][Co-WCo<sub>3</sub>] was synthesized via exchanging the bromide of the [q-PEI-hexyl]Br with the high negatively charged {Co-WCo<sub>3</sub>}<sup>12</sup> of Na<sub>12</sub>[Co-WCo<sub>3</sub>] POM moiety. The [q-PEI-hexyl]Br is synthesized by the quaternization of polyethyleneimine with hexyl bromide (1:100) in the microwave at 100 °C, thus obtaining a water-insoluble viscous liquid which is highly soluble in polar organic solvents such as methanol/1,2-dichloroethane. A saturated aqueous solution of POM was mixed with the 1,2-dichloroethane (DCE) solution containing [q-PEI-hexyl]Br and swirled for 5 min to obtain [q-PEI-hexyl][Co-WCo<sub>3</sub>] from the DCE layer after washing 2 times with DI water. The raw materials of [q-PEI-hexyl][Co-WCo<sub>3</sub>] can be prepared on a large scale and so [q-PEI-hexyl][Co-WCo<sub>3</sub>] hybrid with this facile method at room temperature. Furthermore, the purity, composition, and homogeneity of [q-PEI-hexyl][Co-WCo<sub>3</sub>] were investigated using FT-IR, NMR spectra, thermogravimetric analysis (TGA), and X-ray photoelectron spectroscopy (XPS) analysis. The XPS spectrum of [PEI][Co-WCo<sub>3</sub>] revealed the presence of tungsten (W), cobalt (Co), nitrogen, carbon and oxygen, and bromine (Fig. 5B.S4) The XPS shift to lower values in [q-PEI-hexyl][Co-WCo<sub>3</sub>] {W 4f (34.41 and 36.5 eV), Co 2p (780.32 and 799.96 eV)} compared to parent Co-WCo<sub>3</sub> {W 4f (35.24 and 37.36 eV), Co 2p (781.27 and 797.29 eV)} can be attributed to the dispersion of electron density due to the relatively less electrostatic interaction of [q-PEI-hexyl] with Co-WCo<sub>3</sub> POM (Fig. 5B.S3). TGA indicates the thermal stability of [q-PEI-hexyl][Co-WCo<sub>3</sub>] up to 225 °C and total weight loss of ~74.5% up to 600 °C. The composition of Co-WCo<sub>3</sub> is ~25 wt.% in [q-PEI-hexyl][Co-WCo<sub>3</sub>] obtained from the comparison of TGA of [q-PEI-hexyl] and Co-WCo<sub>3</sub> POM. After evaporating solvent, [q-PEI-hexyl]Co-WCo<sub>3</sub>] shows strong adhesion to glass and aluminium surfaces, which can be recycled using methanol (Fig. 5B.4a/4b). An optical microscope shows the microrod-type structures after grinding, which shows crystalline nature under monochromatic light (Fig. 5B.4c/4d).

These microrods vary in size from 10 to 50 microns. Interestingly, when grinding in the presence of few drops of methanol, these microrods form helical structures (Fig. 5B.4c). These nanocubes then undergo self-assembly to form microrod-like structures as observed in FE-SEM (Fig. 5B.4e). Nanocubes thus can be considered as highly positively charged macromolecules with Br lying outside which were further confirmed from energy dispersive spectroscopy (EDS). The EDS mapping result of microrods demonstrated that [PEI][Co-WCo3] was composed of W, N, and O along with Br, and these elements were dispersed uniformly (Fig. 5B.4f). Further, the dispersion of [q-PEI-hexyl][Co-WCo3] in methanol and then drying leads to cracks at the higher thickness of [q-PEI-hexyl][Co-WCo3], indicating cohesion is stronger in dried

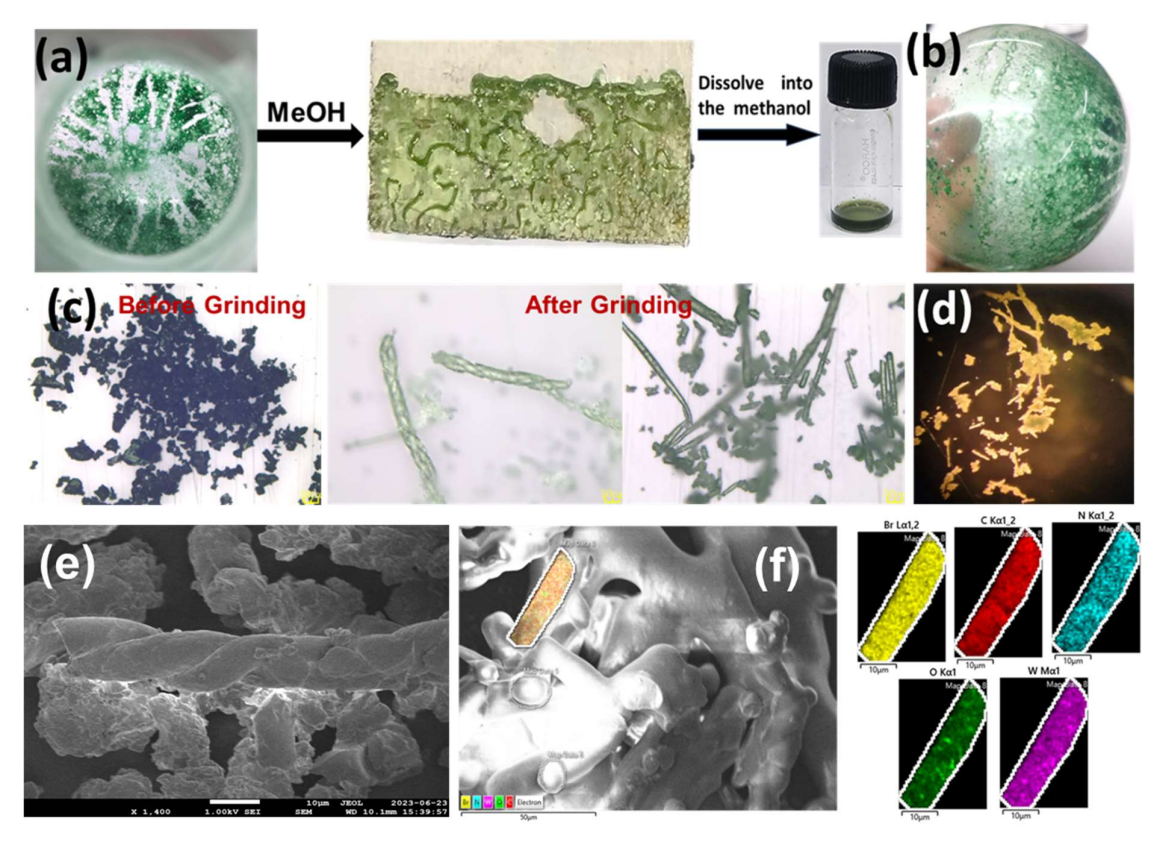


**Figure 5B.4** (a, b) Optical images of [q-PEI-hexyl]Co-WCo<sub>3</sub>] showing strong adhesion to glass/aluminium surface (c) Optical images showing [q-PEI-hexyl]Co-WCo<sub>3</sub>] before and after grinding (d) optical images under monochromatic light. (e) FE-SEM images along with (f) corresponding EDS of [q-PEI-hexyl]Co-WCo<sub>3</sub>].

[q-PEI-hexyl][Co-WCo<sub>3</sub>], a necessary condition for an adhesive (fig 5B.5a). The hydrophobicity as well as sticky nature indicates that the [q-PEI-hexyl][Co-WCo<sub>3</sub>] can be useful as an underwater adhesive. After drying, there was no solvent, and the multilevel

noncovalent interactions of [q-PEI-hexyl][Co-WCo<sub>3</sub>] were fixed when [q-PEI-hexyl][Co-WCo<sub>3</sub>] was coated between two substrates. The flexibility of [q-PEI-hexyl][Co-WCo<sub>3</sub>] due to the polymeric chains along with long alkyl groups contacting the substrate, combined with strong cohesion and adhesion, endowing the hybrid with good adhesive performance. The underwater adhesive characteristics of the [q-PEI-hexyl][Co-WCo<sub>3</sub>] can be seen in Figure 5B.5b depicting a petri dish immersed in water showing almost instant adhesion to a piece of wood with [q-PEI-hexyl][Co-WCo<sub>3</sub>] layer spread over it gets stuck to it while submerged in the water. Similarly, instant adhesion (30 sec) of two glass slides in the presence of water can be seen in Fig. 5B.5c with [q-PEI-hexyl][Co-WCo<sub>3</sub>] dissolved in a few drops of methanol. Also, the adhesion can be sustained in liquid nitrogen, as shown in Figure 5B.5d, indicating its stability at very low temperatures. The [q-PEI-hexyl][Co-WCo<sub>3</sub>] hybrid dissolved into

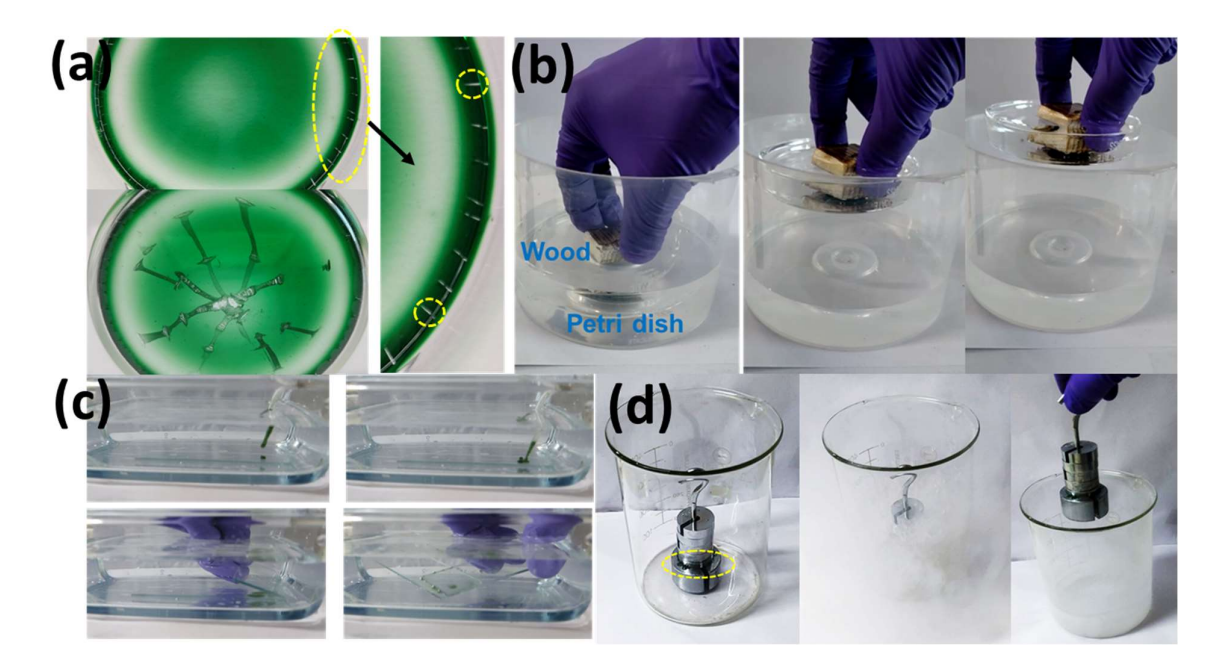


**Figure 5B.5** (a) Scratching effect and cracks observed at glass surface showing the adhesive nature of the hybrid; [q-PEI-hexyl]Co-WCo<sub>3</sub>], (b) underwater adhesion in the presence of water at wood and (c) glass surface (d) underwater adhesion in the presence of liquid nitrogen.

## (Our lab is working on the self-assembly of [q-PEI-hexyl]Co-WCo<sub>3</sub>] to understand various applications: few small works on POM-PEI overlaps with another thesis (Diksha) from our lab)

the different solvents and measured the adhesion strength using the universal tensile machine (UTM) by lab shear test at the glass surface. The adhesion strength using different solvents, methanol, THF, CHCl<sub>3</sub>, and dichloromethane, was found to be 2.36, 2.04, 1.83, and

1.47 MPa, respectively (Fig 5B.6a), indicating methanol as the best solvent for adhesion. Hence, further studies were done using methanol as the solvent of choice. [q-PEI-hexyl][Co-WCo<sub>3</sub>] was dissolved in the methanol and applied at different substrates like stainless steel, aluminium, glass, and PMMA sheet and the adhesion strength was found to be 3.94, 2.92, 2.32, and 0.91 MPa respectively (Figure 5B.6b). The driving force for the adhesion was mainly attributed to the van der Waals force, hydrogen bonding, and metal complexation. The adhesion strength on the glass substrate is slightly less compared to the aluminum due to the high surface energy of glass surface. Consequently, water interacts strongly through hydrogen bonding and van der Waal forces at glass surface due to the abundance of charged polar groups, making it difficult for the [q-PEI-hexyl][Co-WCo<sub>3</sub>] to be replaced. Furthermore, the adhesion strength of the [q-PEI-hexyl][Co-WCo<sub>3</sub>] coated a glass substrate was measured after keeping it for 12 h at different

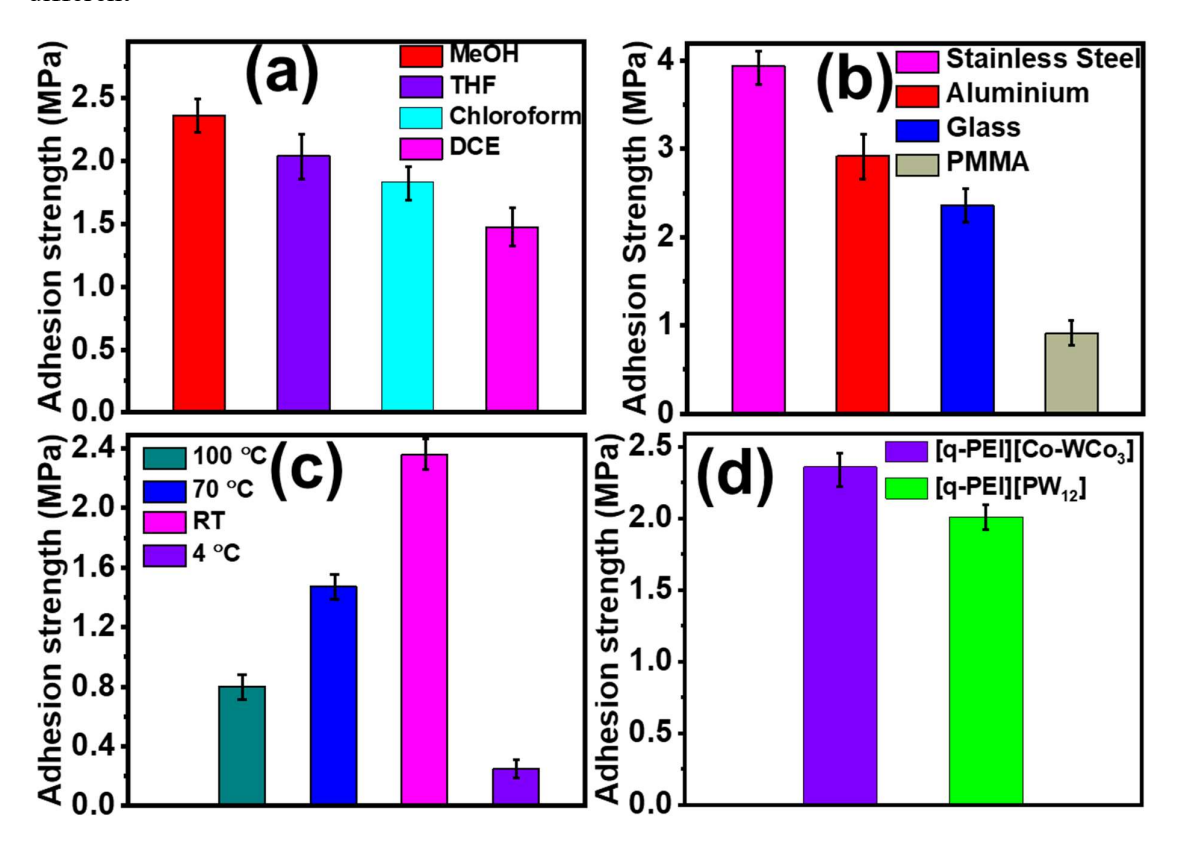


**Figure 5B.6** (a) Adhesion strength in different solvents analysed by the lap shear test; (b) Adhesion strength at different substrates; (c) Adhesion strength at different temperatures (d) Adhesion strength of sandwich and Keggin POMs at glass substrate.

temperatures, 100, 70, 25, and 4 °C were found to be 0.8, 1.47, 2.36, and 0.25 MPa, respectively, suggesting that the highest adhesion strength can be achieved at room temperature

along with appreciable adhesion strength in a wide temperature range (Fig. 5B.6c). The adhesive [q-PEI-hexyl][Co-WCo<sub>3</sub>] containing highly charged sandwich POMs has higher adhesion strength (2.36 MPa) compared to Keggin based POMs; [q-PEI-hexyl][PW<sub>12</sub>] (2.01 MPa) at the glass surface probably due to higher electrostatic interactions (Fig. 5B.6d). After addition of methanol, [q-PEI-hexyl][Co-WCo<sub>3</sub>] adhesive can be redissolved and reused thus revealing the reversibility without losing the adhesive strength.

## Seawater adhesion and anti-corrosion study

The adhesive nature was checked in seawater as well as in (artificial) simulated urine samples. The adhesion strength was found to be 3.57 MPa in seawater and 0.76 MPa in artificial urine samples (Fig. 5B.7a). The underwater adhesion of the hybrid in seawater shows good adhesion in seawater even after 15 days confirmed by the adhesion strength in seawater,

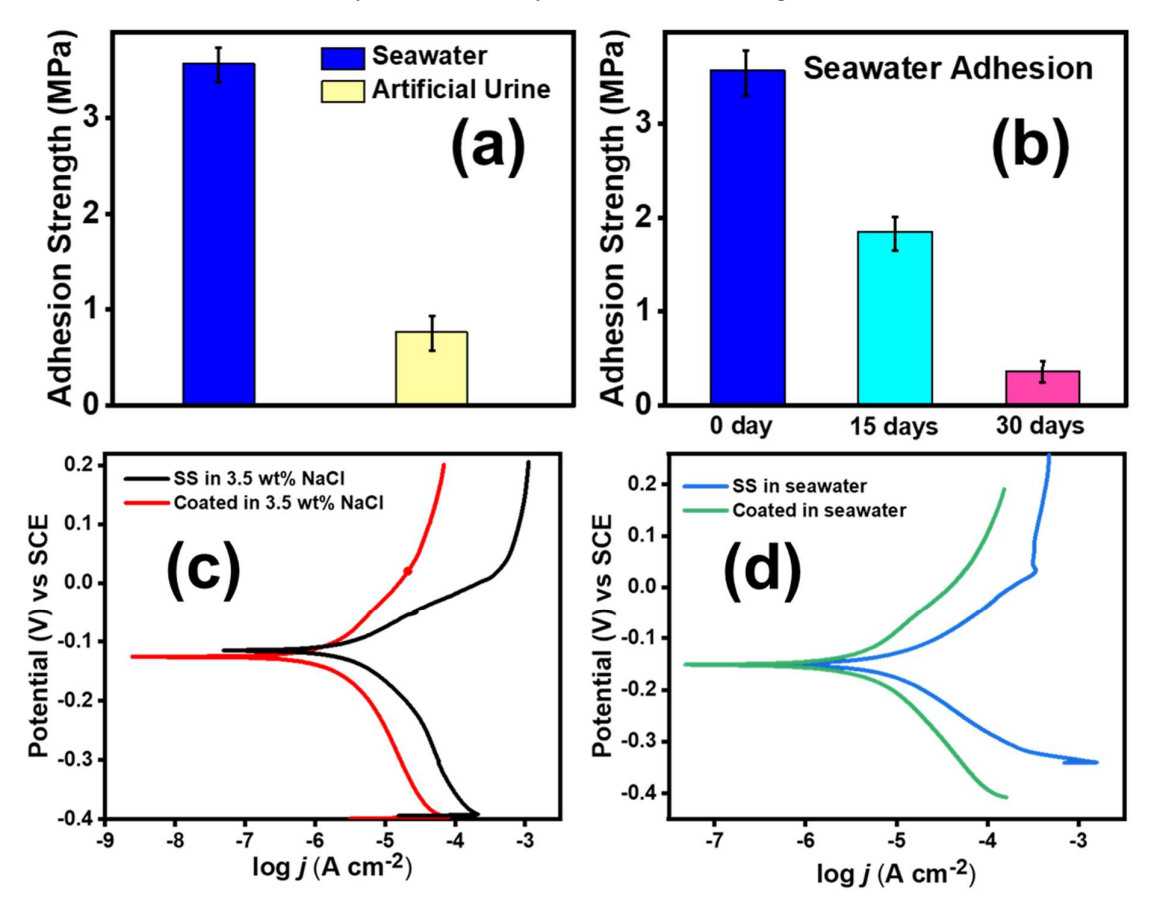


**Fig. 5B.7** (a) Adhesion strength in seawater and simulated urine samples (b) Adhesion strength in seawater after keeping for 15, 30 days. Linear polarization of (c) uncoated SS304 and coated [q-PEI-hexyl][Co-WCo<sub>3</sub>]/SS in 3.5 wt% NaCl and (d) uncoated SS304 and coated [q-PEI-hexyl][Co-WCo<sub>3</sub>]//SS in seawater.

which decreased to 1.85 MPa from 3.57 MPa (Fig. 5B.7b). To further confirm the anticorrosion ability and the stability of adhesive material in seawater, its corrosion study was performed on stainless steel (SS). Cathodic and anodic kinetics for corrosion of stainless steel and [q-PEI-hexyl][Co-WCo<sub>3</sub>]/SS in 3.5 wt% NaCl and seawater have been studied using potentiodynamic polarization. The corresponding corrosion current density (I<sub>corr</sub>) and corrosion potential (E<sub>corr</sub>) were fitted by the Tafel extrapolation method, and obtained results are listed in Table 5B.1. E<sub>corr</sub> for uncoated SS substrate in 3.5 wt% NaCl was found to be -0.115 V while E<sub>corr</sub> for [q-PEI-hexyl][Co-WCo<sub>3</sub>] coated SS shifted to the cathodic region as shown in Fig 5B.7a with significantly lower I<sub>corr</sub> of 1.3 μA cm<sup>-2</sup> as compared to uncoated SS of 15.2 μA cm<sup>-2</sup> <sup>2</sup>. This suggests that the coating provides significant corrosion protection to the SS substrate with a corrosion inhibition efficiency ( $\eta$ ) of 91%. Similarly, corrosion studies were carried out in seawater to demonstrate the corrosion protection ability of [q-PEI-hexyl][Co-WCo<sub>3</sub>] on SS. As it can be seen from Fig 5B.7b, E<sub>corr</sub> of uncoated SS and [q-PEI-hexyl][Co-WCo<sub>3</sub>]/SS are similar, however, [q-PEI-hexyl][Co-WCo<sub>3</sub>]/SS shows a lower I<sub>corr</sub> of 3.82 μA cm<sup>-2</sup> as compared to 25.72 µA cm<sup>-2</sup> of uncoated SS with corrosion inhibition efficiency of 85% indicating that [q-PEI-hexyl][Co-WCo<sub>3</sub>] coating imparts corrosion protection to SS even in corrosive seawater.

Table 5B.1 Electrochemical parameters obtained from polarization curves for various Al anodes in								
4M KOH								
Specimen	E <sub>corr</sub> (V)	I <sub>corr</sub> (μA cm <sup>-2</sup> )	$R_{\rm p}$ (k $\Omega$ cm <sup>-2</sup> )	CR (µm/year)	η%			
Bare SS in 3.5 wt% NaCl	-0.12	15.2	4.6	109.6	-			
Coated SS in 3.5 wt% NaCl	-0.13	1.3	9.8	19.1	91			
Bare SS in seawater	-0.15	25.7	3.7	69.8	-			
Coated SS in seawater	-0.15	3.80	4.8	44.6	85			

#### 5B.3 Conclusion

In conclusion, a highly versatile and stable [q-PEI-hexyl][Co-WCo<sub>3</sub>] hybrid was prepared through a facile ion exchange method at room temperature, which strongly interacts with different substrates such as stainless steel, polymers, and glass, effectively with high adhesion strength up to 4 MPa. The multilevel electrostatic and van der Waal interactions endowed them with strong cohesion, thus exhibiting good adhesive performance underwater and at ultralow temperatures, along with high corrosion resistance efficiency in seawater. This adhesive could be easily removed and recycled up to 10 times without compromising the adhesion strength. Thus, the development of more complex adhesion geometries is made possible by these flexible

self-assembled [q-PEI-hexyl][Co-WCo<sub>3</sub>] hybrids, which show great promise as an adhesive material for usage in various industries and daily life.

## **5B.4 Experimental Section**

#### 5B.4.1 General Information and Instrumentation

#### 5B.4.1a Materials and Methods

PEI (Polyethylenimine) (Sigma aldrich, Mw = 25,000, 99 %), hexylbromide (spectrochem, 99 %), Aliquat 336 (Formula taken as  $C_{25}H_{54}N^+Cl^-$ ), The transition metal salts used in synthesis were obtained from Alfa Aesar (purity > 99.9%) and used without further purification.

## 5B.4.1b Instrumentation

**SEM-EDX analysis:** SEM analysis was conducted on the powder specimen using a JEOL JSM-6610 LA (JEOL, Japan). Integrated JEOL Analysis Station software was used to collect and analyze the X-ray data. The coated sample itself was fixed onto an aluminum stage, ensuring that the carbon-coated surface was in good contact with the holder. All analyses (spot and line) were performed under a high vacuum. The detector used for the EDX spectrometer was an Oxford Inca X-act. EDX line scans were conducted on different points of the sample. The specific voltages and respective resolutions are mentioned in images wherever necessary.

Water contact angle (WCA): WCA values were measured on polymer thin films coated on glass slides using a Laurell Model WS-650MZ-23NPPB programmable spin coater. For measurement, a sessile syringe was used to deposit water drops on polymeric films. The sessile water drop method was used to measure contact angles by Kyowa contact angles meters DMe-211 plus. The average WCA ( $H_2O$ ) value was measured from five separate samples of the same hybrid material in a 1.5  $\mu$ L volume using a 0.305 mm wide needle and the solvent contact angle (SCA) was determined using hexadecane liquid in a 1.5  $\mu$ L volume.

**NMR** spectra were collected using a JEOL JNM-ECS 400 spectrometer at ambient probe temperatures and are referenced as follows: 1H: residual internal CHCl<sub>3</sub> 7.26 ppm, D<sub>2</sub>O 4.79 ppm.

**Adhesion property:** The adhesion strength of the hybrid material was studied by lap shear test using Zwick Roell universal tensile testing machine. The surfaces of the substrates like glass, aluminium, PMMA washed with acetone. The material was adhered between the two substrates

with lap lengths at different lengths. The specimens were extended at 0.5 mm/min at room temperature. All measurements were repeated at least 3 times for each sample.

Other instrumentations are mentioned in section 2.4.1b (chapter 2).

## 5B.4.1c Synthesis

Synthesis of Na<sub>12</sub>[WCo<sub>3</sub>(H<sub>2</sub>O)<sub>2</sub>(CoW<sub>9</sub>O<sub>34</sub>)<sub>2</sub>]. {Na<sub>12</sub>[Co-WCo<sub>3</sub>]} The synthesis of Na<sub>12</sub>[Co-WCo<sub>3</sub>] was performed under microwave heating. Teflon microwave vials was charged with a mixture of Na<sub>2</sub>WO<sub>4</sub>.2H<sub>2</sub>O (16.000 g, 48.48 mmol), 60 mL of H<sub>2</sub>O and 2 mL of conc. HNO<sub>3</sub> and microwave irradiated for 30 min at 80-85 °C. After cooling to room temperature, the solid Co(NO<sub>3</sub>)<sub>2</sub>.6H<sub>2</sub>O (3.656 g, 12.56 mmol) was added and further microwave irradiated for 30 minutes at 85-90 °C. The obtained hot solution was filtered and the filtrate was allowed for crystallization. After 2-3 days deep-green coloured needle shaped crystals were collected by filtration. The obtained crystals were recrystallized from water, and dried at ~80 °C under high vacuum to obtain the title compound Na<sub>12</sub>[Co-WCo<sub>3</sub>] (1.562 g, 48.38%).

**Synthesis of (C25H54N)12[WC03(H2O)2(C0W9O34)2]. {(C25H54N)12[C0-WC03],** C25H54N; aliquat-336 cation} - A thick-wall glass tube was charged with Na<sub>12</sub>[C0-WC0<sub>3</sub>] (0.050 g, 0.01 mmol) and dissolved in 1 mL water. To the clear greenish solution, 1 mL 1,2-dichloroethane solution of Aliquat-336 (0.052 g, 0.13 mmol) was added and stirred for 2 h at room temperature. The crude reaction mixture was then extracted with 1,2-dichloroethane and the organic solvent was evaporated. The obtained greenish viscous solid was dried at 70 °C under vacuum for 1 h to obtain (C25H54N)12[C0-WC03] (0.085 g, 91.0%).

Synthesis of (C25H54N)12[WC03(H2O)2(C0W9O34)2]. {(C25H54N)12[C0-WC03], The polymeric material [q-PEI-hexyl]Br is synthesized by the quaternization of polyethyleneimine (Molecular weight = 25,000) with hexyl bromide (1:100) in the microwave at 100 °C, thus obtaining a water-insoluble highly viscous liquid that is highly soluble in polar organic solvents. Typically, a saturated solution of water-soluble POM was mixed with the 1,2-dichloroethane solution containing [q-PEI-hexyl]Br thus swirling to obtain the hybrid from the 1,2-dichloroethane layer. The purity, composition, and homogeneity of [q-PEI-hexyl][Co-WC03] were analyzed by TGA, XPS, FTIR, and EDAX. The FTIR spectra of [q-PEI-hexyl][Co-WC03] show the characteristic peaks of POM and q-PEI with slight variations due to strong electrostatic interactions as well as hydrogen bondings. The three distinctive absorption bands occurred at 914 (W=O), 860 (W-O-W), and 2926.5, 2852.2 cm<sup>-1</sup>, indicating the interactions between (quaternized) amine groups of [q-PEI-hexyl]Br with anionic Co-WC03 POM. The dominant primary driving force for hydrogen bonding interactions is due to

W=O···H-N between terminal/bridged oxygens of Co-WCo<sub>3</sub> framework and quaternized as well unquaternized N-H of PEI.

## **5A.5 References**

- 1. Katsoulis, D. E. J. C. R., A survey of applications of polyoxometalates. *Chem. Rev.* **1998**, *98* (1), 359-388.
- 2. Ji, X.; Ahmed, M.; Long, L.; Khashab, N. M.; Huang, F.; Sessler, J. L., Adhesive supramolecular polymeric materials constructed from macrocycle-based host–guest interactions. *Chem. Soc. Rev.* **2019**, *48* (10), 2682-2697.
- 3. Zhao, Y.; Wu, Y.; Wang, L.; Zhang, M.; Chen, X.; Liu, M.; Fan, J.; Liu, J.; Zhou, F.; Wang, Z., Bio-inspired reversible underwater adhesive. *Nat. Commun.* **2017**, *8* (1), 2218.
- 4. Hofman, A. H.; van Hees, I. A.; Yang, J.; Kamperman, M., Bioinspired underwater adhesives by using the supramolecular toolbox. *Adv. Mater.* **2018**, *30* (19), 1704640.
- 5. Chen, Y.; Meng, J.; Gu, Z.; Wan, X.; Jiang, L.; Wang, S., Bioinspired multiscale wet adhesive surfaces: structures and controlled adhesion. *Adv. Funct. Mater.* **2020**, *30* (5), 1905287.
- 6. Majumder, A.; Sharma, A.; Ghatak, A., A bioinspired wet/dry microfluidic adhesive for aqueous environments. *Langmuir* **2010**, *26* (1), 521-525.
- 7. Zhang, Q.; Shi, C.-Y.; Qu, D.-H.; Long, Y.-T.; Feringa, B. L.; Tian, H., Exploring a naturally tailored small molecule for stretchable, self-healing, and adhesive supramolecular polymers. *Sci. Adv.* **2018**, *4* (7), eaat8192.
- 8. Dai, Z.; Ding, S.; Lei, M.; Li, S.; Xu, Y.; Zhou, Y.; Zhou, B., A superhydrophobic and anti-corrosion strain sensor for robust underwater applications. *J. Mater. Chem. A* **2021**, *9* (27), 15282-15293.
- 9. Zhang, F.; Li, Z.; Wang, X., Mechanically tunable organogels from highly charged polyoxometalate clusters loaded with fluorescent dyes. *Nat. Commun.* **2023**, *14* (1), 8327.
- 10. Zhou, Y.; Zhang, C.; Gao, S.; Zhang, B.; Sun, J.; Kai, J.-j.; Wang, B.; Wang, Z., Instant and strong underwater adhesion by coupling hygroscopicity and in situ photocuring. *Chem. Mater.* **2021**, *33* (22), 8822-8830.
- 11. Li, X.; Deng, Y.; Lai, J.; Zhao, G.; Dong, S., Tough, long-term, water-resistant, and underwater adhesion of low-molecular-weight supramolecular adhesives. *J. Am. Chem. Soc.* **2020**, *142* (11), 5371-5379.
- 12. Dompé, M.; Cedano-Serrano, F. J.; Heckert, O.; van den Heuvel, N.; van Der Gucht, J.; Tran, Y.; Hourdet, D.; Creton, C.; Kamperman, M., Thermoresponsive complex coacervate-based underwater adhesive. *Adv. Mater.* **2019**, *31* (21), 1808179.
- 13. Ju, G.; Cheng, M.; Guo, F.; Zhang, Q.; Shi, F., Elasticity-dependent fast underwater adhesion demonstrated by macroscopic supramolecular assembly. *Angew. Chem. Int. Ed.* **2018**, *57* (29), 8963-8967.
- 14. Biedermann, F.; Uzunova, V. D.; Scherman, O. A.; Nau, W. M.; De Simone, A., Release of high-energy water as an essential driving force for the high-affinity binding of cucurbit [n] urils. *J. Am. Chem. Soc.* **2012**, *134* (37), 15318-15323.
- 15. Li, X.; Du, Z.; Song, Z.; Li, B.; Wu, L.; Liu, Q.; Zhang, H.; Li, W., Bringing hetero-polyacid-based underwater adhesive as printable cathode coating for self-powered electrochromic aqueous batteries. *Adv. Funct. Mater.* **2018**, *28* (23), 1800599.
- 16. He, P.; Xu, B.; Liu, H.; He, S.; Saleem, F.; Wang, X., Polyoxometalate-based supramolecular gel. *Sci. Rep.* **2013**, *3* (1), 1833.
- 17. Liu, Q.; Wang, X., Precise Assembly of Polyoxometalates at Single-cluster Levels. *Angew. Chem. Int. Ed.* **2023**, *135* (11), e202217764.
- 18. Xu, J.; Li, X.; Li, J.; Li, X.; Li, B.; Wang, Y.; Wu, L.; Li, W., Wet and functional adhesives from one-step aqueous self-assembly of natural amino acids and polyoxometalates. *Angew. Chem. Int. Ed.* **2017**, *129* (30), 8857-8861.

- 19. Liu, J.; Wang, S.; Liu, N.; Yang, D.; Wang, H.; Hu, H.; Zhuang, J.; Wang, X., Au-Polyoxometalates A-B-A-B Type Copolymer-Analogue Sub-1 nm Nanowires. *Small* **2021**, *17* (4), 2006260.
- 20. Zhang, S.; Shi, W.; Yu, B.; Wang, X., Versatile inorganic subnanometer nanowire adhesive. *J. Am. Chem. Soc.* **2022**, *144* (36), 16389-16394.
- 21. Zhang, S.; Wang, X., Sub-1 nm: a critical feature size in materials science. *Acc. Mater. Res.* **2022**, 3 (12), 1285-1298.
- 22. Cui, Y.; Yin, L.; Sun, X.; Zhang, N.; Gao, N.; Zhu, G., A universal and reversible wet adhesive via straightforward aqueous self-assembly of polyethylenimine and polyoxometalate. *ACS Appl. Mater. Interfaces* **2021**, *13* (39), 47155-47162.
- 23. Singh, G.; Adhikary, S. D.; Mandal, D., Stabilization and activation of polyoxometalate over poly (vinyl butylimidazolium) cations towards electrocatalytic water oxidation in alkaline media. *Chem. Commun.* **2023**, *59* (32), 4774-4777.
- 24. Wilker, J., Positive charges and underwater adhesion. Science 2015, 349 (6248), 582-583.

# **Annexure - VII**

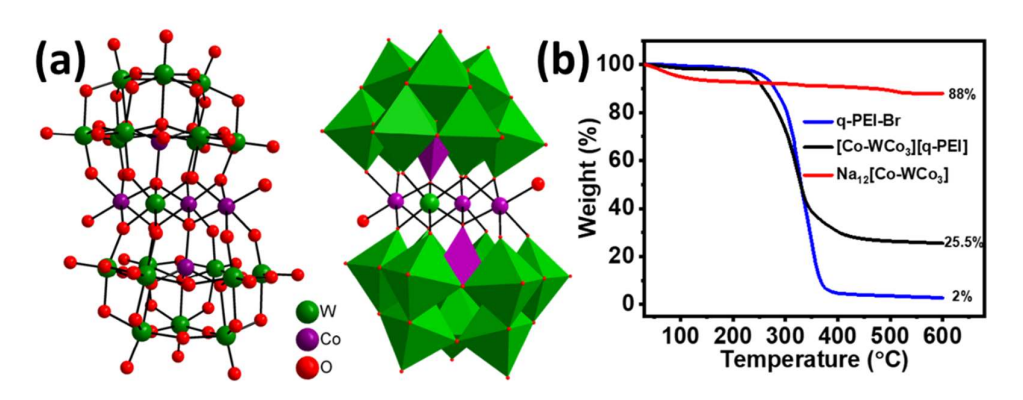


Figure 5B.S1 (a) Ball-and-stick and combined polyhedral/ball-and-stick representation of the single-crystal X-ray structure of polyoxometalate anion  $[WCo_3(H_2O)_2(CoW_9O_{34})_2]^{12}$ -  $[Co-WCo_3]$  (W = green; O = red; Co = purple;  $WO_6$  = golden yellow octahedra;  $CoO_4$  = purple tetrahedra); counter ions and hydrogen atoms of water are omitted for clarity. (b) TGA curve of  $Na_{12}[Co-WCo_3]$ ,  $[q-PEI-hexyl][Co-WCo_3]$  and [q-PEI-hexyl][Br].

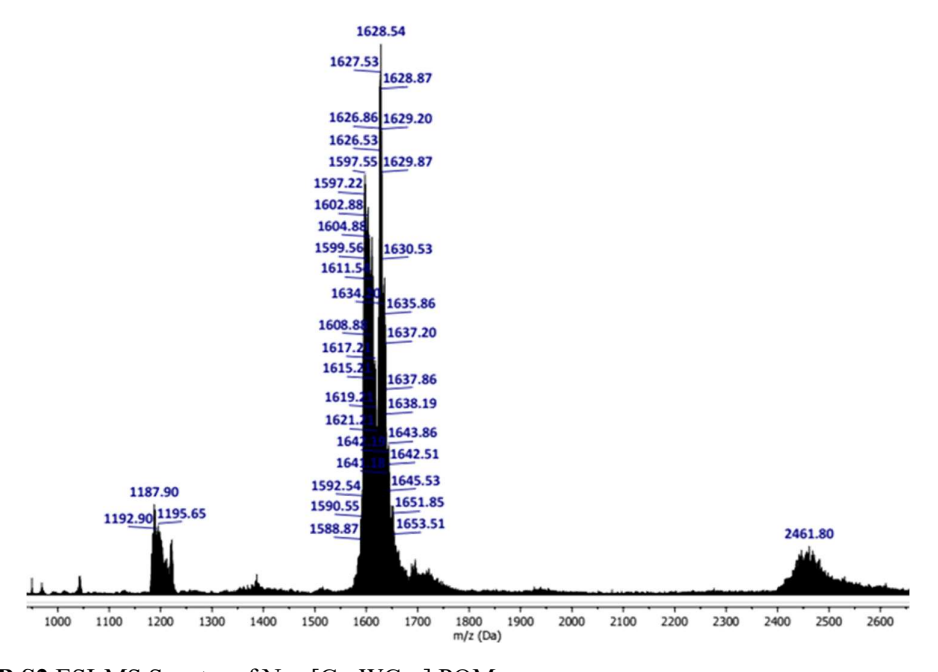
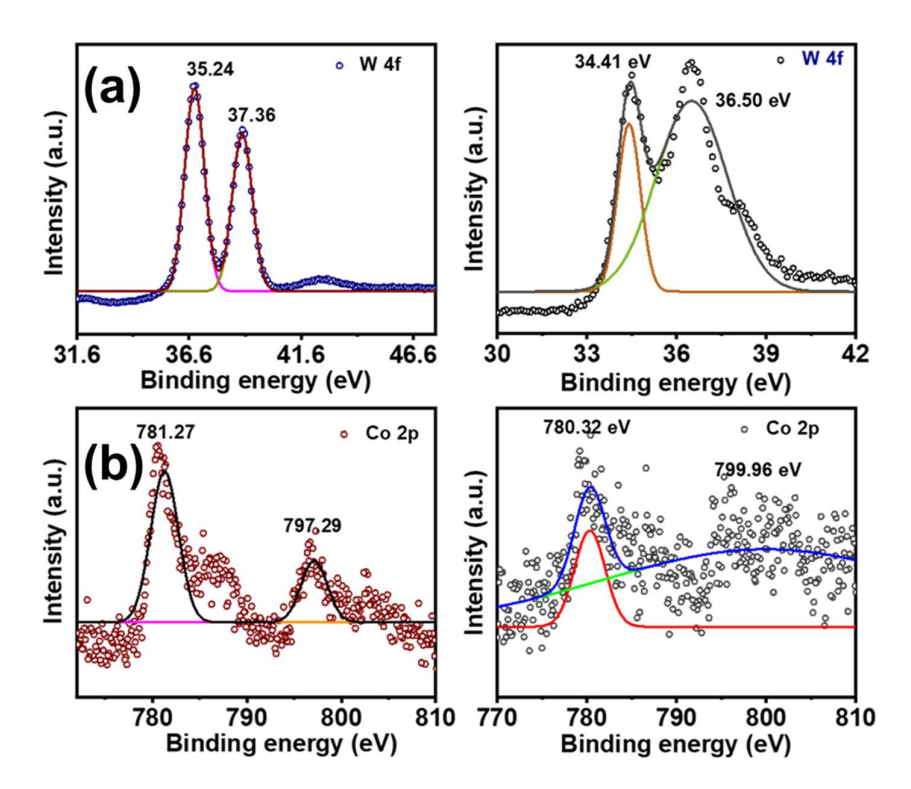
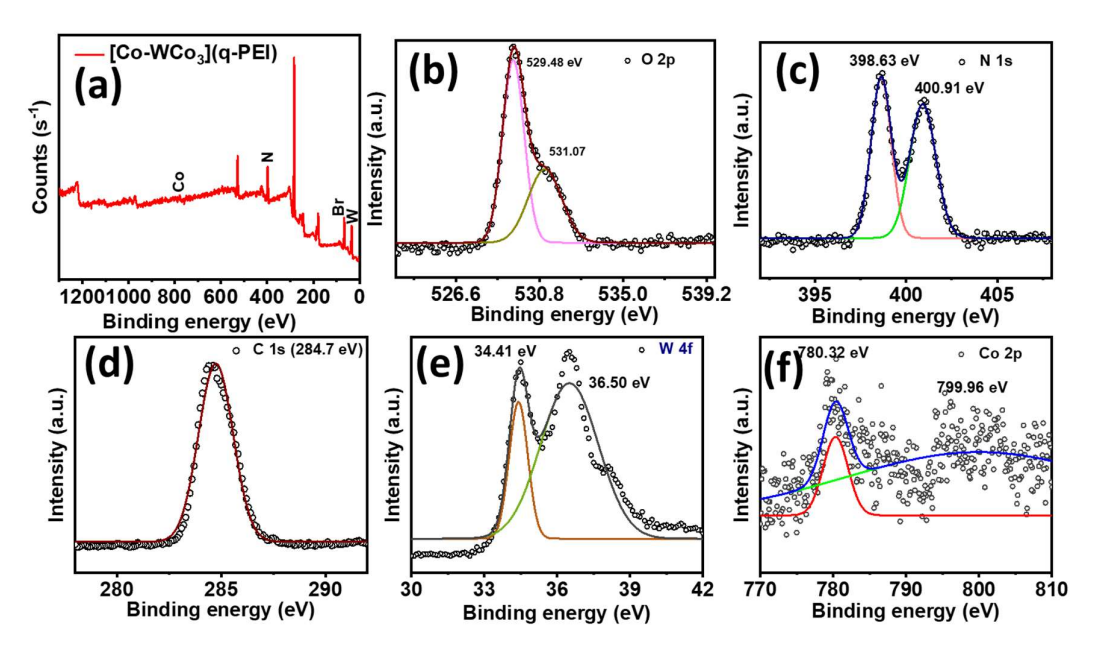


Figure 5B.S2 ESI-MS Spectra of Na<sub>12</sub>[Co-WCo<sub>3</sub>] POM.

Table 5B.S1 ESI mass spectrum and peak assignments for Na <sub>12</sub> [Co-WCo <sub>3</sub> ]				
Fragment	Mol. Wt.	Z	m/z (cal.)	m/z (obs.)
${[WCo_3(CoW_9O_{34})_2]+9H}^{3-}$	4884.36	-3	1628.12	1628.54
${[WCo_3(CoW_9O_{34})_2]+9H+K}^{2-}$	4923.34	-2	2461.67	2461.80



**Figure 5B.S3** Comparison of XPS of (a) W 4f and (b) Co 2p for Na<sub>12</sub>[Co-WCo<sub>3</sub>] POM (left) and [q-PEI-hexyl][Co-WCo<sub>3</sub>] (right).



**Figure 5B.S4** XPS of [q-PEI-hexyl][Co-WCo<sub>3</sub>] with the presence of (b) oxygen, (c) nitrogen, (d) carbon, (e) tungsten and (f) cobalt.

# **Chapter 6**

**Conclusion and Future Prospects** 

#### 6.1 Summary

Polyoxometalates (POMs) have gained significant attention due to their advancements in in material science, including photo and electrocatalysis. Extensive research has been reported on tetrasubstituted sandwich POMs;  $[(TM)_4(H_2O)_2(XW_9O_{34})_2]^{10}$  across various catalytic applications, including sensing, energy conversion and storage devices. To further enhance the catalytic performance of these sandwich POMs, orbital engineering becomes very crucial, as their catalytic activity highly depends on the transition metal core at the sandwich position and the addenda framework.

Orbital engineering in POMs has emerged as a versatile strategy, enabling fast electron transfer and large electron storage capacity compared to conventional tungstate-based POMs. Orbital engineering in POMs can be achieved through several approaches: (I) incorporating mixed addenda atoms (Mo/W or W/V) in the framework, (II) employing various combinations of transition metal substitutions, (III) counterion exchange, etc. In this thesis we have investigated various possibilities of transition metals incorporation into sandwich POMs and examined the orbital engineering of these POMs using both experimentally and DFT studies.<sup>1</sup>

Towards orbital engineering, we employed a cooperative mixed-metal approach that proved to be a versatile synthetic strategy for synthesizing mixed metal-mixed addenda POMs. This approach effectively influences the overall band gap, charge transfer, modulation of electron density, and frontier orbitals, as complemented by DFT calculations. Through this strategy, we successfully synthesized a series of transition metals-substituted sandwich POMs (TMSPs) by systematic variation of pH, salts concentrations, and counterions. Overall, we have explored more than 45 new POMs in this thesis, including different frameworks such as Keggin, Sandwich, Banana, Krebs and POM-based 1D frameworks, and studied their optoelectronic properties through various spectroscopic techniques and DFT studies. Our study provides a comprehensive investigation of the rational design and engineering of band gaps and redox properties, along with the effect of tuning the addenda framework compositions (Mo:W) and transition metals. Our comprehensive findings are supported by rigorous DFT calculations, ensuring the reliability of the experimental results. We also extended the cooperative mix-metal approach for synthesizing mixed metal-mixed addenda polyoxometalates (POMs) in sandwich-type architectures and POM-based coordination frameworks (POMCF), such as 1D/3D-frameworks, which recently have gained attention. Additionally, we explored the synthesis of mixed addenda Banana-type POMs, a previously unexplored POM framework. Synthesis of these mixed-metal mixed-addenda TMSPs revealed

two critical factors playing crucial role in the self-assembly: (a) the charge density of trivacant lacunary part due to the heteroatom, and (b) the cooperative effects of transition metals (TMs) at the sandwich position.

Some of the key insights regarding the synthetic strategies for these transition metal substituted sandwich POMs are as follows: (1) Transition metals as heteroatoms (Zn, Co) create high charge density trivacant lacunary POMs (e.g. ZnW<sub>9</sub>O<sub>34</sub>), while phosphorous as heteroatom results in low charge density trivacant lacunary POMs (e.g. PW<sub>9</sub>O<sub>34</sub>). (2) High charge density lacunary POMs formed with transition metals as heteroatom preferentially bind with transition metals in high oxidation state (e.g., W<sup>6+</sup>, Ru<sup>4+</sup>, Fe<sup>3+</sup>) at internal sandwich positions to form TMSPs. Conversely, using a transition metal in lower oxidation states tends to produce 1-D frameworks based on sandwich POMs. (3) Phosphorous-based low charge density lacunary POMs favor binding with low oxidation state transition metals (e.g., Zn<sup>2+</sup>, Co<sup>2+</sup>, etc.) at both internal and external sandwich positions. However, when transition metals with high oxidation states (e.g. Mn<sup>3+</sup>/Fe<sup>3+</sup>) are used, they tends to form banana POMs in Phosphorous as heteroatom due to the cooperative effect of mixed metals.

One significant contribution of our study is the use of mixed addenda sandwich POMs to precisely lower the overall band gap, allowing the tailored control of LUMO energy levels. This reduction in the LUMO energy levels has profound implications to lower the onset potentials for reduction and enhances absorption at higher wavelengths. Overall, altering transition metals at sandwich or heteroatom positions within these TMSPs or incorporating Mo addenda greatly influences bandgap modulation. For example, moving from right to left across 3d transition metals (Zn to Mn), altering the transition metal at the individual sandwich (whether internal or external) or heteroatom position systematically lowers the band gap - a trend also supported by DFT calculations. Notably, incorporating Mo in mixed addenda POMs not only decreases the bandgap but also shifts the LUMO position. While both factors contribute to bandgap reduction, transition metals at the internal sandwich position (e.g., Fe to Mn) exert more pronounced impact on lowering the bandgap and providing a lower-lying LUMO than Mo incorporation alone, as confirmed by DFT studies. The heteroatom effect is most pronounced with Co, while the external sandwich position shows a comparatively less influence on the bandgap modulation.

Following the trends of decreasing band gap, TMSPs with Co as heteroatom, Mn at the internal sandwich position, and mixed addenda exhibit the lowest band gap, which was indeed experimentally observed in Na<sub>14</sub>[(Co<sub>e</sub>)<sub>2</sub>(Mn<sub>i</sub>)<sub>2</sub>(H<sub>2</sub>O)<sub>2</sub>(CoMo<sub>x</sub>W<sub>9-x</sub>O<sub>34</sub>)<sub>2</sub>].19H<sub>2</sub>O (1.29 eV)

among all the TMSPs reported here. This reduction is attributed to the combined effect of with Co, Mn<sup>3+</sup>, and W/Mo. This cooperative effect was further extended in organic ligands along with transition metals at sandwich positions, leading to the successful isolation of the Mo-based sandwich POM framework for the first time using the synergy between transition metals and organic ligands. This finding highlights the importance of cooperative-effect between transition metals at the sandwich position in the formation of new inorganic-organic hybrid architectures.

#### **6.2 Future Perspective**

We believe that this thesis work lays a strong foundation through the implications of our orbital engineering strategy for future advancements in the field of POMs-based photo and electrocatalysis. The potential for further exploration through counterion exchange and composite design involving various dimensional materials is really vast, and we are confident that this approach will help in substantial progress for the development of POM-based novel heterogeneous materials. Our study also opens the door for a broader spectrum of structural modifications, allowing for diverse functionalities by varying substituted transition metals and heteroatoms.

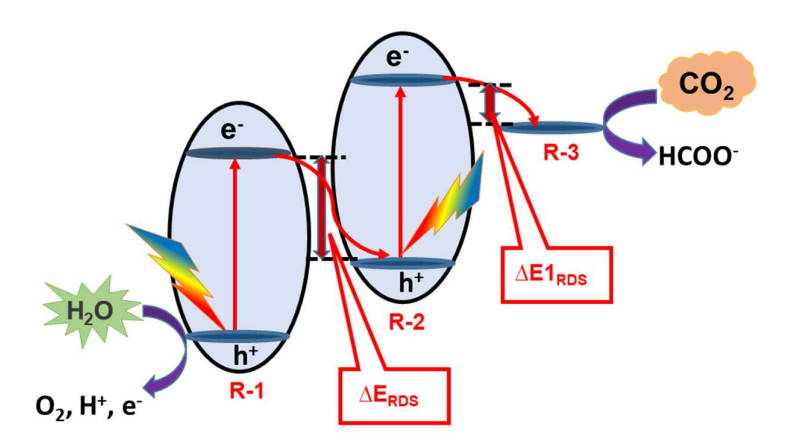


Figure 6.1 Pictorial representation of Z-scheme in heterogeneous catalysis.

Orbital engineering through mixed addenda in sandwich POMs opens up new possibilities, enabling them to incorporate Mo addenda to enhance electron storage and UV-visible light absorption. The rational design through mixed addenda changes the directionality of electrons towards Mo, thus increasing the overall excited state lifetime and improving proton-coupled electron transfer (PCET) processes.<sup>2</sup> Moreover, orbital engineering using our cooperative

mixed metal mixed addenda approach effectively modulates the bandgap, which influence the energy of rate-determining steps ( $\Delta E_{RDS}$ ) (Figure 6.1). his modulation can optimize the electron transfer rate and enhance catalytic efficiency in Z-scheme system by regulating PCET (Figure 6.1).<sup>3-4</sup>

We believe that our cooperative mixed-metal approach offers a robust synthetic analogy suitable for designing new POM and Hybrid POM complexes with tunable orbitals for designing more active catalysts. This approach will facilitate significant progress in developing POM-based novel heterogeneous materials, and opens the access to a wider range of structural modifications with diverse functionalities. Additionally, the di-oxygen activation and binding capability of these sandwich POMs provide an exciting opportunity to investigate oxidation reactions using molecular oxygen as oxidizing agent.<sup>5</sup>

Furthermore, the self-assembly of Mo-based sandwich POMs opens new avenues in materials science through copolymerization and post-functionalization, enabling applications in a broad range of fields. Highly charged POMs clusters can be modified through electrostatic interactions to create POM-based hydrophobic inorganic-organic hybrids, with potential uses in various applications such as underwater adhesive, energy conversion and storage devices as observed in Chapter 5B. This work establishes a pathway for future innovations in the design of versatile and high-performance POM-based materials.

#### 6.3 References

- 1. Singh, G.; Mandal, D., Modulation of the Band Gap and Redox Properties by Mixed Addenda in Sandwich Polyoxometalates. *Inorg. Chem.* **2023**, *62* (48), 19648-19663.
- 2. Odella, E.; Secor, M.; Reyes Cruz, E. A.; Guerra, W. D.; Urrutia, M. N.; Liddell, P. A.; Moore, T. A.; Moore, G. F.; Hammes-Schiffer, S.; Moore, A. L., Managing the redox potential of PCET in grotthuss-type proton wires. *J. Am. Chem. Soc.* **2022**, *144* (34), 15672-15679.
- 3. Zhang, W.; Mohamed, A. R.; Ong, W. J., Z-Scheme photocatalytic systems for carbon dioxide reduction: where are we now? *Angew. Chem. Int. Ed.* **2020**, *59* (51), 22894-22915.
- 4. Zhou, J.; Chen, W.; Sun, C.; Han, L.; Qin, C.; Chen, M.; Wang, X.; Wang, E.; Su, Z., Oxidative polyoxometalates modified graphitic carbon nitride for visible-light CO2 reduction. *ACS Appl. Mater. Interfaces* **2017**, *9* (13), 11689-11695.
- 5. Singh, G.; Das Adhikary, S.; Mandal, D., Physico-and Electrochemical Properties of First-Row Transition-Metal-Substituted Sandwich Polyoxometalates. *Inorg. Chem.* **2023**, *62* (22), 8551-8564.

# **Publications**

- Singh G, Adhikary S D, Mandal D; Physico-and Electrochemical Properties of First-Row Transition-Metal-Substituted Sandwich Polyoxometalates. *Inorg. Chem.*, 2023, 62 (22), 8551–8564.
- **Singh G**, Adhikary S D, Mandal D; Stabilization and activation of polyoxometalate over poly (vinyl butylimidazolium) cations towards electrocatalytic water oxidation in alkaline media. *Chem. Commun.*, **2023**, *59* (32), 4774-4777.
- **Singh G**, Mandal D; Modulation of the Band Gap and Redox Properties by Mixed Addenda in Sandwich Polyoxometalates, *Inorg. Chem.*, **2023**, *62* (48), 19648–19663.

# Poster/oral presentation or participation in conferences

- Attended Research Conclave organized by Indian Institute of Technology Ropar, Punjab, India during April 20 21, 2019.
- Attended ACS on Campus virtual India event, organized by American Chemical Society, on August 10, 2020.
- Participated in scientific writing workshop, organized by ACS publication in collaboration with IIT Bhilai, in Virtual mode, on September 20, 2021.
- Oral presentation at 58th Annual Convention of Chemists, 2021 & International Conference on "Recent Trends in Chemical Sciences (RTCS-2021)" organized by the Indian Chemical Society, Kolkata, India during December 21 - 24, 2021.
- Participated in Modern Trends in Inorganic Chemistry, Banaras Hindu University and presented a poster on 'Designing and synthesis of phosphomolybdates based sandwich Polyoxometalates' December 15-17, 2022.
- Participated in International Conference on Polymers for Advanced Technology, APA and presented a poster on 'Polyoxometalates based inorganic-organic hybrid polymeric materials for underwater adhesion' February 23-25, 2023
- Oral presentation 'Redox Tuning the Belt Chemistry in Sandwich Polyoxometalates' at ChemFest 2023, organized by Indian Institute of Technology Ropar, Rupnagar, Punjab, India on March 09, 2023.

# **Curriculum Vitae**

# Ganga Singh

Ph. D. Scholar, Department of Chemistry

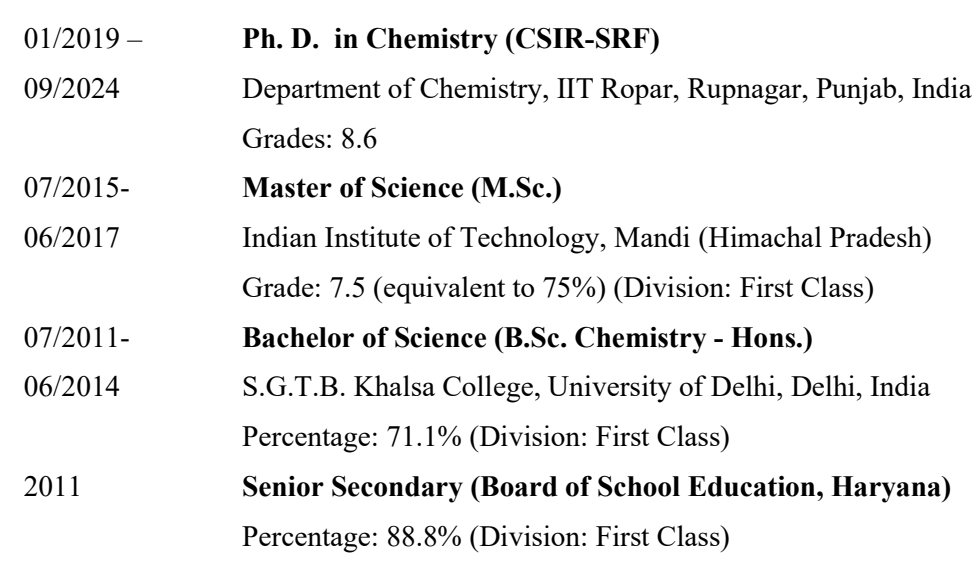
Indian Institute of Technology Ropar

Nangal Road, Rupnagar, Punjab-140001, India

Email ID: ganga95.singh@gmail.com, 2018cyz0015@iitrpr.ac.in

Contact No: +91-8219208079

#### **Academic Records**



#### **Research Experience**

## **Indian Institute of Technology Ropar**

Punjab, India

Supervisor - Dr. Debaprasad Mandal

01/2019 - 10/2024

Thesis Title – Synthesis, Structure-Property Relationship, and Orbital Engineering of Transition Metal-Substituted Sandwich Polyoxometalates.

Projects handled During PhD:

- Design and synthesis of Polyoxometalates (POMs)-polymers/POMs-2D materials-based nanocomposites for artificial photosynthesis (water oxidation coupled CO<sub>2</sub> reduction using Z-scheme), urea synthesis etc.
- Orbital engineering in sandwich POMs by mixed addenda for PCET (proton-coupled electron transfer) tuning in various energy conversion reactions.

- Synthesis of POMs-polymers/ionic liquids inorganic-organic hybrid materials/ionogels for the underwater adhesive application.
- Incorporation of higher oxidation state metals/mixed metals in sandwich POMs for small molecule activation, organic group transformations, Optoelectronic applications.
- Design and synthesis of reduced POMs for energy storage devices.
- Theoretical investigations of electronic properties of POMs.

## **Indian Institute of Technology Mandi**

Himachal Pradesh, India

07/2015 - 06/2016

Supervisor – Prof. Pradeep Parmeswaran

Minor Project

Polyoxometalates-based metal-organic framework and their applications in diverse fields.

**Major Project-** 07/2016 – 06/2017

Development of New Polyoxometalate - Imidazolium/Sulfonium Ionic

Liquids based Hybrids Materials for Photochromic Applications

#### **Scholarly Achievements**

**Publications** 

- **1. Singh G**, Adhikary S D, Mandal D; Physico-and Electrochemical Properties of First-Row Transition-Metal-Substituted Sandwich Polyoxometalates. *Inorg. Chem.*, **2023**, 62 (22), 8551–8564
- **2. Singh** G, Adhikary S D, Mandal D; Stabilization and activation of polyoxometalate over poly (vinyl butyl imidazolium) cations towards electrocatalytic water oxidation in alkaline media. *Chem. Commun.*, **2023**, 59 (32), 4774-4777.
- **3. Singh G**, Mandal D; Modulation of the Band Gap and Redox Properties by Mixed Addenda in Sandwich Polyoxometalates, *Inorg. Chem.*, **2023**, 62, 48, 19648–19663.
- **4. Singh G**, Chaudhary R, Mandal D; Construction of Mixed Addenda Polyoxometalates by Cooperative Self-Assembly and Tuning of Their Optoelectronic Properties; (*Inorg. Chem.*, Manuscript under revision)
- **5. Singh G**, Sharma D, Singh R, Sinha A, Mandal D; Self-assembled Polyoxometalate-based Nanohybrids for Corrosion-Resistant Underwater Adhesive. (Manuscript submitted)
- **6. Singh G**, Chaudhary R, Mandal D; Microwave-assisted synthesis of transition metals substituted sandwich Phosphomolybdates and its optoelectronic application. (manuscript under preparation)
- **7. Singh G**, Chaudhary R, Mandal D; Framework Switch in Trimetallic Sandwich Polyoxometalates Control by Heteroatom and Oxidation State. (manuscript under preparation).

- Participated in Indo-UK Workshop on "Advanced Nanomaterials for energy, health and sustainability" held in IIT Mandi and delivered my research topic, on Oct. 3-6, 2016.
- Oral presentation 'Polyoxometalates based electron transfer modulation for artificial photosynthesis' at 58th Annual Convention of Chemists, 2021 & International Conference on "Recent Trends in Chemical Sciences (RTCS-2021)" organized by the Indian Chemical Society, Kolkata, India, Dec. 21-24, 2021.
- Participated in 'Modern Trends in Inorganic Chemistry, Banaras Hindu University and presented a poster on 'Designing and synthesis of phosphomolybdates based sandwich Polyoxometalates' Dec. 15-17, 2022.
- Participated in International Conference on Polymers for Advanced Technology, APA and presented a poster on 'Polyoxometalates based inorganic-organic hybrid polymeric materials for underwater adhesion' Feb. 23-25, 2023.
- Oral presentation 'Redox Tuning the Belt Chemistry in Sandwich Polyoxometalates' at ChemFest organised by Indian Institute of Technology Ropar, Rupnagar, Punjab, India on March 09, 2023.

#### **Skills**

Instrumentations:

**Hands on experience** (CRF instruments) - Single crystal X-ray diffraction, SC-XRD (Bruker, July 2022- Sep 2024), Raman Spectrometer (Horiba, Feb 2020 – June 2022)

Hands on experience (Department instruments) - Powder X-ray diffraction-PXRD (Bruker), Gas Chromatography techniques GC-MS/TCD/FID (Shimadzu) and System GC - methanizer (Shimadzu), Electrochemical workstations (Autolab 302N potentiostat/galvanostat), UV-visible spectrometer (Perkin Elmer), Diffuse Reflectance Spectroscopy DRS-UV/Vis/NIR (Perkin Elmer), FT-IR spectrophotometer (Perkin Elmer, Bruker ATR), Water contact angle-WCA (Kiowa), Zeta potential and Dynamic light scattering (DLS) (Anton Paar), Thermogravimetry analysis-TGA (Mettler Toledo), Fluorescence spectroscopy (Perkin Elmer), Glovebox (Bruker), Photochemical reactors, Four Probe Instrument, Spin-coater, Schlenk Line techniques.

**Others** - Universal Testing Machine (Linus), Gel Permeation Chromatography (GPC)

Softwares/Tools:

Crystal software (APEX-4, WinGX, Olex 2, Ortep 3, Mercury, Diamond, Crystal maker, Avogadro, Shelxle, X'pert-Highscore, EXPO2014) Chem Draw Professional 15.0, Theory study (Gauss View, Materials studio), Nova 2.1, EC Lab (Electrochemistry), LabSpec (Raman), Mest ReNova (NMR/mass), LabSolutions (GC), EndNote, Origin 2021, MS office software (Word, Powerpoint, Excel), Image processing software (GIMP, Paint, ImageJ) and computer Languages (Basic knowledge of Python, Unix, and Linux commands).

Synthetic:

Various synthetic methods such as microwave, hydrothermal, Sol-gel, and conventional synthesis, different crystallisation techniques for the synthesis of POMs

Teaching and mentoring experience:

- Teaching assistant (TA) for Introduction to Environmental Science and Engineering (GE-111) and training students with safety techniques and practices for laboratory for B.Tech, Masters and Ph.D. students at IIT Ropar for 3 years.
- TA for CRF (central research facility) instruments (Raman, SC-XRD) and department instruments (GC-MS).
- Mentored three M. Sc. Students; minor and major projects (Swarnima, Jiyad KM, Naseeb Araham); two PhD students (Ruchika, Amit) and intern students (Saziya, Shambhavi).

## **Awards and Funding**

- DST inspire fellowship (top 1% students board exam) (2011-2014)
- Qualified IIT-JAM (Joint Admission Test for M.Sc. entrance, 2014 & 2015, All India rank 403)
- Qualified Graduate Aptitude Test in Engineering (GATE 2018, All India Rank 502)
- Qualified National Eligibility Test (Lecturership-NET, Jun 2016, All India Rank 24)
- Qualified National Eligibility Test (CSIR JRF, Dec 2017, All India Rank 53)
- Junior (01/2019 12/2020) and senior research fellowship, CSIR (01/2021 01/2024)
- Prof. G. Gopalarao's centenary Young Scientist Award for the oral presentation entitled "Polyoxometalate based electron transfer modulation for artificial photosynthesis" at the International Conference of Indian Chemical Society.

#### **Personal Details**

Father's name: Shri Bane Singh | Mother's name: Smt. Hiro Kanwar

Sex: Male | Date of Birth: 25-04-1994 | Marital Status: Unmarried | Languages: Hindi, English

#### **Declaration**

I hereby declare that the above-mentioned information is correct to my knowledge.

Date: 26/10/2024

Place: Ropar Ganga Singh